Experimental Investigations of Crack-Trapping in Brittle Heterogeneous Solids

by

Todd Matthew Mower

B.S.M.E., University of New Hampshire (1983)
S.M.M.E., Massachusetts Institute of Technology (1985)
M.E., Massachusetts Institute of Technology (1987)

Submitted to the Department of Mechanical Engineering
in partial fulfillment of the requirements for the degree of

Doctor of Philosophy in Mechanical Engineering

at the

MASSACHUSETTS INSTITUTE OF TECHNOLOGY

May 1993

Signature redacted

Author .....
Department of Mechanical Engineering
May 7, 1993

Signature redacted

Certified by .....
Ali S. Argon
Quentin Berg Professor
Thesis Supervisor

Signature redacted

Accepted by .....
Ain A. Sonin
Chairman, Departmental Committee on Graduate Studies

Experimental Investigations of Crack-Trapping in Brittle Heterogeneous Solids

by

Todd Matthew Mower

Submitted to the Department of Mechanical Engineering
on May 7, 1993, in partial fulfillment of the
requirements for the degree of
Doctor of Philosophy in Mechanical Engineering

Abstract

Over the past two decades many mechanisms of toughening have been considered for brittle solids. Some of the most prominent ones applicable to either monolithic materials or fiber-reinforced composites include deformation-induced local transformations, micro-cracking, crack trapping, crack bridging, and fiber pull-out. Few if any of these have been studied in the past in a manner which permitted evaluation of the effects of individual mechanisms in the absence of other interacting mechanisms. Here we present the development, analysis and results of an experimental study of toughening by the process of crack trapping by second-phase particles (spheres and fibers) of such toughness that make them impenetrable by probing cracks, forcing the cracks to bow around the obstacles with increasing applied load.

The model fracture specimens employed here were wedge-loaded double cantilever beams cast of a brittle epoxy, containing macroscopic (3 mm-diameter) inclusions of Nylon or polycarbonate having similar elastic properties to the matrix. The tests were performed at $-60°C$ to achieve controlled, stable crack propagation. Images of the crack fronts advancing at velocities of about 10^{-4} m/s were recorded with good resolution, providing a continuous record of crack-front shapes during the evolution of the crack-trapping process from the initial pinning configuration through the transition to crack-flank bridging. Remarkable agreement between these images and crack-front shapes predicted by the numerical simulation of Bower & Ortiz is demonstrated. A parametric approach was adopted to study the influence of obstacle spacing, surface adhesion and thermally-induced residual stresses upon the observed crack-front behavior and enhanced stress intensity required to propagate the cracks past these obstacles. Analysis of the quantitative data has demonstrated that, in brittle matrices containing particle volume fractions of approximately 0.2, toughness enhancement by over a factor of two, relative to neat matrix values, may be achieved through the crack-trapping mechanism alone, provided that a high level of adhesion can be maintained between the matrix and the tough reinforcing particles.

Thesis Supervisor: Ali S. Argon
Title: Quentin Berg Professor

Acknowledgements

The Department of The Air Force has sponsored this research through a program at Lincoln Laboratory for employees enrolled in graduate degree programs at M.I.T. For that support I am very grateful, since I would not have been able to complete this work without it. I thank Richard Cerrato, of the Director's Office at Lincoln, whose administration of the program fosters its continuance. Moreover, I thank Dr. Bob Davis, my Group Leader, and Milan Vlajinac, Division Head, for approving my enrollment in the program and tolerating the attendant drain on their budgets which must have resulted. Their belief in the value of education is appreciated.

I am extremely grateful for the opportunity to have worked with Professor Argon. His guidance has been the most fruitful academic or professional relationship which I have ever experienced. I have benefited greatly from his broad understanding of material behavior, both through his influence upon my research and from his classroom teaching. Of equal significance to me has been the positive and cheerful attitude with which Professor Argon approaches teaching, the "making of science", and the people he works with. Since my prior academic training was in related but different fields, whatever knowledge of material behavior I possess has accrued under the tutelage of Professor Argon, and for that, I am very thankful.

I have also benefited greatly from discussions with my thesis committee members, Professors David Parks and Mary Boyce, who helped resolve uncertainties which arose in the course of this research on more than one occasion. Their invested time, continued interest and insightful comments are appreciated. I would also like to acknowledge the guidance of Professor Victor Li during the first few months of my enrollment as a doctoral candidate; I thank him not only for his advice, but also for the suggestion that I explore the phenomenon of crack trapping.

While I was developing experimental techniques to measure the effects of crack trapping, sophisticated computational simulations were being developed by Professors Alan Bower and Michael Ortiz at Brown University. Initially unaware of each others' efforts, we ultimately communicated our results. Professors Bower and Ortiz kindly generated simulations corresponding to the particle interspacings used in the experiments reported here. The resulting comparisons augmented our understanding of the crack-trapping mechanism and enhanced the credibility of the independent investigations. The generosity of Bower and Ortiz is appreciated, and several enlightening discussions with them are acknowledged.

The experimental nature of this research has necessarily involved many aspects which required assistance from people with specific skills or access to specialized resources. I have been very fortunate to be working at Lincoln Laboratory, where the wide variety of expertise available has enabled me to overcome nearly every obstacle in my path. The people who have helped me have not only been very adept at what they do, but have also been very willing to offer what time they had available. At the risk of forgetting to credit someone who may have helped me along the way, I shall single out some of the people who have most directly assisted me.

Beginning with people in Group 75, Al Traniello machined with precision several test fixtures, including the compression cage. Robert Steeves and Robert Perle have skillfully provided computer hardware. George Haldeman and Mark Perutz helped a great deal with computer software for data acquisition. The help of these people is appreciated, and I thank Bob Davis for allowing them to apportion some of their time to me.

Still within the Engineering Division, I thank John Milne for making available to me many facilities and personnel within Group 72. In particular, this work would not have been possible without access to the Materials Processing Lab, where I spent a thousand-plus hours casting epoxy specimens and testing them. The generosity and flexibility of Ken Hill, who supervises that lab, is greatly appreciated. Peter Anderson and Edwin LeFave initiated me to the procedures required to fabricate optical quality castings of epoxy; their instruction, knowledge of processing techniques, friendship, and tolerance of my extended presence is immensely appreciated. The observation of fracture phenomena within the epoxy specimens required the finishing of their surfaces; I thank Scott Hillis for his patience while polishing countless specimens to

near perfection. Several groups of specimens which I tested were machined by the shop under the supervision of Don Paquet. His fitting of my jobs into a busy schedule is appreciated, as are the professional conduct and production of the many machinists.

Within the Solid State Division, Bill Dinatale provided expert scanning electron microscopy. I thank him for his skill, perfectionism and eagerness to please. Bob Murphy provided the electron-beam gold-coatings necessary for SEM imaging of non-conductive surfaces. Preparation of the large number of specimens which I tested during the evolution of this research required a great deal of machining on my part. Access to a milling machine and lathe was therefore a critical issue for me. Through the benevolence of the late Don Kolesar, I had nearly exclusive use of such machines, sometimes for days on end. His generosity and skillful advice will be remembered.

The Publications Group has provided a tremendous volume of support to me, but what is appreciated most is the quality of that work. I am sure that every member of the Photography Lab has worked on at least one or more of my tasks, from photographers to processors. Paula Cerrone managed to squeeze my jobs into a very crowded schedule, and that flexibility has always been appreciated. The expertise of her staff is evident, and the efforts of all on my behalf are gratefully acknowledged. A great deal of high quality, still photography was provided for me by Jack Mahoney, Jon Barron, and Mike Imbeault. Of greatest significance, however, was the cinemaphotographic skill and perseverance of Mike Imbeault, which enabled the recording of crack-front shapes during the process of crack trapping. To Mike and all the photographers, I give many thanks. The other side of visual information processing is its presentation. For that, I thank Bill Breen for scheduling my tasks into an obviously over-worked department, and I thank Ed Sullivan for directing my work to the able hands of Chester Beals. His skillful manipulation of digital imagery and robust expertise with the graphic arts software, PhotoShop©, created the photographic images reproduced in this document. Thank you, Chet.

Lastly, I thank the members of my family. I thank my parents, Lyman and Karen, for the continued love and support that they have provided to me, in many ways, while I have been going to college for ten of the past thirteen years. My wife, Alice, I thank for her even temperament, friendship and love. I thank my sisters, Amy and Robin, for encouragement and blind faith. Finally, I thank my children, Kate and Matthew, for laughing in the background and sneaking into my study to see me.

Part I

The Crack-Trapping Experiments

Contents

List of Figures

List of Tables

Chapter 1

Introduction

1.1 Statement of Principal Thesis Objectives

Toughening of brittle solids as a consequence of heterogeneous microstructures has been a major focus of investigation for decades. Materials of interest have possessed heterogeneities ranging from locally anisotropic grain structures in monoliths such as rocks, ceramics and glass spinels, to particulate and/or fiber-reinforced metals, ceramics and polymers [1, 2, 3]. Sources of toughness in these materials can be grouped into two categories, depending upon the location of microstructural events. Crack-wake phenomena include all toughening mechanisms which transpire in the region immediately behind an advancing crack tip. In this category are traction-carrying mechanisms such as crack-face bridging and frictional sliding. Crack-tip interactions include all mechanisms which occur at the tip of an advancing crack, including "process" events immediately ahead in the concentrated stress field. Included in this grouping are dilatations due to cavitation, microcracking, debonding or strain-induced transformation. Additionally, toughness increments can arise from the local impediment to crack growth by dispersed particles having a fracture toughness greater than that of the bulk matrix. It is this last mechanism, often referred to

as "crack-trapping" or "crack-pinning," which is the focus of this thesis.

Most investigations centered upon determining sources of material toughness have, in the past, followed the *modus operandi* of testing the fracture toughness of a material of interest, performing microscopy on the fracture surface, and then ascribing the measured levels of toughness to inferred sequences of events. While much information can be gathered from *post mortem* fractography, it is always difficult, if not impossible, to separate the effects of mechanisms which may be operative in unison. A further complication to this approach is that some mechanisms may be synergistic, while others may be annihilative.

To date, all investigations of fracture toughness in particulate-reinforced brittle solids have followed some variation of the aforementioned procedures, so no definitive experimental measurements of the effects of crack-trapping exist. The *central goal* of this thesis was to fill this void by performing carefully planned and executed experiments, with *macroscopic model specimens*, to measure the driving force required to advance a trapped crack past discrete obstacles in a brittle matrix, while recording the shape and position of the crack tip on moving film. This data would then provide a measure of toughness induced by crack-trapping in the absence of all other mechanisms. Additionally, this information could provide both inputs and corroboration for numerical simulations being developed by other researchers.

A second experimental goal of this research arose from the desire to measure the adhesion between a matrix and an included particle. No prior particulate-toughening research (which the author is aware of) has included quantification of adhesive strengths; rather, they have relied upon fractographic information for qualitative rankings only. To avoid repeating this shortcoming, an experimental method was sought to measure the adhesion in the bimaterial systems used in the crack-trapping experiments. Because all "standard" adhesion tests incorporate a stress singularity in the nature of an edge, they cannot be used to measure adhesion strengths

which are governed (limited) by brittle failures. Such tests are suited only for relative ranking of adhesive systems and provide no meaningful absolute strength data. Consequently, a test specimen was developed which allowed the true adhesion strength between particle and matrix to be determined under conditions of hydrostatic tension.

In the course of developing the central experimental methods, supporting efforts have resulted in significant new information. Initial measurements of modulus, yield strengths and fracture toughness of epoxy formulations which were candidate brittle matrix materials were pursued to greater depth. As a result, large-strain behaviors of epoxies were characterized as a function of temperature, strain-rate, cure and aging; data was analyzed in light of recent molecular deformation theories, and (possibly never-reported) strain-hardening rates were determined and correlated to fracture toughness. While attempting to determine residual stresses in model composite systems by using classical photomechanics, inconsistencies were noted which prompted further attempts to separate elastic from inelastic behaviors. While not entirely conclusive, this effort revealed several *caveats* for the use of photomechanics, and as such is included in this thesis.

1.2 Organization of Documentation

The next chapter begins with a brief review of some of the published research concerning toughening through the crack-trapping mechanism. In the first section, analytical models which have been developed to account for crack-trapping induced toughness are summarized. Recently performed numerical simulations are then discussed, and the magnitudes of toughening predicted by them are related. Then, a synopsis is presented of some of the many research efforts regarding toughening of brittle materials by the inclusion of tough, second-phase particles. The reports selected to discuss are ones which most prominently involve the crack-trapping mechanism, either because

crack-trapping appears to have been operative in the materials studied, or because it was *thought* to have been operative. Experimental procedures are glossed over, but key results are highlighted. In addition, the common trend of attributing measured toughness to assumed micromechanisms is emphasized. Another theme pointed up is the absence of any numerical data pertaining to levels of adhesion between particles and matrices in the research summarized. The chapter closes with a discussion which establishes the motivation for the use of macroscopic model specimens to investigate the micromechanical effects of crack-trapping.

A summary of the physical properties of materials incorporated into the model specimens is provided in Chapter 3. The first section presents data pertaining to the individual components: the epoxy used as a matrix material, and the rods and spheres used as inclusions. The second section summarizes the adhesive strengths between the inclusion materials and the epoxy, as determined with an experimental technique developed expressly for that purpose. The final section summarizes the calculated magnitudes of residual (thermal) stresses generated in the model specimens. The information contained in this chapter is included at this point to aid the reader in understanding the nature of the crack-trapping specimens; details of all methodologies are discussed in appendices.

The development of the crack-trapping experiments is summarized in Chapter 4. Several specimen geometries and loading arrangements are discussed, and the difficulties associated with attaining crack stability and planarity are analyzed. Details of instrumentation and data acquisition are included where appropriate or important for correct analysis of the experimental results. Efforts to record crack-front configurations with high-speed video and film cameras are summarized. Considerations leading to the final specimen geometry and the execution of the experiments at cryogenic temperatures are explained. Apparently anomalous features of the epoxy matrix near inclusions are shown; conclusive evidence is given which establishes that

plasticization of the epoxy by diffusion of water from the inclusions was the culprit. (Subsequently, inclusions were thoroughly dried prior to casting of the specimens.) Low magnification fractographs from a few of the model specimens are presented to provide some qualitative behaviors of crack-trapping. (Higher magnification microscopy presented in Appendices A & B provides surface characterization of the particles used in the models and of the fracture surface of the epoxy matrix.) In short, this chapter is intended to provide sufficient description of the crack-trapping experiments to address any questions which may arise during interpretation of the results, which is pursued at length in the next chapter.

Chapter 5 embodies qualitative and quantitative analysis of results from the crack-trapping experiments, and then extends these results to models predicting the fracture toughness of brittle solids with micro-scaled particulates. The chapter begins with consideration of the effects of residual (thermal) stresses and adhesion on crack growth in the model specimens. Example imagery is reproduced from the 16-mm movies which recorded crack shapes and positions during the experiments. Correlation of these images with the recorded load data establishes the stress intensities required to force the advance of the cracks into bowed configurations. Also presented are examples of digitized images, which facilitate measurement of local crack extension, shape and area swept. These parameters are then compared, as a function of applied stress intensity, to predictions from an analytical model developed by Rice and Gao at Harvard University [4, 5] and to numerical simulations generated by Bower and Ortiz at Brown University [6, 7]. The experimental results are further analyzed to reveal the influences of particle shape, spacing and adhesion. Peak stress intensities occurring at maximum penetrations provide an explicit measure of the toughening effects achievable by crack-trapping. These results are then correlated to a semi-empirical toughening model, based in part on the essential-work-of-fracture and in part on numerical simulations.

An overview of toughening mechanisms which may develop in quasi-brittle solids with heterogeneous microstructures is provided in Chapter 6. The purpose of this chapter is to place in perspective the experimental results obtained in the research reported here, providing an indication of the importance of crack trapping relative to other mechanisms which are known to be available for the toughening of brittle solids. To this end, the first section in the chapter discusses mechanisms which transpire at or in front of crack tips in the process zone. Microcracking, cavitation and transformation toughening are described and results of analytical models which predict their crack-tip shielding effects are summarized. The second section discusses how crack-flank bridging processes contribute both to a reduction in crack-tip stress intensity and to an increase in fracture energy. Repercussions of simultaneously occurring mechanisms are discussed, and the difficulties associated with predicting the toughening produced by combinations of mechanisms is pointed out. In the final section, microstructural conditions which might enable or inhibit the maximum level of crack-trapping toughening to develop are explained.

The summary chapter encapsulates the principal results obtained from the experimental techniques developed in this research effort.

The characterization of physical properties of materials incorporated into the model specimens is contained in Appendix A. The first section presents measurements and analyses of the matrix material, DGEBA epoxy, as cured for use in the models as well as in a variety of other cures. The thermal analyses used to determine glass transition temperatures and thermal strains are summarized, followed by a description of uniaxial compressive tests performed to generate modulus and yield stress data. These data are summarized as a function of temperature, strain-rate, cure and aging, and then analyzed in light of recent molecular deformation theories. Strain-hardening rates are determined from this analysis and then correlated, with the yield stress data, to fracture toughness measurements obtained on tapered

double-cantilever beam (constant-K) specimens. Two methods of measuring crack velocity in these specimens were pursued and are included for completeness. Presented in the next section are physical property measurements for materials used as inclusions in the model specimens. To enable calculation of residual stresses in the model specimens, thermal strains are determined for the inclusion materials over the temperature intervals from the matrix glass transition temperatures to the temperatures at which the crack-trapping experiments were performed. To determine the elastic modulus of the inclusions, uniaxial tests were executed in tension with the rods and in compression with the spheres. Following this information is a discussion of the merits and compatibility of materials used in the model specimens.

Appendix B details the development of the experimental technique used to measure the adhesive strengths between the epoxy and the inclusion materials used in the crack-trapping model specimens. The appendix begins by establishing the motivation for measuring particle/matrix adhesive strength through discussions of the influence of adhesion upon crack trapping and the lack of adhesive strength measurements in prior research. The following section describes tests commonly performed to measure adhesive strengths, and an explanation is given of how stress concentrations exist in the "standard" tests which render them incapable of measuring absolute magnitudes of adhesion. Next follows a review of the essential background work upon which the technique developed herein is based. The experimental procedure is then described; details of specimen fabrication are included. A finite element analysis used to determine magnitudes of radial stresses generated at the matrix/particle interface is described, and contour plots of stress fields within the neck specimens are reproduced. Tables are then presented which summarize the experimental data and strengths determined for adhesion between epoxy and soda-lime glass, delrin, nylon and polycarbonate with various surface preparations. Fracture surfaces of tested specimens are then characterized with both optical and scanning electron microscopy. It is shown that this information allows the adhesion technique developed here to be

extended to the determination of the interfacial fracture toughness of the bimaterial systems tested.

The determination of residual thermal stresses in composite materials is pursued in Appendix C. The first section applies analytical models derived from the literature to the calculation of residual stresses in the matrix material surrounding both spherical and cylindrical inclusions in the crack-trapping model specimens. The balance of this appendix explores the use of photomechanics for the determination of residual stresses in composites with birefringent matrices. The question arises of whether the stresses near an inclusion are actually the magnitudes indicated by photomechanics. This uncertainty exists due to the stress *and* strain dependence of birefringence as well as the viscoelastic/plastic nature of polymers. Experiments performed to resolve these questions are presented and analyzed; tentative conclusions are reached regarding the photomechanical determination of residual stresses in composite systems.

Chapter 2

Background: Previous Crack-Trapping Research

This chapter provides a concise review of background information pertaining to previous research involving the crack-trapping mechanism. Summarized first are results from theoretical models, both analytical and numerical, which have been devised to explain the toughening effect which results from crack-front pinning by tough obstacles. Several experimental investigations are discussed next, both to present the range of measurements observed and to highlight the uncertainties which accompany most research regarding toughening in particulate-reinforced composite materials. These difficulties and shortcomings are then singled out as the motivating factors for performing the primary research reported in this thesis.

2.1 Theoretical Modeling

2.1.1 Analytical Developments

2.1.1.1 Line-tension theory

The earliest formal, published recognition of the crack-trapping mechanism appears attributable to Lange [8]. The similarity of the bowed shape which a crack front acquires as it is forced between tough particles to the shape of a dislocation which is impeded by pinning obstacles[1] suggested to Lange that a crack front may have a line tension associated with it in a manner similar to the line tension concept used to explain the work done by forces while moving bowed dislocation segments (see, *e.g.* [11, 12]). By considering the strain energy corresponding to a curved crack with radius, c, Lange deduced that the line energy it possesses is equal to

$$T = \frac{2}{3} c \gamma_o \,, \tag{2.1}$$

where γ_o is the surface energy of the matrix. The fracture energy of the material was deemed to be comprised of two components: the innate surface energy, plus a part due to the line energy per distance, d, between pinning obstacles, *i.e.*

$$G_{Ic} = 2\left(\gamma_o + \frac{T}{d}\right) = 2\gamma_o\left(1 + \frac{2c}{3d}\right) . \tag{2.2}$$

Inspection of this equation indicates that the line tension concept leads to predicted toughening which is linear with inverse particle separation, $1/d$, independent of the size of particles. (The parameter c was estimated as being equal to the crack size.) Lange presented fracture energy data from composites of silica-glass containing alumina particles ranging from 3 to 44 μm in size; within each grouping of particle size, the data plotted linearly *versus* $1/d$ over a limited range [13]. Fractographs showing

[1] See, *e.g.* microphotographs of dislocation pinning on pages 52 & 65 of [9], and diagrams of the dislocation bowing process on pages 174 & 631 of [10].

oriented cleavage steps near particles were presented as evidence that crack trapping had taken place. Nonetheless, the increased fracture energy could have resulted from crack trapping, microcracking, crack-flank bridging or some combination thereof. Moreover, most fracture data obtained subsequently from particulate composites has demonstrated strong dependency upon volume fraction, independent of particle size.

Evans extended the line tension analysis much further by calculating the influence of particle size to spacing upon the line energy associated with cracks forced into bowed configurations between obstacles [14]. Evans then developed expressions for the fracture stress required to advance flaws past obstructing obstacles, which predict that the toughening due to crack trapping increases with increasing particle size to spacing, but that the rate of increase drops sharply following the initial toughening due to finite particle concentrations. Green *et al.* performed numerical computations of Evans' expressions and predicted that, for impenetrable particles, toughening by a factor of two should result from $R/L \approx 0.08$, where R is the particle radius and L is the distance between particle centers [15]. At $R/L \approx 0.16$, the trapping-induced toughness was predicted to be about 2.7.

The models based upon the line tension concept are questionable both on theoretical grounds and on the basis of comparison to experimental observations. Though the bowed shapes of dislocations and pinned crack fronts are quite similar, the analogy should not be considered further. Dislocations can store energy through their interaction with surrounding elastic media, even when they close upon themselves in a loop or terminate at a free surface. In contrast, a crack front cannot store energy nor support a tension; the strain energy associated with a crack is released from the structure when the crack driving force is removed. Though the line tension model as implemented by Green *et al.* predicts toughening magnitudes which appear to be in agreement with some data at low volume fractions of particles, the decreasing slope with increasing volume fraction does not agree with most experimental data.

2.1.1.2 Linear perturbation theory

Gao and Rice have obtained analytical solutions for the remotely applied stress intensity required to advance crack fronts between obstacles which have either finite or infinite toughness, as a function of particle spacing [5]. Their approach is based upon the linear perturbation analysis developed by Rice [4], which poses the trapping situation as an elastic boundary value problem for which a potential exists. Therefore, the solution procedure incorporates a crack-front shape which varies sinusoidally, along which boundary conditions are specified which determine solutions to Laplace's equation. In this approach, the elastic properties of the particles and matrix are taken to be equal, though finite toughness of obstacles is permitted. Rice cautions that solutions based upon this method have "limited validity" [4]; predictions are strictly valid only for local, bowed penetrations which are much less than the particle spacing.

The most significant aspect of the solutions based upon the linear perturbation theory is that they enable mathematical representation of trapping by particles with finite toughness, which become partially penetrated as the remote loading is increased. Maximum crack-trapping induced toughness is generated by impenetrable particles, however, and is the case appropriate for comparison to the experiments developed here. The linear perturbation theory result for impenetrable particles is plotted in Chapter 5. Though predicting toughening magnitudes in reasonable agreement with the data at low particle volumes (a few percent), the trend with increasing volume fraction is a decreasing slope, which does not correlate well to the data.

2.1.1.3 Work-of-fracture model

A direct approach to determining the toughness of a brittle material containing tougher heterogeneities has been suggested by Rose, who based his approach upon

the representation of discrete regions of higher toughness by a network of distributed springs [17]. Rose presented his results in terms of a simple rule of mixtures, or line-weighted fraction, of the fracture energies of constituent materials. Though Rose modifies the rule of mixtures expression with a factor designed to produce the correct asymptotic behavior of the springs which represent particles, the approach is not strictly based upon physical processes: during pure crack trapping, crack tips do not sample the fracture energy of the obstructing particles. Similar to the perturbation theory predictions, the fracture energy approach predicts magnitudes of toughening which are in reasonable agreement with the data at low volume fractions, but the trends with increasing volume fraction of particles do not correlate well with experimental evidence.

2.1.2 Numerical Simulations

A numerical implementation of the perturbation theory representation of crack trapping has been developed by Fares, in which the assumptions of linear, first order perturbation have been relaxed [16]. The model assumes that impenetrable particles are perfectly bonded to a matrix having the same elastic properties. The numerical solution method employs a boundary element formulation which, representing opening displacements as dislocation sources, calculates local stress intensity factors along discretized crack front regions. The crack front shapes are assumed to be sinusoidal, but no restriction is placed upon their amplitude. Crack growth is simulated by increasing the remote loading upon a given crack configuration, determining the stress intensity along the crack front, and then adjusting the mesh so that the new crack shape results in the critical stress intensity being generated along the front.

The results of this numerical analysis indicate that the analytical, linear perturbation method provides accurate results when the amplitude-to-wavelength ratio does

not exceed 0.2 [16]. Effective toughening due to crack trapping with particle radius to center separations of $R/L = 0.25$ was determined to be a factor of 2.35 (normalized by the matrix toughness, K_{Ic}^{matr}). The maximum stress intensity which the leading edges of particles were subjected to was calculated to be $3.52\,K_{Ic}^{matr}$.

The most detailed numerical simulations, to date, have been generated by Bower and Ortiz [6]. Their idealized model also consists of elastically similar, impenetrable particles perfectly bonded to a host matrix. (Though the perfect bonding assumption can be replaced with a force-displacement relation.) The numerical solution technique employed by Bower and Ortiz proceeds in the following manner. The discretized crack front initially is straight when it encounters circular regions which have the constraint imposed upon them of zero opening displacement. The crack front shape is perturbed until the shape is acquired which satisfies the fracture criterion at all points along the front within the matrix ($K_I^{local} = K_{Ic}^{matr}$). The unknown pressures over the circular pinning domains are then determined by solving a system of integral equations based upon the relationship between crack-opening displacements and point wedge forces. The force resultant of these pressures is then used to calculate the stress intensity along the periphery of the pinning particles. The equivalent, remotely applied stress intensity necessary to create the current crack configuration is finally determined from the ensemble average of the stress intensity across the crack front.

A significant aspect of the Bower and Ortiz model is that the crack front shape is not assumed prior to the solution procedure. Therefore, the method has the opportunity to predict crack front shapes which result from the crack-trapping process. Such computed shapes will be compared to the experimental data presented in Chapter 5. The numerical data which results gives slightly higher values than were predicted by Fares, for a particle spacing of $R/l = 0.25$ (equivalent volume fraction, $V_p \approx 0.25$). For this spacing, the method of Bower and Ortiz predicts an overall toughening factor of 2.59, with the peak stress intensity generated at particles of $3.93\,K_{Ic}^{matr}$[7]. With

more dilute particle spacings of $R/L = 0.125$ ($V_p \approx 0.06$), the predicted toughening factor is about 1.67 with a peak particle stress intensity of about $3.2\,K_{Ic}^{matr}$. Data generated by Bower and Ortiz specifically for the particle spacings used in the experiments developed here are reproduced in Chapter 5, along with the experimental data, to enable comparison between the two.

2.2 Prior Experimental Evidence

2.2.1 Ceramic Matrices

The most widely researched method of improving the fracture toughness of brittle ceramics is through the addition of well-bonded ductile particles that will remain intact after a crack front passes them by, so that traction is exerted across the crack flanks. Examples include alumina reinforced with aluminum particles [18, 19, 20], silicon carbide containing aluminum [21], and tungsten carbide containing a dispersed binder phase of cobalt [22]. In these systems, the measured enhancement of toughness (usually in terms of fracture energy) is typically found to reach a factor of three or four times the matrix toughness, and is attributed to plastic deformation of bridging ligaments. This view is supported by analytical models of toughening due to crack-face tractions [23, 24], but ignores the possible contribution from the crack-trapping mechanism. In brittle matrices containing ductile particles this omission is probably justified, since any crack trapping which occurs would be prematurely terminated by relaxation of the opening constraint as the highly stressed particles deform. In ceramics containing rigid particles, however, toughening by crack trapping may become more significant.

The fracture toughness of titanium boride composites containing dispersions of B_4C particles was measured using the Vickers indentation technique [25]. The re-

ported data indicate that a maximum enhanced fracture toughness of $K_{Ic} = 1.12\,K_{Ic}^{matr}$ occurs at a particle volume fraction of 0.20. Based upon edge-view profiles of the crack path, the source of the toughness was attributed to crack-tip deflection by residual strain fields surrounding the second-phase particles. A similar investigation with silicon carbide containing yttria and alumina particles achieved much greater toughness enhancements, reaching about 70% at particle volume fractions of 0.16 [26]. The toughening was again ascribed to crack-tip deflection, and was compared to the crack-deflection model of Faber and Evans [27]. The excess measured toughness, relative to theoretical predictions, was explained as resulting from the angular shape of the actual grains, as opposed to the spherical particles assumed by the model [26]. It seems quite likely that an additional source of toughness (perhaps crack trapping) contributed to the overall toughening produced by crack/particle interactions in these materials, particularly in the latter case, where the toughening exceeded the theoretical predictions by 25 to 50%.

The toughness of ceramics containing dispersions of zirconia particles can be increased significantly (by up to a factor of 4 or 5) through a dilatational phase transformation in the zirconia, providing crack-tip shielding [28, 29]. In alumina/zirconia composites, the zirconia particles additionally present regions of superior toughness to cracks probing through the more brittle alumina. Therefore, conditions exist which would enable the crack trapping mechanism to be operative [30]. Contributions from crack trapping are ignored in virtually all explanations of the enhanced toughness of ceramics containing zirconia particles, undoubtedly because the contributions from transformation toughening are far greater. (Additionally, crack deflections over tough grains or along weak interfaces would minimize contributions from crack trapping.)

2.2.2 Inorganic Matrices (silicate glasses)

Early investigations of the mechanical properties of silicate glasses containing rigid particles focused upon (fracture) strength measurements. Frey and Mackenzie determined that the modulus of rupture was increased by additions of alumina or zirconia particles to soda zinc and borosilicate glasses [31]. Davidge and Green determined that the fracture stress of silicate glasses containing thoria spheres decreased with increasing particle size [32]. Their data appeared to exhibit a linear dependence upon the square root of particle size, so that Griffith-type flaws may have been created by stresses in the glass surrounding the particles, or within the particles themselves. In neither of the two reports just related were adhesive strengths determined; relative adhesive strengths in the two types of material systems might explain the difference in reported behavior. Moreover, fracture toughness measurements were not obtained, so the possibility of crack-trapping influences can not be assessed from these reports.

In the work cited earlier in relation to the line-tension model, Lange reported fracture energy measurements obtained with double cantilever beam specimens of a silicate glass containing dispersed particles of alumina [13]. Enhancements in the fracture energy by a factor of approximately two were determined at particle volume fractions of 0.1; the fracture energy increased to about three times that of the matrix at volume fractions of 0.25. These values are well within the realm of toughening achievable by the crack-trapping mechanism (as demonstrated by the experiments reported here), but the fractographic evidence offered by Lange to support the claim that crack trapping was indeed responsible was not very convincing. Though Lange argued that surface roughness and plastic deformation could add little to the fracture energy, crack-face bridging (by intact particles left in the wake of the cracks) can not be ruled out.

Swearengen *et al.* measured the fracture toughness of a borosilicate glass containing dispersed alumina spheres using precracked, single edge-notched beam specimens tested in three-point bending. They found that the plane strain fracture toughness increased linearly with increasing volume fraction of particles, such that $K_{Ic} \approx 2\,K_{Ic}^{matr}$ at a particle volume fraction of 0.2 [33]. This toughening behavior was found to be independent of the residual stresses resulting from glasses having thermal expansion coefficients equal to, slightly greater than or slightly less than that of the alumina inclusions. Crack-front shapes produced during interaction with particles were recorded on the fracture surfaces by imposing artificial Wallner lines with ultrasonic stress waves during testing of the specimens. Fractographs reproduced in [33] clearly show that the crack fronts acquired bowed shapes while being restrained by particles. Consequently, the mechanism responsible for the observed toughening appeared to be crack trapping. The fracture energy data rose linearly with increasing volume fraction, whereas the line tension model as modified by Evans was shown to predict increasing slope at low volume fractions and decreasing slope at high volume fractions (though the magnitudes of experimental data were in reasonable agreement with the theory) [33].

The ultrasonic fractography technique was also used by Green *et al.* to reveal crack/particle interactions during fracture of a silicate glass containing tough particles [34]. The particles in their model material were nickel spheres, which, from measurements of composite moduli, were determined to be so poorly bonded that they behaved as pseudo-voids. Fractographs of crack interaction with particles exhibiting finite adhesive strength indicated that the crack trapping mechanism was initiated, but premature breakaway of the bowed crack fronts from the pinning obstacles resulted from the low adhesive strengths. The measured toughening levels reached $K_{Ic} \approx 1.30 K_{Ic}^{matr}$ at a particle volume fraction of 0.10, and showed little rise with further increases in particle concentration. Particle adhesive strength to the matrix material was not measured, so the effect of adhesion can not be determined.

2.2.3 Organic Matrices (polymeric glasses)

A large number of investigations have focused upon the toughening processes in particle-reinforced polymeric glasses. In one of the earliest studies, Broutman and Sahu used tapered double cantilever specimens to measure the fracture energies of epoxies containing glass spheres which had various surface treatments to modify their adhesive strengths [35]. In cases of unmodified or adhesion-enhanced surfaces, they found a maximum toughness enhancement of a factor of approximately 3. In the case of composites prepared from spheres with reduced adhesion, they found a further enhanced fracture energy, to a factor of about 5. The principal mechanism proposed to be responsible for the basic (factor of 3) increase in fracture energy was crack trapping; the additional increases observed in systems with poor adhesion were attributed to greater fracture surface area resulting from rougher surfaces containing debonded hemispheres. Recent statistical analyses of toughening due to increased surface area caused by deflection along grain boundaries in ceramics suggest that, at best, such increases in surface area can be expected to account for only a 15% rise in fracture energy [36]. To explain the increases in toughness measured by Broutman and Sahu, it may be more reasonable to suggest that a combination of mechanisms may have occurred in unison.

First, Broutman and Sahu reported increases in fracture *energy*, which is related to the stress intensity factor (in the ideally elastic case) through the relation $K^2 = GE$. All other factors being equal, if crack trapping in all of their specimens produced uniform enhancements in K_{Ic}, then a reduction in modulus due to debonding would clearly cause an augmented energy release rate, G. Additionally, debonded spheres would act as pseudo-voids, causing stress concentrations at their equators which would promote local yielding in the glassy polymer; this is now thought to be a principle toughening mechanism in both rubber-toughened [37] and particulate-filled epoxies [38]. Because the magnitudes of these additional sources of toughness are not

known for the specimens fractured by Broutman and Sahu, it is unclear as to what extent crack trapping actually took place in their specimens with reduced adhesion. Moreover, it is entirely likely that reduced adhesion minimized fracturing of the glass particles, therefore allowing more trapping sites to be active.

A similar investigation was undertaken by Spanoudakis and Young, who used double torsion specimens to measure the critical stress intensity in epoxy filled with glass (4.5 and 62 μm) spheres having various surface treatments [39]. They found that K_{Ic} increased nearly linearly with particle volume fractions, such that a maximum of $K_{Ic} \sim 3\,K_{Ic}^{\text{matr}}$ was reached at $V_p \approx 0.4$. This toughening behavior resulted regardless of the surface preparation of the spheres and was attributed primarily to crack trapping. Spanoudakis and Young reported a maximum increase in fracture *energy* by about a factor of two in cases of spheres with unmodified or enhanced adhesion; in the case of spheres with reduced adhesion, the maximum fracture energy enhancement reported was about a factor of four. They attribute the additional factor of two to a reduction in modulus by about 20% for the composites containing release-coated spheres. The discrepancy in the accounting of sources of fracture energy might be resolved by including some of the effects previously mentioned (*e.g.* enhanced yielding), but the key result from Spanoudakis and Young's work was an apparent invariance of crack-trapping induced stress intensity as a function of adhesion. Similar to Broutman and Sahu though, Spanoudakis and Young did not have a measure of the adhesive strengths exhibited by their composite materials; rather, they relied upon fractographic evidence showing adherence of matrix to particles as their indicator of adhesive strengths.

Other investigations of toughening by glass spheres in brittle epoxies have concluded that little difference results in the composite's improved toughness (K_{Ic}) as a function of the apparent adhesive strength of the beads to the matrix. The primary mechanisms suggested to contribute to overall toughness are crack trapping

and crack-tip blunting, where the total toughness results from a competition between these two mechanisms modulated by the degree of adhesion [38, 40, 41]. Measurement of critical stress intensities (in particulate composites) that do not vary greatly with apparent adhesive strengths is *not* evidence that crack trapping is unaffected by adhesion levels; rather, with decreasing adhesion other mechanisms may become operative while crack trapping becomes less effective.

Toughening of epoxy by alumina particles has also been investigated: enhancements of K_{Ic} by a factor of ~ 2 were reported due to inclusion of a 30% volume of alumina ($6\,\mu$m) particles [42]. The toughening was attributed to crack trapping, which was assumed to be less effective in specimens containing particles with reduced adhesion, resulting in slightly (15%) lower toughening behavior. The actual adhesive strengths, however, were not measured.

2.3 Motivation for New Experimental Work

The purpose of developing the crack-trapping experiments was to generate discrete crack-trapping phenomena under carefully controlled conditions in a manner which would enable the toughening effects of crack trapping to be measured accurately in the absence of other mechanisms. As indicated in the preceding discussions, the coexistence of multiple toughening mechanisms in multi-phase materials results in the inability to separate entirely the effects of individual mechanisms from all others. In the technique developed here, it was hoped that testing of macroscopic model specimens fabricated from a brittle matrix which does not craze or microcrack would enable measurement of the effects of crack trapping without the occurrence of those processes. Use of inclusion materials with elastic moduli similar to that of the matrix would prevent interactions between approaching crack tips and stress concentrations. Additionally, it was recognized that because the matrix material used in the crack-trapping experiments developed here had a plane strain plastic zone size (at the test temperature of $-60°C$) of less than one μm, toughening by localized plastic flow would be insignificant.

It was hoped that the effective toughening resulting from the crack-trapping process could be determined from the applied loading required to advance a crack front between obstacles in the macroscopic model specimens. In order for this to be possible, the testing of the specimens would have to be conducted in a manner which would result in a quasi-static fracture process, so that the applied loading could be measured accurately and so that dynamic fracture events would not interfere with the crack-trapping process. To quantitatively determine the effects of adhesive strength upon the crack-trapping mechanism, and in so doing, overcome a deficiency of previous particle-toughening research, it was deemed necessary to develop a companion experimental technique with which to measure the 'true' adhesive strengths between the matrix and the particles used in the crack-trapping model specimens. The con-

trolling influence of particle spacing upon crack-trapping induced toughening could be revealed by changing the spacing of particles within the model specimens. By using different materials as inclusions, the differential thermal strains in the matrix material surrounding the inclusions could be varied to determine the effect of residual stresses upon crack growth and interaction with obstacles. Moreover, another goal was the recording of high quality images of the bowed crack-front configurations, so that interactions between cracks and obstacles would be revealed. In view of some authors' statements that 'There is little direct evidence for this crack pinning mechanism' [43], it was felt that a related goal would be to convince disbelievers that the crack-trapping mechanism indeed does exist.

Chapter 3

Summary of Materials Characterization

This chapter summarizes results of the measurements performed to characterize relevant mechanical and thermal properties of materials which were used in the fabrication of the crack-trapping model specimens. More complete discussions of materials, methods and data are provided in the Appendices, which include appropriate references; the information presented here is intended as a convenient reference to aid understanding of the crack-trapping experiments and results.

3.1 Constituent Materials

3.1.1 Selection Criteria

The selection of an appropriate matrix material was based upon its inherent brittleness, lack of material-specific damage mechanisms and ease of fabrication. It is emphasized here that we strive to isolate the crack-trapping toughening mechanism while suppressing all others; hence, brittle crystalline materials (*e.g.* ceramics) which undergo microcracking and glassy polymers which craze (thermoplastics) were avoided. A transparent, brittle epoxy was deemed the material of choice.

A standard DGEBA epoxy (Shell 815) cured with a bifunctional polyamide (V-40) was employed so that partial curing at room temperature would occur, in order to position obstacles in the desired locations within the specimens. Subsequent post-cures, at elevated temperatures, activate the secondary amines and achieve the final cross-linking of unreacted epoxy groups. To achieve maximum possible brittleness with this combination of resin and hardener, a V-40 concentration of 33 parts per hundred resin and a post-cure temperature of 135°C were used.

The materials used for included particles (obstacles) were chosen to be tough, so that crack-trapping would indeed result when crack-fronts encountered them, and had closely similar elastic properties to those of the epoxy matrix, so that there would be no distant interactions between particles and the crack before actual contact, making the analysis and interpretation of data more direct. Materials available in both spherical and rod forms which fit this description were polycarbonate (PC) and Nylon 6. These two materials also adhere to the epoxy with different strengths, allowing the effect of adhesion upon crack-trapping to be explored.

3.1.2 Thermal Properties

The glass transition temperatures, T_g, of the constituent materials were determined by differential scanning calorimetry (DSC) and by thermal mechanical analysis (TMA). Measured T_g's of the epoxy, Nylon and polycarbonate (PC) were approximately 80, 50 and 145°C, respectively. To enable the calculation of residual thermal stresses in the composite model specimens, thermal strains were determined for the constituent materials over the two relevant temperature intervals: from the T_g of the epoxy to room temperature, and from there to −60°C, at which temperature the crack-trapping experiments were performed. A summary of the measured thermal strains is listed in Table 3.1.

Table 3.1: Average thermal strains of materials used in model specimens.

			80°C to 20°C		20°C to −60°C	
Material	*Form*	*Orientation*	$-\varepsilon$ (10^{-6})	*St.Dev.*	$-\varepsilon$ (10^{-6})	*St.Dev.*
Epoxy	bulk	isotropic	7204	532	5625	307
Nylon	sphere	radial	8086	429	6301	270
	rod	radial	6080	126	5606	107
	rod	long.	7610	86	6530	109
PC	sphere	radial	4111	34	4916	113
	rod	radial	4357	29	5073	90
	rod	long.	4387	72	5117	195

3.1.3 Mechanical Properties

To determine the Young's modulus, E, and yield strength, σ_y, of the epoxy used as the matrix in the model specimens, uniaxial compression tests were performed upon cylindrical (25.4 mm-high $\times$ 12.7 mm-diam.) specimens cast from the same material. Because polymers are rate-sensitive, measurements were performed at strain rates ranging from 10^{-4} to 10^{-1} s^{-1} and at temperatures ranging from 40°C down to −60°C. Fracture toughness of the epoxy was measured over the same temperature range using tapered double cantilever-beam specimens at displacement rates ranging from 0.1 to 10 mm/min. With these specimens, it was found that the jerky, unstable fracture of the epoxy subsided with decreasing temperature, so that stable, continuous fracture was consistently produced at −60°C. As a consequence, the crack-trapping experiments were performed at this temperature.

The elastic moduli of the Nylon and PC rods and spheres, used as obstacles in the model specimens, were measured at −60°C using compressive tests for spheres and tensile tests for rods. Table 3.2 lists approximate values of the measured physical properties of materials used in the composite models; more exact values are given in Appendix A. Included in this table, for completeness, are yield stress and fracture toughness data for PC and Nylon, derived from the literature.

Table 3.2: Physical properties of constituent materials at −60°C.

Material	T_g (°C)	E (GPa)	σ_y(MPa)	K_{Ic}(MPa$\sqrt{\text{m}}$)
Epoxy	80	3.5	145	0.5
PC	145	3.0	90 [44]	1.9 [44, 45]
Nylon	50	3.6	140 [46]	3.3 [46, 47]

3.2 Adhesive Strengths

The strengths of the adhesive bonds between the inclusion materials and the epoxy were determined with a novel experimental technique which is described in detail in Appendix B. The technique involves embedding a sphere of the candidate material in the center of an epoxy bar which is machined with an NC lathe to a natural neck profile. The contoured bar is strained in tension while an image of the sphere is recorded. The radial stress corresponding to the applied load when debonding occurs is then determined by means of a finite element solution of the deformation problem. Because no stress singularities exist at the interface prior to debonding, as is often the case with the usual popular tests, the technique used here provides a measure of the "true" adhesive strength for the bimaterial systems employed.

Using the same epoxy formulation as used in the crack-trapping experiments, specimens tested contained either Nylon or polycarbonate spheres. All spheres were solvent cleaned and dried prior to inclusion in test specimens. Analysis of the test results indicates that the Nylon/epoxy system exhibits an adhesive strength, σ_a, of approximately 31 ± 5 MPa. Various attempts to enhance the adhesion through acid etching and/or primers did not result in adhesive strengths outside of the indicated range. Polycarbonate/epoxy systems consistently exhibited higher adhesive strengths, such that $\sigma_a > 54 \pm 2$ MPa. Modification of the PC surface with one coat of release agent lowered the strength to $\sim 28 \pm 4$ MPa; a second coat resulted in $\sigma_a \approx 22 \pm 3$ MPa.

3.3 Residual (Thermal) Stresses

Due to different thermal contractions exhibited by the materials used, excursions in temperature generate stresses in and around the inclusions within the epoxy. Residual thermal stresses in the model specimens at the surface of inclusions (*i.e. maximum matrix stresses*) have been calculated using analytical models discussed in Appendix C and the thermal strains reported in Table 3.1. The room-temperature Young's moduli used for epoxy, Nylon and PC (measured as previously described) were 2.5, 2.9 and 2.4 GPa, respectively; moduli at −60°C were as listed in Table 3.2. Poisson's ratio was assumed to be 0.37 for the epoxy and 0.35 for the inclusions. Computed values of maximum matrix stresses are given in Table 3.3 for each of the indicated temperature intervals.

The actual thermal stresses present in the model specimens were equal to the sum of the stresses generated during the initial cooling, reduced by some unknown amount of inelastic relaxation, plus the stresses generated during the cooling from room temperature to −60°C. Although the stress relaxation behavior of the epoxy used here is not known, experiments with a similar epoxy (EPON 828, TETA) have demonstrated a relaxation time constant, τ_r, in excess of 10^{10} min at room temperature [48]. Assuming similar behavior here, the stresses in model specimens which have been stored for several months will not have time to relax appreciably. (Since $\sigma_{relax} \propto \sigma_o\, e^{-t/\tau_r}$) Therefore, the residual stresses during the crack-trapping experiments are taken to be the sum of those generated during the two cooling stages.

Table 3.3: Calculated matrix thermal stresses (MPa) at inclusion surfaces.

		80°C to 20°C		20°C to −60°C		Final	
Inclusion	*Material*	σ_r	σ_θ	σ_r	σ_θ	σ_r	σ_θ
Spheres	Nylon	2.3	-1.1	2.4	-1.2	4.6	-2.3
	PC, 1/8"	-7.6	3.8	-2.4	1.2	-10.	5.0
		σ_r	σ_z	σ_r	σ_z	σ_r	σ_z
Rods	Nylon	-1.0	-0.1	-0.4	-0.3	-1.4	-0.4
	PC	-3.7	0.55	-1.0	0.15	-4.7	0.7

Chapter 4

Development of The Crack-Trapping Experiments

This chapter begins with descriptions of some of the initial tests performed here to investigate the process of crack-trapping. Qualitative results from these initial experiments are presented, and considerations which led to the successful specimen configuration and testing procedure are discussed. The execution of the final crack-trapping experiments is then detailed, from the fabrication of specimens to the reduction of data. The procedure used to determine the enhanced stress intensity, due to crack trapping, is explained and justified. Interpretation of the results is developed in the following chapter.

4.1 Initial Experiments

4.1.1 Qualitative Observations

To obtain some initial, qualitative observations of the effects of crack trapping, several specimens similar to the one shown in Figure 4.1 were fabricated and fractured. These specimens were double cantilever-beams having a square cross-section of 63 × 63 mm and a height of 90 mm, containing rows of two or three 8-mm Nylon spheres. Each specimen had a 20-mm long starter crack machined across the full width of the epoxy and sharpened with a razor blade. Loading was accomplished with a 30-degree, polished steel wedge at a rate of 0.5 mm/min on a displacement-controlled test machine at room temperature.

The resulting fractures in these specimens were dynamic, one-step events. It may be seen from the roughness of the initial portion of the fracture surface in Fig 4.1 that the fracture initiation was accompanied by an excessive amount of strain energy, despite the razor-sharpening. Crack growth in this specimen proceeded from several co-linear starting points, passed the first row of obstacles, and coalesced into a single front which propagated at a high velocity (of order 100 m/s), as indicated by the frosted, non-reflective nature of the fracture surface. The interaction of the crack front with the second row of particles produced one of the tell-tale signs of crack-trapping: "tails" were generated on the down-stream side of the obstacles as bifurcated crack fronts re-joined from surfaces with slightly different elevations. Multiple tails emanating from an individual obstacle is a strong indication that a crack has propagated along the particle/matrix interface, rather than causing debonding (simultaneous separation of the surfaces) to occur after circumventing the obstacle and forming a single tail. The only fracture arrest line that is evident on the fracture surface in Figure 4.1 is nearly at the end of the specimen; it is clear that this specimen geometry and testing procedure could not be used to measure directly the effect upon

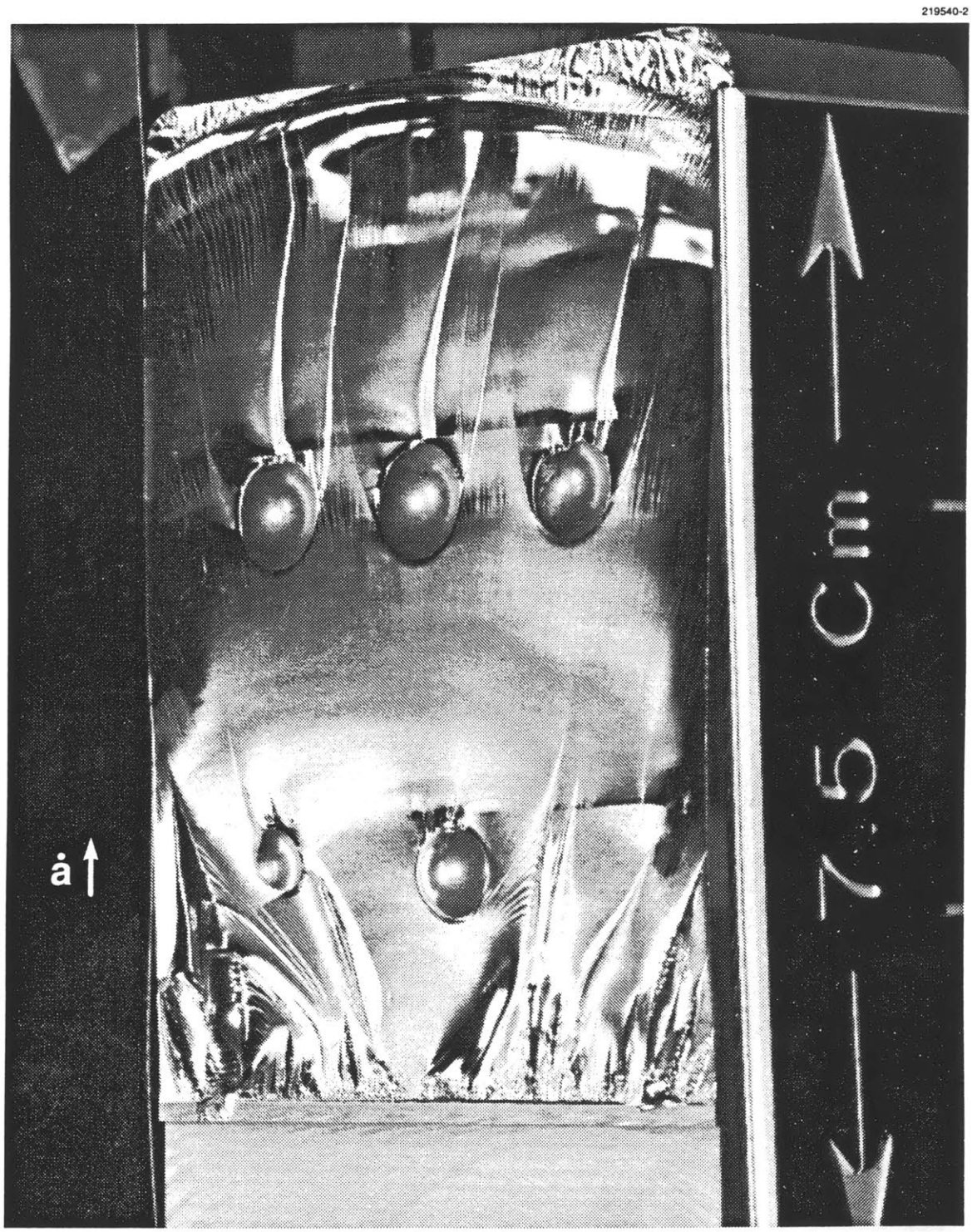

Figure 4.1: Fracture surface (gold-coated) from typical specimen tested to generate qualitative features of crack trapping by tough obstacles.

global fracture toughness of the interaction between the crack front and the impeding obstacles.

Nonetheless, several examples of fractographic evidence of the process of crack trapping were obtained. Shown in Figure 4.2 is another example of tails generated by rejoining of individual crack fronts after advancing beyond particles. Here again, multiple tails were formed behind each obstacle as a result of two or more local fracture paths developing along each particle/matrix interface. Following the fracture of the interfaces, the local crack fronts extended along different planes which eventually join, leaving behind ledges or "tails."

The second major fracture-surface artifact of crack trapping is created when fracture arrests occur while a crack is in the bowed configuration. Several such bowed arrest lines may be seen between the particles shown in the photograph of Figure 4.3. After several successive jumps through the spaces between the particles, the crack fronts escaped the center particle but continued to be trapped by the outer particles, as evidenced by the faintly visible, bowed pseudo-arrest line between them.

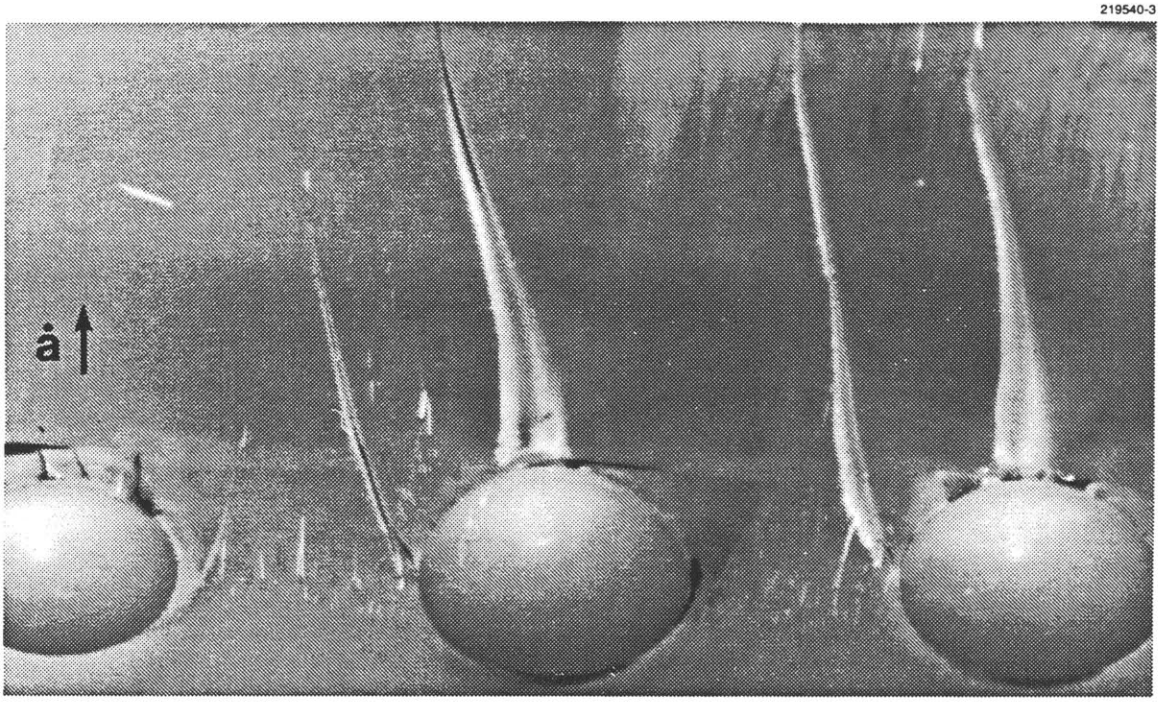

Figure 4.2: Fracture surface with multiple "tails" created by rejoining of individual crack fronts after traveling around and over particles.

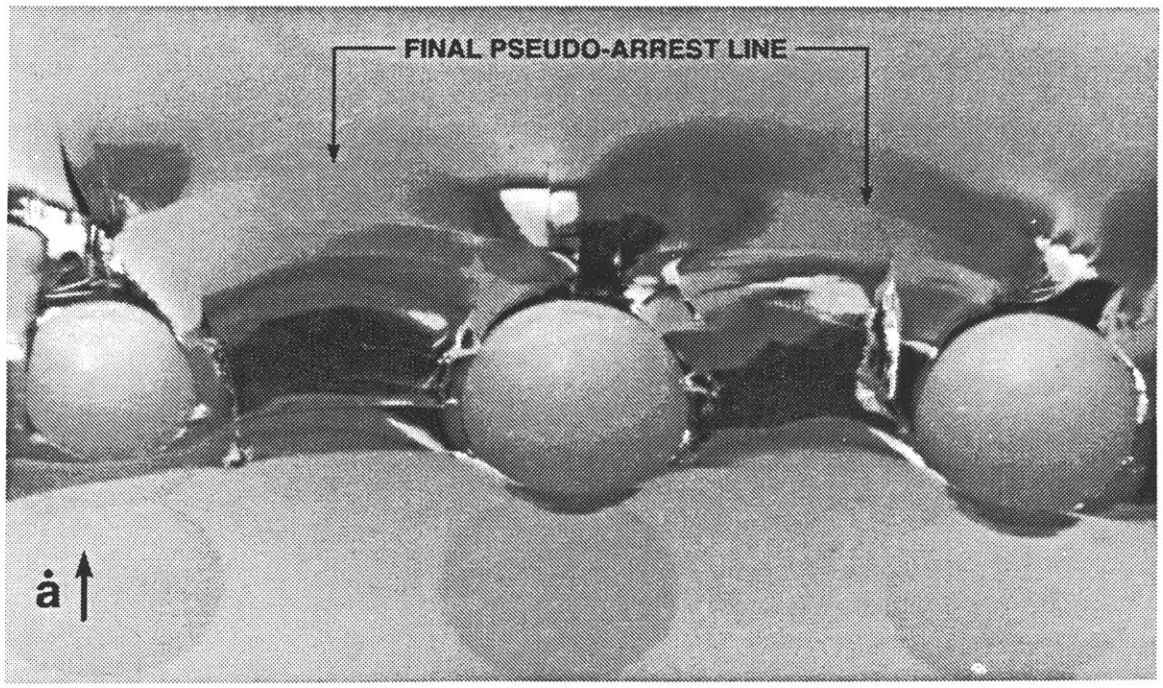

Figure 4.3: Fracture surface with bowed lines created by temporary arrest of crack growth while being trapped by tough particles.

4.1.2 Attempted Quantitative Measurements

To attempt to obtain quantitative measurements of toughening induced by crack trapping, a second series of specimens was fabricated with a more slender profile to encourage multiple arrests within each specimen. The hoped-for strategy was to place rows of tough particles within the specimens at crack length positions which might coincide with arrests. The measured stress intensity required to re-initiate crack growth from the trapped configurations would then be compared to the stress intensity required to initiate crack extensions in the neat matrix, thus providing a measure of crack-trapping toughness.

Double cantilever-beam specimens were again cast from epoxy, with a square cross-section of 13 × 13 mm and a height of 74 mm. Pairs of Nylon or silica-glass particles were positioned along the anticipated crack plane. To force the crack growth to remain planar, 1.5-mm thick strips of glass-mat reinforced epoxy (G-10) plates were bonded to the sides of the specimens. Side grooves were then cut through the thickness of the plates, along the edges of the crack plane. This technique proved very successful in causing planar crack growth; it also created such constraint upon the crack-tip strains that the edges of the crack front actually grew in advance of the center.[1] This effect is evidenced by the fracture arrest lines seen in Figures 4.4 and 4.5, which contain photographs of fractured halves of four different specimens which were gold-coated and mounted in pairs for examination with an SEM.

[1]This is in contrast to crack growth in non-side grooved specimens, where conditions of plane stress at the surface raise the effective fracture toughness (through greater plastic flow) and cause the edges of crack fronts to lag behind the crack growth in the center.

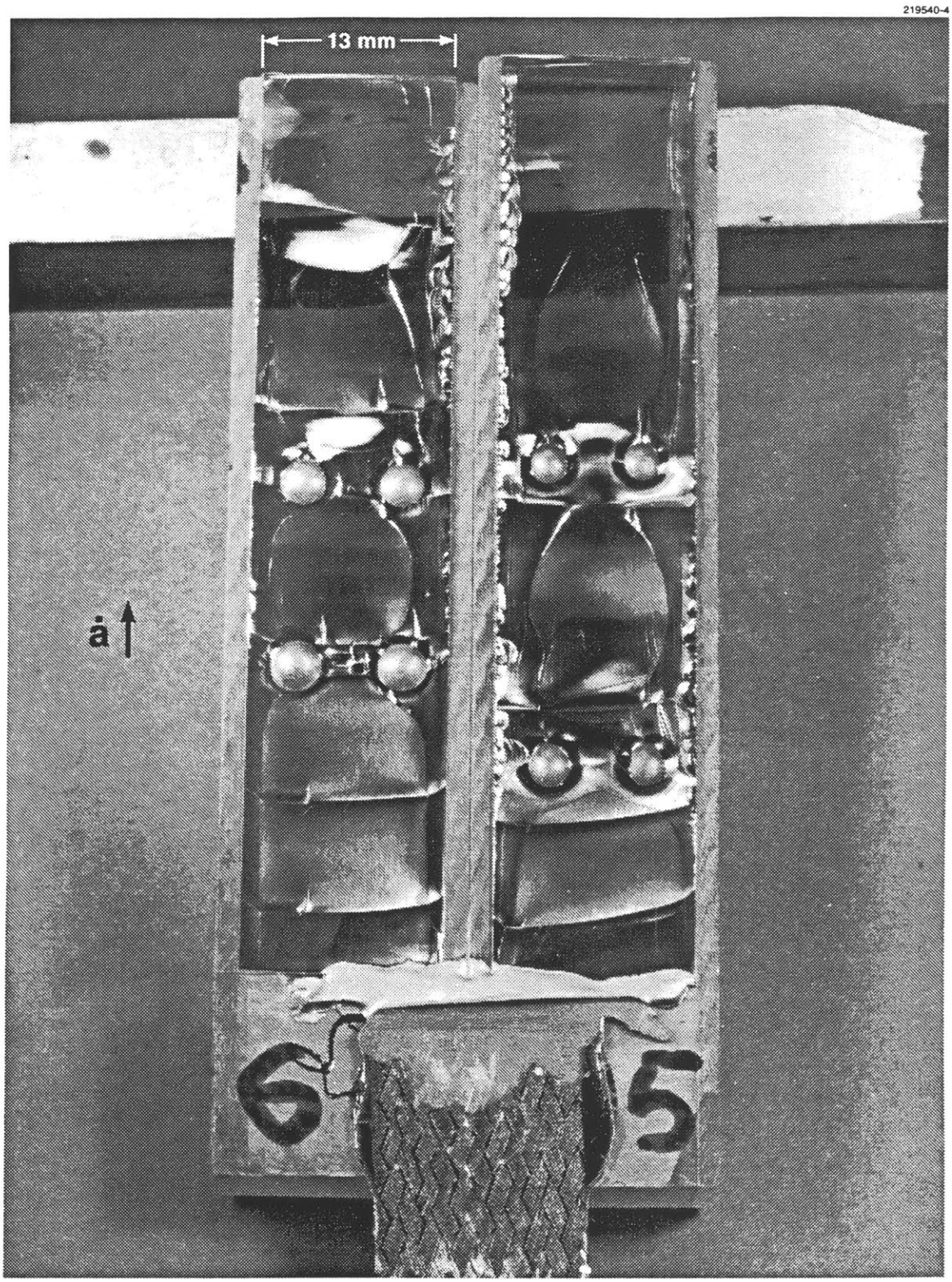

Figure 4.4: Fracture surfaces (gold-coated) from two typical 13-mm DCB specimens containing 3.17-mm diameter Nylon spheres.

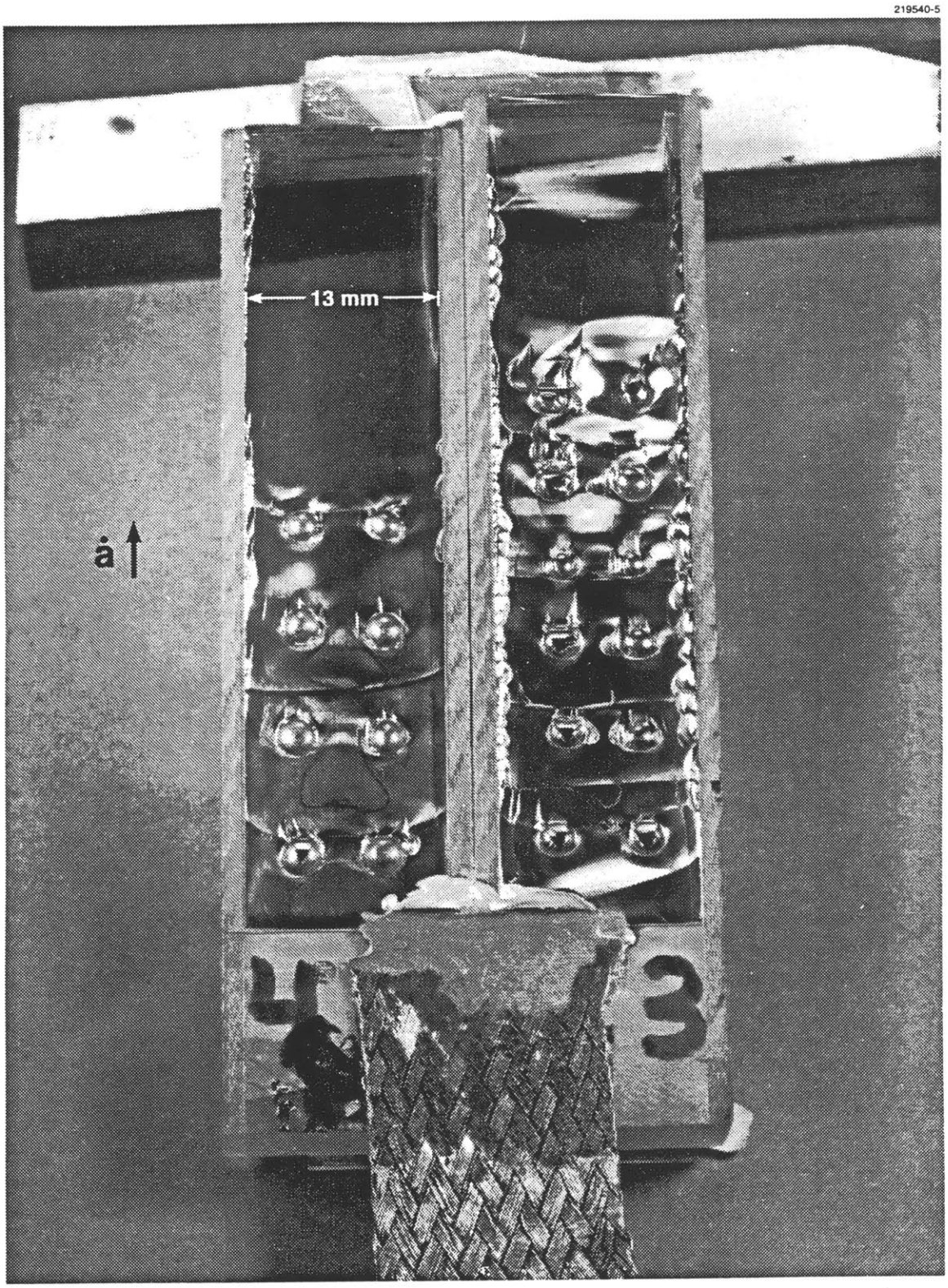

Figure 4.5: Fracture surfaces (gold-coated) from two typical 13-mm DCB specimens containing 3-mm diameter silica-glass spheres; left specimen contains spheres which had adhesive strength reduced by a release agent.

Fracture surfaces of two specimens which contain Nylon spheres are shown in Figure 4.4. Many complex, detailed features may be seen on these surfaces, but first note that several sequential fracture arrests and re-initiations were generated within each specimen, as hoped for. In general, however, the arrests resulted from the consumption and dissipation of strain energy during the very jerky form of crack advance and not from the quasi-static interaction of the crack with particles, so that in only one instance (for the specimens shown in this figure) was there a coincidence of crack arrest with particle position. In this instance, the crack was trapped by the particles and made three short, jerky advances before reaching a stable trapped configuration. This sequence is easily seen in the electron micrograph reproduced in Figure 4.6.

Fracture surfaces of two specimens containing silica-glass spheres are shown in Figure 4.5. In the specimen-half shown on the right-hand side of this figure, the spheres adhered with a strength of about 60 MPa to the epoxy matrix (see Appendix B). This level of adhesive strength was sufficient to transfer enough stress intensity at the tip of the propagating crack to fracture the majority of particles in the crack's path; additionally, no arrests occurred at particle positions in this specimen. In contrast, the specimen-half shown on the left side of Figure 4.5 contains silica-glass spheres which had their adhesive strength to epoxy reduced to about 30 MPa by treatment with a release agent. As a consequence, only one particle was fractured and two arrests occurred at locations where particles were present. The reduction in adhesive strength apparently eliminated (reduced) the option for the crack to bypass the trapping configuration by fracturing the brittle particles.[2] Enough adhesion still exists to enable the crack-trapping mechanism to be operative, as evidenced by the bowed arrest lines at the first and last rows of particles in the specimen shown in the left side of Figure 4.5. This observation may be counter intuitive: rather than "turning off"

[2]The room-temperature fracture toughness of the epoxy is about 1.0 MPa$\sqrt{\text{m}}$, and that of the soda-lime glass is about 0.7 MPa$\sqrt{\text{m}}$.

the crack-trapping mechanism, the effect of reduced adhesion *with brittle particles* is to prevent their fracture and thus make crack trapping possible, provided enough adhesion is still present, so that the crack does not go "over" the particle by premature debonding. In these specimens (with $K_{Ic}^{int} \approx 0.9\, K_{Ic}^{part}$ and $K_{Ic}^{part} \approx 0.7\, K_{Ic}^{mat}$), the particles fractured before the crack trapping mechanism could evolve because the process of crack trapping increases the local K_I applied to the trapping particle. Reduction in the interfacial toughness, by about a factor of two, permitted crack trapping to occur by reducing the K_I applied to the glass particles via deflection of the crack tip into the interface. Due to the orientation of the interface relative to the loading direction, increased loading was necessary to promote the interfacial crack growth, which was accompanied by local bowing of the crack front between the particles.

An electron micrograph of the final bowed arrest line (in the specimen with release-treated glass spheres) is reproduced in Figure 4.7. In addition to the obvious bowed arrest line, this magnified image reveals a faint, secondary arrest in a more elliptical shape at a deeper penetration past the obstacles. An interesting feature of this fractograph is that the "river" lines leading away from the primary arrest line are not normal to it. Local crack growth usually proceeds in a direction perpendicular to arrest lines. The markings seen here which lead away from the arrested crack indicate that the re-initiated crack growth was drawn ahead in an outward direction, influenced by the strong constraint (and accompanying enhanced stress intensity) created by the grooved, high-modulus side plates. Closer examination of the sole release-coated glass particle which fractured, isolated in the micrograph in Fig 4.8, revealed the likely cause of its failure. Shown in Fig 4.9 is a magnified view of a hole in the surface of the glass sphere at the origin of its fracture. The presence of this flaw elevated the stress intensity developed within the silica glass to a level above its fracture toughness, in spite of the limited stress it experienced as a result of the reduced adhesion.

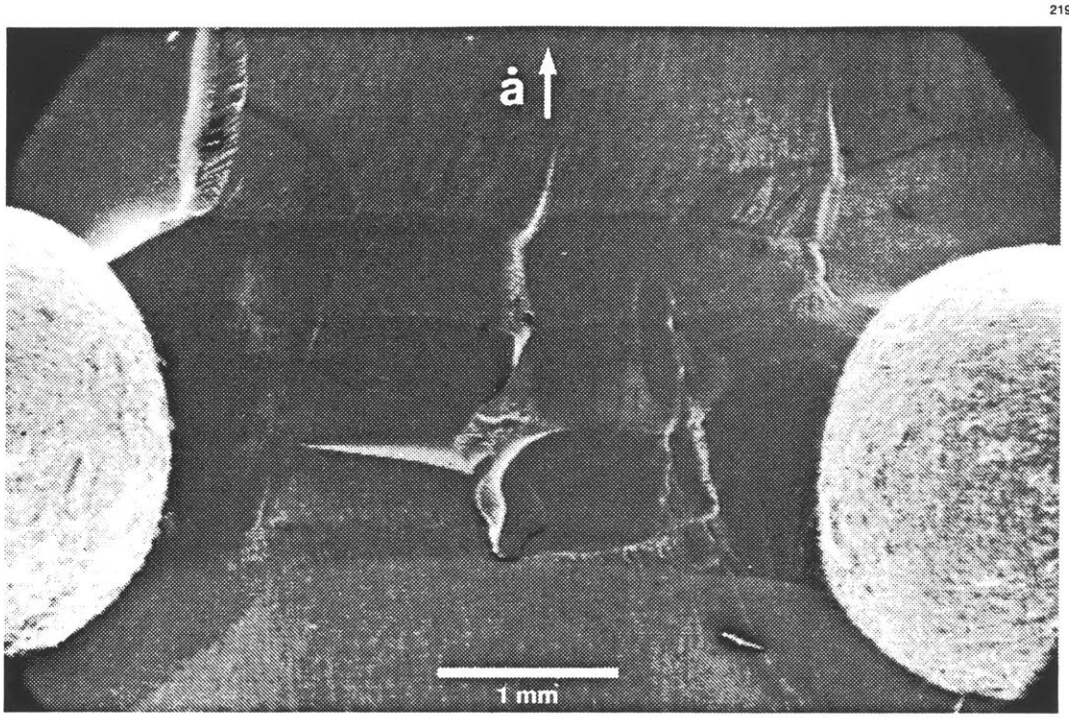

Figure 4.6: SEM photomicrograph of crack-trapping by Nylon particles in specimen shown in left portion of Figure 4.4.

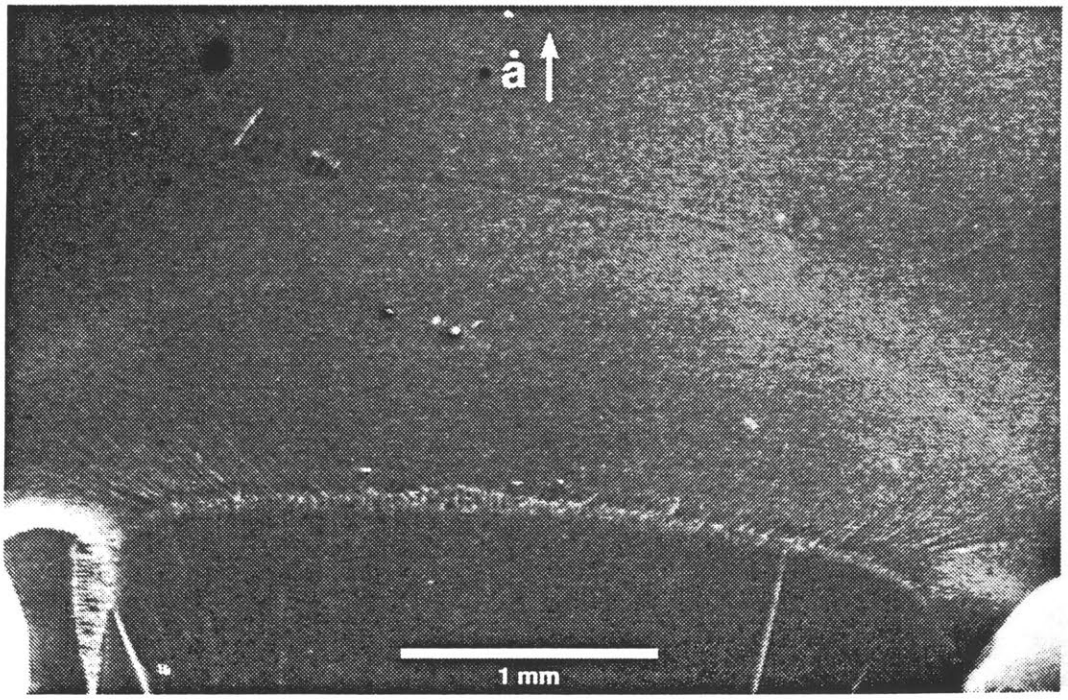

Figure 4.7: SEM photomicrograph of crack-trapping by glass particles (with reduced adhesion) in specimen shown in left portion of Figure 4.5.

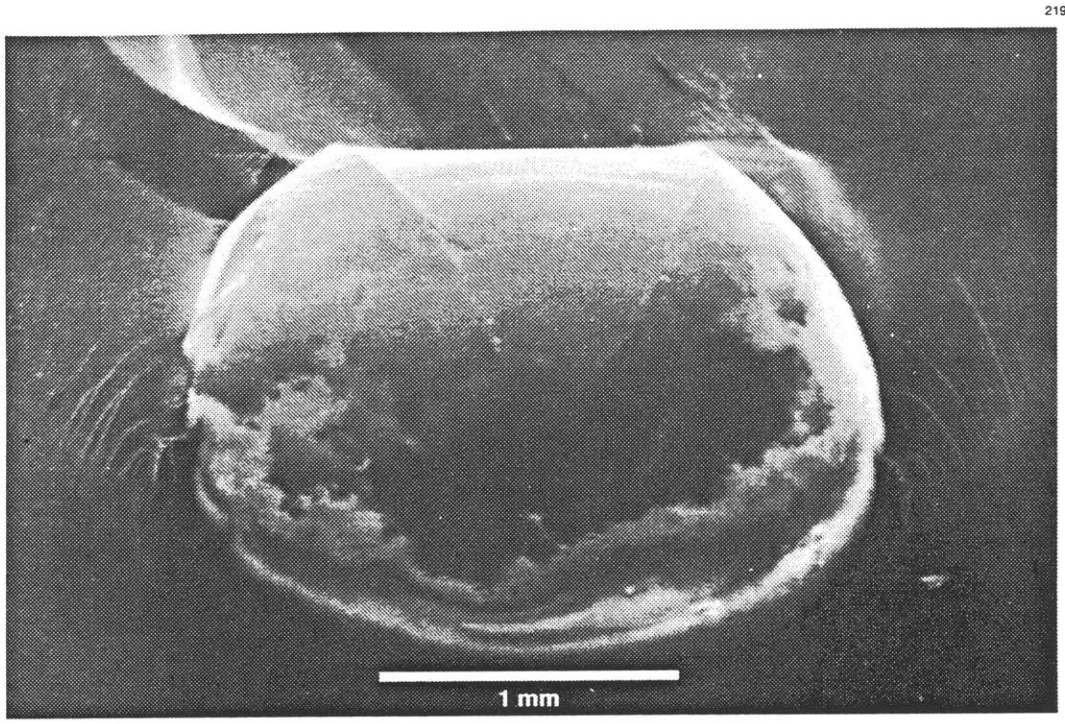

Figure 4.8: SEM photomicrograph of the only glass sphere to fracture in the specimen shown in left portion of Figure 4.5, with deliberately reduced adhesive strength.

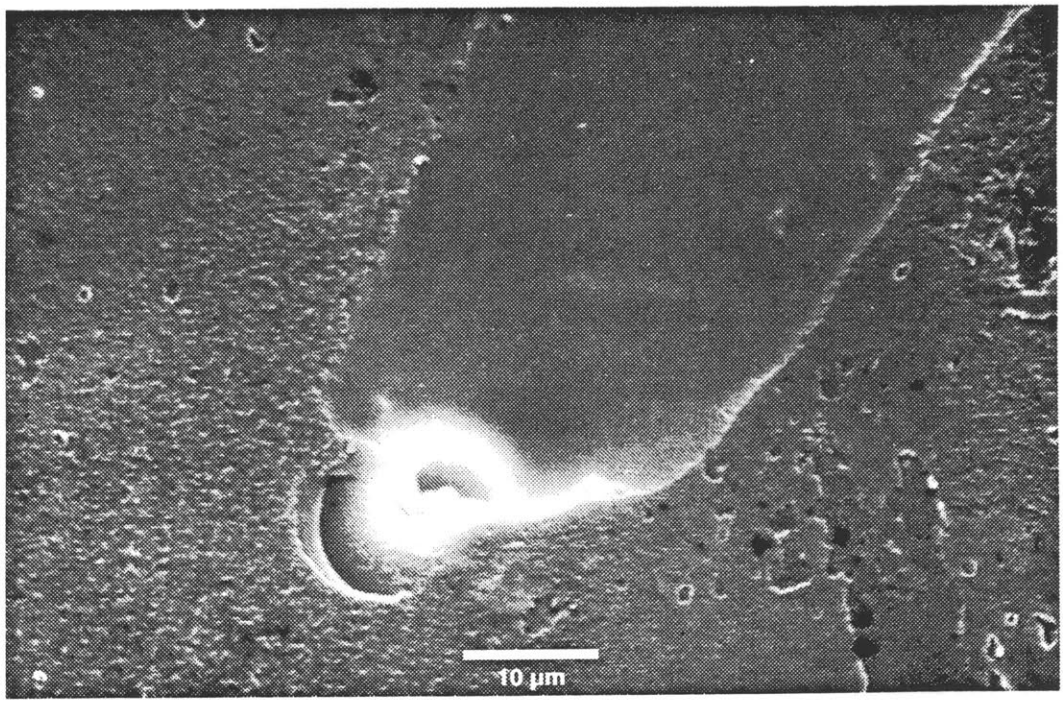

Figure 4.9: SEM photomicrograph of flaw on glass sphere which resulted in the fracture of the glass sphere shown above.

There are many other features worthy of note on the surfaces of the specimens shown in Figures 4.4 and 4.5, including artifacts of apparent dynamic effects and stress-wave reflections from interfaces. A striking feature which was repeatedly produced in specimens containing Nylon spheres, but not in those containing glass spheres, was a "halo" around the particles. This smooth, annular region around Nylon particles may be seen more easily in the light optical fractograph reproduced in Figure 4.10 than in the electron micrograph of the same area, shown previously in Figure 4.6. The cause of this halo region will be discussed in the next section.

The calculated values of stress intensity associated with the trapping events generated in these (13-mm) specimens were only 10 to 20% in excess of the stress intensity calculated for crack initiation in neat portions of the specimens. This range is similar to the scatter in the neat values, so no meaningful quantitative data can be derived from this series of tests, particularly when the conditions for arrest and re-initiation of the crack front could not be relatively established.

Attempts with these specimens to record the evolution of crack-front shapes while interacting with obstacles were also unsuccessful. A high speed video (Spectra Physics, @1000 frames per second) image was recorded during fracture of a few of the 13-mm specimens. Pairs of sequential recorded images, such as those reproduced in Figure 4.11, indicate that crack jumps from particle-row to particle-row took place in less than one millisecond, so that a faster framing speed would be required to record stages of crack growth which involve particle interactions.

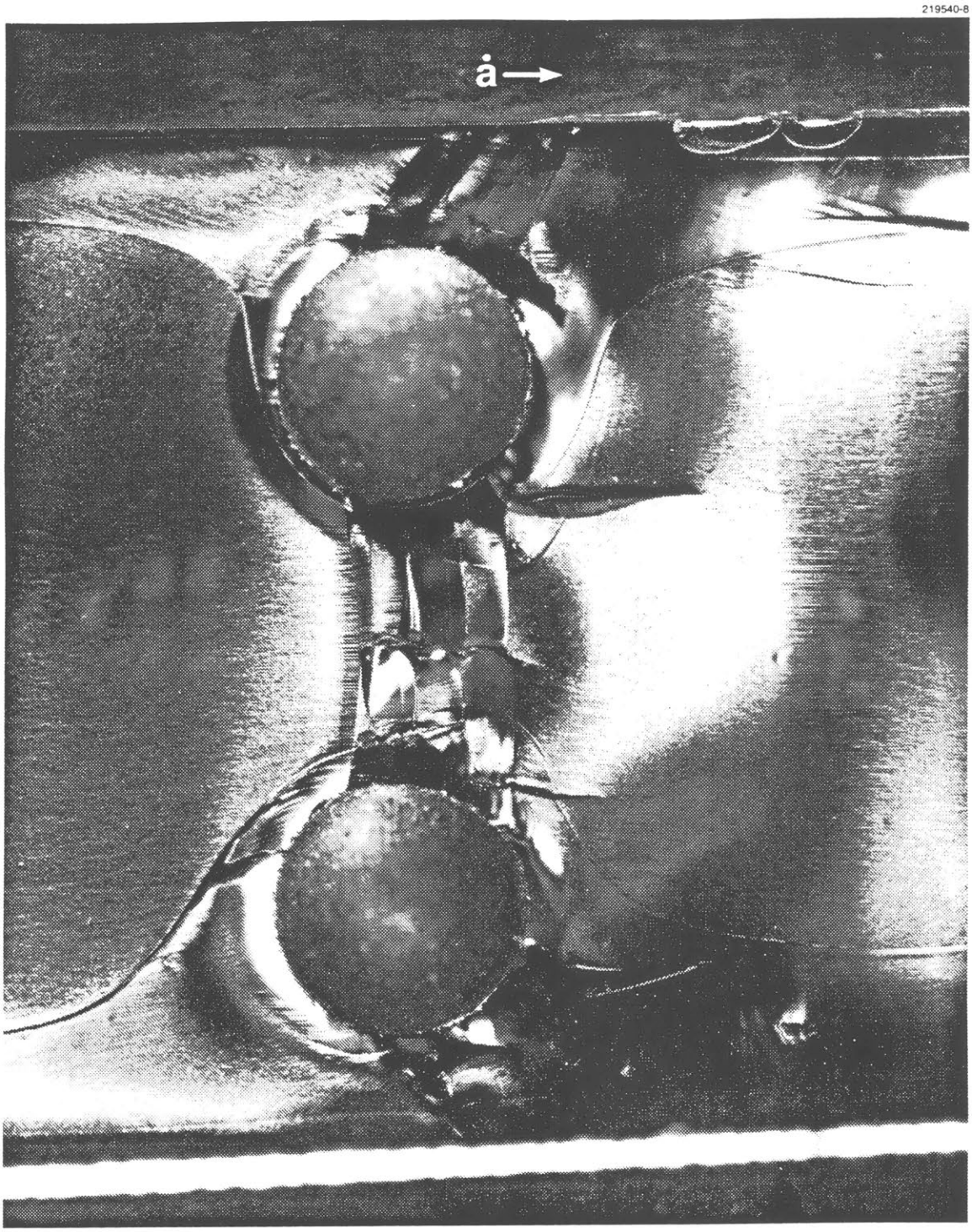

Figure 4.10: Light micrograph of the fracture surface previously shown in Figure 4.6. Note the concentric, smooth "halos" around each Nylon sphere.

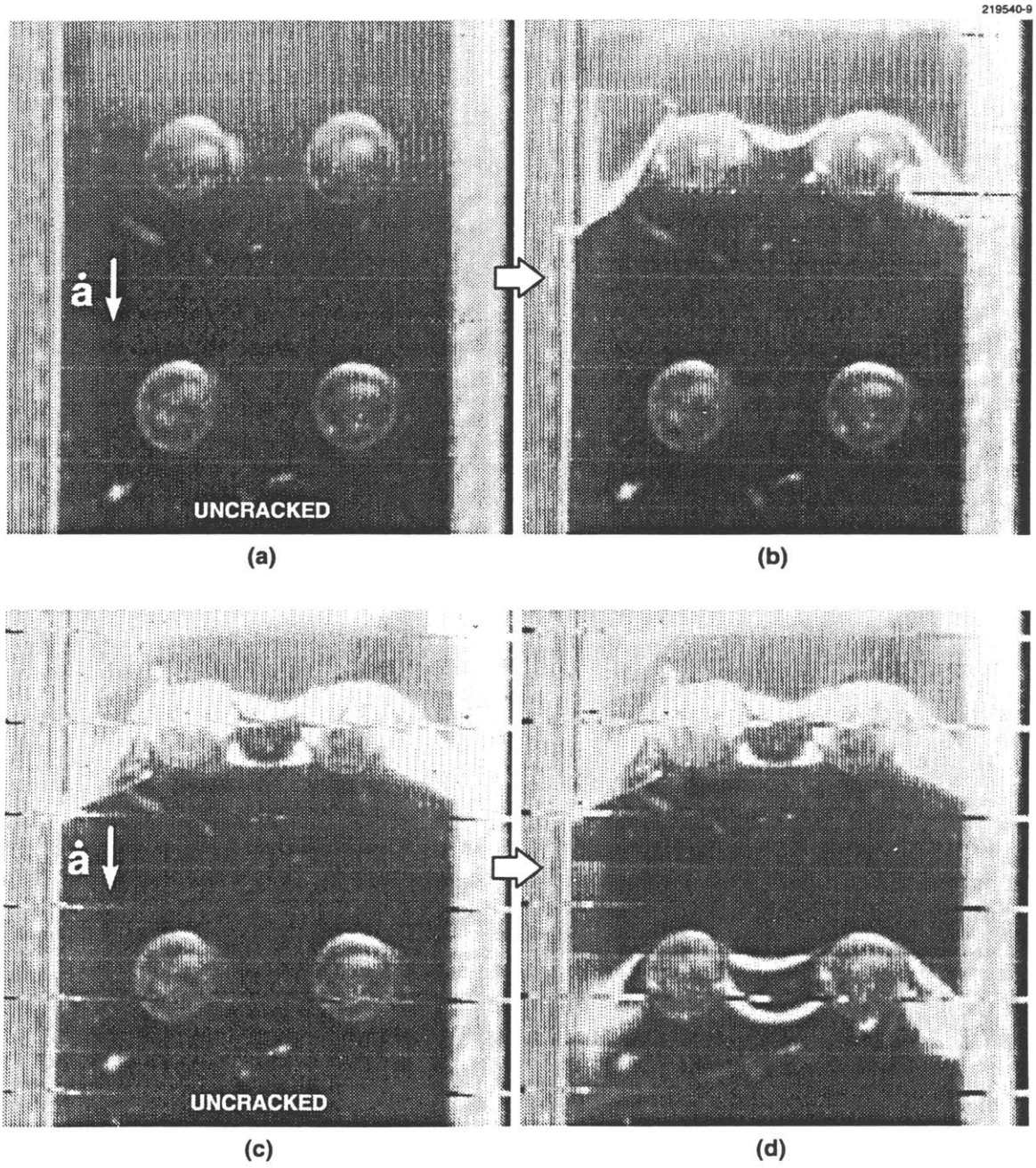

Figure 4.11: High speed (1000 fps) video of fracture in 13-mm DCB specimens. Sequential frames from (a) to (b) and from (c) to (d) demonstrate that crack growth was too rapid to record interactions between crack front and particles with this specimen and technique.

A faster framing rate was attained with a high speed 16-mm movie camera (Hy-Cam, @6200 frames per second), which was used to record crack-front images during fracture of larger specimens. These specimens were also epoxy DCB's containing Nylon or silica-glass spheres, and had dimensions of $38 \times 38 \times 90$ mm. Crack growth in these specimens also proceeded in jumps which were too rapid to allow identification of the crack-trapping configurations and critical interaction with particles from recorded film sequences. Two pairs of sequential images which demonstrate this are reproduced in Figure 4.12.

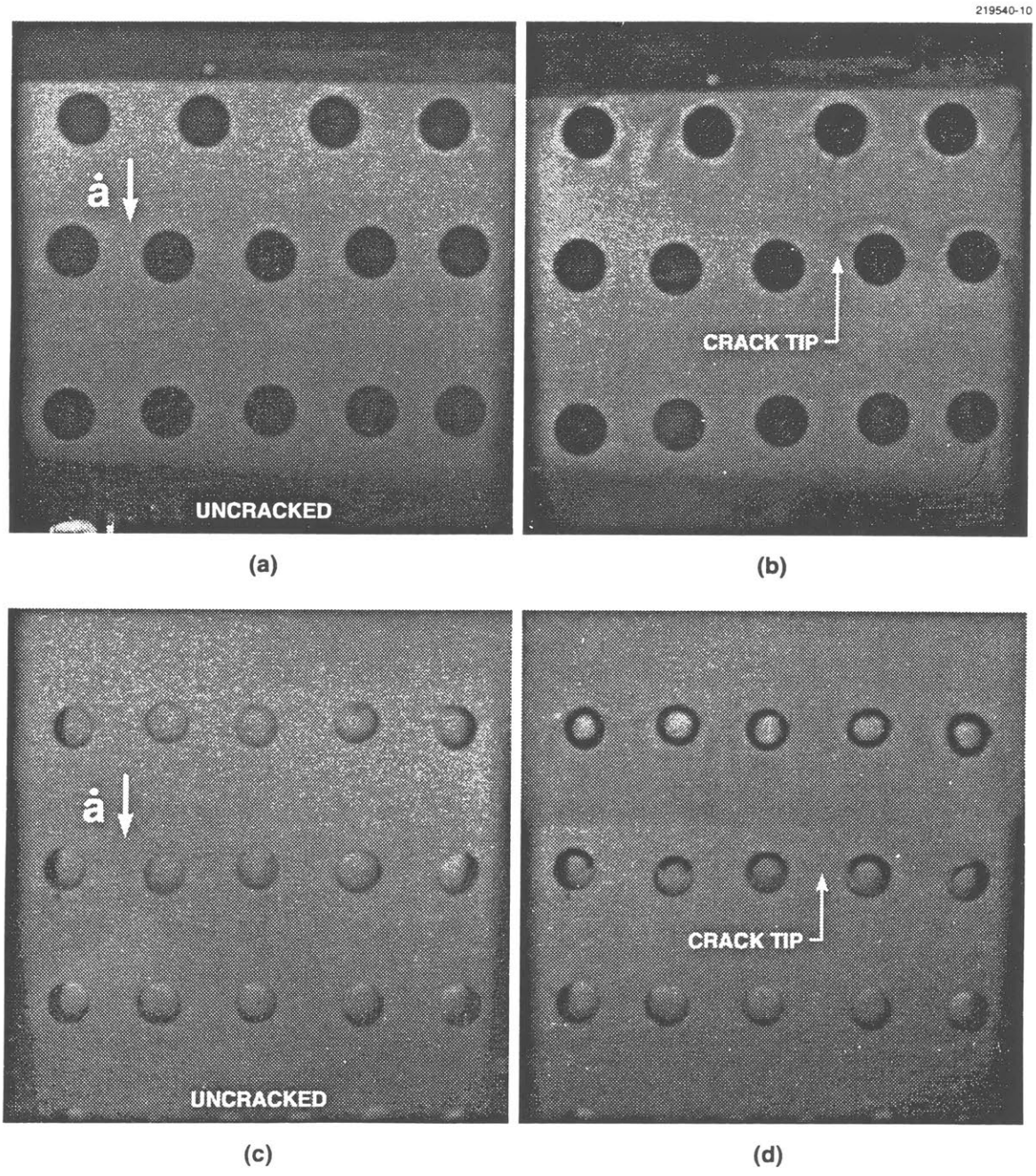

Figure 4.12: High speed (6200 fps) 16-mm images of fracture in 38-mm DCB specimens. Sequential frames from (a) to (b) and from (c) to (d) demonstrate that crack growth was too rapid to record the key interactions between crack front and particles with this specimen and technique.

4.1.3 Analysis of "halos"

Smooth annular regions surrounding Nylon particles were observed on all of the fracture surfaces in the 13-mm specimens. Additionally, in all of these specimens (both fractured and unfractured) the epoxy within approximately one radius of Nylon particles is of a much lighter color than the bulk epoxy. This three-dimensional effect indicates that some reaction took place between the Nylon and the epoxy, probably during curing. Initial speculation that the epoxy may not be fully cured in regions close to the Nylon was evaluated with the following analyses.

Microhardness tests were performed upon fracture surfaces containing these halo regions. Little variation in hardness was determined between the smooth halo regions and regions far away from the particles. This result does not indicate that the material was in a uniform state of cure: compression tests subsequently obtained and discussed in Appendix A show little variation in yield stress as a function of T_g for epoxies *of the same formulation* but cured at different temperatures.

To obtain a more sensitive measure of the state of cure of the material adjacent to the Nylon particles, differential scanning calorimetry (DSC) was performed upon small quantities of epoxy removed from the halo regions. These measurements revealed glass transition temperatures that were reduced by 20°C or more from the T_g of the bulk epoxy. Chemical reactions between epoxy and Nylon at temperatures below the Nylon melting temperature have not been documented; the most likely cause of the T_g-depression was deemed to be diffusion of water from the Nylon, which is known to be very hygrophobic, during post-curing of the epoxy.

Plasticization of epoxy by the presence of water has been well-documented in the literature [49, 50]. Reduction of the T_g in epoxies by 30–40°C has been observed to occur as a result of the presence of just 1% (by weight) of H_2O [51]. Though the precise cause of this effect remains unclear, reasonably accurate predictions of T_g-depression can be made on the basis of a modified rule-of-mixtures approach which incorporates the glass transition temperature of water ($\sim 134\,K$) [51, 52].

Final proof of the culpability of water was obtained by thoroughly drying Nylon particles prior to their inclusion in model specimens; after postcuring the epoxy, no halos were observed around the particles. The most significant aspect of the plasticized halo regions is that their fracture toughness is approximately double that of the more fully cured epoxy. (See Appendix A.) Thus, during the crack-trapping experiments the halo regions would have the effect of increasing particle diameters. To eliminate this variable and the effect it might have on results, all particles subsequently incorporated into model specimens were thoroughly dried, at 80°C for a period of ten or more days.[3]

[3]Though it might be interesting to explore how this effect could be used to enhance toughness, epoxies containing significant plasticized regions would have reduced moduli and thermodynamic stability relative to their homogeneous, more fully cured states, and would, therefore, not be desirable to have.

4.1.4 Principal effects to overcome

The most significant difficulty to surmount in the crack-trapping experiments was the unstable, jerky nature of crack extensions in the model specimens. Despite the use of wedge-loaded DCB's, which are geometrically stable fracture specimens (because in them cracks extend in a decreasing K-field), crack extensions in all of the initial experiments were very rapid. The consequences of dynamic crack growth were twofold: images of crack-front interactions with particles could not be recorded, and the accompanying effects upon applied loading could not be measured accurately.

Through a series of fracture toughness tests and examination of the available literature,[4] it became clear that fracture in epoxies is influenced by an inherent material instability. At room temperature, most epoxies fracture in an unstable, jerky manner which results from alternate crack-tip blunting of stationary cracks, followed by energetically "supercharged" extensions of sharp cracks, only to be blunted again upon arrest. This mode of fracture gives way to stable, continuous fracture as the yield stress is increased, either as a result of increased loading rates or as a result of reduced testing temperatures. In the epoxy used here, stable fracture was consistently found to occur at a temperature of $-60°C$. Because stable fracture was required, both to enable photographing the crack front as it interacted with the obstacles and to measure accurately the resulting increases in toughness, the crack-trapping experiments were performed at $-60°C$.

[4]Both of which are discussed in Appendix A.

The enforcement of planar crack growth in the crack-trapping specimens was the second difficult requirement to achieve. The tendency of double cantilever specimens to spall, or fracture away from the center plane, results from the very high bending stresses generated at the surface of the individual beams, in the plane of crack growth. Slight perturbation of a short crack away from the center plane in a DCB subjects it to higher tensile stresses than the out-of-plane stresses which promote planar extension. Consequently, short cracks in DCB's will most often spall away from the center plane with a curvature whose magnitude is indicative of the ratio of in-plane to out-of-plane stresses.

The technique initially employed of reinforcing the sides of DCB specimens with glass-fiber composite plates was successful in promoting planar crack growth at room temperature. At reduced temperatures, however, the difference in thermal expansions between the epoxy matrix and the reinforcing plates was so great that the resultant thermal stresses caused specimen failures prior to any externally applied loading. When the glass-fiber plates were removed and side grooves were cut to a depth of 10% of the specimen width, crack extensions once again spalled more often than not.

To characterize the tendency of cracks to spall as a function of crack length, an approximate stress analysis of the DCB was performed by subdividing the geometry into the two beams of the cracked portion, in which the in-plane (σ_x) stresses are generated, and the lower, uncracked beam in which the out-of-plane (σ_y) stresses are present. The ratio, σ_y/σ_x, was computed as a function of normalized crack length, including the compressive component of force from the (frictionless) wedge. The plot in Figure 4.13 shows that, for short crack lengths (less than beam height) this ratio is very low, which is consistent with the spalling tendency of short cracks. The ratio does not reach unity, which indicates an ambivalence of the crack for planar *versus* curved growth, until the crack has grown to over 75% of the specimen length. Such long cracks are undesirable because they introduce complications of compliance and shear

of the "built-in" cantilever ends into the stress intensity determination. Consequently, an initial crack length of about 65% of the specimen length was adopted; σ_y/σ_x was augmented by cutting deep side grooves (33% of the specimen width, in total) and by using a center support. Details of this final specimen geometry are given in the next section.

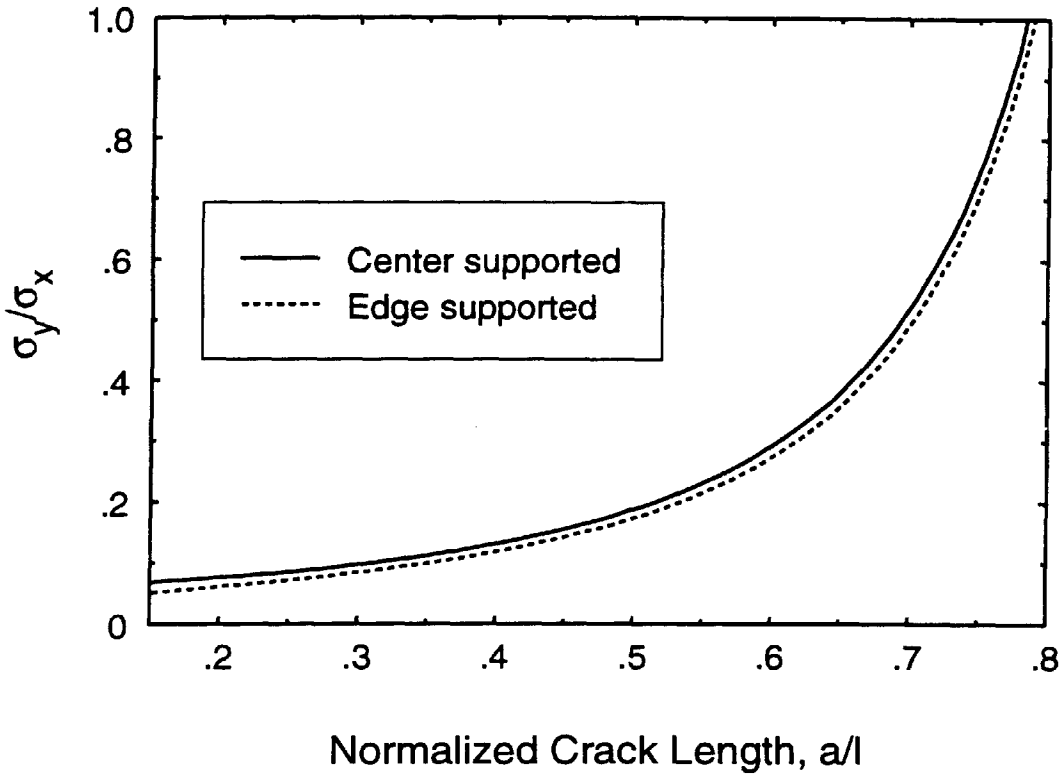

Figure 4.13: Approximate ratio of out-of-plane to in-plane beam stresses at crack tip of DCB specimen loaded with 30-degree wedge.

4.2 Final Experimental Technique

4.2.1 Specimen Fabrication

The final crack-trapping specimens were double cantilever-beam specimens having a square cross section of 38 mm×38 mm and a height of 89 mm. In the initial fabrication step, the resin and curing agent were heated to approximately 65°C, mixed for at least five minutes, and then evacuated until most degassing activity ceased. The liquid was then poured into aluminum molds which had been coated with a release agent. In the case of specimens containing rods, the molds were filled and then placed under vacuum until all bubbles were evacuated. In the case of specimens containing spheres, a two-step process was required. The molds were filled to the centerline and evacuated, sufficient time was allowed for gelation to commence, the spheres were placed in the desired locations, and further gelation was allowed. Prior to vitrification, the molds were filled with a newly-prepared batch of epoxy and again evacuated. In this manner, spheres could be incorporated into the center plane of specimens which contained no discernible mechanical interface.

All rods and spheres used as obstacles were solvent cleaned and then thoroughly dried prior to their inclusion into the specimens to prevent plasticization of adjacent epoxy by diffusion of water from the inclusions during curing of the epoxy. Inter-particle spacings (R/L, as defined in Figure 4.14), of 0.125, 0.187 and 0.250 were used, corresponding to equivalent volume fractions of approximately 0.06, 0.14 and 0.27.

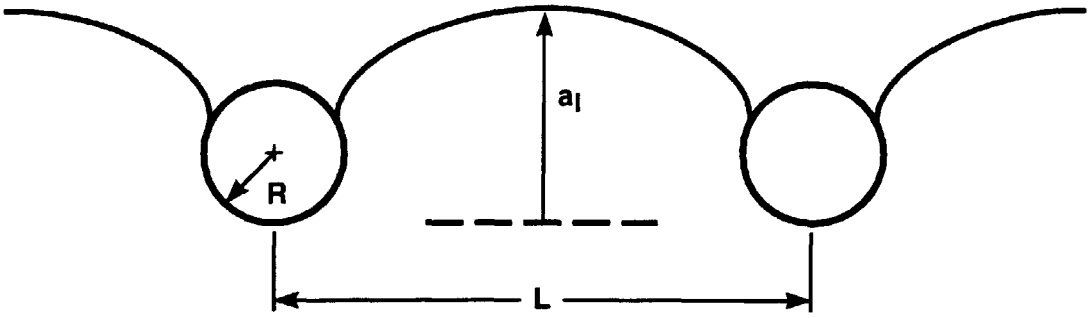

Figure 4.14: Geometry of particle spacing and local (bowed) crack advance.

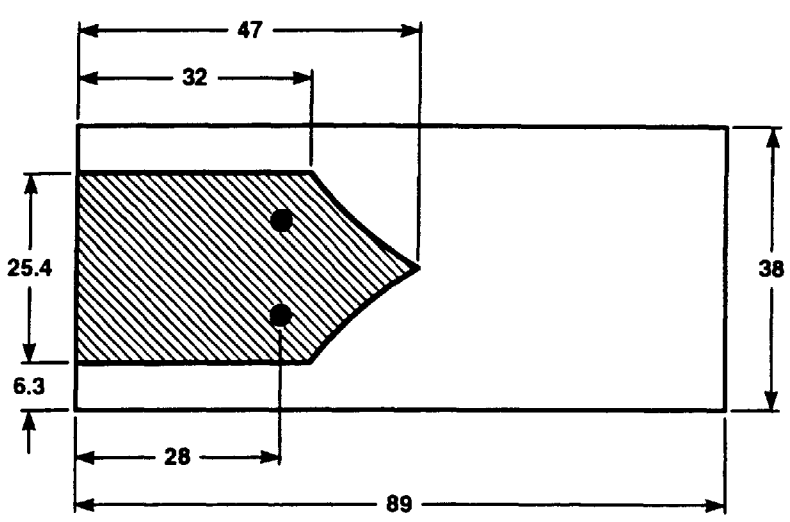

DIMENSIONS ARE IN MILLIMETERS

Figure 4.15: Dimensions of DCB crack-trapping specimens. Cross-hatching indicates fracture area remaining after cutting side grooves and starter notch.

Following a room-temperature cure of at least 24 hours, the filled molds were post-cured for one hour at 135°C and cooled at a rate of approximately 10°C/hour in a programmable oven. Specimens were then milled to the dimensions indicated previously and shown in Figure 4.15. A semi-circular groove was machined across the bottom of each specimen, parallel to the crack plane, to accommodate a pin to provide vertical support during testing. To promote planarity of crack growth, side grooves were then cut with a 0.5-mm thick slitting saw to a depth of 6.3 mm. A chevron-shaped starter crack was cut to a length of 43 mm, so that when the propagating crack reached the full width, the crack length would be about two-thirds of the specimen length. During the casting of specimens, the particles were placed just beyond this point, so that the measured effects of crack-front/particle interactions would not be corrupted by end effects in the DCB.

After all machining operations had been completed, the specimens were sanded and then polished with alumina paste. Photographs of a typical specimen containing Nylon rods are reproduced in Figure 4.16. In these photographs, the cross-section of the rods is evident as a light colored circle. In the normal view, darker regions surrounding the circles are projected by parallax along the rods; this artifact merges with the true cross-section of the rods in the cinematography obtained during the experiments. Photographs of a typical specimen containing polycarbonate spheres are reproduced in Figure 4.17.

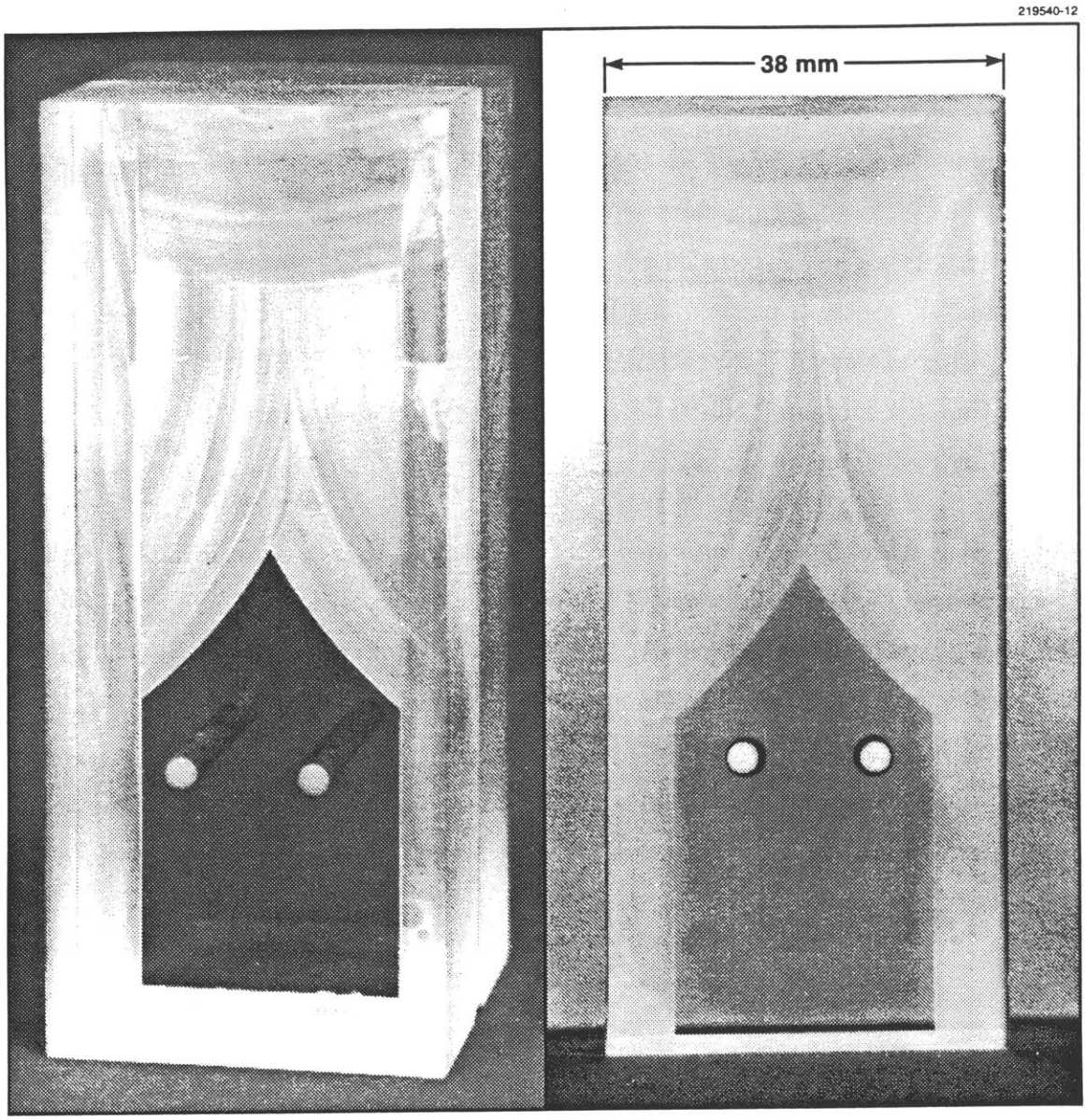

Figure 4.16: Crack-trapping specimen containing Nylon rods. In the normal view, note the actual cross-sectional rod area compared to the area projected by parallax.

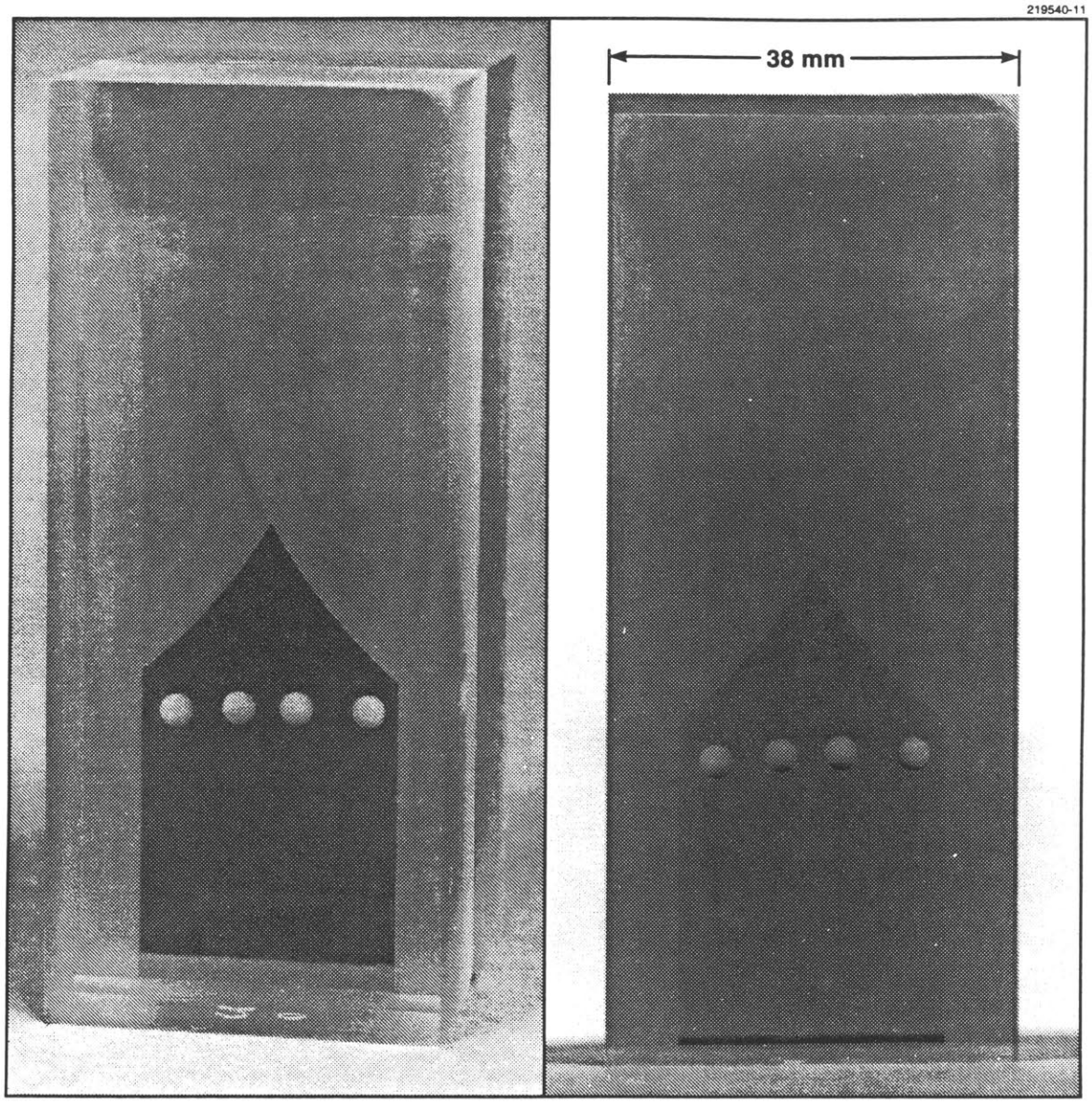

Figure 4.17: Crack-trapping specimen containing polycarbonate spheres.

4.2.2 Testing Procedures

The crack-trapping experiments were performed at $-60°C$ in a temperature-controlled chamber. Cooling was accomplished with forced convection of liquid nitrogen boil-off vapor, and was maintained to within $\pm 2°C$ with a controller utilizing a thermocouple placed adjacent to the specimens. Testing was performed with a screw-driven (displacement-controlled) machine operated at a constant cross-head velocity of 2.5 mm/min. Loading of the specimens was performed with a polished, stainless steel 30-degree wedge lubricated with molybdenum disulphide. Specimens were supported with a cylindrical steel pin positioned parallel to the fracture plane.

The load was directly recorded by a load cell, while the wedge displacement was measured with a linear potentiometer sensing the relative motion between the wedge and the load cell platen. To prevent sticking of the actuator, a resistive film heater was mounted on the potentiometer housing. Both load and displacement data were digitally recorded and stored at a sampling rate of 100 Hz.

Images of the crack front and its interaction with obstacles were recorded on 16-mm film at a frame rate of 24 fps. Two cameras were used: one with a normal view (looking along the axis of the rods) to image the crack front, and one looking down upon the specimens at an angle of approximately 25 degrees in order to record possible debonding along the rod/epoxy interfaces. Lighting for the crack-front images was provided by light from a tungsten lamp reflected by a heated mirror (to increase the spot size) and passed through a diffuser plate. Lighting for the debonding images was provided by a fiber-optic light source aimed directly at the surface of the obstacles where crack intersection was anticipated. The elapsed time from crack initiation to specimen failure was typically about 40 s, so approximately 1000 photographic images were obtained during the crack growth in each specimen.

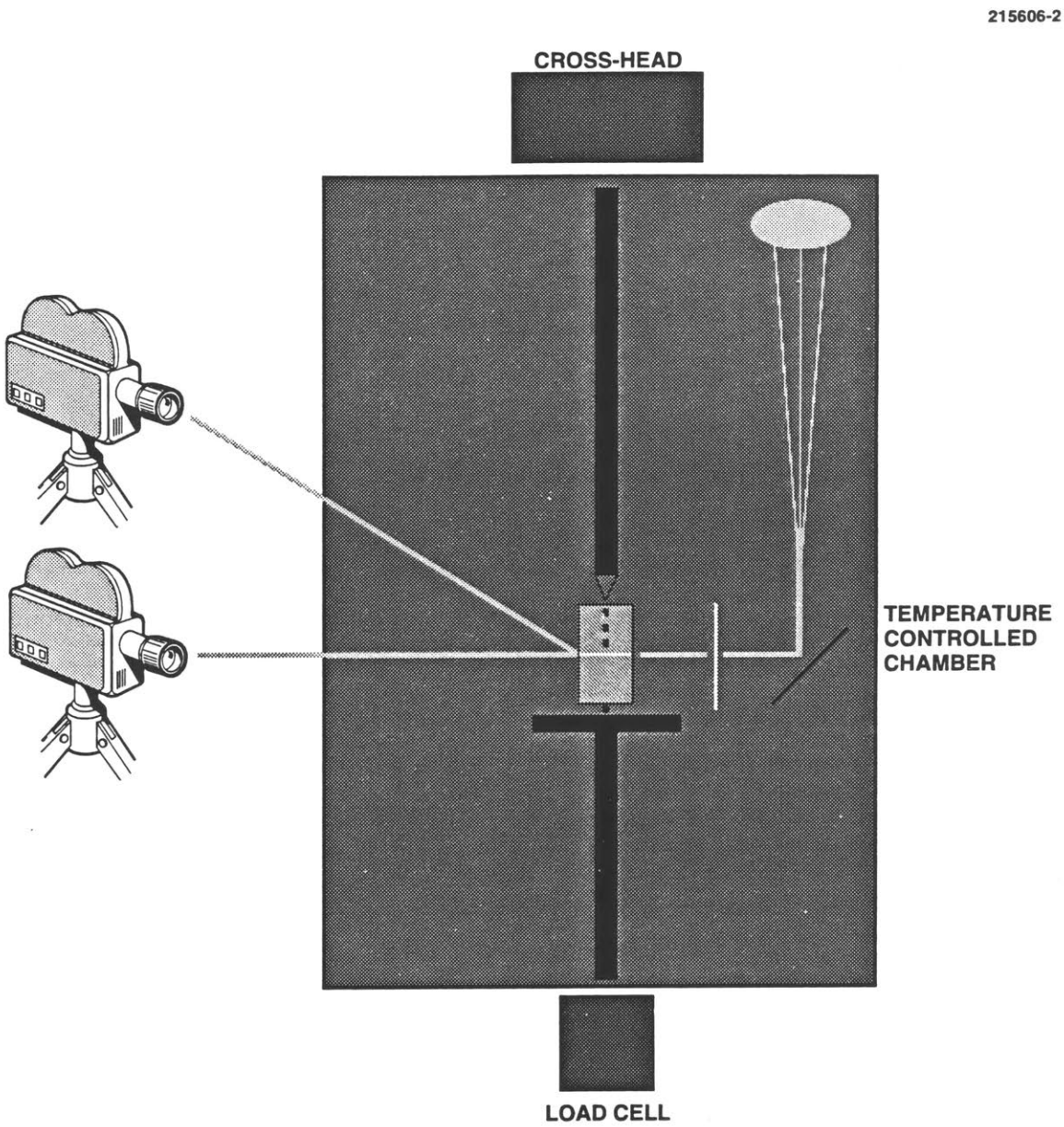

Figure 4.18: Schematic of set-up for crack-trapping experiments.

4.2.3 Reduction of Data

A typical load *versus* displacement ($P-\delta$) trace from testing of a specimen containing no obstacles is reproduced in Figure 4.19. As the crack extends through the Chevron starter section its width increases, resulting in a nonlinear rise in load. The maximum load is reached when the crack reaches the full width of the specimen (end of Chevron), and is followed by a steady drop in load during crack extension. A precipitous drop in load results as the crack approaches the end of the DCB and final specimen cleavage occurs.

A typical $P-\delta$ trace from a specimen containing two polycarbonate rods is reproduced in Figure 4.20. The slight reduction in load at the initiation of fracture ("pop-in") can be seen in this figure. Following the drop in load from the maximum, the crack front reaches the rods and becomes "trapped", causing the load to rise once again. As a result of this rise in applied load (and hence, stress intensity), the crack front begins to advance past the obstacles and assumes a locally bowed configuration. Further load increase causes the local crack front to continue to grow in a bowed shape until the breakaway configuration is reached. At this point, one or more of the obstacles are left behind (or fractured, if the toughness of the particle, K_{Ic}^{part} , is less than the locally-induced stress intensity) and the previously-independent crack fronts coalesce into one and continue to grow. If the impeding obstacle was tough enough to be left intact and if it is sufficiently well-bonded to the matrix, then bridging of the crack flanks takes place.

A similar history of sequential events can be seen in the $P-\delta$ trace shown in Figure 4.21, corresponding to testing of a specimen containing two PC spheres. In this instance, the spheres had their adhesive strength reduced from above 54 MPa to about 22 MPa by the application of a release agent, resulting in a decreased load induced by trapping, relative to specimens with full adhesive strength.

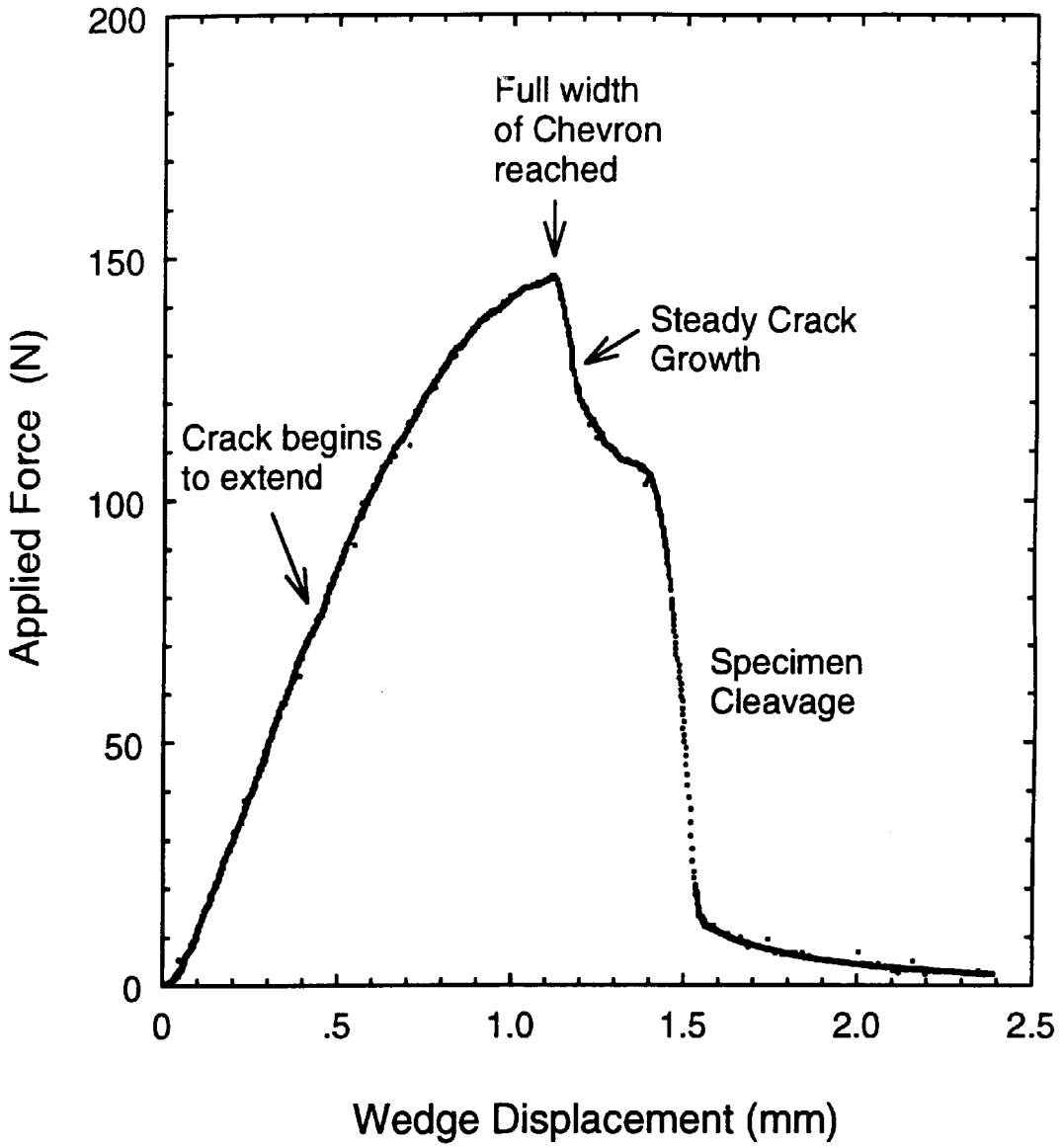

Figure 4.19: Typical load *vs.* displacement plot from testing a crack-trapping specimen containing no obstacles (neat matrix only).

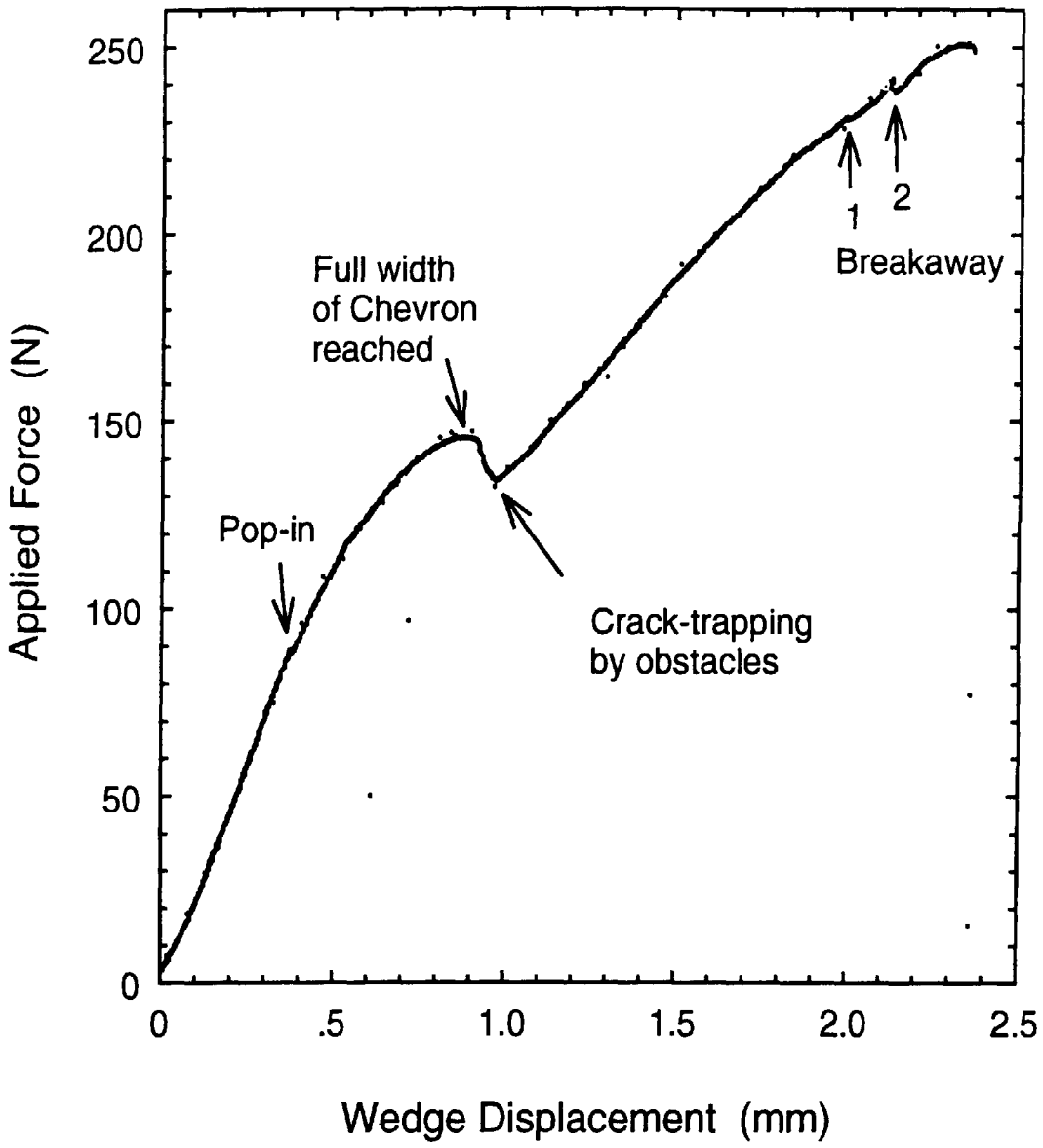

Figure 4.20: Typical load *vs.* displacement plot from testing a crack-trapping specimen containing two PC rods. $R/L = 0.125$.

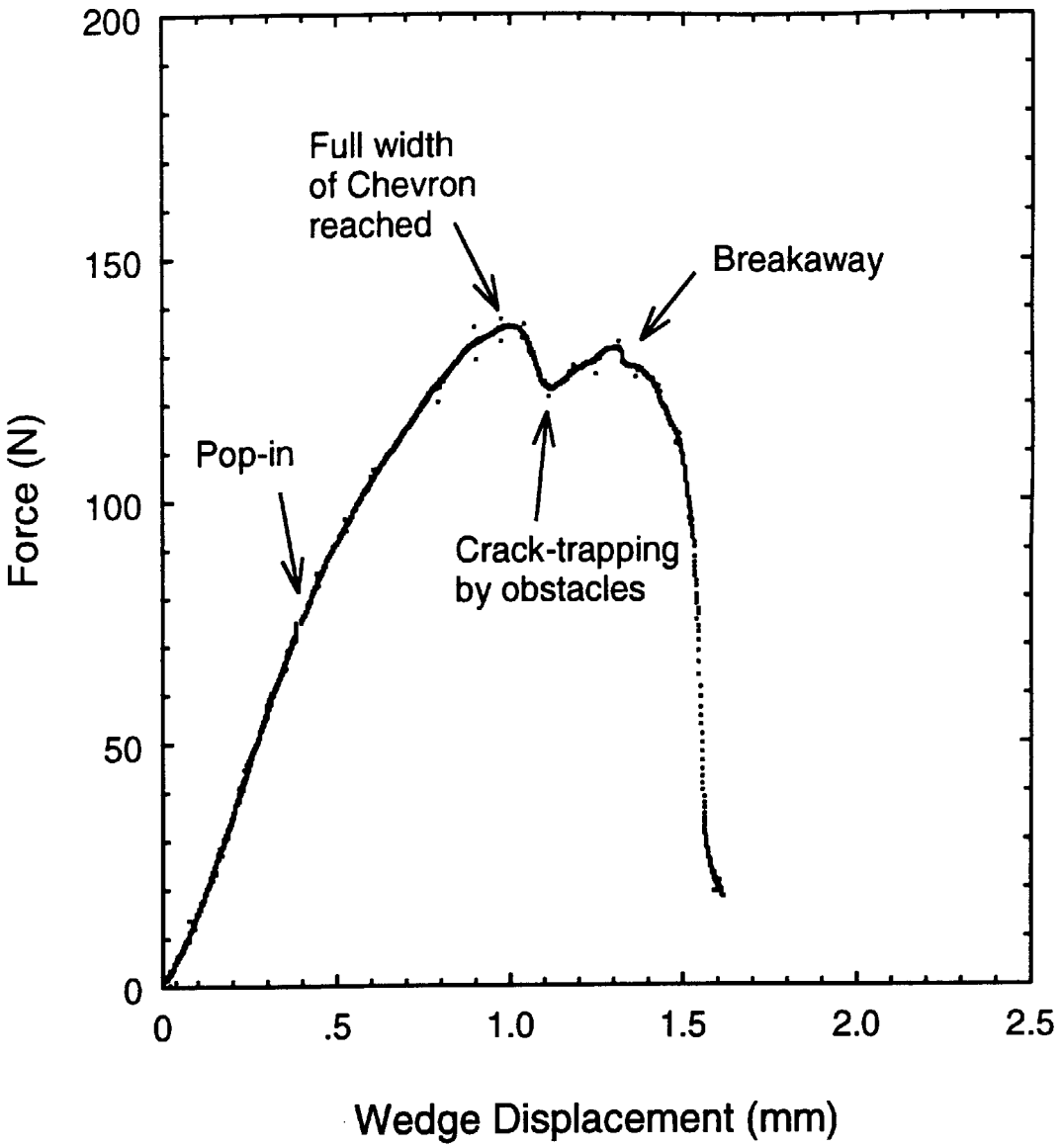

Figure 4.21: Typical load *vs.* displacement plot from testing a crack-trapping specimen containing two PC spheres with reduced adhesion. $R/L = 0.125$.

During the testing of the crack-trapping specimens, 16-mm movie images of crack growth were recorded. These cinematographic images provide clear histories of the crack-front interactions with the obstacles in each of the model specimens. Examples of typical images are reproduced in Figures 4.22 and 4.23, which show crack fronts trapped by Nylon and PC rods, respectively. These images are unaltered (but digitized) second generations of the original negatives; though the contrast in these reproductions is low, the bowed crack fronts are clearly apparent.

Digitization of images affords the opportunity not only to enhance image quality, by adjusting the contrast and intensity of selected pixel types, but also enables precise quantification of selected groups of pixels. Digitized reproductions of excerpted frames from the testing of a typical specimen with Nylon rods are shown in Figure 4.24. These sequential images give direct evidence for the complete evolution of the crack-trapping mechanism, from the initial "pinning" of the crack faces to the final breakaway configuration and transition to bridging, once the crack front has gone around the obstacles and has left them behind. Similar images obtained with specimens containing PC rods and spheres are shown in Figures 4.25, 4.26, and 4.27. Included in these figures are the digitally enhanced portions of the original images, which were used to determine the area swept out by the crack fronts as they advanced past the obstacles.

The load data were registered with the movie images by utilizing the data acquisition rate, the filming frame rate, and correlated starting positions. As a result, the applied load is known corresponding to all of the images of crack growth and interaction with obstacles. Through the method explained in the next section, these data are used to compute the toughening induced by crack-trapping.

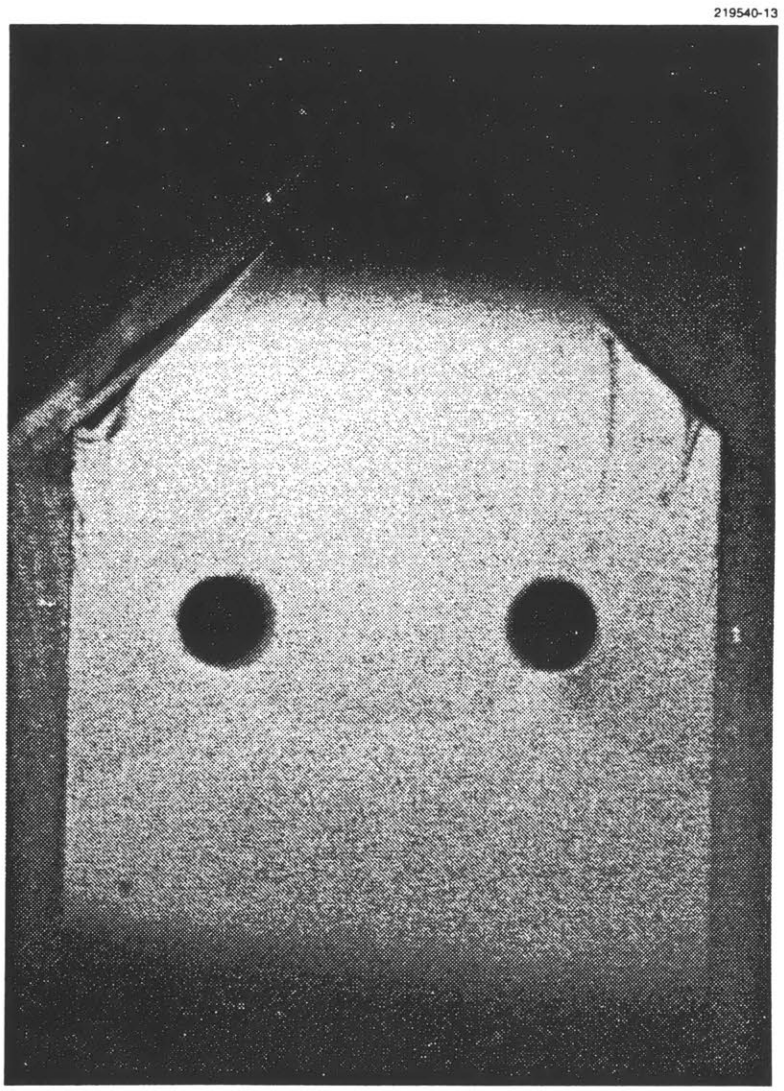

Figure 4.22: Typical 16-mm film image obtained at a frame rate of 24 fps during crack-trapping experiments. Un-retouched (not digitally enhanced) image of trapping by Nylon rods.

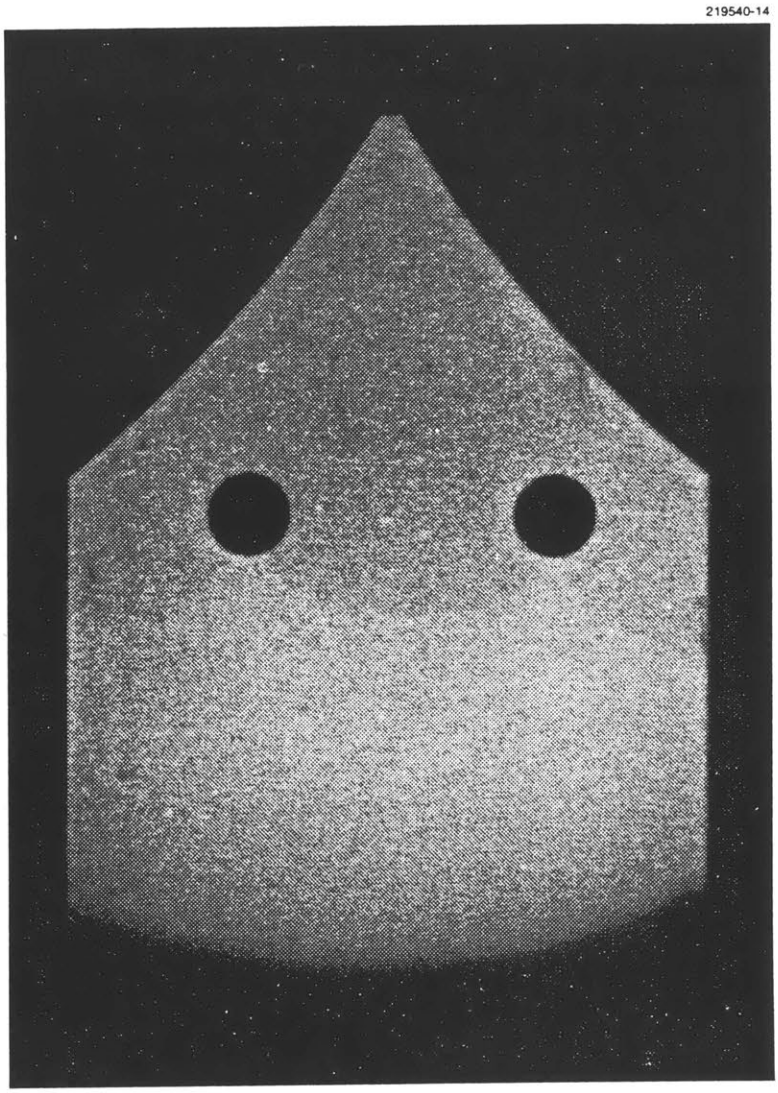

Figure 4.23: Typical 16-mm film image obtained at a frame rate of 24 fps during crack-trapping experiments. Un-retouched (not digitally enhanced) image of trapping by PC spheres.

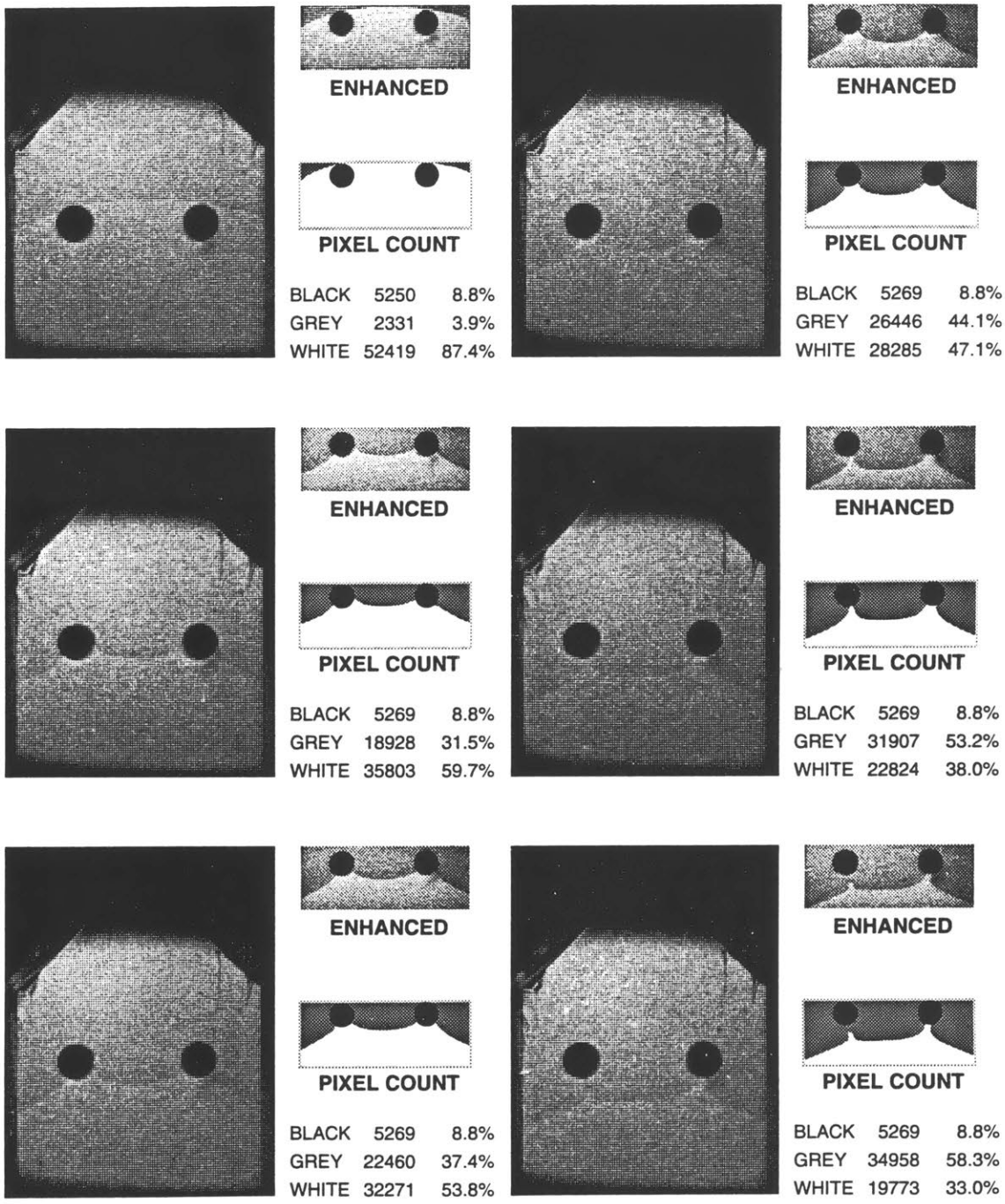

Figure 4.24: Digitized images from 16-mm film, showing trapping of crack in epoxy by 3.17-mm Nylon rods. Histograms of pixels enable areas swept by local crack fronts to be determined. Obstacle spacing, R/L = 0.125.

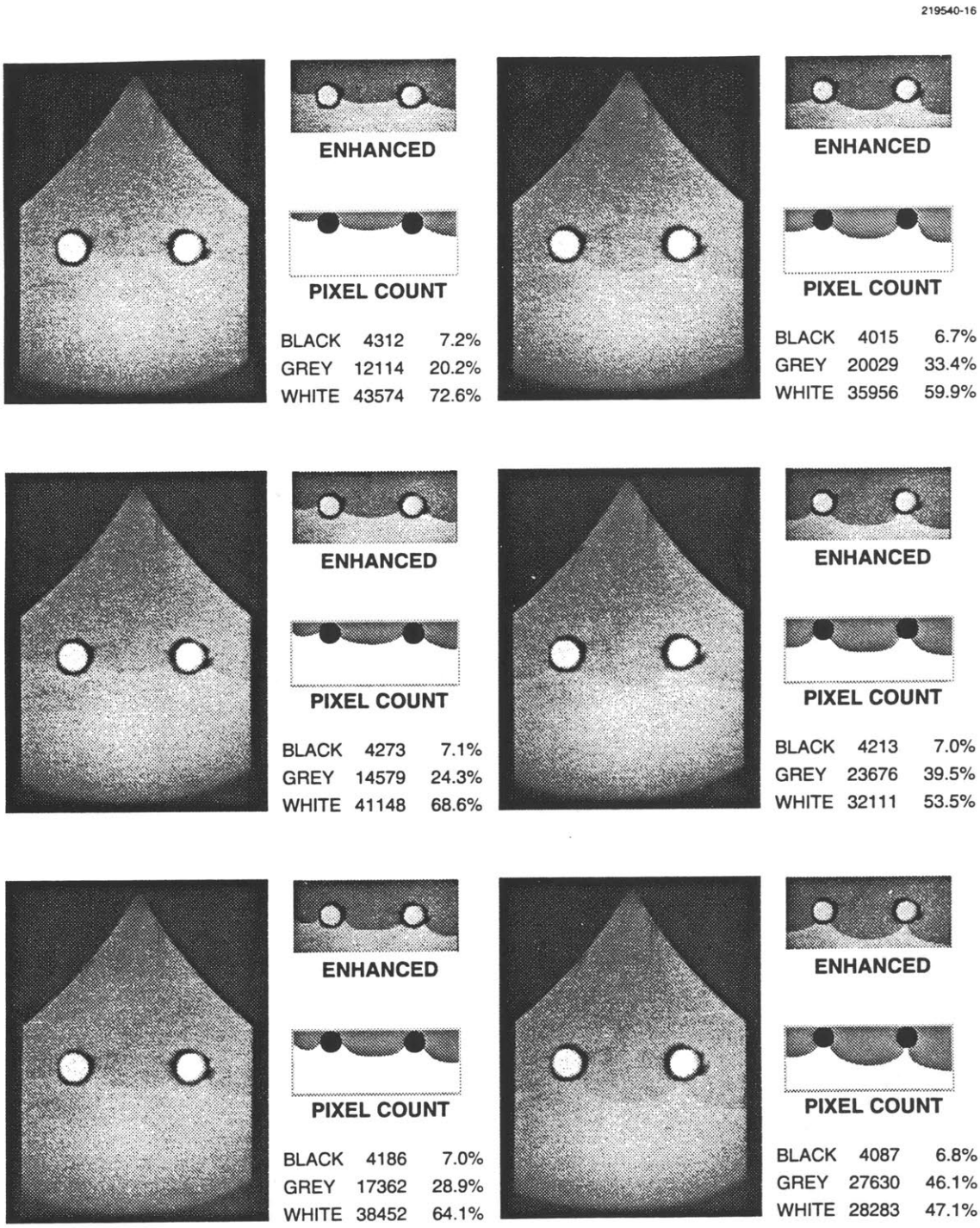

Figure 4.25: Digitized images from 16-mm film, showing trapping of crack in epoxy by 3.17-mm PC rods. Histograms of pixels enable areas swept by local crack fronts to be determined. Obstacle spacing, R/L = 0.125.

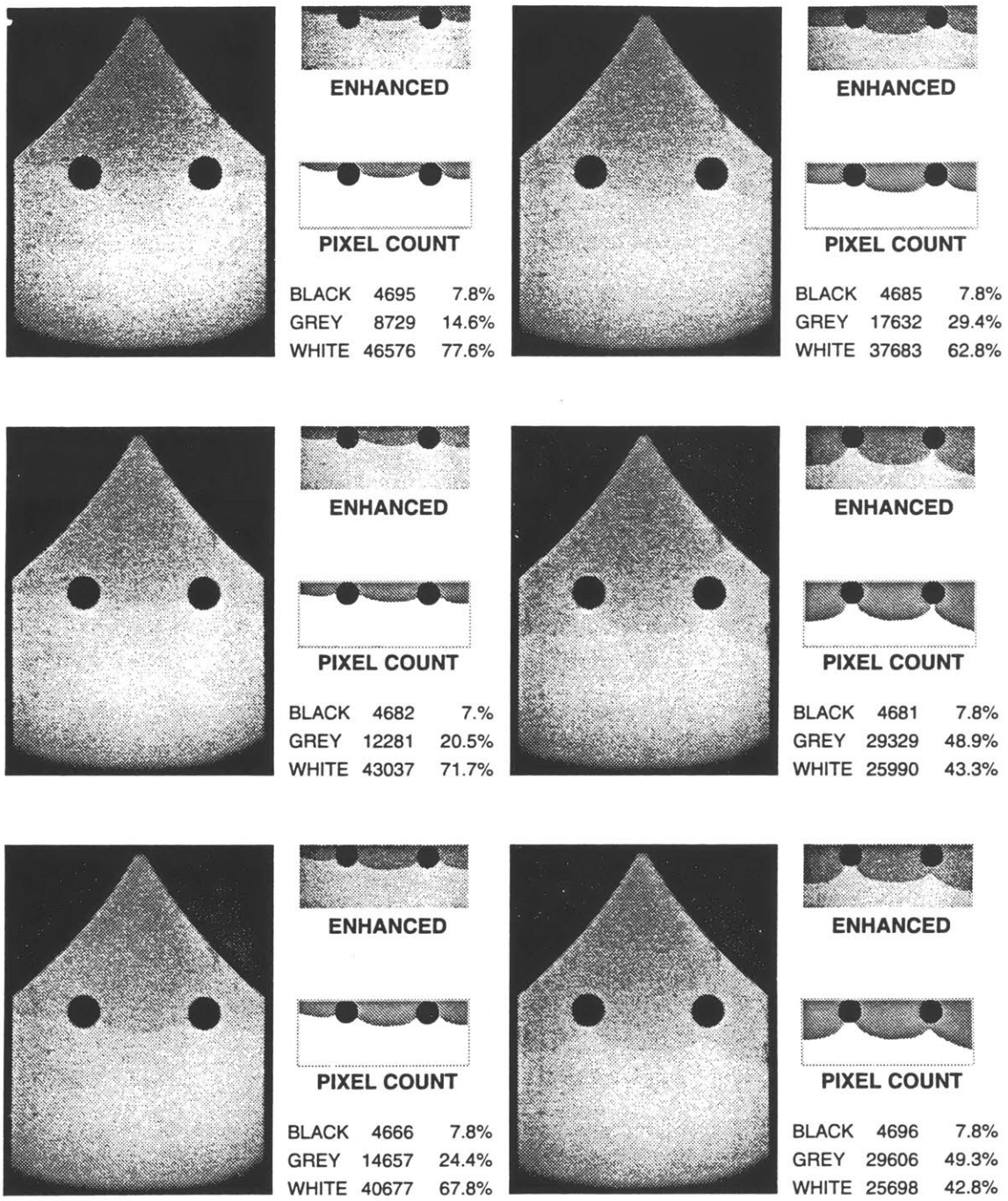

Figure 4.26: Digitized images from 16-mm film, showing trapping of crack in epoxy by 3.17-mm PC spheres. Histograms of pixels enable areas swept by local crack fronts to be determined. Particle spacing, R/L = 0.125.

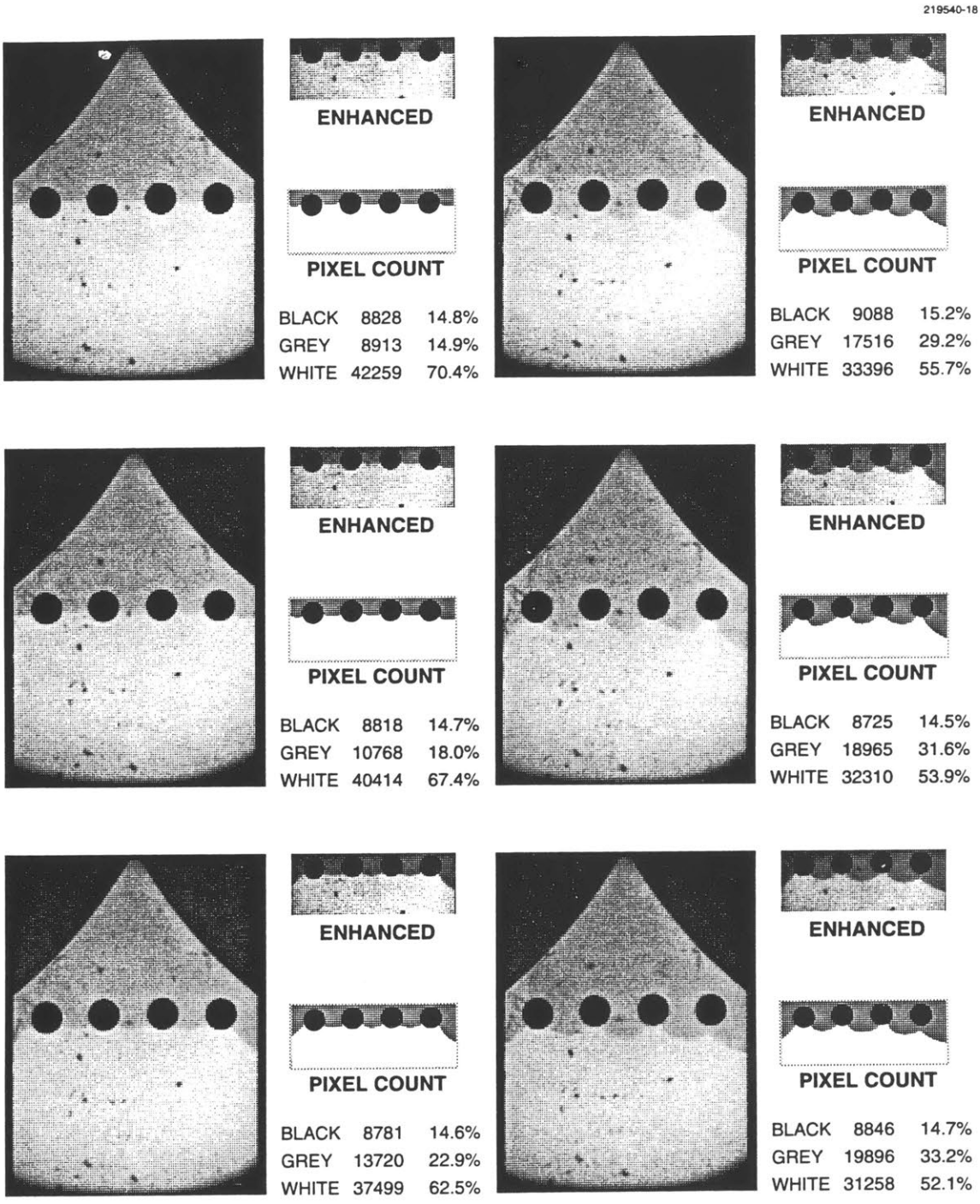

Figure 4.27: Digitized images from 16-mm film, showing trapping of crack in epoxy by 3.17-mm PC spheres. Histograms of pixels enable areas swept by local crack fronts to be determined. Particle spacing, $R/L \approx 0.250$.

4.2.4 Determination of Stress Intensity

In the interpretation of the results, the accurate determination of the elevation of stress intensity due to the crack-path obstacles in the specific DCB specimens requires taking note of the special features of the specimen and its mode of separation.

The simple beam theory solution does not account for shear deformations or the compliance of the "built-in" cantilever ends. (*c.f.* Eqn. A.26) A more exact analysis considering these problems was developed by Kanninen using the model of a beam resting upon an elastic foundation [53]. Kanninen's equation, which was derived for crack extension under conditions of constant opening displacement, becomes

$$K_I = \left(\frac{P\,a}{1-\nu^2}\right)\left(\frac{12}{B^2\,h^3}\right)^{1/2}\Psi\,, \tag{4.1}$$

where the correction term, Ψ, is a function of the ratio of ligament length to beam height and is not reproduced here; its minor influence in these experiments is explained below. Following convention, P represents the applied load, B and h are the beam width and height, and a is the crack length.

Although the application of Equation 4.1 to data obtained from fracture in the neat portions of the DCB specimens results in K_{Ic} values which are in exact agreement with the value (0.5 MPa$\sqrt{\text{m}}$, at -60°C) obtained from the TDCB fracture tests (discussed in Appendix A), a procedure was adopted to eliminate the effects of minor specimen-to-specimen differences. The toughness enhancements due to trapping of the crack-front by tough particles were determined by the ratio

$$\left(\frac{K_I^{\infty}}{K_{I_c}^{\text{matr}}}\right) = \frac{P\,a\,\Psi}{P_{\text{o}}\,a_{\text{o}}\,\Psi_{\text{o}}}\,, \tag{4.2}$$

where the numerator is evaluated throughout the crack-growth experiment, while the denominator is evaluated at the point where the crack just reaches the obstacles. The validity of this approach is now explained.

Stable crack growth in homogeneous materials progresses at a constant stress intensity in the absence of dynamic effects and inelastic deformations. Restated, since K_{Ic} is uniform throughout a homogeneous material, the driving force causing stable crack growth in a homogeneous material must remain constant. Hence, in the DCB specimens used here, Equation 4.1 should remain constant over portions of specimens in which no crack/particle interaction takes place. In the absence of end effects, the apparent condition is simply that the product $P \cdot a$ equals a constant.

To assess the validity of this representation of crack driving force in the crack-trapping specimens, two specimens *without obstacles* were tested to measure the variation in $P \cdot a$ during crack growth over the lengths corresponding to particle positions in the composite model specimens. In Figure 4.28(a), it may be seen that $P \cdot a$ during crack growth in neat specimens remained nearly constant in comparison to the increase in $P \cdot a$ due to crack-trapping in typical specimens containing obstacles. If we now account for possible end effects, modification of $P \cdot a$ by the correction term Ψ is shown in Figure 4.28(b) to have a relatively minor, but beneficial, influence upon representing a constant fracture toughness during crack extension in the neat specimens. Because the product '$Pa\Psi$' is seen to be constant during neat matrix fracture over the region of crack length where cracks interact with obstacles in the crack-trapping specimens, the use of Equation 4.2 is an accurate approach.

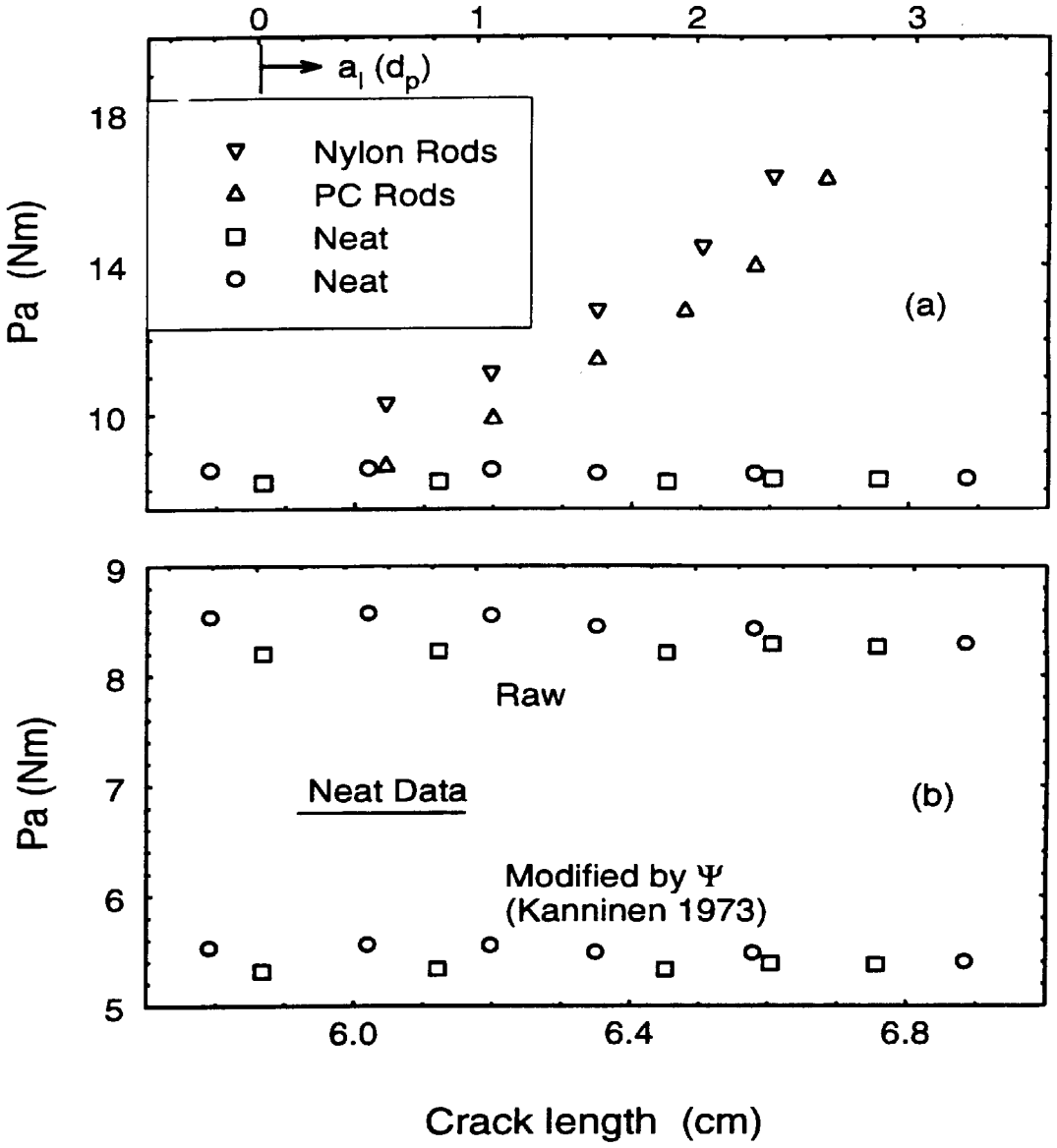

Figure 4.28: Experimental evidence for assuming $P \cdot a \propto K_I^{\infty}$: a) Comparison of $P \cdot a$ determined from neat specimens *vs.* typical specimens containing obstacles. b) Effect of modifying $P \cdot a$ in neat specimens by correction factor, Ψ, to account for shear deformations and rotation of cantilever ends.

Chapter 5

Crack-Trapping Results

This chapter presents the principal results obtained from the crack-trapping experiments. The influence of residual stress and adhesion upon crack interaction with obstacles is qualitatively described. Analysis of crack images is detailed, including comparison of bowed crack-front shapes with numerical predictions provided by Profs. Bower & Ortiz of Brown University. The peak value of trapping-induced toughness is determined as a function of particle spacing, and is compared to analytical models. It is emphasized here that the model matrix material does not craze or microcrack and was truly brittle at the test temperature of $-60°$C: the calculated plane-strain plastic zone size ($r_p \approx (K_{Ic}/\sigma_y)^2/6\pi$) is less than one μm. Consequently, toughening by local plastic flow or any mechanism other than crack trapping was inconsequential in the model specimens.

5.1 Effects of Residual Stresses

5.1.1 Influence of Residual Stresses on Crack Growth

Residual (thermal) stress values near the inclusions in the crack-trapping specimens are calculated in Appendix C and were summarized in Table 3.3. Though the magnitude of residual thermal stresses in the vicinity of the obstacles in the model specimens was quite small in comparison to crack-tip stresses, their effect upon crack growth was noticeable and qualitatively predictable. The compressive longitudinal stress (-0.4 MPa) in the epoxy adjacent to the Nylon rods caused a slight retardation in the rate of crack growth as the rods were approached. In contrast, the longitudinal tensile stress (0.7 MPa) near PC rods caused slight accelerations in crack growth. The effect of these stresses upon the shape of crack fronts approaching rods may be seen in the photographs reproduced in Figures 5.1 and 5.2.

In the case of spheres, the effect of residual stresses was more dramatic. With PC spheres, the tensile, tangential matrix stress (4 MPa) attracted approaching cracks to the sphere equators. In addition, the residual tension in the epoxy caused a very slight jump in the crack growth from a position about one half-radius away to the surface of the spheres. Thereafter, crack growth continued steadily. The combination of compressive tangential (-2 MPa) and tensile radial (4 MPa) stresses near the surface of Nylon spheres caused approaching cracks to spall away from the obstacles, so that no crack trapping was induced in these specimens.

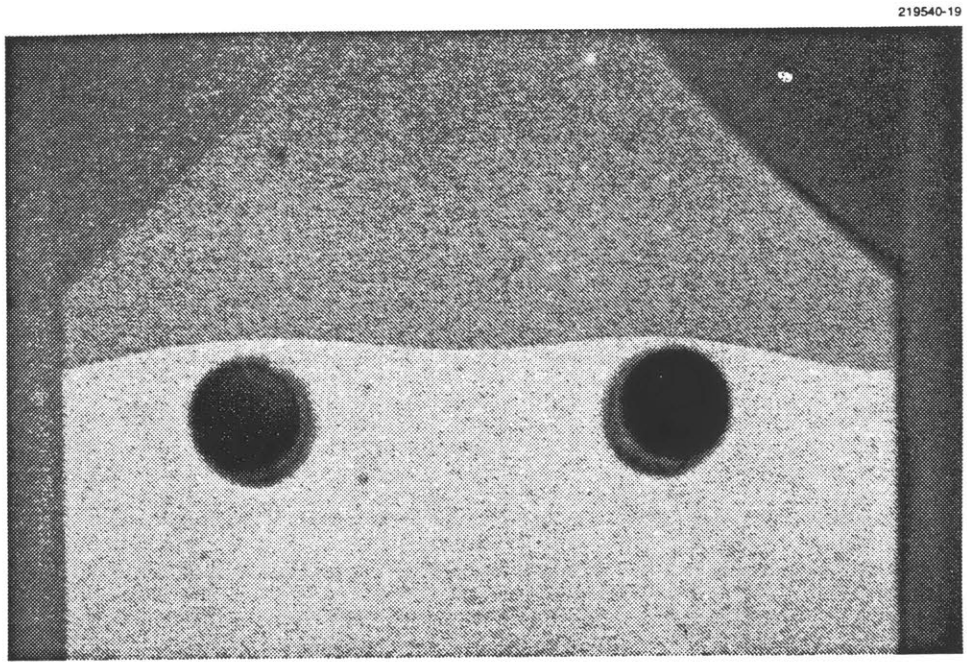

Figure 5.1: Example of slight retardation of crack growth due to compressive residual (axial) stresses near Nylon rods.

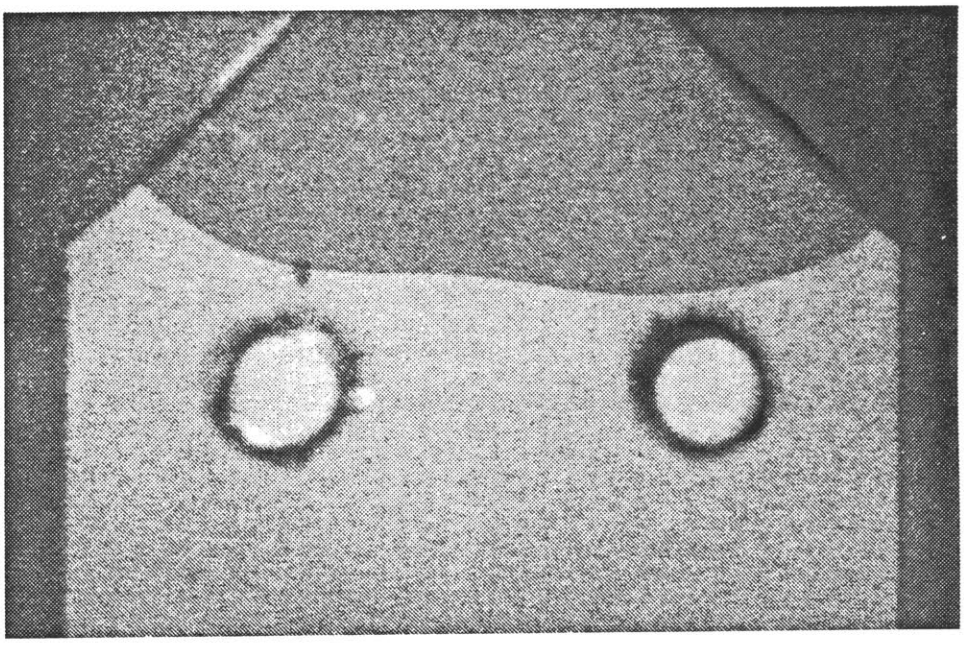

Figure 5.2: Example of slight attraction of crack growth into tensile residual (axial) stress fields surrounding PC rods.

5.1.2 Residual Stresses in Determination of Stress Intensity

Residual stresses can affect the remote loading necessary to propagate a crack in structures or test specimens. When a crack tip begins to separate material which is in a state of residual compression, a higher applied load will be required to continue crack extension than would be the case if no residual stresses were present. In particulate or fiber-reinforced materials, a compressive residual matrix stress can impart a toughness enhancement of 10–50% and has been regarded as a toughening mechanism in and of itself [54]. A more precise view would consider the compressive stress as an agent that *enables mechanisms*, such as deflection or trapping, to occur.

In the model specimens tested here, residual stresses affected the applied load required to advance cracks past the trapping obstacles. The magnitude of this effect was small: the load corresponding to crack extension to the leading edge of Nylon rods was about 6% greater than the load corresponding to similar extensions in specimens containing no obstacles; residual tensile stresses near PC rods effected a reduction in load by about 12% . Though no mechanism other than crack trapping was operative, the effect of residual stresses upon crack-tip stress intensity must be analytically eliminated to enable the accurate determination of toughness induced by crack trapping alone. The procedure which was employed is now explained.

Linear elastic crack-tip fields are assumed, substantiated by the small scale yielding previously related, so that the superposition of stress intensity is invoked as

$$K^{\text{tip}} = K^{\infty} + K^{\sigma_{\text{res}}} \quad . \tag{5.1}$$

This expression is evaluated by approximating the stress intensity created by residual stress, $K^{\sigma_{\text{res}}}$, as proportional to the difference in applied load between specimens with obstacles and those without, at crack extensions corresponding to the leading edge of obstacles. Thus it is conceived that an effective load experienced by the crack tip, P^{tip}, is equal to the sum of the current loading, P, and the difference between applied

load with and without residual stresses. This approximation is written as

$$P^{tip} \approx P + \left(P_o^{\sigma_{res}=0} - P_o^{\sigma_{res}} \right) \ , \tag{5.2}$$

where the subscript circle indicates evaluation at the crack length corresponding to particle contact. This procedure evaluates the effect upon load (and crack tip) of residual stresses when cracks just reach the obstacles, and implicitly assumes this effect remains constant during continued crack growth. This is not the case in reality; as more of the residual stress field is intersected by the crack front, the effects will become proportionally greater. Nonetheless, because residual stress effects in the model specimens were relatively minor (of order 10%), changes in their representation should be of second order.

Incorporating the effect of residual stresses through the preceding logic, Equation 4.2 is modified so that the stress intensity established by the trapping mechanism in the model specimens is determined by

$$\left(\frac{K_I^{trap}}{K_{I_c}^{matr}} \right) = \frac{\left[P + \left(P_o^{\sigma_{res}=0} - P_o^{\sigma_{res}} \right) \right] a \, \Psi}{P_o^{\sigma_{res}=0} \, a_o \, \Psi_o} \ . \tag{5.3}$$

5.2 Effects of Adhesion

Crack trapping by Nylon rods was accompanied by limited, albeit steady, debonding (fracture) of the Nylon/epoxy interface, which has a measured adhesive strength of about 31 MPa. The process of debonding and interfacial separation was recorded by the upper camera as a bright area growing from the point of crack contact, along the interface to a distance of approximately one rod diameter. Examples of debonding in specimens containing Nylon rods are shown in Figure 5.3. These images show the initial debonding, when cracks just contact the Nylon rods, and the full extent of debonding when the maximum trapping is reached. Though the crack faces remain "pinned" at the trailing edges of the obstacles (as seen in the crack-front images), the action of the partial debonding is to reduce the effective R/L and thus diminish the toughening from the levels that would be achieved with "perfect" bonding.

In contrast, apparently perfect bonding was exhibited by the specimens containing polycarbonate rods. The measured adhesive strength of >54 MPa was sufficient to prevent debonding from occurring in any of the tests, even after the crack front had reached the breakaway configuration and passed beyond the PC rods. Continued loading of these specimens produced ring cracks in the epoxy below the main fracture surface at a depth of approximately one rod-radius; ultimately, fracture of the PC rods resulted with no evidence of debonding or fracture of the PC/epoxy interface. Reduction of the PC/epoxy adhesive strength to about 28 MPa, by treating the rod surfaces with a release agent, did not enable any debonding to occur. Further reduction, by a second coat, to about 22 MPa still did not result in any debonding. No moderation in trapping-induced toughness resulted from reduced adhesion of PC rods. Evidently, the *toughness* of the PC/epoxy interfaces remained high enough to prevent the probing cracks from prying open the interface. In contrast, the Nylon/epoxy interfacial toughness must be sufficiently lower to enable the limited debonding that developed in those specimens. (These observations are substantiated

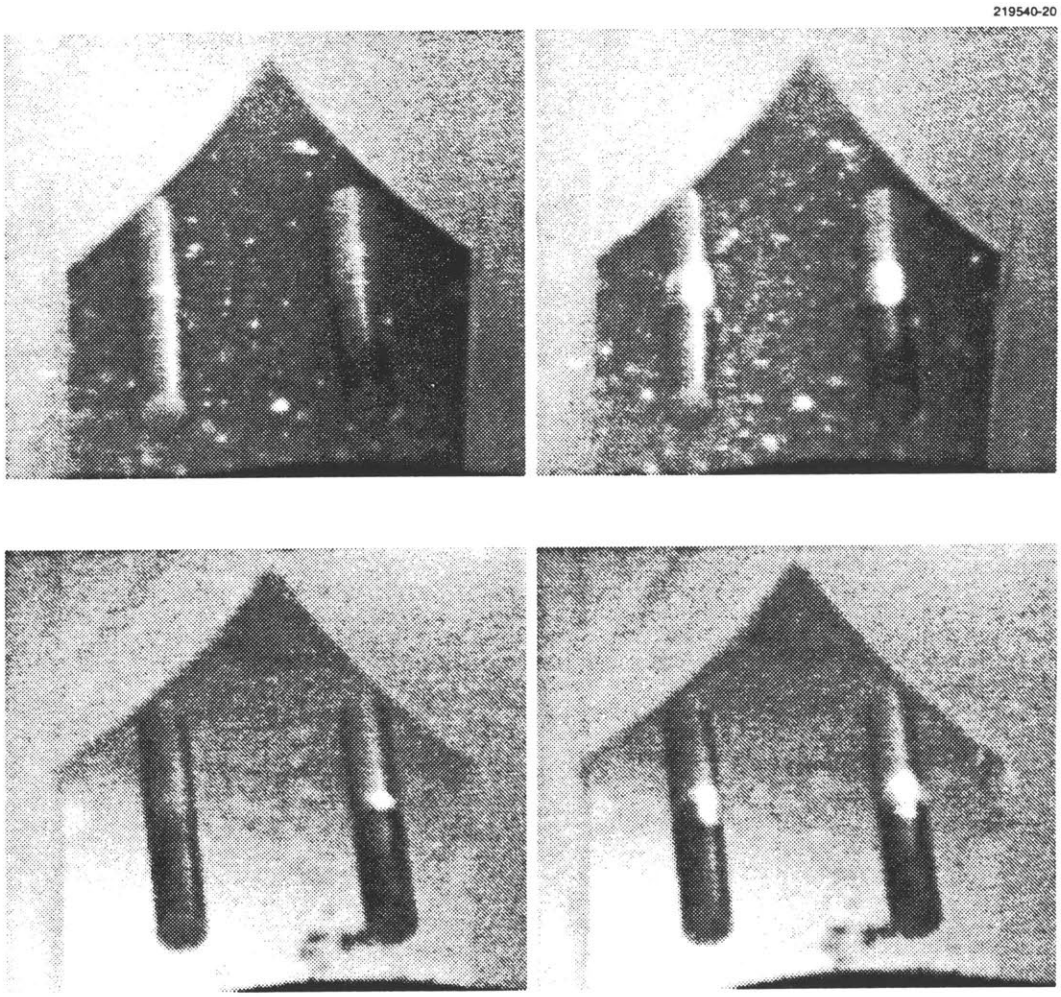

Figure 5.3: Two examples of limited debonding in specimens with Nylon rods. In the left photographs, the cracks (not seen at this angle) have made contact with the rods and debonding has just begun along the interface of one rod in each specimen. The right photographs correspond to the breakaway configuration of the crack front, and therefore indicate the maximum extent of interfacial separation accompanying crack trapping in specimens containing Nylon rods. Specks are patches of "snow" which have condensed upon specimen surfaces.

by measurements and analysis presented in Appendix B.)

No debonding was ever observed during crack trapping by PC spheres with full (>54 MPa) adhesion. When loading in these specimens was continued well beyond the point of breakaway from the trapping configuration, the PC spheres fractured with no indication of interfacial failure. PC spheres with adhesive strengths reduced to about 22 MPa were still able to trap advancing crack fronts, but to a diminished extent. The maximum toughening resulting from trapping by PC spheres with reduced adhesion was only about 15% of the toughening level attained with full adhesion.

A phenomenological explanation for the difference in trapping behavior observed as a function of adhesion with spherical *versus* cylindrical obstacles follows. When cracks encounter and are trapped by spherical obstacles, they begin probing the strength and toughness of the interface while commencing the bowing process. Any perturbation of the crack tip from the diameter of a spherical obstacle subjects the interface to an opening mode of stress intensity. Thus, at any time during additional remote loading, a crack front has the option of following whatever path offers the least *local* resistance over, around, or through the obstacles. When the obstacles are cylindrical, relatively little K_I is applied to the interface if it is perpendicular to the crack-growth direction, and the full level of trapping-induced toughness is easily reached.

5.3 Analysis of Crack-Trapping Images

5.3.1 Local Crack Shapes

5.3.1.1 Enhanced (digitized) images

Digitized images of crack-front shapes recorded during testing of four typical specimens are reproduced in Figures 5.4 to 5.7. These images have been enhanced to increase the contrast between the cracked and uncracked portions of the specimens, and to determine from pixel histograms the areas swept by the locally bowed cracks.

In the first series of images, it appears that the side-grooving and residual compressive stresses near the Nylon rods have combined to cause the center of the crack front to initially lag behind the edges. As the load increases, the crack becomes trapped by the tough obstacles and assumes a slightly bowed shape between them. With further loading, the bowed front becomes elliptical, eventually extending outward a full diameter past the obstacles while still remaining trapped. Finally, the local crack fronts grow to the extent that they attract each other and coalesce behind the obstacles. This entire process represents the evolution of toughening by crack-front trapping and the transition to crack-flank bridging.

In the remaining three series of images included here, similar crack-front histories are apparent from crack trapping by PC rods and spheres. In these images, however, the side-grooving does not tend to cause as severe an edge effect as in specimens with Nylon rods. In fact, prior to the highest levels of load, the edge cracks in specimens with PC obstacles behave as if image particles were present on either side. Since the side-grooving was identical in all specimens, this difference in behavior is attributed to the lower adhesive strength of the Nylon rods.

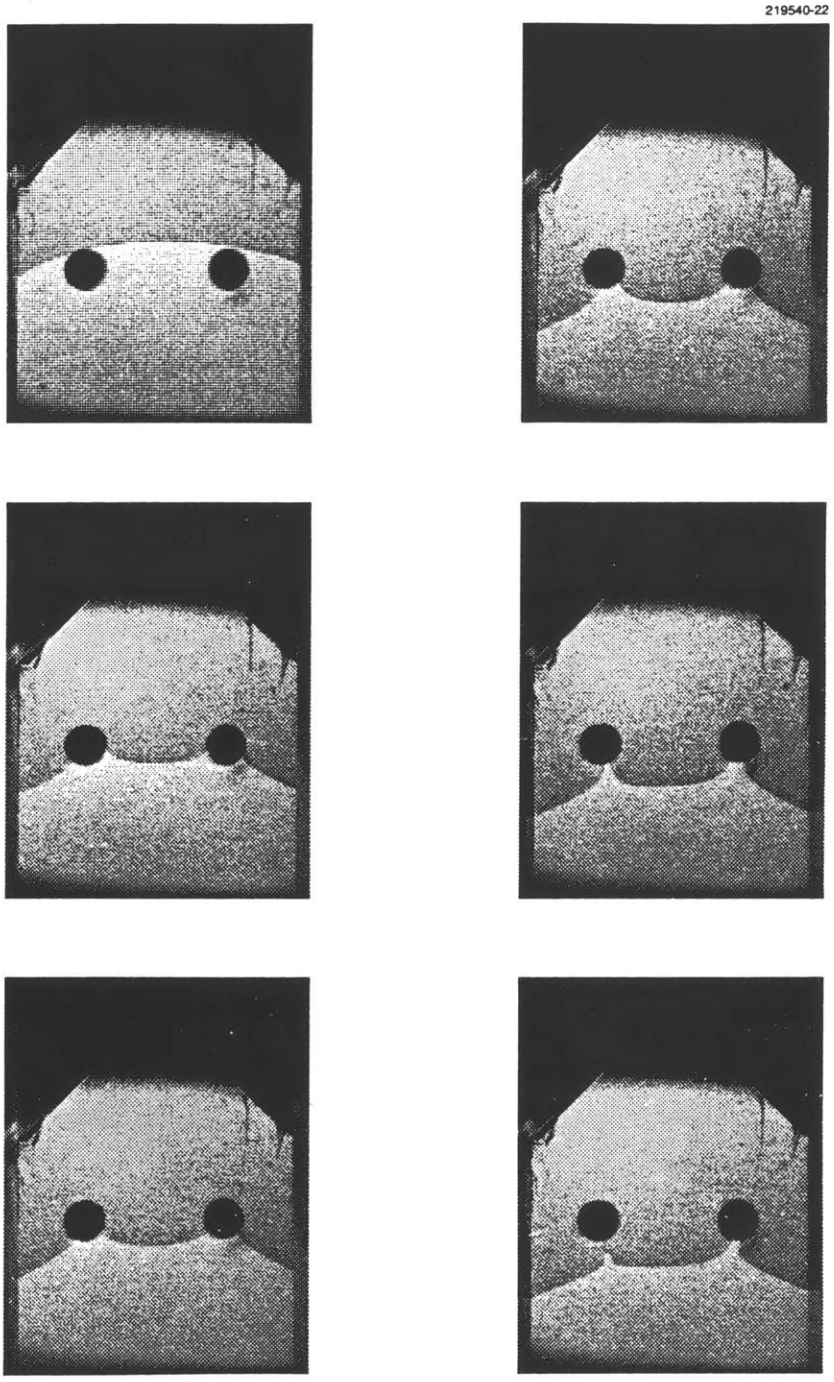

Figure 5.4: Enhanced, digitized images from 16-mm film, showing evolution of local bowing of brittle matrix crack past tough Nylon rods. $R/L = 0.125$.

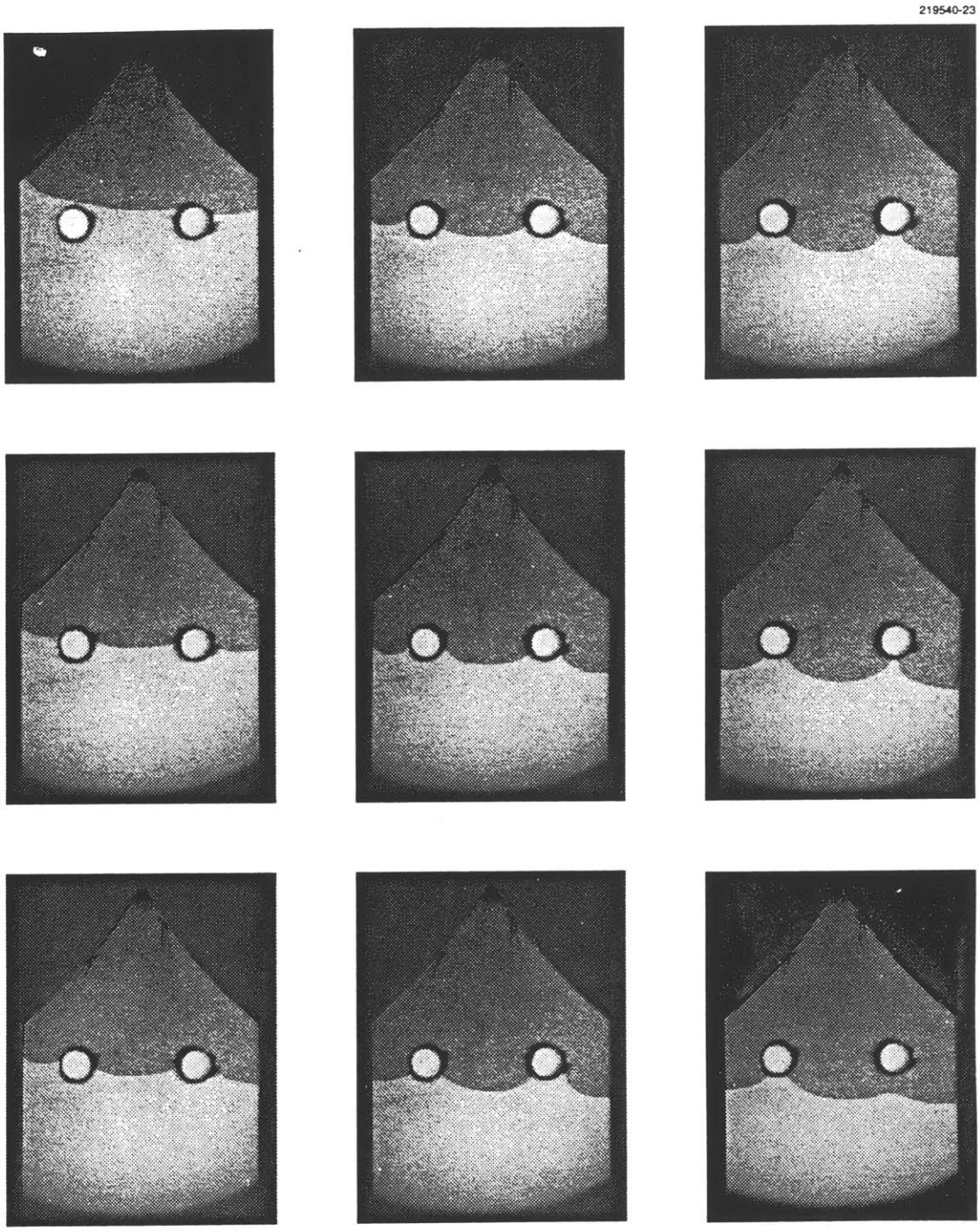

Figure 5.5: Enhanced, digitized images from 16-mm film, showing evolution of local bowing of brittle matrix crack past tough PC rods. $R/L = 0.125$

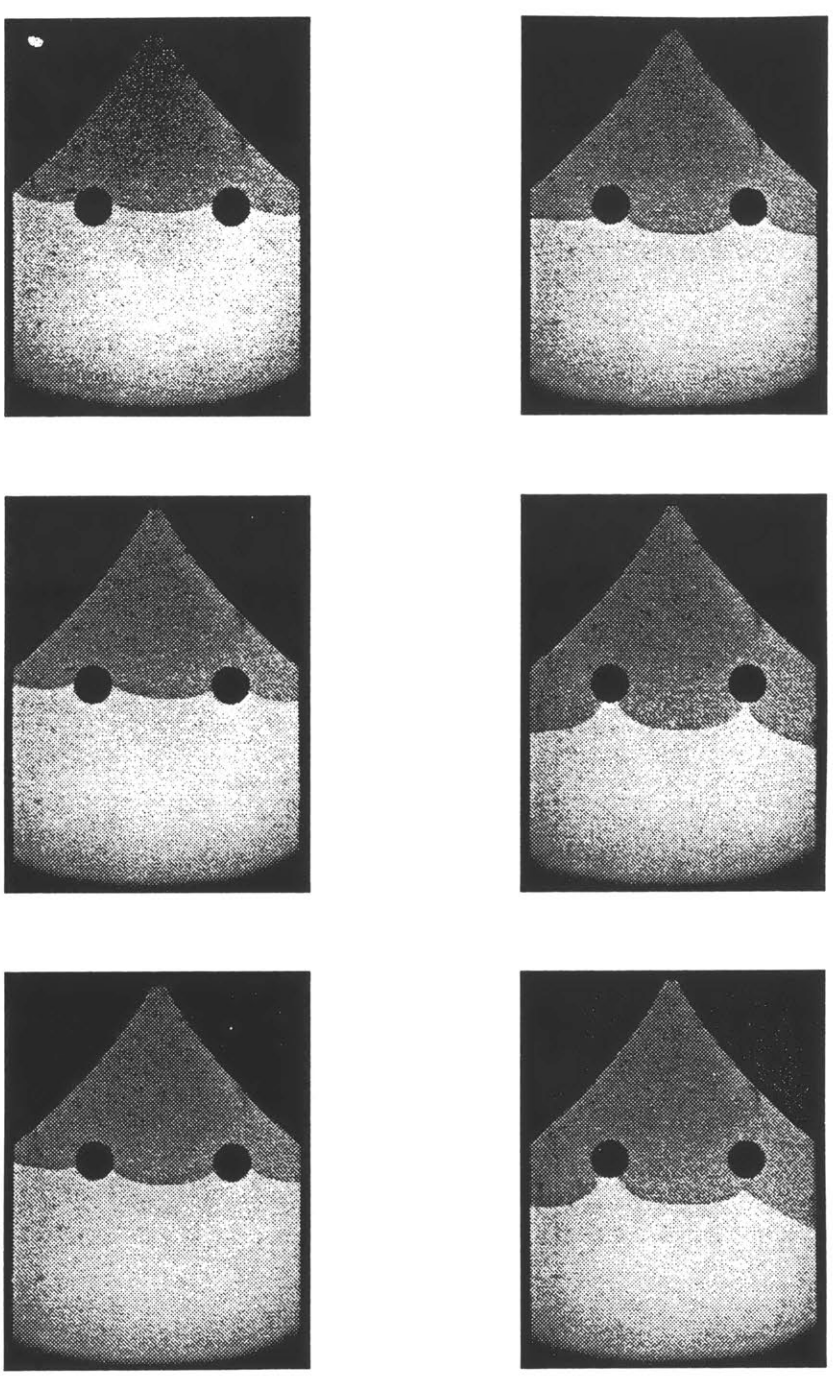

Figure 5.6: Enhanced, digitized images from 16-mm film, showing evolution of local bowing of brittle matrix crack past tough PC spheres. $R/L = 0.125$.

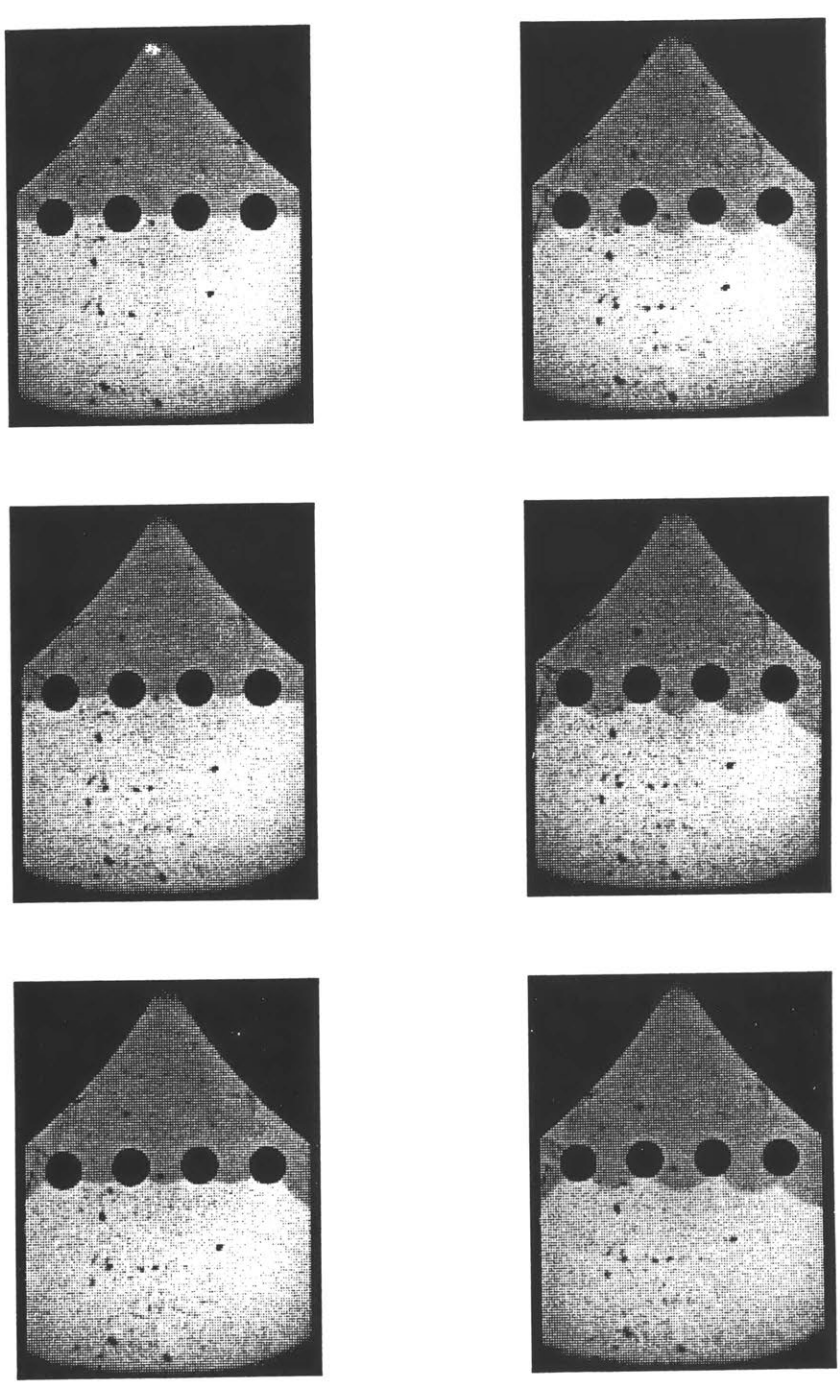

Figure 5.7: Enhanced, digitized images from 16-mm film, showing evolution of local bowing of brittle matrix crack past tough PC spheres. $R/L \approx 0.250$.

5.3.1.2 Breakaway configurations

The shapes of local crack fronts just prior to "escape" from the trapping obstacles in all cases are elliptical, with a maximum penetration of approximately two particle diameters. Therefore, when characterized in terms of the particle center-to-center spacing, L, the breakaway configurations reach a maximum penetration which varies quite linearly with particle spacing, as illustrated by the data plotted in Figure 5.8.

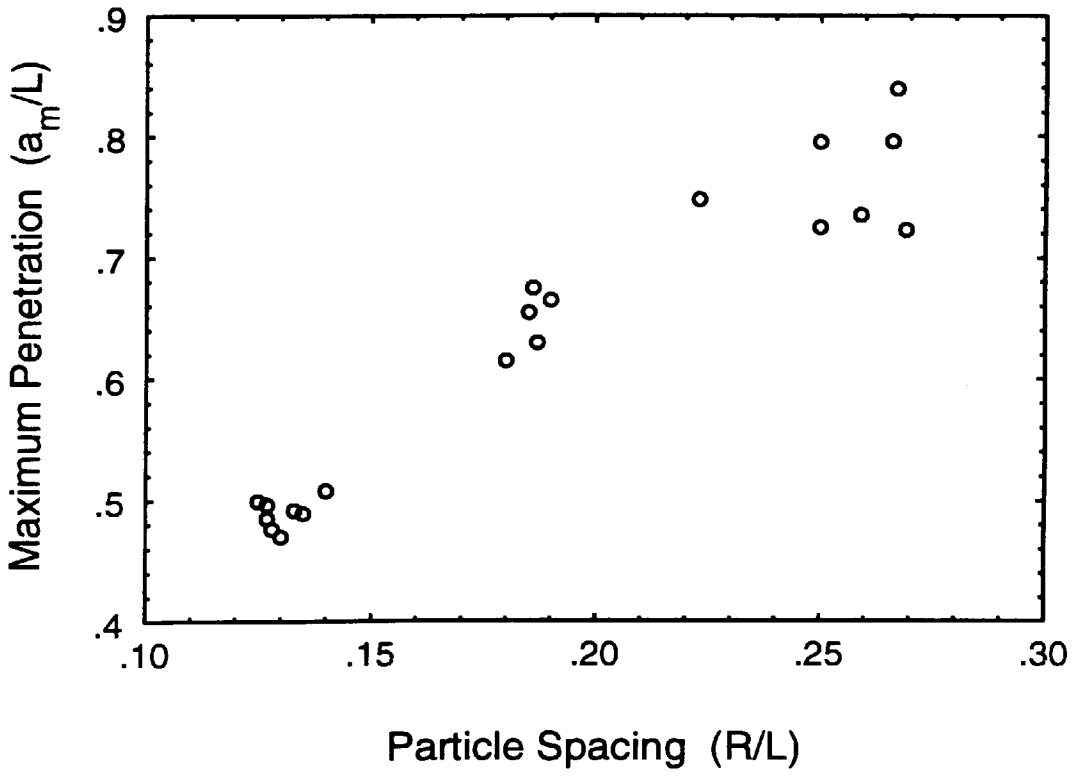

Figure 5.8: Maximum penetration reached by local crack front at breakaway from trapping configuration, as a function of particle spacing.

5.3.1.3 Transition to Bridging

After a crack front has passed obstructing particles and broken free from the trapping configuration, the particles will continue to carry traction if they remain intact and well bonded to the matrix. This traction exerts a negative stress intensity on the crack tip, effectively increasing the overall material fracture toughness. The chief action of bridging forces, however, is to dissipate energy as the crack flanks separate. In a continuum approach which assumes that discrete bridging forces are uniformly "smeared" across the crack face, the contribution of bridging work to the fracture energy, per unit area of crack face, is given simply as [55]

$$\Delta G = f \int_0^{u_c} \sigma(u)\, du \ , \tag{5.4}$$

where f is the area fraction of bridging material with a characteristic stress-separation function, $\sigma(u)$, which vanishes at the critical separation, u_c. The determination of $\sigma(u)$ under conditions of 3-D constraint [56] has led to predictions [57] of increased fracture toughness (K_{Ic}) by up to a factor of six in lead-particle reinforced glass. Moreover, enhancement of energy release rate ($\mathcal{G}_c$) by as much as a factor of sixty has been reported due to addition of particles of aluminum in a brittle glass [58].

The representation of the contribution to fracture energy made by bridging, given by Equation 5.4, indicates that little or no such contribution can be made during the process of crack trapping because the crack faces remain pinned at particle peripheries; du at a given pinning particle remains negligible until the crack front escapes it. Obstacles left intact and fully bonded after the crack front has passed may begin to flow plastically, or in the case of fibers, develop slippage between the fiber and the matrix. Additionally, the coalescing local crack fronts may rejoin from fracture planes at different elevations, thus forming ridges or "tails" behind the particles.[1]

[1]These features are often the only obvious evidence left on a fracture surface which indicates that crack trapping was involved in the fracture process. Fractographs showing tails were included in Chapter 4.

Images showing tails generated in a crack-trapping model specimen are reproduced in Figure 5.9. The transverse fractures evident in the second frame indicate that traction was carried by ledges, or ligaments, formed by the joining of the local cracks. The ligaments continued to carry traction even when they had extended to a length of approximately two particle diameters. This traction clearly reduced the local stress intensity, for the crack front seen in the first frame lags sharply behind at the ligament positions. Nonetheless, the contribution to fracture energy through bridging, made by these remnants of crack trapping, is expected to be negligible in materials whose matrix has a low tensile strain-to-failure. The additional surface area generated by these tails would increase the fracture energy by a small amount; this increase would vary linearly with volume fraction of second-phase particles and might account for improvements in energy release on the order of a few percent.

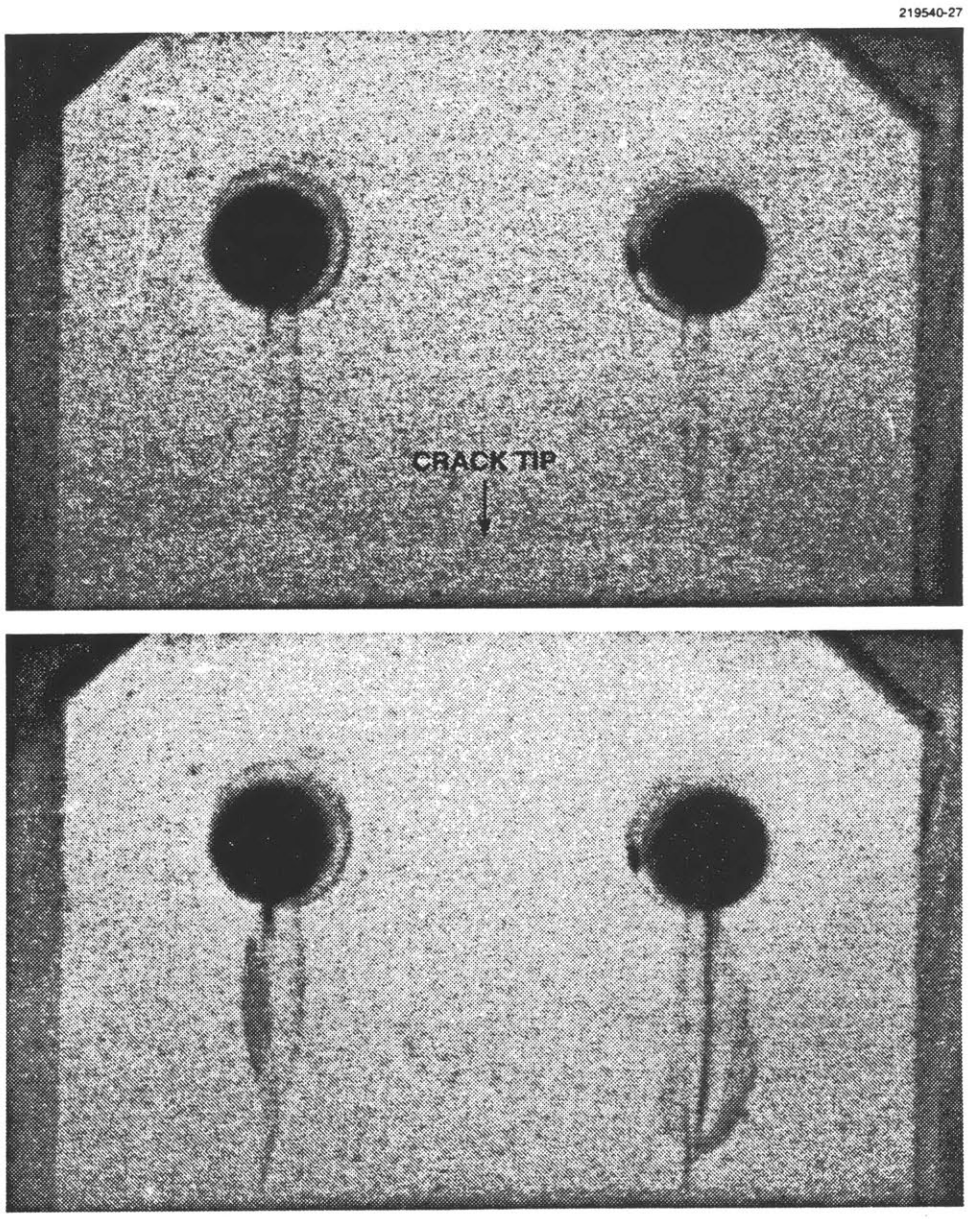

Figure 5.9: Example of tails generated by rejoining of trapped crack fronts at different elevations. The transverse fractures seen in the second (lower) frame indicate that traction was being carried by an intact ligament in the first frame.

5.3.2 Local Crack Penetration

Registration of the recorded crack-front images with the applied loading provides the magnitude of remote load corresponding to the crack configuration recorded in each image. The applied load and average crack length were identified for many sequential images obtained from each of the tested specimens. These parameters were then used, with Equation 5.3, to calculate the effective stress intensity corresponding to each of the crack-trapping configurations. This effective stress intensity, normalized by the matrix toughness, has the (minor) effects of residual stress removed and therefore represents the level of toughness enhancement produced by the evolving stages of crack trapping.

Shown in Figures 5.10 to 5.13 are enlarged reproductions of the images shown earlier, with corresponding values of $K_I^{\text{eff}}/K_{I_c}^{\text{matr}}$ indicated for each frame. Superimposed upon these images are crack-front profiles which are predicted by the numerical simulation developed by Bower & Ortiz [6], who kindly provided numerical data for the particle spacings used in these experiments [7]. In their model, the elastic properties of the matrix and of the trapping particles are taken to be equal, and the particles are assumed to be impenetrable and perfectly bonded to the matrix (though this condition may be relaxed). The computational procedure imposes the constraint of zero-opening displacement over the area representing particles, perturbs the crack so that it acquires the shape which corresponds to the fracture criterion being met along the front within the matrix, and then determines the remote toughening which results from the pressures required to maintain the constraint within the circular domains. As demonstrated by the figures, excellent agreement exists between the numerical predictions and actual crack shapes and penetration distances. In each series of images, nearly perfect matching of crack shapes is seen to persist at stress intensities up to about 70% of the maximum achieved prior to breakaway. Systematic trends in crack penetration as a function of effective stress intensity are discussed next.

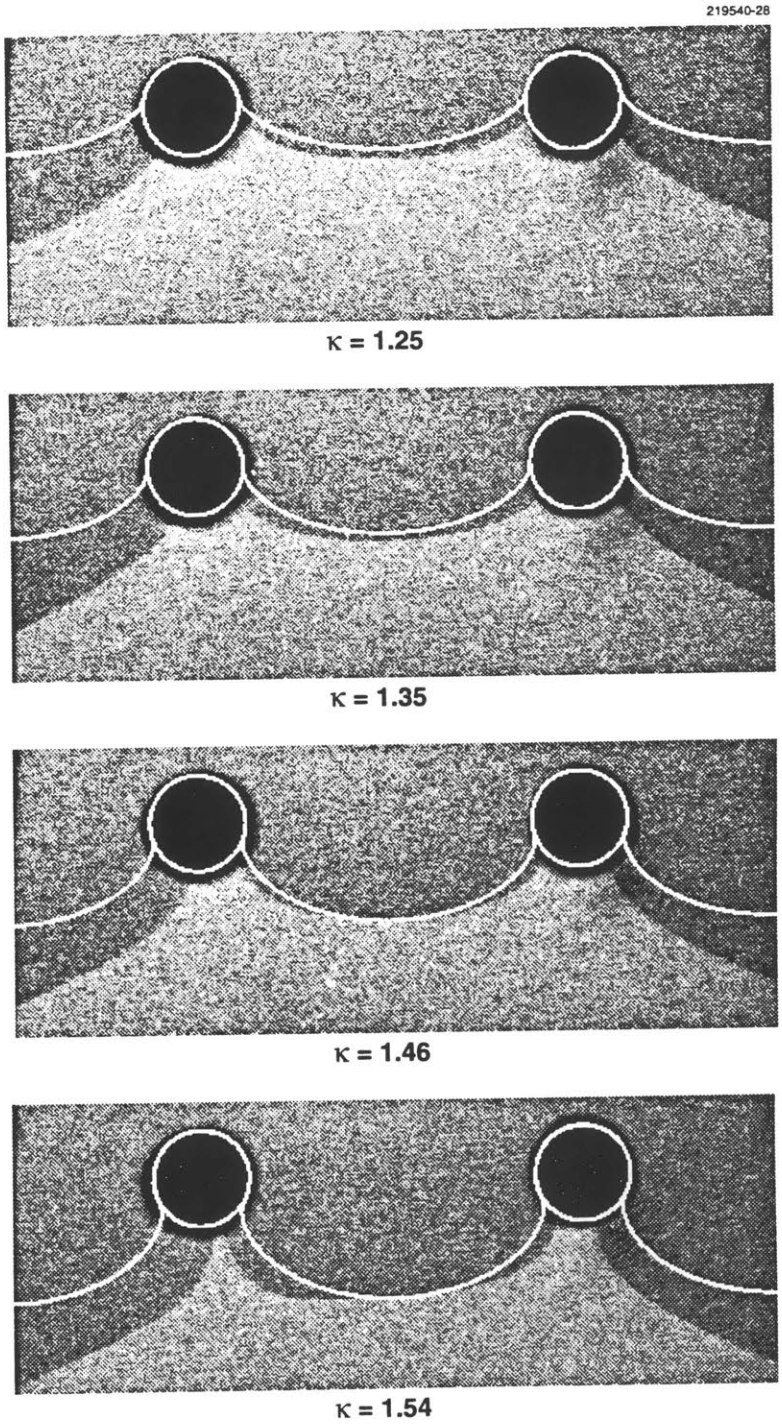

Figure 5.10: Superposition of crack-front profiles predicted by the Bower & Ortiz numerical model with digitized images of trapping in epoxy by Nylon rods. Effective crack-tip stress intensities are indicated by $\kappa = K_I^{eff.} / K_{Ic}^{mat.}$.

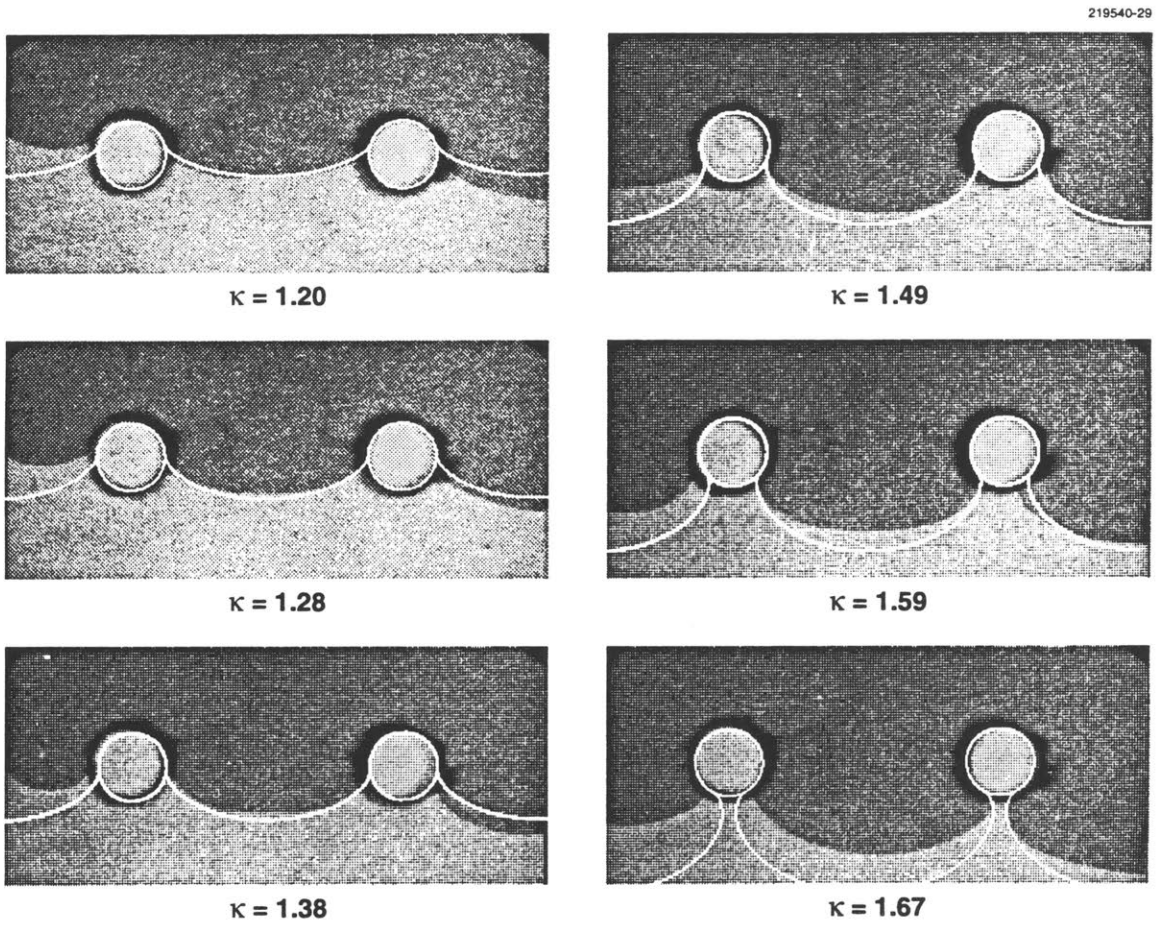

Figure 5.11: Superposition of crack-front profiles predicted by the Bower & Ortiz numerical model with digitized images of trapping in epoxy by PC rods. Effective crack-tip stress intensities are indicated by $\kappa = K_I^{eff.} / K_{Ic}^{mat.}$.

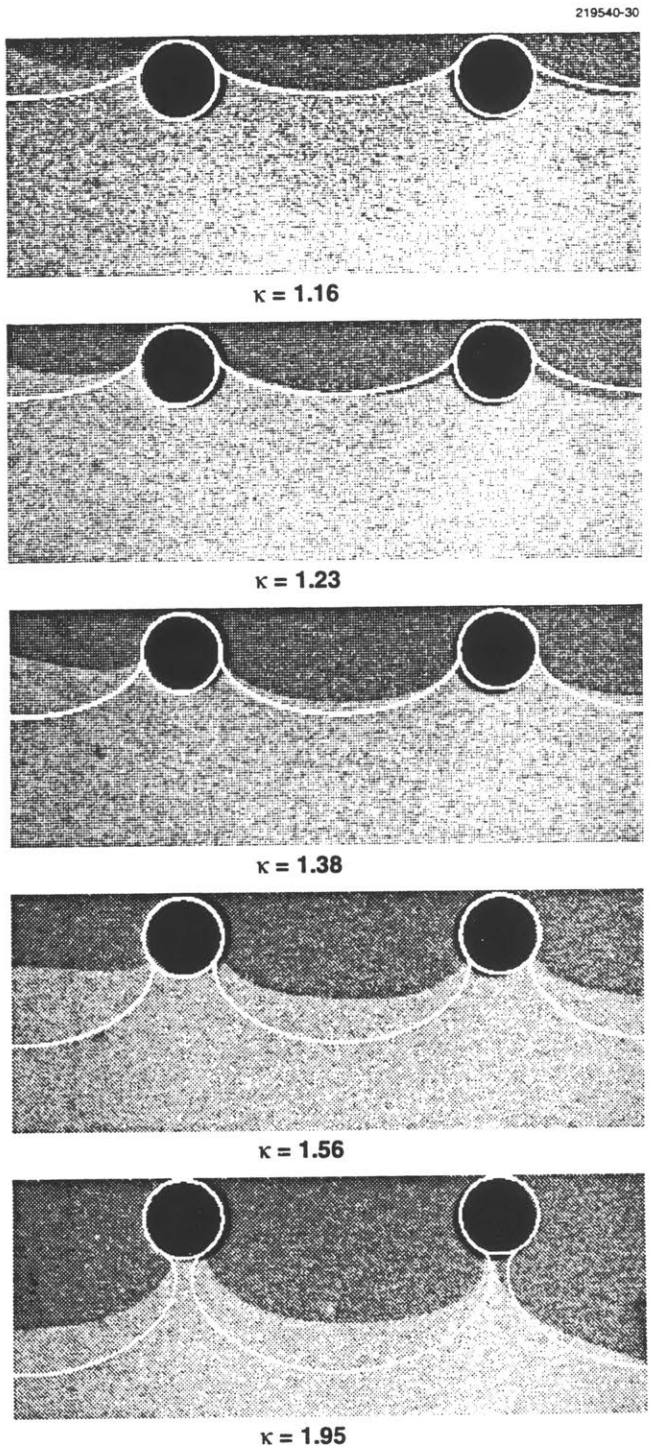

Figure 5.12: Superposition of crack-front profiles predicted by the Bower & Ortiz numerical model with digitized images of trapping in epoxy by PC spheres. Effective crack-tip stress intensities are indicated by $\kappa = K_I^{eff.} / K_{Ic}^{mat.}$.

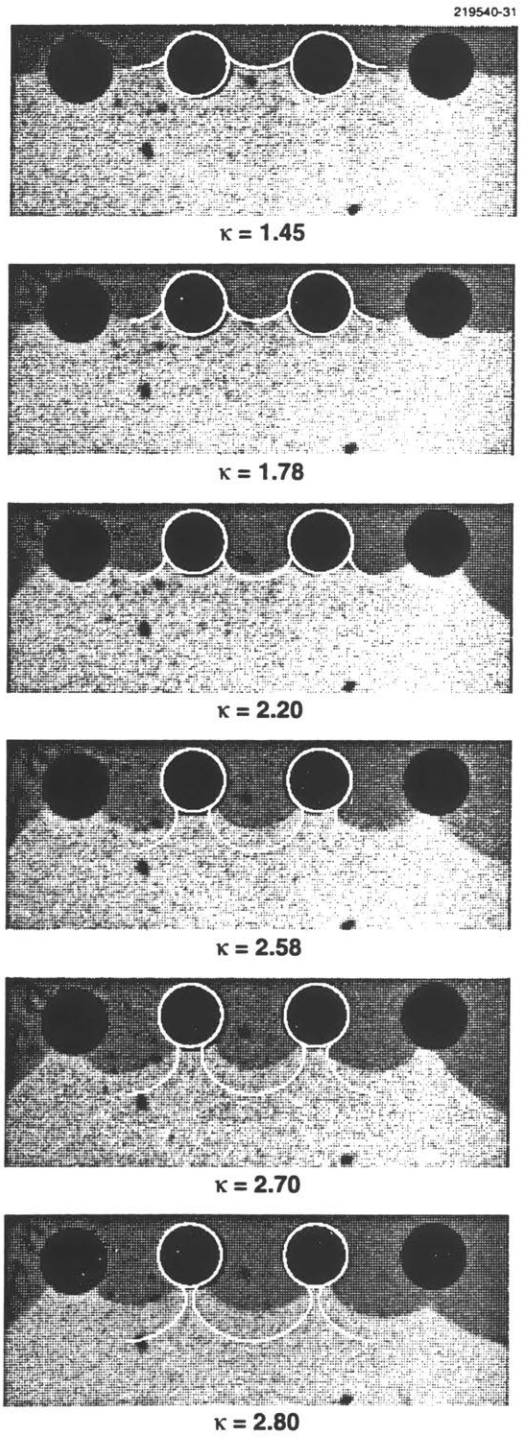

Figure 5.13: Superposition of crack-front profiles predicted by the Bower & Ortiz numerical model with digitized images of trapping in epoxy by PC spheres. Effective crack-tip stress intensities are indicated by $\kappa = K_I^{eff.} / K_{Ic}^{mat.}$.

The effective toughening due to crack trapping in specimens containing Nylon rods, at a spacing of $R/L = 0.125$, is plotted in Figure 5.14 as a function of local (bowed) crack advance, a_l. Included in this figure are the results from numerical simulations performed by Bower & Ortiz [6, 7], which assume perfect bonding between brittle matrix and tough particles with identical elastic properties. The data indicate that, at a given applied stress intensity, the local crack-fronts were able to advance slightly farther than the numerical model predicts. This advance was accompanied by the limited debonding of the Nylon/epoxy interface which was shown and discussed earlier. The crack-front images indicate that, in spite of this limited debonding, the crack faces remain "pinned" at the trailing edges of the obstacles. Nonetheless, comparison of the experimental data with the numerical predictions indicate that the action of the partial debonding is to reduce the effective R/L and thus diminish the toughening from the levels that would be achieved with "perfect" bonding.

Apparently perfect bonding was exhibited by the specimens containing polycarbonate rods. No debonding was ever observed in these specimens, and the effective toughening levels corresponding to local crack advances, shown in Figure 5.15, compare quite well with the numerical predictions up to the stages where the crack approaches the final breakaway configuration. At this point, the toughening observed in the model specimens begins to exceed the predictions by as much as 15%. The reasons for this discrepancy are not clear. Although the numerical method encounters an instability at the breakaway configuration, the discrepancy occurs well before that point. A likely explanation is that the numerical model is based upon a representation of an infinite array of particles, while the experimental data incorporate some finite-size effect which manifests itself at the highest load levels.

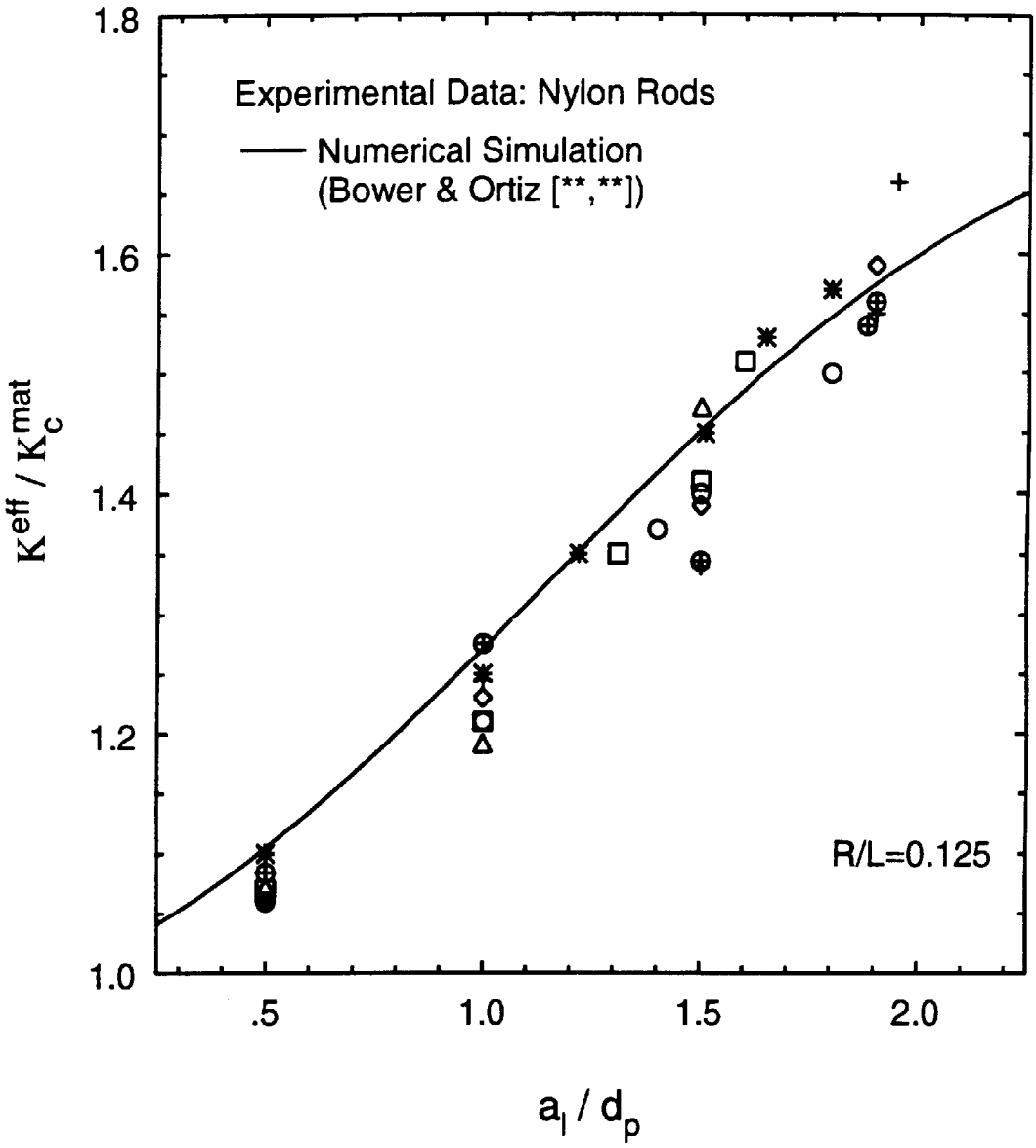

Figure 5.14: Effective toughening enhancement resulting from crack trapping by Nylon rods, as a function of local crack advance normalized by particle diameter in specimens with $R/L = 0.125$.

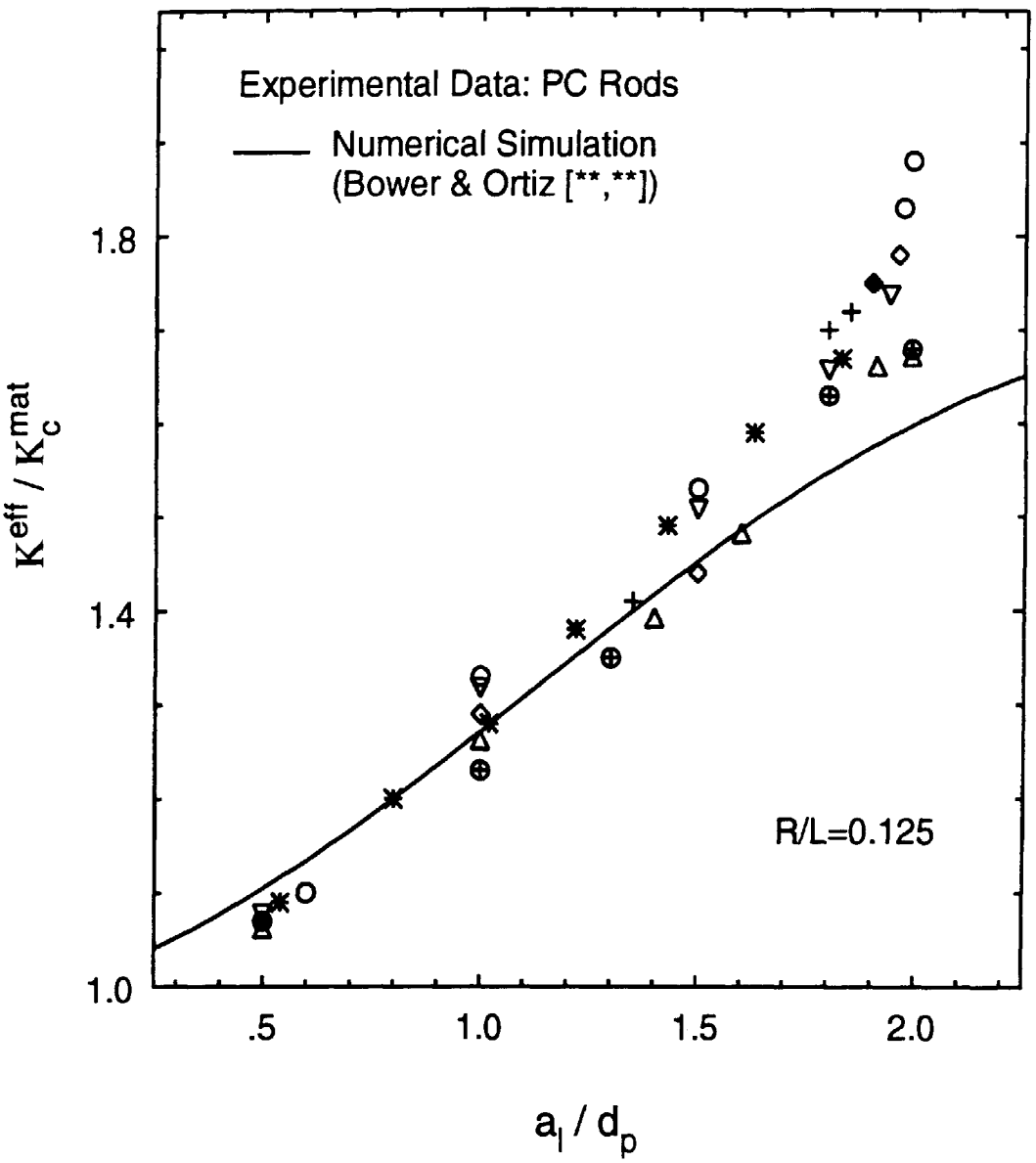

Figure 5.15: Effective toughening enhancement resulting from crack trapping by polycarbonate rods, as a function of farthest local crack advance (a_l) normalized by particle diameter, in specimens with $R/L = 0.125$.

It is difficult to conceive of a mechanism which would result in a higher load being required for a given crack advance than is predicted by the numerical model. Both plastic deformation of the trapping particles and debonding of interfaces would have the effect of relaxing the displacement constraint placed upon the crack faces at the periphery of particles; this effect, in turn, would reduce the applied load necessary to extend local crack fronts. The elastic moduli of the epoxy and the Nylon rods are nearly equal. The polycarbonate, however, has a modulus which (at the test temperature) is about 15% lower than that of the epoxy. Consequently, the matrix material near PC rods must share proportionately more of the crack-tip tensile stresses; this condition would tend to favor increased extension of the local cracks at a given applied loading, which is opposite to the behavior actually observed.

The higher loading as a function of crack advance in the model specimens, relative to the numerical model, was more pronounced with PC spheres than it was with PC rods. The relative behaviors are more clearly illustrated when the local crack advance is characterized in terms of average local crack lengths, $<a>$. This parameter was computed by determining the area swept by local crack advances and then dividing that by the particle separation distance, L. Shown in Figure 5.16 are results from representatives of the three types of trapping specimens and results from the numerical simulation of Bower & Ortiz. Once again, consideration of the limited debonding of the Nylon rods implies excellent agreement with the numerical results. The PC obstacles, in contrast, clearly create more of an impediment to the local crack growth than the numerical simulation predicts. A similar plot of data for obstacle spacings of $R/L = 0.25$, shown in Figure 5.17, also indicates that the PC spheres provided superior crack-trapping toughness.

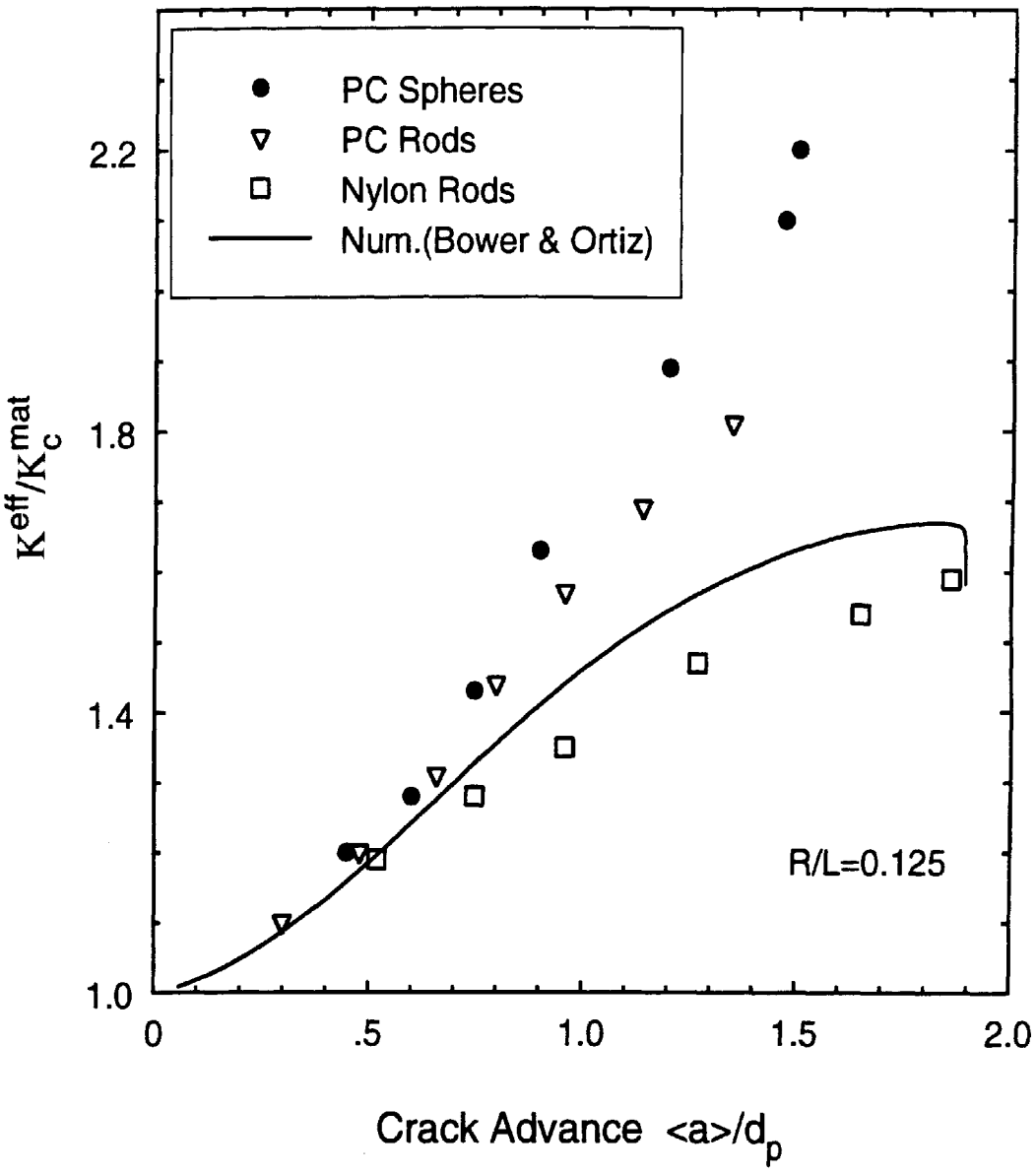

Figure 5.16: Effective toughening enhancement resulting from crack trapping in specimens with $R/L = 0.125$, as a function of average local crack advance, $<a>$, normalized by particle diameter.

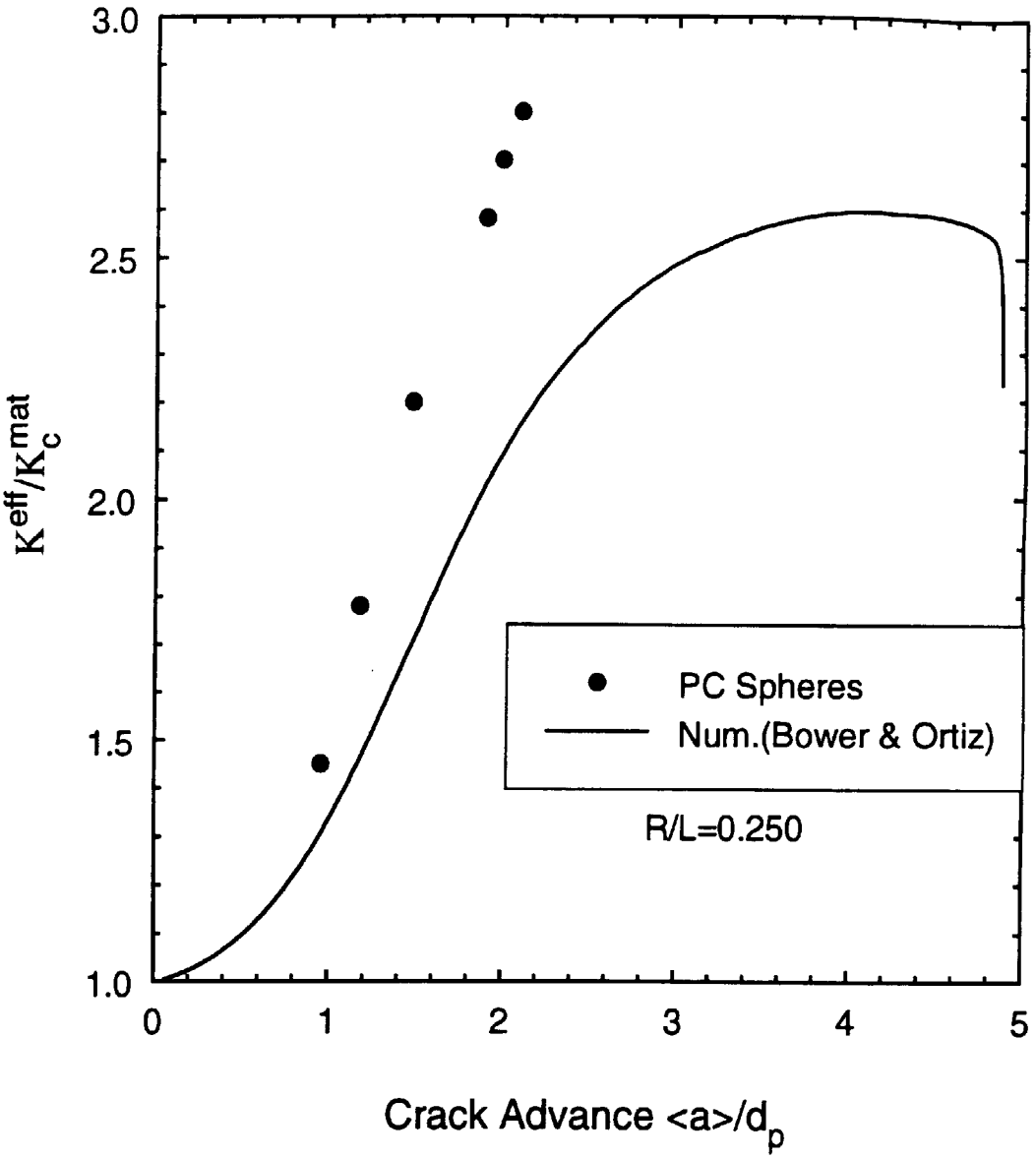

Figure 5.17: Effective toughening enhancement resulting from crack trapping in specimens with $R/L = 0.25$, as a function of average local crack advance, $<a>$, normalized by particle diameter.

5.4 Maximum Toughness Enhancement Achievable by Crack Trapping

5.4.1 Effect of Adhesion

The relative behavior of the specimens containing Nylon rods *versus* those containing PC rods is consistent with the measured adhesive strengths of 31 and >54 MPa, respectively. An unexpected result was that reduction of the PC/epoxy adhesive strength to about 28 MPa, by treating the rod surfaces with a release agent, did not enable any debonding to occur. Further reduction, with a second coat, to about 22 MPa still did not result in any debonding or decrease in trapping-induced toughness. Evidently, the *toughness* of the PC/epoxy interfaces remained high enough to prevent the probing cracks from prying open the interface. In contrast, the Nylon/epoxy interfacial toughness must be sufficiently low enough to enable the limited debonding that occurred in those specimens.

These observations are supported by the interface toughnesses which were approximately determined with the adhesion tests described in Appendix B. In those experiments, the toughness of the release-coated PC/epoxy interface was found to be about 20% greater than the toughness of Nylon/epoxy interface, even though the two systems exhibited similar adhesive strengths.

Reduction of the adhesive strength of spherical particles had a much more dramatic effect upon their ability to trap cracks, as illustrated by the load-displacement traces reproduced in Figure 5.18. When the adhesive strength of spheres was reduced from above 54 MPa to about 22 MPa, crack trapping was still exhibited but the cracks were able to bypass the obstacles by fracturing along the interfaces. As a result, the maximum levels of toughness enhancement achieved in such specimens was only on the order of 10–15%.

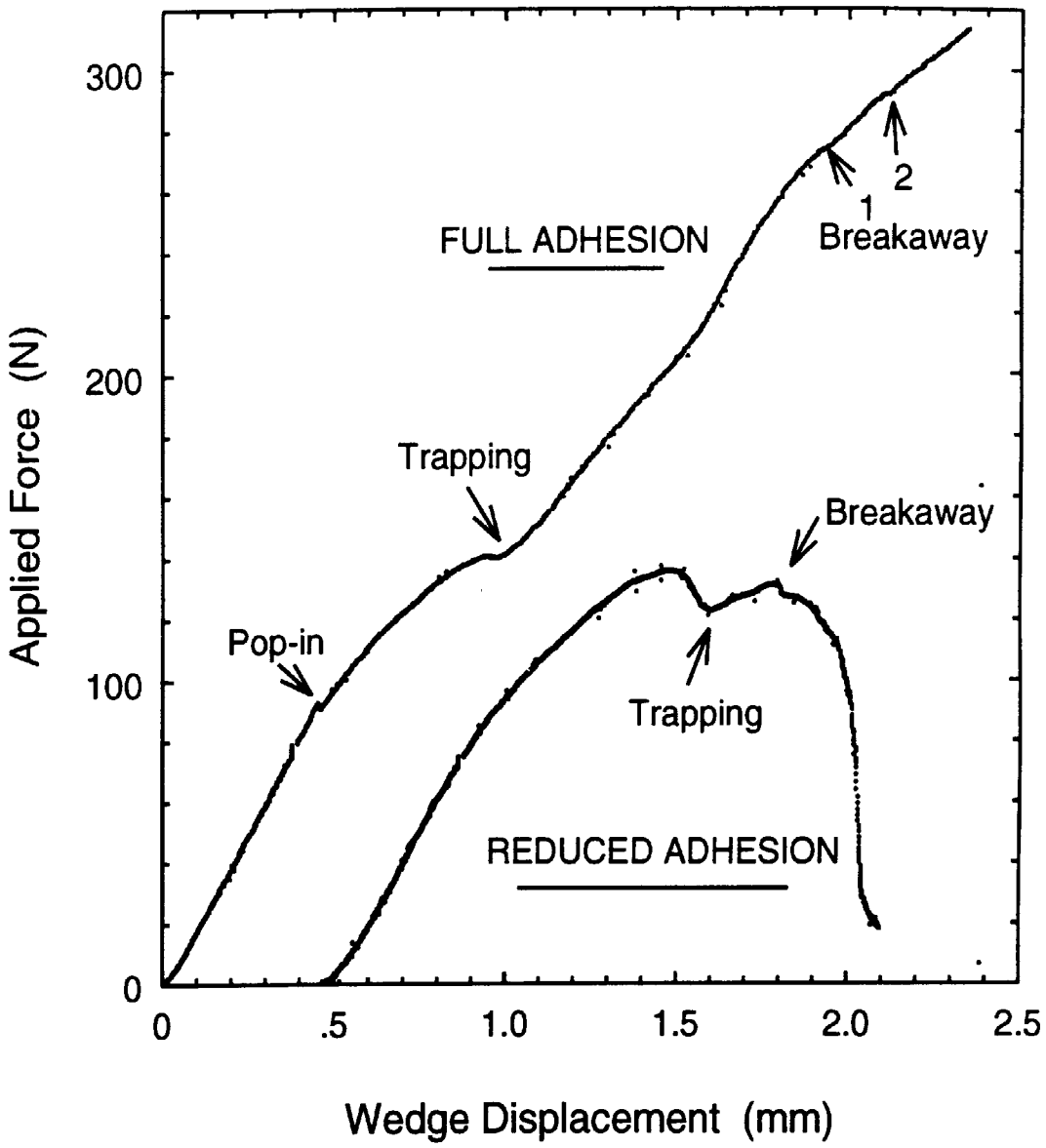

Figure 5.18: Effect of adhesion on load-displacement data obtained from testing two specimens containing PC spheres: one with full (>54 MPa) and one with reduced (22 MPa) adhesion. $R/L = 0.125$.

5.4.2 Comparison of Experiment with Theory

A summary of the measured values of the maximum toughness induced by crack trapping is plotted in Figure 5.19 as a function of interparticle spacing. The experimental data indicate that toughness enhancements of over a factor of two can be achieved by the crack-trapping mechanism alone with reasonable (0.15–0.20) volume fractions of tough particles dispersed in a brittle matrix.

Several analytical models have been proposed recently to represent the magnitude of toughening by crack trapping as a function of particle spacing. Rice has developed a model based upon linear perturbation theory [4] which, assuming that semicircular crack-front segments break away upon reaching a local penetration equal to the interparticle spacing, yields a prediction for effective toughness which can be rewritten as

$$\left(\frac{K_I^{\text{trap}}}{K_{I_c}^{\text{matr}}}\right) = \left\{ 1 - \frac{\frac{\pi}{4}\,(1-2R/L)}{\ln\left[\frac{1+\sin\left\{\frac{\pi}{2}(1-2R/L)\right\}}{\cos\left\{\frac{\pi}{2}(1-2R/L)\right\}}\right]} \right\}^{-1} . \tag{5.5}$$

It is emphasized [4, 5] that this approach is invalid for both very dilute and very high concentrations of particles, but it can be seen from the plot in Figure 5.19 that the predicted toughness ratio (~ 1.5) in the volume fraction range of 0.06–0.10 approaches the values measured here.

A model suggested by Rose, based upon the line-fraction work of fracture (energy release) predicts that [17]

$$\left(\frac{K_I^{\text{trap}}}{K_{I_c}^{\text{matr}}}\right) = \left\{ \left(1 - \frac{2R}{L}\right) + \left(\frac{K_{I_c}^{\text{part}}}{K_{I_c}^{\text{matr}}}\right)^2 \frac{2R}{L} \right\}^{1/2} . \tag{5.6}$$

When this expression is plotted out it agrees well with the data, and is certainly applicable to composites in which energy is dissipated through the fracture of particles.

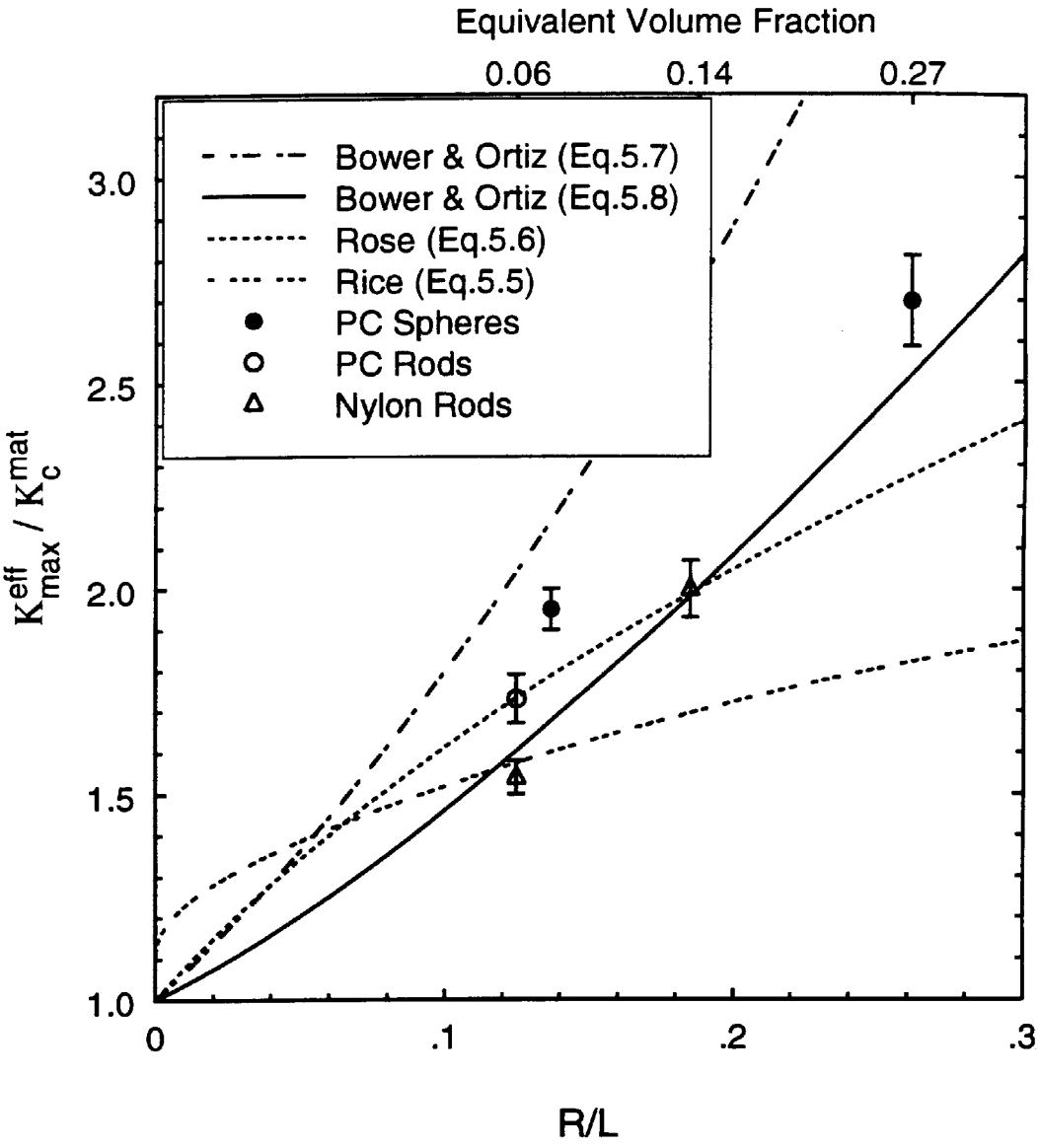

Figure 5.19: Maximum crack-trapping toughening as a function of inter-particle spacing. Experimental data reported here *versus* model predictions as identified.

Unfortunately, this expression has no physical basis for describing the toughening by pure crack trapping, since trapping by tough (impenetrable) particles does not allow the crack to probe the particle properties.

The numerical analysis of Bower and Ortiz represents trapping and bridging of cracks by regular arrays of tough particles by fully enforcing conditions of zero crack-flank opening displacement over circular peripheries of the rods [6]. Their representation of simulations which allow particles to carry traction even after the crack front has passed them by yields an expression for the peak toughening ratio due to trapping and bridging combined:

$$\left(\frac{K_I^{\text{trap}}}{K_{Ic}^{\text{matr}}}\right) = 1 + 3.09\,\frac{R}{L}\,\frac{K_{Ic}^{\text{part}}}{K_{Ic}^{\text{matr}}}\,. \tag{5.7}$$

Incorporating an "effective particle toughness" [7] of $K_{Ic}^{\text{part}} = (2.1+4.8R/L)\ (\text{MPa}\sqrt{\text{m}})$, this expression predictably overshoots the data reported here by a substantial amount.

The best analytical representation results from substituting the effective particle toughness into Rose's line-fraction weighted work-of-fracture model. The resulting expression becomes [7]

$$\left(\frac{K_I^{\text{trap}}}{K_{Ic}^{\text{matr}}}\right) = \left\{ \left(1 - \frac{2R}{L}\right) + \left(2.1 + 4.8\,\frac{R}{L}\right)^2 \frac{2R}{l} \right\}^{1/2}\,, \tag{5.8}$$

which agrees quite well with the data, as seen in Figure 5.19. This expression for toughening by crack trapping now represents the particle toughness by a pure geometric factor, as it must, since the crack can no longer sample the properties of the particles. While the effective particle toughness notion is a useful empirical fit to numerical simulations, it leaves unanswered the mechanistic justification of it.

5.4.3 Assessment of Validity of Experimental Data

5.4.3.1 Experimental errors

The determination of stress intensity in the crack-trapping specimens required the measurement of only two variable parameters, the crack length and the applied load. The applied load was measured with a load cell which was calibrated with weights equivalent to the force at which crack-trapping began to occur in the experiments ($\sim 130\,\mathrm{N}$). The weights, in turn, were measured with a digital scale having an accuracy of $\pm 0.2\%$. Effects of any "drift" in the load cell amplifier were mitigated by the technique employed of normalizing the trapping toughness by the matrix toughness determined for each specimen. The linearity of the load cell output is specified as being within 0.5% by the manufacturer (Instron), so a reasonable value of experimental error possibly contributed by the measurement of load would be about 1%.

The measurement of two crack lengths were required for each toughness determination: the length, a_o, when the crack first contacts the obstacles, and the crack length during the evolution of crack trapping. When the first contact was made, the crack fronts were fairly straight and measurement could be made to within $\pm 0.2\,\mathrm{mm}$; this translates to about $\pm 0.3\%$ of $a_o \approx 59\,\mathrm{mm}$. The measurement of the evolving crack length was subject to considerably more error, since the crack front becomes locally bowed during the trapping process. An effective (average) crack length was determined for each bowing configuration analyzed by visually fitting a straight line so that the cracked area beyond the line was approximately equal to the uncracked area behind the line. It is estimated that, with this procedure, the measured crack lengths were determined to within $\pm 1\,\mathrm{mm}$; this translates to about $\pm 1.6\%$ of the total crack length. The sum of the individual uncertainties brings the total estimated range of experimental error to approximately $\pm 3\%$.

5.4.3.2 Nonlinear Influences

The ideal behavior of the crack-trapping specimens would be to create upon the crack front the effect of the presence of image particles on either side of the specimen. In practice, this condition was often apparently fulfilled, but it is clear that the side-grooving created an enhanced stress intensity at the edges which partially disrupted the image condition. Nonetheless, this effect was continuous, and presumably constant, throughout the crack growth in each specimen; once again, the procedure of normalizing the trapping toughness by the matrix toughness measured from the same specimen should nullify errors introduced by edge effects.

Debonding of the particle/matrix interfaces would allow further penetration of crack fronts into the matrix between particles, and thus produce less trapping-induced toughness than could be achieved with "perfect" bonding. This, as described previously, is exactly what occurred with specimens having obstacles which were Nylon rods. No debonding occurred at any of the PC obstacle interfaces, so this effect can not be considered a source of "error" in those tests.

A final influence on the measured values of crack-trapping toughness might be variable toughness of the epoxy matrix, caused by changes in the crack propagation velocity. This factor is considered because the matrix toughness is inferred, for each specimen, when the crack reaches the obstacles and is travelling at a constant rate of $\dot{a} \approx 1\,\mathrm{mm/s}$, whereas the trapping toughness is determined while the crack is travelling at approximately one-quarter this velocity. Because greater plastic deformation (and hence, toughness) accompanies slower crack propagation in materials with rate-dependent deformation, it is possible that the method used here to calculate the trapping-induced toughness may include some toughening due to local velocity changes. Despite the rate-sensitivity of deformation and fracture in epoxies, experiments have shown that, in DGEBA epoxies with several different cures, changes in crack velocity by three [59] to nine [60] orders of magnitude result in variation of the

critical stress intensity by only 5 to 20%. Moreover, a constant critical energy release rate ($\sim 80\,J/m^2$) was measured in an amine-cured DGEBA epoxy during crack growth rates ranging from 10^{-4} to about 3 m/s [61]. Thus, it is realized that the changes in crack propagation velocity produced during the crack-trapping experiments were accompanied by negligible changes in the toughness of the epoxy matrix.

5.4.3.3 Crack-Trapping mechanism isolated

A problem common to many experimental investigations of toughening mechanisms is that several mechanisms may be operative in unison, thus making the measurement of the effect of a single, individual mechanism difficult, if not impossible. This situation is reviewed more fully in Chapter 2, where the coexistence of multiple toughening mechanisms in particulate-reinforced epoxies is highlighted, along with the tendency of investigators to emphasize the effects of the particular mechanism(s) which they are intent upon studying. Here, we point up the utility of the model specimens to isolate one particular toughening mechanism, crack trapping.

During growth of the cracks in the model specimens, no crack branching occurred. Examination of the fracture surface with an electron microscope showed no evidence of microcracking and indicated that cleavage fracture took place with no discernible plastic deformation. No dynamic effects were generated in these experiments, since the crack propagation was stable and controlled to rates on the order of 1 mm/s. No strain-induced transformations are known to occur in epoxy; any similar mechanism, if it existed, would be accounted for by the procedure of normalizing the crack-trapping toughness by the matrix toughness measured with each specimen. No dilatations due cavity growth were possible, since great care was exercised in removing voids from the epoxy during fabrication of the specimens. In short, the measurements obtained with these macroscopic specimens isolated the toughening effects of crack trapping and demonstrated its transition to crack-flank bridging.

Chapter 6

Overview of Toughening Processes in Quasi-Brittle Solids

The aim of this chapter is to place in perspective the role of crack trapping in determining the fracture resistance of brittle materials with heterogeneous microstructure. Many processes may evolve during the growth of cracks in brittle solids containing second-phase particles. The various mechanisms may be grouped into two primary categories, depending upon whether they occur at locations in front of or behind the crack tip, as illustrated in Figure 6.1. Mechanisms which occur in front of crack tip, in the "process zone," impart toughness primarily by shielding the crack tip from applied stress through a region of reduced stiffness, by generating additional surface area, or by increasing the volume of material which yields under the influence of the concentrated crack-tip stresses. Behind the crack tip, traction carried across the flanks by intact ligaments, particles or fibers acts both to reduce the crack-tip stress intensity and to dissipate work through plastic deformation or frictional phenomena. Directly at the crack tip, trapping may occur. In the following, the conditions under which each toughening mechanism may be dominant is discussed, and the possible contribution of crack-trapping relative to the other mechanisms is evaluated.

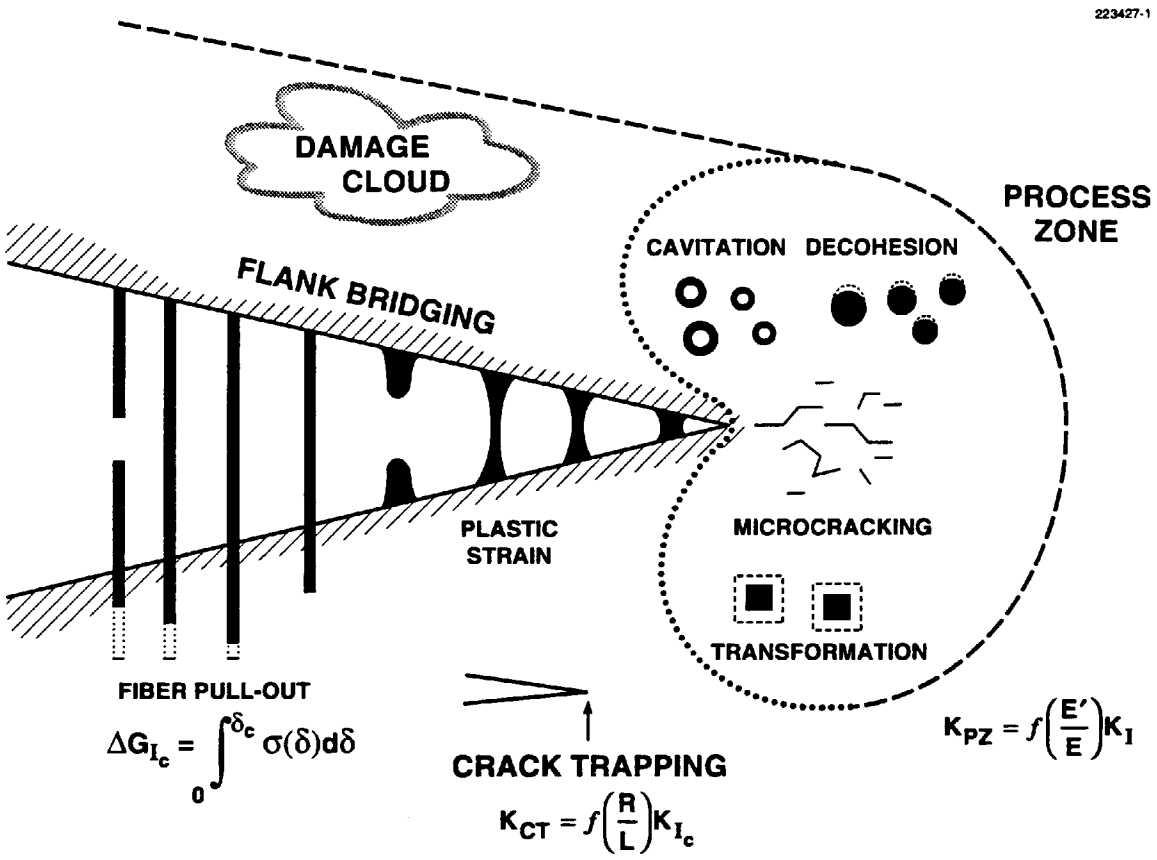

Figure 6.1: Schematic of principal toughening processes which may contribute to the toughness of a brittle solid containing tough heterogeneities.

6.1 Crack-Tip Processes

6.1.1 Process Zone Mechanisms: Shielding

6.1.1.1 Microcracking

Brittle crystalline materials, such as ceramics and rocks, may often crack along grain boundaries or at the interface between the bulk matrix and second-phase particles. This "microcracking" may nucleate from residual stresses incurred during fabrication, or may result from applied stress during service. In either case, one of the consequences is a reduction of the effective elastic modulus of microcracked material loaded in tension, so that less stress is transmitted to the crack tip than if the surrounding material were undamaged. In general, a reduced stress intensity at the crack tip results, but the average apparent toughness of the material may, in fact, not be improved because of macrocrack-microcrack interactions and the coalescence of coplanar microcracks into the advancing crack tip. Analytical developments put forth in recent years have not created a unanimous viewpoint on the extent to which toughening actually results from microcracking.

The simplest approach to modeling the toughening effect of microcracking in the process zone assumes that the damaged material remains linear-elastic (only more compliant), so that the crack-tip shielding which results for a stationary crack is simply [62]

$$K_{tip}^2 = \frac{\tilde{E}'}{E'} K_\infty^2 , \tag{6.1}$$

where $\tilde{E}'$ is the plane-strain modulus of the microcracked region, as given by a separate development [63]. With a microcrack density defined as $f = N < a^3 >$, where N is the number per unit volume of microcracks having radius a, this model predicts only a 5% increase in K_{Ic} at a microcrack density of $f = 0.3$. A more detailed

analysis of this problem, also incorporating the effect of a reduced modulus in the process zone due to microcracking, predicts crack tip shielding (reduced K_{tip}) ranging from 30 to 40% (with $f = 0.3$) for isotropic, randomly orientated microcracks nucleating upon attainment of critical mean or maximum normal stresses [64]. Models which incorporate microcracks that nucleate on planes perpendicular to maximum principal stress [65, 66] or which represent the modulus of microcracked material by a stress-dependent function [67] predict slightly higher shielding for a similar degree of microcracking.

Analytical models of the interaction between microcracks and the primary crack tip show that the crack tip stress intensity fluctuates, from shielding to amplification, as a function of microcrack orientation and distance from the crack tip [68]. Numerical simulations [69] of microcracks coplanar with the macrocrack show that the interaction effect is strictly amplification (~10–40%); in the case of parallel but non-coplanar microcracking, similar amplification of the stress intensity of the main crack resulted. In the same numerical study, shielding of crack-tip K_I by approximately 5% resulted from a random distribution of randomly oriented microcracks at a density of $f = 0.35$. Changing the orientation of microcracks such that their plane was perpendicular to the maximum stress increased the shielding to about 12%.

The toughening resulting from microcrack-shielding may be partially or even completely offset by the accumulation of damage zones which link up with the macroscopic crack. By representing microcracked material directly in front of a crack tip as a cohesive zone having a traction-displacement behavior dependent upon microcrack density, Ortiz used a J-integral analytical approach to estimate the reduction in K_{Ic} resulting from accumulated, planar microcracking [70]. A key result of this analysis was that crack-tip "shielding and toughness degradation seem to counterbalance each other almost exactly," for the case of planar crack growth. More precisely, a net toughening effect of a few percent was predicted for microcrack densities up to about 50%. Beyond this density, toughness degradation dominated so that embrittlement

was predicted for planar cracks. Introduction of crack deflection (along grain boundaries, *e.g.*) reduced the toughness degradation effect so that some ($\sim 20\%$) shielding was preserved over nearly the entire range of microcrack densities [70].

All of the aforementioned results pertain to shielding due to microcrack-induced modulus reduction in a process zone directly ahead of stationary crack tips, and do not include the reduction of crack-tip stress intensity resulting from modulus reduction of material along the flanks of growing cracks. The increase in crack-tip shielding of growing cracks over stationary cracks, due to microcrack-induced modulus reduction, has been shown to be on the order of 40% [64]. An additional mechanism which contributes strongly to the fracture toughness of materials with growing cracks (resistance curve effect) is the irreversible dilatation that accompanies microcracking in residual stress fields, which is mechanically similar to a transformation strain.

6.1.1.2 Transformations

Inelastic, dilatational microcracking accompanies the growth of microcracks in (tensile) residual stress fields, regardless of whether such microcracks are nucleated spontaneously by thermal stresses during fabrication of a heterogeneous material, or are generated by crack-tip stresses. The relief of residual stress by microcracking results in an inelastic, non-recoverable volumetric strain, $\mathcal{E}^p_{ii}$, which is indistinguishable on a macroscopic level [64] from a transformation strain, $\mathcal{E}^T$, such as accompanies the phase transformation of zirconia from tetragonal to monoclinic [29], or as accompanies the shear-induced crazing of thermoplastics [71, 72].

Cracks which grow into regions which have experienced a permanent dilatation ($\mathcal{E}^T$, either due to release of residual stresses or to material phase transformations) develop, with increasing crack length, crack-tip stress shielding which may become several times greater than the shielding due to a modulus reduction alone [62]. This

effect results from what may be considered an augmented, residual energy density [62] or inelastic compressive strains [28, 73] in a zone flanking the length of the crack behind the tip. The damaged, or transformed wake zone extends to a height, H. on each side of the crack tip, given by [64, 73]

$$H = \frac{\sqrt{3}\,(1+\nu)^2}{12\,\pi}\,(\frac{K}{\sigma^c})^2\,, \tag{6.2}$$

where K is the applied stress intensity factor and σ^c is the critical mean stress which is required to initiate the dilatational microcracking (or transformation).

The crack tip stress intensity induced by dilatation of a particle with radius, b, located at (r,θ) in relation to a crack tip, may be written as [73]

$$\Delta K_I^{\text{tip}} = \sqrt{\left(\frac{\pi}{8}\right)}\,\frac{Eb^2\Omega}{(1-\nu^2)r^{3/2}}\cos\frac{3}{2}\theta\,, \tag{6.3}$$

where the equivalent plane-strain dilatation (cross-sectional area expansion of a cylindrical inclusion) is given by $\Omega = (2/3)(1+\nu)\,\varepsilon^T$.

The angular dependence of this expression for ΔK_I^{tip} indicates that dilatations in a 120° fan ahead of crack tips will slightly elevate the crack-tip stress intensity,[1] while dilated material left behind in the wake of an advancing crack will continue to exert a reduction of K_I^{tip}[73]. Thus, transformation toughening becomes operative only for cases of growing cracks, and manifests itself as an apparent R-curve in toughness testing. A steady state condition is reached with little crack growth, however, such that a peak value of toughness is asymptotically reached after crack extensions of typically only two to four times the wake height [28]. By numerically integrating Equation 6.3 over a complete contour enclosing a crack, the steady state, peak effect of transformation toughening has been predicted to be [64, 73]

$$\frac{K_I^{\text{tip}}}{K} = 1 - 0.2143\,\frac{Ec\varepsilon^T}{(1-\nu)}\frac{\sqrt{H}}{K}\,, \tag{6.4}$$

[1] An alternate analysis suggests that dilating material ahead of crack tips, in a zone with a double-lobe shape determined by a contour of constant crack-tip hydrostatic stress, generates no influence at all upon K_I^{tip}[28].

where c is the volume fraction of transforming material.

The level of toughening induced by dilatational transformations can be significant. A great deal of experimental data concerning the toughening of ceramics by the inclusion of stress-transformable ($\mathcal{E}^T = 0.04$) zirconia grains as precipitates or included particles is summarized in Reference [29]. Ceramics which have been toughened in this manner include alumina, cubic zirconia, CaO, MgCa, MgO, Y_2O_3, and others. As an example, a variety of composites consisting of an alumina matrix containing zirconia particles demonstrate toughening increments ranging up to $6\,\mathrm{MPa}\sqrt{\mathrm{m}}$, as a function of volume fraction of ZrO_2 and the developed steady-state wake height [29]. Since K_{Ic} of the alumina is approximately $5\,\mathrm{MPa}\sqrt{\mathrm{m}}$, achievable levels of zirconia transformation toughening appears to be in excess of 100%. In addition, trends in toughening increments scale linearly with $c\sqrt{H}$ [29], in accordance with Equation 6.4.

Experiments with ZrO_2-toughened alumina, magnesia and other ceramics universally demonstrate toughening increments which are 50–80% greater than is predicted by Equation 6.4 [28, 73, 74]. A portion of this additional toughness may be assigned to difficulties in determining some of the parameter values required by the toughening model [73], but the principal source of the excess measured toughness must be attributed to other mechanisms which are operative in unison with the transformation process. The most likely other mechanisms are microcracking and deflection (discussed below), but models of these mechanisms when operating independently suggest possible toughening increments of just a few percent. This situation raises the issue of toughening by a combination of mechanisms, which is quite complicated and can not be determined by a simple summation of the individual effects [74], since the consequences of each mechanism upon the material microstructure influence the ability of other mechanisms to operate.

6.1.1.3 Decohesion

Decohesion of particles may produce different effects upon the global toughness of the material containing them, dependent upon the location of the particle relative to the crack tip when decohesion occurs. If the adhesive strength between matrix and particle is low enough so that decohesion occurs prior to the crack reaching the particle, then the effects upon toughness will be identical to those produced by microcracking. If no residual stresses are present, then the dilatation resulting from the interfacial separation will be almost completely elastic, and the primary contribution to toughness will be through modulus-reduction shielding. The presence of tensile residual stresses in the matrix will cause a non-recoverable dilatation to develop upon decohesion, which will further augment the toughness through the strain-transformation mechanism.

Another source of toughness which accompanies decohesion of particles in the absence of contact with a crack stems from the generation of new surfaces. This effect also accompanies microcracking along grain boundaries. The formation of new surfaces within material near a crack tip requires energy, and so contributes to the energy release rate of a growing crack. The magnitude of energy involved relative to $\mathcal{G}_c$ is minimal, however, and is usually ignored.

The separation of particles from their host matrix by the probing of concentrated crack-tip stresses can contribute to the overall material toughness through an increased fracture surface area and through greater plastic dissipation accompanying the interfacial fracture process than the cleavage fracture of the matrix. If the particle modulus is lower than the modulus of the matrix, or if residual (thermal) stresses place particles under hydrostatic pressure, then crack tips will be attracted to the particle equators. The crack tip then has the option of fracturing the particle, fracturing the interface, or waiting until the particle debonds from radial stresses at the poles. If the latter process does not occur, then the crack may propagate along the

interface if

$$\frac{\mathcal{G}^{\text{int}}}{\mathcal{G}_c^{\text{int}}} \geq \frac{\mathcal{G}_I^{\text{part}}}{\mathcal{G}_{Ic}^{\text{part}}} \,. \tag{6.5}$$

Since a hemispherical fracture path will traverse twice the area that would have been exposed by an equatorial fracture, conditions which promote interfacial fracture as opposed to cleavage of particles can result in the dissipation of more energy during fracture.

6.1.1.4 Cavitation

Another mechanism which can contribute to the toughness of brittle, heterogeneous materials stems from the cavitation of either the matrix or included particles. Brittle organic glasses have been toughened by, for example, the dispersion of small (1–10 μm) rubber particles throughout the polymer matrix [37,72,75–80]. The process of particle cavitation itself consumes energy, contributing to $\mathcal{G}_c$ a modest amount which has been estimated [81] to be $\Delta\mathcal{G}_c = 4\,c\,\Gamma_t$, where Γ_t is the "tearing" energy of the cavitating particles.

More recent analyses of the relative magnitudes of contributing toughening mechanisms in rubber-modified polymer glasses suggest that the energy consumed by particle cavitation itself is negligible [82], but that the process is instrumental in activating two other energy-absorbing mechanisms which are of major importance in such materials [75]. The principal role of cavitating particles, which behave nearly as voids, is to concentrate stresses at their equator due to the modulus mismatch [83, 84] and to lower the yield stress of the adjacent matrix material by relaxing the plane strain constraint through the dilatation process [77, 80]. Similar dilatation could, of course, accompany the decohesion of rigid particulates in a more compliant matrix. The dilatation of particles which remain bonded, and do not cavitate in the manner of elastomers, will be enhanced for particles with lower Poisson's ratio. This effect has been found to be more dramatic than a modulus mismatch, so that the stress

concentration due to a void is greater than that produced by a rubber particle [83, 85].

The result of stress concentrations at particle locations and the unconstrained yield stress near those that cavitate, dilate or debond is the promotion of extensive shear yielding at crack tips. A secondary consequence is the growth of voids in the hydrostatic stress field which accompanies crack tips, absorbing energy in the process. The mechanism of plastic void growth in an epoxy matrix has been modeled by Huang and Kinloch, who find that this contribution to the toughness of a rubber-toughened epoxy is negligible at reduced temperatures [75]. As T_g of the epoxy was approached, however, the inelastic growth of voids became the major consumer of energy due to the sharp reduction in yield stress.

Some thermoplastics under stress develop a damage mechanism which resembles cavitation. When local stresses in, for example, polystyrene (PS) or polymethylmethacrylate (PMMA) reach critical levels, polymer fibrils are drawn out in highly aligned bunches that bridge the faces of thin, microscopic slits, or voids [71]. These crack-like "crazes" are oriented such that the load-bearing fibrils contained within are parallel to the maximum principal stress. Fracture of crazable polymers may initiate by the nucleation of crazes at stress concentrators such as included dust particles, and proceeds by the necking and rupture of craze matter until the remaining crazes become unstable [72]. While the inadvertent generation of crazes is deleterious, the fostering of crazes in a controlled manner can, in fact, be employed to toughen brittle glassy polymers which are capable of crazing.

Though discrete, localized crazes represent potential failure sites, promotion of global crazing can increase the strain-to-fracture of some brittle polymers through a dilatational process viewed as "craze plasticity". Concentric, spherical particles composed of a copolymer blend having a relatively high compliance were incorporated into a high molecular weight polystyrene, resulting in a dramatic (300%) reduction of the yield (craze) stress and a similar increase in the failure strain of specimens

tested in uniaxial tension [86]. The promotion of extensive crazing (indicated by macroscopic yielding) in the PS composites was enabled by radial tensile stresses generated at the surface of particles due to differential thermal contractions during processing, and by the stress concentration resulting from the low bulk modulus of the special, two-phase particulates [86]. The enhanced toughness in these materials is characterized in terms of lowered craze growth rates which accompany the reduced stresses required to promote crazing via a particle-induced cavitation mechanism [72].

6.1.2 Localized Yielding

Plastic flow of brittle, rigid solids such as ceramics and rocks does not play a significant role in their toughening processes because the yield stresses of those materials are sufficiently high enough to prevent any useful volume of material to deform. On the other hand, brittle organic glasses typically have a much lower yield stress (though it is a higher fraction of the stiffness), enabling local stress concentrations to promote plastic dissipation which can be a major contributor to the energy release rate of brittle polymers.

This toughening mechanism becomes dominant in composite materials with brittle matrices which are capable of some crack-tip plasticity in the absence of second-phase particles [75, 80]. For extensive localized yielding to occur, however, requires a dispersion of stress concentrators in front of the crack tip. Careful preparation of thin sections of fractured rubber-modified organic glass (PC) has revealed that, in such materials, the stress field ahead of advancing crack tips first promotes cavitation and debonding of particles (which then perform still greater stress concentration) and then links up the stress concentrations with thick bands of yielding matrix material [78]. This process has been predicted with finite element analyses [83, 84] to occur in a similar fashion.

Analytical modeling of the stress distributions and deformations in the process zone of a rubber-modified epoxy indicates that as much as half of the predicted toughness may come from shear banding, with the balance arising from plastic void growth, tearing energy of the particles and bridging of the crack faces [75]. The measured toughness enhancements ($\Delta\mathcal{G}_c$) of rubber-modified epoxies range from 50 to 400% of the toughness of the neat resins, and, in general, can not be accounted for by simple summation of individual mechanisms. Synergistic effects shall be discussed below.

6.1.3 Deflection

When cracks impinge upon grain boundaries, second-phase particles or any sharply defined discontinuity in fracture toughness, an option is presented for the direction of continued crack propagation. If the intercepted boundary provides a path of least resistance, then the crack tip will deflect along it, creating a local perturbation in what otherwise might have been a smooth fracture surface. If this process is repeated extensively along the length of a crack in a brittle solid, then the increased surface area due to such crack deflection may constitute enough additional energy to be considered a toughening mechanism.

An analytical model of the effect of crack deflection on local stress intensity factors and the resulting fracture path predicts a maximum toughening ($\Delta\mathcal{G}_c$) effect due to increased surface area alone of about 15% (asymptote reached at c$\sim$ 0.25) in ceramics with tough, dispersed grains [36]. When the energy release rate due to combined modes of induced stress intensity is computed, the toughening effect predicted rises to about 40% for $c = 0.25$. Experiments performed to test this theory measured the increase in $\mathcal{G}_c$ of silicon nitride composites containing grains with varying aspect ratios, and of lithium-alumino-silicate glass ceramics containing elongated crystals [87]. The results of these measurements showed that $\mathcal{G}_c$ could be nearly doubled by changing

the aspect ratio of grains from equiaxed to an aspect ratio of 6. This degree of toughening could not be accounted for by the measured crack-path deflections alone, and so must result from a synthesis of other mechanisms including microcracking (which was observed) and crack trapping.

The increase in surface area resulting from debonding or semispherical fracturing of spherical particle interfaces can be easily estimated by considering particles with radius, R, dispersed with center-to-center separations of L. If stress conditions favor crack-tip attraction to the equators, resulting in exposure of entire hemispheres, then the increased surface area normalized by the unperturbed, planar area is

$$\frac{\Delta A}{A} = \frac{(2-1)\pi R^2}{\pi (L/2)^2} = 4\left(\frac{R}{L}\right)^2 = A_f = c\,. \tag{6.6}$$

The normalized increase in surface area, due to debonding or crack deflection over spheres, is simply equal to the area fraction of particles. The area fraction of particles on a representative material section is identical to the volume fraction of particles [88], so that the potential increase in area resulting from crack deflection over spherical particles is equal to c.

Consideration of the repercussions of crack deflection suggest that it may do more harm than good. Forcing (or allowing) crack tips to circumnavigate second-phase particles will prevent the possibility of mechanisms developing which require intimate, sustained contact of crack tips with particles. Crack trapping, crack-tip blunting (shear-yielding) and, to some extent, transformations and microcracking all require or are augmented by contact between crack tips and impeding particles. Since these mechanisms have the potential to develop normalized toughening increments far in excess of the volume fraction of particles which create them, it is clear that crack deflection is the least efficient mechanism which is available to toughen brittle materials.

6.1.4 Crack Trapping

Tough particles or distributed regions of superior toughness in a brittle solid can present formidable obstacles for a crack front to overcome. By constraining the crack faces to zero opening displacement at discrete locations, impenetrable particles force crack tips to advance past them by forming locally bowed crack-front segments. To accomplish this type of crack advance requires elevation of the remote driving force, K, to generate $K_I = K_{Ic}$ along the bowed segments by counterbalancing the negative K_I^{tip} created by the imposed islands of zero opening displacement. As a consequence, the stress intensity around the periphery of the pinning regions is increased several-fold, and the effective global toughness of the material is augmented by an amount that is determined primarily by the volume fraction of tough heterogeneities.

This toughening mechanism has been recognized for over two decades as having potential importance [8, 14], but the magnitude of its contribution to overall toughness and the conditions necessary to promote its operation have not been clarified because experimental measurements aiming to do so have universally involved materials in which a multitude of toughening mechanisms operate simultaneously. Fracture toughness measurements with ceramics containing tough grains or particles[25, 26], or with silicate glasses containing ceramic inclusions [13, 33] may include the effects of microcracking and/or deflection. Measurements with inorganic glasses containing tough metallic particles [15, 34, 89] are likely to include toughness contributions from plastic deformation of the reinforcements and crack-bridging by intact particles. A host of investigations have been performed with particle reinforced polymeric glasses [35–43] to determine contributions of individual mechanisms and overall levels of toughness improvement. In these composite materials it is nearly impossible to selectively activate individual mechanisms or to determine their contributions from measurements of overall toughness. Consequently, definitive measurement of the toughening effect of crack trapping has remained elusive.

Analytical modeling of the crack trapping process has indicated that increased applied stress intensity is indeed required to promote the local bowing processes, such that an effective toughness enhancement in the range of 70% is reached with impenetrable, perfectly bonded particles at a volume fraction of $c = 0.2$ [4, 5]. Detailed numerical simulations suggest that the toughness enhancement may be greater, predicting $\left(\frac{K_I^\infty}{K_{I_c}^{matr}}\right) \approx 2.3$ under similar assumptions [6]. The experiments reported in the previous chapter support the magnitude of this prediction, and provide information concerning the conditions necessary to generate respectable levels of crack-trapping toughness. Implications of these results are discussed further in a later section.

6.1.5 Material Separation: Role of K_{Ic}

The most important consequence of all the mechanisms considered thus far is to modulate the near-tip stress fields in cracked materials. In quasi-brittle materials, in which the extent of the process zone remains small relative to structural dimensions and the crack length, the near-tip stresses are scaled linearly by the crack-tip stress intensity, K_I^{tip}. The maximum tensile stress is developed a short distance ahead of the traction-free crack tip, and is determined by K_I^{tip}, which may be reduced, or shielded, from the remotely applied K by processes which develop at or in front of the crack tip. Therefore, material separation and the progression of crack growth is directly determined by the effectiveness of crack-tip toughening processes. This is to be contrasted with mechanisms that exert traction across the flanks of growing cracks: while generating a negative K_I^{tip} by applying closure forces behind the crack tip, crack-flank processes also continue to dissipate energy at constant, or decreasing tractions, thereby contributing to the fracture energy inelastic increments in excess of a $\mathcal{G}_c$ which would otherwise be equal to $(1 - \nu^2)K^2/E$.

6.2 Crack-Flank Processes

6.2.1 Bridging: Transition from Crack Trapping

After a crack front has passed obstructing particles and broken free from the trapping configuration, the particles will continue to carry traction if they remain intact and well bonded to the matrix. This traction exerts a negative stress intensity on the crack tip, effectively increasing the overall material fracture toughness. With increasing load, the crack front will advance to the next trapping positions, while the first, bypassed obstacles develop greater stresses and contribute more load sharing though bridging of the crack faces. As the reinforcing particles become more highly stressed, they may fail either by fracture or by necking, or may debond from the matrix. Eventually, a steady state condition will be reached, where crack trapping evolves at the crack tip, a transition of particles from trapping to bridging is continually occurring, and a constant (on average) number of particles are involved in the bridging of the crack flanks. This process has been numerically simulated by work of Bower and Ortiz, wherein the steady state condition including bridging is predicted to develop 50–100% more toughening effect (with tough, perfectly bonded particles that are elastically similar to the matrix) than crack trapping alone [6]. The actual magnitude of the prediction is, of course, dependent upon the volume fraction of particles.

6.2.2 Bridging: Continued Dissipation

The chief action of bridging forces is to dissipate energy as the crack flanks separate. This may be accomplished through the plastic deformation of ductile particles [57, 98, 20], frictional sliding among grains [99–101], through the pull-out of debonded fibers resisted by shear forces [102, 103], or by the promotion of additional matrix yielding at the base of stressed fibers [104, 105]. The most commonly used approach

to model the contributions of these processes to fracture energy assumes that discrete bridging forces can be represented as tractions "smeared" across the crack face, so that the contribution of bridging work to the fracture energy, per unit area of crack face, may given simply as [19, 23, 55]

$$\Delta G = f \int_0^{u_c} \sigma(u)\, du \ , \tag{6.7}$$

where f is the area fraction of bridging material with a characteristic stress-separation function, $\sigma(u)$, which vanishes at the critical separation, u_c. The most difficult aspect of modeling the behavior of materials which exhibit non-zero crack face tractions is the determination of an appropriate stress-separation relation [106]. The determination of $\sigma(u)$ under conditions of 3-D constraint [56] has led to predictions [57] of increased fracture toughness (K_{Ic}) by up to a factor of six in lead-particle reinforced glass. Moreover, enhancement of energy release rate ($\mathcal{G}_c$) by as much as a factor of sixty has been reported due to addition of particles of aluminum in a brittle glass [58]. Experiments with aluminum composites reinforced with unidirectional alumina fibers have demonstrated improvements in K_{Ic} from about 12 to nearly $30\,\mathrm{MPa}\sqrt{\mathrm{m}}$ [104]. (We note, however, that the lengths of crack extension required to generate such high fracture resistance were greater than the thickness (5 mm) of the specimens tested; therefore, the use of the LEFM parameter K_{Ic} to characterize the toughness of these materials is not strictly appropriate.)

6.2.3 Work of Fracture: $\mathcal{G}_{Ic}$

Though crack-bridging mechanisms do reduce K_I^{tip} by applying closure forces behind the crack tip, their principal effect is enhancement of the fracture energy which accompanies growing cracks. This is manifested by R-curve effects during the fracture-toughness testing of composite materials containing fibers or compliant particles. The steady state level of the fracture energy, or "work of fracture", can be an order of magnitude or more greater than the energy release rate associated with crack initi-

ation in such materials. This inelastic increase in $\mathcal{G}_c$ clearly can not be related to K_I^{tip} through linear elastic fracture mechanics. The increasing $\mathcal{G}_c$ that accompanies the growth of cracks which carry traction across their flanks provides a stabilizing mechanism which encourages crack arrest. Once $d\mathcal{G}_c/da = 0$ is reached, however, materials toughened by bridging behave as any material with constant $\mathcal{G}_c$, so that further increases in applied loading will result in catastrophic failure.

Another source of dissipation which may contribute to the work of fracture arises from the presence of damaged material along the flanks of cracks which have grown into process zones. Material which has suffered microcracking, decohesion of cavitation will posses some degree of inelastic behavior upon unloading due to asperities and plastic strains which prevent material interfaces from fitting together again in their original positions. As crack tips extend, enveloping new material in process zones, the material left behind in a damage wake, or cloud, will be subject to decreasing levels of stress. This unloading process will, on a microscopic scale, develop a hysteresis in the material stress-strain curve, resulting in a dissipation equal to the enclosed area. The magnitude of this energy contribution to the overall work of fracture will, of course, vary from material to material and would be difficult to evaluate since the extent of the nonlinear material behavior would have to be determined *in situ*.

6.3 Combined mechanisms

The effect upon overall material toughness of mechanisms which operate simultaneously is difficult to ascertain. This is to be expected, since the operation of one mechanism is sure to influence the existence or efficiency of others. An example of cooperative mechanisms is the promotion of shear yielding by stress concentrations enhanced through the cavitation or debonding of particles. A counterproductive effect would be created by crack deflection along weak interfaces, which would prevent

the operation of crack trapping.

Many of the research endeavors cited in this chapter focused upon one or two potential toughening mechanisms, and in so doing, neglected or down-played the possibility of contributions from other sources. A recent attempt to perform better book-keeping recognized that the majority of toughness improvement in rubber particle-modified epoxies arises from massive shear yielding, plastic void growth, and cavitation of the particles [75]. The summation of model predictions for each of these mechanisms provided a good approximation to the measured toughness values of the composite material, but the measured values were consistently 20–30% higher. It has previously been pointed out that simple summation of coexisting mechanisms may not be correct or insightful due to nonlinear, unknown interactions between the mechanisms involved [74].

The suggestion has been made that a multiplicative effect may develop between bridging mechanisms and process zone, or shielding mechanisms, so that the resulting toughness increment is greater than the sum of its parts [107]. This is an appealing prospect, but the principle of energy conservation implies that the total dissipation (energy release rate) from two mechanisms can only be greater than their sum if some other energy sink exists which is not being accounted for. Alternatively, simultaneous mechanisms could enhance each other so that they each absorb more energy than they would if existing alone. An example where this might be true is the combined action of plastic void growth and shear banding of polymeric glasses. This would explain the deficit in the book-keeping of [75]. It appears that the synergism between mechanisms may only be fully accounted for empirically, by obtaining detailed experimental measurements of the damage mechanisms that actually transpire in concert [108].

6.4 Conditions Which Promote Crack Trapping

The maximum potential toughening by crack trapping can be induced in brittle solids only by heterogeneities which are tougher than the host matrix, so that crack penetration of the heterogeneities is prevented. In addition, the heterogeneities must have moduli equal to or greater than the modulus of the matrix, so that the opening displacement can be suppressed at regions along a crack front. If either of these two conditions are not met, than the evolution of crack trapping will be prematurely terminated by escape of the crack front from the pinning positions, and the maximum toughening effect will not be attained.

A further requirement necessary for the operation of crack trapping is that the tough heterogeneities be sufficiently well bonded to the matrix. The experiments performed in this study have shown that if the reinforcements are highly elongated and aligned perpendicular to the crack plane, then "perfect" bonding is not necessary, since the crack tip has no escape route it can follow to avoid the obstacles. As long as the adhesive strength between rod-like inclusions and the matrix is high enough to prevent pull-out of the rods, then opening displacement of the crack front is prevented at the periphery of the rods, and crack trapping ensues. Partial debonding of the rods was observed to reduce the level of stress intensity required to advance cracks past rods by only 5–10%. When the tough heterogeneities are equiaxed particles, adhesive strength becomes a more critical issue.

If the adhesive strength between a matrix and equiaxed particles is low, than the crack front can easily avoid being pinned either by debonding the particles ahead of it in the triaxial stress field, or by following the interfaces through interfacial fracture processes when particles are reached. The experiments performed here indicate that an adhesive strength of above 50 MPa between spheres and the matrix comprising the model specimens was sufficient to enable crack trapping to fully evolve and transit

to bridging. Reduction of the sphere/matrix adhesive strength to about 25 MPa enabled crack fronts to skirt around the obstacles after exhibiting only a very limited amount of crack trapping. To extrapolate this information to other matrix/particle systems, which may have significantly higher moduli than the materials used here (and hence, would generate higher stresses at particle interfaces) we emphasize that crack trapping is produced by imposed localized regions of minimal crack opening displacement. Since extensive plastic flow at crack tips would permit the relaxation of such constraints, the strength of adhesive bonds between a matrix and second-phase particles which is required to permit crack trapping to occur must be considered relative to the flow stress of the matrix material. In the model specimens containing spherical particles, adhesive strengths of approximately $\sigma_y/3$ produced the effects of "perfect" bonding. Reduced adhesive strengths of $\sigma_a \sim 0.16\,\sigma_y$ diminished the toughening produced by crack trapping to about 10% of its potential. Thus, it may be expected that adhesive strengths which are on the order of 30% of the yield strength of the host matrix are required to generate the maximum toughness which can be provided by crack trapping.

In order for crack trapping to occur, crack tips must come in contact with the dispersed inclusions. If the inclusions are long fibers oriented normal to the crack plane, then the crack tip will obviously be impeded. If, on the other hand, the inclusions are either short fibers or particulates randomly dispersed throughout the matrix, then favorable stress conditions which attract crack tips to the particles are necessary for crack trapping to occur. Residual stresses established during fabrication must be radially compressive at the particle surfaces (expansion coefficient of particle less than that of matrix) so that tensile tangential stresses in the matrix attract crack tips to the equators of particles. These stresses must be high enough to counterbalance the stresses created by modulus mismatch stress concentrations, since the latter will tend to attract cracks to the poles of particles which are more rigid than their host matrix. (The stress concentrations created by more compliant particles favor crack growth toward particle equators, but particles which are more compliant than the

matrix will not effectively constrain the crack front opening displacement.) The residual tensile tangential stresses should not, however, be so great as to cause radial cracks to nucleate from the particles [109].

For the contribution to overall toughness made by crack trapping to be significant, the relative toughening by other mechanisms should be less so. For instance, in polymeric glass composites which derive significant gains in toughness from shear yielding promoted by stress concentrating particles, the contribution made by crack trapping may by modest, both on a relative basis and on an absolute basis since plastic straining at the crack tip may relax the displacement constraint necessary to generate crack trapping. Crystalline materials with weak grain boundaries may gain most of their toughness by microcracking, while obviating the possibility of crack trapping to occur by deflecting crack tips over tough grains.

The experiments performed here have shown that brittle materials containing tough, second-phase particles can experience more than a doubling of their fracture toughness through the crack trapping mechanism alone. The toughness enhancement resulting from crack trapping has been demonstrated to be a function solely of volume fraction of particles, provided that the heterogeneities are tough enough and stiff enough to enforce islands of inhibited opening displacement at crack tips. Crack-trapping toughness increases monotonically with volume fraction of well-bonded particles, and develops twice the toughness of the matrix at a volume fraction of $c = 0.2$. Experimental results indicate that the toughness enhancement can be doubled again, to an effective toughness equal to thrice the neat value, with an increase in particle volume fraction to $c = 0.3$. In order for similar levels of toughening to be realized in a "real" material with dispersed micro-constituents, optimum combinations of materials would be required to cause maximum crack trapping behavior to occur.

Chapter 7

Summary

In the principal focus of this thesis, experiments were developed in which the crack-trapping mechanism was studied in the absence of other, distracting mechanisms. By quasi-statically propagating a crack in macroscopic model specimens fabricated from a brittle matrix containing tough, elastically similar obstacles, magnitudes of crack-trapping induced toughening were determined during the continuous process of crack-front/particle interaction. The maximum crack-trapping toughness was determined as a function of particle spacing and adhesive strength to the matrix.

With sufficiently well-bonded particles, it was found that crack trapping would produce toughness levels of about 1.7 times the matrix toughness at particle spacings of $R/L = 0.125$, which corresponds to an equivalent volume fraction of particles equal to 0.06 (based upon representative volume (area) elements having radius $L/2$). Increasing the equivalent volume fraction to about 0.26 increased the resulting crack-trapping toughness to about $2.7\,K_{Ic}^{\text{matr}}$. The adhesive strength required to create these (maximum) levels of crack-trapping toughness with spherical particles was determined, with an auxiliary experimental technique, to be in excess of 50 MPa, which is approximately one-third of the yield strength of the matrix. Reduction of this adhesive strength by a factor of two resulted in the diminishing of the effectiveness

of the crack-trapping mechanism by an order of magnitude. In the case of elongated particles (rods) oriented perpendicular to the crack fronts, adhesive strengths (over the range of 25 to 50 MPa) were found to have minimal influence since crack tips could not circumnavigate the obstacles.

The crack-trapping experiments also provided high quality images of the crack-front shapes while interacting with the trapping obstacles. From these images, the complete evolution of the crack-trapping process was revealed, from the initial pinning of the crack front to the coalescence of the local, bowed fronts behind the obstacles, forming the transition to the crack-bridging mechanism. The shapes of crack fronts generated during crack trapping were compared to predictions obtained from the numerical simulations of Bower and Ortiz. In general, excellent agreement was demonstrated. Limited debonding of Nylon rods during the crack-trapping process allowed crack fronts in those experiments to advance slightly farther than the numerical predictions. In model specimens with polycarbonate obstacles demonstrating "perfect" adhesion, excellent agreement between the experimental data and numerical predictions existed up to the point where the maximum local crack bowing was reached (breakaway configuration); beyond this point, the experiments provided crack-trapping toughening levels which exceeded the numerical predictions by 15–20%.

In accompanying developments (presented in appendices), an experimental technique was developed to measure the "true" adhesive strength between transparent matrices and included spherical particles. By subjecting the candidate particle to a triaxial stress field with no singular stress concentrations, the radial stress causing debonding to occur was determined. Analysis of the data obtained from these experiments provided not only the particle/matrix adhesive strength, but also an estimate of the interfacial fracture energy.

Extensive characterization of the deformation and fracture behavior of the epoxy

used as a matrix material in the crack-trapping experiments was performed as a supportive effort. Yield stress measurements were obtained as a function of temperature and strain rate, and were correlated to the Argon molecular theory of polymer deformation. Strain-hardening behavior of the epoxy was characterized, and it was found that the trend of increasing strain-hardening rate with increasing glass transition temperature was paralleled by the trend of increasing brittleness. Fracture toughness tests performed as a function of deceasing temperature demonstrated that the notorious room-temperature, jerky fracture behavior of epoxy subsided with increasing yield stress.

Limited experiments concerning the use of photoelasticity for the determination of thermal misfit stresses in the vicinity of inclusions have demonstrated the existence of two effects which should be taken account of. The first effect (which is not discussed in the literature, possibly because it is relevant only to resins which cure in two stages) concerns the creation of a birefringent field solely due to molecular conformation to topographic constraints imposed during polymerization of the main carbon-carbon chains. This birefringence becomes locked in place during subsequent cross-linking of the epoxy groups, and cannot be removed by annealing; hence, the final birefringence includes a component from this source. The second phenomenon is that of photomechanical creep (and relaxation), which is well documented but sometimes ignored. In viscoelastic/plastic, birefringent materials, isochromatic fringes resulting from strains which are imposed for a long period of time become fixed in place, so that intersection of the strain fields by a traction-free surface results in little perturbation of the fringes. This is the very same effect which enables the "stress-freezing" technique which is used to determine three-dimensional stresses with photoelasticity. Nonetheless, rates of photomechanical creep differ from mechanical, viscoelastic creep rates and must be determined for specific materials when photomechanical measurements are to be made over great lengths of time.

Bibliography

[1] Evans, A.G., "Perspective on the development of high-toughness ceramics," *Journal of the American Ceramic Society,* **73**, (2) (1990), 187–206.

[2] Ibrahim, I.A., Mohamed, F.A. and Lavernia, E.J., "Particulate reinforced metal matrix composites – a review," *Journal of Materials Science,* **26** (1991), 1137–1156.

[3] Garg, A.C. and Mai, Y.-W., "Failure mechanisms in toughened epoxy resins–A Review," *Composites Science and Technology,* **31** (1988), 179–223.

[4] Rice, J.R., "Crack fronts trapped by arrays of obstacles: solutions based upon linear perturbation theory," in *Analytical, Numerical and Experimental aspects of Three Dimensional Fracture Processes,* eds. Rosakis *et al.* (ASME AMD-Vol. 91 1988), 175–184.

[5] H. Gao and J. R. Rice, "A first-order perturbation analysis of crack trapping by arrays of obstacles," *Journal of Applied Mechanics,* **56** (1989), 828–836.

[6] Bower, A.F. and Ortiz, M., "A three-dimensional analysis of crack trapping and bridging by tough particles," *Journal of Mechanics and Physics of Solids,* **39**, (6) (1991), 815–858.

[7] Bower, A.F. and Ortiz, M., *personal communications* (1992).

[8] Lange, F.F., "The interaction of a crack front with a second phase dispersion," *Philosophical Magazine,* **22** (1970), 983–992.

[9] *Flow and Fracture of Metals and Alloys in Nuclear Environments,* ASTM STP 380, (ASTM 1965).

[10] McClintock, F.A. and Argon, A.S., *Mechanical Behavior of Materials* (Addison-Wesley 1966).

[11] *Idem, ibid*, 110.

[12] Martin, J.W., *Micromechanisms in Particle-Hardened Alloys*, (Cambridge 1980), 50–63.

[13] Lange, F.F.,"Fracture energy and strength behavior of a sodium borosilicate glass-Al_2O_3 composite system," *Journal of the American Ceramic Society*, **54**, (12) (1971), 614–620.

[14] Evans, A.G., "The strength of brittle materials containing second phase dispersions," *Philosophical Magazine*, **26** (1972), 1327–1344.

[15] Green, D.J., Nicholson, P.S. and Embury, J.D., "Fracture of a brittle particulate composite *(Part 2)*," *Journal of Materials Science*, **14** (1979), 1657–1661.

[16] Fares, N., "Crack fronts trapped by arrays of obstacles: numerical solutions based on surface integral representation," *Journal of Applied Mechanics*, **56** (1989), 837–843.

[17] Rose, L.R.F., "Toughening due to crack-front interaction with a second-phase dispersion," *Mechanics of Materials*, **6** (1987), 11–15.

[18] Flinn, B.D., Rühle, M. and Evans, A.G., "Toughening in composites of Al_2O_3 reinforced with Al," *Acta metallurgica*, **37**, (11) (1989), 3001–3006.

[19] Dalgleish, B.J., Trumble, K.P. and Evans, A.G., "The strength and fracture of alumina bonded with aluminum alloys," *Acta metallurgica*, **37**, (7) (1989), 1923–1931.

[20] Anderson, C.A. and Aghajanian, M.K., "The fracture toughening mechanism of ceramic composites containing adherent ductile metal phases," *Ceramic Engineering Science Proceedings*, **9**, (7–8)(1988), 621–626.

[21] Flom, Y. and Arsenault, R.J., "Effect of particle size on fracture toughness of SiC/Al composite material," *Acta metallurgica*, **37**, (9) (1989), 2413–2423.

[22] Sigl, L.S. and Exner, H.E.,"Experimental study of the mechanics of fracture in WC-Co Alloys," *Metallurgical Transactions A*, **18** (1987), 1299–1308.

[23] Sigl, L.S., Mataga, P.A., Dalgleish, B.J., McMeeking, R.M. and Evans, A.G., "On the toughness of brittle materials reinforced with a ductile phase," *Acta metallurgica*, **36**, (4) (1988), 945–953.

[24] Evans, A.G. and McMeeking, R.M., "On the toughening of ceramics by strong reinforcements," *Acta metallurgica,* **34**, (12) (1986), 2435–2441.

[25] Kang, E.S. and Kim, C.H., "Improvements in mechanical properties of TiB_2 by the dispersion of B_4C particles," *Journal of Materials Science,* **25** (1990), 580–584.

[26] Kim, D-H. and Kim, C.H., "Toughening behavior of silicon carbide with additions of yttria and alumina," *Journal of the American Ceramic Society,* **73**, (5) (1990), 1431–1434.

[27] Faber, K.T. and Evans, A.G., "Crack deflection processes–I. Theory," *Acta metallurgica,* **31**, (4) (1983), 565–576.

[28] McMeeking, R.M. and Evans, A.G., "Mechanics of transformation-toughening in brittle materials," *Journal of the American Ceramic Society,* **65**, (5) (1982), 242–246.

[29] Green, D.J., Hannink, R.H.J. and Swain, M.V., *Transformation Toughening of Ceramics,* (CRC Press 1989).

[30] Wang, J. and Stevens, R., "Review: Zirconia-toughened alumina (ZTA) ceramics," *Journal of Materials Science,* **24** (1989), 3421–3440.

[31] Frey, W.J. and Mackenzie, J.D., "Mechanical properties of selected glass-crystal composites," *Journal of Materials Science,* **2** (1967), 124–130.

[32] Davidge, R.W. and Green, T.J., "The strength of two-phase ceramic/glass materials," *Journal of Materials Science,* **3** (1968), 629–634.

[33] Swearengen, J.C., Beauchamp, E.K. and Eagan, R.J., "Fracture toughness of reinforced glasses," in *Fracture Mechanics of Ceramics, Vol. 4,* eds. R. C. Bradt *et al.* (Plenum Press 1978), 973–987.

[34] Green, D.J., Nicholson, P.S. and Embury, J.D., "Fracture of a brittle particulate composite *(Part 1),*" *Journal of Materials Science,* **14** (1979), 1413–1420.

[35] Broutman, L.J. and Sahu, S., "The effect of interfacial bonding on the toughness of glass filled polymers," *Materials Science and Engineering,* **8** (1971), 98–107.

[36] Faber, K.T., Evans, A.G. and Drory, M.D., "A statistical analysis of crack deflection as a toughening mechanism," in *Fracture Mechanics of Ceramics, Vol. 6,* eds. R. C. Bradt *et al.* (Plenum Press 1983), 77–91.

[37] Kinloch, A.J., Maxwell, D.L. and Young, R.J., "The fracture of hybrid-particulate composites," *Journal of Materials Science,* **20** (1985), 4169–4184.

[38] Cantwell, W.J., Smith, J.W., Kausch, H.H. and Kaiser, T., "Examination of the process of deformation and fracture in a silica-filled epoxy resin," *Journal of Materials Science,* **25** (1990), 633–648.

[39] Spanoudakis, J. and Young, R.J., "Crack propagation in a glass particle-filled epoxy resin *(Part 2: Effect of particle-matrix adhesion),*" *Journal of Materials Science,* **19** (1984), 487–496.

[40] Moloney, A.C., Kausch, H.H., Kaiser, T. and Beer, H.R., "Review: Parameters determining the strength and toughness of particulate filled epoxy resins," *Journal of Materials Science,* **22** (1987), 381–393.

[41] Amdoudi, N. *et al,* "Coated glass beads epoxy composites: influence of the interlayer thickness on pre-yielding and fracture properties," *Journal of Materials Science,* **25** (1990), 1435–1443.

[42] Moloney, A.C., Kausch, H.H. and Stieger, H.R., "The fracture of particulate-filled epoxide resins (Part 1)," *Journal of Materials Science,* **18** (1984), 208–216.

[43] Cantwell, W.J., and Roulin-Moloney, A.C., "Fractography and failure mechanisms of unfilled and particulate filled epoxy resins," in *Fractography and Failure Mechanisms of Polymers and Composites,* ed. Roulin-Moloney (Elsevier 1989), 233–290.

[44] Pitman, G.L. and Ward, I.M., "Effect of molecular weight on crack shape and fracture toughness in polycarbonate," *Polymer,* **20** (1979), 895–902.

[45] Brown, H.R., "A model for brittle-ductile transitions in polymers," *Journal of Materials Science,* **17** (1982), 469–476.

[46] Mai, Y. and Williams, J.G., "The effect of temperature on the fracture of two partially crystalline polymers; polypropylene and Nylon," *Journal of Materials Science,* **12** (1977), 1376–1382.

[47] Kinloch, A.J. and Young, R.J., *Fracture Behavior of Polymers,* (Elsevier 1988), 344.

[48] Theocaris, P.S., "Time dependence of creep recovery in cross-linked polymers," *Rheologica Acta,* **6**,, (2) (1967), 246–251.

[49] Moy, P. and Karasz, F.E., "Epoxy-water interactions," *Polymer Engineering and Science,* **20** (4), (1980), 315–319.

[50] Peyser, P. and Bascom, W.D., "The anomalous lowering of the glass transition of an epoxy resin by plasticization with water," *Journal of Materials Science,* **16** (1981), 75–83.

[51] Moy, P. and Karasz, F.E., "The interactions of water with epoxy resins," in *Water in Polymers,* ed. Rowland, S.P. **ACS 127** (American Chemical Society Wash., D.C. 1980), 505–513.

[52] Ellis, T.S. and Karasz, F.E., "Interaction of epoxy resins with water: the depression of glass transition temperature," *Polymer,* **25** (1984), 664–669.

[53] Kanninen, M.F., "An augmented double cantilever beam model for studying crack propagation and arrest," *International Journal of Fracture,* **9**, (1) (1973), 83–92.

[54] Taya, M. *et al.*, "Toughening of a particulate-reinforced ceramic-matrix composite by thermal residual stress," *Journal of the American Ceramic Society,* **73**, (5) (1990), 1382–1391.

[55] A. G. Evans and R. M. McMeeking, "On the toughening of ceramics by strong reinforcements," *Acta metallurgica,* **34**, (12) (1986), 2435–2441.

[56] Ashby, M.F., Blunt, F.J. and Bannister, M., "Flow characteristics of highly constrained metal wires," *Acta Metallurgica,* **37**, (7) (1989), 1847–1857.

[57] Bannister, M. *et al.*, "Toughening in brittle systems by ductile bridging ligaments," *Acta Metallurgica,* **40**, (7) (1992), 1531–1537.

[58] V. V. Krstic, P. S. Nicholson and R. G. Hoagland, R. G. , "Toughening of glasses by metallic particles," *Journal of the American Ceramic Society,* **64**, (9) (1981), 499–504.

[59] Phillips, D.C. and Scott, J.M., "Determination of the K, v diagram of epoxide resins," *Journal of Materials Science Letters,* **9** (1974), 1202–1205.

[60] Young, R.J. and Beaumont, P.W.R., "Failure of brittle polymers by slow crack growth," *Journal of Materials Science,* **10** (1975), 1343–1350.

[61] Gledhill, R.A. and Kinloch, A.J., "Crack growth in epoxide resin adhesives," *Journal of Materials Science Letters,* **10** (1975), 1261–1263.

[62] Evans, A.G. and Faber, K.T., "Crack-growth resistance of microcracking brittle materials," *Journal of the American Ceramic Society,* **67**, (4) (1984), 255–260.

[63] Budiansky, B. and O'Connell, R.J., "Elastic moduli of a cracked solid," *International Journal of Solids and Structures,* **12** (1976), 81–97.

[64] Hutchinson, J.W., "Crack tip shielding by micro-cracking in brittle solids," *Acta metallurgica,* **35**, (7) (1987), 1605–1619.

[65] Ortiz, M., "A continuum theory of crack shielding in ceramics," *Journal of Applied Mechanics,* **54** (1987), 54–283.

[66] Ortiz, M. and Giannakopoulos, A.E., "Maximal crack tip shielding by microcracking," *Journal of Applied Mechanics,* **56** (1989), 279–283.

[67] Charalambides, P.G. and McMeeking, R.M., "Finite element method simulation of crack propagation in a brittle microcracking solid," *Mechanics of Materials,* **6** (1987), 71–87.

[68] Dolgopolsky, A., Karbhari, V. and Kwak, S.S., "Microcrack induced toughening–an interaction model," *Acta metallurgica,* **37**, (5) (1989), 1349–1354.

[69] Laures, J.-P. and Kachanov, M., "Three-dimensional interactions of a crack front with arrays of penny-shaped microcracks," *International Journal of Fracture,* **48** (1991), 255–279.

[70] Ortiz, M., "Microcrack coalescence and macroscopic crack growth initiation in brittle solids," *International Journal of Solids and Structures,* **24** (1988), 231–250.

[71] Argon, A.S., "Sources of Toughness in Polymers," in *Advances in Fracture Research (ICF7),* **4**, eds. K. Salama *et al.* (Pergamon 1989), 2661–2681.

[72] Argon, A.S. and Cohen, R.E., "Crazing and Toughness of Block Copolymers and Blends," in *Advances in Polymer Science,* **91/92**, ed. H.H. Kausch (Springer-Verlag 1990), 301–351.

[73] Budiansky, B., Hutchinson, J.W. and Lambropoulos, J.C., "Continuum theory of dilatational transformation toughening in ceramics," *International Journal of Solids and Structures,* **19**, (7) (1983), 337–355.

[74] Evans, A.G. and Cannon, R.M., "Toughening of brittle solids by martensitic transformations," *Acta metallurgica,* **34**, (5) (1986), 761–800.

[75] Huang, Y. and Kinloch, A.J., "Modelling of the toughening mechanisms in rubber-modified epoxy polymers: II," *Journal of Materials Science,* **27** (1992), 2763–2769.

[76] Kinloch, A.J., Maxwell, D.L. and Young, R.J., "Micromechanisms of crack propagation in hybrid-particulate composites," *Journal of Materials Science Letters,* **4** (1985), 1276–1279.

[77] Kinloch, A.J., Shaw, S.J., Tod, D.A. and Hunston, D.L., "Deformation and fracture behavior of a rubber-toughened epoxy: 1. Microstructure and fracture studies," *Polymer,* **24** (1983), 1341–1354.

[78] Parker, D.S., Sue, H-J., Huang, J. and Yee, A.F., "Toughening mechanisms in core-shell rubber-modified polycarbonate," *Polymer,* **31** (1990), 2267–2277.

[79] Sue, H-J., "Craze-like damage in a core-shell rubber-modified epoxy system," *Journal of Materials Science,* **27** (1992), 3098–3107.

[80] Pearson, R.A. and Yee, A.F., "Sources of toughness in modified epoxies," in *Proceedings of the ACS Division of Polymeric Materials: Science and Engineering,* **63** (ACS 1990), 311–314.

[81] Kunz-Douglass, S., Beaumont, P.W.R. and Ashby, M.F., "A model for the toughness of epoxy-rubber particulate composites," *Journal of Materials Science,* **15** (1980), 1109–1123.

[82] Li., D., Li., X. and Yee, A.F., "The role of cavitation in rubber particles in the deformation of rubber toughened epoxy resins under constrained conditions," *Proceedings of the ACS Division of Polymeric Materials: Science and Engineering,* **63** (ACS 1990), 311–314.

[83] Guild, F.J., and Young, R.J., "A predictive model for particulate filled composite materials," *Journal of Materials Science,* **24** (1989), 2454–2460.

[84] Huang, Y. and Kinloch, A.J., "Modelling of the toughening mechanisms in rubber-modified epoxy polymers: I," *Journal of Materials Science,* **27** (1992), 2753–2762.

[85] Yee, A.F., "Fracture behavior and toughening of rigid/rigid polymer alloys," *Proceedings of the ACS Division of Polymeric Materials: Science and Engineering,* **63** (ACS 1990), 311–314.

[86] Gebizlioglu, O.S., Argon, A.S. and Cohen, R.E., "Craze plasticity and toughness of particulate block copolymer blends," *Polymer,* **26** (1985), 529–542.

[87] Faber, K.T. and Evans, A.G., "Crack deflection processes–II. Experiment," *Acta metallurgica,* **31**, (4) (1983), 577–584.

[88] DeHoff, R.T. and Rhines, F.N., *Quantitative Microscopy,* (McGraw-Hill 1968).

[89] Stett, M.A. and Fulrath, R.M., "Mechanical properties and fracture behavior of chemically bonded composites," *Journal of the American Ceramic Society,* **53**, (1) (1970), 5–13.

[90] Moloney, A.C., Kausch, H.H. and Steiger, H.R., "The fracture of particulate-filled epoxide resins (Part 2)," *Journal of Materials Science,* **19** (1984), 1125–1130.

[91] Moloney, A.C. and Kausch, H.H., "Direct observations of fracture mechanisms in epoxide resins," *Journal of Materials Science Letters,* **4** (1985), 289–292.

[92] Young, R.J., Maxwell, D.L. and Kinloch, A.J., "The deformation of hybrid-particulate composites," *Journal of Materials Science,* **21** (1986), 380–388.

[93] Maxwell, R.J., Young, R.J. and Kinloch, A.J., "Hybrid particulate-filled epoxy-polymers," *Journal of Materials Science Letters,* **3** (1984), 9–12.

[94] Spanoudakis, J. and Young, R.J., "Crack propagation in a glass particle-filled epoxy resin *(Part 1)*," *Journal of Materials Science,* **19** (1984), 473–486.

[95] Dekkers, M.E.J. and Heikens, D., "Shear band formation in polycarbonate-glass bead composites," *Journal of Materials Science,* **19** (1984), 3271–3275.

[96] Dekkers, M.E.J. and Heikens, D., "The effect of interfacial adhesion on the mechanism for craze formation in polystyrene-glass bead composites," *Journal of Materials Science,* **18** (1983), 3281–3287.

[97] Lange, F.F. and Radford, K.C., "Fracture energy of an epoxy composite system," *Journal of Materials Science,* **6** (1971), 1197–1203.

[98] Krstic, V.D., "On the fracture of brittle-matrix/ductile-particle composites," *Philosophical Magazine,* **48**, (5) (1983), 695–708.

[99] Mai, Y-W. and Lawn, B.R., "Crack-interface grain bridging as a fracture resistance mechanism in ceramics: Part II, Theoretical fracture mechanics model," *Journal of the American Ceramic Society,* **70**, (4) (1987), 289–294.

[100] Swanson, P.L., Fairbanks, C.J., Lawn, B.R. and Mai, Y-W., and B. J. Hockey, "Crack-interface grain bridging as a fracture resistance mechanism in ceramics: Part I, Experimental study on alumina," *Journal of the American Ceramic Society,* **70**, (4) (1987), 279–289.

[101] Bennison, S.J. and Lawn, B.R., "Role of interfacial grain-bridging sliding friction in the crack-resistance and strength properties of nontransforming ceramics," *Acta metallurgica,* **37**, (10) (1989), 2659–2671.

[102] Evans, A.G. and He, M.Y., "Interface debonding and fiber cracking in brittle matrix composites," *Journal of the American Ceramic Society,* **72**, (12) (1989), 2300–2303.

[103] Llorca, J. and Elices, M., "A cohesive crack model to study the fracture behavior of fiber-reinforced brittle-matrix composites," *International Journal of Fracture,* **54** (1992), 251–267.

[104] Cao, H.C., Yang, J. and Evans, A.G., "The mode I fracture resistance of unidirectional fiber-reinforced aluminum matrix composites," *Acta metallurgica,* **40**, (9) (1992), 2307–2313.

[105] Hu, M.-S., Yang, J., Cao, H.C., Evans, A.G. and Mehrabian, R., "The mechanical properties of Al alloys reinforced with continuous Al_2O_3 fibers," *Acta metallurgica,* **40**, (9) (1992), 2315–2326.

[106] Li, V.C. and Ward, R.J., "A novel testing technique for post-peak tensile behavior," in *Fracture Toughness and Fracture Energy,* ed. Mihashi (A. A. Balkema Pubs. 1989).

[107] Amazigo, J.C. and Budiansky, B., "Interaction of particulate and transformation toughening," *Journal of the Mechanics and Physics of Solids,* **36**, (5) (1988), 581–595.

[108] Evans, A.G., Ahmad, Z.B., Gilbert, D.G. and Beaumont, P.W.R., "Mechanisms of toughening in rubber toughened polymers," *Acta metallurgica,* **34**, (1) (1986), 79–87.

[109] Krstic, V.D. and Vlajic, M.D., "Conditions for spontaneous cracking of a brittle matrix due to the presence of thermoelastic stresses," *Acta metallurgica,* **31** (1983), 139–144.

Part II

Supportive Measurements

Appendices To

Experimental Investigations of Crack Trapping
in
Brittle Heterogeneous Solids

by
Todd M. Mower

Contents

List of Figures

List of Tables

Appendix A

Mechanical Characterization of Materials Used in Model Specimens

This appendix documents the measurement of physical properties of materials used to fabricate the model specimens employed in the crack-trapping experiments. The data are discussed both in light of the use of the materials in those experiments, and in the context of material behavior in general.

The principal motivation for the careful determination of constituent properties is that in order to enable correct interpretation of the behavior of composite models, the relevant behaviors of the individual components must be known with confidence. Also of major importance is the desire to ensure compatibility (*e.g.* elastic similarity) of the components, thus simplifying the analysis. Additionally, accurate knowledge of thermal properties allows analytical determination of stress states in the model specimens in the conditions under which they are tested. The mechanical behavior of the matrix, epoxy, is investigated and discussed at length due to its industrial importance. Specifically, efforts were directed to increasing the information available regarding the effects of cure, aging, strain-rate and temperature on deformation and fracture behavior.

A.1 Matrix Material (DGEBA Epoxy)

A.1.1 Criteria for Selection as Matrix Material

The major emphasis of this thesis is the experimental study of crack-trapping by tough particles in brittle materials. The selection of an appropriate matrix material for this purpose is based upon its inherent brittleness, lack of material-specific damage mechanisms and ease of fabrication. While it is obvious that inherent brittleness should be a selection factor, it is emphasized here that we strive to isolate the crack-trapping toughening mechanism by suppressing all others; hence, brittle crystalline materials (*e.g.* ceramics) which microcrack and glassy polymers which craze (thermoplastics) should be avoided. One suitable alternative is epoxy.

With proper resin/hardener ratios and heat curing, epoxy can be a very brittle matrix material. Initial fracture toughness tests with specimens cast from Epon 815 (Shell Chemical Co.) yielded critical stress intensity factors in the range of 0.5 to $1.0\,\mathrm{MPa\,m^{\frac{1}{2}}}$, with critical energy release rates on the order of 200 to 400 $\mathrm{J/m^2}$. Being an amorphous (glassy) solid composed of huge molecules, epoxy has no crystal microstructure along which microcracks can form. High crosslink density between molecular chains suppresses crazing to the extent that reports of crazing are sparse and speculative [1, 2, 3]. Epoxy does possess plastic characteristics, however, exhibiting crack-tip blunting [4, 5, 6] and shear banding [7, 8, 9], which are thought to be the principal toughening mechanisms in unreinforced resins [10, 11]. Both of these mechanisms occur to some extent in most materials which exhibit any degree of plasticity [12]. Because these mechanisms operate on a microscopic scale, their occurrence in the epoxy (macroscopic) model systems used in this study will not compromise the models' ability to produce generic crack-front effects induced by particles. In addition, epoxy has tremendous commercial value not just as an adhesive, but also (when reinforced) as a structural material used in many industries.

A.1.2 Specification of Components

A.1.2.1 DGEBA epoxy resin

The epoxy chosen for use as a matrix material in the model specimens was a widely-used member of the large family of "diglycidyl ether of bisphenol-A" (DGEBA) resins. The specific resin used carries the trade name "EPON 815," and was provided in bulk by Shell Chemical Co. This resin consists primarily of the chemically-pure EPON 828, which has the viscosity of molasses (13 Pa s) @ STP, but is diluted with 15% butyl glycidyl ether to a consistency of light syrup (0.6 Pa s) @ STP [13]. The diluted resin (815) was favored for the fabrication of model specimens in order to facilitate complete evacuation of air which becomes entrapped during mixing. (Viscosity can, of course, be lowered by heating the resin but that reduces the working "pot" life available for specimen fabrication.) The differences in mechanical properties between the cured solids of the pure and diluted versions are slight, as indicated in the Shell reference bulletin [13]. The molecular weight of EPON 815 is about 380; because it is a difunctional resin, the epoxide equivalent weight (used for determining stoichiometry) is about 190 [13]. In general, higher molecular weight resins stimulate chain extension and result in more flexible cured solids; the low molecular weights of EPON 815 and 828 favor cross-linking and result in brittle materials. Great variation in the properties of cured epoxies is, however, achieved through the use of different curing agents.

A.1.2.2 Curing agents

The curing agent used for all of the model specimens was a polyamide provided by Shell under the trade name of "V-40". This curing agent, with a viscosity of 12 Pa s @ STP, is a "condensation product of polyamines and dibasic acids produced by the polymerization of unsaturated fatty acids [13]." The exact constituents and proportions are unknown (perhaps just proprietary), but V-40 is essentially a bifunctional diamine [14]. The feature of V-40 most useful for the fabrication of model specimens

is that its primary amines generate a room-temperature cure, allowing the positioning of particles on or below the surface while gelation occurs. Subsequent post-cures, at elevated temperatures, activate the secondary amines and achieve the final cross-linking of unreacted epoxy groups.

The stoichiometry of EPON 815/V-40 is determined by balancing the epoxide equivalent weight (190 mg epoxide/mequiv.) with the available amine hydrogens (145 mg/mequiv.) [15]. Thus, a stoichiometric mix would be about 3 parts EPON 815 mixed with 4 parts V-40. Nevertheless, Shell recommends concentrations of 33 to 100 parts (curing agent) per hundred resin (phr), and indicates that highest toughness is achieved with equal proportions. Because brittleness was sought for the matrix of the model specimens, a V-40 concentration of 33 phr was used. (This concentration is hereafter referred to as 3:1–resin:curing agent.) Most specimens cast for characterization purposes had 3:1 proportions, but due to the widespread use of EPON 828/V-40 in proportions of 3:2, some specimens were also cast with a 3:2 ratio. Three different post-curing temperature schedules were utilized for the V-40 specimens and are schematically shown in Figure A.1.

A second, fundamentally different type of curing agent has also been used in this research to fabricate specimens for use in evaluating the toughening produced by microparticles. This second curing agent was boron triflouride monoethylamine (BF_3MEA), and was provided by the Miller Stephenson Co. BF_3MEA is a salt-complex member of the Lewis Acid family, and catalyzes homopolymerization of epoxy resins at elevated temperatures to a much greater degree than can be obtained with amines; hence, epoxies cured with BF_3MEA can withstand higher temperatures, but are more brittle [16]. BF_3MEA is a solid at room temperature and slowly dissolves in epoxy resin at a temperature of 90° C, whereupon the mixture remains as a stable liquid for months until heated to the catalytic temperature. For all specimens cured with BF_3MEA, a concentration of 3% (by weight) was used and the temperature schedule shown in Figure A.1 was followed, according to the manufacturer's recommendations [17].

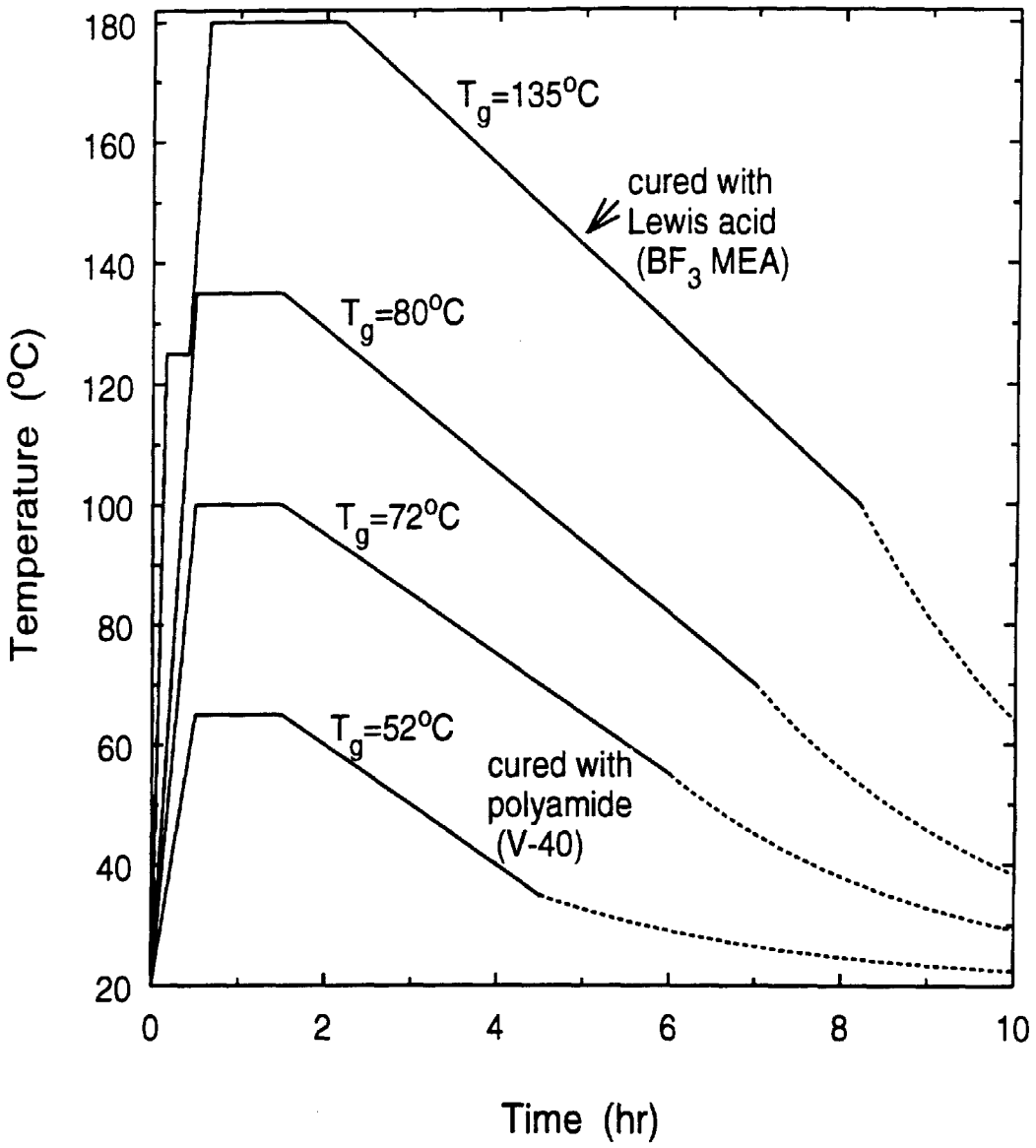

Figure A.1: Thermal curing schedules for the epoxy formulations investigated. Lower three schedules were used as post cures following 24^+ hr, room-temperature curing with a bifunctional (V-40) polyamide. Solid lines represent programmed oven-control; dashed lines approximate exponential natural cooling. Glass transition temperatures indicated for EPON 815 resin cured with 3% BF_3MEA and with V-40 at a 3:1 mix ratio.

A.1.3 Thermal Measurements

A.1.3.1 Glass transition temperatures

Cured epoxies are amorphous, glassy polymers. As such, their response to mechanical stimuli is strongly dependent upon temperature and must be discussed with reference to their glass transition temperatures. Glass transition temperatures (T_g) are not necessarily unique material properties, but are dependent upon the cooling rate at which the liquid approaches the solid state [18]. As shown in the generic plot of specific volume (or enthalpy) *versus* temperature in Figure A.2, faster cooling rates give rise to higher transition temperatures. Furthermore, the physical transformation from liquid to solid states does not occur sharply (as in a melt or crystallization), but takes place over a rather broad temperature region of 30°C or more in extent.

The apparent difficulties in specifying T_g are surmounted by following conventions. Because measured T_g's vary by only a few degrees for an order of magnitude change in cooling rate [19], only slight discrepancies are observed between research reports on similar materials utilizing different rates. As long as one rate is used in determining transition temperatures of materials being compared, then the exact rate of cooling is of little consequence. The matter of selecting a discrete temperature to label 'T_g' is resolved by choosing the temperature corresponding to the intercept between the solid and liquid state asymptotes, as indicated by the points H and H′ in Figure A.2 [18, 20, 21]. This temperature will coincide with the midpoint of the observed S-shaped discontinuity in expansion coefficient or specific heat *versus* temperature which is schematically shown in Figure A.3.

Of the many thermal analysis techniques available, the ones most commonly used for determination of glass transition temperatures are dynamic modulus measurement [22], differential scanning calorimetry (DSC) [24] and thermal expansion measurement. Dynamic modulus measurements typically exhibit $tan\,\delta$ peaks at temperatures exceeding T_g by 15 to 20°C [25, 26], and were not used here. Thermal expansion and DSC measurements were employed instead and are related as follows.

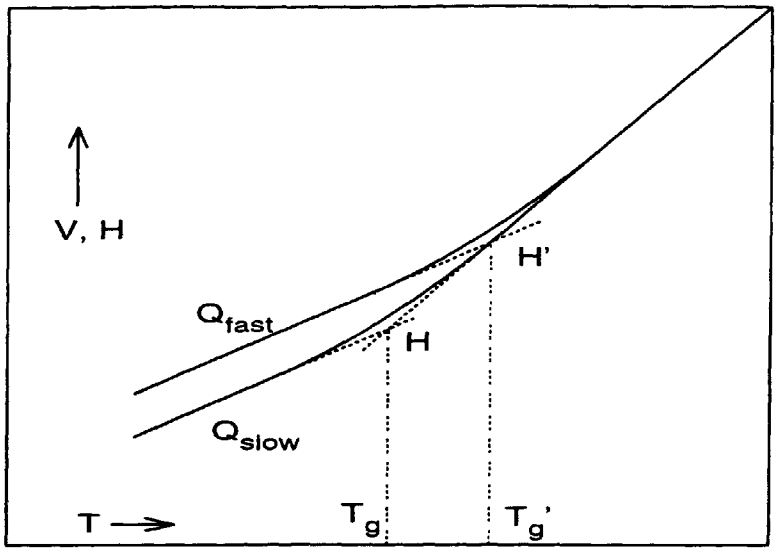

Figure A.2: Glass transition behavior of a glassy substance as a function of two cooling rates, Q_{fast} and Q_{slow}. Adapted from Ref. [20]

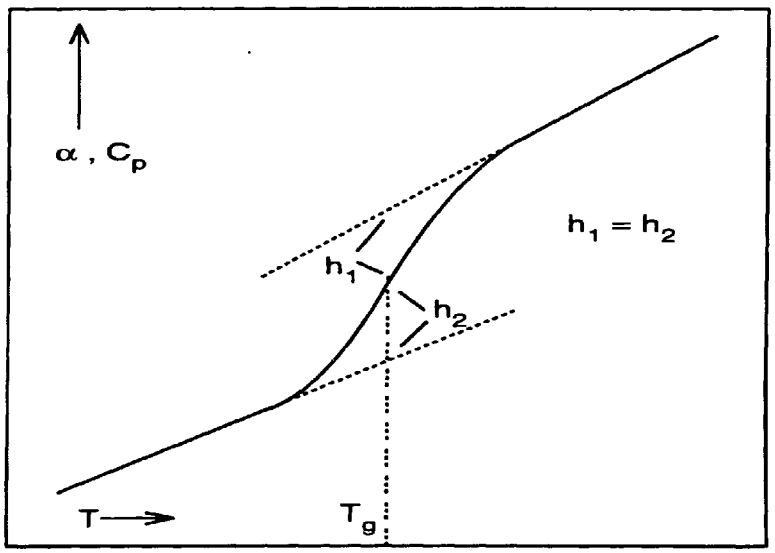

Figure A.3: Glass transition behavior as determined from measurement of either specific heat or expansion coefficient.

DSC data Despite the fact that true glass transition temperatures can only be determined from measurements made while *cooling* a material, the most common method utilized today is to measure the specific heat of a specimen while heating it in a differential scanning calorimeter (DSC). This technique yields "essentially similar results [20]" (to cooling-based methods), but in fact may measure a "fictive temperature," T_f, which corresponds to the hypothetical temperature at which the material would be in thermodynamic equilibrium [25]. (This concept is attributed by Plazek to Tool [27].) Though such a distinction may be real, it has little practical importance because T_f scales with T_g and is never more than a few degrees lower [25].

Calorimetric data were acquired here initially with a Perkin-Elmer DSC-4 and later with a Thermal Analysis Instruments (TA, formally a branch of DuPont) DSC-2900. These instruments monitor the power required to raise the temperature of a specimen, at a constant rate, relative to that required for a standard. Specimens consisting of approximately 10 mg of film or powder were dried under vacuum[1] at room temperature and were scanned at a rate of 10°C/min. These widely-used parameters are thought to produce the most sensitive and accurate results [24,28–30]. The well-known [31–35] phenomenon of endothermic peaks occurring as the glass temperature is passed through (due to structural relaxation during aging), was observed and was handled in the following manner. After an approximate T_g was determined for a particular material, similar specimens subsequently received a 'first scan' at a rate of 30°C/min to a temperature about 20°C above T_g, and were then quenched at a rate of 50°C/min. Second scans were then immediately performed at a rate of 10°C/min. The brief annealing procedure ("rejuvenation" [36]) erased the effects of physical aging yet produced little or no additional curing of the specimen material. (All of the epoxies studied here were cured at temperatures 20–60°C above their resulting T_g's.) Typical traces showing first and second-scans are shown in Figure A.4. Also shown in this figure is the determination of T_g by use of the midpoint-method. Six or more specimens were tested for each of the epoxy formulations investigated; reproducibility of T_g was within ±2°C. Table A-1 summarizes the data acquired in this manner.

[1] As discussed in chapter 4, small amounts of water absorbed by epoxy were determined to have reduced T_g by about 20°C; published reports indicate that absorption of just 1% H_2O can lower T_g by as much as 30°C [23].

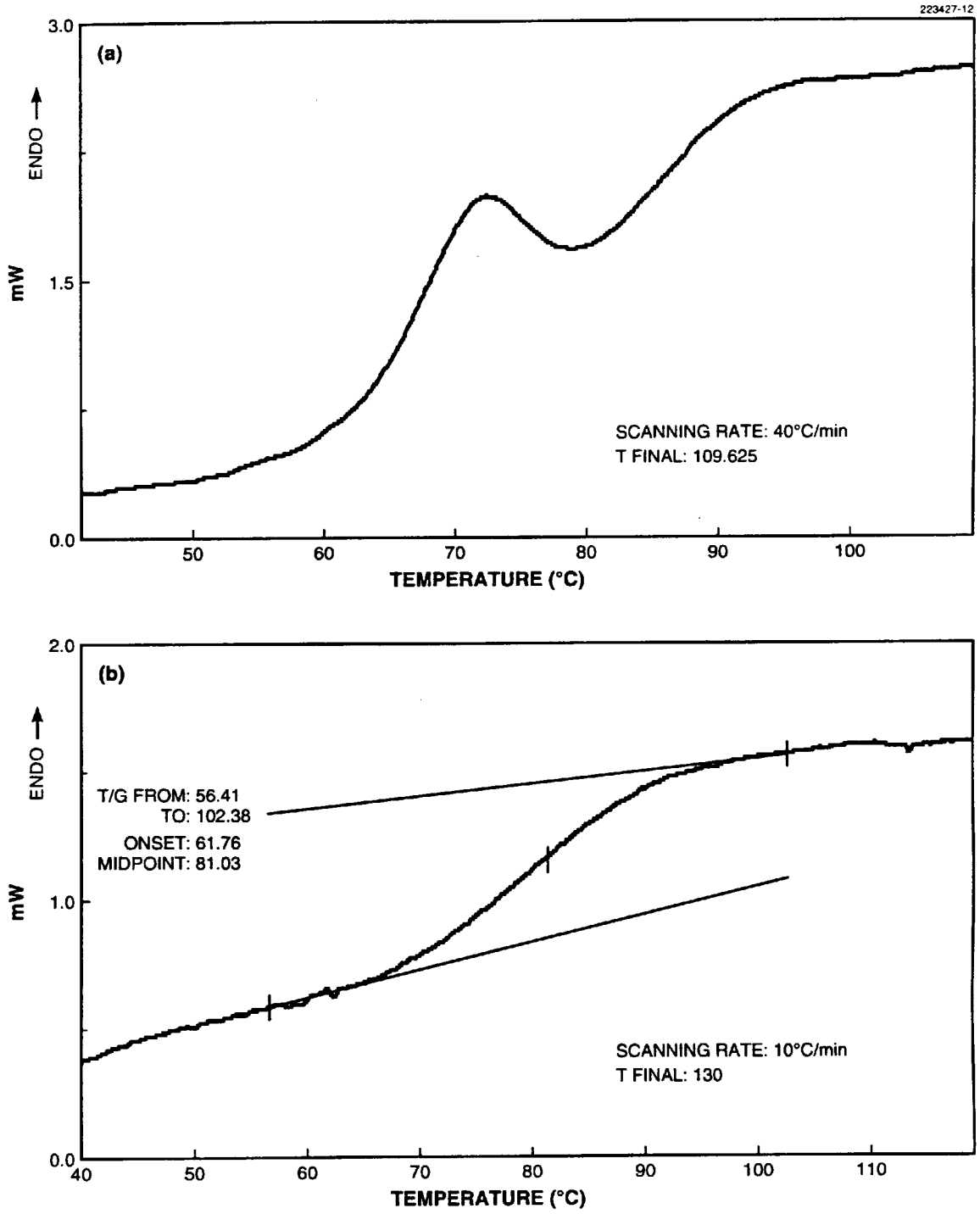

Figure A.4: Typical DSC traces; (a) showing first (rapid) scan executed to anneal away the effects of ageing, and (b) second (slower) scan to determine glass transition temperature.

TMA data Glass transition temperatures were also determined from thermal expansion data, which were obtained with a TA 2940 Thermomechanical Analyzer (TMA). This is an instrument which measures the expansion of a specimen as it is heated (or cooled) at a controlled rate. The length measurement is accomplished with an LVDT which has a resolution of 10^{-8} m, and the temperature chamber is controlled by a feedback loop utilizing a thermocouple which is located adjacent to the specimen. (As opposed to a thermocouple in the heater.)

Because of the low thermal conductivity of epoxies, the uniformity of sample temperature is a concern. Greater temperature gradients within a sample will have the effect of spreading out thermal transitions over wider temperature intervals, and a transition temperature such as T_g will appear to occur later in time. To minimize this effect, samples were sized such that at least one dimension was on the order of 1 to 2 mm. To determine the optimum temperature ramp rate, measurements were performed at increasingly slower rates until little effect upon the indicated T_g was noted. In this manner, an optimum rate of 2°C/min was chosen for most of the specimens. Relaxation peaks were noted in the expansion behavior as the temperature was increased through T_g, but T_g's were determined from cooling measurements only. For the reason noted previously, samples were dried under vacuum prior to testing. The general procedure followed was to heat the specimens at a rate of 20°C/min to about 20°C above T_g, equilibrate the temperature for one minute, and then ramp down at 2°C/min. Typical TMA plots are reproduced in Figure A.5.

Table A.1: Summary of epoxy glass transition temperatures.

Components	*Mix Ratio*	*Max. Cure Temp.* (°C)	T_g (°C)	
			DSC	*TMA*
EPON 815/V-40	3:1	135	78	80
	3:1	100	72	73
	3:1	65	52	52
	3:2	100	49	50
	3:2	65	43	45
EPON 815/BF_3MEA	3%	180	133	135

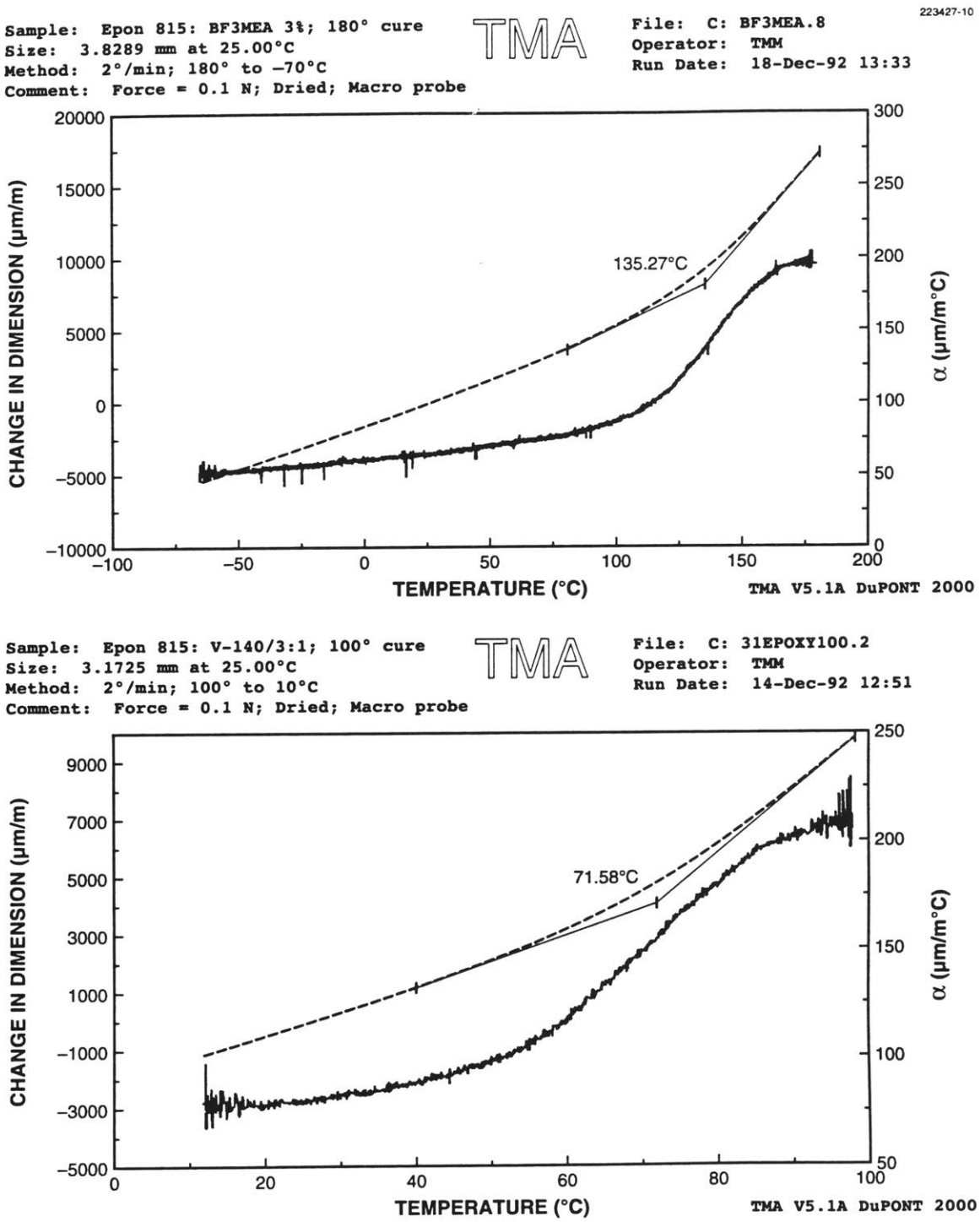

Figure A.5: Typical TMA traces; showing cooling from above T_g to ambient temperature. Midpoint of α discontinuity is seen to coincide with intercepts of expansion asymptotes.

A.1.3.2 Thermal strains

TMA data To enable the calculation of thermal stresses in the composite model specimens, thermal strains were determined for the epoxies used over two temperature intervals of interest. The simplest, and most exact, temperature span is from ambient (taken to be a cool 20°C) to the temperature at which the crack-trapping experiments were performed, -60°C. The second temperature interval of interest is that during which thermal stresses are built up during fabrication of the specimens. Based upon the fact that thermosets have a finite modulus even when well above their T_g, Nairn has maintained that thermal stresses begin building up in epoxies as they are cooled down from the curing temperature, T_c [37, 38]. On the other hand, it has been recognized that the stresses generated while cooling from T_c to T_g must be negligible due to the modulus reduction by two orders of magnitude [39]; this hypothesis has been confirmed by experiments [40]. For the epoxy used here in model specimens, the reduction in modulus at temperatures above T_g is almost three orders of magnitude [41]. Thus it seems most appropriate to consider that thermal stresses in these specimens are built up while cooling from T_g to ambient temperatures.

To obtain the required strain data, TMA scans were performed from temperatures above T_g's to -70°C. To prevent moisture condensation on samples while being measured, helium purge gas was passed through the heater chamber during testing. Specimens were previously dried under vacuum, and scan rates of 2°C/min were used. Five or more specimens were measured for each of the epoxy formulations used in model specimens. Typical TMA scans and determination of strains are reproduced in Figure A.6. A summary of the relevant thermal strains is tabulated below.

Table A.2: Average thermal strains of epoxies used in model specimens.

Components	*Mix Ratio*	*Max. Cure Temp.* (°C)	T_g (°C)	$-\varepsilon$ (10^{-6})	
				T_g to 20°C	20 to -60°C
EPON 815/V-40	3:1	135	80	7204	5625
EPON 815/V-40	3:1	100	72	5380	5497
EPON 815/BF_3MEA	3%	180	135	9778	4751

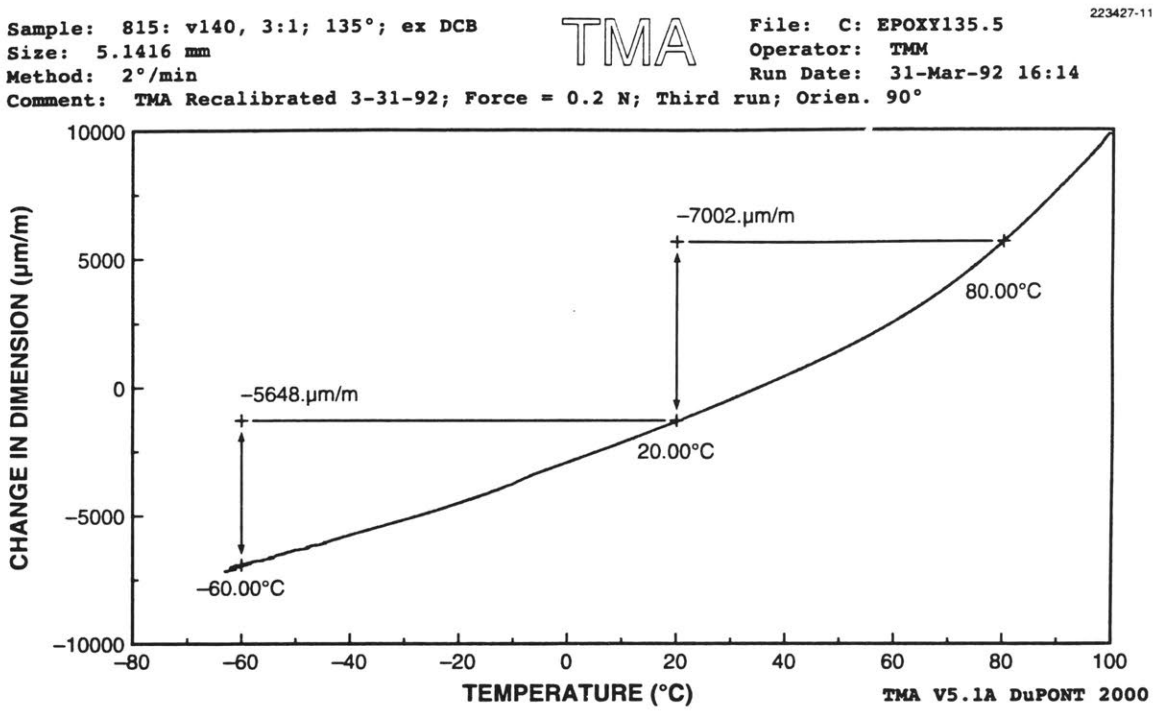

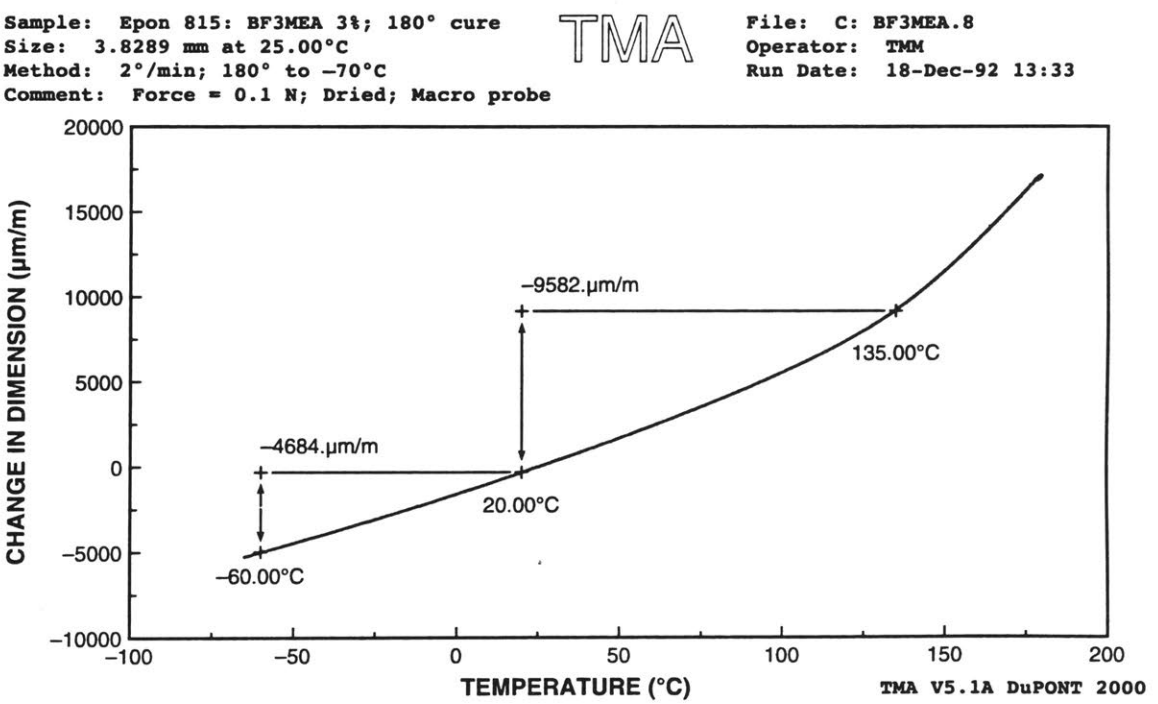

Figure A.6: Typical TMA traces; showing cooling from above T_g to –70°C. Strains are indicated for intervals from T_g to 20°C and from 20° to –60°C.

A.1.4 Uniaxial Compressive Tests

A.1.4.1 Motivation

The measurement of mechanical properties of candidate epoxies began with tensile tests intended to provide elastic modulus and yield strength data. These tests were performed in accordance with ASTM procedure D638 using dogbone-shaped specimens cast in molds machined to the specified dimensions [42]. Testing was performed in a screw-driven Instron 1125, with specimen gauge lengths instrumented with a clip-on strain-gauge extensometer. Results immediately indicated that the brittle nature of the epoxy caused the measurements to be prematurely terminated by brittle fractures which emanated from tiny voids or surface imperfections. While is was possible to determine moduli from these tests, it was realized that probing yield and post-yield behavior of the epoxies would require testing in compression in order to suppress fracture.

A.1.4.2 Specimen preparation

Compression specimens were prepared in the following manner. The epoxy resin and curing agent were heated to about 65°C, thoroughly mixed by stirring and then degassed in a vacuum desiccator for about 20 min. The liquid was then poured into aluminum molds with cylindrical cavities which had been coated with durable, 0.08-mm films of teflon.[2] These were then placed under vacuum again, until all noticeable degassing activity ceased. The molds were then placed into a computer-controlled programmable oven with several large bars of aluminum to increase the thermal mass of the oven's contents, thus slowing the rate of natural cooling after

[2]Use of glass tubes, sprayed with a release agent, created several problems. Insufficient heat transfer from the exothermic curing reactions caused specimens molded in glass tubes to have both vertical and radial gradients of extent of cure, as evidenced by coloration gradations. Adequate thicknesses of release agent to permit removal of the cured epoxy also resulted in contamination of the specimen by transferred flakes of teflon; lesser amounts of release agent prevented full release, so that breaking glass was a hazard.

the completion of program sequences. The thermal cure cycles used were presented earlier, in Figure A.1.

The cured epoxy rods were machined on a lathe to right cylinders having height of 25.4 mm and width of 12.7 mm. Final surface cuts were made with water as a lubricant, so that very smooth surfaces resulted. The chosen aspect ratio of 2:1, also used by others [35, 44, 45, 46], is a good compromise between squat specimens, which exhibit pronounced end effects due to friction, and tall specimens, which may buckle or prematurely shear over. The finish-machined specimens were placed in a glass desiccator, under vacuum at room temperature, until just prior to testing.

A.1.4.3 Description of apparatus

Initial compression tests resulted in several specimens shearing over and spurious extensometer indications. These difficulties were attributed to non-parallelism of the platens and instabilities in the load-train. Consequently, a precision compression cage was fabricated to enable compression testing between parallel platens with the testing machine in tensile mode. The cage, shown in the photograph of Figure A.7, features polished, stainless steel platens which are drawn toward each other with 25-mm diameter, centerless ground stainless rods which pass through close-tolerance holes bored in the platens.

Displacement between the platens was measured with a linear potentiometer. Because the resistive element of this device is a continuous film, it theoretically has an infinite resolution. This resolution is, of course, limited by the resolution of whatever instrument is reading the signal. In this case, data were acquired on a PC equipped with 16-bit Analog-to-Digital boards which effectively limited the resolution to about 0.0047 mm. The load cell signal was picked up directly from the amplifier board in the Instron 1125 and also fed to an A/D board in the PC. The acquisition rate was varied from 1 to 2000 Hz (dependent upon strain rate), so that 5000 data points were stored for each test.

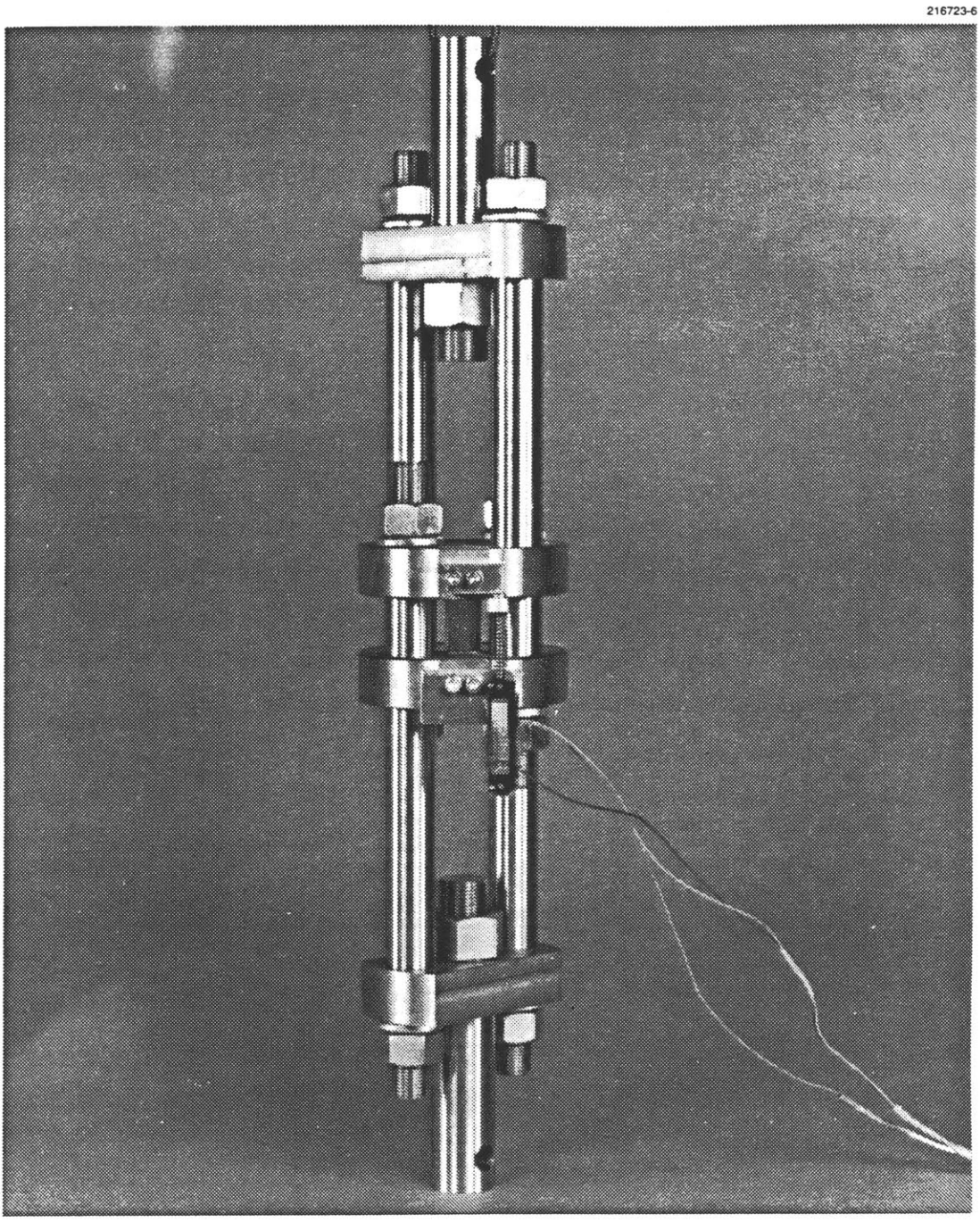

Figure A.7: Custom-built precision compression cage. Cylindrical specimen (25-mm high × 12.7-mm diameter) is shown between polished stainless steel platens. Extensometer is a linear potentiometer.

An environmental chamber was used to provide test conditions at sub-ambient and elevated temperatures. Cooling was accomplished with liquid nitrogen boil-off vapor introduced with a fan powered by a control unit which monitored the temperature with a thermocouple located adjacent to the specimen. Heating was provided with a resistance heater, fan-convected in a similar manner. The compression tests were performed after the temperature had stabilized to within $\pm 2°C$.

A.1.4.4 Testing procedures

A routine procedure was followed for testing of the compression specimens. After the temperature of the environmental chamber had stabilized at the desired testing temperature, the extensometer was re-calibrated with machinists height-blocks and the load-cell output was re-zeroed. Specimens were taken directly from the storage desiccator and a drop of molybdenum disulphide oil was placed on each end.[3] They were then centered, with a positioning jig, on the similarly-lubricated platens. The data-acquisition system was then activated and the deformation begun.

A.1.4.5 Parametric variations

Several groups of specimens cured with V-40 were tested, each group consisting of either a different mix ratio or different post-cure temperature. No variations in mix or cure temperature were explored with specimens cured with BF_3MEA. In recognition of the well-established densification of glassy polymers resulting from physical ageing [47], and in particular the concomitant embrittlement of epoxies [33, 35, 46], groups of specimens were tested at 'ages' ranging from one day to one year. Because the effects of aging rapidly accelerate as the aging temperature approaches T_g [25, 47, 48], little effect of aging was anticipated for these specimens, which were all stored at ambient temperature. Nonetheless, this issue was pursued due to the importance of aging at

[3]This lubricant was found to give "essentially zero friction" [43] and is simple to apply; available as *'GLOBO'* from Casten Enterprises, Elgin, Ill.

ambient temperatures.

Compression tests were performed at temperatures of −60, −20 and 20°C. At these temperatures, all of the materials tested were in the glassy domain since the lowest T_g of any specimen was 45°C. The applied strain rates were controlled by changing the crosshead speed of the testing machine; since a screw-driven machine without a feedback loop was being used, it was not possible to impose a constant strain rate. Instead, the strain rate was constantly increasing as a function of the decreasing specimen length. Nominal (initial) strain rates utilized ranged over three decades, from 1.67×10^{-4} to 1.67×10^{-1} (s^{-1}). Strain rates at yield, accurately noted in following figures, were approximately 6 to 8% faster.

A.1.4.6 Reduction of data

Raw data were recorded in computer files consisting of load, P, and engineering strain, $\varepsilon_{\text{eng.}} \equiv (l_o - l)/l_o$. These data were converted to true-stress, true-strain data in the conventional manner, as follows. The true strain experienced at any given compressed length, l, is defined as

$$\varepsilon_{\text{true}} = \int_{l_o}^{l} \frac{dl}{l} = \ln \frac{l}{l_o} \tag{A.1}$$

and is calculated through use of the engineering strain as

$$\varepsilon_{\text{true}} = \ln \frac{l}{l_o} = \ln \left(1 - \frac{l_o - l}{l_o} \right) = \ln (1 - \varepsilon_{\text{eng.}}) . \tag{A.2}$$

The true stress is calculated on the basis of conservation of volume as

$$\sigma_{\text{true}} = \frac{P}{A} = \frac{P}{A_o} \frac{l}{l_o} = \frac{P}{A_o} (1 - \varepsilon_{\text{eng.}}) . \tag{A.3}$$

The assumption of constant volume throughout each measurement is quite valid, since inelastic deformation processes in polymeric glasses are activated principally by deviatoric stress components (shear) [49, 50], and the measurements were all performed at constant (atmospheric) pressure.

The measure of stiffness derived from these uniaxial compressive measurements is taken to be time-independent, though it is a function of applied strain rate. At small strains, up to about 0.02, the stress-strain behavior remains quite linear and may be approximated by a tangent modulus, E. As the imposed strain rate approaches the limit of impact, or the test temperature approaches the limit of absolute zero, E approaches what is referred to as the *glassy modulus*, E_g [51]. The calculation of moduli from the measurements reported here was performed in a consistent manner for all the data obtained. To avoid artifacts produced by nonlinear contact phenomena, data at strains below 0.005 were ignored. A least-squares fit was performed upon data up to a strain of 0.015, which is well prior to any detectable effects due to viscoelasticity or plastic deformation. This procedure is illustrated in Figure A.8 for a set of measurements obtained at room temperature with three different strain rates, as noted in the figure. The procedure is further illustrated in Figure A.9 for a pair of tests performed at room temperature and at -60°C.

A.1.4.7 Discussion of data

Typical stress-strain curves obtained at room temperature and at a nominal strain rate of $0.0167\,s^{-1}$ are plotted in Figure A.10. Very distinct behaviors are evident in this figure for the three different epoxy formulations. The specimen cured with Lewis Acid (BF_3MEA) not only exhibits a relatively high yield stress, but also shows little evidence of strain softening. In addition, its strain (orientation) hardening is quite pronounced. The pair of specimens cured with V-40, at a 3:1 ratio, demonstrate both strain softening and strain hardening, with an extended intermediate region of flow at an essentially constant level of stress. For these specimens, little difference in behavior may be seen (in this plot) as a function as a function of different T_g's (due to different post-cure temperatures). Specimens cured with V-40 at a 3:2 ratio show substantial strain softening, which is evidence of localized deformations occurring throughout the specimen volume [52, 53]. The softening in these specimens became so great that it enabled barreling to occur, at which point the tests were consequently halted relatively early.

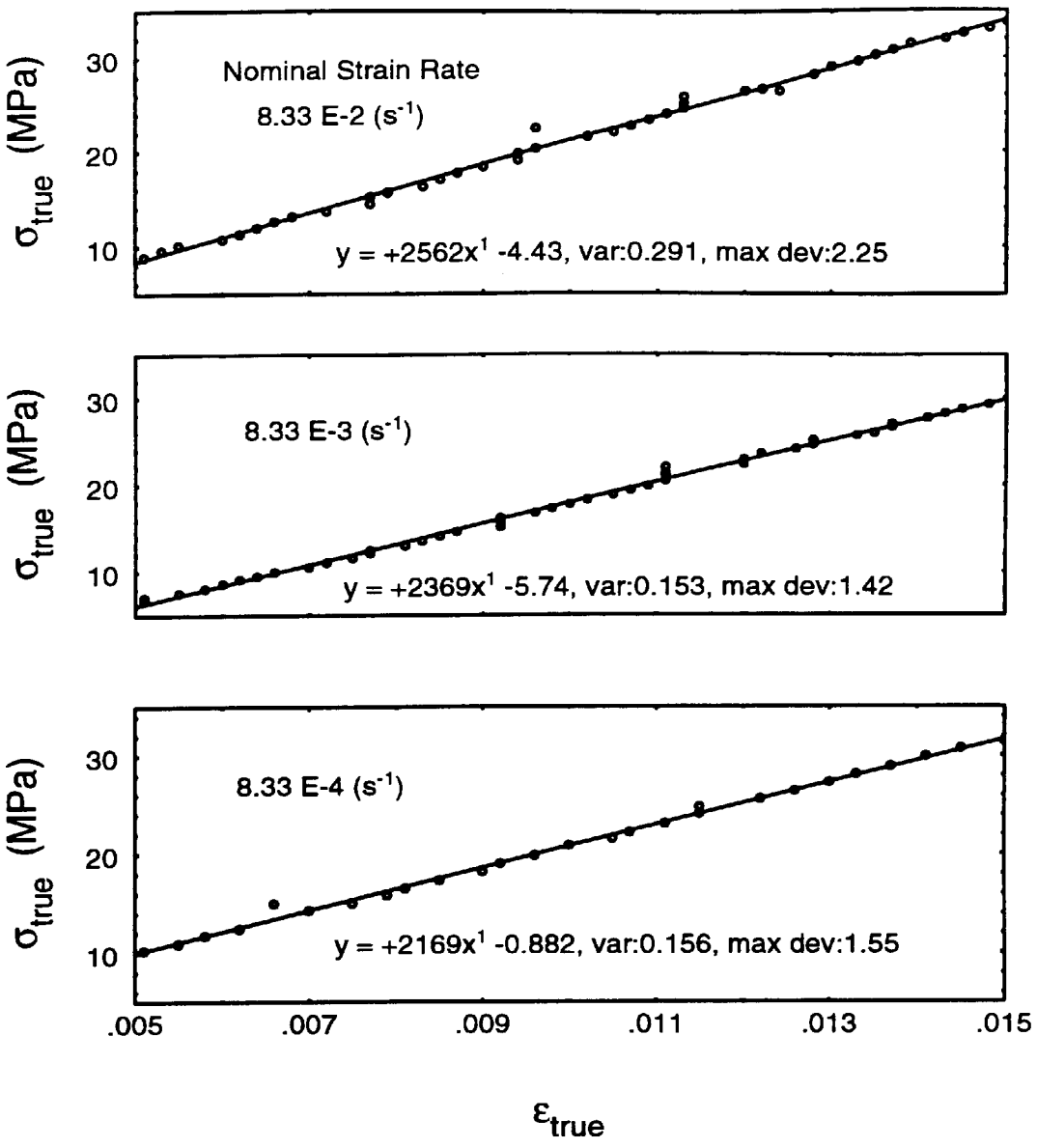

Figure A.8: Examples of elastic modulus determination from stress-strain curves (EPON 815:V-40/3:1, T_g= 72°C) obtained at room temperature, at nominal (initial) strain rates as indicated. All specimens were aged 48 days at room temperature.

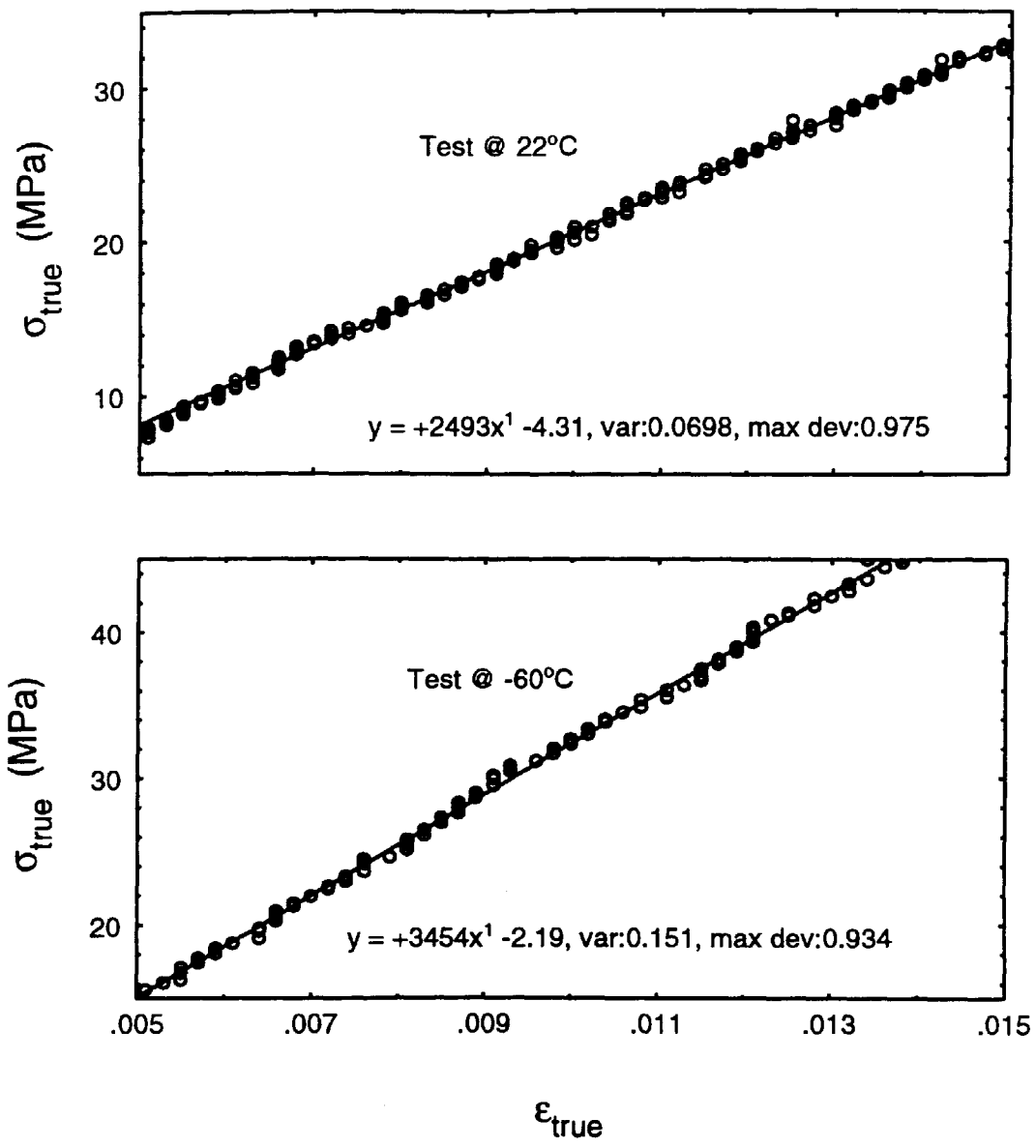

Figure A.9: Examples of elastic modulus determination from stress-strain curves (EPON 815:V-40/3:1, T_g=80°C) obtained at ambient and sub-ambient temperatures, at a nominal (initial) strain rate of $1.67 \times 10^{-3}\,s^{-1}$. Both specimens were aged 80 hours at room temperature.

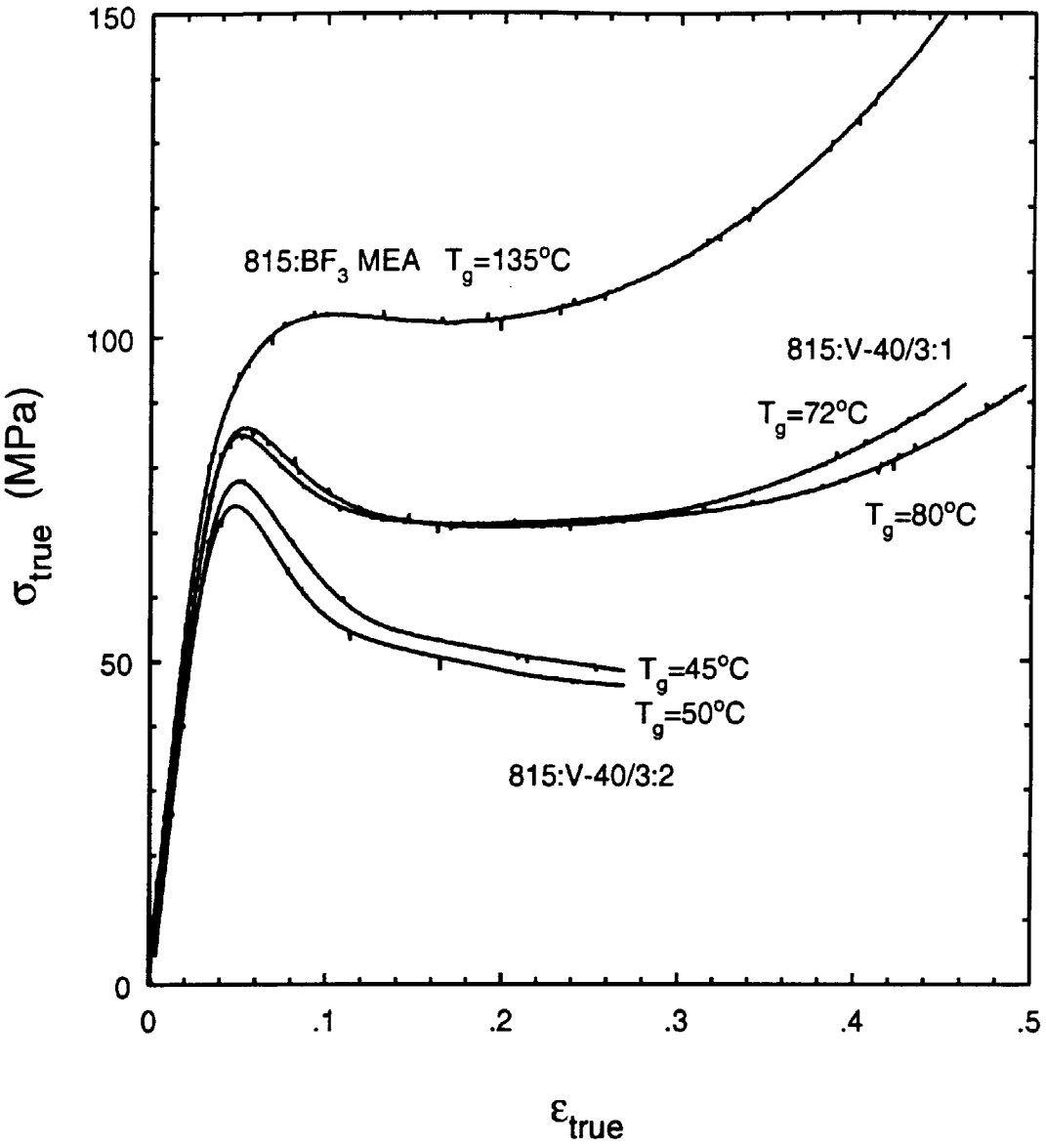

Figure A.10: Typical stress-strain curves obtained at room temperature, at a nominal (initial) strain rate of $0.0167\,s^{-1}$. All three epoxy formulations are based on the DGEBA EPON 815, with curing agents and glass transition temperatures as noted in the figure.

This extensive softening behavior indicates that increasing the concentration of polyamide curing agent (from 3:1 to 3:2) results in an epoxy solid that is less crosslinked, and therefore contains a higher density of regions capable of large localized deformation. As an aside, it is repeated at this point that the model specimens used in the crack-trapping experiments were cast with the stiffer, more brittle formulation of 3:1 (cured to $T_g = 80°C$).

Modulus The effect of curing agent and cure temperature upon the measured uniaxial modulus is shown in Figure A.11 for specimens based upon EPON 815. Clearly the Lewis Acid (BF_3MEA) generates the most rigid epoxy solid (presumably by promoting complete polymerization of the epoxy groups and fully cross-linking all adjacent chains). The log-linear dependency upon strain rate is obvious; this rate sensitivity is greater for specimens with the lower T_g's (regardless of whether the lower T_g results from lower cure temperature or from higher polyamide concentration). Also evident is the softening resulting from the higher concentration of polyamide (V-40), which promotes chain extension at the expense of crosslinking.

The deformation behavior of epoxy is, of course, markedly affected by changes in temperature. Shown in Figure A.12 are families of stress-strain curves obtained at 22°C and −60°C, for one formulation (815:V-40/3:1, T_g=80°C) of epoxy at four different strain rates. As expected, stiffness and yield strength are enhanced by a reduction in test temperature. In addition, inspection of the curves indicates that, at the lower temperature, no region of constant flow stress is produced. Rather, the strain-softening region is spread out over a greater strain interval, and is immediately followed by strain hardening at lower levels of strain.

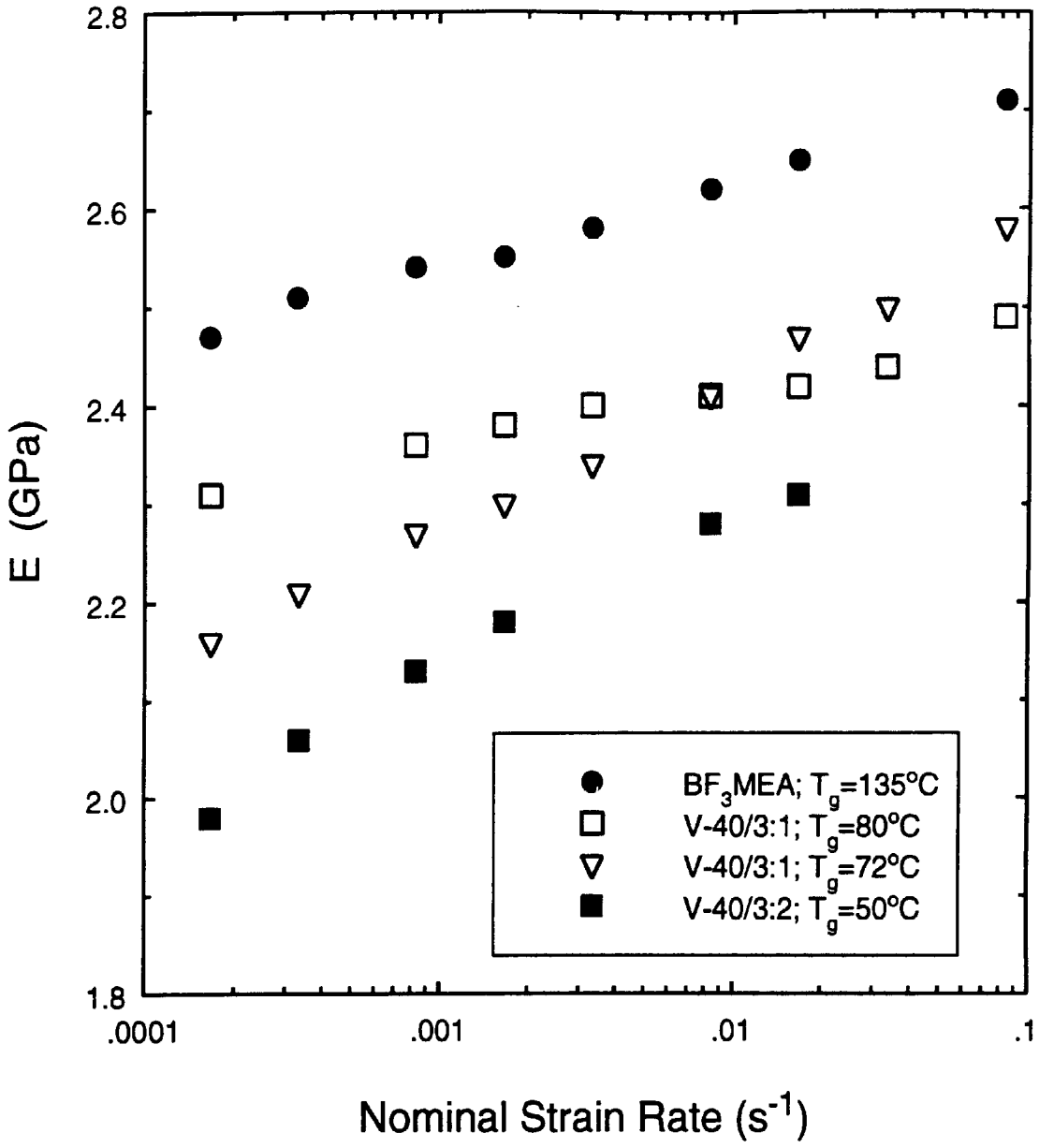

Figure A.11: Effect of curing agent, concentration and cure temperature on the uniaxial compressive modulus of epoxies based upon EPON 815. Measurements were obtained at 22°C.

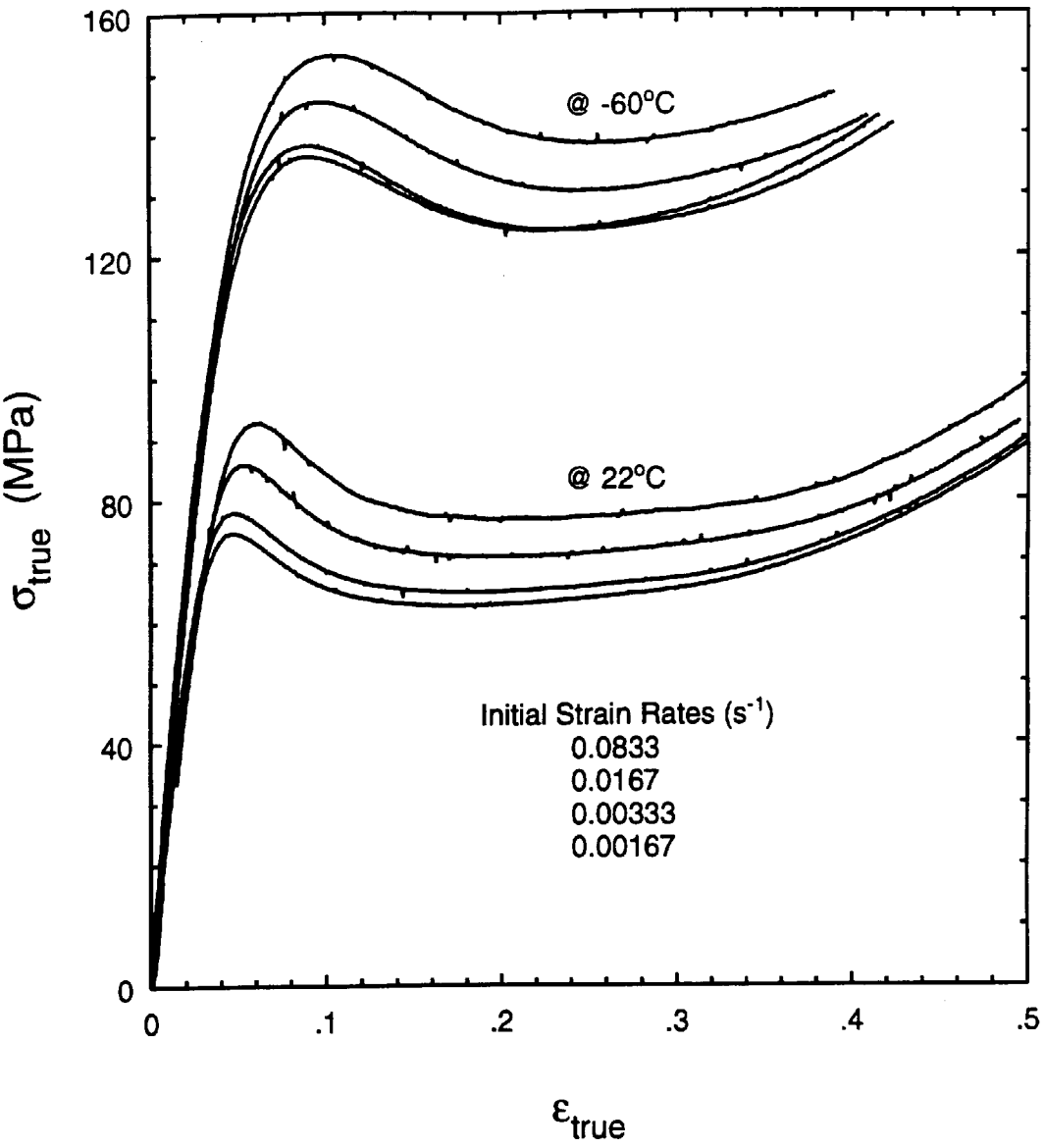

Figure A.12: Stress-strain curves (EPON 815:V-40/3:1, $T_g = 80°C$) obtained at ambient and sub-ambient temperatures, at nominal (initial) strain rates as indicated.

The measured dependency of modulus upon temperature is shown in Figure A.13 for 815:V-40/3:1, $T_g = 72°C$. This figure clearly indicates that temperature has a more pronounced effect than strain rate upon the modulus exhibited by the epoxy specimens. The decrease in modulus is nonlinear with increasing temperature, and rate sensitivities become reduced as the temperature is increased through ambient. A comparison of moduli measured for the two similar formulations, having different T_g's due to different curing temperatures, is shown by the plot in Figure A.14. At room temperature, these epoxies have an elastic modulus of about 2.5 MPa, while at -60°C (the temperature at which the crack-trapping experiments were performed) the modulus increases to about 3.5 MPa. The small modulus difference between the two materials at room temperature becomes slightly greater at reduced temperatures.

The effect of aging at room temperature on the modulus of these epoxies is modest, but noticeable stiffening does result as the glassy materials densify with age. This evolution is shown in Figure A.15 by values of E measured at room temperature for 815:V-40/3:1, $T_g = 72°C$ specimens whose ages ranged from 48 to 377 days. The observed increase in stiffness with time is to be expected from discussions of physical aging of glassy polymers in general [47, 54], and reports of embrittlement of similar epoxies [25, 33]. More specifically, the data are consistent with reports of E increasing by about 10% due to aging in a DGEBA epoxy cured with piperidine [46]. Data in Figure A.15 indicate that low strain rates generate the greatest differences in modulus as a function of age; this is evidently due to decreasing strain-rate sensitivity with increasing age.

Yield Stress The influence of temperature, rate and aging on the yield stresses of these epoxy materials will now be presented and discussed. The combined effect of temperature and rate upon yield stress, reduced by modulus, will be explored through discussions of molecular deformation theory in a following section. For the present, it is of interest to summarize the yield stresses of the various epoxies studied as a function of individual engineering parameters.

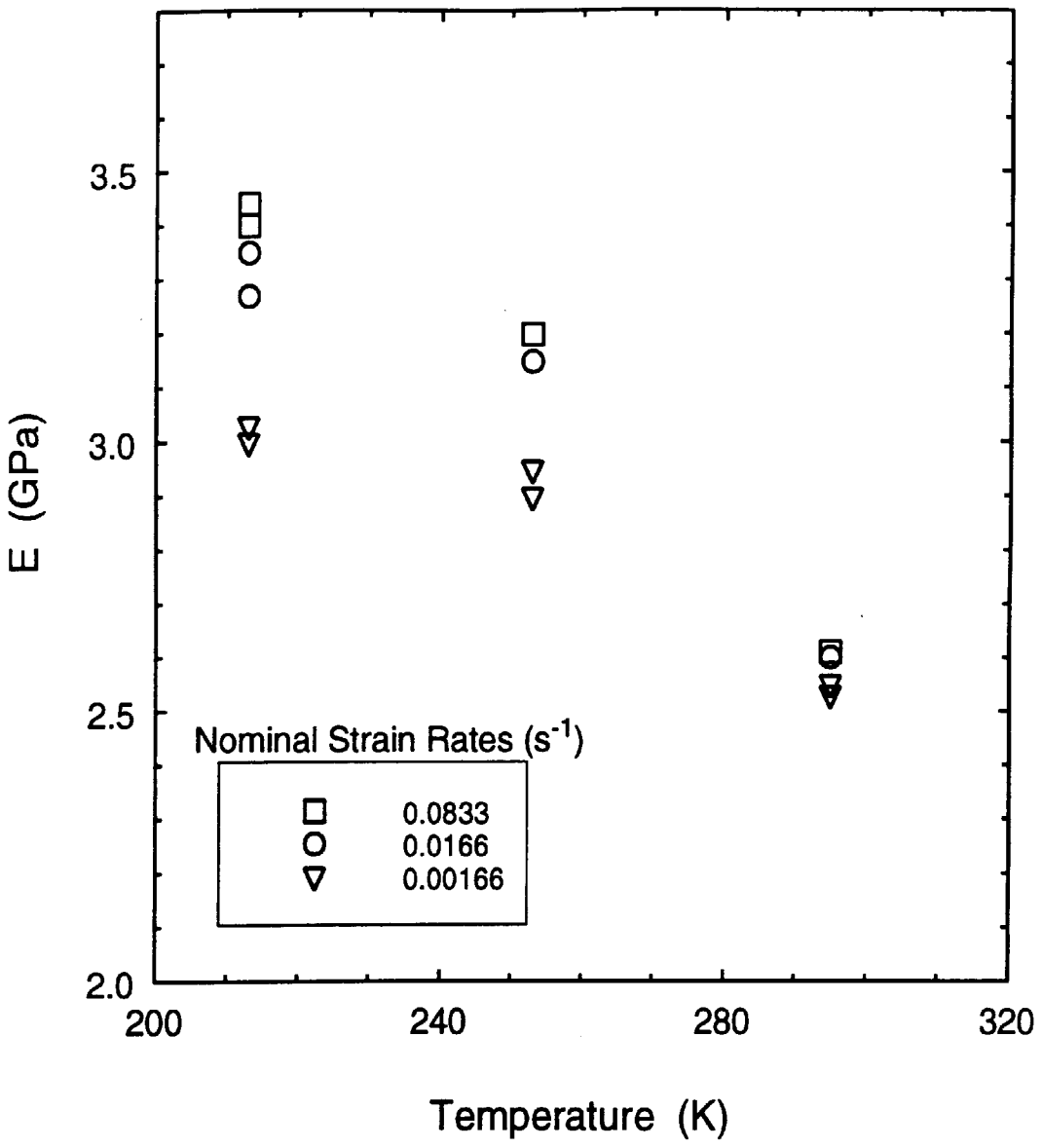

Figure A.13: Temperature dependence of uniaxial compressive modulus (EPON 815:V-40/3:1, $T_g = 72°C$) obtained at ambient and sub-ambient temperatures, at nominal (initial) strain rates as indicated. All specimens were aged 377 days at room temperature.

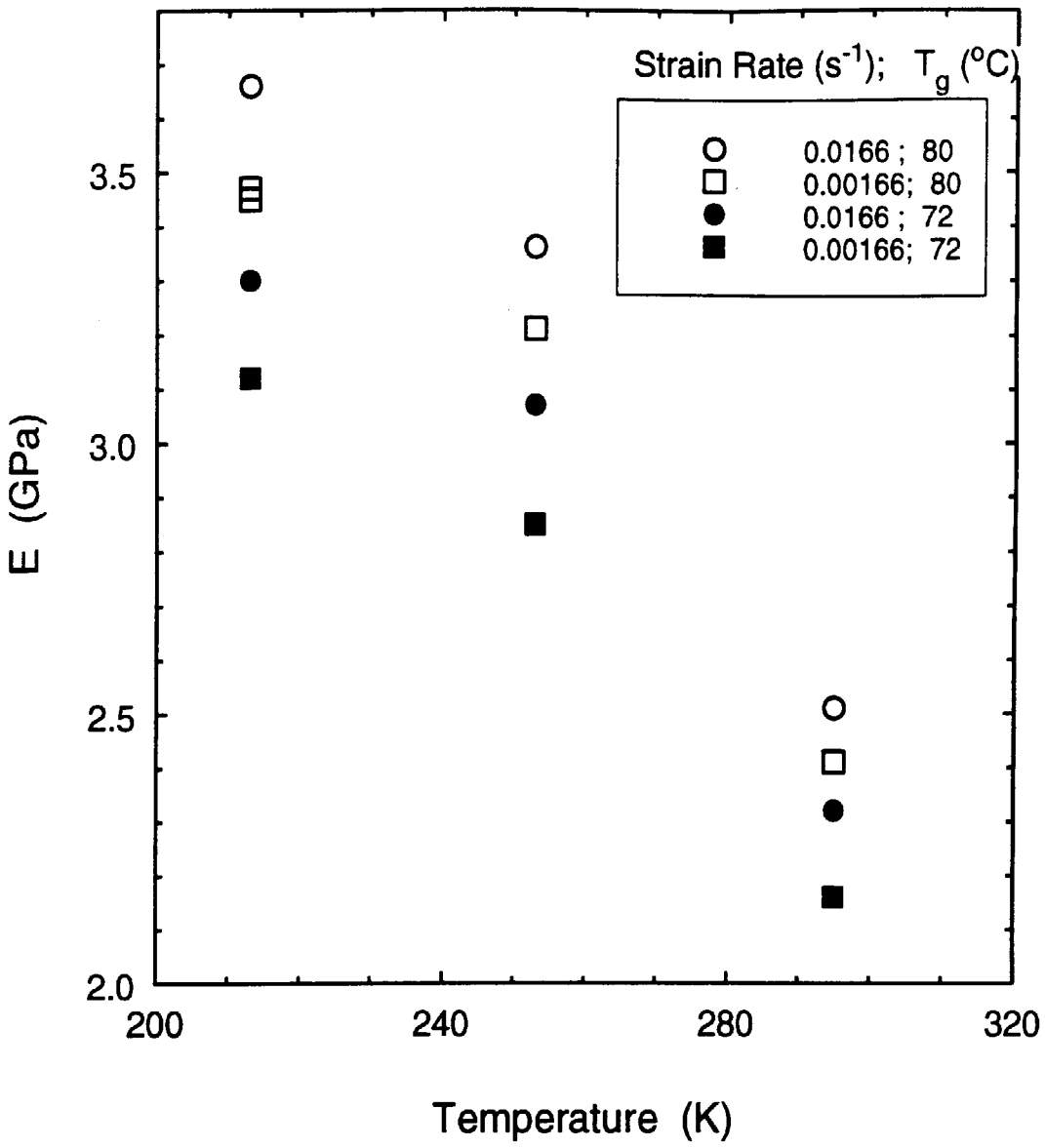

Figure A.14: Comparison between the measured moduli of specimens made from the same formulation of epoxy (EPON 815:V-40/3:1), but cured at different temperatures resulting in the two glass transition temperatures as indicated. All specimens were aged 20 hours at room temperature.

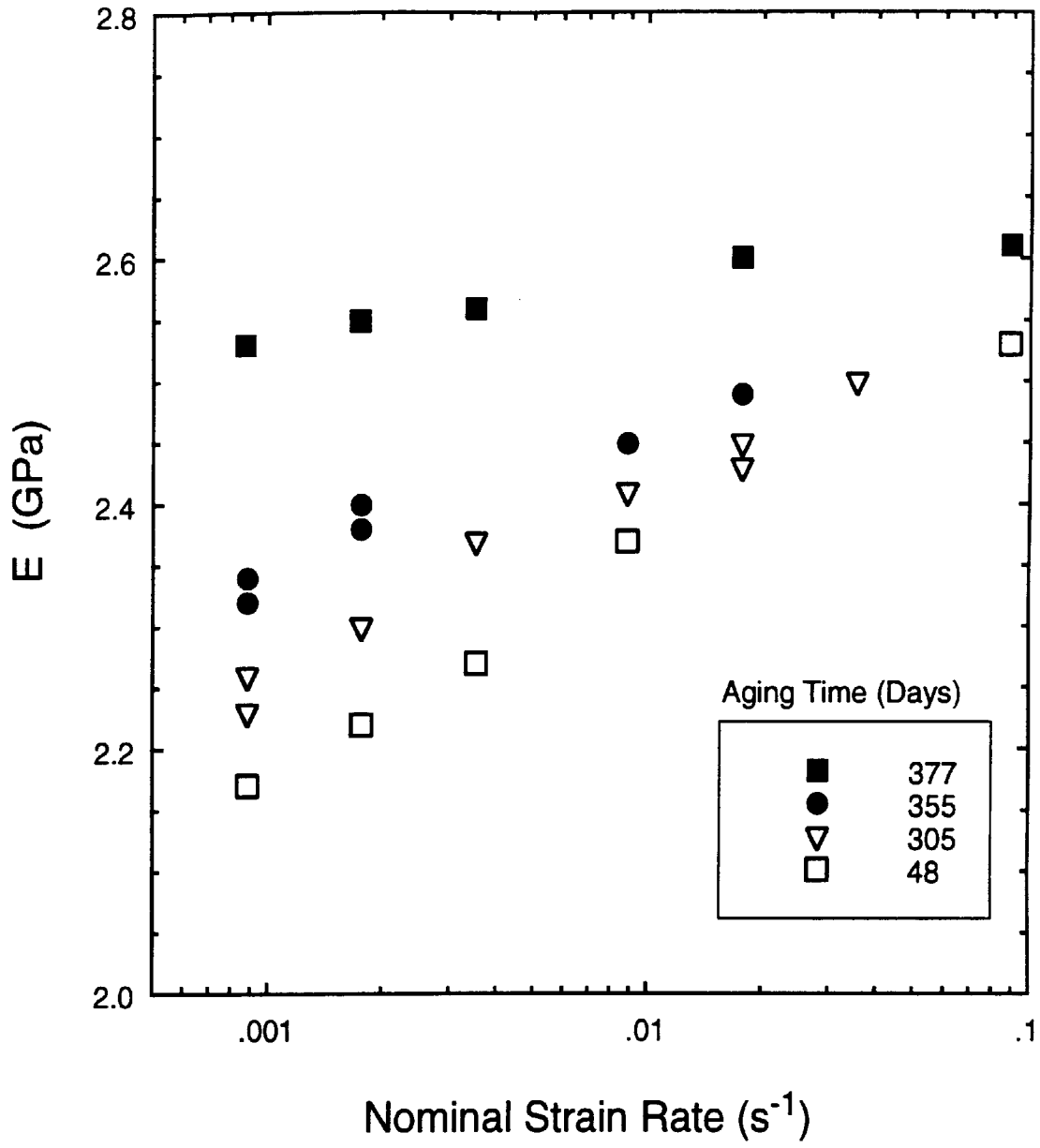

Figure A.15: Effect of physical aging at room temperature on the measured moduli of 815:V-40/3:1, $T_g = 72°C$. Measurements obtained at room temperature with an initial strain rate of strain rate of $1.67 \times 10^{-3}\,s^{-1}$.

The specification of a yield stress on a stress-strain curve of a polymer would be compounded by viscoelastic effects if an offset intercept was used, as is commonly done for metals. An unequivocal point results if, instead, the peak stress prior to softening is specified as the yield stress. This is not only a convenient point to specify, but it is the most logical, because on a true stress, true strain curve, the peak pre-softening stress corresponds to the intrinsic yield point, which is indicative of the onset of global plastic deformation [55]. In all of the discussions which follow, σ_y represents this definition of yield stress.

The yield stresses measured at room temperature for EPON 815 specimens cured with BF_3MEA and with V-40 (cured to T_g=80°C) are plotted in Figure A.16 as a function of strain rate. This figure indicates that the Lewis Acid produces cured solids with yield stresses that are some 20% greater than those of the polyamide-cured solids, and can exceed 100 MPa. The log-linear dependencies of σ_y upon strain rate is quite apparent; many other polymers have also been found to obey the relationship $\sigma_y = A + B \log \dot{\varepsilon}_y$ [56]. Similar to the modulus behavior, the yield stress proved to be significantly more rate-sensitive in specimens cured with V-40 than with BF_3MEA. Specimens cured with V-40 to T_g's of 72°C and 80°C demonstrated nearly identical yield behavior; the 72°C data was omitted to avoid cluttering the figure.

The effect of temperature upon σ_y in these epoxies is shown in Figure A.17 for 815:V-40/3:1, $T_g = 72$°C and in Figure A.18 for 815:V-40/3:1, $T_g = 80$°C. The first figure shows a monotonic, nearly linear increase in σ_y as a function of decreasing absolute temperature; at −60°C , an enhancement of nearly 100% relative to room temperature values is observed. The second figure indicates that the log-linear rate sensitivity persists at reduced temperature, and parallels that measured at ambient. Inspection of the two figures reveals that values of σ_y measured for the two cures of 815:V-40/3:1 are nearly identical at equal temperatures and strain rates.

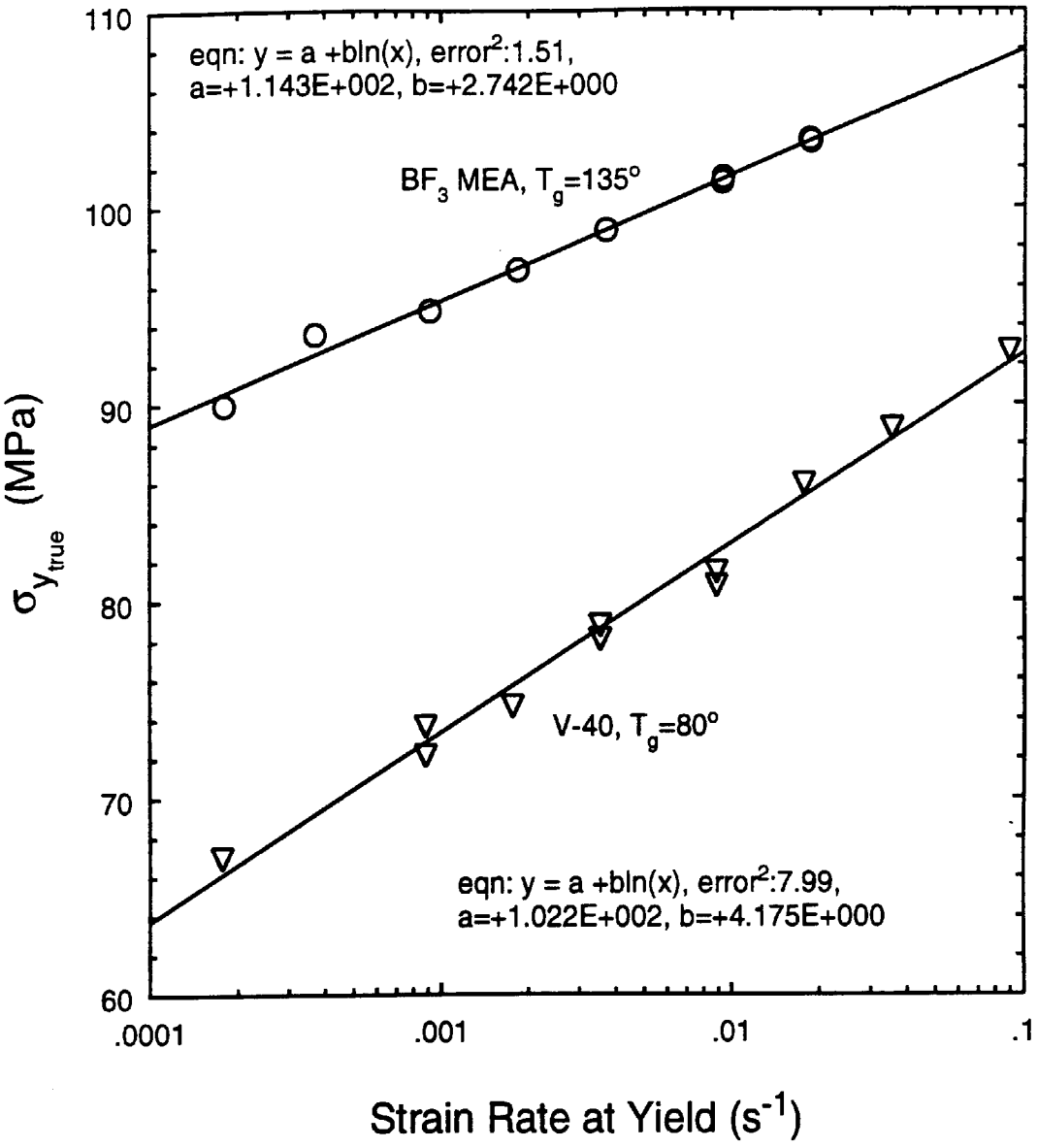

Figure A.16: Effect of curing agent upon the rate-sensitive yield stresses of epoxy (EPON 815) specimens measured at room temperature (22°C).

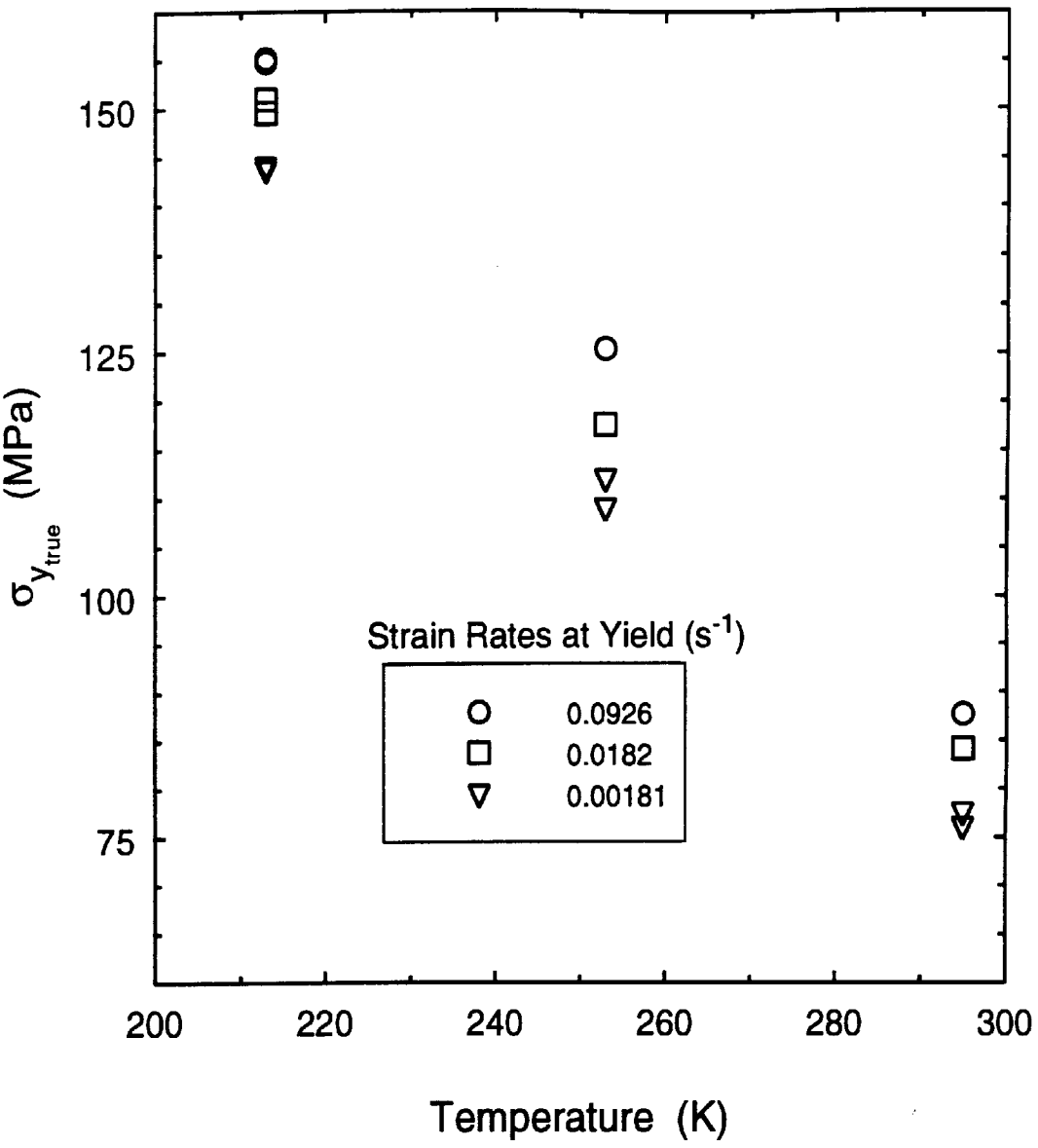

Figure A.17: Temperature dependence of yield stresses measured with epoxy (815:V-40/3:1, T_g=72°C) specimens aged 377 days at room temperature.

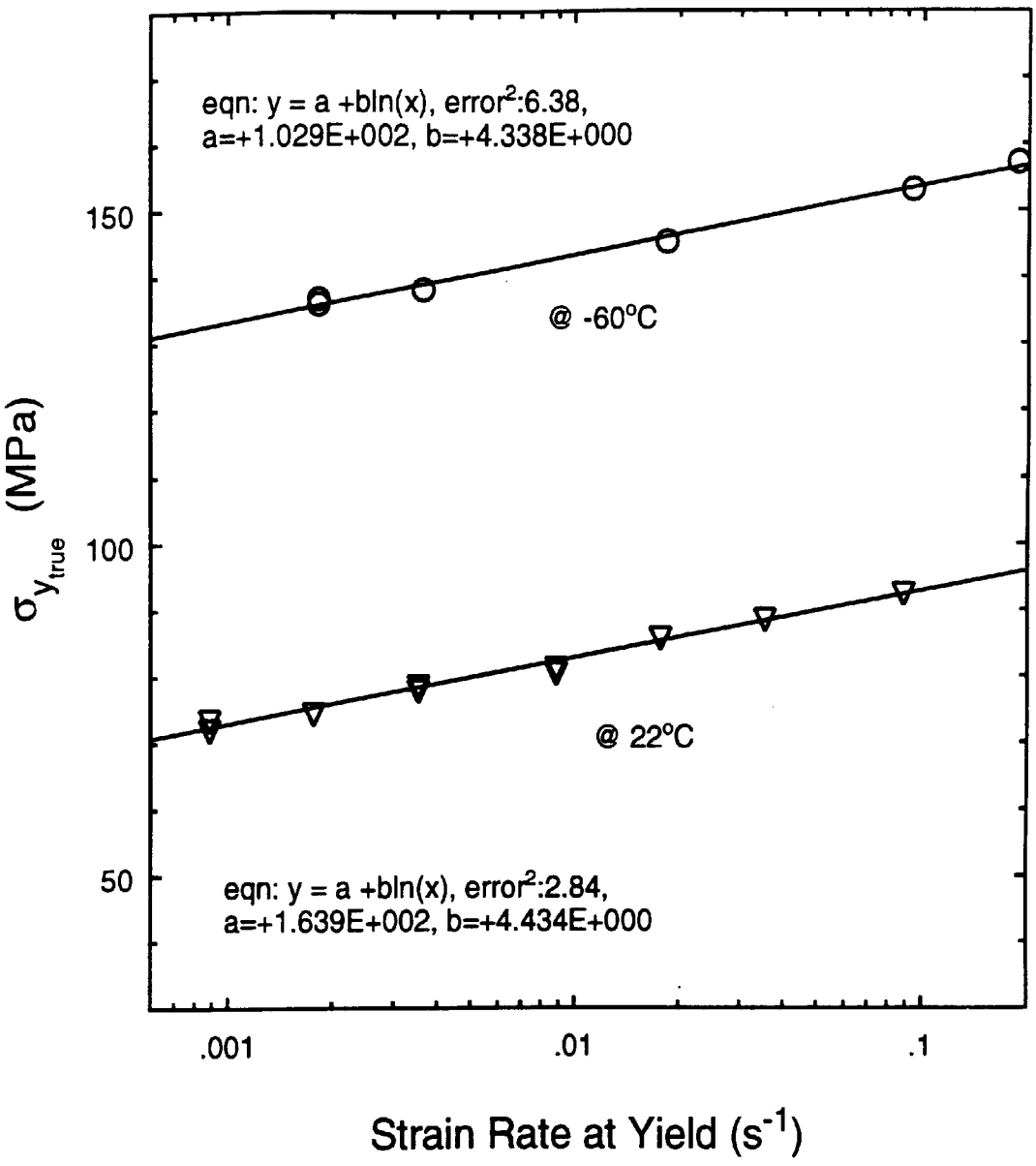

Figure A.18: Effect of temperature on the rate-sensitive yield stress of the epoxy formulation (815:V-40/3:1, $T_g = 80°C$) used in the crack-trapping experiments. All specimens were aged 66 days at room temperature.

The effect of aging upon yield behavior is demonstrated in Figure A.19 by typical stress-strain curves obtained from 815:V-40/3:1, $T_g = 72°C$ specimens aged for different lengths of time at room temperature. The expected rise in stress at yield, due to aging, is seen to persist and become even greater at large strains. Increasing σ_y with age, due to densification [47, 54] (or alternatively, reduction in free volume [21, 32]) has been reported before for similar epoxies [33, 35, 46, 57]. (The embrittlement accompanying aging [33, 46] shall be discussed in a later section.) A summary of the enhancement of σ_y with increasing age, at room temperature, for 815:V-40/3:1, $T_g = 72°C$ is presented in Figure A.20. While there is undoubtedly some scatter, the overall trend of rising σ_y with age is obvious, but only on the order of 5% for aging periods of about one year. Truong and Ennis [46] report somewhat higher (10%) increases, but at elevated ageing temperatures which were about 30°C below the epoxy's T_g's. At temperatures closer to the glass transition, molecular rearrangements are made increasingly more rapid and so it is not surprising that manifestations of aging, such as enhanced σ_y , are increased.

Aging (below T_g) is one form of thermal history which a material can experience; annealing (above T_g) is another thermal treatment which can alter the mechanical response of a polymeric glass. Sufficiently long exposure times to temperatures at or above T_g will remove the effects retained in polymeric glasses due to physical aging and mechanical deformation influences [21, 47]. To explore this phenomenon in the epoxy studied here, compression specimens which had all been aged at room temperature for 377 days were exposed to different heat treatments. Stress-strain curves obtained from their testing at room temperature are shown in Figure A.21 and Figure A.22. The most striking observation is that the annealing treatments have all mitigated the mechanisms which promote deformation localization, as evidenced by the reduced softening behavior. A speculative cause for this reduced localization is that the annealing treatments may have relaxed stress concentrations that could have built up during aging by densification of the amorphous polymer around tiny hard inclusions (dust, or network "nodules"). As expected, annealing does reduce the yield stress (through anti-aging, or rejuvenation). The order of annealing/machining proved to be of little significance.

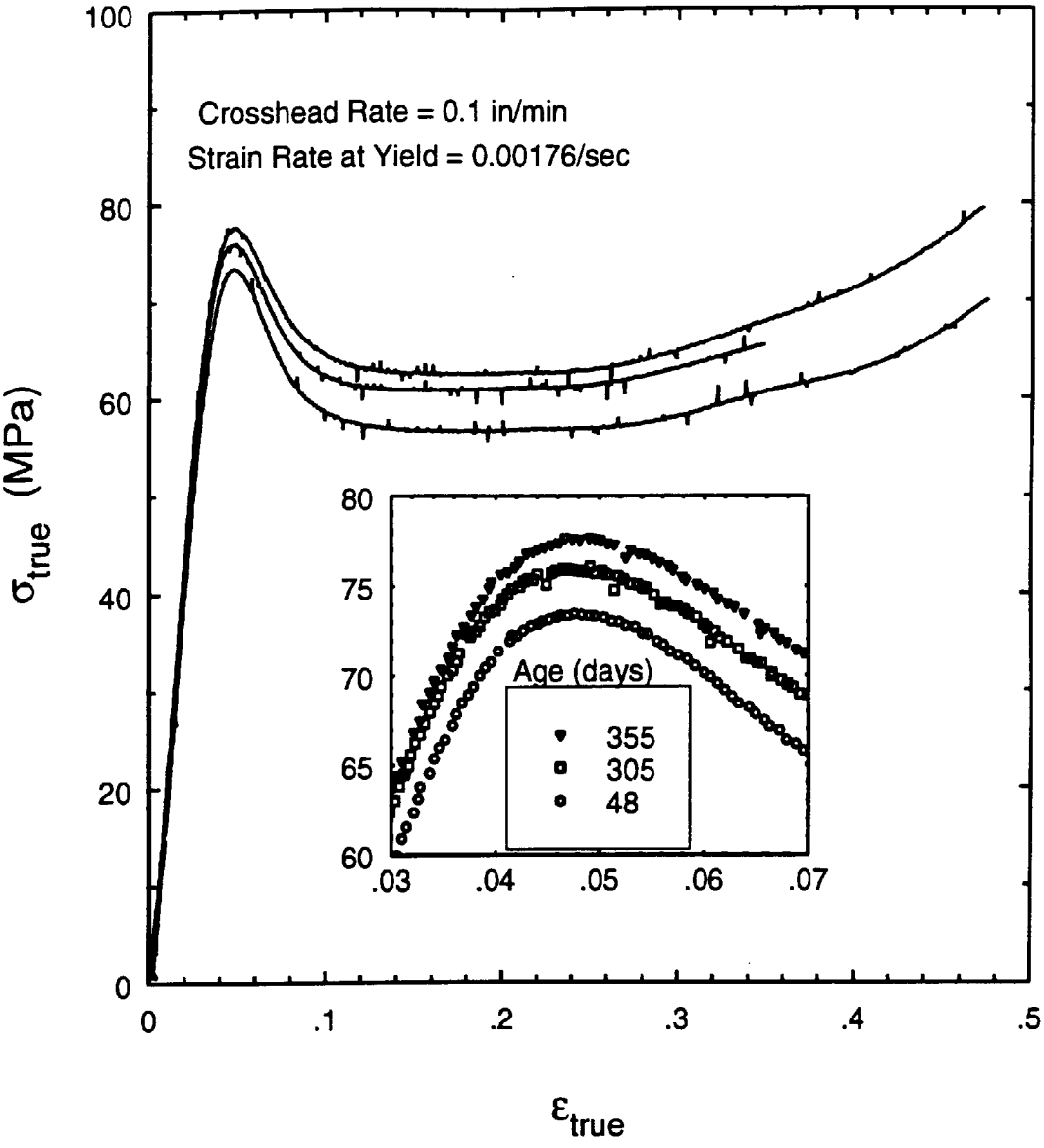

Figure A.19: Effect of aging on yield and post-yield behavior of epoxy, demonstrated by stress-strain curves obtained at 22°C with 815:V-40/3:1, $T_g = 72°C$ specimens aged at room temperature for the times indicated.

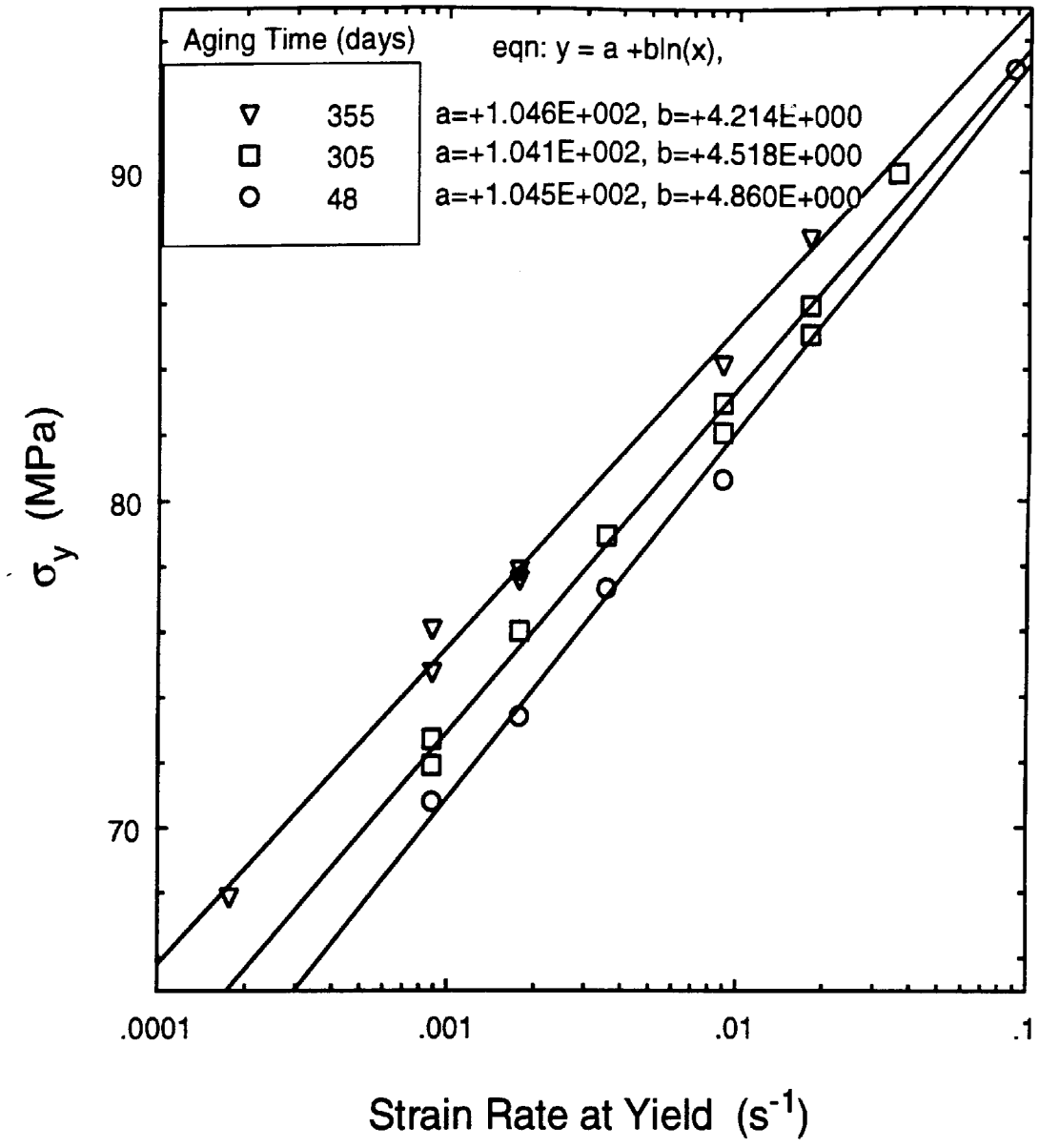

Figure A.20: Effect of aging on the rate-dependent yield stresses measured at 22°C with epoxy (815:V-40/3:1, $T_g = 72°C$) specimens aged at room temperature for the times indicated.

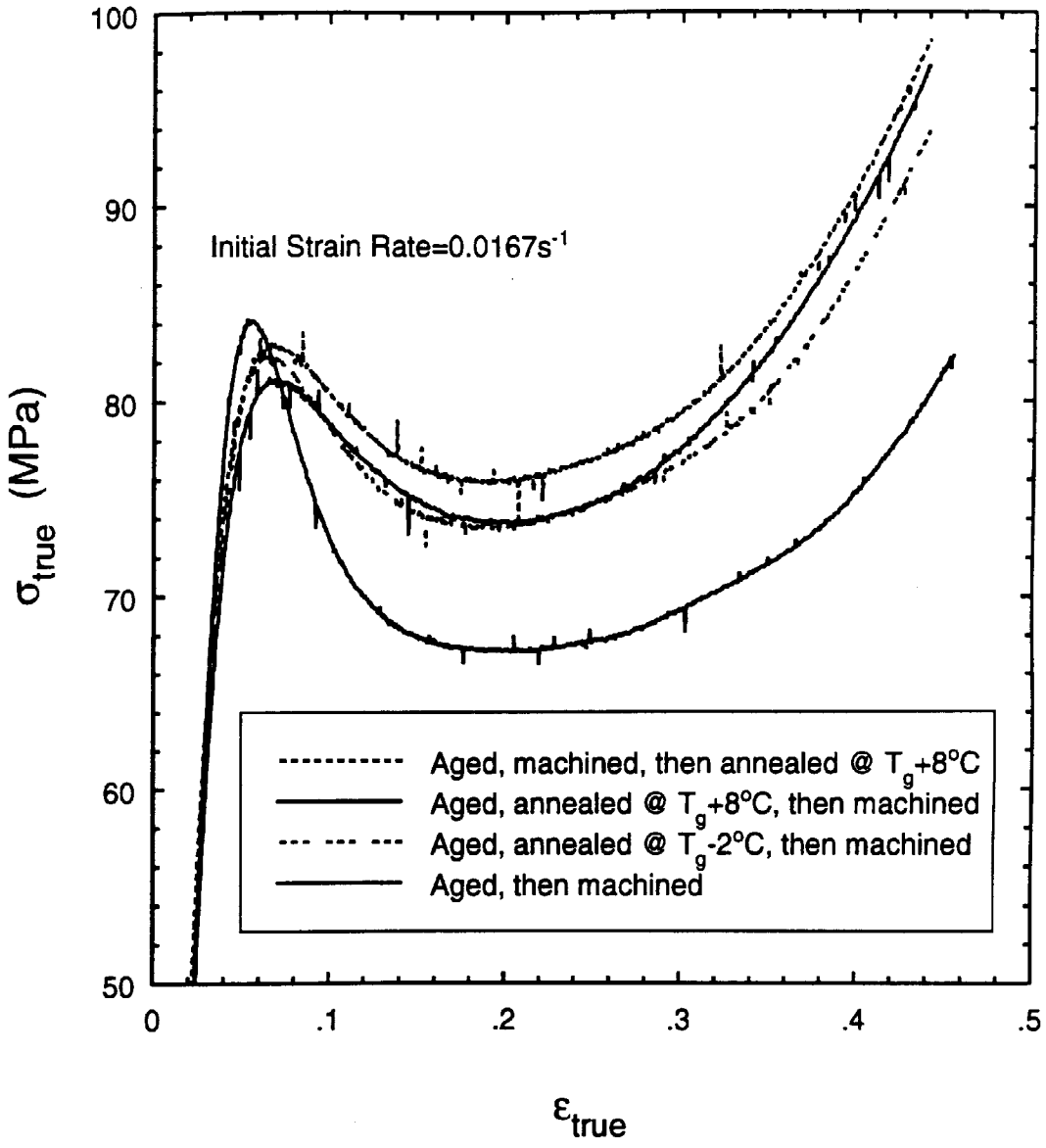

Figure A.21: Deformation behavior measured at 22°C of epoxy specimens (815:V-40/3:1, $T_g = 72°C$) which were aged 377 days at room temperature and then annealed at the temperatures indicated for 12 hours.

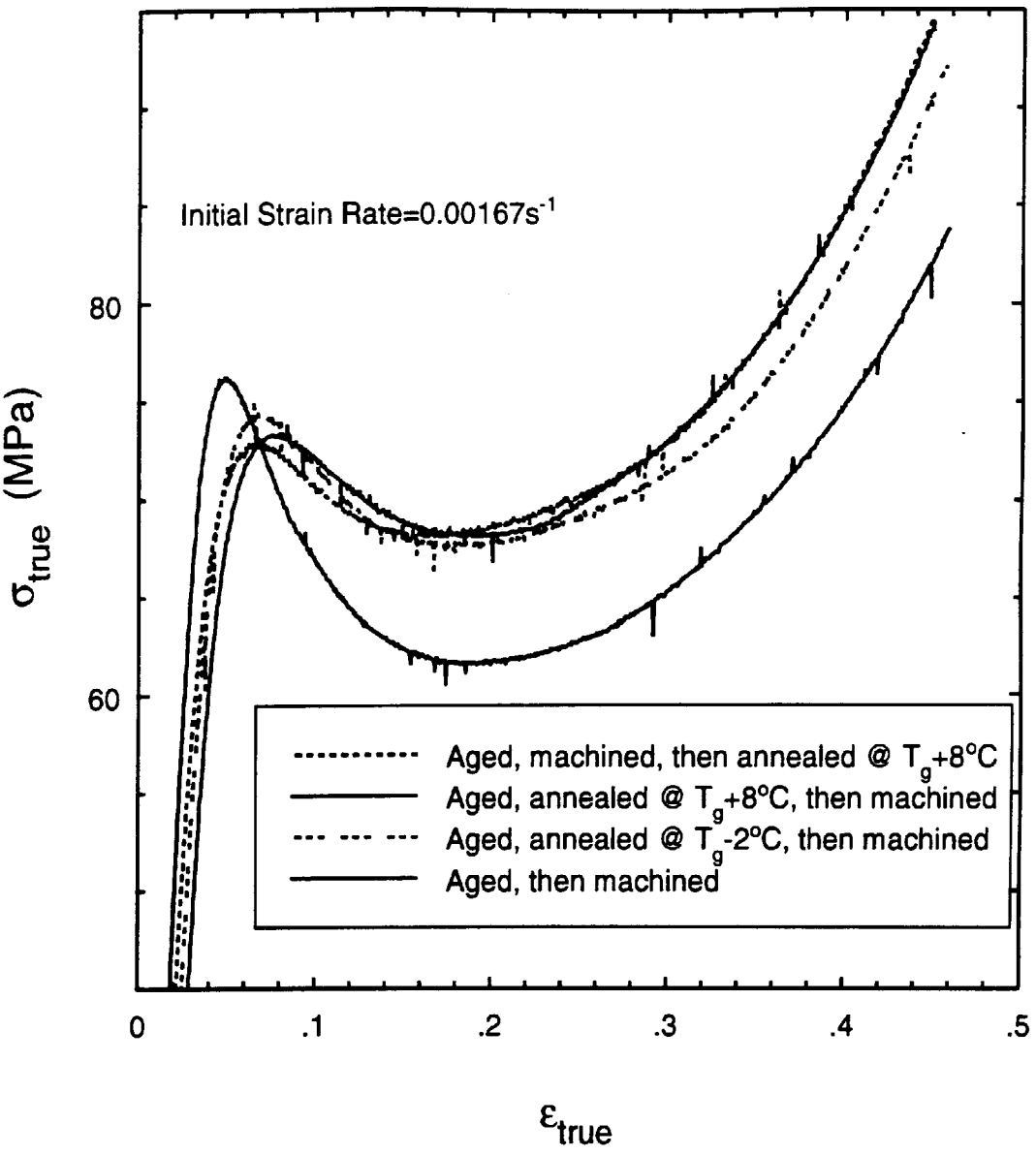

Figure A.22: Deformation behavior measured at 22°C of epoxy specimens (815:V-40/3:1, $T_g = 72°C$) which were aged 377 days at room temperature and then annealed at the temperatures indicated for 12 hours.

A.1.4.8 Correlation of data to the Argon theory of deformation

A theory which is to successfully model the deformation behavior of a solid must incorporate an appropriate dependency of molecular restructuring energies upon the shear strain, which is the driving force, and the shear modulus, which scales the energy barrier (and storage). Such a theory was developed by Argon, who proposed that deformation in amorphous polymers takes place by paired kinking of chain segments, which was modeled as wedge-like regions of misfitting strain [59]. The activation free enthalpy, ΔG_f^*, was computed from a solution obtained earlier for the free energy of a disclination loop (having molecular radius a) by calculating its interaction with an elastic medium resulting from the strain imposed by the nucleation of molecular kinks bending through an angle ω. The final expression, dependent upon Poisson's ratio, ν, shear modulus, μ, and yield stress in shear, τ, was presented as [59]

$$\Delta G_f^* = \frac{3\,\pi\,\mu\,\omega^2\,a^3}{16\,(1-\nu)}\left[1 - 8.5\,(1-\nu)^{5/6}\left(\frac{\tau}{\mu}\right)^{5/6}\right] . \qquad \text{(A.4)}$$

The dependence of deformation upon absolute temperature, T and shear strain rate, $\dot{\gamma}$, was introduced by utilizing standard rate theory in the form

$$\dot{\gamma} = \dot{\gamma}_o \exp\left(-\frac{\Delta G_f^*}{kT}\right) , \qquad \text{(A.5)}$$

where $\dot{\gamma}_o$ is a pre-exponential frequency factor. Rewritten in this form, Equation A.4 becomes [60]

$$\frac{\tau}{\mu} = \frac{0.077}{(1-\nu)}\left[1 - \frac{16(1-\nu)kT}{3\pi\mu\omega^2 a^3}\ln\left(\frac{\dot{\gamma}_o}{\dot{\gamma}}\right)\right]^{6/5} . \qquad \text{(A.6)}$$

This expression relates the plastic resistance in shear of a polymer to its modulus, temperature, rate of straining and the relevant molecular geometries involved in the deformation. A linear dependence of flow stress, reduced by modulus, upon temperature can be extracted by rewriting this equation as [60]

$$\left(\frac{\tau}{\mu}\right)^{5/6} = A - B\,(T/\mu) , \qquad \text{(A.7)}$$

where terms have been collected as

$$A = \left\{ \frac{0.077}{(1-\nu)} \right\}^{5/6} , \tag{A.8}$$

and

$$B = A \left\{ \frac{16(1-\nu)k}{3\pi\omega^2 a^3} \ln\left(\frac{\dot{\gamma}_o}{\dot{\gamma}}\right) \right\} . \tag{A.9}$$

We note here that the leading term, A, is the ratio of ideal shear stress to modulus, reduced by the exponent 5/6; *i.e.*

$$\hat{\tau} = \frac{0.077}{(1-\nu)} \mu . \tag{A.10}$$

It can be seen from Equation A.7 that, in addition to the linear dependence of reduced flow stress upon temperature, the theory predicts a common value of $[0.077/(1-\nu)]$ will be exhibited by all polymers at 0 K or at strain rates which approach $\dot{\gamma}_o$.

Equation A.6 may be simplified somewhat and rewritten as

$$\left(\frac{\tau}{\mu}\right)^{5/6} = \left(\frac{0.077}{(1-\nu)}\right)^{5/6} \left\{ 1 - \frac{5}{6} \frac{(1-\nu)}{0.077\, E} \left(\frac{\tau}{\hat{\tau}}\right)^{-1/6} \frac{kT}{\Delta V_\sigma^*} (2.3) \log\left(\frac{\dot{\gamma}_o}{\dot{\gamma}}\right) \right\} , \tag{A.11}$$

by introducing the stress activation volume (the basic unit of thermally-activated material experiencing shear transformation, which in the Argon theory is modeled as a pair of kinks in the polymer chain) as [59]

$$\Delta V_\sigma^* = \left[\frac{\partial \Delta G_f^*}{\partial \tau} \right]_{p,T} = \frac{3\pi}{16} \left(\frac{5}{6}\right) \frac{\omega^2 a^3}{0.077} \left(\frac{\tau}{\hat{\tau}}\right)^{-1/6} . \tag{A.12}$$

We now recognize, from Equation A.10 and the epoxy data presented earlier, that the term $\left(\tau/\hat{\tau}\right)^{-1/6} \approx 1.15$ over the ranges of temperature and strain rates explored. If we further assume that the modulus is invariant enough to take as a constant on the right hand side (a reasonable assumption since, over three decades of $\dot{\varepsilon}$, changes in E [at constant temperature] are only on the order of 10%), then we can combine the constant terms (taking $\nu = 0.36$) of Equation A.11 and rewrite it as

$$\left(\frac{\tau}{\mu}\right)^{5/6} = A \left\{ 1 - \frac{C(T,\mu)}{\Delta V_\sigma^*} \log\left(\frac{\dot{\gamma}_o}{\dot{\gamma}}\right) \right\} , \tag{A.13}$$

where

$$C(T,\mu) \;=\; 2.535 \times 10^{-22}\,\frac{T(\mathrm{K})}{\mu(\mathrm{Pa})}\,. \tag{A.14}$$

Data acquired in uniaxial compression may be compared to the Argon theory by transforming the normal yield stress, σ_y, normal strain, ε and Young's modulus, E to their shear analogs. Utilizing the elastic relationship $\mu = E/2(1+\nu)$ and the equivalence of flow stress (from the Mises condition) $\tau = \sigma_y/\sqrt{3}$, some of the epoxy data presented earlier is recalled.

In our first pass at comparing the epoxy data to the Argon theory, we examine some room-temperature data only. An additional parameter which is needed to plot data according to Equation A.13 is the pre-exponential frequency factor, which is taken to be[4] $\dot{\gamma}_o = \sqrt{3}\cdot 10^{12}\,s^{-1}$. Using this value, data are plotted in Figure A.23 for room-temperature measurements obtained over three decades of strain rate. We note here that, using equations presented in [59], the pre-exponential frequency factor was calculated from $(\partial \ln\dot{\gamma}/\partial\tau)_{p,T}$ measured for the epoxies investigated here, and was determined to be in the range of $10^{12} - 10^{13}$. Further, it is noted that changes in $\dot{\gamma}_o$ by an order of magnitude influence the intercept of straight-line fits to the data by only a few percent, and do not change the slopes at all.

[4]Estimated by the product of atomic frequency $\nu_a \approx 5\times 10^{12}\,s^{-1}$, $\omega \approx 2$, and volume fraction of deforming segments, $\alpha \approx 0.1 \rightarrow 0.2$.

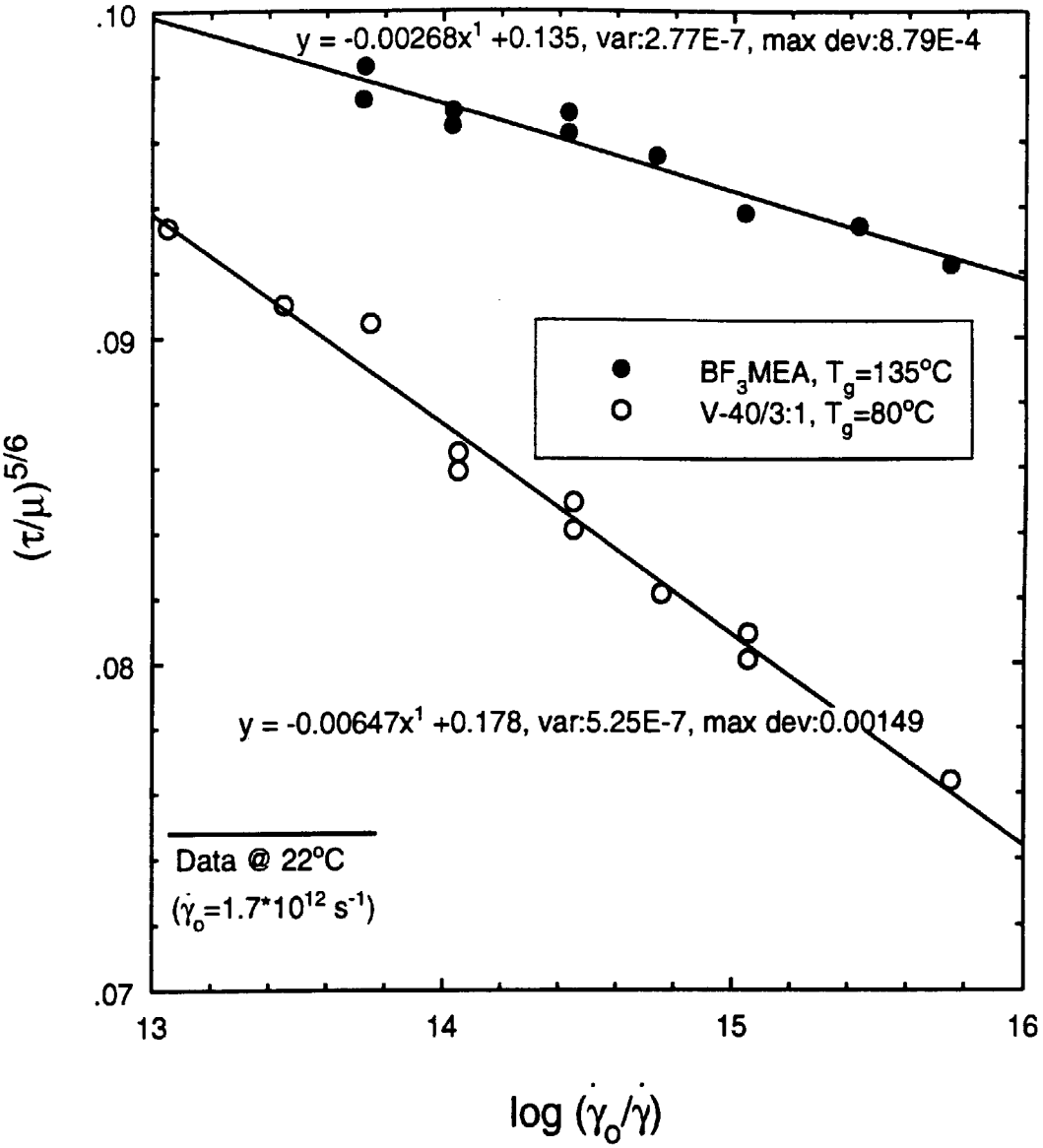

Figure A.23: Normalized yield data of two cures of EPON 815 measured at 22°C. Straight lines are least-squares fits, whose intercepts determine the ideal shear resistance and whose slopes determine the activation volumes, ΔV_f^*, via Equation A.13.

The immediate observation to be made from Figure A.23 is that the data do indeed plot on a straight line as predicted by the theory. This in itself is remarkable, since the theory is based upon the enthalpy associated with bending of polymer backbone chains, and makes no account of the effects of crosslinking, which must reinforce the molecular chains by restricting their mobility (and hence, modes of deformation). The intercepts of the straight-line fits are in good agreement with the theoretical value of 0.171. The epoxy specimens cured with polyamide to a $T_g = 80°C$ produced an intercept of 0.178, which groups this material among flexible carbon-chain polymers (*e.g. PC, PS, PET, PMMA*) whose intercepts were determined [59, 60, 61] to be in the range of 0.17–0.18. The epoxy specimens cured with BF_3MEA produced an intercept of 0.135, which is indicative of a fundamentally different molecular geometry, as observed in [60] for a class of aromatic polymers (Kapton, PPO, DFO) that produced intercepts in the range of 0.13–0.14. These aromatic polymers all possessed T_g's which were significantly greater than those of the carbon-chain materials (in general, by about 100°C), which is in direct correlation to the behavior of the epoxies whose measurements are shown in Figure A.23.

A similar investigation of epoxies was reported, by Yamini and Young, in which data obtained well below T_g also could be modeled well by the Argon theory [44]. In that study, one curing agent (TETA) was used to generate cured epoxy solids with increasing T_g as a result of increasing curing agent concentration. (In contrast to the reverse effect with the polyamide curing agent [V-40] used here.) The data reported in [44] were plotted as a function of (T/μ) and displayed a steady trend of increasing intercepts with increasing T_g, which is opposite to the trend exhibited by the epoxies reported here and by the varied group of polymers reported in [59, 60]. This difference in behavior might be reconciled by the observation that both E and σ_y decreased as a function of increasing T_g in [44]. In contrast, the present study shows that epoxy specimens cured with BF_3MEA (having T_g=135°C) have a significantly higher E and σ_y than the V-40/3:1, T_g=80°C materials. The two completely different curing agents used assuredly result in cured epoxy solids with fundamentally different structures. As mentioned earlier, the Lewis Acid promotes complete homopolymerization of the epoxy groups by catalyzation, whereas the polyamide links together epoxy groups

by reaction with the amine molecules. The intercept value of 0.135 displayed by the Lewis Acid-cured epoxy, in the range with the aromatic polymers that have a large molecular volume, is consistent with the concept that its *effective* molecular volume is enhanced due to extensive crosslinking. The extent of crosslinking is evidenced by the brittleness of BF_3MEA-cured epoxy, to be presented later. The large effective molecular volumes are reflected by the experimentally-determined activation volumes, which are discussed next.

The stress activation volumes may be determined from Equation A.13 and the slopes of the lines in Figure A.23. Using Equation A.14 and taking the temperature to be 295 K, for specimens cured with BF_3MEA (taking $E = 2.6$ GPa) the constant of Equation A.13 becomes $C = 2.88 \times 10^{-29}$. For 815:V-40/3:1, $T_g = 80°C$ specimens (taking $E = 2.4$ GPa), the constant becomes $C = 3.12 \times 10^{-29}$. Utilizing the experimentally-determined values of A, these considerations lead to values of $\Delta V_\sigma^* = 1450\,\text{Å}^3$ for the BF_3MEA epoxy and $\Delta V_\sigma^* = 858\,\text{Å}^3$ for the V-40, T_g=80°C epoxy, which is consistent with the observation made in the previous paragraph that the more heavily crosslinked epoxy behaves as if it had a much larger effective molecular volume. Indeed, if we use Equation A.12 and assume that $\omega = 2$ (since [60] the mean valence angle of a C-C bond is $\sim 115°$), we find that the two epoxies have effective molecular radii of a_o=3.69 and 3.09 Å. The larger of these two values, for the Lewis Acid-cured epoxy, agrees well with the molecular radii determined by Yamini and Young, who reported [44] ranges of 3.98–4.38 Å for their epoxy, which they determined to have slightly higher ($\sim 20\%$) values of E and σ_y (at similar strain rates) than were measured for the Lewis-acid cured specimens here. The low value of a_o=3.09 Å determined for the specimens cured with V-40 is indicative of more localized modes of deformation in the polymer chains, and is consistent with its lower modulus and yield stress and its higher strain-rate sensitivity.

The effect of aging upon the parameters of the Argon theory was investigated for a series of 815:V-40/3:1, $T_g = 72°C$ epoxy specimens, whose data are plotted in Figure A.24. Evidently, aging has little effect upon the parameters deduced for the theory, as no systematic pattern emerges from the data in the figure. The rational

explanation for the lack of an apparent influence due to aging is that aging has a similar effect upon the modulus and yield stress of this epoxy, both in terms of magnitude and in terms of strain-rate sensitivity as shown earlier. The four straight-line fits in Figure A.24 may best be interpreted as bracketing the experimental error, in which case the average intercept is 0.149 and the average slope determines that ΔV_σ^*=1003 Å^3 and a_o=3.25Å. The values of ΔV_σ^* determined for the epoxies here are in good agreement to a report of ΔV_σ^* = 900 Å^3 for other crosslinked networks [62]. In contrast, another report [63] has presented ΔV_σ^* values on the order of 10^4 Å^3 for an epoxy identified as "Araldite MY 753 resin and HY 951 hardener," which had strength and stiffness similar [64] to that of the V-40-cured specimens studied here.

The epoxy data presented here can also be compared to the Argon theory as a function of temperature, which has a more profound impact upon material properties than does the strain rate. If the data are plotted against temperature, reduced by modulus, then plots such as shown in Figure A.25 can be interpreted through Equation A.7. For the two sets of data acquired at strain rates of $\dot{\gamma}$=3×10^{-2} and 10^{-3}, the activation volumes computed from the slopes and intercepts of Figure A.25 are as follows. The specimens cured to T_g = 80°C produce ΔV_σ^* =3857 and 3525 Å^3 for the faster and slower strain rates, respectively, which result in computed mean molecular radii of a_o=5.1 and 4.95 Å. The specimens cured to T_g = 72°C produce ΔV_σ^* =2469 and 2198 Å^3, and a_o=4.40 and 4.23 Å. We observe first that both cures of epoxy specimens display a reduction, by about 10%, of the computed parameters as a result of the reduction of strain rate by a factor of ten. Additionally, it is apparent that closer agreement with the parameters determined from the Yamini and Young data is obtained from these data than from the room temperature data discussed earlier.

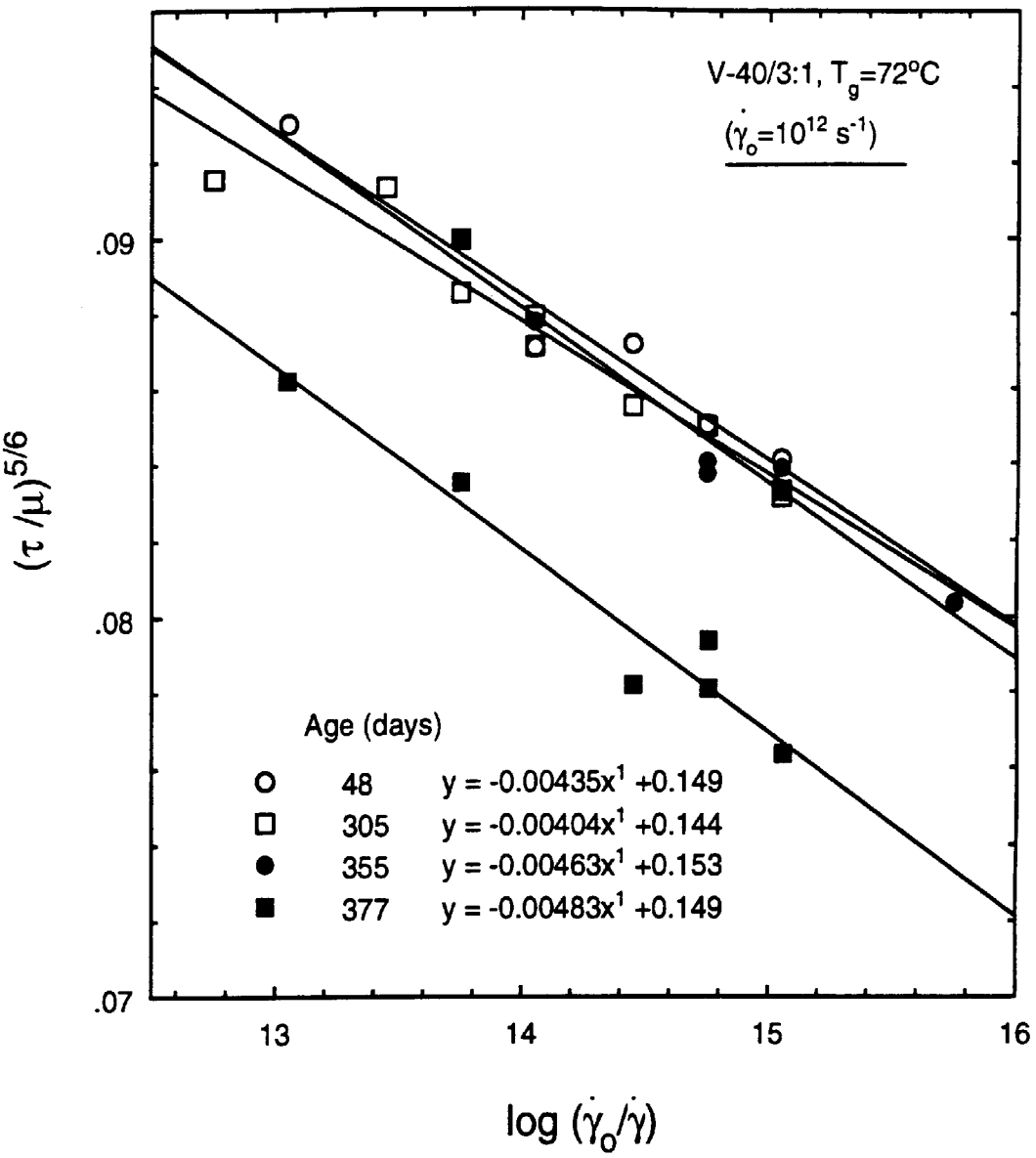

Figure A.24: Yield data of 815:V-40/3:1, $T_g = 72°C$ specimens aged for the indicated times and tested at 22°C. Data normalized in the same manner as in Figure A.23.

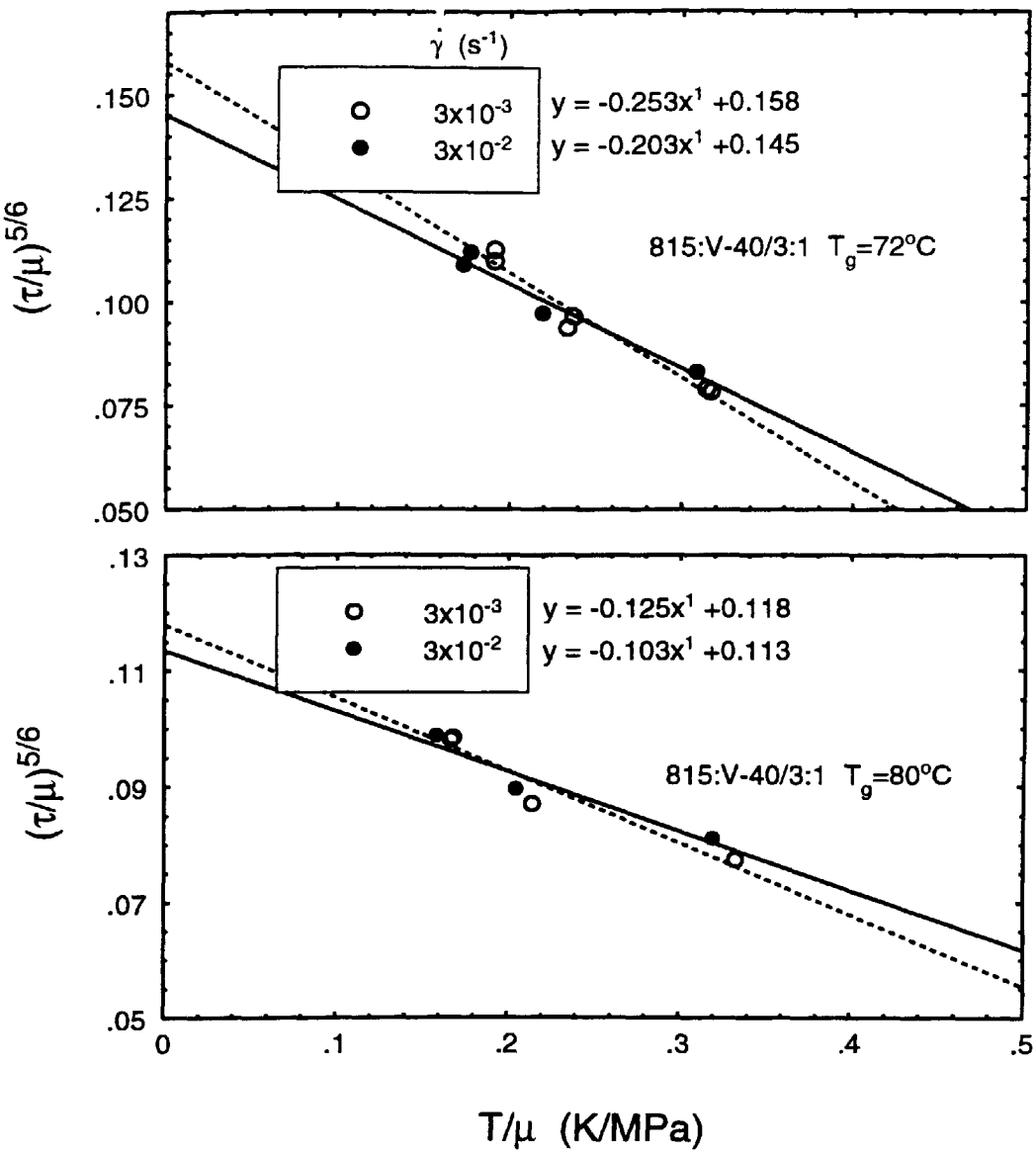

Figure A.25: Yield data of 815:V-40/3:1 specimens tested at nominal strain rates of $\dot{\gamma} = 0.03, 0.003 s^{-1}$. Data normalized according to Equation A.7.

A.1.4.9 Rate sensitivities

Data presented earlier indicate that the epoxies investigated here exhibit log-linear dependencies of both E and σ_y upon strain rate (at a fixed temperature). Referring to Figures A.16, A.18 and A.20, it may be seen that the relationship $\sigma_y = A + B \log \dot{\varepsilon}_y$ is followed extremely closely. This behavior may be utilized to deduce other material characterizing parameters, such as apparent activation volumes and, in crystalline materials, the force-distance curves of dislocations impeded by obstacles. In the paragraphs below, activation volumes determined solely from the rate sensitivity of yield stress, as formulated in the Eyring model, are calculated and compared with the values determined earlier on the basis of the Argon theory.

Activation Volumes The formulation of the Eyring model of plastic flow in polymers is based on the concept that molecular segments are vibrating over an energy barrier (activation enthalpy, ΔH^*) whose height is reduced by the effects of applied stresses. The model predicts that the shear strain rate is described by a standard Arrhenius rate equation, modified by a hyperbolic sine, giving an equation of the form [55]

$$\dot{\gamma} = \dot{\gamma}_o \exp\left(-\frac{\Delta H^*}{kT}\right) \sinh \frac{\Delta V_\sigma^* \tau}{2kT} . \tag{A.15}$$

For large stresses (high strain rates and/or low temperatures) differentiation of Equation A.15 leads to

$$\Delta V_\sigma^* = \frac{2\,k\,T}{\left(\frac{\partial \tau}{\partial \ln \dot{\gamma}}\right)_{p,T}} = \frac{2\,k\,T\sqrt{3}}{\left(\frac{\partial \sigma_y}{\partial \ln \dot{\varepsilon}}\right)_{p,T}} . \tag{A.16}$$

Physical significance for ΔV_σ^* in the Eyring model may be more easily interpreted if Equation A.15 is modified slightly and rewritten as [63]

$$\dot{\gamma} = \dot{\gamma}_o \exp\left[-\left(\Delta H^* - \int_0^\tau \Delta V_\sigma^* d\tau\right)/kT\right]_p . \tag{A.17}$$

From this equation it becomes more apparent that ΔV_σ^* is the effective volume throughout which stress acts to reduce the energy barrier to molecular motions. The view has been expressed however, that ΔV_σ^* is not a true volume, but is simply a

proportionality constant between the work done at the molecular level during deformation and the applied stresses [65].

The Eyring activation volumes can be computed from the slopes, $(\partial\sigma_y/\partial \ln \dot{\varepsilon}\,)_{p,T}$, determined in the plots presented earlier. The specimens cured with Lewis Acid (BF_3MEA) yielded a slope of 2.742 MPa at room temperature, from which a value of ΔV_σ^*=5143 Å^3 is computed with Equation A.16. Similarly, specimens cured with V-40 to T_g's of 72 and 80°C produce values of 2902 and 3378Å^3, respectively. These activation volumes are comparable to those determined through the Argon model, but are consistently higher by a factor of $\sim$ 3. A similar trend is displayed nonetheless, with the material having the highest σ_y and lowest rate-sensitivity (Lewis Acid-cured) generating the highest experimentally-determined ΔV_σ^*. The softer and more rate-sensitive materials (V-40-cured) have lower activation volumes, which, as discussed earlier, is characteristic of more localized deformation mechanisms. This conclusion, reached from activation parameter analysis, is also reached directly from inspection of the typical stress-strain curves exhibited by the classes of epoxies investigated.

The argument might be made that determination of $(\partial\sigma_y/\partial \ln \dot{\varepsilon}\,)_{p,T}$ should be done with strain-rate-change experiments on single specimens, rather than with several specimens over a range of rates. The explanation in favor of the argument is that the data should be acquired not just at constant temperature and pressure, but also at constant material *structure*. In addition, rate-change experiments enable the acquisition of multiple data points from a single specimen. An argument for the use of data from specimens tested at a constant rate, with many specimens over a range of rates, is that this procedure will smooth out any specimen-to-specimen variations and experimental errors. Furthermore, little variation in structure is expected between amorphous polymer specimens which are all fabricated simultaneously.

Several strain-rate-change experiments were performed with specimens of each of the epoxy formulations. Typical stress-jumps are shown in Figure A.26 for tests which were performed at room temperature by changing the crosshead speed on the testing machine by a factor of ten. Changes were executed at the point on the stress-

strain curve when the yield stress (inflection point) was just reached, and additionally thereafter. Values of $(\partial\sigma_y/\partial \ln \dot{\varepsilon}\,)_{p,T}$ determined at the yield points on these plots were about 30% greater than the slopes[5] obtained from Figures A.16, A.18 and A.20. A possible explanation for this discrepancy is that the feature of the test machine being used which enables changing the crosshead speed *"Times 10"* in reality became something like *"Times 13."* However, previous measurements with PVC have also shown that values of $(\partial\sigma_y/\partial \ln \dot{\varepsilon}\,)_{p,T}$ obtained from multi-specimen testing are 30–40% smaller than those values obtained from single (strain-rate-change) specimens [66]. If the assertion is adopted that the rate-change testing is the more appropriate method, then the activation volumes computed here from $(\partial\sigma_y/\partial \ln \dot{\varepsilon}\,)_{p,T}$ would be reduced significantly and hence would be in better agreement with values of ΔV_σ^* determined from the Argon theory. These rate-change data also provide the additional information that, as the level of straining increases, ΔV_σ^* decreases. This is evidenced by the increasing magnitudes of the stress-jumps at greater strains. The reduction in ΔV_σ^* is indicative of a reduction in ΔH^* due to stored strain energy *and* a rise in temperature, since the testing is essentially adiabatic (due to the low thermal conductivity of epoxy).

[5]The equations indicated in the referenced figures include the conversion: $\ln 10 = 2.303$.

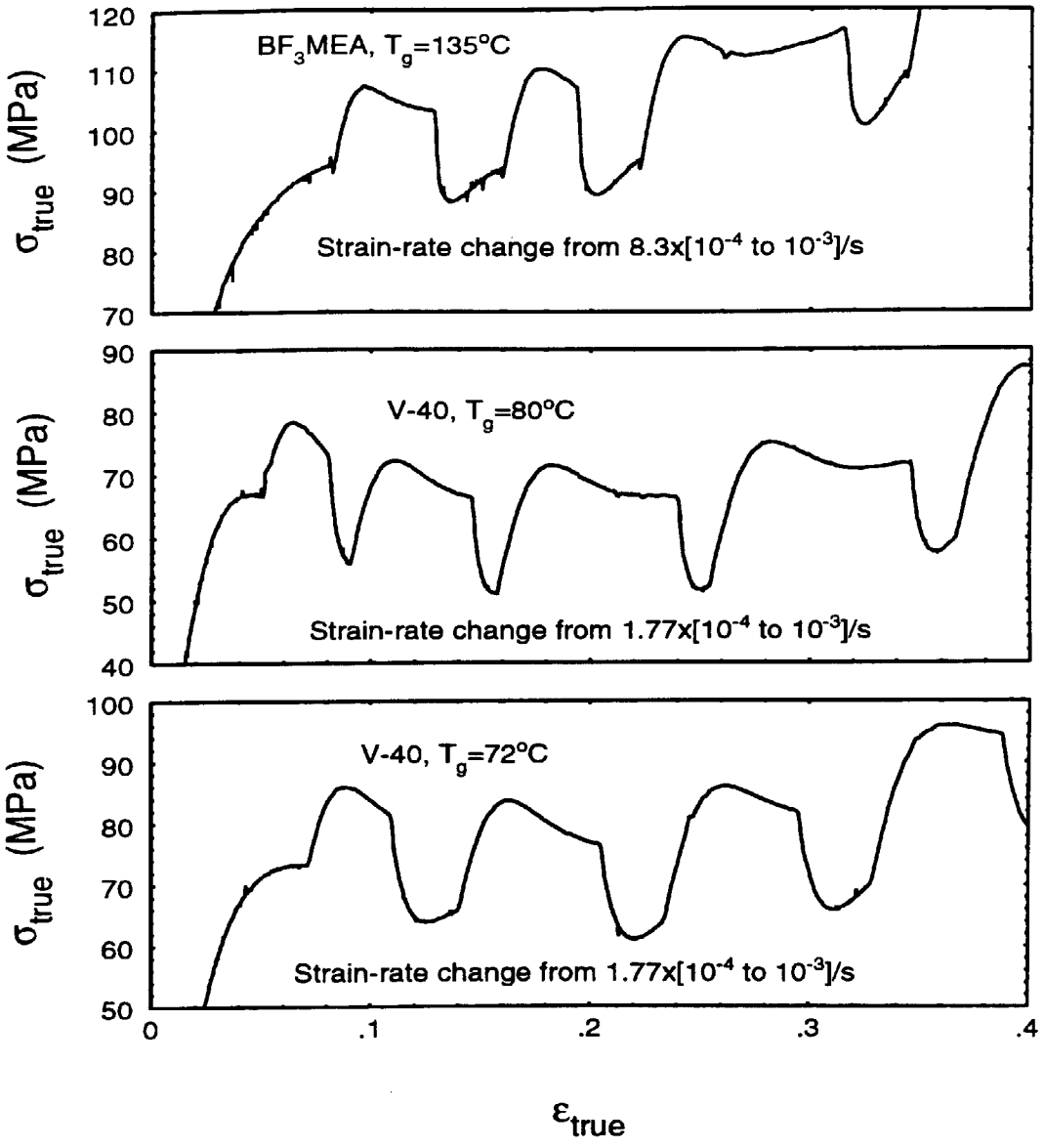

Figure A.26: Example strain-rate change data from experiments performed at room temperature on the three cures of epoxies studied.

Strain Hardening The characteristic stress-strain curves (see Figure A.10) for the different cures of epoxy examined here show wide variations in the softening and hardening behaviors. Specimens cured with V-40 at a 3:2 ratio produced such extensive strain softening that the tests were terminated before orientation effects could be witnessed. Specimens cured with V-40 at a 3:1 ratio demonstrated both strain softening and strain hardening, with an extended intermediate region of flow at an essentially constant level of stress; this may be the result of the competing effects of softening and hardening occurring simultaneously. Epoxy solids cured with Lewis Acid (BF_3MEA) showed little evidence of strain softening, but their strain (orientation) hardening was very high. In addition to the high magnitude of hardening in these materials, another striking feature was the relatively low level of strain at which the hardening began. (Typically at $\varepsilon \approx 0.2$, as opposed to the higher strains (0.4–0.5) at which hardening in amorphous glassy polymers usually tends to occur [55].) The balance of this section shall quantify these hardening behaviors as a function of a strain-hardening exponent.

The strain hardening of these epoxies shall now be characterized directly by empirical means. We seek to match the stress-strain curves with a functional fit using the usual (plastic, rate-independent) power-law equation

$$\sigma^{\mathrm{P}} = \sigma_{\circ} \left(\frac{\varepsilon}{\varepsilon_{\circ}} \right)^{n} , \tag{A.18}$$

where $\sigma_{\circ}$ and $\varepsilon_{\circ}$ are reference values of stress and strain, taken at the yield point, and n is the adjustable parameter which represents the degree of hardening. For most metals, n ranges between 0.1 and 0.4 [67]. Published values of n for plastics are sparse and indeed elusive for epoxies in particular, though when a value is required, values on the order of 0.1 are usually assumed [68]. If such values of n are used to attempt to fit Equation A.18 to the post-yield portion of typical stress-strain curves obtained from the two classes of epoxy cures studied here, then curves such as shown in Figure A.27 result. The plots in this figure immediately make clear the difficulty presented by trying to match the deformation behavior of these epoxies by an equation with a single adjustable parameter. Due to the softening in these materials, the exponential rise in the fitting curve immediately begins to deviate from the material curve. In

addition, a power-law fit which uses any exponent less than unity will not represent the inflection and strongly rising portion of the stress-strain curve.[6]

The aforementioned difficulties may be overcome by use of a modified power-law equation which is capable of representing the flow at essentially constant stress (following any initial softening), and then matches the upturning portion through an exponent greater than one. Such an equation would have the form

$$\sigma^{\mathrm{p}} = \sigma_{\mathrm{s}} + H(\varepsilon_{\mathrm{h}}) \left(\frac{\varepsilon}{\varepsilon_{\mathrm{h}}} \right)^{h} , \tag{A.19}$$

where σ_{s} is the steady flow-stress exhibited after yield, ε_{h} is the strain at which hardening begins, and H is the Heaviside step function with its usual meaning. A first impression of this equation might be that the hardening is not represented by any physical basis, *i.e.* that the hardening is no longer represented by a proportionality to the yield stress. Nonetheless, because the hardening in polymers is a direct consequence of molecular orientation, the stress-independent strain term may, in fact, have some reasonable physical basis.

Typical hardening curves obtained from epoxies cured with the different curing agents are shown in Figures A.28 and A.29. The least-squares fits of Equation A.19, which are included in the figures, are seen to approximate the material behavior extremely well. Values of the exponent, h, are in the range of 3–5 and are summarized in Table A.3 as a function of strain rate for the epoxies investigated here. From the indicated values of h, it is apparent that the Lewis Acid-cured epoxies experience much greater orientation hardening than specimens cured with V-40.

[6]The constitutive model developed in Reference [53] might be adapted to characterize the complete evolution of softening and hardening behavior in these epoxies.

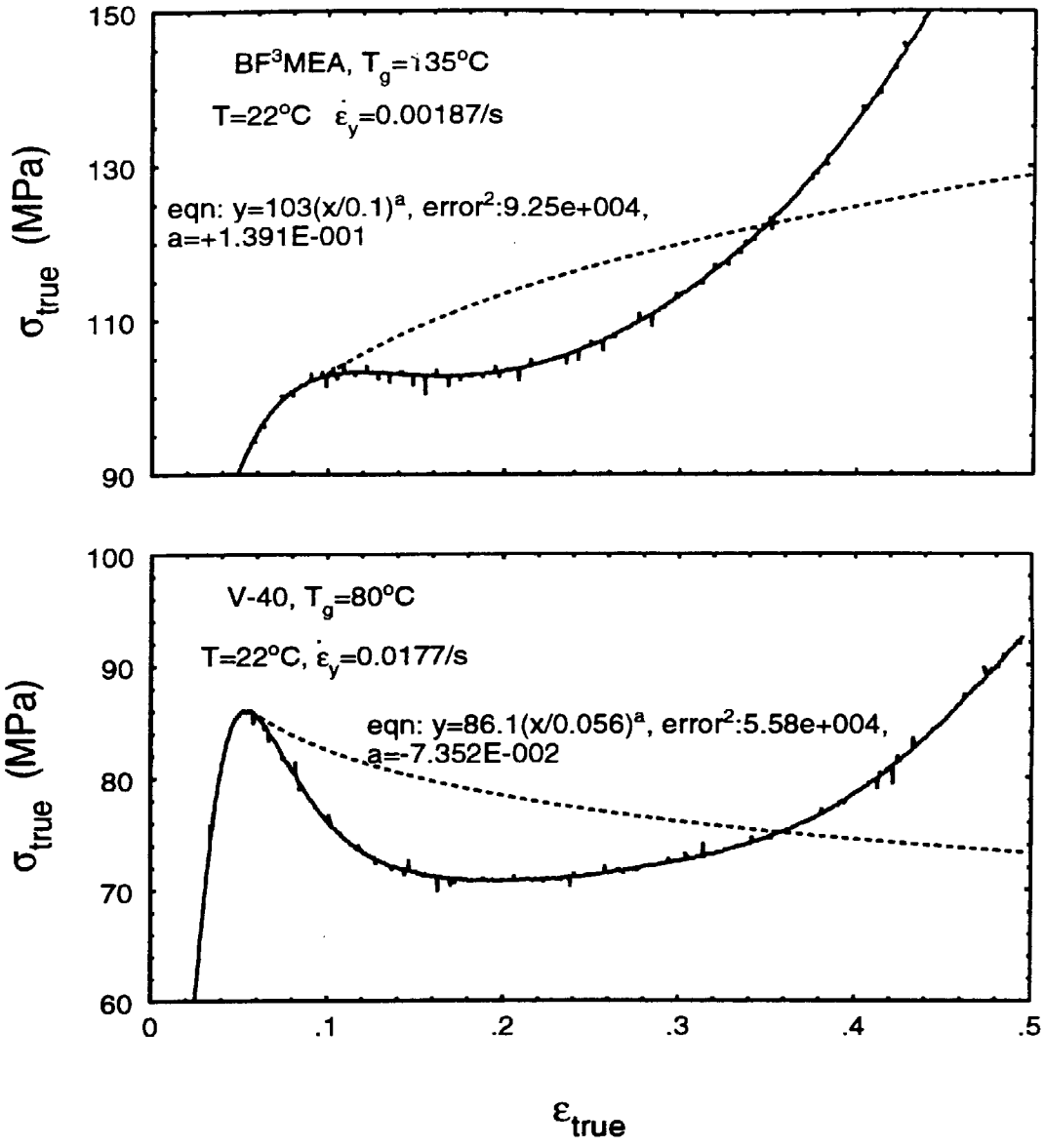

Figure A.27: Post-yield portions of epoxy stress-strain curves, with least-squares fit of Equation A.18.

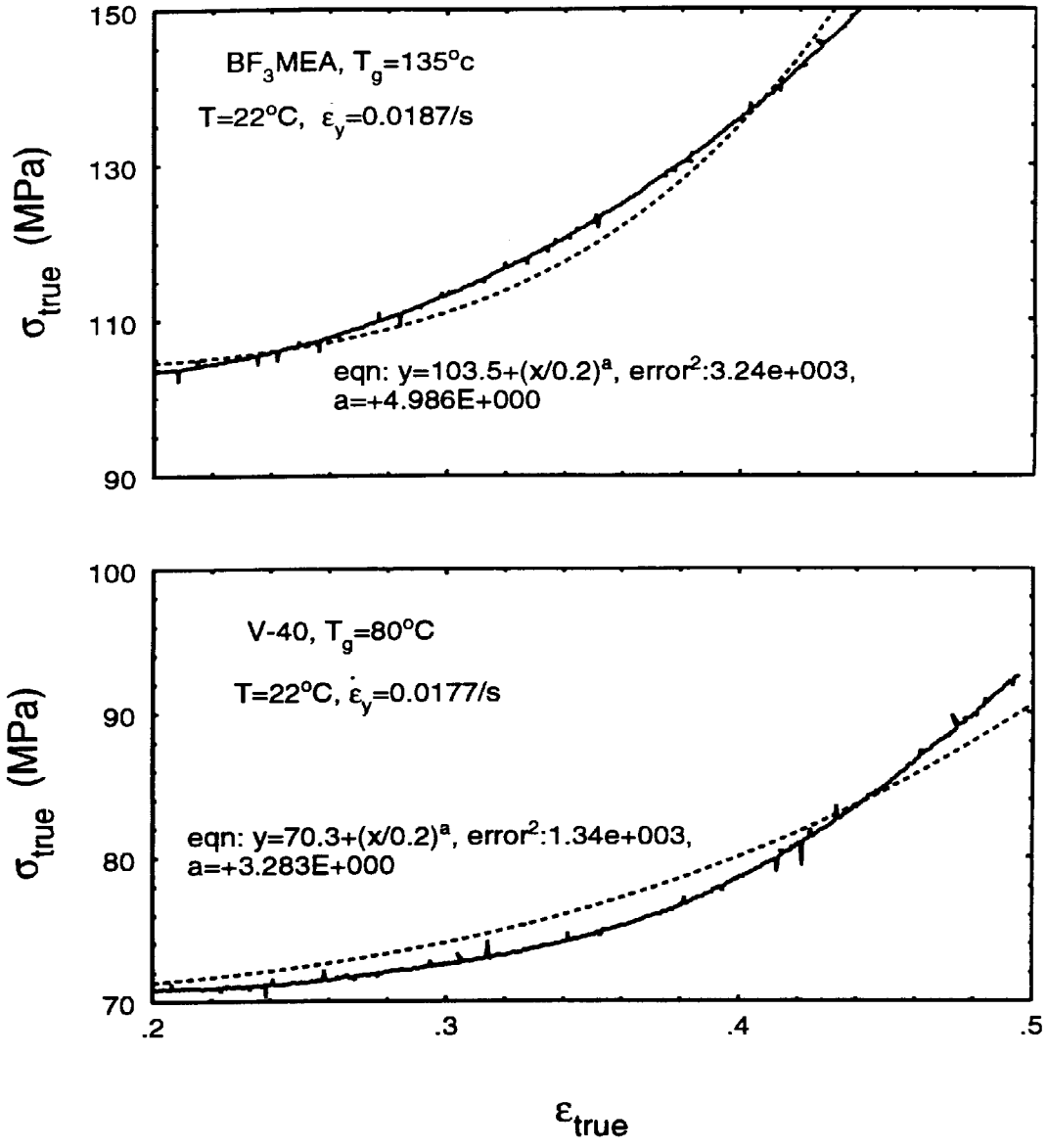

Figure A.28: Hardening portions of epoxy stress-strain curves; dashed lines are least-squares fit of Equation A.19.

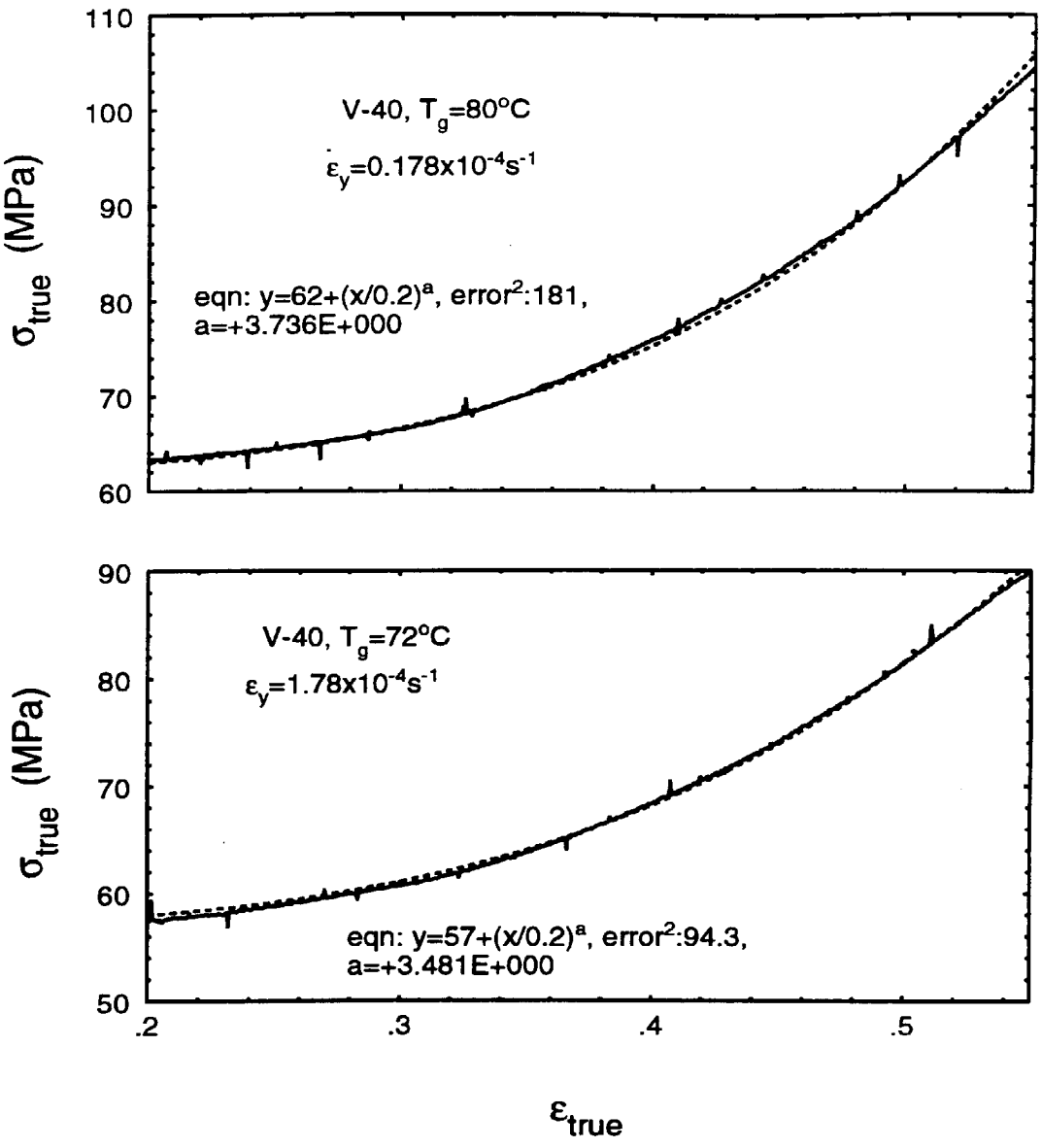

Figure A.29: Hardening portions of V-40-cured epoxy stress-strain curves; dashed lines are least-squares fit of Equation A.19.

The physical significance of the standard strain hardening expression, where the rate of hardening is proportional to the yield stress, may be restored by simply shifting the hardening portion of Equation A.18 to the strain at which hardening commences. In this case, the expression would be

$$\sigma^{\mathrm{p}} = \sigma_{\mathrm{s}} + H(\varepsilon_{\mathrm{h}})\sigma_{\mathrm{s}}\left[\left(\frac{\varepsilon}{\varepsilon_{\mathrm{h}}}\right)^{n'} - 1\right], \tag{A.20}$$

which incorporates the flow stress following softening but will not reflect the strongly upturning rise in stress that results from large strains. Typical least-squares fits to this equation are shown in the plots included in Figure A.30. Although the functionality of the curves do not match, levels of stress are approximated reasonably well by Equation A.20. Values of n' determined in this manner are included in Table A.3, which also contains least-squares fits of n, as used in the standard power law relation (Equation A.18). Clearly, ability of the standard power law to adequately represent hardening is confounded by the presence of softening, as indicated by negative values of n. Use of the modified-standard relation results in meaningful values of n' that display two obvious trends. The Lewis Acid-cured epoxy consistently exhibits the most rapid hardening, and all of the epoxies tend to harden more rapidly at slower strain rates and higher T_g's.

Table A.3: Hardening exponents determined by fitting Equations A.18, A.19 and A.20 to the epoxy compressive stress-strain data.

Hardening Exponent	*Epoxy Cure*	*Nominal Strain Rate* (s^{-1})		
		1.67×10^{-4}	1.67×10^{-3}	1.67×10^{-2}
n	BF_3MEA, $T_g = 135°C$	0.24	0.19	0.14
	V-40, $T_g = 80°C$	-0.0042	-0.015	-0.073
	V-40, $T_g = 72°C$	-0.0067	-0.078	-0.061
h	BF_3MEA, $T_g = 135°C$	4.9	4.7	4.9
	V-40, $T_g = 80°C$	3.7	3.5	3.4
	V-40, $T_g = 72°C$	3.5	3.4	3.4
n'	BF_3MEA, $T_g = 135°C$	0.50	0.44	0.36
	V-40, $T_g = 80°C$	0.38	0.30	0.20
	V-40, $T_g = 72°C$	0.32	0.21	0.19

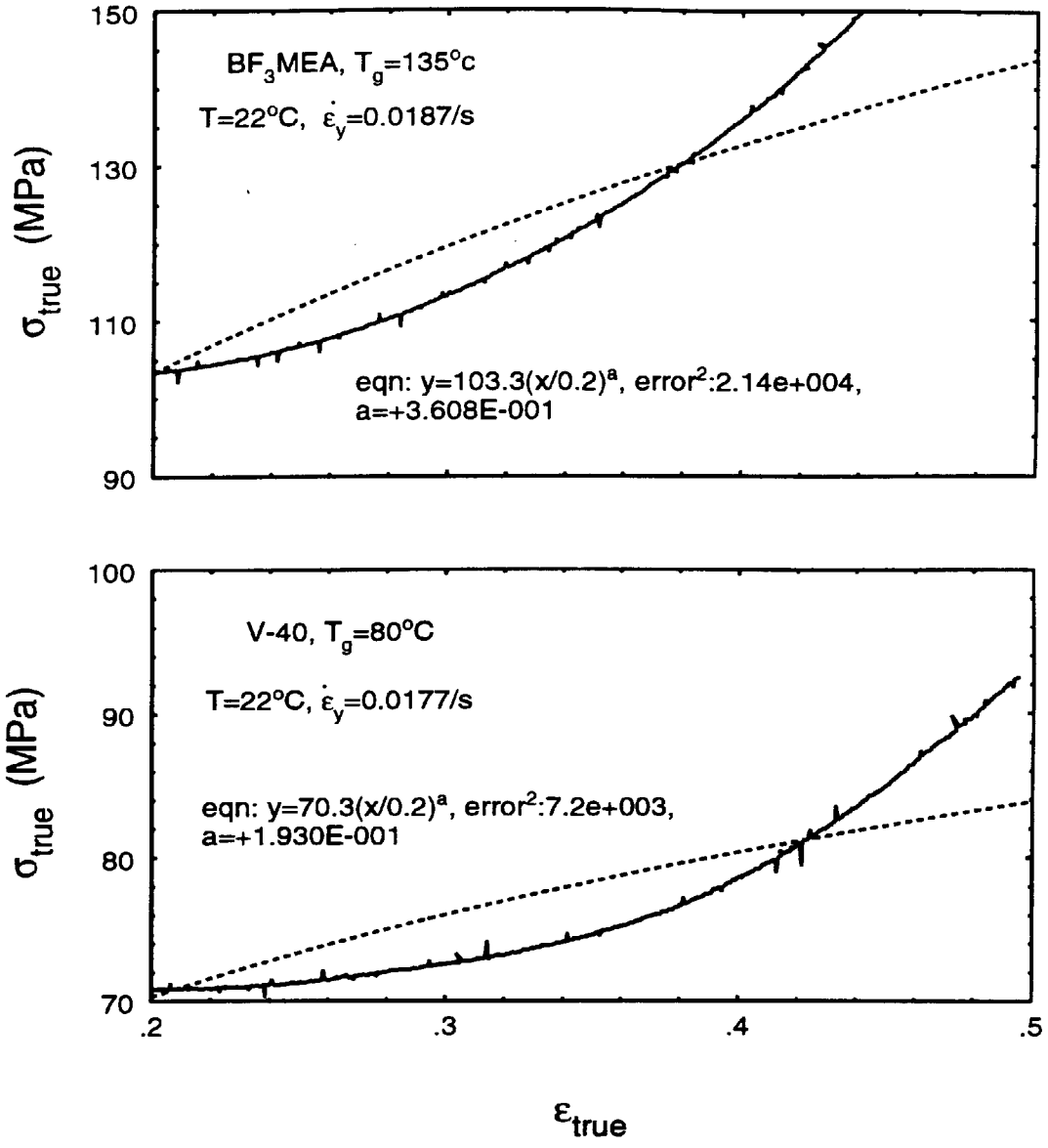

Figure A.30: Hardening portions of epoxy stress-strain curves; dashed lines are least-squares fit of Equation A.20.

A.1.5 Fracture Toughness Tests

A.1.5.1 Double cantilever beam specimens (DCB)

The initial efforts to measure the fracture toughness of the epoxies discussed in this appendix were pursued in order to establish the suitability of such materials for use as a matrix in the crack-trapping experiments. The first type of specimen used was the double cantilever beam (DCB), which is illustrated schematically in Figure A.31.

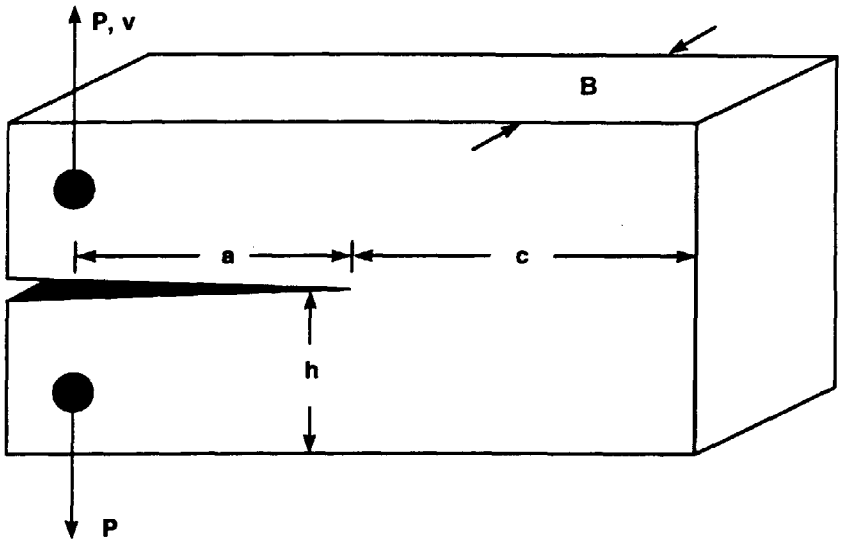

Figure A.31: Schematic description of the double cantilever specimen.

Background The nomenclature of the figure is defined as follows: P is the applied load, acting through the displacement, v (which is relative between the two points of load application), a is the crack length, h is the height of each beam (in the cracked portion), and B is the specimen thickness. It can be shown quite simply that the "energy release rate," G, is proportional to the change in compliance, $C = v/P$, with increasing crack length [69]:

$$G = \frac{P^2}{2B}\frac{\partial C}{\partial a}\,. \tag{A.21}$$

This relation is valid for all loading configurations of cracked elastic bodies. It is noted here that G is the *crack driving force*, equal to twice the new surface energy (2Γ) created by fracture of an ideally elastic solid. Simple engineering beam analysis of the DCB results in

$$G = \frac{12\,P^2\,a^2}{E\,h^3\,B^2}\,. \tag{A.22}$$

A necessary condition for crack extension is that enough energy be available to drive the crack; thus G must be equal to or greater than 2Γ. This, however, is not a *sufficient* condition, for the material at the crack tip must be ready and able to separate. This additional condition is obviously one of stress. Because the stress field

$$\sigma_{ij} = \frac{K_I}{\sqrt{2\pi\,r}}\,f_{ij}(\theta) \tag{A.23}$$

immediately ahead of a crack tip (subject to the opening mode, I) is scaled by the *stress intensity factor* K_I, the logical stress criterion for fracture to occur is that a critical value of K_I be reached.[7] This critical value, denoted K_{Ic}, is referred to as the "plane strain fracture toughness," and is determined as the critical value of K_I required to promote crack extension in a material specimen whose thickness (or smallest dimension) is sufficient to ensure that conditions of plane strain exist at the crack tip. This minimum dimension d is usually specified as [69] approximately $15\,r_{\rm p}$, where $r_{\rm p}$ is the radius of plastic deformation surrounding a sharp crack tip in plane stress, *i.e.*

$$d > 2.5\frac{K_I^2}{{\sigma_y}^2} \approx 2.5(2\pi r_{\rm p})\,. \tag{A.24}$$

For materials in which no dissipative processes take place, there is an exact equivalence between the energy and the stress conditions, so that, in plane strain [69]

$$K_I^2 = \frac{G_I\,E}{(1-\nu^2)}\,. \tag{A.25}$$

In reality, of course, dissipation occurs in all materials, so this equation is never exactly correct for real materials. For many materials it is nearly exact though, and

[7] For thorough discussions of this approach, the reader is referred to References [69, 70].

the appropriateness of its use may be characterized by the size of the inelastic zone, r_p, produced ahead of a fully developed crack. For brittle materials, r_p is on the order of 100 μm or less, and the methods of *linear elastic fracture mechanics* (LEFM) outlined here are appropriate. For materials which develop larger values of r_p, or for specimens whose dimensions are on the order of r_p, nonlinear fracture mechanics [71] and other methods of characterization [72] must be applied. In the case of the epoxies investigated here, r_p is on the order of 50 μm; therefore LEFM analysis and procedures were followed.

In the case of the DCB specimen, the application of Equation A.25 to Equation A.22 results in

$$K_I = \frac{2\sqrt{3}}{(1-\nu^2)} \frac{P}{h^{3/2}} \frac{a}{B} . \tag{A.26}$$

This expression, based upon simple beam theory, is only approximate and does not account for the compliance of the "built-in" cantilever ends nor does it account for shear deformations and possible inertial effects. A more exact analysis developed by Kanninen, based upon the model of a beam resting upon an elastic foundation, results in a correction term, Ψ, applied to the right hand side of Equation A.26. For crack extension under conditions of constant opening displacement, the correction factor reduces to [73]

$$\Psi = \left\{ \frac{1 + 0.64(h/a)}{1 + 1.92(h/a) + 1.22(h/a)^2 + 0.39(h/a)^3} \right\} \tag{A.27}$$

for short cracks or slender specimens where c, the uncracked ligament length, is greater than $2h$. Replacing the load point displacement with the engineering beam-theory equivalent load (*i.e.* $\delta = Pa^3/3EI$), Kanninen's equation (11) becomes

$$K_I = \left(\frac{P\,a}{1-\nu^2} \right) \left(\frac{12}{B^2\,h^3} \right)^{1/2} \Psi . \tag{A.28}$$

This equation was applied to the initial testing of the fracture toughness of epoxies, described below.

Experimental Procedures Several DCB specimens of each of the candidate epoxy formulations were fabricated and tested at room temperature. The specimen dimensions were, approximately: B=1 cm, W=6 cm and L=9 cm. Starter cracks were cut with a 0.5 mm-thick slitting saw on a milling machine to initial crack lengths, a_o, of 2 cm. These notches were then sharpened with a razor blade to provide initial cracks as sharp as possible. Loading was performed with a polished stainless steel wedge having an angle of 30°.

Testing was performed on an Instron 1125 machine, using the strip-chart to record data. Since the test machine is "screw-driven", and low loads were required to fracture the specimens (hence, minimal energy is stored in the machine load-train) conditions of displacement control prevailed. A displacement loading rate of $\sim$ 0.5 mm/min was used during most of the tests.

Discussion of Data Most of the tests resulted in a single crack extension which led to complete fracture of the specimens; hence, only one data point could be obtained with each specimen. A summary of the average computed values of K_{Ic} and G_{Ic} obtained with the DCB specimens is given in Table A.4. Significant scatter in the data existed and was judged to be the result of minor, but unavoidable, differences between the sharpness of the initial cracks.

To overcome this difficulty, and generate more reproducible data, it was resolved to adopt the use of a specimen that would allow multiple fracture initiations and arrests per test. Such crack growth would then, in theory, enable the initiation of all crack advances (subsequent to the first) to be made from natural cracks of identical sharpness. Moreover, the feature of multiple data points obtainable from a single specimen was desired.

The DCB specimens did provide additional useful information, in the form of characterizations of the fracture surface by electron microscopy. Typical micrographs of the epoxy fracture surfaces are shown in Figures A.32 and A.33. These photos clearly show cleavage steps and whiskers, indicative of the brittle nature of the fracture

process. The photos of mating surfaces display matching features on both halves, down to the scale of a few microns, demonstrating that almost no plastic deformation occurred during crack extension. The arrest line shown in Figure A.33 is about 30 μm in width and is an indication of the size of the crack-tip plastic zone (at room temperature, in $T_g = 72°C$ epoxy).

Table A.4: Average fracture toughness parameters determined for epoxy (815:V-40/3:1), from initial measurements with DCB specimens.

Cured T_g (°C)	80	72	52
K_{Ic} (MPa m$^{1/2}$)	0.9	1.3	2.8
G_{Ic} (J m^{-2})	298	669	3231

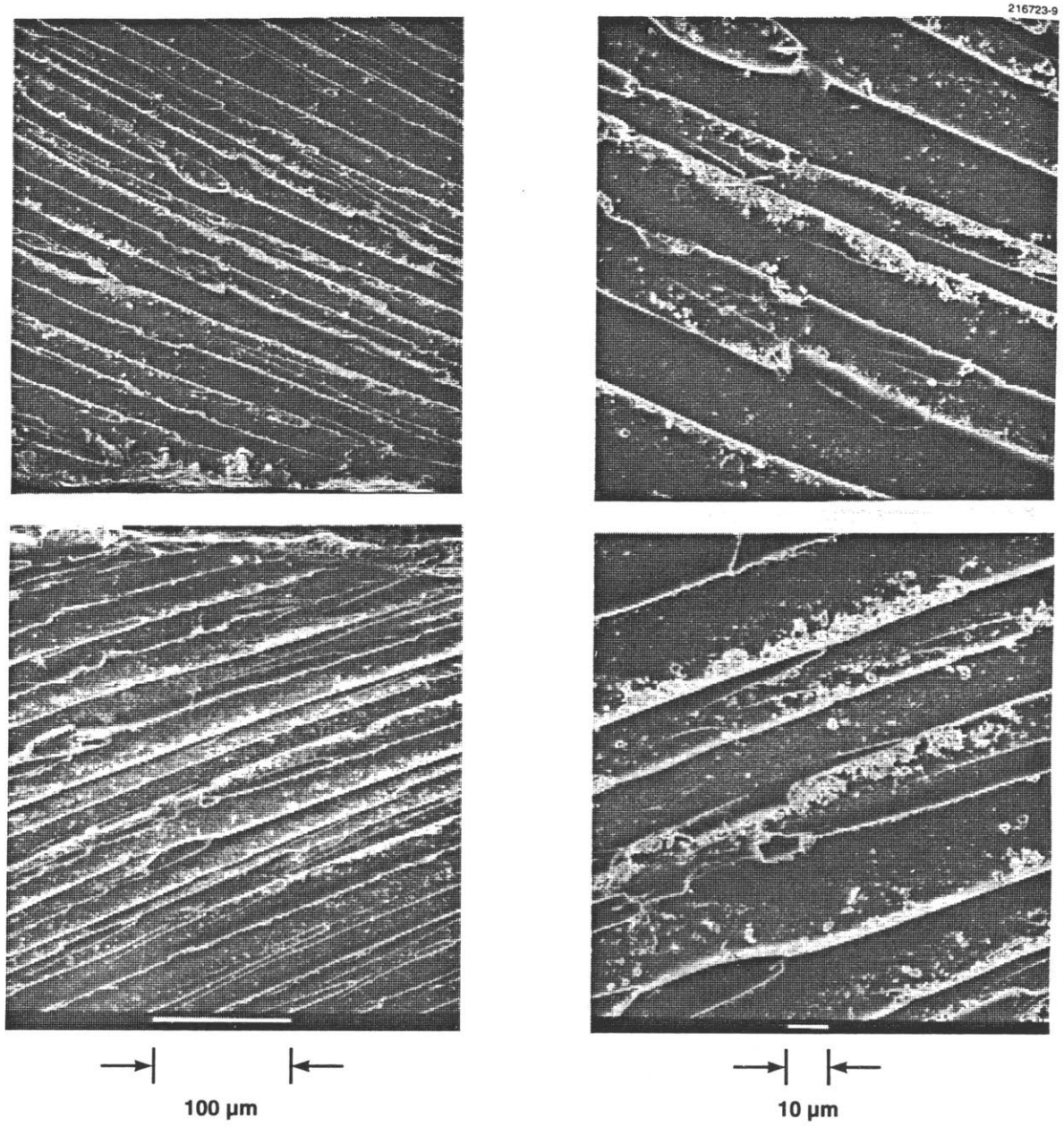

Figure A.32: Scanning electron micrographs of epoxy fracture surfaces. Photos from mating surfaces, showing lack of plastic deformation.

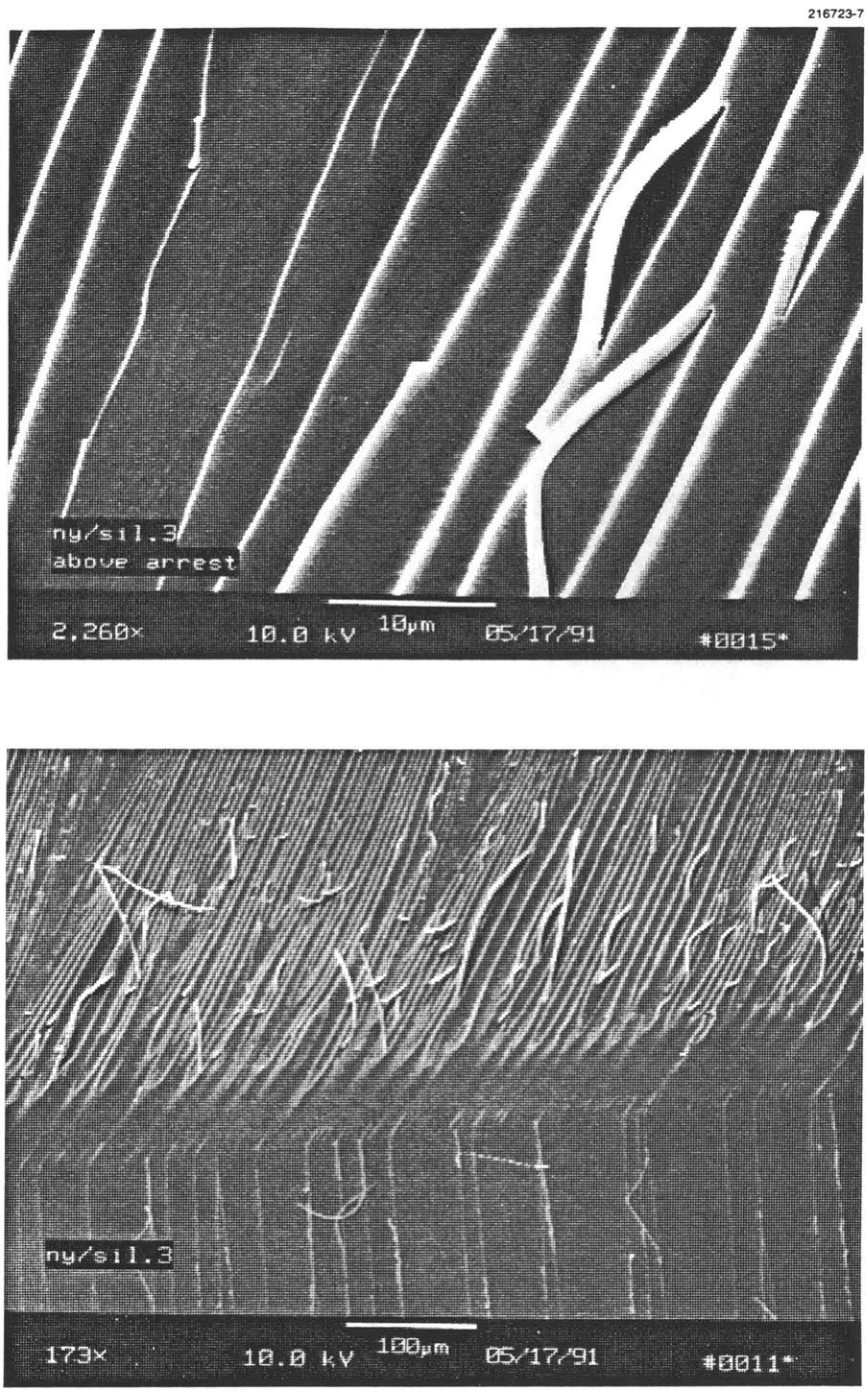

Figure A.33: Scanning electron micrographs of epoxy fracture surfaces. Upper photo shows sharply defined cleavage steps and whiskers. Lower photo shows arrest line to be ~50 μm in width, similar to the plastic zone size.

A.1.5.2 Constant-K specimens (TDCB)

Background The standard double cantilever beam specimen may be modified to make a specimen which produces a constant crack driving force (K, or G) by designing the specimen dimensions such that the change in compliance with crack length is constant. Such a specimen should cause a crack to propagate at constant load. Equation A.22 shows that the desired behavior can be achieved by either making $h^3 \propto a^2$ or $a/B = const.$ Though it is possible to fabricate specimens with the required changing width, they would consume a large volume of material. A much better choice is to modify the height of the specimen as a function of crack length.

The tapered double cantilever beam specimen was introduced and experimentally developed by Mostovoy *et al.* [74]. Their beam analysis included the effects of shear deflection, and resulted in the conclusion that a constant K specimen must be contoured such that

$$3\frac{a^2}{h^3} + \frac{1}{h} = m\,, \tag{A.29}$$

where m is a constant that determines the slenderness (height *vs.* length) of the specimen. Mostovoy *et al.* suggested that a large value of m (slender specimen) was appropriate for the testing of adhesives, with adherends bonded along the centerline of the specimen, but that the testing of monolithic materials required steeper angles (due to arm breakage). Using specimens shaped with m=4, they performed an experimental validation of the linear increase of compliance with crack length, and found that linearity was exhibited for crack lengths ranging from one to three inches. The dimensions of their TDCB, shown in Figure A.34, show that this length range comprises a significant portion of the length of the specimen.

The experimental work of Mostovoy *et al.* further demonstrated that the calculated values of m were slightly lower than the values m' which were actually measured. With aluminum specimens machined to m=4 and having side grooves such that the narrow section, B_n, was equal to $0.9B$, they determined that $m' \approx 5.5$. Using their

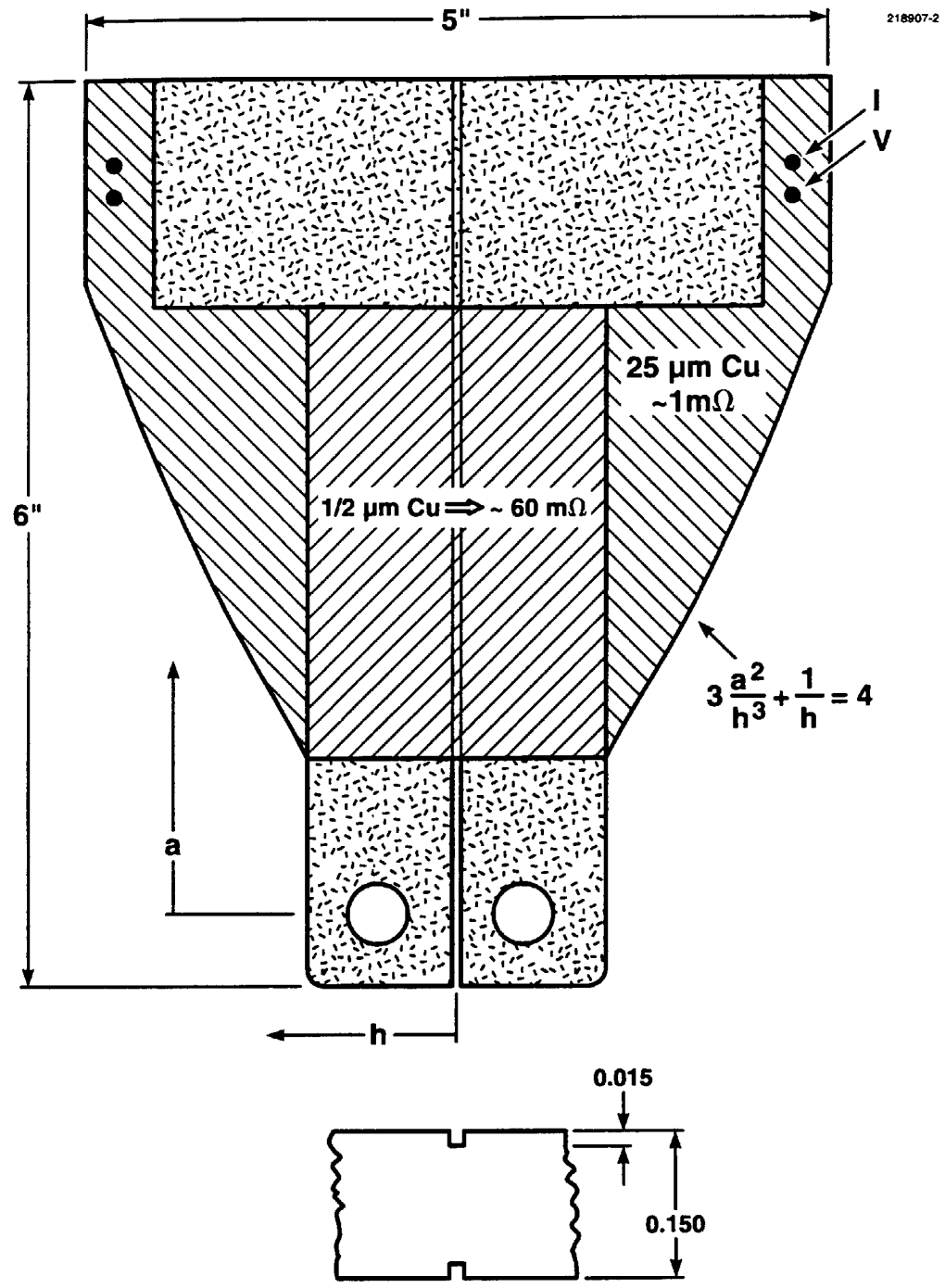

Figure A.34: Details of tapered double cantilever specimen (TDCB). Cross-hatched areas indicate portions which were plated with copper for crack propagation velocity measurements. Designed using English units after [74].

expression [74] for the energy release rate

$$G_{Ic} = \frac{4\,P_c^2}{E\,B B_n} m' \,, \tag{A.30}$$

a modulus-independent expression for the fracture toughness determined with the TDCB may be written as

$$K_{Ic} = \frac{2\,P_c}{(1-\nu^2)} \left(\frac{m'}{B_n B} \right)^{1/2} \,. \tag{A.31}$$

This equation indicates that the TDCB should produce crack extension at constant load in specimens with uniform toughness along the crack line.

Specimen Preparation Molds with the dimensions indicated in Figure A.34 were machined on a numerically-controlled milling machine (to produce the curved contour with m=4) from 6 mm-thick aluminum plates. The plates were drilled with through-holes so that they could be bolted together, each forming one side of two castings. Surfaces of these plates which would come in contact with epoxy were then fine-sanded. The molds were then coated with high-temperature films of teflon (*Durafilm*) so that they would not need to be repeatedly coated with spray-on release agents (which often tend to transfer contaminating particles into the mold contents).

Epoxy resins were mixed with curing agents, evacuated, cured and post-cured as described in the procedures for fabrication of the compression specimens. After de-molding the specimens, rough edges were lightly filed off, the wide edge of the specimens (from the tops of molds) were milled flat, and the loading pin holes were drilled. The initial notch-length of 25 mm and the side grooves were then cut with a 0.38 mm-thick carbide (for stiffness) slitting saw on a milling machine. Specimens were stored in a desiccator until just prior to testing, when the initial crack was sharpened with a razor.

Testing Procedures The TDCB specimens were tested with a commercial testing machine (Instron 1125) using a sensitive (222-N max.) load cell. The standard tensile procedure of using a universal joint to minimize moments was employed. Load and crosshead displacement data were digitally recorded in a manner similar to that in the compression experiments. Displacement rates of 5, 0.5 and 0.05 mm/min were utilized, with most data taken at the intermediate rate. The first phase of this testing took place at room temperature ($22 \pm 2\,^{\circ}$C), but later testing was performed at reduced temperatures using the temperature-controlled chamber.

Discussion of Data Typical load *vs.* displacement curves obtained at room temperature are reproduced in Figure A.35. It is readily apparent from these traces that the fracture processes in these TDCB specimens did not take place smoothly under constant load. Rather, each specimen displayed a large drop in load at each fracture initiation, with a correspondingly large jump in crack length. The V-40-cured specimens with the lowest T_g (72°C) allowed only one fracture event per specimen, since the crack either jumped beyond the limit of compliance linearity, or the specimen failed completely. Crack jumps in the V-40, T_g=80°C specimens were somewhat smaller in extent, so that these specimens often arrested once in the region of the TDCB that exhibits linear compliance. Here, determination of K_{Ic} from a "natural" sharp crack could be made. The most brittle specimens, cured with the Lewis Acid, generally displayed much smaller crack extensions at each initiation, so that three to four K_{Ic} values could be determined with each specimen.

In spite of the jerky nature of the fracture in these specimens at room temperature, several noteworthy points are to be made from the data, plotted in Figure A.36. First, despite the fact that the fracture was unstable, much less scatter in the data developed than did with the untapered DCB specimens. No trend in the critical extension loads was observed as a function of whether crack extensions occurred from natural cracks or starter cracks. Values of K_{Ic}, calculated using Equation A.31 and extension loads, show a slight trend of decreasing as displacement rate increases, and display a very strong trend of decreasing as the material T_g increases.

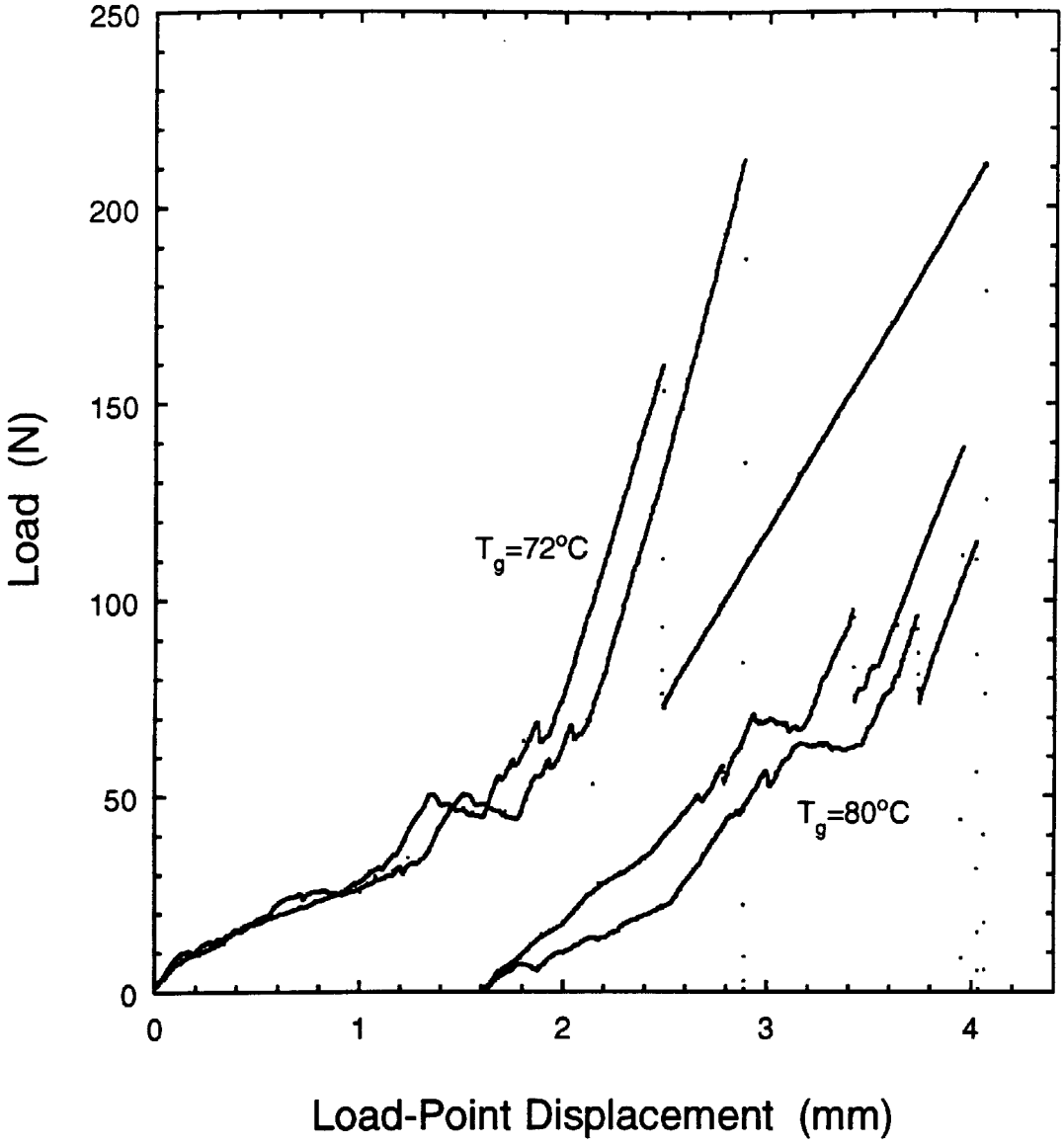

Figure A.35: Typical room-temperature load *vs.* displacement traces obtained with TDCB specimens cast from 815:V-40/3:1 epoxy with T_g's as indicated. Saw-tooth form is a result of the intrinsic, jerky fracture behavior of many epoxies at room temperature.

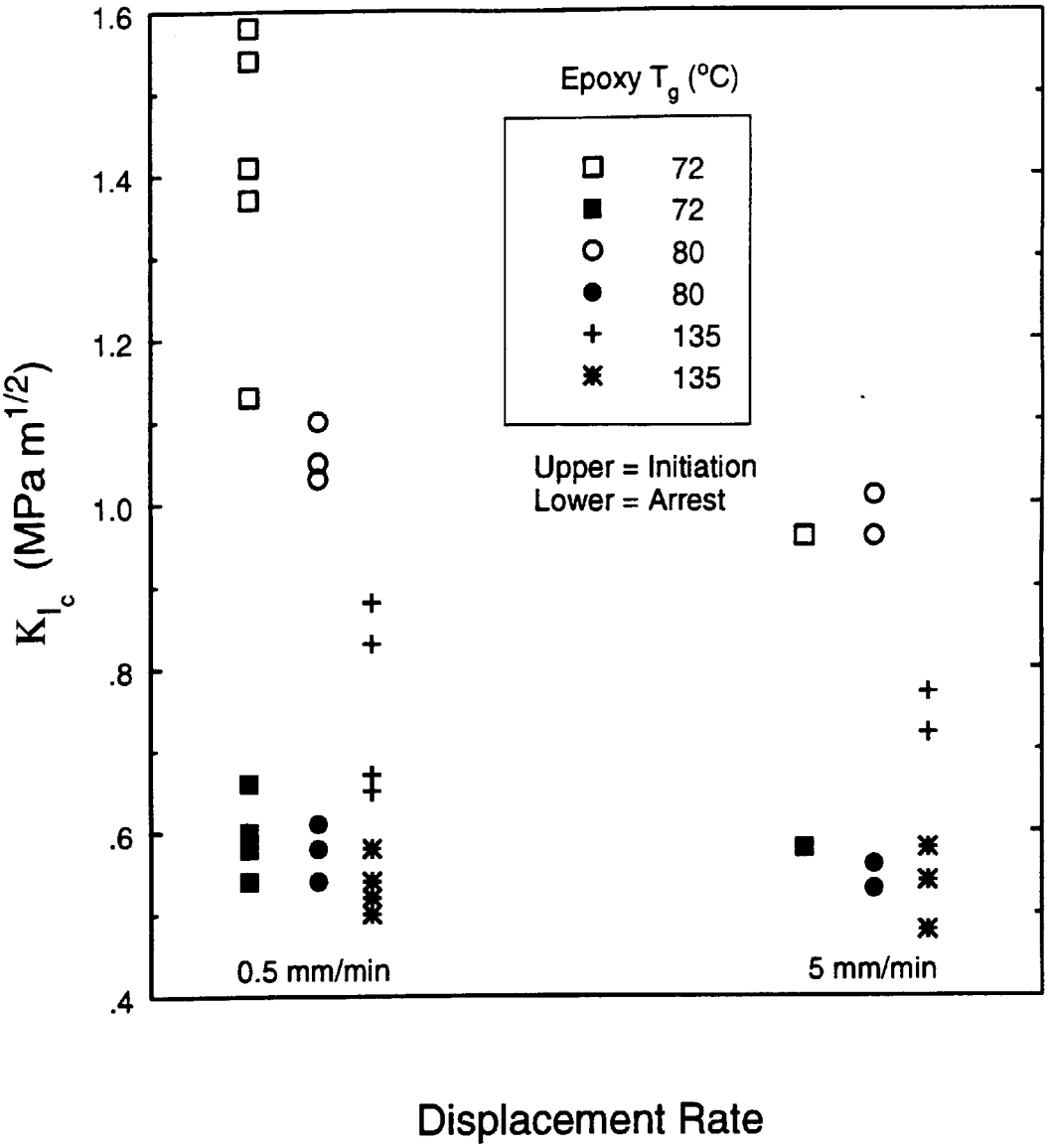

Figure A.36: Room-temperature fracture toughness (K_{Ic}) measured with TDCB specimens, for 815:V-40 and 815:BF_3MEA epoxy with T_g's as indicated. *Note: Magnitudes of data should be reduced by* $\sim 15\%$ *, per the compliance calibration of Figure A.43.*

Another feature to be observed in Figure A.36 is that the values of toughness calculated from the quasi-static equilibrium loads at the moment of fracture *arrest* are relatively constant. Additionally, it appears that the decreasing values of initiation toughness tend towards the arrest values of roughly K_{Ic}=0.5 MPa m$^{1/2}$. An obvious conclusion is that the process responsible for the increased initiation toughness is not operative during extension and crack arrest.

A further point noted here is that the trends exhibited by the initiation toughness parallel the trends observed in the hardening behavior of these epoxies. The epoxy with the greatest hardening (BF_3MEA-cured) has the lowest initiation toughness, and as the rate of hardening in the (V-40-cured) epoxies decreased, the initiation toughness correspondingly increased. Thus, the process of fracture initiation may be influenced by strain hardening.

It is clear that the higher toughnesses measured at crack initiation than at crack arrest were not a result of insufficiently sharpened starter cracks, as several of the higher values measured were from naturally sharp cracks. Therefore, the phenomenon which gives rise to the unstable, jerky crack growth must be intrinsic to the epoxy material under the given test conditions. Indeed, this type of fracture behavior has been observed extensively [5,46,75–79], and has been given the somewhat misleading name of "stick-slip" behavior.

The higher toughness associated with crack initiation certainly is a consequence of processes which do not have sufficient time to develop during crack extension and arrest. Kinloch and Williams [11, 80] have developed a model which attribute the initiation behavior to plastic yielding (blunting) at the crack tip while it is stationary. As the blunting progresses, the crack tip radius is enlarged so that higher levels of loading are required to generate the critical stress intensity necessary for crack extension. The model incorporates two critical parameters which characterize material toughness, as opposed the single criterion of either K_{Ic} or G_{Ic}: it is envisaged that a critical stress, σ_c, is developed in the material at a critical distance, r_c, in front of the crack tip. Using values of $\sigma_c \sim 380$ MPa and $r_c \sim 2\,\mu$m (proportional to the

calculated crack opening displacement, $cod = K_{Ic}^2/E\sigma_y$), their model accounts for some measured fracture initiation toughness values quite well [5, 80].

An alternate explanation for the unstable crack growth observed in epoxies is based upon thermal effects [81]. Due to the low thermal conductivity of epoxy, fracture processes occur under essentially adiabatic conditions which can lead to a reduction of the yield stress due to energy dissipation. Using generic polymer values for specific heat, density and thermal conductivity, Williams [82] has analyzed the temperature rise at a moving crack tip in polymers. His model predicts that, as cracks velocities approach (and exceed) $\sim$ 100 m/s, thermal reduction of the yield stress will result in increases of toughness on the order of 100% . This analysis explains quite well the observed increases in toughness at higher velocities in many polymers. Velocity-induced thermal effects have little to do with the stick-slip behavior in epoxies, as is suggested in [81], since it is a peculiarity of the initiation of cracks from stationary positions.

The temperature at which epoxy fracture occurs is known to influence whether it occurs in a continuous, stable manner or occurs in the jerky fashion discussed above. Kinloch and Williams [80] pointed out that a transition from the jerky to a continuous behavior is seen to develop as the yield stress of the material increases above about 100 MPa. The observation seems to be valid for material-to-material differences as well as for increasing σ_y in a given material as a result of increasing loading rate or decreasing test temperature. Indeed, extensive testing of an amine-cured DGEBA epoxy over three decades of loading rate with constant-K (double-torsion) specimens, at test temperatures from ambient to $-200°$C, demonstrated conclusively that such behavior exists [83]. At all loading rates, and for all formulations of epoxy specimens, any unstable "stick-slip" behavior at room temperature began to attenuate at temperatures around $-20°$C and disappeared entirely around $-50°$C.

Because stable crack growth was necessary for the crack-trapping experiments of the present work, fracture toughness testing was pursued at reduced temperatures to seek, and characterize, stable fracture behavior of the V-40-cured epoxy material.

(Which, it is reminded here, allows room-temperature curing so that model specimens containing inclusions can be fabricated). Testing was carried out with the TDCB specimens at reduced temperatures in the temperature-controlled chamber described in the compression testing procedures. Typical load *vs.* displacement curves obtained from these tests are shown in Figure A.37.

The loading traces in this figure illustrate clearly the fracture-mode transition which occurs. The room-temperature unstable fracture of 815:V-40/3:1, $T_g = 80°C$ is seen to steadily fade as the temperature of the test specimen decreases. Following the fracture of the Chevron starter notch and attainment of the full specimen width, the fracture process at $-60°C$ is continuous and progresses at nearly constant load. Computed critical stress intensity factors are plotted in Figure A.38, in which it may be seen that the initiation values are lowered to the arrest values by the reduction of temperature. The arrest toughness seems to be temperature independent, at a level of $\sim 0.5\,\mathrm{MPa\,m^{1/2}}$. At -60°C, this translates into an energy release rate of $\sim 60\,\mathrm{J/m^2}$; the plane strain plastic zone size, $r_p \approx (K_{Ic}/\sigma_y)^2/6\pi$, is calculated to be *less than one* μm. These parameters indicate that, at $-60°C$, this epoxy is a truly brittle material.

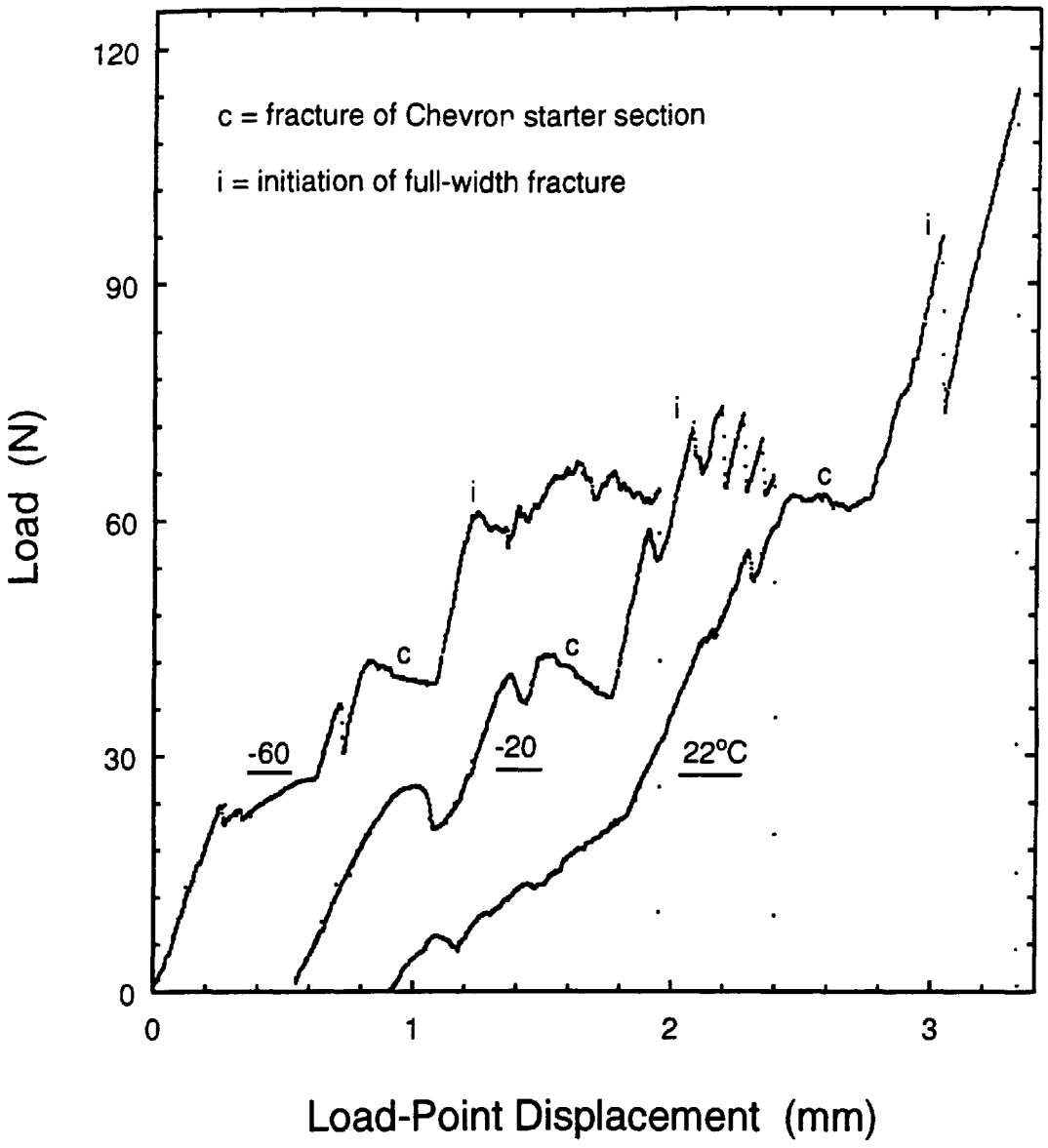

Figure A.37: Typical load *vs.* displacement traces obtained with TDCB specimens cast from 815:V-40/3:1, T_g=80°C epoxy as a function of temperature, showing transition from jerky fracture behavior at ambient temperature to continuous fracture at low temperature.

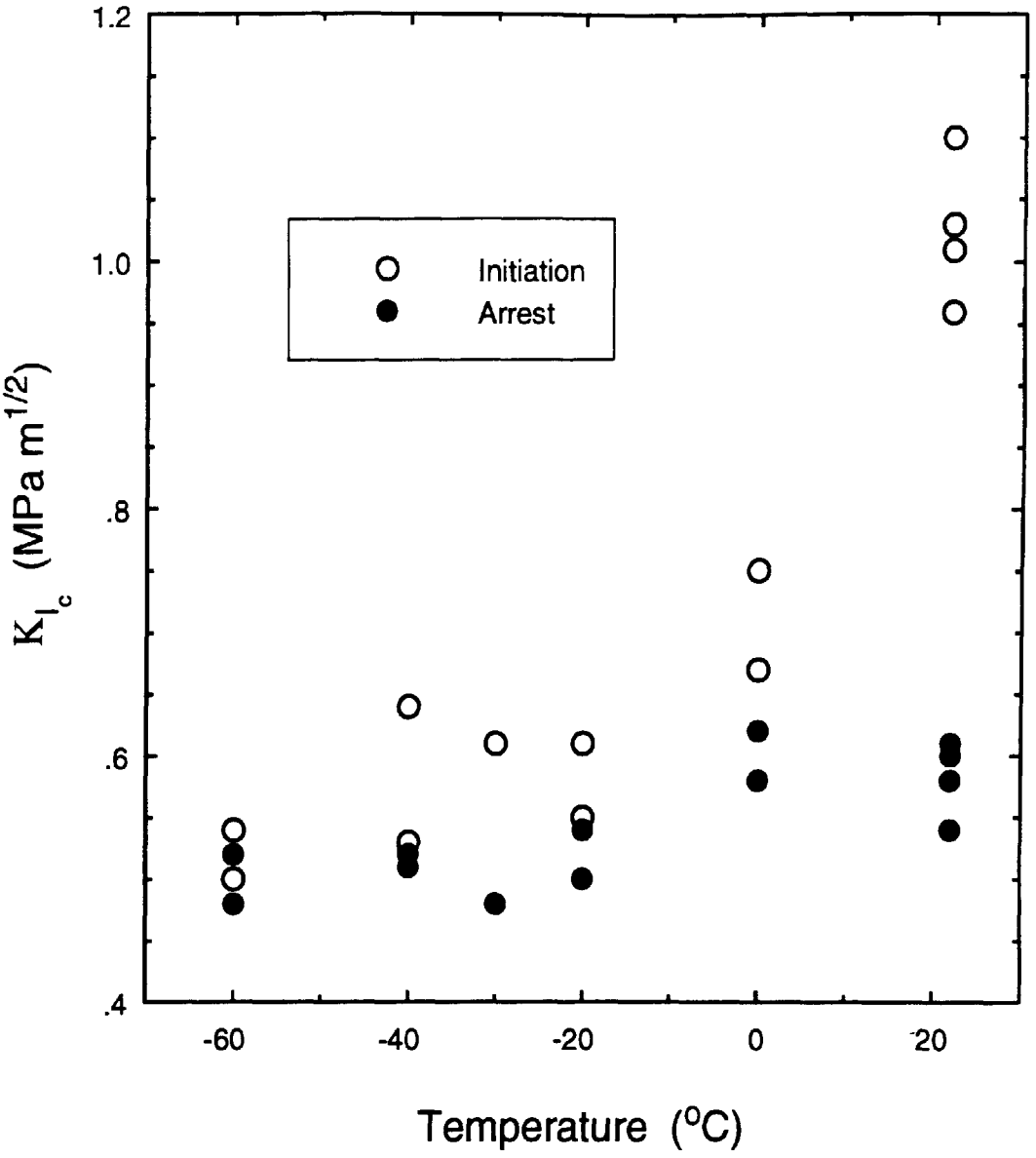

Figure A.38: Fracture toughness (K_{Ic}) measured with TDCB specimens, for 815:V-40/3:1, T_g=80°C epoxy as a function of test temperature. *Note: Magnitudes of data should be reduced by* $\sim 15\%$ *, per the compliance calibration of Figure A.43.*

A.1.5.3 Crack propagation velocity measurements

Fracture in epoxies has been shown to take place in quite different manners, dependent upon whether or not the process is unstable or continuous. Associated with these modes are two very different ranges of crack propagation velocity. In the stable, continuous regime, crack velocities on the order of 10^{-4} to 10^{-2} m/s are seen to occur. The unstable, dynamic behavior produces velocities too rapid to observe with the naked eye, but the limiting velocity is approximately $0.38(E/\rho)^{1/2} \sim 500$ m/s [70]. Because such a wide range of behavior exists, it seems possible that quantifying the velocities as a function of driving force, K_{Ic}, may shed some light upon the different conditions that lead to the very different modes of crack growth. Additionally, it seemed prudent to develop a means of measuring crack velocities for the current research, in order to have the ability to assess the effect of crack/particle interactions upon crack velocities.

Many methods of crack velocity measurement have been developed, ranging from sophisticated high-speed cameras used to study extremely rapid crack velocities [84], to simple load-relaxation techniques which are sufficient for measuring slow crack growth [85]. It is not the purpose here to review all the available methods[8], but to relate the methods employed in this work and the results obtained. First, the essence of what has previously been observed regarding the velocity of crack growth in epoxies shall be stated.

When epoxies fracture in a stable manner, either due to reduced temperature or to the nature of the particular cured-solid chemistry, the resulting crack tip velocity can be extremely slow but varies quite strongly with stress intensity. Using load-relaxation of double-torsion test specimens, one study of "a common DGEBA" epoxy found that increasing K_{Ic} from 0.65 to 0.75 MPa m$^{1/2}$ caused a rise in crack velocity from 10^{-5} to 10^{-3} m/s [85]. A similar study of both neat and silica-filled epoxy found that $\log v \propto K_{Ic}$, such that a rise in K_{Ic} from 1.6 to 2.2 MPa m$^{1/2}$ produced increases in velocity from 10^{-9} to 10^{-2} m/s [87].

[8] A brief review of the methods is provided in Reference [86].

When epoxies fracture in an unstable manner, much greater crack tip velocities are generated. Using crack-tip positions recorded with a high-speed multiple-spark camera to determine velocities, and the methods of dynamic photoelasticity to characterize the instantaneous stress intensity, Kobayashi and Dally measured a range of crack velocities in two classes of epoxies: one which (at room temperature) exhibited the brittle, jerky behavior and one in which the fracture process was brittle but continuously stable [84]. Their results were similar for both materials, and indicate that a constant stress intensity caused crack velocities ranging from zero to 200 m/s. (The epoxy which fractured in a continuous manner had $K_{Ic} \approx 1\,\mathrm{MPa\,m^{1/2}}$; the epoxy exhibiting unstable fracture had $K_{Ic} \approx 0.5\,\mathrm{MPa\,m^{1/2}}$.) Velocities in excess of 200 m/s were produced by nonlinearly increasing increments of stress intensity. Velocities of over 400 m/s were created by a doubling of the initial stress intensity, and resulted in the crack forming branches (bifurcating). Other researchers have reported [88] experimental results "with no clear relationship being apparent between K_{Ici} and velocity." Their data, obtained using the D.C. potential technique and double torsion specimens, created a "shotgun plot" of K_{Ic} *versus* velocity but was reconciled by a conversion to stored elastic energy *versus* velocity. A linear rise in crack velocity, from 80 to 340 m/s, resulted from stored energies at fracture initiation ranging from .02 to .08 J. Using single edge-notched specimens, the same authors found a similar relationship, except that a nonlinear increase in stored energy was necessary to cause increases in velocity beyond 300 m/s [89].

In consideration of the above information, it seemed clear that crack propagation velocities in the epoxies studied here might be extremely fast, difficult to control and possibly equally difficult to measure with any reasonable resolution. Nonetheless, two standard methods were attempted in this work. The first method utilizes ripple markings on the fracture surface, created during fracture by an ultrasonic transducer, to provide a permanent record of the crack velocity (which was proportional to the spacing of the ripple lines). The second method utilizes a conductive coating (grid, or gauge) which is severed by the advancing crack, so that measurement of an electric potential rise across the crack plane gives an instantaneous indication of the crack position. The use of these two methods shall now be described.

Ultrasonic Fractography Brittle fracture surfaces sometimes feature faint, curved lines transverse to the propagation direction, which result from interactions between the advancing crack and elastic stress waves that may reflect from edges, inclusions, voids or other imperfections. According to Döll [90], these lines were first described by H. Wallner in 1938 and are therefore named after him. Analysis of naturally-forming Wallner lines for the determination of crack velocities was reported by Smekal in 1950 [91]. The use of artificially-induced Wallner lines was developed by Kerkhof in the early 1950's and was reported by him in 1969 in a succinct paper regarding the crack velocities, v, in an inorganic glass [92].

Ultrasonic fractography utilizes the fact that materials separate in tensile mode, causing cracks in homogeneous materials to propagate in a direction normal to the maximum tensile stress. If a fracture specimen has a device attached to it which superimposes stress waves at a frequency, f, on top of the usual loading, then disturbances will (in theory) be created upon the fracture surface at regular spacings. Example configurations of the technique are schematically illustrated in Figure A.39.

In the ultrasonic fractography attempted here, piezoelectric transducers (PZTs) were affixed to the TDCB specimens in the configuration of Figure A.39 (b), so that a small component of shear was added to the stress experienced by the crack tip. The PZTs were single crystals fashioned into thin (1-mm) disks of 25-mm nominal diameter, as commonly used for security system sensors (Radio Shack). Mounting of the crystals was accomplished with a cyanoacrylate adhesive, which bonds quickly, breaks off easily, and avoids damping which would be caused by, *e.g.* tapes.

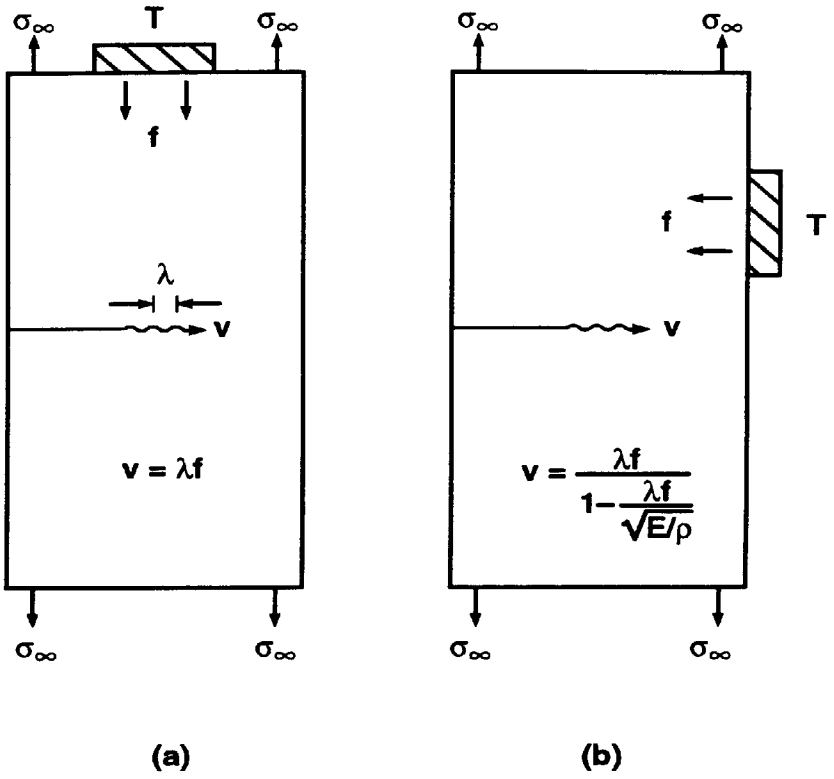

Figure A.39: Illustration of fracture surface modulation by superimposed (a) normal stress waves and (b) shear stresses. The transducer, T, sends stress waves at frequency, f, which interact with the crack traveling at velocity, v, producing periodic surface ripples with spacing of λ.

Excitation of the PZTs was in the form of square pulses from an HP-214A, 250-W pulse generator. To obtain the maximum amplitude of stress waves in the specimen, the frequency of the generator was varied while observing on an oscilloscope the signal received at the opposite end of the specimen through another crystal acting as a sensor. In cases where just one transducer was used, the driving frequency was usually $\sim$ 14.3 kHz. In other cases, two transducers (and a second generator) were used: one driven at $\sim$ 71.4 kHz with moderate amplitude and one at $\sim$ 7.2 kHz with maximum amplitude, so that a major marking might be laid down on the fracture surface at every tenth minor marking. Testing of the specimens was performed at room temperature using crosshead displacement rates of 0.5 and 5 mm/min.

The results obtained with this method were disappointing. The primary problem encountered was that the fracture surfaces created at the high velocities produced have a slightly frosted appearance, so that the very faint timing marks are not visible. At room temperature, all three formulations of epoxy tested fracture in the brittle, unstable manner. As a result, very high velocities are generated immediately after fracture initiation, creating a smooth but non-reflective surface. As the crack driving force diminishes, the velocity slows down and the surfaces generated become highly reflective just prior to arrest. Only in this region were satisfactory surface markings created by the transducers. Examples of such features may be seen in the two photographs reproduced in Figures A.40 and A.41. Using the mm-scale and the indicated transducer frequencies, it is easily determined that the crack velocities in the decelerating region were from about 70 m/s down to a few m/s just prior to crack arrest. In addition to the lack of reflective surfaces, an additional problem with the ultrasonic method surely is the damping of the superimposed waves by the viscoelastic nature of the material. Indeed, Döll states that, for these very reasons, the application of ultrasonic fractography to polymers is very limited [90]. Perhaps this method would be well suited for use with these materials at reduced temperatures.

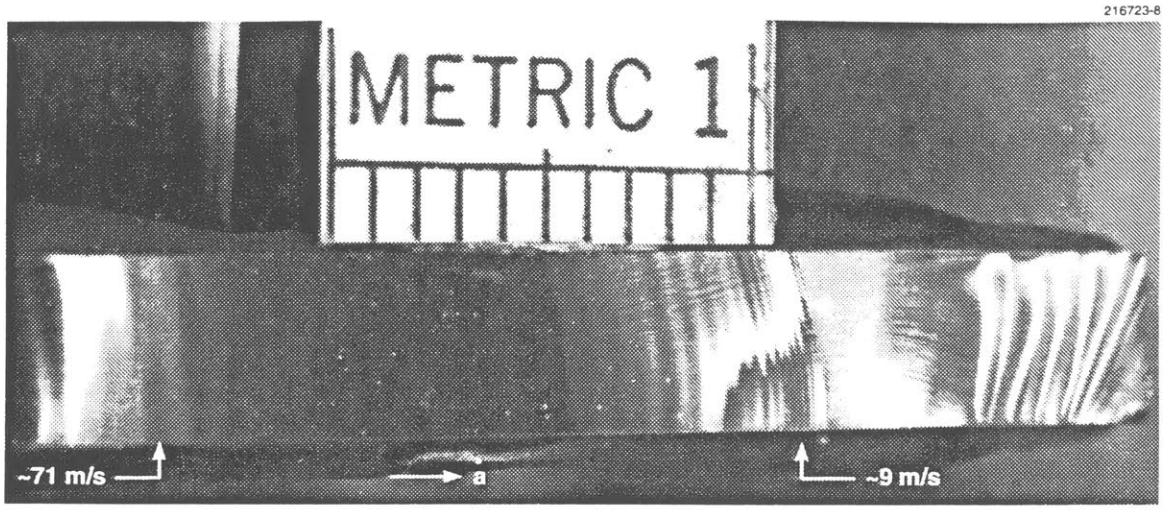

Figure A.40: Surface from TDCB specimen of 815:V-40/3:1, T_g = 72°C epoxy fractured at room temperature. Modulations from peizoelectric transducer pulsing at 71.4 MHz indicate the crack velocities shown.

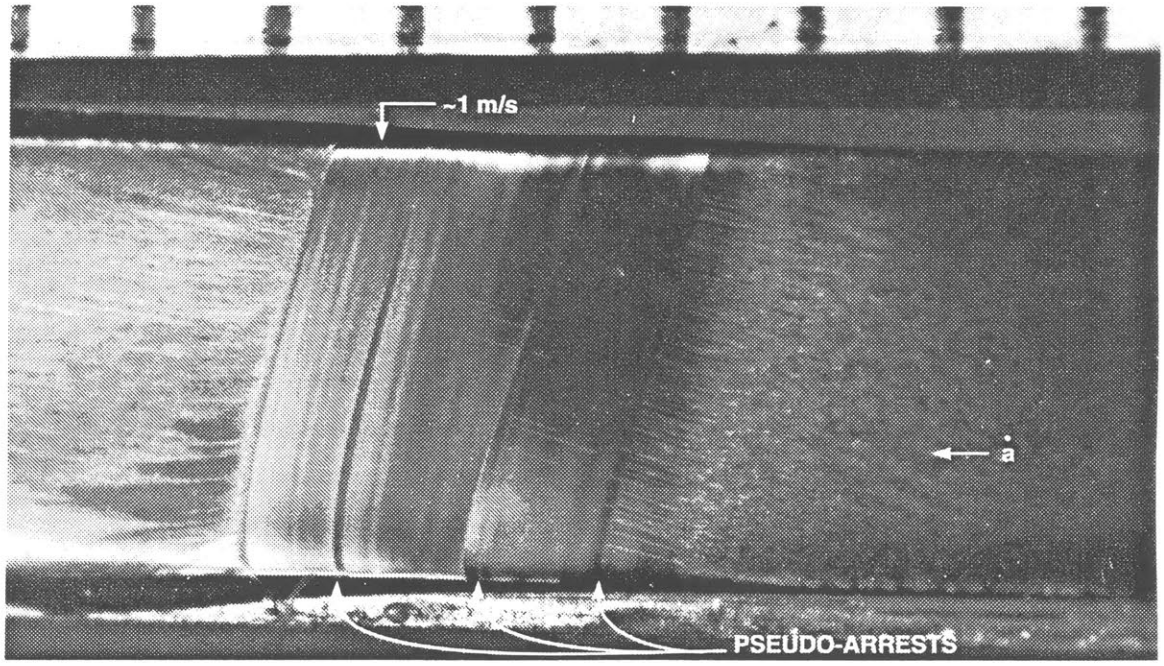

Figure A.41: Surface from TDCB specimen of 815:BF_3MEA, T_g = 135°C epoxy fractured at room temperature. Modulations from piezoelectric transducer pulsing at 20 MHz indicate the crack velocity was about 1m/s as it hesitated three times before finally arresting.

Electric Potential Method One method of monitoring crack growth in conductive materials is to pass a source of constant electric current through the specimen and measure the changing potential across the crack surface. By comparison to calibration data or finite element solutions of the electric field, the crack position can be determined with reasonable accuracy [93]. This same technique can be applied to non-conductive materials by coating the surface of the region to be cracked with a conductive film, or "gauge" [94].

Through application of the conductive coating, crack velocities have been measured in many polymers. Graphite velocity gauges have been used in: Charpy impact testing of PC & PMMA [95] and polyamide & filled epoxy [86]; single edge-notched and three-point bend specimens of epoxy [89]; and double torsion specimens of neat and filled epoxy [88]. Most recently, the use of the graphite gauge has been applied to the study of crack velocities in bimaterial specimens: using specimens fabricated by allowing silicon carbide powder to settle in a low-viscosity epoxy, the deceleration and arrest or deflection of cracks encountering the stiffer medium was recorded [96]. In the works just quoted, the maximum crack velocity recorded in epoxies was usually about 375 m/s.

To obtain velocity measurements here with the electric potential method, the TDCB specimens were modified by the coatings of copper indicated in Figure A.34. The rectangular region bounding the crack plane was coated with a layer of copper approximately 0.5 μm in thickness by an electroless solution technique.[9] Such a thin layer provided the high resistance required to obtain measurements with good resolution, and further, added little to the stiffness of the specimen. Low resistance "bus-bars" were created by electro-plating films of thicker copper ($\sim 25\,\mu$m) on the edges of the specimens as shown. The total resistance of the copper circuit is the sum of the two bus-bar resistances plus the resistance of the central region, which will increase as the crack travels through it. A first order analysis gives $R = R_{BB} + \rho b/tc$, where c is the ligament length and b is the constant width, ρ is the resistivity and t

[9] Vapor deposition methods were not used, since they would not coat the vertical sides of the crack-guiding grooves. The fabrication of these specimens required a great deal of surface preparation, masking and re-masking.

is the thickness of the region bounding the crack. Because we require more accuracy than can be obtained with this expression, a calibration procedure was performed to experimentally determine the variation of R with crack length in these specimens.

To perform the resistance calibration, the growth of a crack through the copper plating was simulated by cutting precisely with a razor increments along the crack-guiding side grooves of a typical TDCB. A constant current through the copper was maintained, while the increasing voltage across the specimen was measured and recorded. Data acquired in this manner are plotted in Figure A.42.

In the upper figure are shown all the data points, along with a curve which has the same form as $R = R_o + const/lig$. Clearly the form of this equation can be fit reasonably well to the data. However, the data at the extremes of ligament length (full ligament, or fully cracked) have the potential to provide unreliable results [86], so the attempt to determine a curve fit to the data shall not include these extremes. Shown in the lower figure are the data over the range of crack lengths that are of most concern. It was found that a simple equation of the form $lig = const/R^m$ fit the calibration data extremely well, as shown by the two curves plotted in the figure. Though this calibration data looks quite smooth and accurate, it can not be used on an absolute basis to convert measured resistance to crack length in all specimens, because there was some specimen-to-specimen variation in initial resistance (presumably due to small differences in thickness of the very thin central copper film). Consequently, the procedure adopted for converting measured resistance to crack length was to use the *form* of the curves that match the calibration data, but modify the constant and exponent in the equation for each specimen so that measured resistances at stationary (and known) crack positions yield the measured crack lengths. This procedure incorporates improved accuracy by defining the resistance/length conversion over the subregions of ligament (*i.e.* individual crack-jump events).

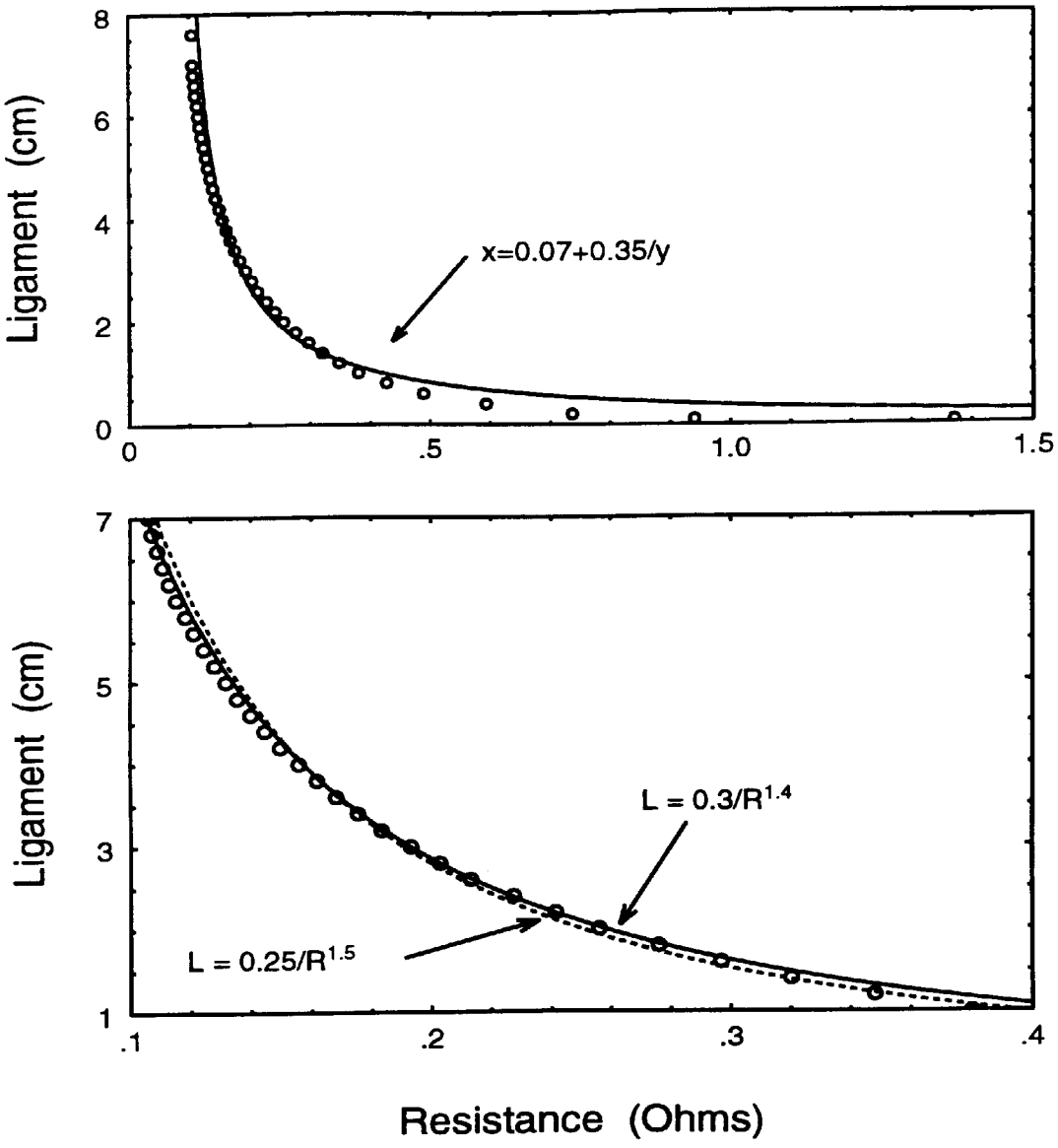

Figure A.42: Calibration of copper-plated TDCB for determination of crack velocities. Semi-infinite plate would display $R = R_o + const/Lig$, plotted in upper graph; specimen-specific curves of form shown in lower graph were used to convert oscilloscope voltage data to crack tip positions.

The concern may be raised that the added stiffness due to the copper plating may affect dC/da and therefore alter the magnitudes of K_{Ic} determined with these specimens. To address this issue, the compliance of both a plated and a plain TDCB specimen were measured after each was slotted to increasing lengths with a thin slitting saw on a milling machine. The measurements so obtained are plotted in Figure A.43, from which two principal conclusions may be reached.

First, the expected decrease in specimen compliance due to the added copper becomes greater with increasing crack length. Thus, there exists a difference in slope, dC/da, due to the copper plating. Though the difference appears slight, its effect upon the calculation of G_{Ic} needs to be determined. By comparing the expression for energy release rate in the TDCB (Equation A.30) with the generic expression, $G = (P^2/2B)dC/da$, we see that the experimentally-determined value m' may be written as

$$m' = \left(\frac{B_n E}{8}\right) \frac{dC}{da} . \qquad \text{(A.32)}$$

Working in English units because the TDCB used here was patterned after the specimen used by Mostovoy *et al.* [74], we find from the linear region (a=1 to 3 in) of Figure A.43 that dC/da=0.775 and $0.732\times10^{-3}\,\text{lb}^{-1}$ for the plain and copper-plated specimens, respectively. Using appropriate values of B_n=0.12 in and E=350 kpsi, we compute that, for the plain TDCB, m'=4.069 (in^{-1}) and for the copper-plated TDCB, $m' = 3.843$. These values indicate that very little effect upon calculation of G_{Ic} or K_{Ic} is caused by the presence of the copper; if an effective E were invoked to account for the higher stiffness of the copper, then the two values of m' might be even closer.

The most important information obtained from Figure A.43 is that the values of m' exhibited by the epoxy TDCB's here are significantly lower than the $m' \approx 5.5$ reported for the aluminum TDCB's which were contoured to exactly the same dimensions with a calculated m=4. An explanation for this difference may be found in the percent of specimen thickness which is in a state of plane stress. The size of the plane stress plastic zone in the epoxies used here is about 30 μm, so less than 2% of the specimen thickness is in plane stress. On the other hand, the plastic zone size in Mostovoy

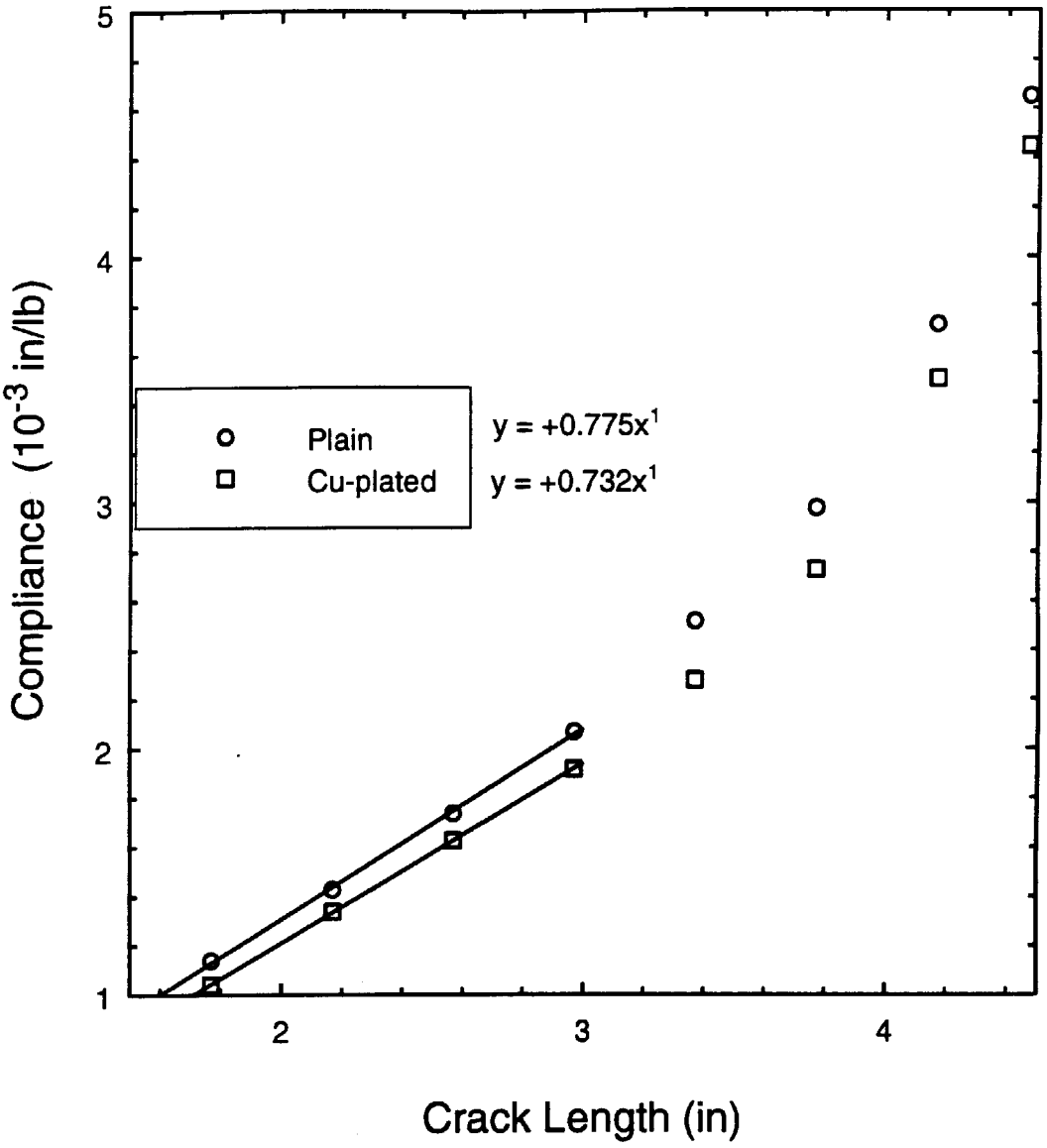

Figure A.43: Compliance calibration measurement of TDCB specimens, both plain and copper-plated. English units used to demonstrate comparison of measured m' to calculated $m = 4\,\text{in}^{-1}$, from Ref. [74].

et al.'s aluminum was slightly less than 1 mm, so their specimens had about 12% of the thickness experiencing plane stress. In addition, aluminum is much tougher than epoxy, so the load/thickness applied to those specimens was about fifty times higher [74], causing greater deformations throughout the specimens than occurs with the epoxy TDCB's. Therefore, the higher values of m' represent a departure of those specimens from pure linear elastic behavior (with small scale yielding at the crack tip). The close agreement of the experimental values of m' determined for the epoxy TDCB's with the calculated value of m=4 is an indication of their brittle, elastic behavior. The final conclusion here is that the values of K_{Ic} determined earlier (plotted in Figures A.36 and A.38) should be reduced by $(4/5.5)^{1/2} \sim 85\%$.

The experimental procedure for the determination of crack velocities with the electric potential method relies upon the use of a sophisticated data acquisition and recording instrument. A high-speed A/D converter and computer could be used, but to limit the quantity and improve the resolution of data accumulated an oscilloscope was used here. A digital, four channel (HP-4094) memory 'scope was utilized because of its versatile triggering capability; the sampling rate used was 2 MHz. One channel monitored the current applied to the copper-plated TDCB's, one channel recorded the transient voltage rise which accompanied crack extensions, and one channel was used to trigger from an extremely sensitive acoustic emission sensor affixed to the specimen. This method of triggering was found to be much more sensitive and reliable than triggering from a voltage-rise threshold.

A necessary condition for the electric potential method is that a constant current source be applied to the conductive path across the crack plane. Because the resistance changes rapidly during crack extension, common power supplies cannot compensate quickly enough to maintain constant current. An example of this is shown in the top photograph of Figure A.44, in which it can be seen that the current dropped off sharply during the fracture event. Simple modification to the power supply (Kepco # JQE 0–15v), per the operator's manual, produced the constant current condition required. This is illustrated in the bottom photograph of Figure A.44.

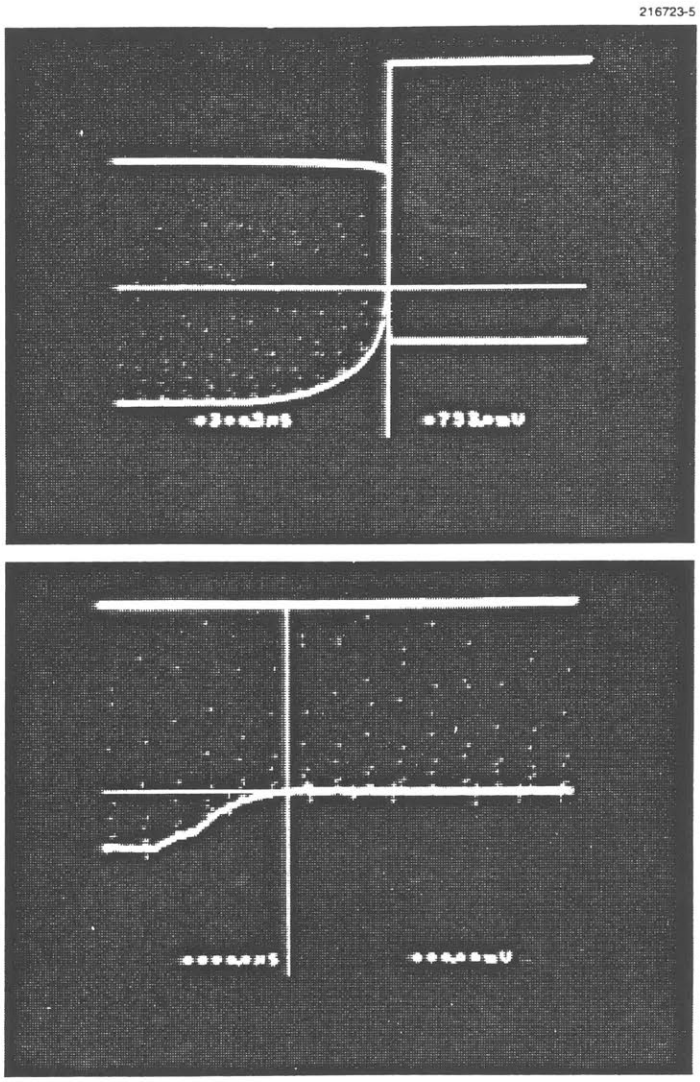

Figure A.44: Oscilloscope traces obtained in electric potential measurement of crack velocity; in each photograph the upper trace is current, with I_0 = 100 mA, and the lower trace is voltage, with V_0 ~10 mV. Upper event shows result of not using a constant current source. Power supply was reconfigured to maintain constant current in spite of rapid resistance change, demonstrated in the lower photograph. Periodic spikes are induced voltages from electric pulses driving the PZT for surface modulation.

The concern may arise that the power dissipated through the copper may increase the temperature of the epoxy sufficiently high that its fracture behavior may be altered. To minimize this possibility, the level of current applied was fixed at 0.1 Amp. Simple calculations show that a steady-state temperature rise of less than 0.05°C is sufficient to convect away the dissipated power.

To eliminate the effect of any slight changes in current or spurious voltage signals, the resistance of the electrical path across the crack plane was determined by dividing the recorded voltage by the actual current recorded. (Instead of dividing by a constant, assumed current.) A typical example of data reduced in this manner is illustrated in Figure A.45 for two fracture events in a 815:V-40/3:1, $T_g = 72°C$ specimen. By consideration of the duration of the voltage transients, and knowing the length of the crack extensions (from arrest lines on the surfaces), average velocities of $\sim$150 and $\sim$210 m/s are determined to have transpired during the crack propagations.

Crack tip positions as a function of time are determined by transforming the resistance data, as shown in Figure A.45, through use of the calibration curves, whose derivation was previously described. Resultant crack tip histories are shown in Figures A.46 and A.47 for specimens of 815:V-40/3:1, $T_g = 72°C$ epoxy. In each fracture event, the crack accelerated rapidly to its peak velocity and then travelled at a relatively constant rate until it approached its arrest position. The peak velocities determined from each of these traces was only about 10% greater than the averages that had been computed from $\Delta a/\Delta t$; this indicates that the cracks do indeed propagate at nearly constant velocity over most of their length.

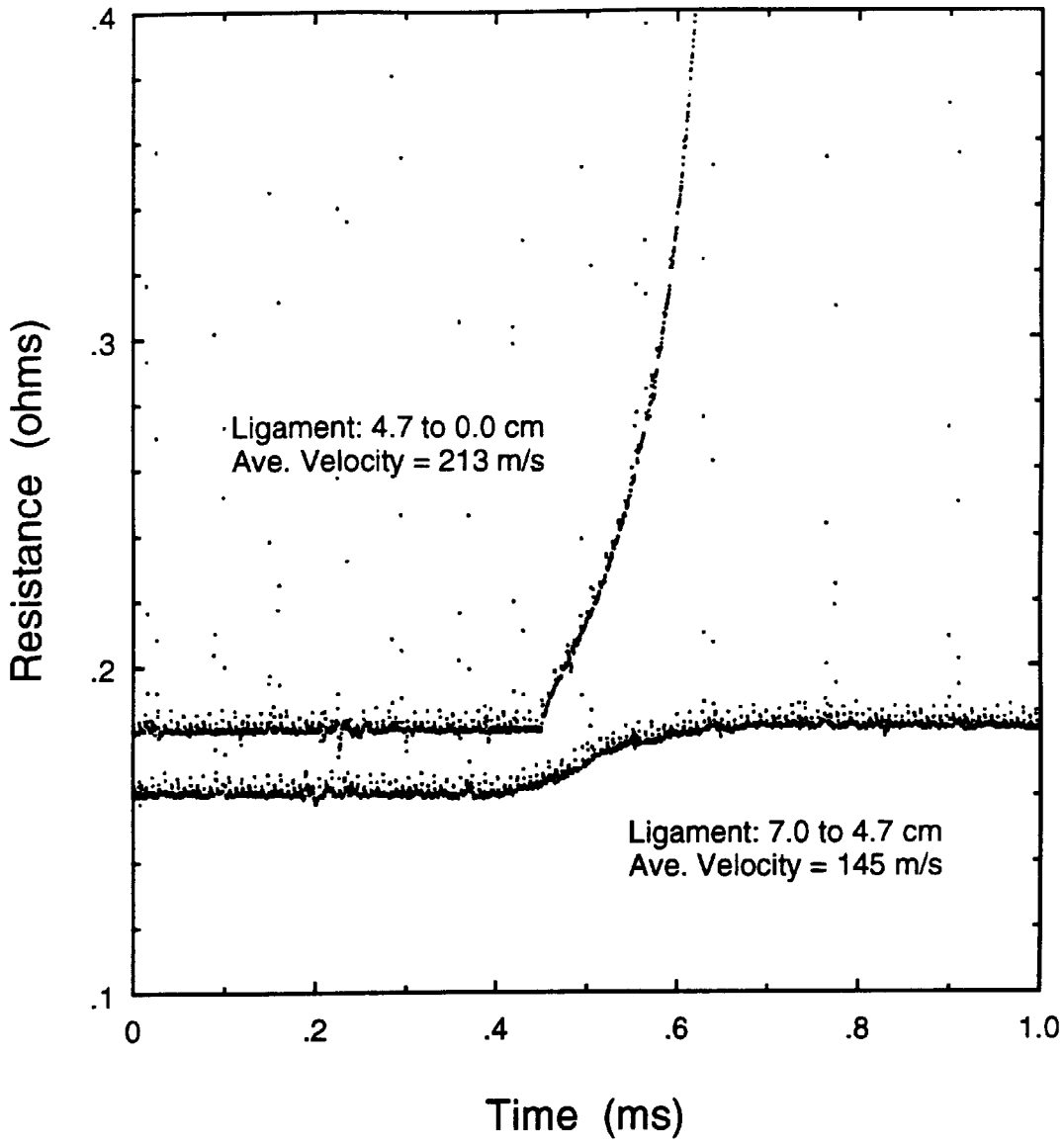

Figure A.45: Oscilloscope records of fracture events, converted to resistance *vs.* time by dividing the voltage trace by the current trace. Two sequential events shown, for which the average velocities are determined by $\Delta a/\Delta t$. Spikes induced from pulse generator are seen at intervals of 14 and 140μs.

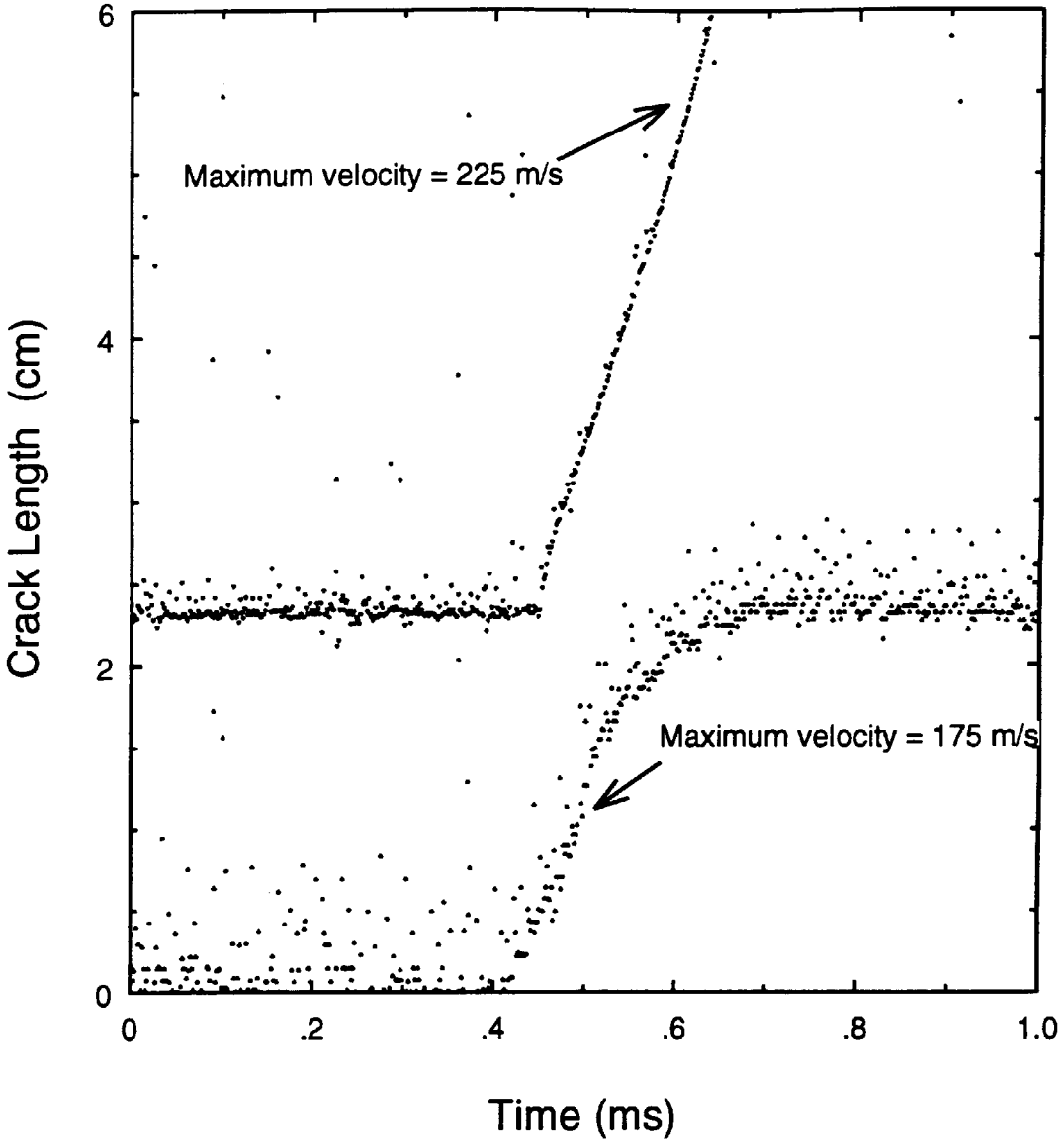

Figure A.46: Data of Figure A.45, converted to crack length *vs.* time by using calibration functions. Cracks reached a peak, relatively constant velocity after a brief acceleration period. Specimen was 815:V-40/3:1, $T_g = 72°C$.

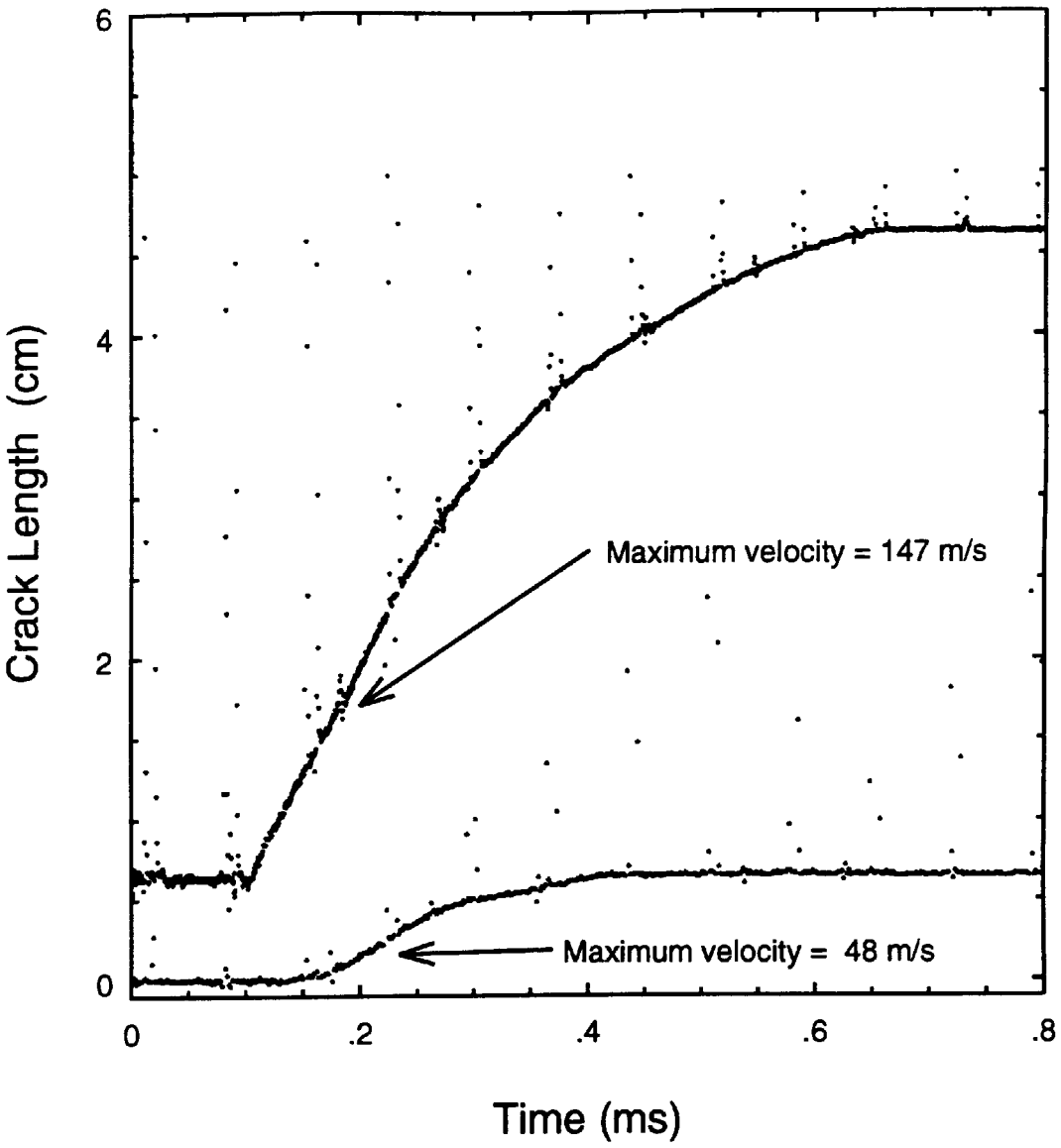

Figure A.47: A second example of the crack velocity determination in an 815:V-40/3:1, $T_g = 72°C$ specimen using the electric potential method.

The maximum crack velocities determined for all of the specimens were in the range of 175 to 300 m/s; no discernible trend developed as a function of epoxy formulation/cure. In another study of crack propagation in epoxy using constant K specimens (double torsion), velocities in a similar range were also reported [88]. Other experiments which have subjected specimens either to dynamic situations (Charpy impact [86]) or to increasing K-fields (SEN [84], 3PB [89]) have generated velocities exceeding 400 m/s. Therefore, it seems that the data generated here are in agreement with the limited published reports.

The techniques adapted here for the measurement of crack velocities were not applied to the central focus (crack-trapping by particles) of this thesis. They could, however, be applied with some modification. The ultrasonic surface modulation technique might prove suitable for reduced temperatures, which cause the fracture surfaces of these epoxies to be smooth and highly reflective, so that the markings would be very easily seen. If the purpose of such experiments were to study the history of crack motions in the vicinity of microparticles, then the effect of the ultrasonic stress waves upon the micromechanisms of fracture should be considered. The electric potential method could be applied to specimens containing microparticles, but the resolution would have to be substantially improved. Improvements over the resolution exhibited here of $\sim$1 mm could be accomplished by increasing the applied current and not using the ultrasonic technique simultaneously. It is doubtful, though, that high enough resolution could be achieved to measure changes in velocities due to crack-tip interactions with microparticles.

A.1.6 Suitability of epoxy as matrix

A major requirement for the material chosen to be the matrix of the crack-trapping specimens was that it be capable of a slow, room-temperature cure, so that inclusions could be manually positioned during the curing process. One resin/curing agent combination which fulfills this requirement is the Epon 815/V-40 which was studied extensively here. The mix ratio of 3:1 and the post-curing schedule with maximum

temperature of 135°C were chosen so that the matrix would be as brittle as possible (with the V-40 curing agent).

Like most polymers, the mechanical behavior of this epoxy is influenced strongly by the temperature at which tests are conducted. At room temperature, uniaxial compressive tests indicate a modulus of $E \approx 2.5\,\mathrm{GPa}$ and a yield stress of $\sigma_y \approx 80\,\mathrm{MPa}$. Using constant-$K$ specimens, the room-temperature fracture behavior was unstable at all loading rates. Toughness values corresponding to fracture initiation were $\sim 1\,\mathrm{MPa\,m^{1/2}}$, while the arrest values were $\sim 0.5\,\mathrm{MPa\,m^{1/2}}$. The plane strain plastic zone size corresponding to arrest is $r_p \approx 9\,\mu\mathrm{m}$. While these figures indicate that this epoxy is quite brittle, its unstable fracture at room temperature made attempts to measure the toughening due to crack trapping by obstacles quite difficult, if not impossible. If an alternate epoxy resin/curing agent could be found that: 1) cured slowly at room temperature, 2) was equally brittle, and 3) fractured in a stable manner at room temperature, then it would be most suited for crack-trapping experiments. Since such an epoxy (or other resin) is not known to us, the crack-trapping experiments were performed at a reduced temperature.

At a temperature of -60°C, uniaxial compressive tests indicate a modulus of $E \approx 3.5\,\mathrm{GPa}$ and a yield stress of $\sigma_y \approx 150\,\mathrm{MPa}$ for 815:V-40/3:1, $T_g = 80°\mathrm{C}$ epoxy. The fracture process at such reduced temperature becomes quite stable, so that propagation occurs at constant load in a constant-K specimen and is controlled by the displacement rate. A relatively constant value of $K_{Ic} \approx 0.5\,\mathrm{MPa\,m^{1/2}}$ is exhibited, which corresponds to an energy release rate of $G_{Ic} \approx 60\,\mathrm{J/m^2}$. The computed plane strain plastic zone size is less than one μm, which indicates that, at reduced temperatures, this epoxy is indeed a most suitable material for the matrix of crack-trapping specimens. Such extreme brittleness, coupled with the lack of material-specific damage mechanisms (such as crazing or micro-cracking) endows this epoxy with the necessary attributes to model fracture processes in generic, ideally brittle materials.

A.2 Inclusion Materials

A.2.1 Criteria for Selection as Inclusions

The selection of materials for use as inclusions in the model specimens employed in the crack-trapping experiments was based upon several requirements. Inclusions were sought in two geometries: cylindrical rods and spheres.

The first requirement was that the elastic modulus of the inclusions be as close to that of the matrix (epoxy) as possible. By minimizing the elastic mismatch, determination of crack-driving forces will not be corrupted by stress concentrations and unequal load-sharing, and valid comparisons can be made to analytical and numerical models which assume equal stiffnesses. A large number of polymeric materials have stiffnesses that will closely match the epoxy modulus, so the selection is not narrowed greatly on that basis alone.

The second requirement was that the toughness of the inclusion material be several times greater than the toughness of the epoxy, so that cracks in the model specimens could, in fact, be trapped. Many unreinforced polymers are brittle and do not meet this criterion. A handful that do are polymethylmethacrylate (PMMA, or Plexiglass©), polyvinylchloride (PVC), polyamide (Nylon 6 or 66), acetal (Delrin©), melamine-formaldehyde, polytetraflourethylene (Teflon©), acrylonitrile-butadiene-styrene (ABS) and polycarbonate (PC). This list, which is not all-inclusive, is further restricted by the availability of materials in rod and spherical form.

An additional, more restrictive requirement was that the adhesion of the material to epoxy be high. Even a tenacious adhesive like epoxy bonds poorly to Delrin and Teflon; in the work here, both PVC and PMMA were used as molds for some epoxy specimens because they were found to separate easily from the cured epoxy. ABS is readily available in sheet form, but no rods or spheres could be found. The remaining three materials, PC, Nylon, and melamine-formaldehyde were found to be available

in both rod and spherical form. Of these, PC and Nylon were most desirable because they have very nearly the same stiffness as epoxy. The adhesion of these materials to epoxy is quantified through use of a novel experimental technique, the development and results of which are described in Appendix B.

A.2.2 Specification of Components

A.2.2.1 Rods

Nylon rods were available from the stockroom at Lincoln Laboratory in diameters as small as 3.175 mm; the manufacturer is unknown, but the thermal strain measurements (discussed in the following section) indicate a T_g of about 50°C, which suggests that the material is Nylon 6 [97]. Polycarbonate rods were purchased in a diameter of 3.175 mm from McMaster-Carr, a vendor who indicated that the material was Lexan©(GE#141). Phenolic/cloth composite rods were also purchased from McMaster-Carr, but no information was available regarding their nature or origin.

A.2.2.2 Spheres

Nylon spheres were purchased from McMaster-Carr in 1.59, 3.175, 4.66 and 6.35-mm diameters. They would not reveal the manufacturer or provide any further identifying information, but the T_g's of the spheres suggest they are also Nylon 6. Polycarbonate spheres were purchased from Clifton Plastics (PA) in 6.35-mm diameters (GE#121) and from Precision Plastic Ball Co. (IL) in 3.175-mm diameters (GE#141). Melamine-formaldehyde spheres in 6.35-mm diameters were purchased from Clifton.

A.2.3 Thermal Strain Measurements

To enable the calculation of residual stresses in the model specimens, thermal strains were measured in each of the materials used over two relevant temperature intervals: from the T_g of the epoxy matrix (80°C) to 20°C, and from 20°C to the temperature at which the crack-trapping experiments were performed (-60°C). Specimens were dried in a small oven for several days at a temperature of 80°C and were then stored in a glass desiccator with fresh desiccant. Measurements were obtained with a TA TMA-2900 in a manner similar to that described for measurements of epoxy. A summary of the mean values of thermal strains recorded for multiple measurements of all the inclusion materials is tabulated on the following page.

Table A.5: Measured average thermal strains of materials used in DCB specimen models.

			80°C to 20°C			20°C to -60°C		
Material	*Form*	*Orientation*	$-\varepsilon$ (10^{-6})	*St.Dev.*	# *data*	$-\varepsilon$ (10^{-6})	*St.Dev.*	# *data*
Epoxy	T_g = 80°C	isotropic	7204	532	13	5625	307	15
Nylon	sphere	random	8086	429	6	6301	270	10
	rod	radial	6080	126	4	5606	107	4
	rod	longitudinal	7610	86	3	6530	109	3
Poly-carbonate	sphere	(1/8") random	4111	34	6	4916	113	6
	sphere	(1/4") random	4419	78	9	5330	112	9
	rod	radial	4357	29	3	5073	90	5
	rod	longitudinal	4387	72	4	5117	195	4
Phenolic	sphere	random	2710	395	7	2484	340	7
	sphere	axis "1"	2600	30	3	2301	12	3
	sphere	axis "2"	3718	17	3	3286	3	3
	sphere	axis "3"	2710	27	3	2484	19	3
	rod	radial, $\parallel$ lam.	1601	147	3	1741	125	3
	rod	radial, $\perp$ lam.	4465	318	3	4307	291	3
	rod	longitudinal	1282	40	7	1410	48	7

A.2.4 Uniaxial Tests

Uniaxial stress-strain curves were acquired for all of the inclusions used in the model specimens so that their moduli could be determined both at room temperature and at -60°C. Naturally, the rods were tested in tension and the spheres were tested in compression. Specimens were dried at 80°C for several days prior to testing.

A.2.4.1 Tensile tests: Rods

Polycarbonate, Nylon and phenolic rods were tested in tension by gripping specimens in standard, cam-tightening flat grips with rough faces. The specimens were all 3.175-mm in diameter and were approximately 125-mm long, so that ~25 mm could be held in each grip while exposing ~75 mm of specimen length between them. A strain-gage extensometer was attached to the central 25-mm portion of this length. The signal from the extensometer was fed through a strain-gage conditioner to an A/D board in a PC. Load data was fed to an A/D board directly from the load-cell amplifier.

Measurements were obtained at both room temperature (22°C) and at reduced temperature (−60°C) in the chamber which was used for the compressive tests of epoxy. Displacement rates from 2.54 to 25.4 mm/min were used, resulting in nominal strain rates from 1.66 to $16.6\times10^{-3}\,s^{-1}$. Three samples of each material were measured at each strain rate. A summary of the average initial moduli, determined from a least-squares fit over the strain interval from 0.005 to 0.015, is given in Table A.6.

Table A.6: Measured initial tensile moduli (GPa) of dry, 3.175-mm rods.

		Nom. Str. Rt. (10^{-3} s^{-1})			
Temp.	*Material*	1.66	3.33	8.33	16.6
22° C	Polycarbonate (GE141)	2.28		2.41	
	Nylon (6)	2.82		2.91	
	Phenolic-cloth	8.63		8.77	
−60°C	Polycarbonate (GE141)	2.78	2.82	2.97	3.0
	Nylon (6)	3.41	3.45	3.57	3.62
	Phenolic-cloth	12.3		13.5	

A.2.4.2 Compression tests: Spheres

Polycarbonate, Nylon and melamine-formaldehyde spheres with a diameter of 6.35 mm were tested in compression with the cage apparatus used for the epoxy compression tests. A linear potentiometer was again used as the extensometer, and data were stored in a PC as before. The stainless steel platens were wiped with a cloth and lubricated with a spot of molybdenum disulphide oil prior to testing of each specimen. Measurements were obtained at both room temperature (24°C) and at reduced temperature (−60°C) in the temperature-controlled chamber. Displacement rates from 0.25 to 12.7 mm/min were used, resulting in nominal strain rates from 0.66 to $33.3 \times 10^{-3}\,s^{-1}$. Two samples of each material were measured at each strain rate.

Typical load *vs.* displacement curves obtained are reproduced in Figure A.48. The extremely nonlinear nature of the spherical contact deformation is evident. Equally apparent are the relative stiffnesses of the materials, and the temperature-sensitivity of the deformation of all three polymeric materials.

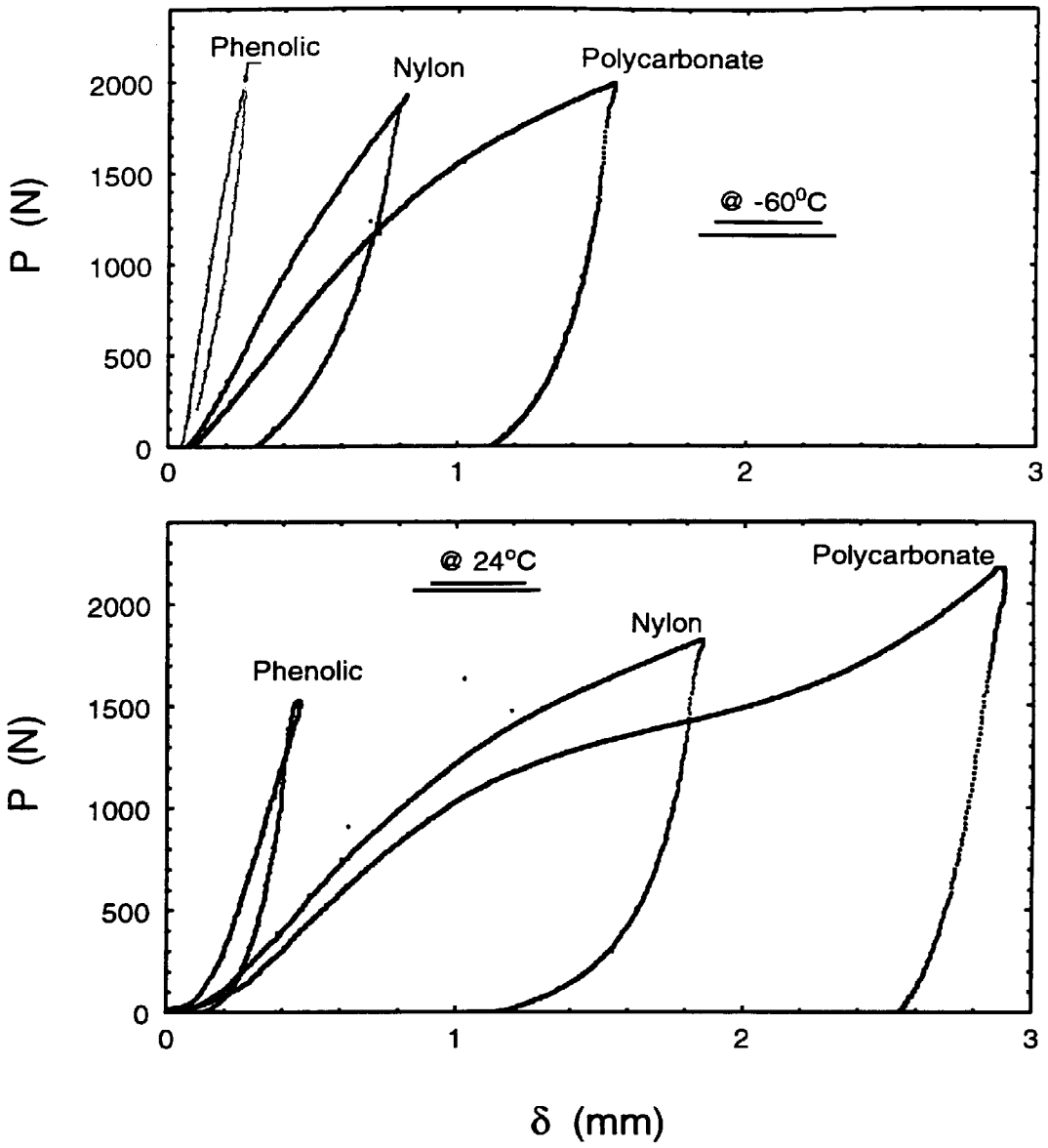

Figure A.48: Typical load *vs.* displacement data obtained from compression of 6.35-mm diameter spheres between two polished steel platens, at a relative displacement rate of 2.54 mm/min.

Quantitative information can be extracted from these curves if the deformation of spherical surfaces is considered. The classical analysis of Hertz, in 1881 [98], considered the contact of two spheres, having radii R_1, R_2 and elastic constants E_1, E_2 and ν_1, ν_2. The relative displacements of the centers of the contacting spheres, under the influence of force, P, can be expressed as [99]

$$u_1 - u_2 = \left\{ \frac{9\,P^2}{16} \frac{R_1 + R_2}{R_1 R_2} \left[\frac{1-\nu_1^2}{E_1} + \frac{1-\nu_2^2}{E_2} \right]^2 \right\}^{1/3} . \tag{A.33}$$

In the case under consideration here, $R_1 = 3.175\,\mathrm{mm}$, $R_2 \to \infty$, $\nu_2 \approx 0.30$ and $E_2 \approx 200\,\mathrm{GPa}$. Because there are *two* contacting surfaces, we substitute for $u_1 - u_2$ the distance of one-half the relative displacement between the platens, $\delta/2$. Adopting a representative value of $\nu_1 = 0.36$ and making all the substitutions, we find

$$\left(\frac{\delta}{2}\right)^{3/2} = \frac{11.58}{\sqrt{\mathrm{m}}} \frac{P}{E_1} + \frac{0.0606\,P}{\mathrm{GPa}\sqrt{\mathrm{m}}} , \tag{A.34}$$

which can be rewritten in a form with which to normalize the data as

$$E = \frac{11.58}{\sqrt{\mathrm{m}}} P \left[\left(\frac{\delta}{2}\right)^{3/2} - \frac{0.0606\,P}{\mathrm{GPa}\sqrt{\mathrm{m}}} \right]^{-1} . \tag{A.35}$$

The second term in the brackets of Equation A.35 represents the deformation of the steel plates, and at first appears quite small due to the presence of the factor (10^9) in the denominator. Nonetheless, using the peak force and deformation values from the phenolic data at $-60°\mathrm{C}$ in Figure A.48, a quick calculation reveals that the deformation of the steel plates can be as high as 20% of the total displacement; consequently this correction term is not insignificant and will be carried along.

When the data of Figure A.48 are normalized through the Hertz contact equation, the curves shown in Figure A.49 result. The initial portions of these curves are now more nearly linear, and allow the determination of an elastic modulus. This will not be a uniaxial modulus, in a strict sense, because the spheres are subjected to a state of multiaxial stress due to the nature of the contact deformation. Nonetheless, the slopes in the initial, linear range of all the data were determined and are summarized in the table below. Examples of the initial portions of the normalized data are shown in Figure A.50, along with the indicated moduli.

Table A.7: Measured compressive moduli (GPa) of dry, 6.35-mm spheres.

		Nom. Str. Rt. (10^{-3} s^{-1})		
Temp.	*Material*	0.66	6.6	33
24° C	Polycarbonate (GE121)		1.75	1.81
	Nylon (6)		1.93	1.98
	Melamine-Phenolic	5.85	6.66	
−60°C	Polycarbonate (GE121)	2.68	2.95	3.24
	Nylon (6)	3.84	4.12	
	Melamine-Phenolic	16.5	20.5	

The numbers in this table are felt to be reasonable fits to the data, but a qualification is in order. The process of transforming the data through Equation A.35 is extremely sensitive to the zero-offset displacement, due to the exponent of 3/2. Shifting the raw data by only 5 μm can change the modulus indicated by the transformed data by over 20%. Great care was taken to adjust the zero displacement to the point where the load was just seen to begin to rise, but the confidence interval for the values given in the table can only be $\pm$10%.

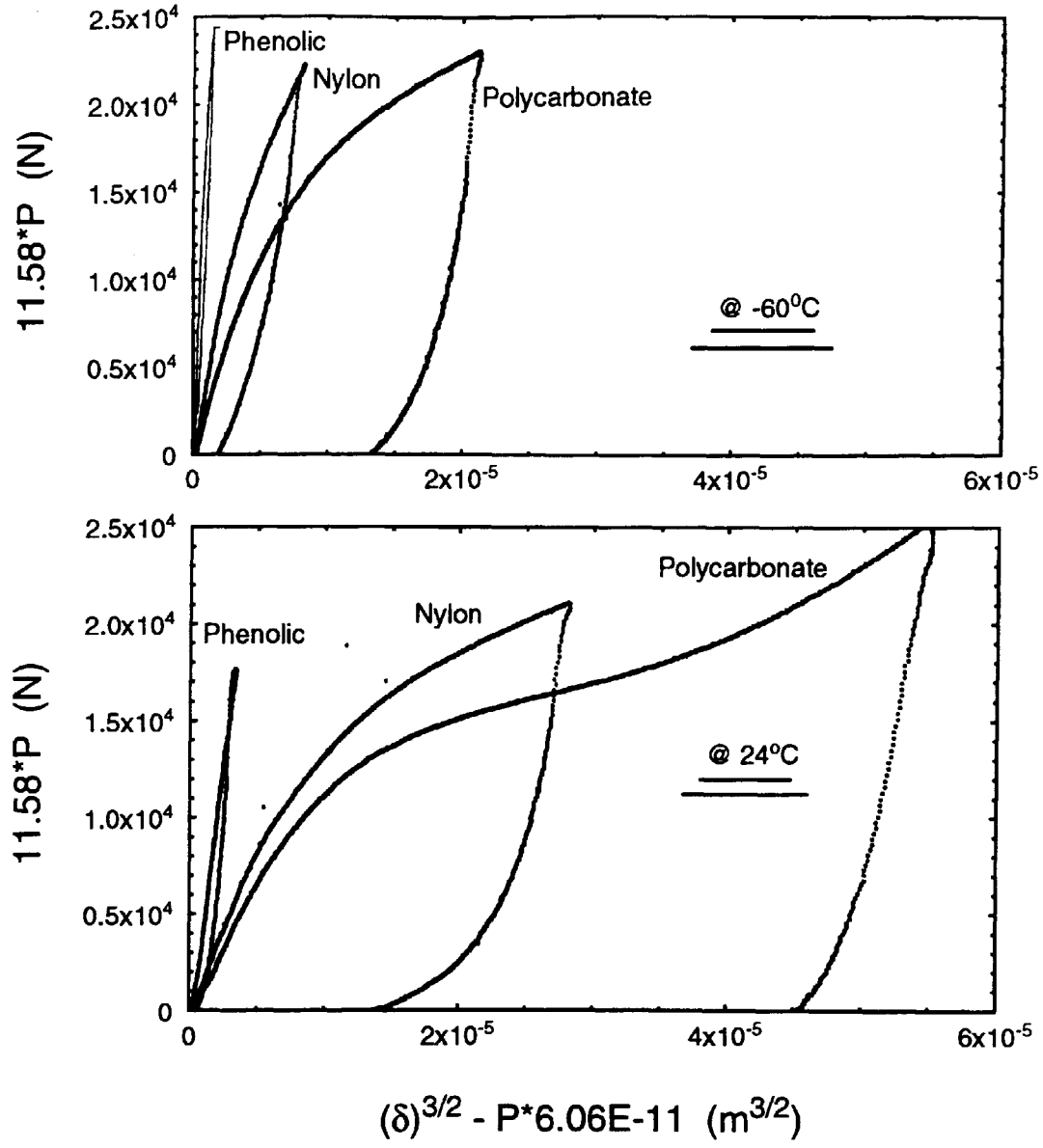

Figure A.49: Data from Figure A.48 (compression of spheres) normalized through the Hertz contact equation (A.35).

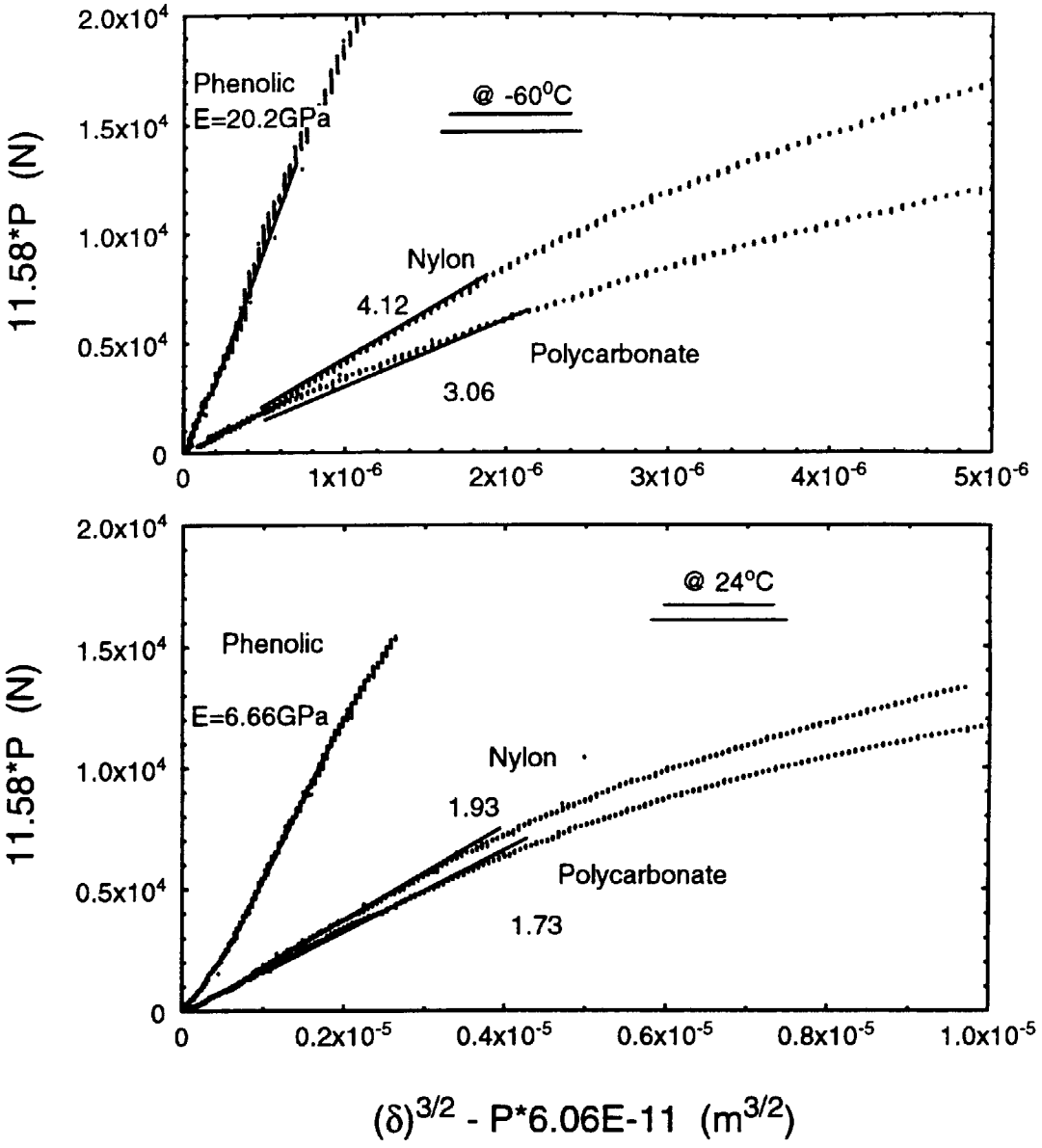

Figure A.50: Initial portions of Hertz-normalized sphere compression data obtained at a relative displacement rate of 2.54 mm/min. Slopes indicated over the linear, pre-yield region of deformation.

An additional concern arises in the compressive testing of spheres: because the contact area is continuously increasing, a yield point is not obvious on a load *versus* displacement curve. Thus, it is necessary to consider yielding within the context of the Hertzian analysis. The maximum stress, $\sigma_{max} = 3P/2\pi a^2$, occurs at the center of the contact area, having radius [98]

$$a = \left\{ \frac{3}{4} \frac{P R_1 R_2}{R_1 + R_2} \left(\frac{1-\nu_1^2}{E_1} + \frac{1-\nu_2^2}{E_2} \right) \right\}^{1/3} . \tag{A.36}$$

The maximum equivalent stress, upon which (Von Mises) yielding depends, occurs along the vertical diameter at a depth of about one-half the contacting radius and is approximately equal to $0.62\sigma_{max}$ [99]. Inserting the expression for a into the above relation for stress and letting $R_2 \rightarrow \infty$, we find the maximum equivalent stress,

$$\overline{\sigma}_{max} \approx 0.62\sigma_{max} = \frac{0.62}{\pi} \left(\frac{6P}{R_1^2} \right)^{1/3} \left(\frac{1-\nu_1^2}{E_1} + \frac{1-\nu_2^2}{E_2} \right)^{-2/3} . \tag{A.37}$$

Making the appropriate substitutions, with $R_1 = 0.003175\,\mathrm{m}$ and $E_1 \sim 2\,\mathrm{GPa}$, we compute that

$$\overline{\sigma}_{max} \approx P^{1/3}\, 28\,\mathrm{MPa}\,(\mathrm{N})^{-1/3} . \tag{A.38}$$

Clearly, the equivalent stress initially rises rapidly in a contact problem, as evidenced by this equation. The room-temperature yield stress of polycarbonate, at the strain rates applied here, is on the order of 66 MPa [100]. The yielding of Nylon is very sensitive to its state of water content, but 70–75 MPa is a reasonable value to assume for the yield stress of Nylon which has been dried [101]. According to Equation A.38, then, yielding will begin to occur in these materials when the force applied (to the spheres) is only about 14 N. Based upon this analysis, only very limited, initial portions of the force *versus* displacement curves can be used to determine moduli.

The situation may not be as dire as it seems. The volume of material which experiences yield is quite small; according to a plot of principal stresses as a function of depth, yielding within the sphere will occur in a volume having a radius of less than $2a/3$ [102]. The contact radius, a, corresponding to a load of, say, 100 N is only about 0.5 mm, so the volume of material which experiences (at this load) $\overline{\sigma} > \sigma_y$ is

approximately 0.1% of the volume of the sphere. This revelation not only indicates that a tiny portion of the sphere is capable of yielding, but further suggests that the effective yield stress of that region may be significantly higher than previously assumed, due to the presence of *constraint* from adjoining, non-yielding material.

Experiments with ductile metals (lead) constrained within glass tubes have demonstrated that the peak stress, prior to yielding, carried by highly constrained materials can be as high as 5 to 6 times their uniaxial yield stress [103]. More recent experiments [104] with the same type of specimens have produced constraint factors slightly greater than 4. (The diminished effect is attributed to slightly reduced bonding between the lead and glass.) Both sets of experiments subjected a ductile material to a high degree of constraint by bonding to a much stiffer material. The present situation of the compression of spheres can be thought of as a small volume of material subject to high stresses, constrained within a larger volume having the same stiffness.[10] Though the stiffnesses are equal, the outer material is not flowing and is as perfectly bonded to the inner region as ever could be possible. So, if we are conservative and adopt a constraint factor of 4, the effect upon the calculated *onset* of yield in the spheres is as follows.

Taking the constrained yield stress now as $\sigma_y' \approx (4)70 = 280\,\text{MPa}$, we see, through application of Equation A.38, that yielding within the spheres may not occur until the applied load is as high as 1000 N. This analysis is certainly approximate, as the constraint of the yielding subregion within the sphere is actually unknown. The simplest solution here, for the determination of moduli, is to restrict attention to the linear portions of the normalized curves as illustrated in Figure A.50.

A final comment here is that the compression of the spheres at reduced temperature produced similar modulus values to the reduced temperature tensile testing of rods. On the other hand, moduli determined from room temperature sphere compression were lower, by about 25%, than the corresponding values determined from tensile

[10] A similar situation develops in front of a crack tip under conditions of plane strain: a region of plastically-deforming material is constrained by adjoining identical material, resulting in a plastic constraint factor equal to 3 [105].

testing of rods. This difference may be attributed to the fact that the rod materials were not identical to the sphere materials, may be due to the different nature of the tests, or could be due to some systematic experimental error.

A.2.5 Suitability of Materials for Inclusions

A.2.5.1 Elastic Similarity

One of the chief requirements for the inclusions to be used in the crack-trapping model specimens is that they have an elastic modulus which is similar to that of the epoxy matrix. The crack-trapping experiments were performed at -60°C, at which temperature the modulus of the epoxy was determined to be 3.45 to 3.65 GPa at strain rates from 1.6 to $16\times10^{-3}\,s^{-1}$. Under similar conditions, the Nylon rods exhibited nearly identical values and the Nylon spheres were about 10% more stiff. The measured moduli of polycarbonate rods and spheres were about 15% lower than the modulus of the epoxy. Therefore, on the basis of the close similarity of elastic moduli, it appears that Nylon and polycarbonate are suitable materials for use as inclusions in the model specimens.

A.2.5.2 Adhesion

The inclusions must adhere to the epoxy matrix, or they will simply behave as voids in response to crack growth in the matrix. Further, it was hoped at the outset of this research that the adhesion level between the inclusions and epoxy could be varied through the use of surface modifications. Preliminary experimentation showed that strong bonding between epoxy and both Nylon and polycarbonate could be achieved and modified. An experimental technique was developed to measure the adhesive strengths of these bimaterial systems under hydrostatic tension; methods employed and results obtained are described in detail in Appendix B.

A.2.5.3 Toughness

The inclusions are further required to be tougher than the epoxy matrix, so that crack propagation in the epoxy will, in fact, be impeded and the crack-trapping/bowing mechanism can be studied. Since $K_{Ic} \approx 0.5\,\mathrm{MPa\,m^{1/2}}$ for the epoxy matrix, a reasonable requirement for the inclusions is that they have $K_{Ic} \approx 2\,\mathrm{MPa\,m^{1/2}}$ or greater. Typical values for polycarbonate exceed this criterion at room temperature, but the reduced temperature toughness is reported to be approximately $1.7\,\mathrm{MPa\,m^{1/2}}$ [106]. The toughness of Nylon is also temperature-dependent, and is greater than that of PC at room temperature [107]. At reduced temperatures, Nylon 6 becomes increasingly brittle as a function of its semicrystallinity [108].[11] As a consequence, Nylon rods occasionally fractured during testing of the model specimens.

Though these materials are not as tough as desired, they are at least three times tougher than the epoxy, and their other characteristics qualify them above all others considered for use in the model specimens.

[11] Annealed, amorphous Nylon will crystallize if heated above 100°C in the presence of water [109]. Nylon rods which had a high moisture content were initially dried at 110°C; they became so brittle that they could be snapped in two with fingertips. Subsequently, all Nylon rods and spheres were dried at 80°C, as recommended by others [110].

Appendix B

An Experimental Technique to Measure the True Adhesive Strength Between Inclusions and Transparent Matrices

This appendix describes in detail the experimental technique developed to measure the adhesive strength between inclusions and the epoxy matrix in the crack-trapping specimens. The incentive for developing this technique was two-fold. First, it was desired to have a means to quantify the adhesive strengths achieved between the materials comprising the composite models used here. Second, though various techniques to measure *fiber*-matrix bond strengths and toughnesses have proliferated, it was recognized that no general methods have been established to measure the adhesive strengths between particulates and resin matrices. After explaining how the technique is executed and analyzed, test results from silica-glass, Delrin, Nylon and polycarbonate spherical inclusions in an epoxy matrix are presented.

B.1 Motivation

B.1.1 Influence of Adhesion on Crack Trapping

A precise understanding of the adhesive strength necessary to promote crack trapping by impenetrable obstacles in brittle solids has still not been reached, despite numerous investigations. By far, the majority of these investigations have focused upon the toughening processes in particle-reinforced epoxies. The principal issues which arise when interpreting results from many of these studies are illustrated in the following discussions.

In one of the earliest studies, Broutman and Sahu used tapered double cantilever specimens to measure the fracture energies of epoxies containing glass spheres which had various surface treatments to modify their adhesive strengths [111]. In cases of unmodified or adhesion-enhanced surfaces, they found a maximum toughness enhancement of a factor of approximately 3. In the case of composites prepared from spheres with reduced adhesion, they found a further enhanced fracture energy, to a factor of about 5. The principal mechanism proposed to be responsible for the basic (factor of 3) increase in fracture energy was crack trapping; the additional increases observed in systems with poor adhesion were attributed to greater fracture surface area resulting from rougher surfaces containing debonded hemispheres. Recent statistical analyses of toughening due to increased surface area caused by deflection along grain boundaries in ceramics suggest that, at best, such increases in surface area can be expected to account for only a 15% rise in fracture energy [112]. It is more reasonable to assume that a combination of other factors were at work.

First, Broutman and Sahu reported increases in fracture *energy*, which is related to the stress intensity factor (in the ideally elastic case) through the relation $K^2 = GE$. All other factors being equal, if crack trapping in all of their specimens produced

uniform enhancements in K_{Ic}, then a reduction in modulus due to debonding would clearly cause an augmented energy release rate, G. Additionally, debonded spheres would act as pseudo-voids, causing stress concentrations at their equators which would promote local yielding in the glassy polymer; this is now thought to be a principle toughening mechanism in both rubber-toughened [113] and particulate-filled epoxies [114]. Because the magnitudes of these additional sources of toughness are not known for the specimens fractured by Broutman and Sahu, it is unclear to what extent crack trapping actually took place in their specimens with reduced adhesion. Moreover, it is entirely likely that reduced adhesion minimized fracturing of the glass particles, therefore allowing more trapping sites to be active.

A similar investigation was undertaken by Spanoudakis and Young, who used double torsion specimens to measure the critical stress intensity in epoxy filled with glass (4.5 and 62 μm) spheres having various surface treatments [115]. They found that K_{Ic} increased with particle volume fractions, to a maximum at $V_p \approx 0.4$ of approximately a factor of three greater than the neat matrix toughness. This toughening behavior resulted regardless of the surface preparation of the spheres and was attributed primarily to crack trapping. Spanoudakis and Young reported a maximum increase in fracture energy by about a factor of two in cases of spheres with unmodified or enhanced adhesion; in the case of spheres with reduced adhesion, the maximum fracture energy enhancement reported was about a factor of four. They attribute the additional factor of two to a reduction in modulus by about 20% for the composites containing release-coated spheres. This discrepancy in the accounting of sources of fracture energy may be resolved by including some of the effects previously mentioned, but the key result from Spanoudakis and Young's work was an apparent invariance of crack-trapping induced stress intensity as a function of adhesion. Similar to Broutman and Sahu though, Spanoudakis and Young did not have a measure of the adhesive strengths exhibited by their composite materials; rather, they relied upon fractographic evidence showing adherence of matrix to particles as their indicator of

adhesive strengths.

Other investigations of toughening by glass spheres in brittle epoxies have concluded that little difference results in the composite's improved toughness (K_{Ic}) as a function of the apparent adhesive strength of the beads to the matrix. The primary mechanisms suggested to contribute to overall toughness are crack trapping and crack-tip blunting, where the total toughness results from a competition between these two mechanisms modulated by the degree of adhesion [10, 114, 116]. Measurement of critical stress intensities (in particulate composites) that do not vary greatly with apparent adhesive strengths is *not* evidence that crack trapping is unaffected by adhesion levels; rather, with decreasing adhesion other mechanisms may become operative while crack trapping becomes less effective.

Toughening of epoxy by alumina particles has also been investigated: enhancements of K_{Ic} by a factor of ~ 2 were reported due to inclusion of a 30% volume of alumina ($6\,\mu$m) particles [117]. The toughening was attributed to crack trapping, which was assumed to be less effective in specimens containing particles with reduced adhesion, resulting in slightly (15%) lower toughening behavior. The actual adhesive strengths, however, were not measured.

Though it seems intuitively necessary to have good bonding between a brittle matrix and tough particles in order to permit trapping to occur, examples suggesting exceptions have been shown. In a silica-glass containing poorly bonded nickel spheres, fracture surfaces with ultrasonically created Wallner lines showed that crack-front growth was slowed by the obstacles and divided into locally bowed fronts between them [118]. The curvature of these local segments between the "pseudo-pores" was similar to curvatures of bowed fronts resulting from trapping by well bonded particles. The enhancement of critical stress intensity, however, was only on the order of 20–25%, which brings into question the nature of its source. Similar results were obtained from fracture experiments with a porus glass, and were simply attributed to the

elastic concentration of stress intensity in the vicinity of the pores [119]. Given that local yielding of the silica-glass matrix can be ruled out, and that trapping-induced toughness by holes is difficult to conceive of, a feasible explanation is that the crack tips were shielded from the remotely applied stress intensity by a region of reduced modulus due to interface separations [120].

It is apparent, from the preceding discussion, that the effect of adhesion upon the crack-trapping mechanism has not been established. No prior research efforts which focus upon toughening mechanisms in particulate-reinforced brittle materials have included quantitative measures of adhesive strengths. Thus, it was deemed necessary to develop a technique which could measure adhesive strengths in model specimens used in the current and in future investigations.

B.1.2 Deficiency of 'Standard' Adhesion Tests

Commonly used techniques of measuring "adhesion" were not considered here for the purpose of determining the adhesive strengths exhibited by the material pairs used in the crack trapping specimens. Such popular tests as lap-shear, butt joint and peel tests possess stress concentrations inherent to their design which render them incapable of generating results which can represent true adhesive strengths. The reason for this deficiency is that failure of the standard test joints always proceeds through fractures initiated at the location of stress concentration; the joints never fail by uniform stressing across the entire surface.

In the case of peel tests or any test with a similar geometry, the nature of the stress concentration is obvious and singular: the test commences with a crack along the interface, and the more flexible member is pulled away from the substrate at some inclined angle. Proper mechanical analysis will obtain the fracture energy of the interface in this type of test [121], but will not provide a measure of adhesive strength.

In the case of lap-shear and butt joint testing geometries, stress concentrations arise from the finite-length interface between materials with differing moduli [122]. The stress distributions and magnitudes of concentration vary with specimen size, adhesive thickness and elastic mismatch, which therefore influence the failure loads. Because these tests have gained such widespread, sometimes naive usage, brief descriptions of their stress distributions and failure trends are provided in the next subsections. Once again, failure in these specimens does not result from a uniform traction reaching a critical level, so that these "standard test methods do not enable the magnitude of intrinsic adhesion forces acting across the interface to be determined [123]."

B.1.2.1 Butt joints

Finite element stress analyses of rigid, cylindrical bars joined across flat end surfaces ("poker chip specimens") with an adhesive having finite modulus and $\nu = 0.34$ indicate that the axial stresses in the adhesive layer are singular at the specimen edge [124]. In specimens with a diameter to adhesive thickness ratio, D/h, equal to 20, the axial stress at a radial position $r \approx 0.49$D is predicted to be about 20% greater than the nominal (F/A) section stress. The strength of this singularity increases with decreasing D/h, so that the fracture stress in butt joints is observed to decrease with increasing adhesive layer thickness [125, 126].

Though the singular stresses at the specimen periphery become less severe with decreasing adhesive thickness, correspondingly the stresses in the central region of the butt joint rise above the nominal section stress. As a consequence, the geometry of these specimens affects not only the failure load, but also the failure mode. In plexiglass-adherend/polyurethane-adhesive poker chip specimens, Anderson *et al.* found that specimens with $D/h > 13$ always failed from debonds initiating at the center; in specimens with $D/h < 4$, failure always originated from the edge [124].

In the same study, Anderson *et al.* demonstrated the sensitivity of butt-joint testing upon eccentricity of load path. Use of special grips, universal joints and precision machining of specimens can optimize only so far the degree to which loading is applied axisymmetrically. Any slight variation in the thickness of a given bondline will cause the joint to be subjected to eccentric loading. Eccentrically applied loading can increase the resulting edge stresses by over a factor of three [124] and result in great scatter in the data. To demonstrate the importance of this effect, Anderson *et al.* tested metal/epoxy/metal buttons both with and without a compliant, rubber link in the load train. Use of the flexible link increased the failure loads by up to a factor of 2, and similarly decreased the variation in data.

B.1.2.2 Lap joints

A complete review of the mechanics of joints formed by the overlapping of substrates with a thin adhesive layer between is provided by Kinloch [127]. In the basic configuration of a single overlap, stress concentrations develop in both the normal stress across the adhesive layer and in the shear stress acting in the direction of loading. Analyses which consider the adherends as rigid beams show that the normal stress in the adhesive at the ends of the overlap section is amplified by a factor of four over the nominal applied shear stress [128]. Solutions based upon plate theory which incorporate finite modulus adherends show that this normal stress concentration can be far greater, particularly if the moduli of the adherends are not similar [129]. This concentration results both from elastic mismatch and from bending moments created by the eccentric loading path of the single overlap geometry. Because the joint failure is driven by the maximum tensile stress, the failure loads (and nominal stresses) in this specimen geometry bear no direct relation to adhesive strengths.

The eccentric loading of lap joints can be eliminated by adding a third adherend, forming a second overlap surface on the other side of the (now) center adherend. This results in a reduction of the stress concentrations and a corresponding increase in the nominal failure stress by about a factor of two [130]. Failure in these double lap specimens, nonetheless, is still governed by concentrated stresses at the ends of the overlap. Moreover, trends in experimental data showing increasing failure loads with decreasing [131] or increasing [121, 132] adherend thickness and increasing adhesive thickness [126, 131] indicate that data from double lap specimens are not related to intrinsic adhesive strengths. The data can, however, be analyzed with fracture mechanics to determine effective interfacial fracture energies, $\mathcal{G}$, which can be used to predict failure loads in similar adhesive pairs which have an existing (or assumed) initial crack length, a_o.

B.2 Adhesion Techniques for Composites

B.2.1 Fracture Mechanics Approach

In response to the growing applications of adhesive joints and the awareness of their inherent stress concentrations, the rapidly growing field of fracture mechanics was applied to the problem of characterizing joint strengths in the late 1960's [133, 134]. These approaches utilized an energy-based approach, wherein the fracture energy of the interface was determined from the applied load required to extend an initial crack along the interface. Early analyses developed for the fracture of bimaterial configurations included only the strain energy stored in point-loaded circular plates (blisters) and simple beams bonded to rigid adherends [133]. These analyses were extended to obtain critical loadings for a variety of double cantilever-beam adhesive geometries and pressure-loaded disks, but still considered the adherend to be rigid and the crack-tip loading to be entirely normal [134]. Nevertheless, this approach was demonstrated experimentally [135] to produce consistent values of adhesive fracture energies, γ_a, through a Griffith-type relation[1] applied to results from adhesive fracture tests incorporating different initial flaw sizes.

Recent fracture mechanics techniques applied to the characterization of adhesive joints have been intended for application to composite materials, and have emphasized the existence of shear stresses at the crack tip resulting from elastic mismatch as well as from the geometry of the joint and the applied loading. The fundamental fracture criterion is the attainment of a critical value of energy release, which for the bimaterial interface is given by [136]

$$\mathcal{G} = \frac{1/E_1' + 1/E_2'}{2\cosh^2 \pi\mathcal{E}}(K_1^2 + K_2^2)\,, \tag{B.1}$$

where $E' \equiv E/(1-\nu^2)$ for each material and $\mathcal{E}$ is a function of the elastic constants.

[1] $\sigma_{cr} = Q\sqrt{2E\gamma_a/\pi a}$, where Q is a geometry factor specific to each test.

In this (bimaterial) case, K_1 and K_2 cannot directly be determined from the normal and shear loadings, as is the case with homogeneous bodies. Rather, K_1 and K_2 are found to be functions of the parameter ε, which is very small for many material pairs [137]. When $\varepsilon \to 0$, K_1 and K_2 recover their usual significance of K_I and K_{II}, and the above equation becomes the familiar expression for homogeneous, isotropic materials.

Recognizing that $\varepsilon \sim 0$ for many material pairs, a simplified approach to characterizing bimaterial fracture was suggested [138], in which the K's have their usual (remote) meaning but the interface crack-tip loading is characterized by the remote "phase angle", $\psi = \tan^{-1}(K_{II}/K_I)$, plus a shift, ω, due to the modulus mismatch. Values of ω for practical material pairs are listed in [138] and range from about -10 to 5°. Following this approach, the fracture criterion becomes the attainment of a critical value, $\mathcal{G}_c$, which is presumed to be a continuous function of ψ.

Theoretical models of the dependence of $\mathcal{G}_c$ upon surface roughness parameters predict that, indeed, $\mathcal{G}_c$ is a monotonically increasing function of the crack-tip phase angle [139, 140]. Due to mechanical interlocking of mating surfaces, crack tips on interfaces with finite asperities are increasingly shielded from mode II stresses as the phase angle increases. Ideally brittle, smooth interfaces receive no shielding from applied K_{II} unless the loading is very nearly pure mode II.

A great deal of effort has recently been expended upon measuring the fracture energy of bimaterial systems as a function of "mixity" of loading; a selected sample of this work is reported in References [138, 141, 142, 143]. These reports provide results from various combinations of metal, ceramic or glass adherends, and, in some cases, a polymer adhesive interlayer. The data universally show a rise in toughness (fracture energy, $\mathcal{G}_c(\psi)$), as a function of increasing shear stress intensity, K_{II}. Though the data have important implications for optimizing the use of specific material pairs in engineered composite materials, they are, nonetheless, applicable only to those material

pairs and only under conditions which closely replicate the testing configurations.

One general feature observed from both the experimental data and the theoretical models previously cited follows. Though the apparent fracture energy of the interface increases as a function of ψ, the effect is relatively minor until K_{II} is nearly equal to K_I: when $\psi \sim 40°$, measured increases in $\mathcal{G}_c$ are on the order of 20–40%; thereafter, with increasing ψ, increases in $\mathcal{G}_c$ become much greater. Similar trends have also been reported for mixed loading of homogeneous specimens [144].

The fracture mechanics approach to characterizing interfaces may provide data and design guidelines for understanding the sources of energy dissipated during the fracture of many composite materials, but the developed methods do not provide any new means of determining the intrinsic toughnesses of interfaces. This point is worth noting, since it is the intrinsic energy required to separate two surfaces (through mode I, or cleavage loading) that very often scales all other dissipation processes attendant to fracture under general (mixed) loading conditions [145]. Additionally, any fracture mechanics approach is based upon the premise that a flaw exists in the body under consideration. Consequently, the developments above do not furnish any information about the conditions under which a flaw on an interface is initiated; *i.e.* fracture mechanics is not a framework for predicting or characterizing adhesive strengths.

Adhesive strengths are the focus of this Appendix. Though at least one author has written that "there is no satisfactory method of measuring the strength of the bond between the fibre and the matrix [146]," a few methods designed to do that are briefly discussed in the next section. The purpose of including those discussions is partly for completeness, but primarily to underscore the existence of several methods having some capability of measuring fiber adhesion, while no suitable techniques have been developed for particles.

B.2.2 Fiber Adhesion Tests

B.2.2.1 Single fiber pull-out

Several techniques which are often used to attempt to measure the adhesive strength between a fiber and a matrix material are variations of the single fiber pull-out test [147]. As the name implies, a fiber is cast into and then pulled out of a block of matrix material while recording the applied load, F. The assumption is made that the fiber will begin to slide, relative to the matrix, when a critical level of adhesive shear stress is reached: $\tau_i = F/l\pi d$, where l is the length of fiber within the matrix. Typically, this calculated value of shear stress is taken as a measure of the chemical bond strength of the interface [148]. In fiber/matrix systems where little or no chemical bonding takes place, the peak shear stress determined from pull-out data has been viewed as resulting from a product of the interfacial pressure and friction [149].

While the simplicity of this procedure is appealing, the actual stress distribution is complicated by discontinuous shear traction at the surface of the matrix where the fiber enters it, and by Poisson contraction of the fiber. As a result, normal stresses act across the fiber/matrix interface which contribute to the initial debonding process and make interpretations of adhesive strengths from this test suspect [150].

A variation of this testing procedure is the "button test", in which a disk which has been cast around a fiber is pushed along the fiber, while the latter is held in grips attached to a load cell [147]. The peak force required to move the disk is interpreted as resulting from the sum of adhesive and frictional forces acting across the interface; the frictional forces are determined from the force required to continue sliding the disk along the fiber. To be expected, finite element studies show that the shear stresses acting along the fiber/matrix interface are greatly concentrated near where the load is applied to the disk [151]. Likewise, normal stresses will be concentrated here as

well, so that measured loads from specimen debonding will not reflect intrinsic, or "true", adhesive strengths.

Analyses of the debonding process in the fiber pull-out test incorporated energy release rate criterion long before the recent emphasis in bimaterial fracture mechanics. For example, in a study of glass rods embedded in a polyurethane matrix, Atkinson *et al.* found good correlation between experimental data and numerical predictions of the energy release rate of an extending interface crack [152]. Additionally, they observed in their experiments that debonding occurred via the growth of cracks initiated at the ends of fibers; as the cracks advanced upwards along the interface, the energy release rate decreased so that crack growth ceased mid-way between the fiber end and the specimen surface. With further increasing load, cracks initiated from the surface and propagated down the interface until debonding was completed.

Independent observation of similar fiber debonding processes gave rise to a recently developed model which defines the conditions necessary for debonding to occur at either end of the embedded length of fiber, and further develops the fiber-debonding stress-displacement relations for use in modeling the fracture behavior of composites [153]. Because this model determines the stress distribution along an unbonded fiber, it could be used to deduce fiber/matrix adhesion strengths from single fiber pull-out data. The authors point out, though, that a fracture-based analysis must be used instead to analyze fiber/matrix pairs having a high interfacial toughness (critical energy release rate).

B.2.2.2 Embedded fiber specimen

The direct measurement of true interfacial fiber/matrix strengths has been pursued with specimens containing fibers completely embedded in a transparent matrix. Broutman describes the use of such specimens to determine the adhesive shear and tensile strengths of boron fibers in an epoxy matrix [154]. The methods used for both cases are essentially similar to the technique developed later in this Appendix.

The procedure used by Broutman was to bond a fiber length into a block of matrix material which was then compressed along the direction of the fiber axis. The surface of the fiber was monitored as the loading was increased until debonding of the interface occurred. For the measurement of shear strength, the specimen shape was a bar with a uniform, square cross-section. Tensile stresses normal to the fiber surface were generated by contouring the bar in a neck fashion, with the narrow central region near to the middle of the fiber. Using these two types of specimens, Broutman found that the tensile bond strength between boron fibers and an epoxy was approximately 5.5 MPa, while the measured shear strength was on the order of 55 MPa [154].

A variation of these procedures is to load a constant cross-section specimen of this type in tension. With sufficient bonding to a brittle fiber, the fiber will begin crack into shorter lengths as the load is increased. Ultimately, a critical length is reached below which no further cracking takes place. The interfacial shear strength is then related to this critical length and the intrinsic fiber fracture stress [150, 155]. The obvious disadvantage of this method is that it requires a brittle fiber, which is subject to statistical variation in fracture strength.

B.2.3 Particle Adhesive Strength Inferences

B.2.3.1 Fractography

Investigations of the effect of adhesion upon the mechanical properties of particulate-reinforced composites have relied exclusively upon either assumed adhesive characteristics or upon fractographic evidence to provide qualitative rankings of adhesive strength levels as a function of surface preparation. This trend can be traced back at least to 1968, when Kenyon reported the influence of modified adhesive strengths upon tensile stress-strain characteristics of a typical (EPON 815) epoxy which was filled with 25 μm glass particles [156]. Kenyon modified the adhesive strengths by coating the glass particles with either release agents or silane coupling agents. The tensile test results showed increasing fracture strains with increasing adhesive strength, which was substantiated by microscopy of fracture surfaces which showed increasing amounts of matrix adhering to the particle free surfaces.

A great deal of research effort has been focused upon improving the fracture behavior of brittle polymers, primarily epoxy, through the use of filler particles. A sampling of these are listed as References [111,113–117,157–160]. In those studies in which adhesive strengths were varied, it is found that, depending upon the materials involved, fracture toughness may increase or decrease as a function of increasing adhesion. In all cases, the adhesive strengths were inferred from examination of fracture surfaces. Though relative adhesive levels are clearly indicated from some particularly enlightening microscopy (*e.g.* [158]), the effect of adhesive strength upon specific toughening mechanisms and overall fracture toughness might become clearer if quantitative measures of particle/matrix adhesive strength were utilized.

B.2.3.2 Dilatation experiments

Attempts to quantify the particle/matrix adhesive strength have been pursued by measuring the dilatation of particulate composites during tensile testing. In 1964 Farris described the construction of a gas dilatometer and its application to the measurement of dilatation in an elastomer filled with rigid particulates (a solid rocket-fuel) [161]. A direct correlation between stress-strain behavior and "dewetting" was reported as a function of testing rate and temperature. While this instrument appears to have provided a sensitive indication of the dilatation of specimens resulting from debonding of particulates, its use should be restricted to materials similar to those which Farris applied it to: nearly incompressible elastomers containing extremely well bonded, rigid particles.

When applied to materials with a Poisson's ratio much less than 0.5, dilatation measurements will incorporate the elastic component, ε_{ii}, which will be difficult to separate entirely from dilatation resulting from many individual debonding events which are distributed in time, and may take place at strain levels below the elastic limit of the matrix. Additionally, the measured rate of dilatation will increase as debonding proceeds, due not to debonding but due to growth of voids already established. A further element which potentially could affect the sensitivity of dilatation measurements used to indicate debonding might be cavitation of the materials themselves, if either the matrix or the particles have a low bulk modulus.

Dilatation measurements have been applied to such glass-filled polymers as epoxy [162], polyethylene [163], and polyamide-6 [164, 165]. Though the data reported seem to provide a measure of bond strength, the Poisson's ratios of these materials were about 0.35; therefore, the measurements may be subject to the uncertainties mentioned above. Furthermore, in these studies the volume change during tensile testing of materials was determined through the use of surface-mounted strain gages. It is

doubtful whether such techniques have the inherent precision required to detect the global effect of such small volume changes as accompany the separation of interfaces.

B.2.4 Film Adhesion tests

A variety of techniques exist for the measurement of bond strength between thin films and substrates. Though many of these have been developed in the course of unrelated research, the measurement and control of interfacial strength and toughness of film coatings on fibers has been suggested as a key component in the optimization of metal-matrix composites [166]. By creating fiber coatings with carefully specified strengths and fracture energies, brittle fibers can be isolated from impinging cracks while still contributing to the load-carrying capability of the material. This design methodology could, in principle, be applied to many types of composite materials, thus increasing the importance of film adhesion control and measurement.

In the standard blister test, the pressure required to propagate a circular crack between a film and substrate is used to determine the interfacial fracture energy [134, 135]. In a recent modification of this technique, the center of the blister is affixed to the substrate at an "island", so that the failure stress of low-strength film materials is not exceeded before the critical pressure is reached [167]. Yet another variation utilizes misfit strains and film thickness to determine $\mathcal{G}_c$ of film/substrate combinations which spontaneously develop blisters during deposition of the film [145].

Methods involving considerably more sophisticated equipment and instrumentation have been developed specifically to measure the adhesive strengths of films. In one technique, a short duration, high amplitude shock wave is applied to the rear of a substrate with an electromagnetic "hammer", which is accelerated by discharge of high voltage capacitors [168]. A second technique subjects the film/substrate interface to a pressure wave which is created by using a laser pulse to vaporize a constrained layer of gold positioned on the back side of the substrate [169]. With both methods, the interfacial adhesive strength is determined from numerical calculation of the magnitude of stress wave which causes debonding.

B.3 Background

The experimental method discussed in the remainder of this Appendix is based upon the work of Argon *et al.* , who determined the adhesive strengths of particulates in bars of copper and steel alloys [170]. By tensile straining bars which had been initially machined to a natural neck profile, they induced a state of triaxial stress upon particles contained within the central portions of the specimens. The fractured bars were sectioned and examined to locate the positions of second-phase particles (Fe_3C, Cu-Cr, TiC) which had separated from the bulk metal, nucleating voids. The furthest axial position (from the neck center) at which particles separated was determined, and the adhesive strength was equated to the radial stress corresponding to this position, which was approximated as [171]

$$\sigma_r \simeq \sigma_y(\overline{\mathcal{E}}^p) + \sigma \,, \tag{B.2}$$

where $\sigma_y(\overline{\mathcal{E}}^p)$ is the flow stress in uniaxial tension of the (hardening) material and σ is the computed negative pressure.

An approximate analytical solution for the plastic stresses and strains in the neck [172] based upon the work of Bridgman [173] gave the distribution of negative pressure (mean normal stress) along the axis as

$$\sigma_{|_{r=0}} = \sigma_y \left\{ \frac{1}{3} + \ln\left[1 + \frac{a}{2R}\right] - 2\ln\left[1 + \frac{z^2}{a(a+2R)}\right] \right\} , \tag{B.3}$$

where z is the axial position from the center, a is the minimum section radius and R is the minimum radius of profile. This expression indicates that σ is proportional to the flow stress, so that a state of pure hydrostatic tension may be expected to develop only after plastic strains are produced in much of the neck. In addition, Argon *et al.* indicate that Equation B.3 is valid only for axial positions near the necked region, where the profile is concave outward [170]. For regions located further away along

the axis, numerical computations [172] based upon the methods of Needleman [174] provided the magnitudes of σ as a function of plastic strain and axial position.

To determine a mathematical representation of the natural neck profile, many ductile copper bars were necked and carefully measured [175]. An empirical fit to these measurements was given as [172]

$$r = a_o \left[1 - v \left(\sqrt{1 + \frac{1}{(\frac{z}{a_o})^2 + v^2}} - 1 \right) \right] , \tag{B.4}$$

with

$$v \equiv \frac{\frac{a}{a_o}(2 - \frac{a}{a_o})}{2(1 - \frac{a}{a_o})} , \tag{B.5}$$

where a is the radius of the central section and a_o is the radius of the rod at a great distance from the neck. By straining specimens with profiles machined according to this expression, a state of triaxial stresses can be generated within the neck region to explore decohesion and cavitation phenomena.

With the adaptation of this technique to glassy, polymer matrices it was anticipated that the adhesive strength between the particles and the matrix might be reached prior to any significant development of plastic strains. Therefore, the use of the Bridgman solution for stress at the neck center would not be fully valid. An alternative might be to use an elastic solution developed by Neuber for circumferentially grooved bars, but that solution was based upon a profile with a constant radius of curvature [176]. An additional complexity arises, in the form of stress concentrations, if the particles included in the neck have a much higher modulus than the polymer which the neck is fabricated from. Consequently, a finite element analysis was employed to determine the state of stress in the natural neck specimens used here.

The overall strategy employed here entailed the casting of a spherical particle of a candidate material at the center of a solid bar of epoxy, which was then machined with

a numerically controlled lathe to the profile given by Equation B.4. The neck was then strained in tension, while an image of the particle surface was continuously recorded. The adhesive strength of the particle/matrix interface was then determined, using the applied load which caused debonding to occur, from the radial stresses computed in the finite element solution.

B.4 Experimental Technique

B.4.1 Fabrication of Specimen

The materials used to fabricate the neck specimens for determination of adhesive strengths were identical to those used in the crack-trapping DCB specimens; they are, therefore, discussed more fully in Chapter 3 and Appendix A. The epoxy matrix used was EPON 815 cured with V-40 at a mix ratio of 3:1. The materials whose adhesive strengths to epoxy were evaluated were Delrin, Nylon, polycarbonate and soda-lime (silica) glass. The polymers were obtained as 3.17 mm-diameter spheres with a sphericity (diameter tolerance) better than 0.5%. The silica-glass particles had a nominal diameter of 2.8 mm; in general, they were quite irregular, but with careful sorting nearly spherical specimens could be found and tested.

The most difficult aspect of specimen fabrication was the placement of the spherical particles in the center, both radially and longitudinally, of a solid bar of epoxy without creating a mechanical interface between two sections of the epoxy, which would cause an inherent structural weakness. The overall scheme followed was similar to the fabrication of the crack-trapping specimens. The height and volume of the required epoxy casting for the neck specimens created additional complications, however, which are addressed in the following description of the methods developed.

The molds used to cast the epoxy rods were thin-walled (1.5 mm) tubes of polymethyl methacrylate, 51 mm in outside diameter and approximately 35-cm long. PMMA was chosen despite some manufacturer's claims that it adhered *well* to epoxy, because casting on *smooth*, thin PMMA plates showed that they could be peeled away from the cured epoxy solid, leaving a glassy-smooth surface. The only disadvantage of this choice of mold material is that the T_g of PMMA is about 110°C. Consequently, a maximum curing temperature of 100°C was used. This resulted in a T_g of the epoxy

solid equal to 72°C, which is 8°C lower than is produced in the curing of the DCB specimens. It is expected that little difference upon adhesive strength results, but that has not been confirmed. An advantage to this choice of mold is that they were disposable: after curing of the epoxy, the PMMA was peeled or broken away from the solid rods.

Aluminum plugs were machined to fit closely the inside diameter of the PMMA tubes. The plugs were coated with a release agent and then inserted into the bottom of the tubes. Epoxy resin was then mixed, degassed, and poured into the tubes up to the half-length of the desired solid rods. The half-filled tubes were then placed in a tall vacuum chamber to degas the contents once again. After all visible bubbles were evacuated, the vacuum was removed and sufficient time was allowed to pass to cause the surface tension to increase (through gelation) enough to support a sphere placed upon the surface.

At this point, one of the candidate spheres (properly solvent-cleaned, dried and, in some cases, surface-modified) was placed upon the conical tip of the teflon positioning jig which is schematically shown in Figure B.1. Vacuum was then applied to the jig to hold the particle in place. A tiny drop of freshly mixed, degassed epoxy was then placed on the sphere. The positioning jig with sphere in place was then inserted into a half-filled mold and slowly pushed in until the sphere made contact with the epoxy surface. The vacuum was then removed from the jig, which was extracted after the stability of the position of the sphere was established.

Vacuum was applied again to remove any bubbles that may have formed on the lower surface of the sphere. Another period of time was allowed so that gelation of the hemispherical bond would occur, but not enough time to allow vitrification; too much curing at this stage would introduce a mechanical interface between halves of

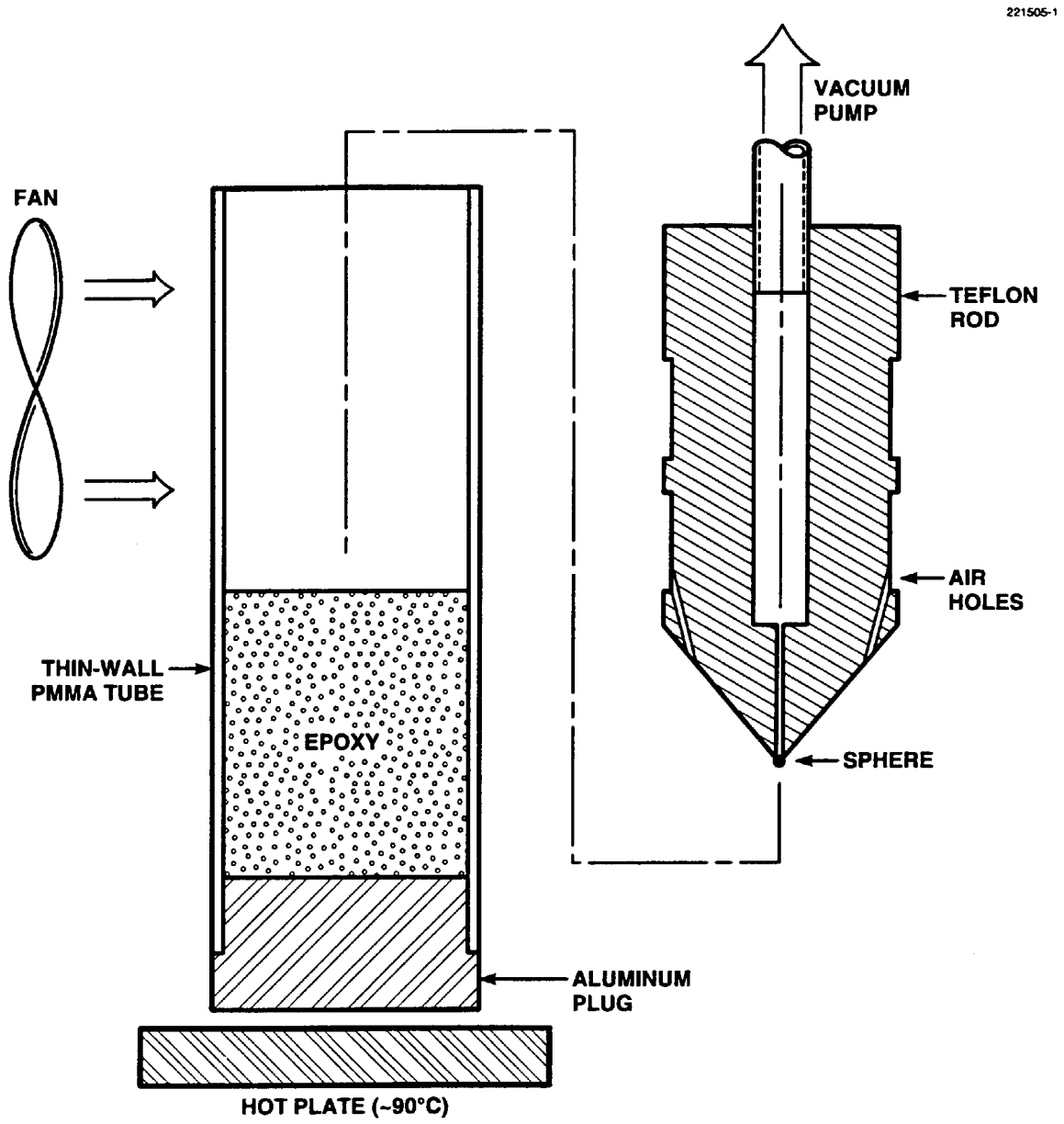

Figure B.1: Schematic drawing of procedure used to cast spheres in center of epoxy rods for adhesive strength neck specimens.

the finished solid. At the appropriate time[2], the molds were filled to within about 3 cm of the top and then evacuated until all bubbles were removed (or at least, removed from regions near the sphere).

The entire casting process was complicated by the exothermic nature of the epoxy curing reaction. Because of the volume of the casting, more heat was generated during the (room-temperature) curing process than could be removed at the surface. Hence, the reaction becomes auto-catalytic, and "runs away" unless the volume temperature is controlled. After each stage of evacuation, during which there was *no* convective heat transfer from the top and side surfaces, the tubes containing epoxy were placed in a chest freezer at $-40°C$ for about ten minutes. This step brought the temperature of the epoxy down to approximately ambient, and prevented vitrification before the casting process was completed.

A second major problem with the casting process was created by the height of the casting ($\sim 30\,cm$). During the room-temperature curing of the epoxy, a significant amount of chemical shrinkage occurs. This shrinkage continues long after adhesion and a shear modulus are established. Consequently, if a high proportion of the casting surface is constrained then shrinkage voids may be formed. In the case of these neck specimens, the only free surface was the cross-section of the tubes, so that just 4% of the surface was free to contract without forming voids. A large meniscus was always formed on the top of the cured epoxy rods, and until a corrective method was developed, large (several cm^3) voids formed in the lower sections.

The procedure adopted to prevent the shrinkage voids was designed to control the vertical temperature gradient in the rods, so that curing would progress from the highly constrained lower sections upward. To do this, the bottom plugs were changed from teflon, which was initially used because of its poor adhesion to epoxy, to more

[2]Determined through experience only.

conductive aluminum. An aluminum base for the vacuum chamber (whose principal component was a large PC tube) was machined and positioned on a laboratory heating plate. With this arrangement, heat could be applied to the lower section of the castings during all phases of fabrication, including degassing. The surface temperature of the aluminum plate was monitored and kept to about 90°C. After the tubular molds were finally filled, evacuated and cooled, they were arranged upon the heated plate with a fan blowing across their upper sections. In this manner, initial curing was forced to proceed from the bottom up, and no voids were formed in the final castings.

Following about twelve hours of this controlled temperature-gradient curing, the specimens were kept at room temperature for at least another day so that all room-temperature reaction could be completed. They were then placed in a programmable oven, which controlled the post-cure temperature to a maximum of 100°C and slowly cooled the specimens down to room temperature again. The molds were then cracked, pried and peeled apart from the finished epoxy rods.

In the next step of fabrication, the rods were machined to a total length of 25.4 cm with the particle located exactly in the center. The length-wise central locating of the spheres was accomplished by sliding a thin aluminum tube, having a pair of narrow hoop-slits at the center, over each epoxy rod. These were held up to a light, and the position of the tube was adjusted until the slits could be seen across the diameter of the sphere. A mark was then inscribed upon the epoxy bar at the ends of the 25.4-cm aluminum tube. Material was then removed from each rod end, to the scribe mark.

Each rod was then machined on a numerically controlled lathe, which had been programmed from data produced by Equation B.4. The radius, a, of the central neck section was prescribed as one-half the radius, a_o, of the distant end to be held by grips. A plot of this profile is shown in Figure B.2, which shows the beveled collars at the ends which provide the gripping surfaces for testing. After the contours

were machined, each specimen was again mounted in a lathe for final finishing. Successively finer grits of wet/dry sandpaper and water were used to smooth the neck surfaces. Final polishing was accomplished with alumina paste and cloths. A few fine scratches were allowed to remain over most of the surface areas; near the central neck region, all scratches were removed to reduce the chance of fracture due to flaws on the highly stressed surface during testing. A photograph showing a pair of finished neck specimens is reproduced in Figure B.3. A magnified view of one of these is shown in Figure B.4, which shows a silica-glass particle contained within the neck.

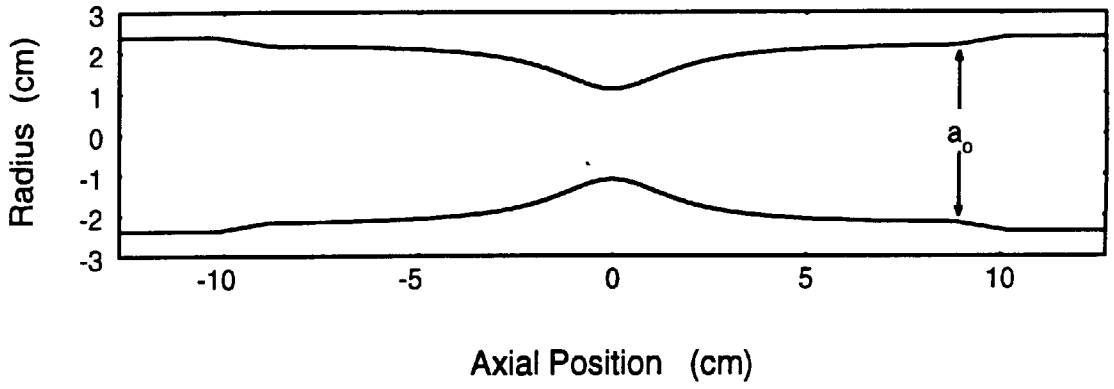

Figure B.2: Profile from Equation B.4, with $a/a_o = 0.5$, used to machine neck specimens with numerically controlled lathe.

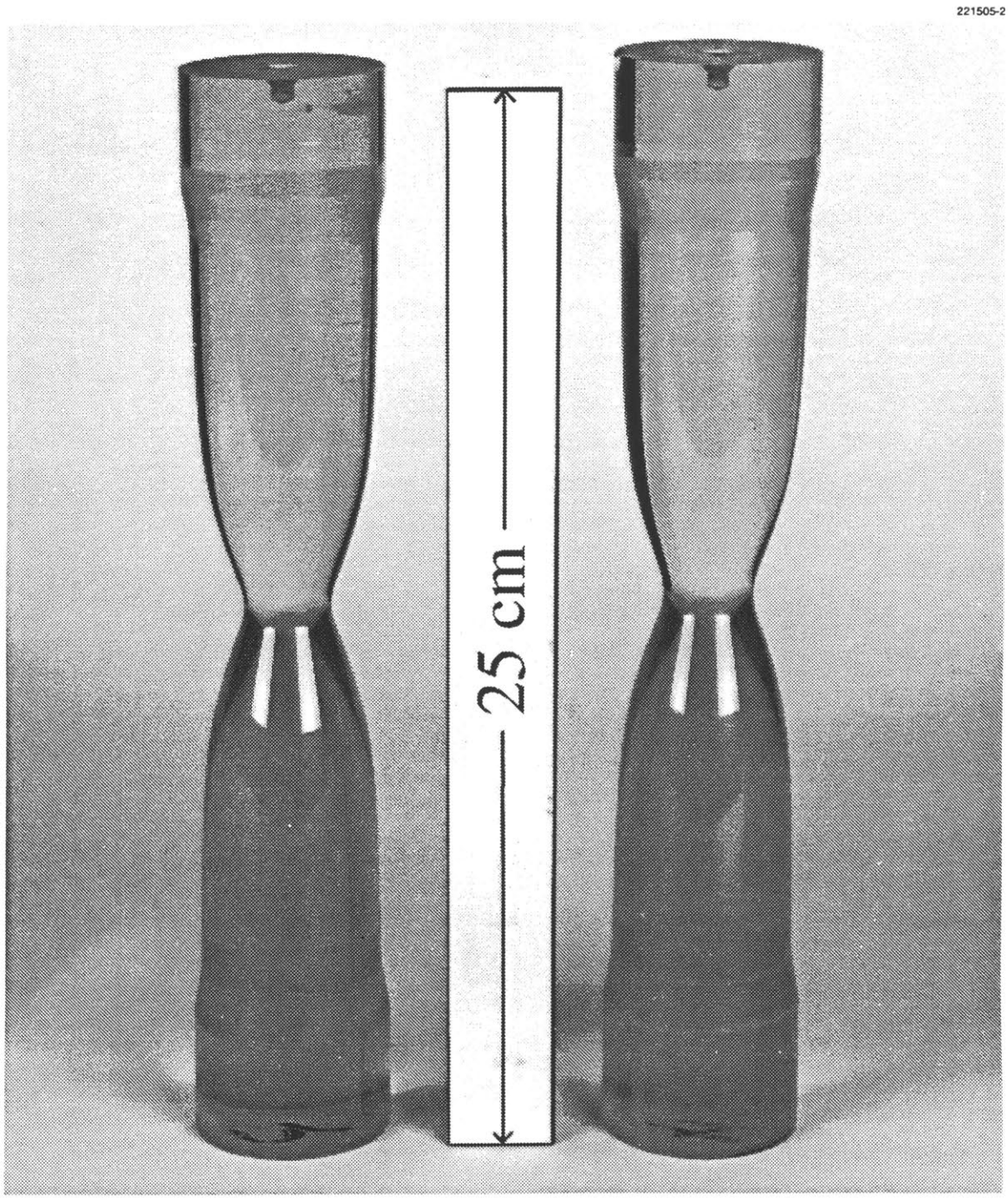

Figure B.3: Two finished neck specimens for measurement of adhesive strengths.

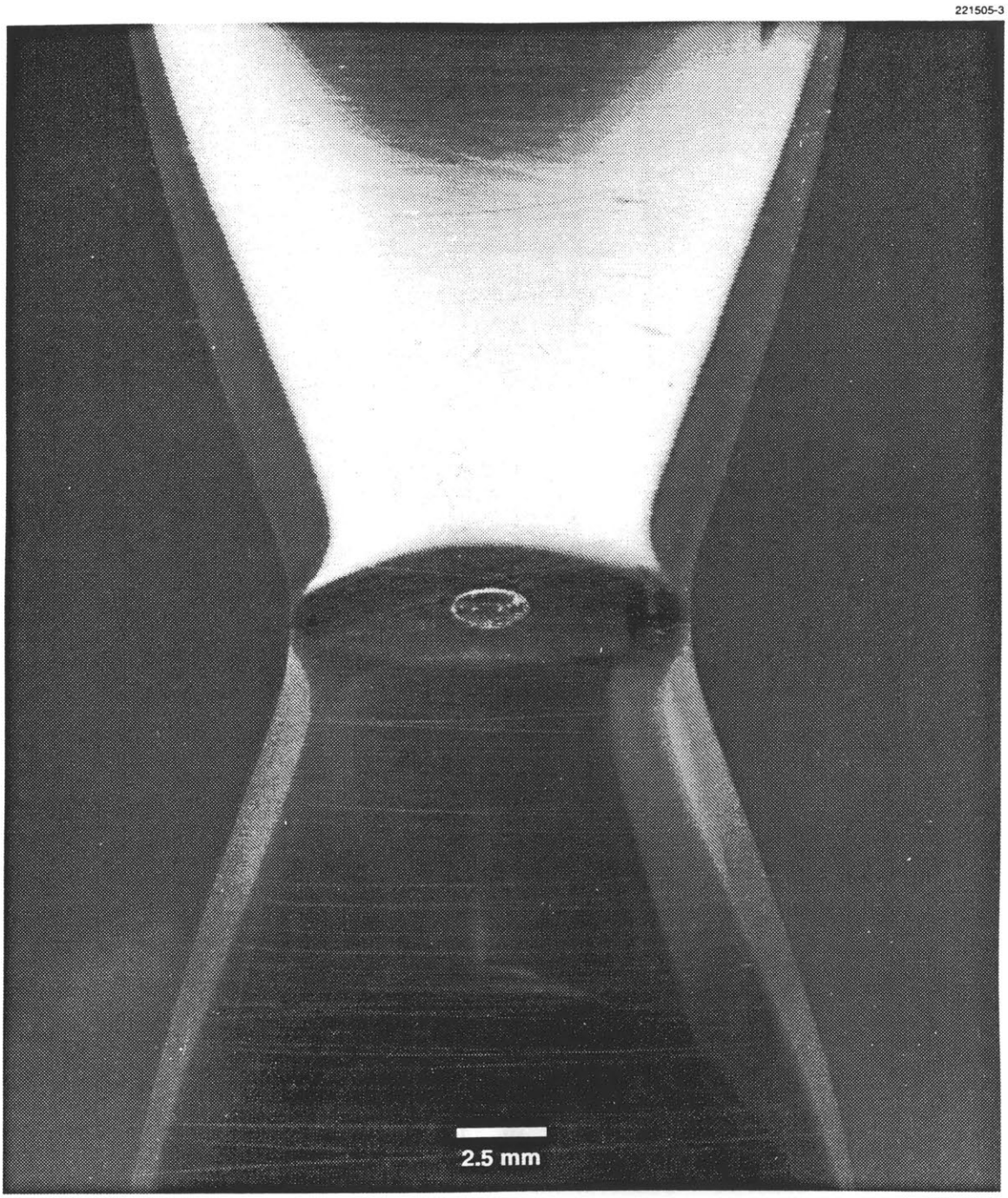

Figure B.4: Close-up of finished neck specimen with glass particle.

B.4.2 Testing Procedure

To apply tensile force to the adhesive strength neck specimens, special grips were machined from aluminum blocks. Each grip consisted of two mating halves, bolted together and bored out to accommodated the contour of the specimen ends. A beveled surface at the bottom of the grips, matching the tapered shoulder of specimens, provided the bearing surface for load transmission. Large (25-mm diameter) pins connected the grips to a standard materials testing machine (Instron 1125).

The neck specimens were strained in tension at room temperature with a grip-displacement rate of 5 mm/min. This translates to a nominal applied strain rate of $\dot{\varepsilon} \sim 3.3 \times 10^{-4}\,\mathrm{s}^{-1}$, based upon uniform deformation of the entire specimen length. Due to the nonuniform diameter of the specimens, the actual strain rate was about an order of magnitude faster (indicated by finite element simulations). Load data were measured with a 45 kN load cell and recorded on a time-based strip chart recorder.

During the applied loading of each specimen, a 16-mm movie image of the sphere was recorded at a framing rate of 24 fps. Lighting was provided by a fiber optic light source. The start of each film segment was synchronized with locations on the strip chart, so that correlation of the film rate and chart speed would provide the magnitude of applied load corresponding to debonding events.

B.4.3 Example Debonding Images

Debond events in neck specimens containing particles with low to modest adhesive strength to epoxy, such as Delrin and Nylon, or PC and silica-glass particles with release-coated surfaces, could usually be observed both in real time and when viewing the recorded films. Debonding always initiated at either or both poles of the sphere. In cases with very low adhesive strength (Delrin), debonding continued to advance over the entire surface, until at least an entire hemisphere was debonded and little traction could be applied to the sphere. In cases with moderate adhesive strength and interfacial toughness, debonding advanced slowly along the interface until conditions became favorable for the crack tip to kink into the epoxy. At this point, the critical crack size for the current stress level had invariably been reached, and rapid fracture ensued across the neck.

A sequence of images recorded during the debonding of a Delrin particle are shown in Figure B.5. In these images, the debonding is manifested by dark patches growing on the surface and by bright reflection of the light incident upon the surface. In the example shown here, the debonding of the Delrin sphere proceeded initially from the South pole, but was joined by debonding from the North pole prior to the unloading of the neck specimen. Photographs reproduced in Figure B.6 show two Nylon spheres which have debonded over hemispheres in a similar manner.

Specimens of PC or silica-glass which had been treated with a release agent also debonded at their poles slowly enough to record the process on film. Images of a treated PC sphere before and after debonding are shown in Figure B.7; in this case, the debonding upper hemisphere did not reflect additional light, but created a faint "ghost" image with a larger radius. Images of a treated glass sphere before and after debonding are shown in Figure B.8; in this case, the debonding lower hemisphere became apparent from a bright, growing patch of reflected light.

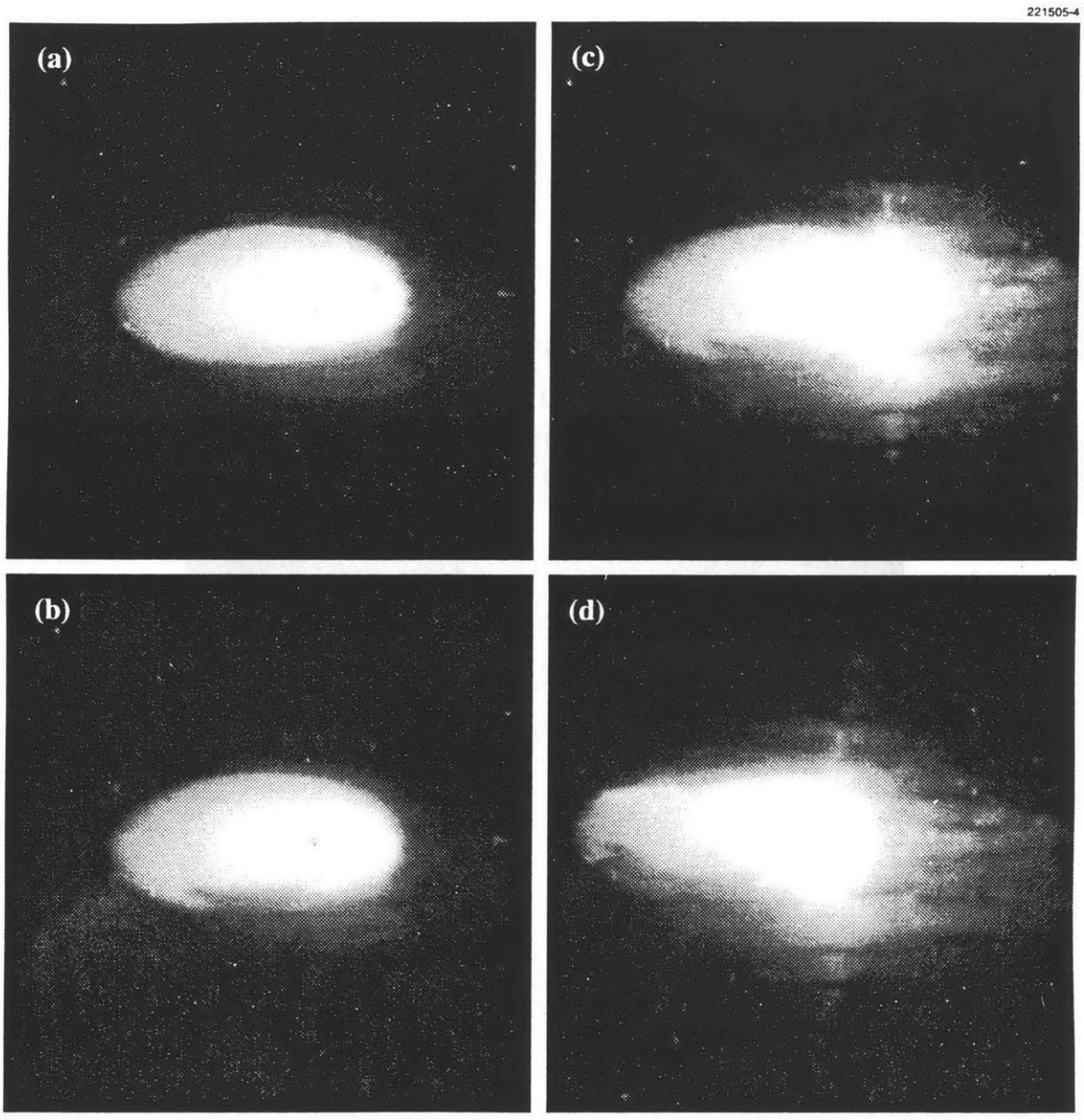

Figure B.5: Sequence (a–d) of 16-mm images recorded during debonding of Delrin sphere in adhesive strength neck specimen.

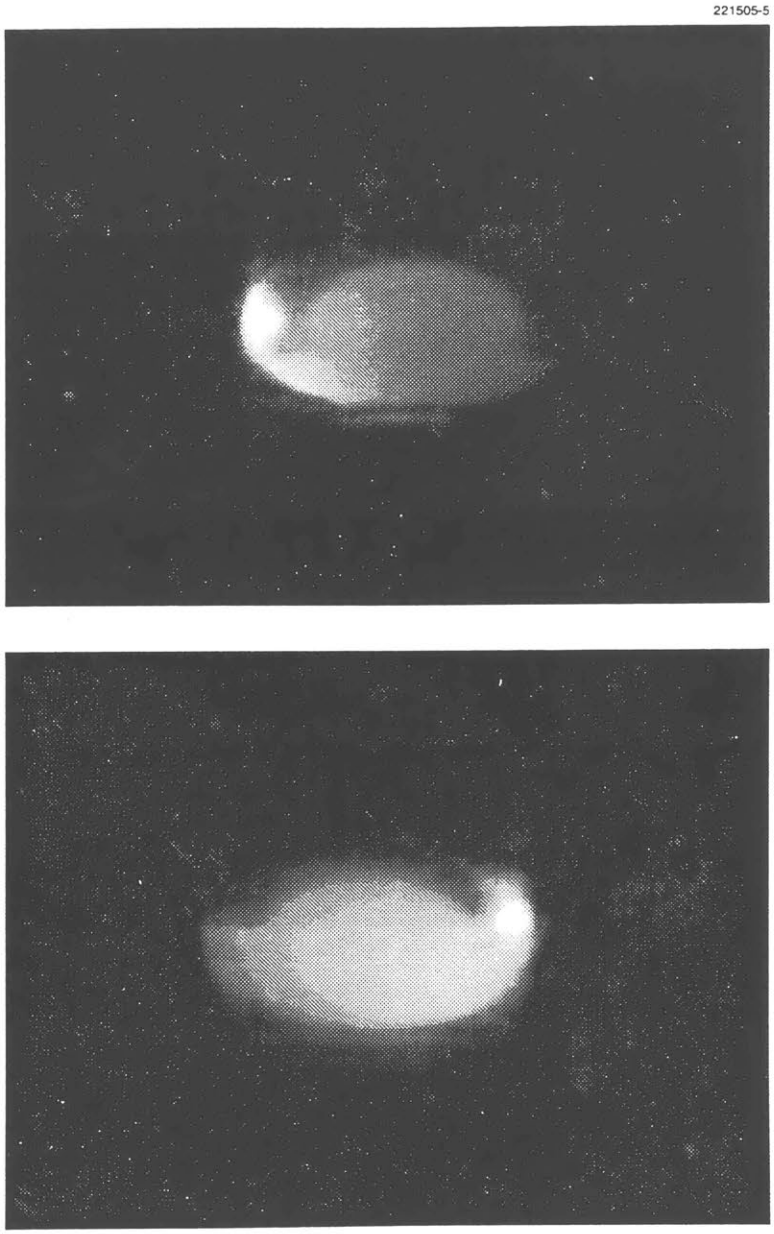

Figure B.6: Typical images of debonded Nylon spheres in two separate adhesive strength neck specimens.

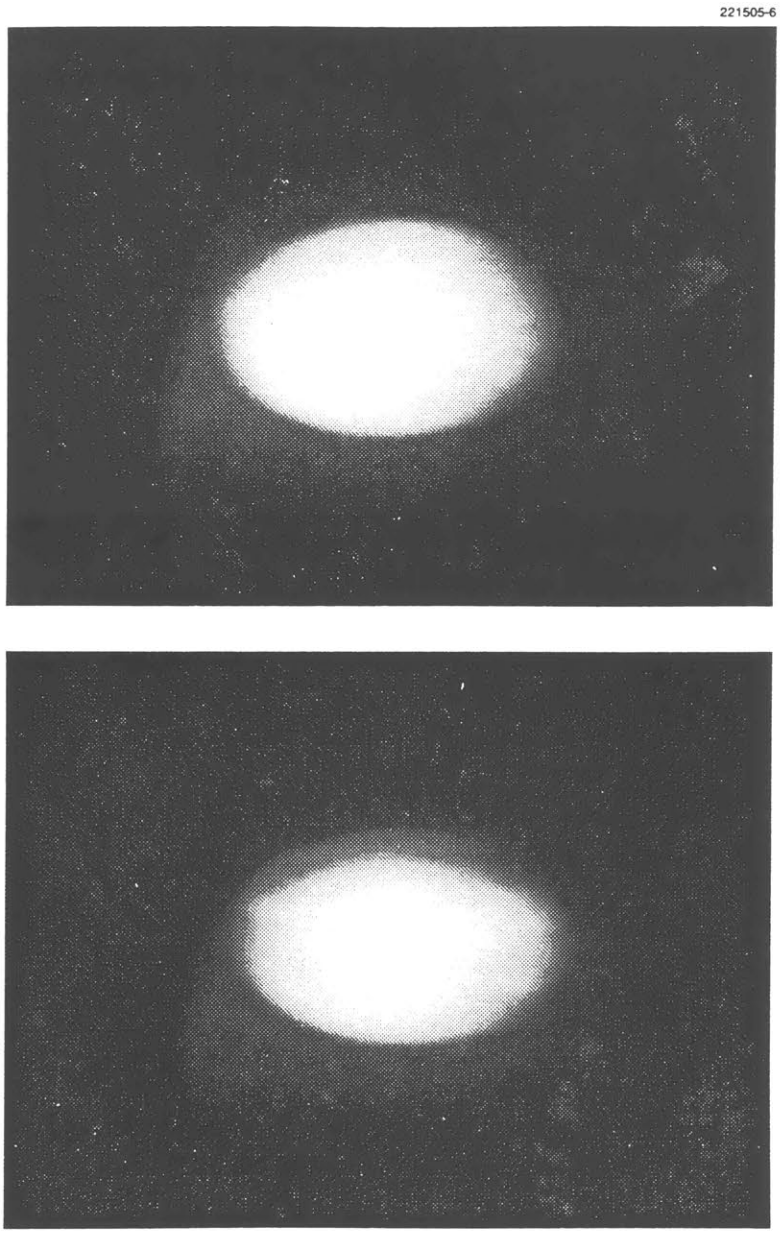

Figure B.7: Example of debonding of PC sphere treated with release agent. Upper image shows before, lower image after debonding near North pole.

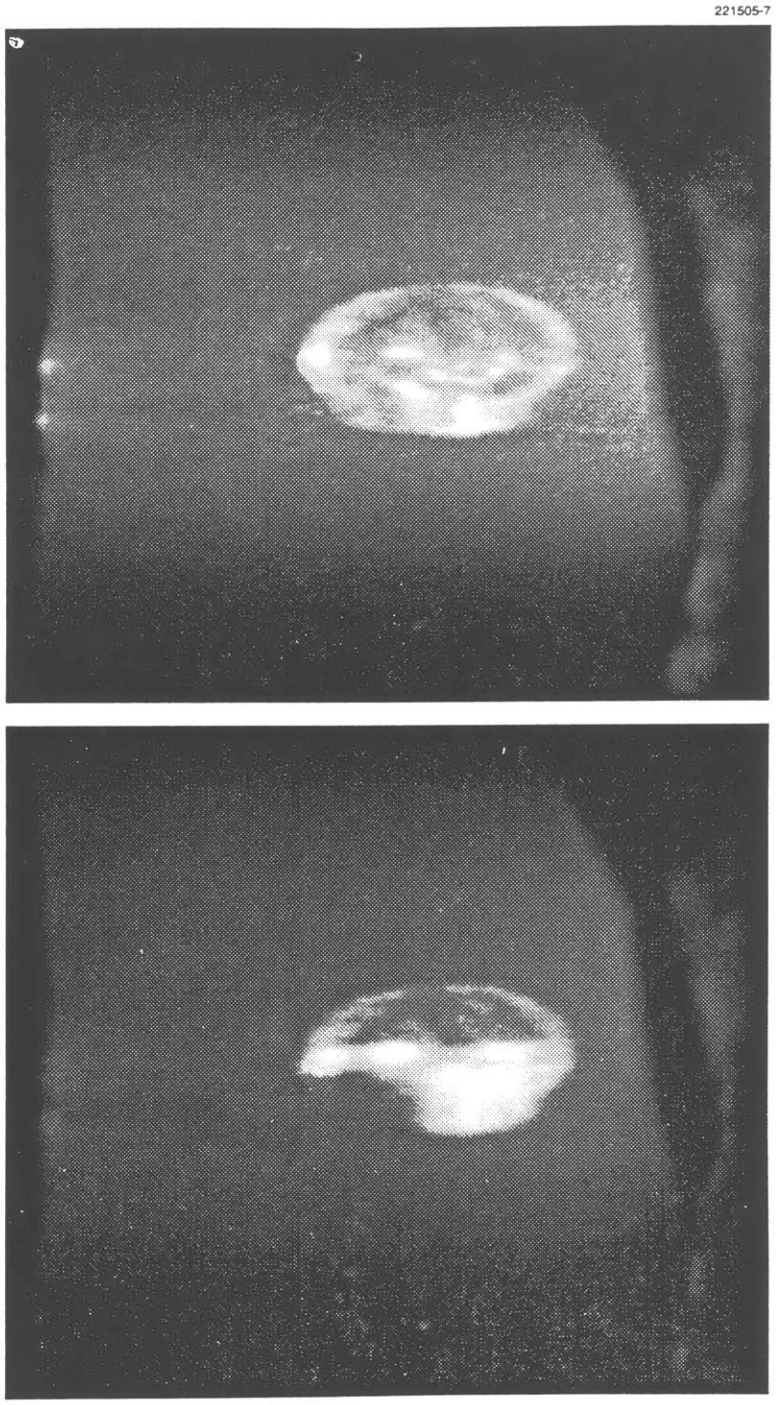

Figure B.8: Example debonding of a silica-glass sphere treated with release agent. Upper image shows before, lower image after debonding near South pole.

In cases of extremely well bonded particles, such as silica-glass or polycarbonate, debonding occurred at such a high applied load that the critical flaw size[3] was quickly reached and rapid fracture of the specimen ensued. In these cases, no debonding images were recorded (due to the slow filming frame rate of 24 fps), and the debonding load was simply determined from the peak load at specimen failure.

A typical example of a fracture resulting from the debonding of a glass sphere in a neck specimen under a high loading is reproduced in Figure B.9. The smallest area seen in the center of this photograph is the debonded region, where the crack travelled along the interface before kinking into the epoxy. When the crack first began propagating in the epoxy, it travelled at a relatively "slow" velocity (less than 100 m/s), leaving a smooth surface. (Directly beneath this area, and having a similar diameter, is the particle remaining in the epoxy. The particle can be seen in the original, color photograph but is not evident in the reproduction shown here.) The crack velocity then approached its limit of about 1/3 the elastic wave speed, $\sqrt{E/\rho}$, and began creating a rougher fracture surface. This surface extends to about one-half the radius, at which point the fracture surface becomes grossly rough, with large chips missing. The location of this transition corresponds well to the meeting of the crack front with the reflection from the free surface of the original stress wave created by the fracture initiation. Similar fracture surfaces were created by the debonding of glass spheres in other neck specimens.

An example of the failure of a specimen due to surface flaws, having no relation to debonding, is shown in Figure B.10. The fracture surfaces reproduced in this photograph show clearly that the failure of the specimen originated at the surface, presumably from a scratch that had not been removed by polishing or from a nick created in subsequent handling. Obviously, such failures resulted in no useful data.

[3]Corresponding to the applied stress and the toughness of the epoxy through the relation $\pi a_{cr} = \left(\frac{K_{Ic}}{\sigma_I}\frac{\pi}{2}\right)^2$, which is derived for a 3-D penny-shaped crack in Ref. [177].

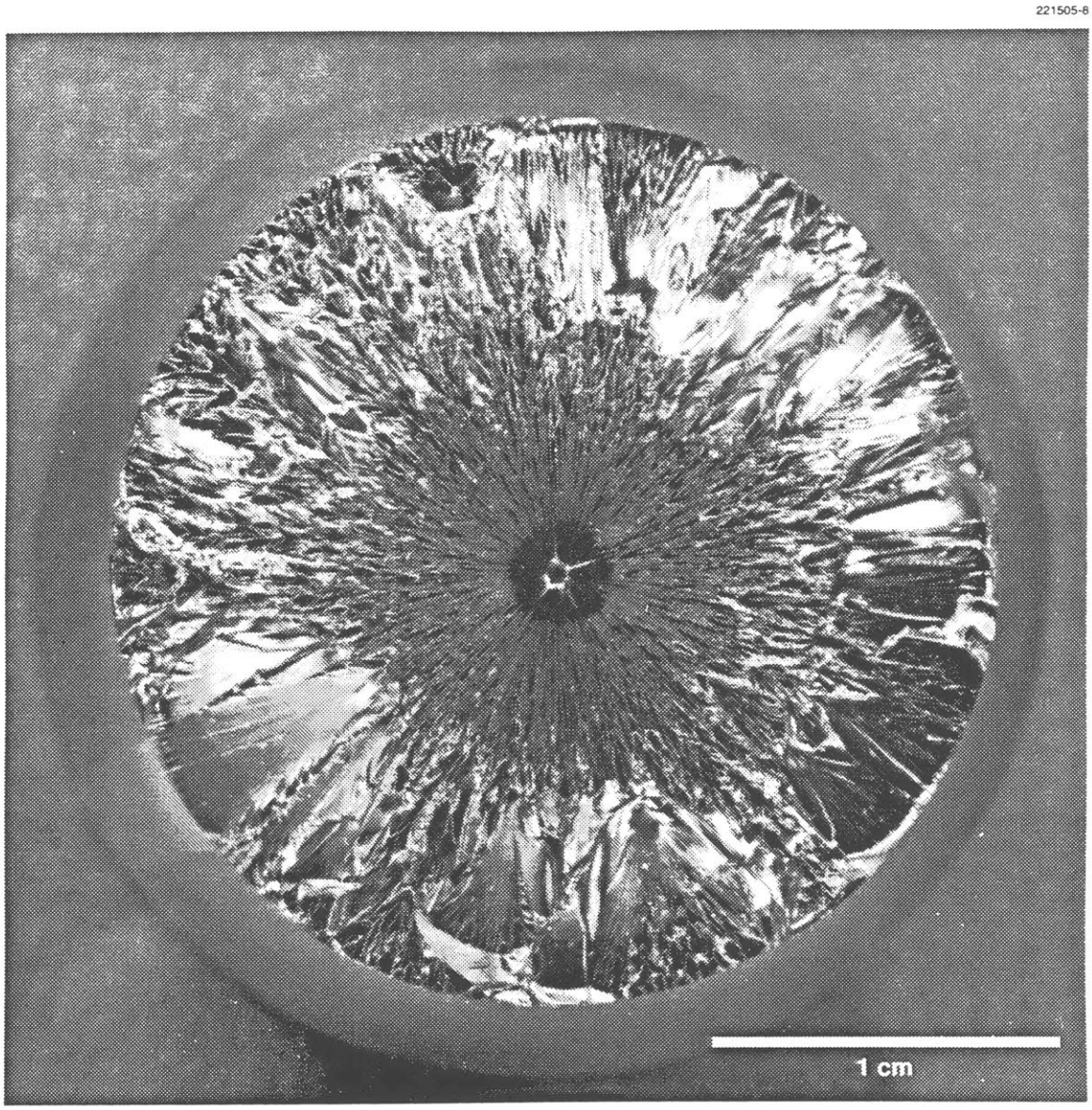

Figure B.9: Typical radial fracture initiated by debonding at pole of glass sphere. Crack travelled along interface a short distance, kinked into the epoxy, and propagated in three distinct modes (discussed in text). Particle remains below the exposed surface.

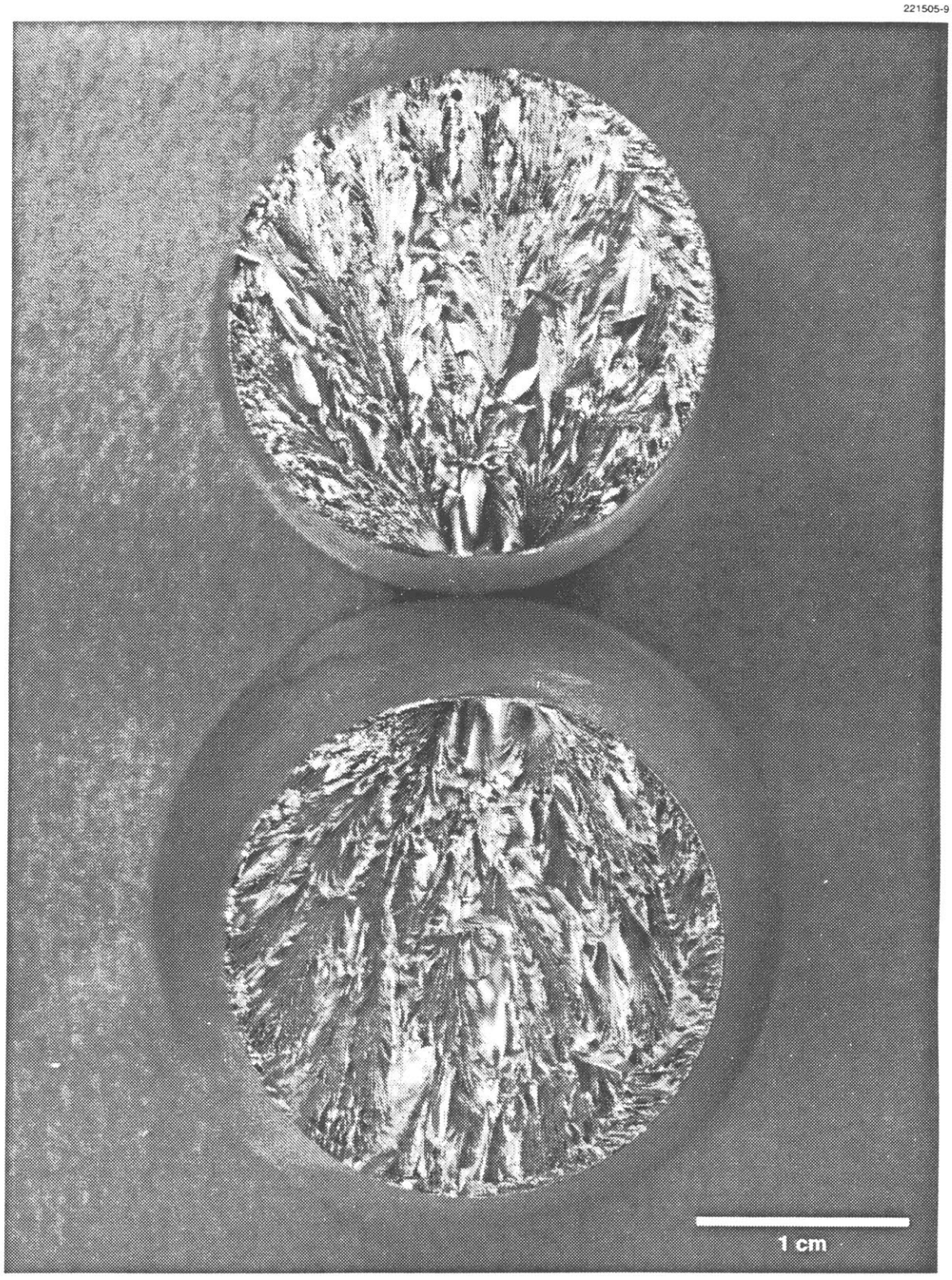

Figure B.10: Typical fracture initiated by surface defect.

B.5 Finite Element Stress Analysis

B.5.1 Elastic solution

A numerical solution for the stresses resulting from deformation of the adhesive strength neck specimens was obtained with the commercial finite element program, ANSYS, which was made available through an academic license [178]. This program was executed on a standard, 386-based PC.

The neck specimen was modeled with eight-noded, isoparametric, quadrilateral elements which naturally represent quadratic displacements. Stresses across these elements, being derivatives of strains, become linearly varying functions. Therefore, these elements provide better solutions to problems where stress gradients or curved surfaces are present than do constant-stress, four-noded elements. The additional number of nodes created by the mid-side nodes of the quadratic elements is more than offset by the opportunity to reduce the size of this (neck) problem through the use of symmetry.

Because the neck is a solid of revolution, it can be represented by axisymmetric finite elements, which reduce the problem to two-dimensions (one layer thick). In addition, the neck is symmetric about its center section. Therefore, boundary conditions of symmetry were applied to the longitudinal (y) axis and to the center radial (x) axis. No displacements or forces were applied to the free, contoured surface. Force loading was applied with equivalent pressures to the end section corresponding to the grip position.

The meshing density was adjusted so that increasingly finer elements were employed as the section radius decreased, as seen in the plot shown in Figure B.11. The central region, shown in Figure B.12, was finely divided with 786 elements, exclusive

of the sphere. The remainder of the neck which is not shown in this mesh plot was incorporated into an elastic superelement. This step greatly reduced computation times in the plastic solutions which required iterative computations. The sphere itself was modeled with 154 elements having edge lengths equal to about 8% of the sphere radius, as shown in Figure B.13.

An elastic finite element solution to the deformation problem of neck specimens containing Nylon spheres showed that, at the maximum debonding load which was experimentally recorded, the equivalent stress ($\overline{\sigma}$) everywhere remained below the rate-dependent yield stresses of both the epoxy and the Nylon. Consequently, just one (elastic) solution for a particular load furnishes stresses which would result from any other load, within the elastic range, simply by scaling the solution according to the applied load. In this elastic analysis, Young's modulus of the Nylon was taken (see Appendix A) to be $E = 2.8\,\text{GPa}$. Poisson's ratio for the Nylon was assumed to be $\nu = 0.34$; for the epoxy, a value of $\nu = 0.36$ was assumed. Young's modulus for the epoxy at the approximate strain rate generated during testing of the necks was taken (from Appendix A) as $E = 2.2\,\text{GPa}$.

Contours of equivalent (Mises) stress[4] generated from the solution of this problem, with an applied load of 16.5 kN, are plotted in Figure B.14. It can be seen from this plot that nowhere is the yield stress ($\approx 60\,\text{MPa}$, at $\dot{\varepsilon} \sim 10^{-3}\text{s}^{-1}$) of the epoxy exceeded. Radial stresses within and immediately adjacent to the Nylon sphere are plotted in Figure B.15, which shows, as expected, that the radial stress is continuous across the interface and is a maximum at the pole.

[4]All FE plots of equivalent stresses shown in this Appendix are unaveraged nodal stresses.

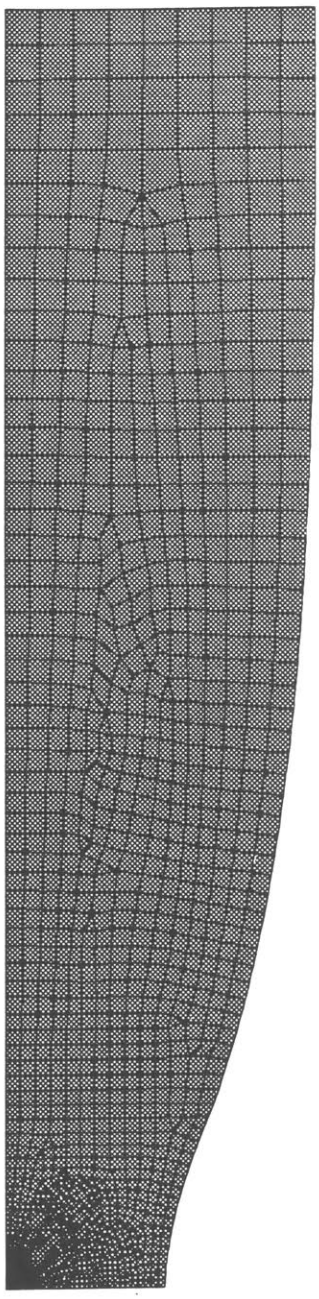

Figure B.11: Meshing used in FE model of the neck specimens used to measure adhesive strengths. A total of 1559 axisymmetric, quadratic (eight-noded) elements were employed, with a total of 4838 nodes.

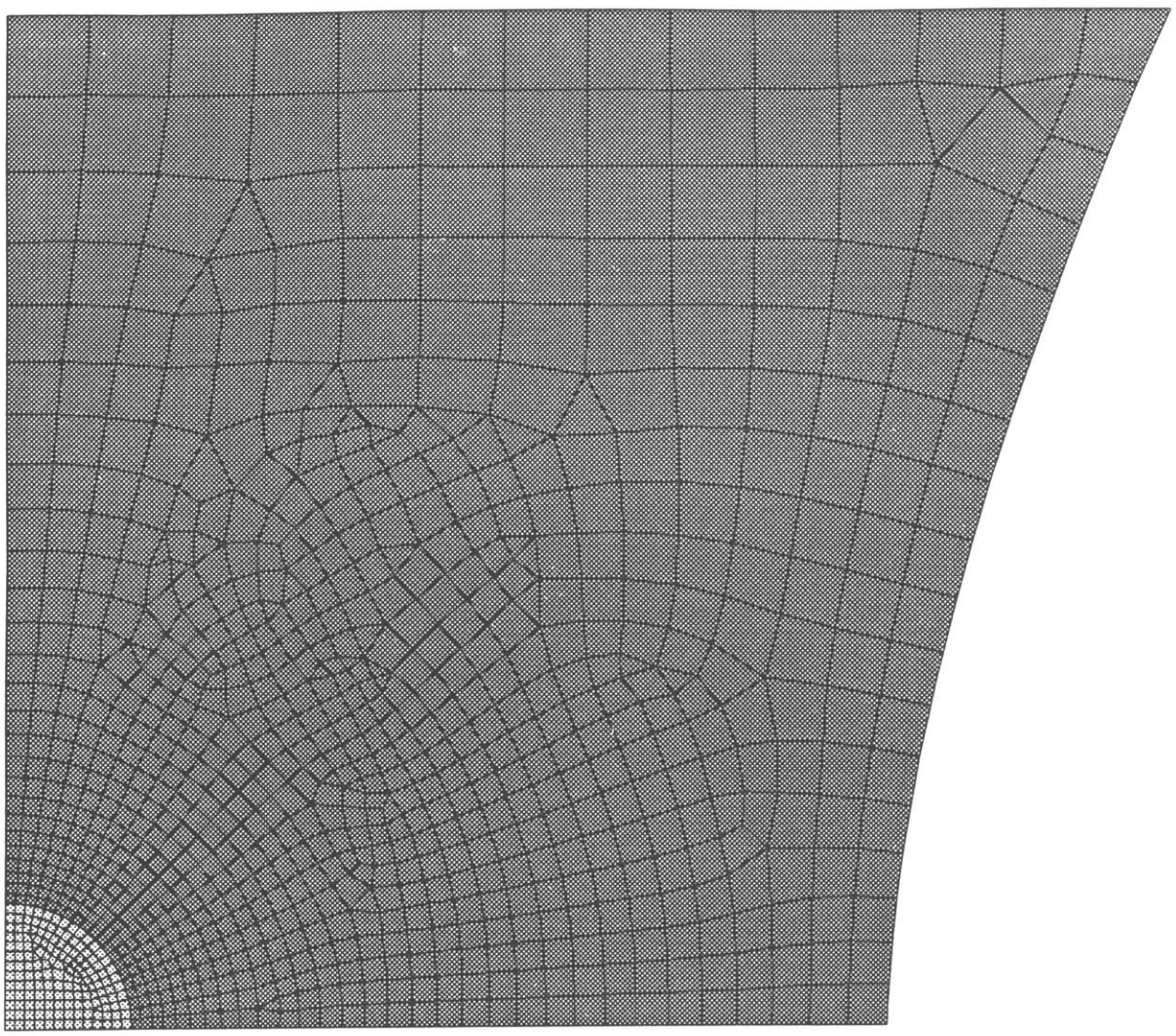

Figure B.12: Meshing used to model central portion of neck specimens. Elements shown here (except those representing sphere) were assigned a bilinear hardening behavior. The remainder of the specimen (*not shown*) was incorporated into an elastic superelement.

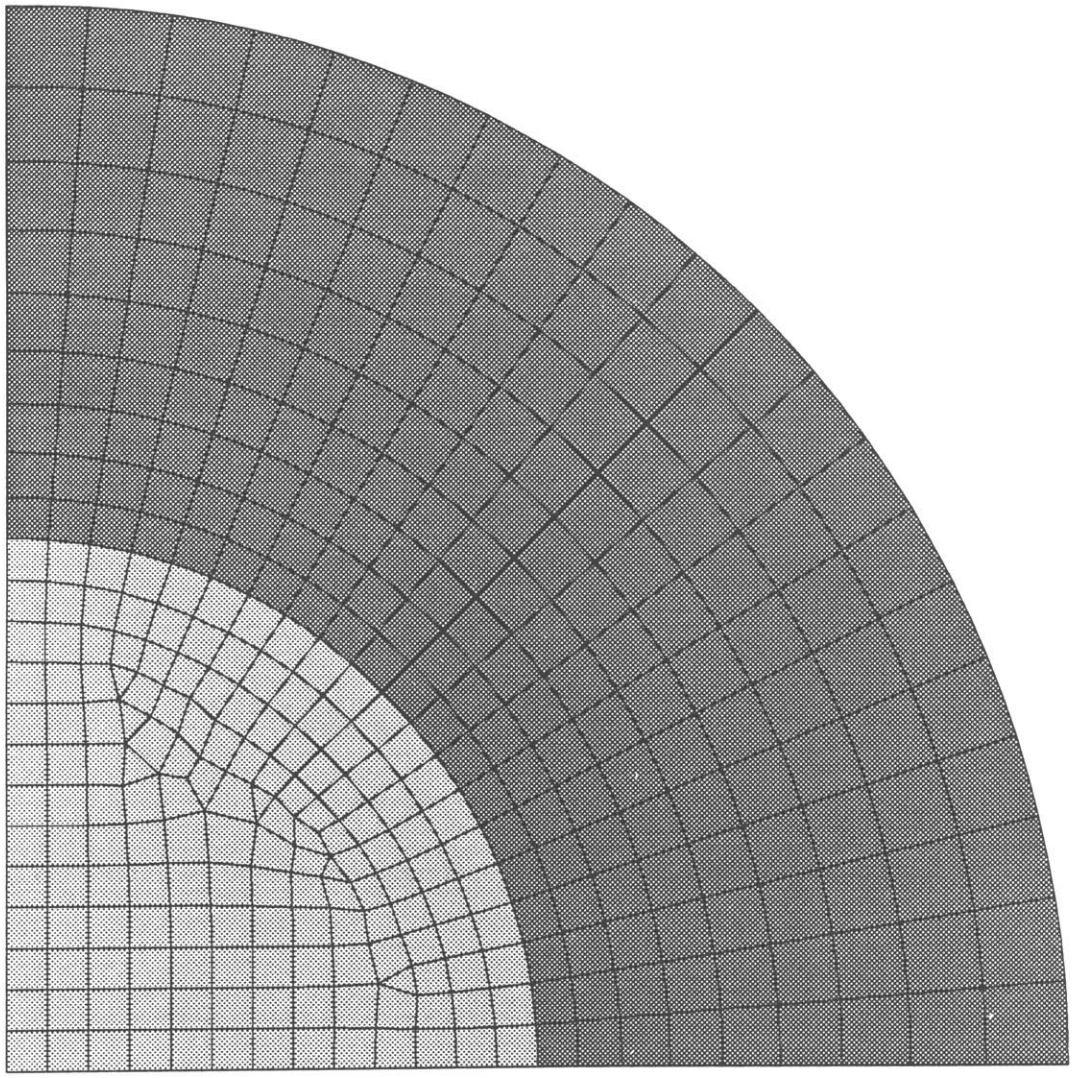

Figure B.13: Meshing used to model sphere and adjacent region of neck specimens. The sphere is represented by 154 axisymmetric, quadratic (eight-noded) elements. Shell surrounding sphere contains 180 similar elements.

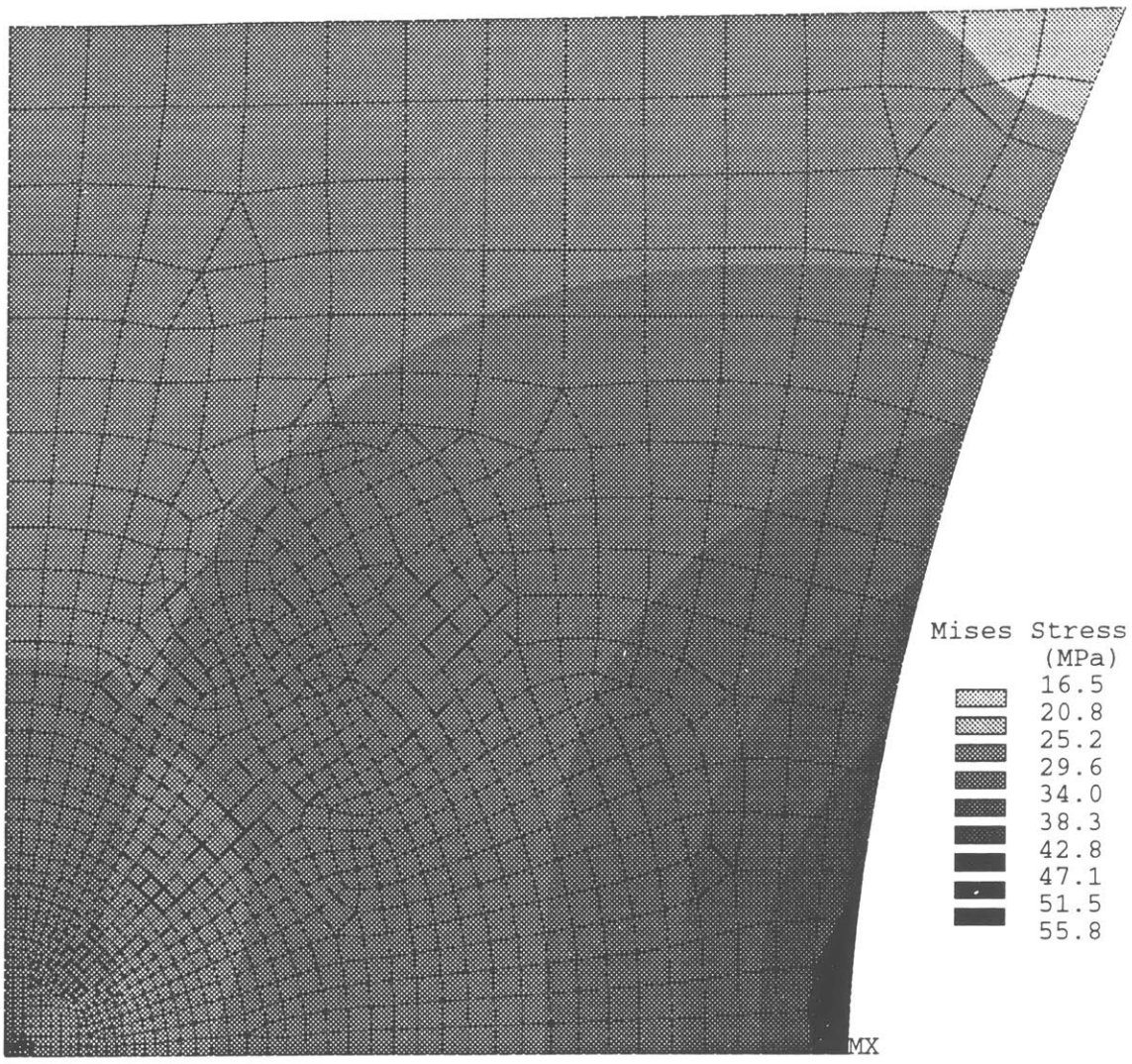

Figure B.14: FE computed equivalent stress, $\overline{\sigma}$, in central region of neck specimen containing Nylon sphere, loaded with pressure on the end section equivalent to a force of 16.6 kN. The approximate yield stress ($\sigma_y \approx 60$ MPa) of the epoxy is not reached anywhere, in this static, elastic analysis.

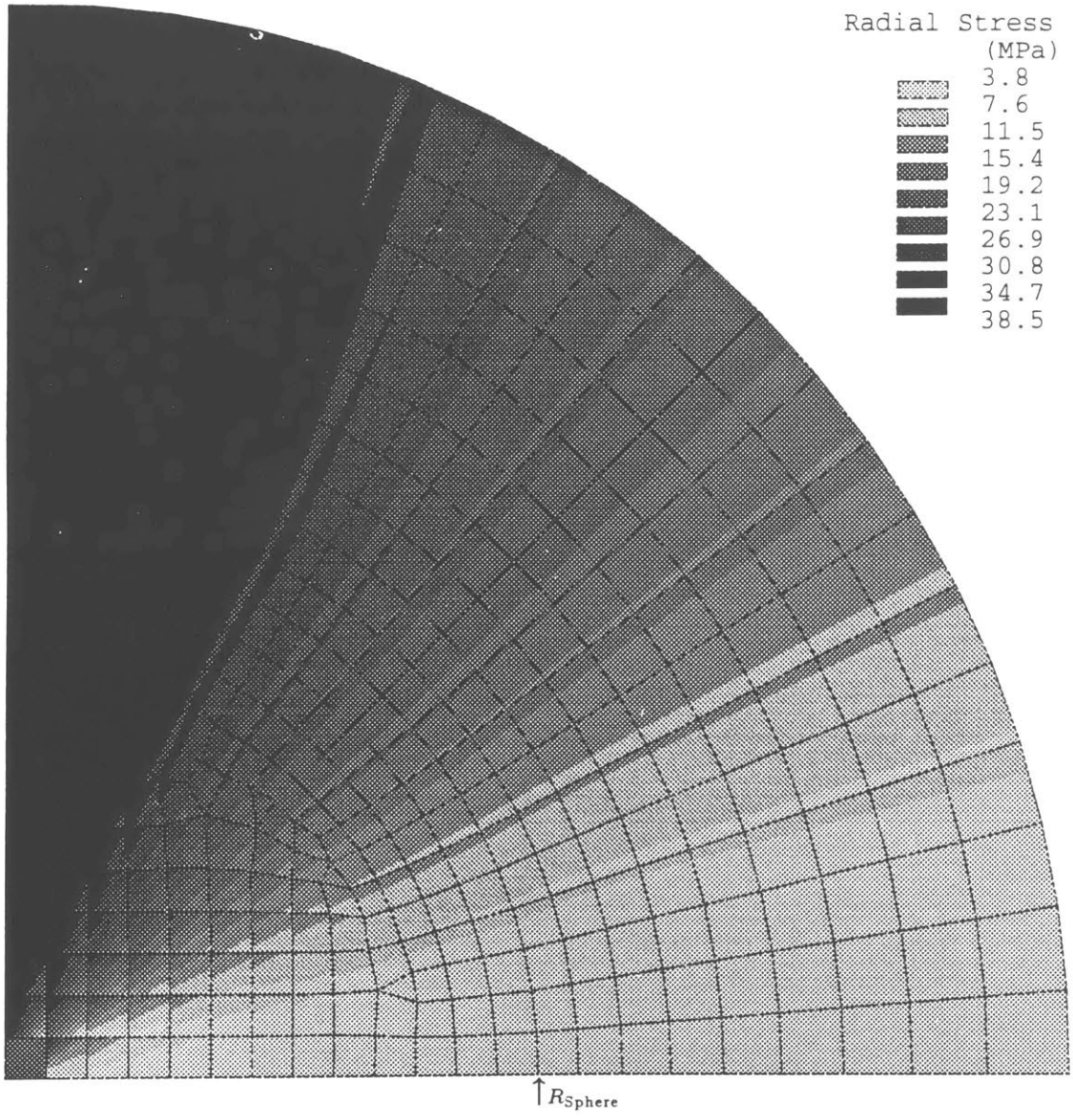

Figure B.15: FE computed radial stress, σ_r, within and outside of Nylon sphere in neck specimen loaded with 16.6 kN. (Unaveraged nodal stresses)

B.5.2 Plastic solution

Analysis of neck specimens containing particles with relatively high adhesive strengths required a plasticity solution, with the adoption of a nonlinear stress-strain property for the epoxy. In the case of necks containing PC spheres, the yield stress of the epoxy was exceeded simply because the debonding load (experimentally observed) was great enough to cause extensive yielding (determined with the FE analysis) to develop at the surface of the neck and spread inward. In the case of silica-glass spheres, much less yielding developed at the surface of the neck, but significant flow in the epoxy was predicted by the FE analysis to occur above the particle itself, due to the (factor of 32) modulus mismatch.

The nonlinear numerical solution was implemented by incrementally applying the load in 1.3-kN load steps. Within each load step, the load vector was incrementally increased and iterative solutions computed. The criterion satisfied for convergence within each load step was that the plastic strain increment be less than 1% of the current elastic strain. Elastic properties assigned for the PC spheres were $E = 2.2\,\text{GPa}$ and $\nu = 0.35$; for the silica-glass spheres, $E = 69.5\,\text{GPa}$ and $\nu = 0.24$.

The softening and hardening behavior of the epoxy was represented by the linear approximations shown in Figure B.16. Also shown in this plot are typical, true stress-strain curves obtained from compression of epoxy specimens identical to the epoxy used in the neck specimens, at a strain rate similar to that experienced by the material in the central region of the necks. Evidence[5] that the yield stress in tension may be lower, by about 15%, than the yield stress in compression is the justification for the model approximation being noticeably lower than the stress-strain curves. The negative slope due to softening could not be incorporated due to the numerical

[5] Wronski and Pick reported measurements from epoxies indicating ratios of yield stress in tension/compression of approximately 0.75 [179]. This ratio was based upon engineering stresses, however. Correcting for true stress at yield strains, a ratio of about 0.85 results.

instability it would create. Therefore, the bilinear hardening model shown was deemed a suitable approximation to the true softening/hardening of the epoxy.

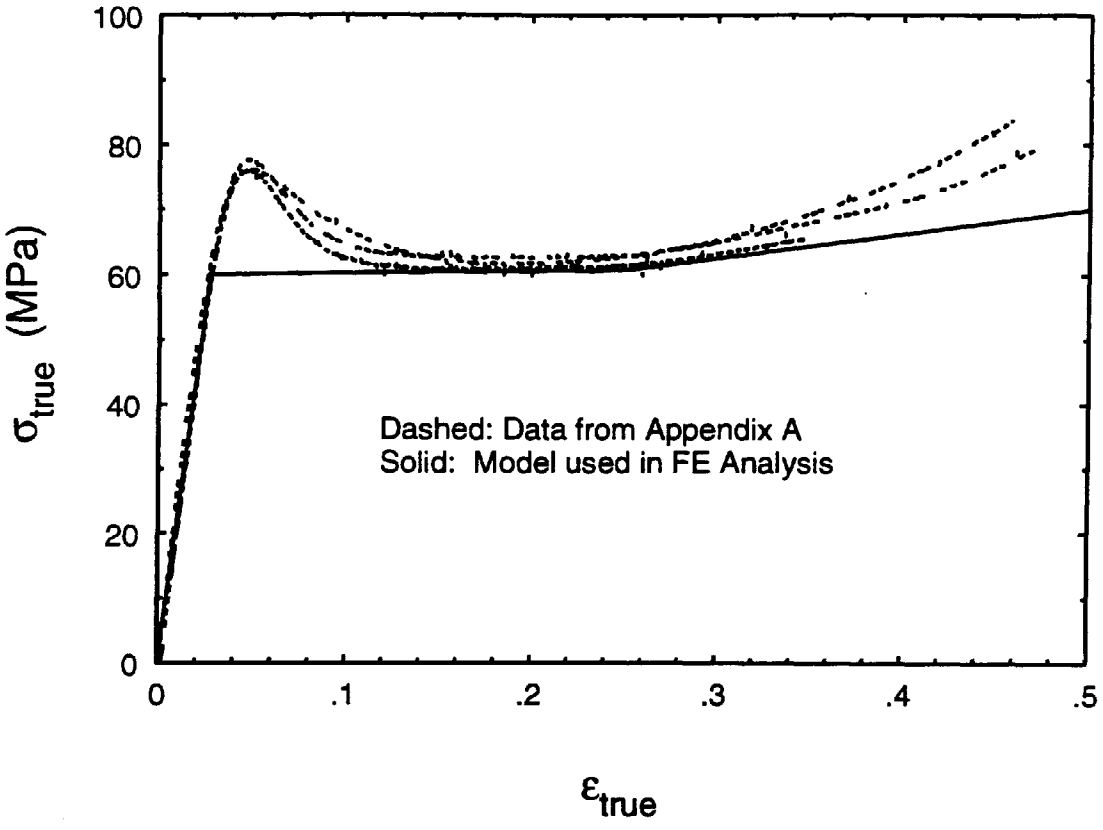

Figure B.16: Stress-strain behavior adopted for epoxy in nonlinear FE solution of neck specimen tensile deformation. Dashed curves obtained from compression of epoxy at $\dot{\varepsilon} \approx 10^{-3}\,\mathrm{s}^{-1}$.

The finite element solutions to the deformation of neck specimens containing PC spheres predict the growth of a region of plastic flow beginning at the surface of least radius and spreading inward towards the longitudinal axis, with increasing load. Reproduced in Figure B.17 is a contour plot of the equivalent stress, $\overline{\sigma}$, computed in the central region of the neck from an intermediate solution of the plasticity problem, corresponding to an applied load of 23.5 kN. It may be seen from the plot that, at this load, the yielding region has developed to only about 15% of the neck radius, and no flow has occurred near the sphere. Two more load steps brought the FE analysis to the highest load sustained by necks containing PC spheres, 26.2 kN. Contour plots of $\overline{\sigma}$ corresponding to this load are shown in Figure B.18, which indicates that the region of plastic flow has spread to about 35% of the neck radius, and still no yielding has occurred near the sphere. A plot of the radial stress within and near the PC sphere at this load is shown in Figure B.19.

Because the peak load experienced by neck specimens containing silica-glass spheres was lower than by those with PC spheres, yielding in the necks with glass spheres was not as extensive. Plastic flow was promoted, however, by the stress concentration resulting from the elastic mismatch between the silica-glass and the epoxy. Figure B.20 shows that $\overline{\sigma}$ resulting from the maximum load applied to necks with glass spheres exceeded the yield stress of the epoxy in three small regions: one at the neck surface of least radius, and two near the sphere. In Figure B.21, one of the plastic regions near the sphere is seen to be directly above the particle and the other is on the particle surface at about 45°. A plot of the radial stress within and near the glass sphere is shown in Figure B.22.

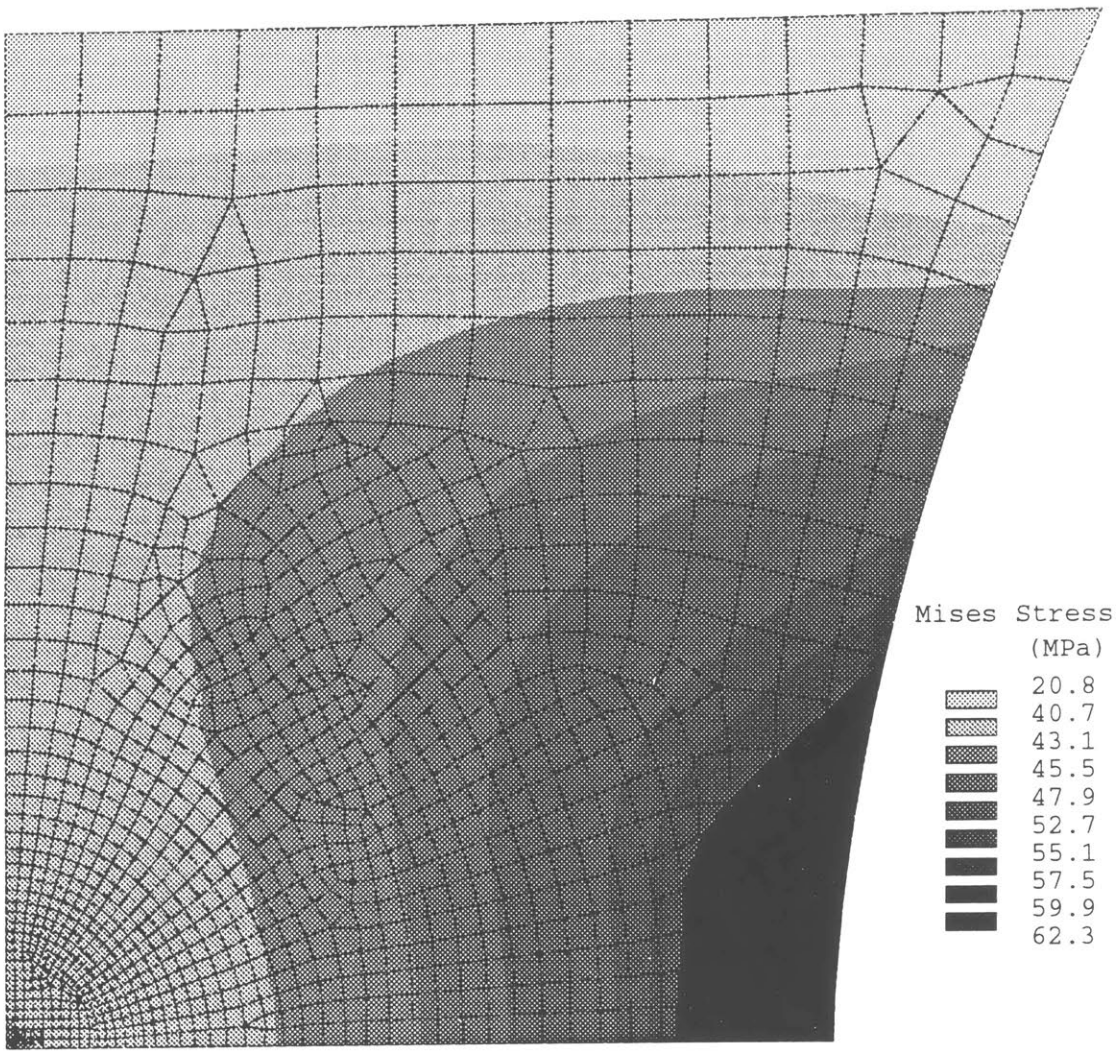

Figure B.17: FE computed equivalent stress, $\overline{\sigma}$, in central region of neck specimen containing PC sphere, loaded incrementally to 23.57 kN. The approximate yield stress ($\sigma_y \approx 59.9$ MPa) of the epoxy is exceeded at the neck surface of smallest diameter and has begun to grow.

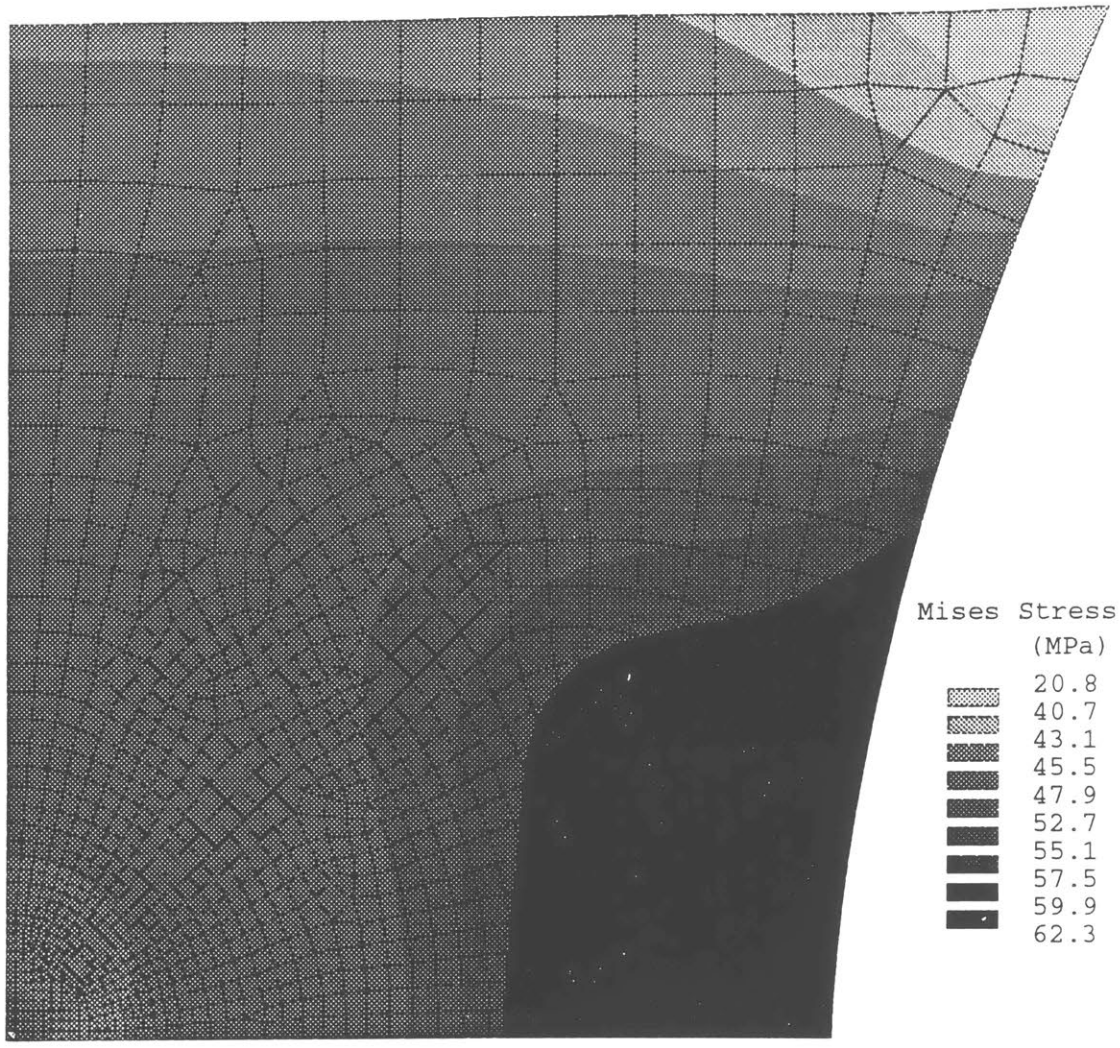

Figure B.18: FE computed equivalent stress, $\overline{\sigma}$, in region near PC sphere in neck specimen loaded incrementally to 26.2 kN. The yielding zone of epoxy has expanded considerably inward from the neck surface; no plastic flow has developed near the sphere.

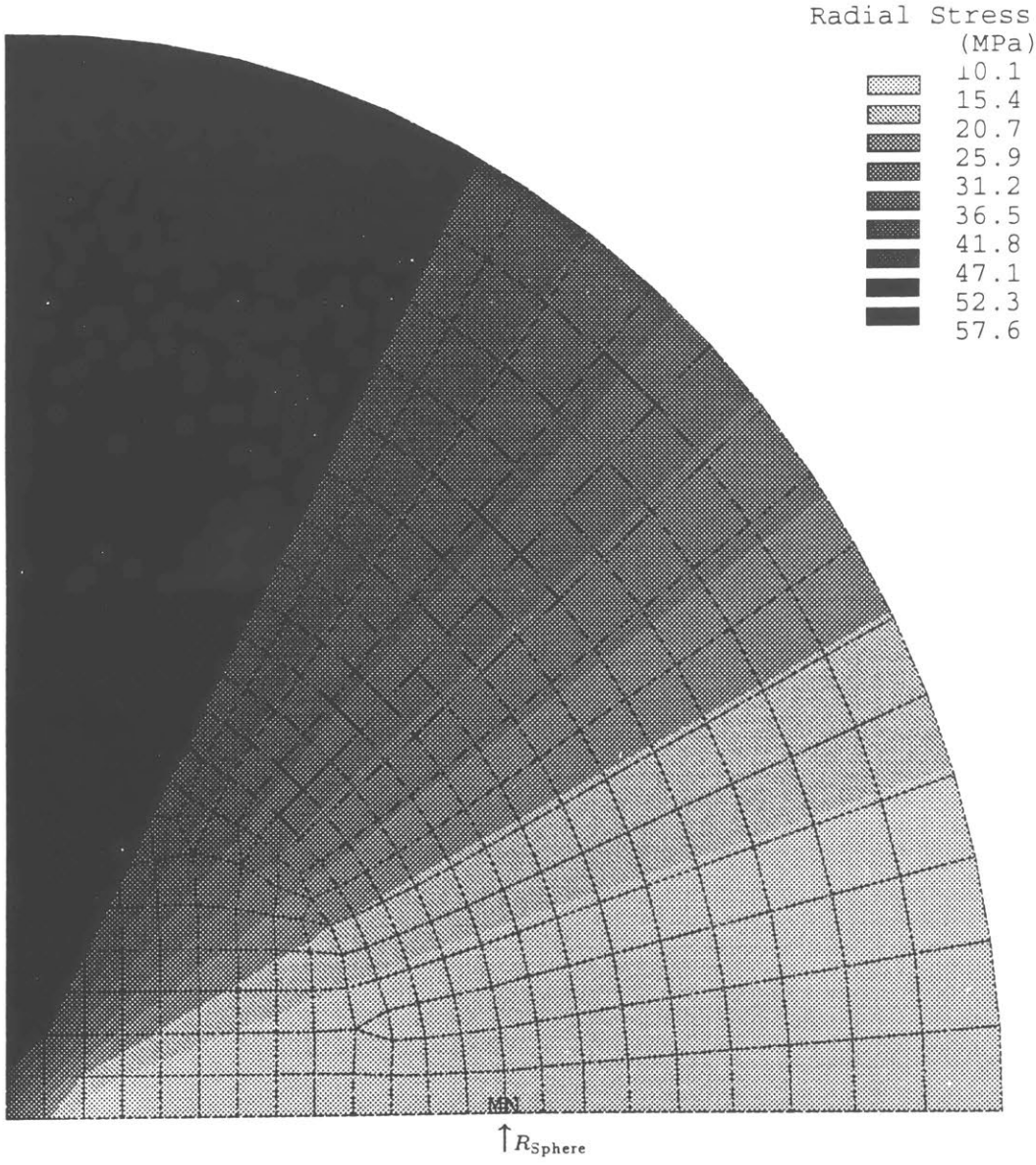

Figure B.19: FE computed radial (averaged) stress, σ_r, within and outside of PC sphere in neck specimen loaded incrementally to 26.2 kN.

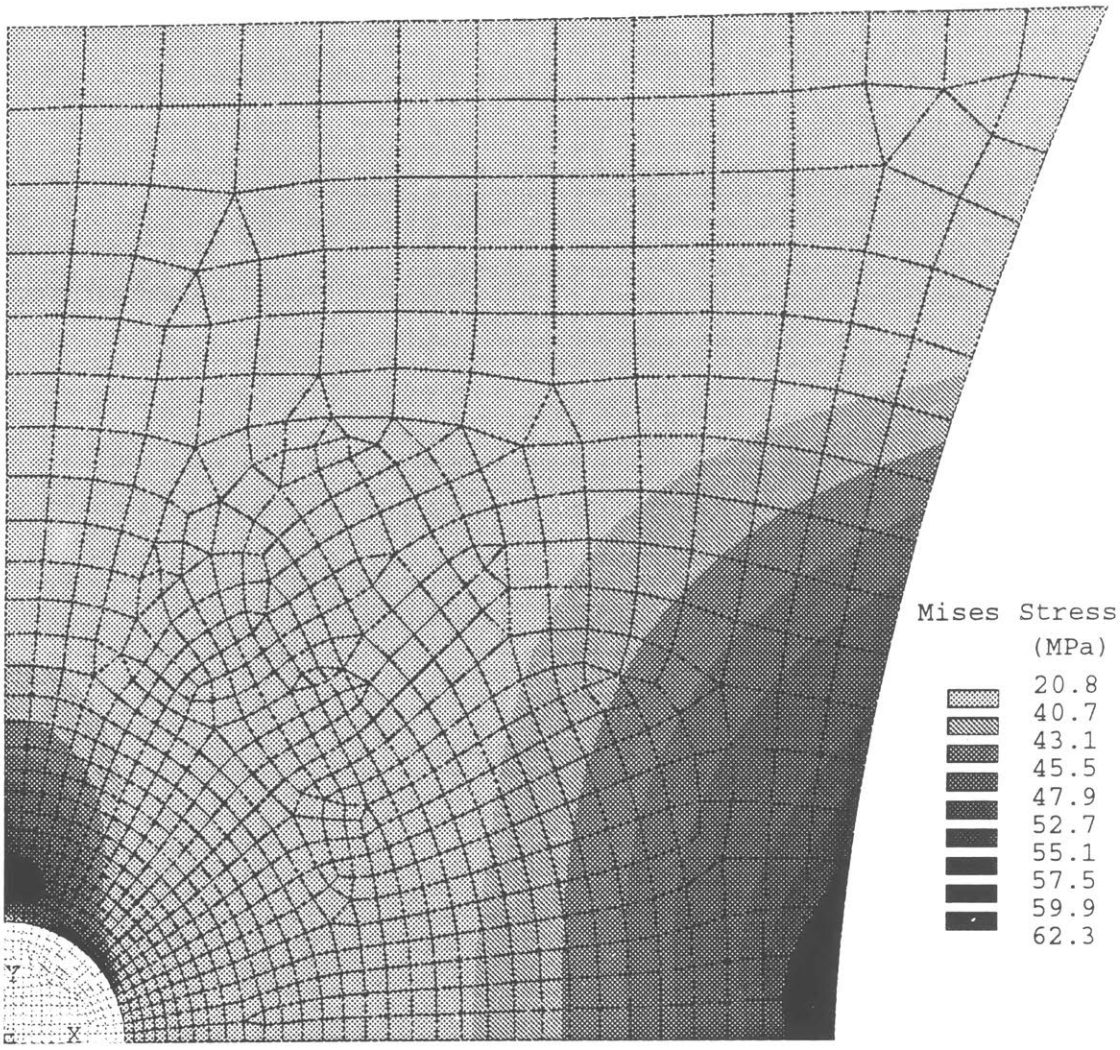

Figure B.20: FE computed equivalent stress, $\overline{\sigma}$, in central region of neck specimen containing glass sphere, loaded incrementally to 20.46 kN. The approximate yield stress ($\sigma_y \approx 60$ MPa) of the epoxy is exceeded at the neck surface of smallest diameter and near the particle.

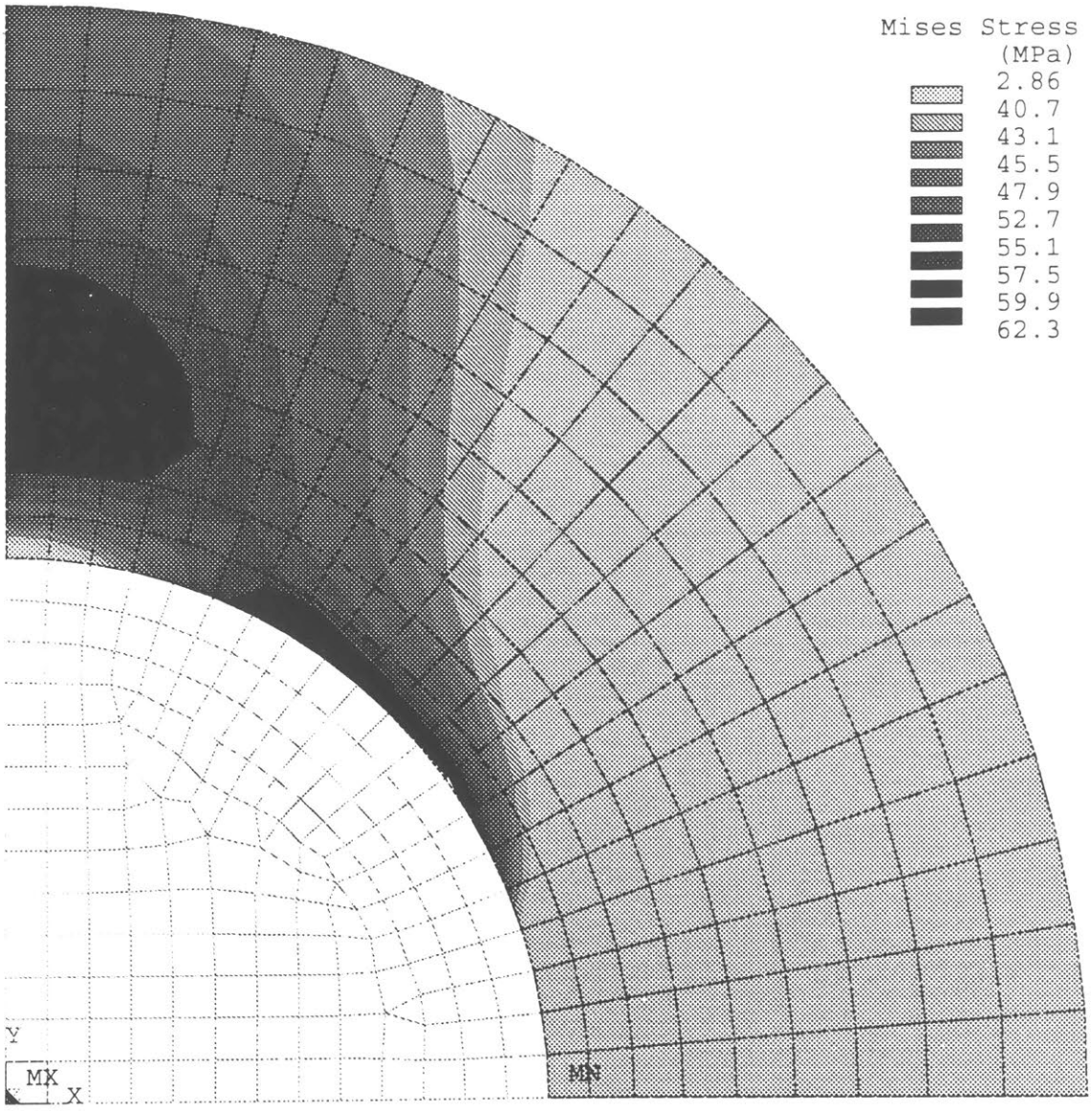

Figure B.21: FE computed equivalent stress, $\overline{\sigma}$, in region near glass sphere in neck specimen loaded incrementally to 20.46 kN. The approximate yield stress ($\sigma_y \approx 60$ MPa) of the epoxy is exceeded above the particle pole and on its surface at $\phi \sim 30 \rightarrow 60°$. Within the glass sphere, $\overline{\sigma} > 62$ MPa.

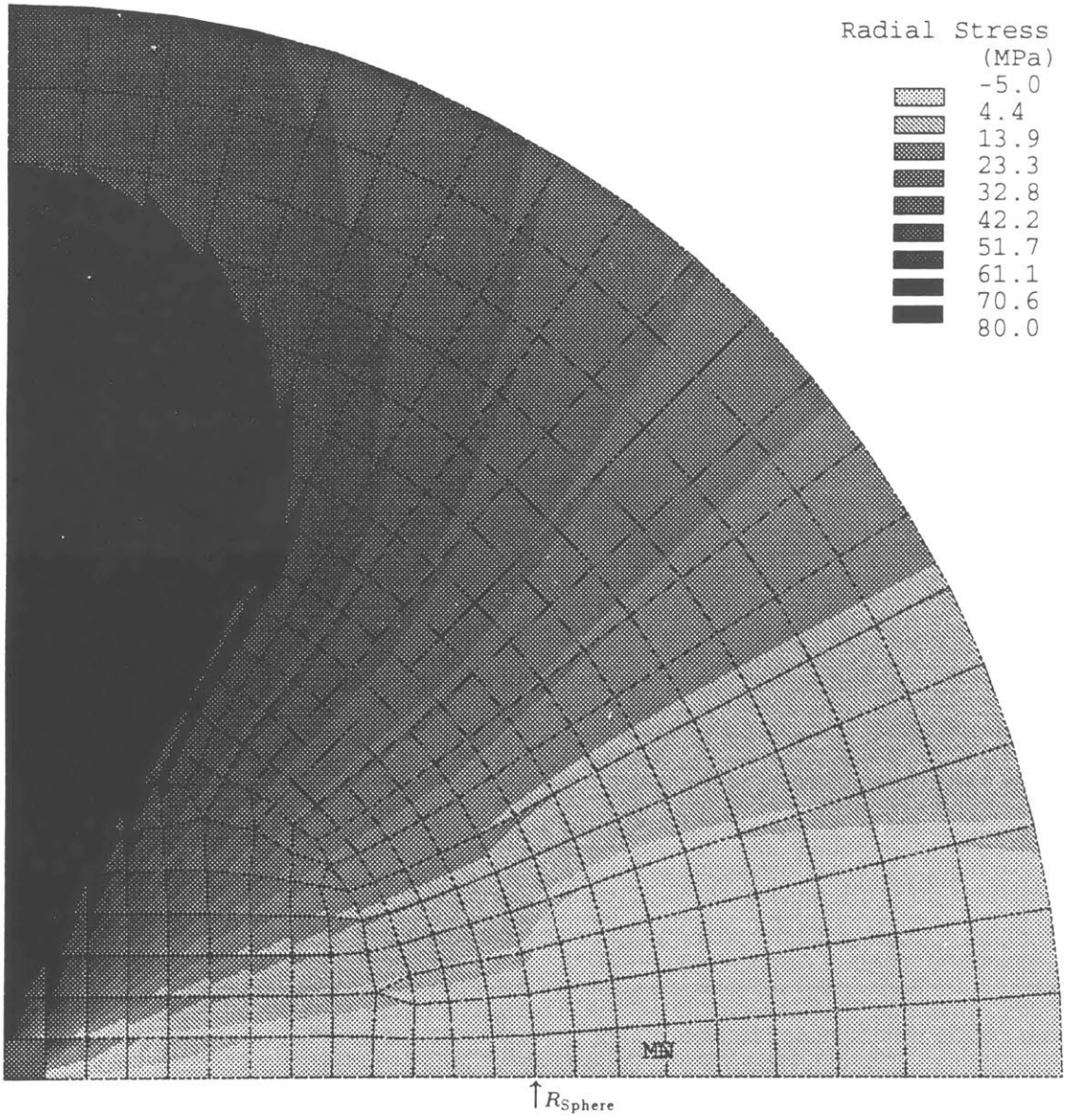

Figure B.22: FE computed radial (unaveraged) stress, σ_r, within and outside of glass sphere in neck specimen loaded incrementally to 20.46 kN.

B.5.3 Stresses @ particle surfaces

In naturally necked cylindrical bars, hydrostatic tension (σ) develops as a consequence of nonuniform strain hardening and deformed geometry. In bars machined to a natural neck profile, the hardness of the material is uniform at the onset of testing, but the contoured shape rapidly concentrates strain in the central region of the neck in a manner that generates triaxial tension [172]. As plastic flow develops throughout the volume of the neck, the triaxial stresses become more nearly equal so that hydrostatic tension results.

Because debonding of the spheres in the adhesive strength neck specimens occurred prior to the development of bulk plastic flow, the radial stresses which caused decohesion can not be represented by the sum $\sigma_y + \sigma$, as in Equations B.2 and B.3. Significantly, though, the state of stress at the surface of spheres in the neck specimens is one of triaxial tension which varies smoothly and has no singularities. The mean negative pressure, σ, computed with the finite element analysis is plotted in Figure B.23 as a function of angular position on the surface of spheres in neck specimens subjected to the maximum load recorded experimentally for debonding of each type of sphere material. The plots indicate that σ is nearly constant over the surface of each sphere, with the following exception. Near the poles and equators, mismatches in Poisson's ratio cause abrupt (computed) changes in the tangential normal stresses which result in similar computed changes in σ.

The radial stresses do not experience abrupt changes, but continuously vary from peak values at the pole to minima at the equator. Plotted in Figure B.24 are computed values of σ_r at the surface of the spheres, resulting from the same experimental maximum loads. The magnitudes of $\sigma_r$remain relatively constant (within $\sim$ 15% of the peak values at the pole) in each case as θ varies from 0 to about 20°. With increasing angular position from the poles, the radial stresses decrease in magnitude

rapidly[6]. Because there is no sharply localized stress concentration at the location where decohesion originates (invariably at the pole), the adhesive strength of the bond between a sphere and the neck material can be characterized well by the magnitude of polar radial stress.

Values of FE-computed σ_r at the poles of the three types of spheres are plotted in Figure B.25 as a function of increasing load on the neck specimen. These data are used in the next section to determine the adhesive bond strengths from experimentally observed decohesion loads.

[6]The radial stresses generated at the surface of spheres would remain more uniform if the flow stress of the neck material was lower than the adhesive strength between it and inclusions.

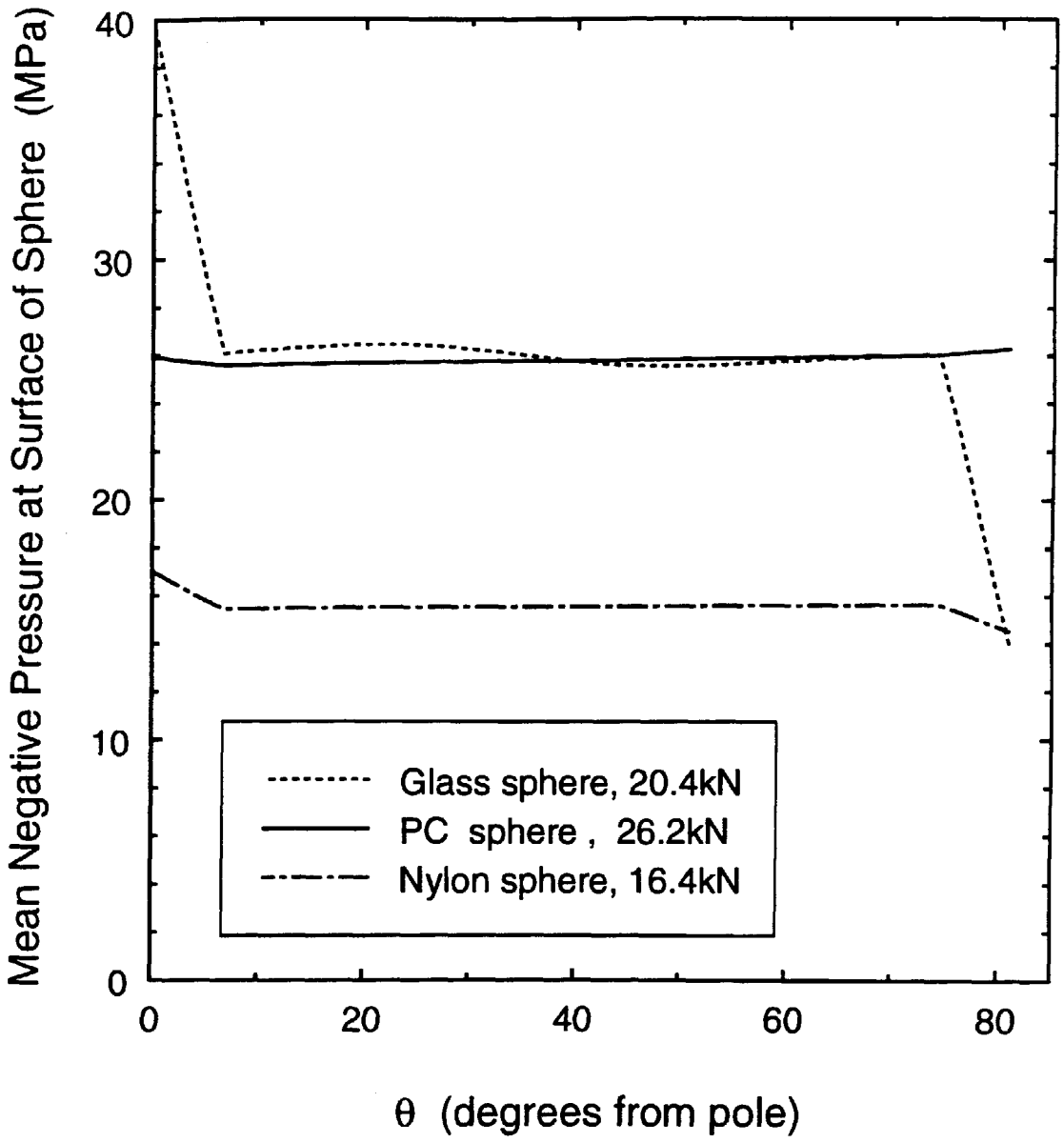

Figure B.23: Mean negative pressure at the surface of spheres in adhesive strength neck specimens subjected to the loads indicated. From FE analysis.

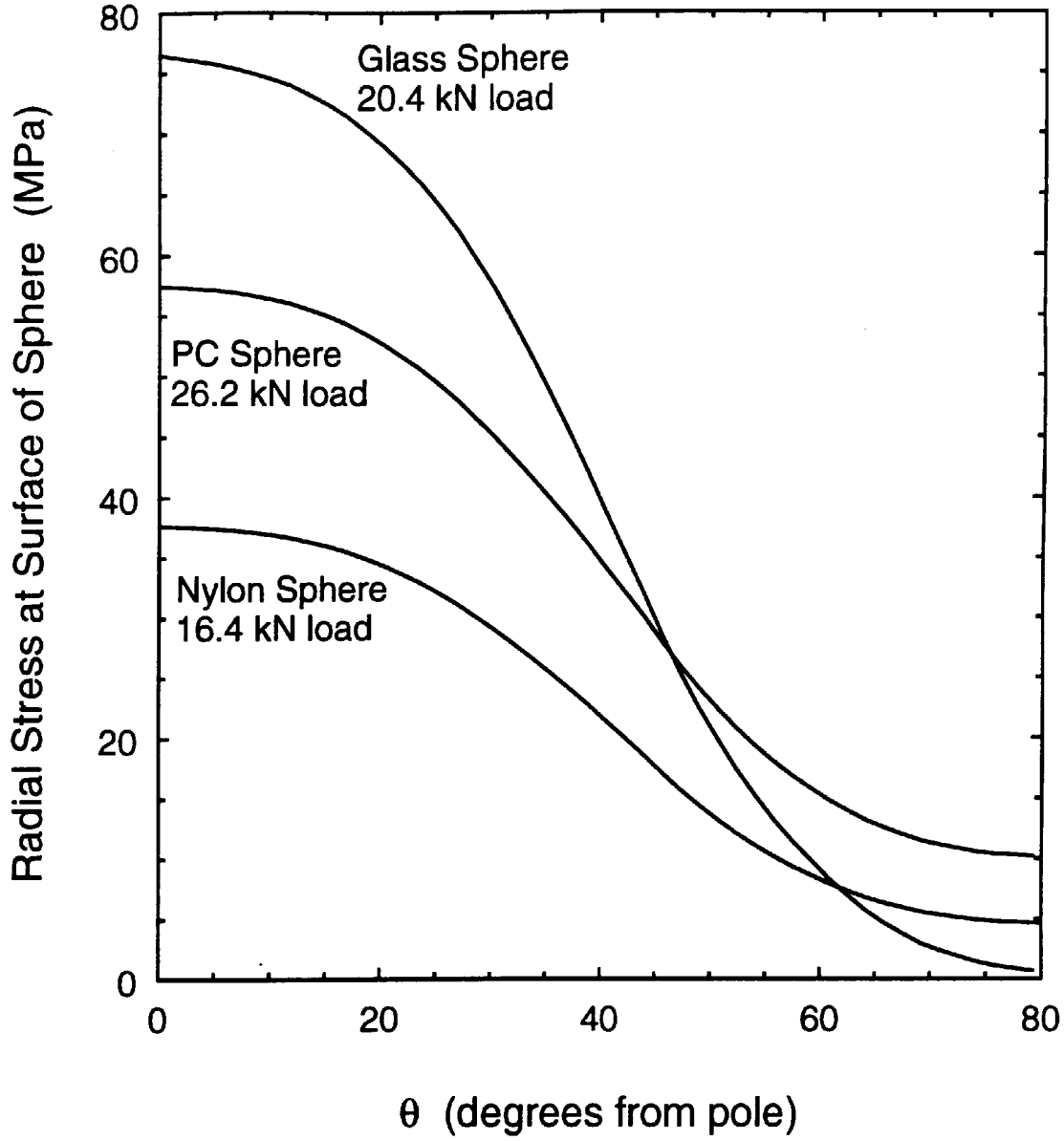

Figure B.24: Radial stress at the surface of spheres in adhesive strength neck specimens subjected to the loads indicated. From FE analysis.

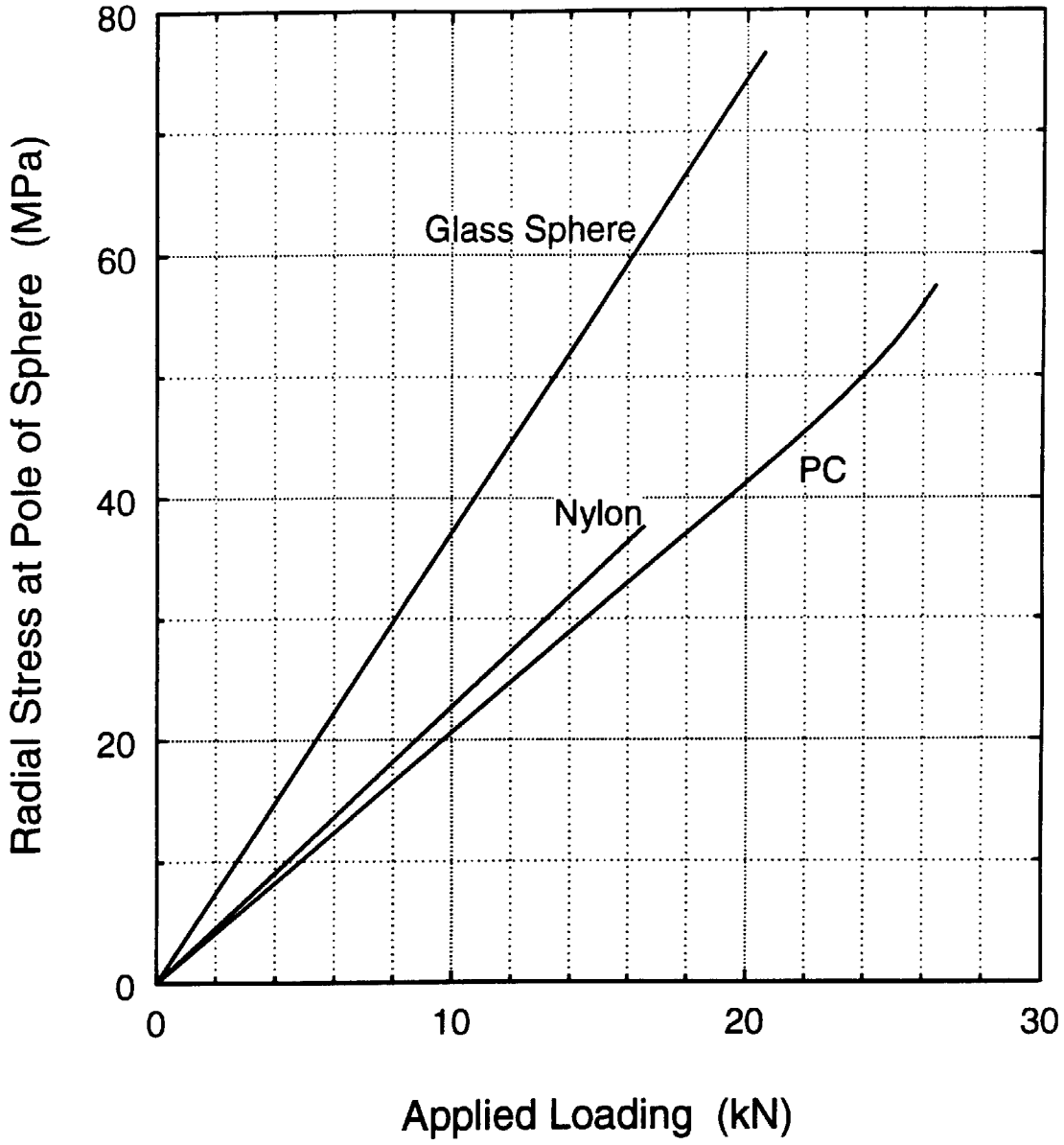

Figure B.25: Radial stress at the pole of spheres in adhesive strength neck specimens as a function of increasing load. From FE analysis.

B.6 Experimental Results

B.6.1 Microscopy of adhesive failures

The testing of the adhesive strength neck specimens resulted in debonding at the pole of all spheres in specimens which did not fail by fractures emanating from flaws in the epoxy. The nature of the process of debonding was similar in all cases. Upon reaching the critical load to cause the polar radial stress to reach/exceed the adhesive bond strength, a debonding flaw developed. This interfacial crack then propagated along the surface of the sphere, under decreasing Mode I loading, until the local stress intensities became favorable for the crack to leave the interface and "kink" into the epoxy neck. The crack then radially fractured the neck section, rapidly gaining velocity as it spread outward. This sequence of events may be seen in the following photomicrographs of the fracture surface of a typical specimen containing a silica-glass sphere.

In Figure B.26 the radial symmetry of fracture through the neck section is immediately apparent. Additionally, the smooth region surrounding the exposed glass surface is contrasted by surface striations which develop after the crack has reached a high enough velocity to cause Mode II components of stress intensity, which force the crack to become nonplanar. With higher magnification, Figure B.27 shows the sharp transition in the fracture path from the interface to the epoxy neck material. The short distance along the interface travelled by the crack is indicative of a tough (relative to the epoxy) interface; the surface of this sphere was solvent-cleaned, but otherwise not modified prior to inclusion in the neck.

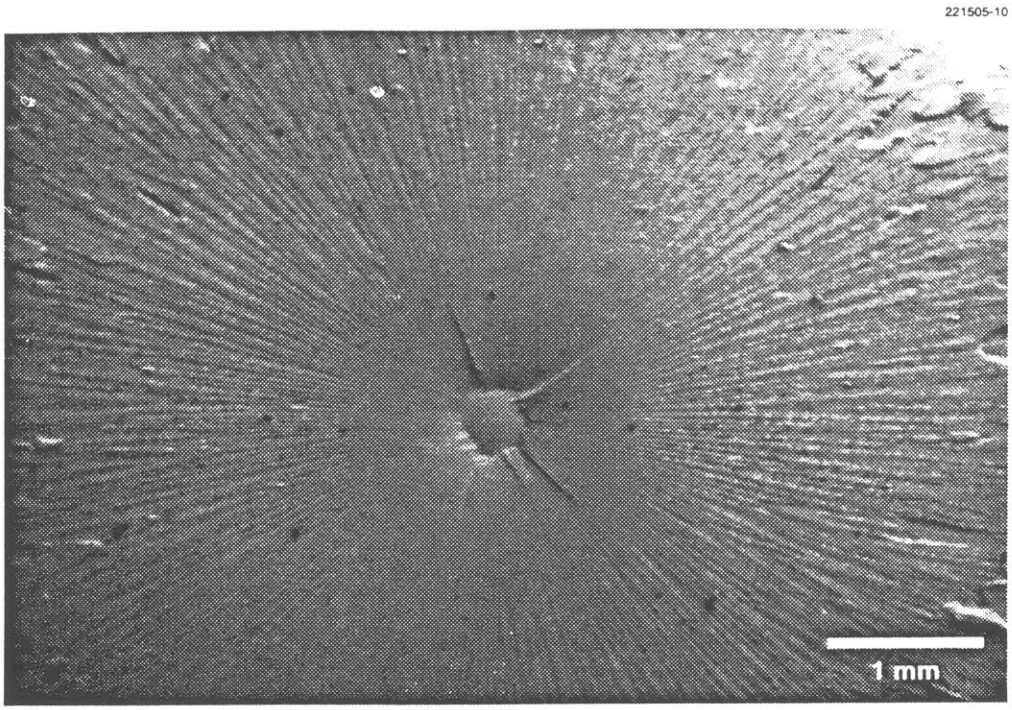

Figure B.26: SEM photomicrograph of typical fracture surface resulting from debonding of silica-glass sphere in adhesive strength neck specimen.

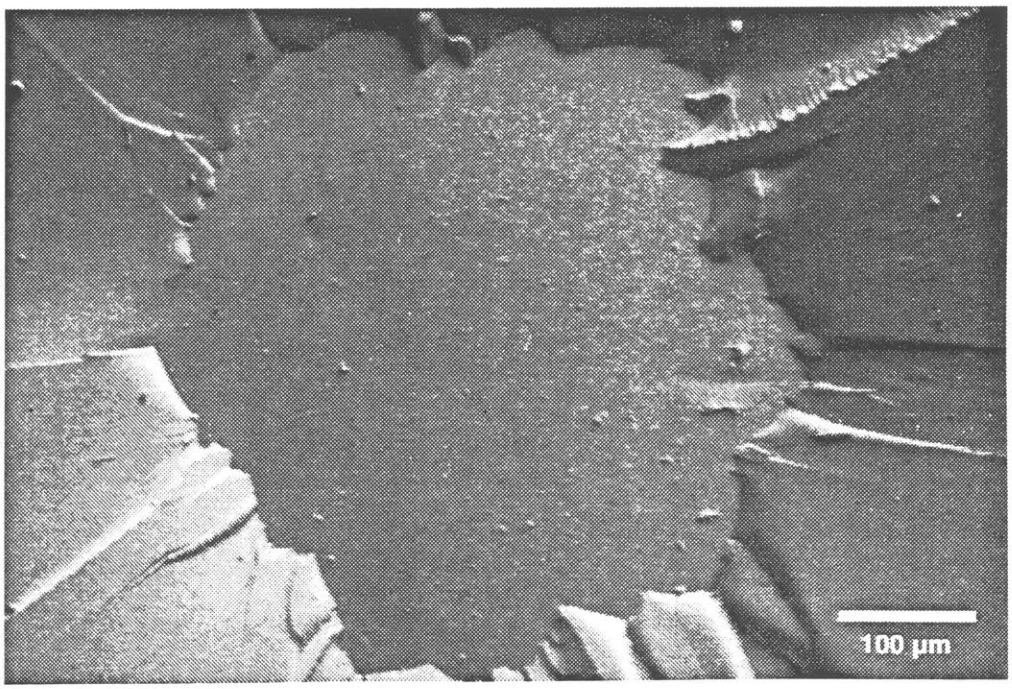

Figure B.27: Higher magnification of surface shown above, showing sharp transition of crack path from the paticle/matrix interface to the bulk epoxy.

Still higher magnifications of this same, silica-glass debonded surface show that the surface of the sphere is quite smooth, indicating that the fracture was adhesive in nature, as opposed to cohesive (through either of the solids in a path parallel to the interface). A few remnants of epoxy still adhere to the surface of the sphere, however, probably mechanically "locked" into pits or depressions in the glass surface which may be seen at the highest magnification shown here.

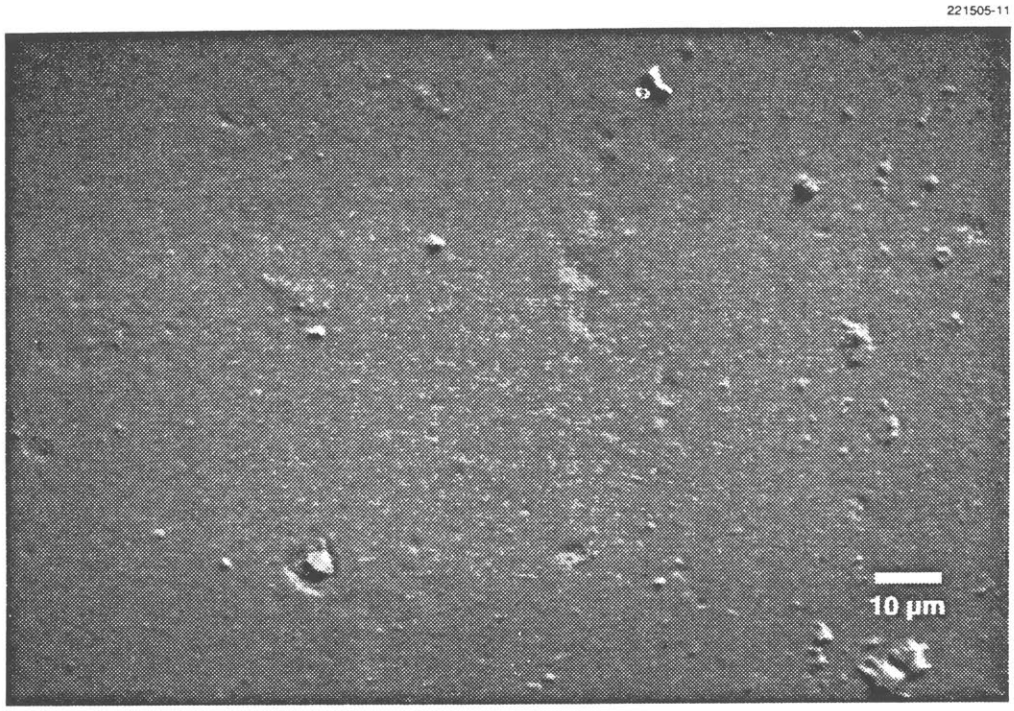

Figure B.28: SEM photomicrograph of debonded surface of silica-glass sphere. Interfacial adhesive failure is apparent, though a few remnants of epoxy are still attached.

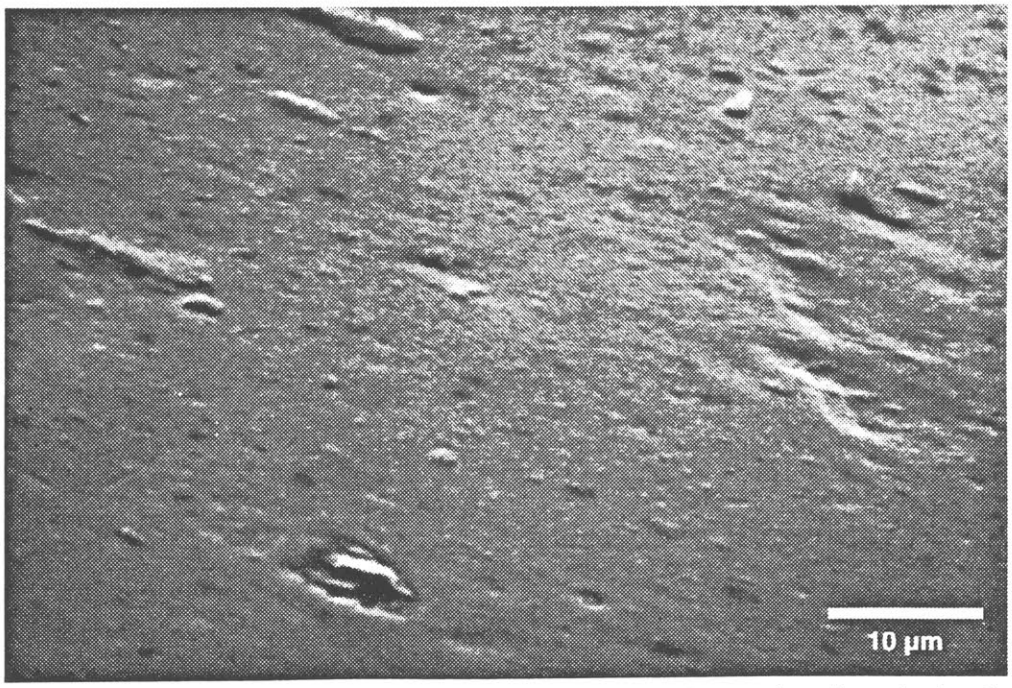

Figure B.29: Higher magnification of surface shown above, showing pits in glass surface and attached shards of epoxy.

Debonding of Nylon spheres produced sequences of fracture behavior similar to those initiated by debonding of glass spheres in the adhesive strength neck specimens. A principal difference results, however, from the much lower bond strength of the Nylon to epoxy than was exhibited by glass. Matching fracture surfaces from a neck specimen containing a Nylon sphere, shown in Figure B.30, demonstrate that the interfacial fracture travelled from the pole nearly down to the equator prior to kinking into the epoxy. This nearly hemispherical debonding, as opposed to the 10–20° arcs exposed on glass spheres, results from two, related causes: the toughness of the Nylon/epoxy interface is lower than the glass/epoxy interface toughness, and the low adhesive strength of epoxy to Nylon results in debonding at a low applied load, so that the critical flaw size (which elevates K_I to K_{Ic}) is not reached until the crack has almost reached the equator of the sphere.

The photomicrograph reproduced in Figure B.31 clearly shows the radial symmetry of the fracture through the epoxy neck section. Also evident is the transition of the crack velocity from "slow" to "fast", at a distance of about one radius from the sphere surface. The rougher, fast-fracture surface is accompanied by radial striations and cleavage whiskers still attached to the surface. Immediately adjacent to the sphere is a very smooth "halo" resulting from plasticization of the epoxy by water diffusion from the Nylon during the elevated-temperature post-curing of the epoxy. Specimens fabricated before this effect was recognized produced adhesive strengths comparable to specimens fabricated subsequently with dried spheres.

An SEM image of the debonded Nylon surface, shown in Figure B.32, indicates that, despite a few fragments of epoxy still adhering to the Nylon, the fracture process was restricted to the interface. During the interfacial separation, damage occurred to both materials: seen in this image is a plate-like layer of Nylon peeled away from the surface. In the higher magnification SEM image shown in Figure B.33, fragments of plastically stretched epoxy may be seen clinging to the Nylon.

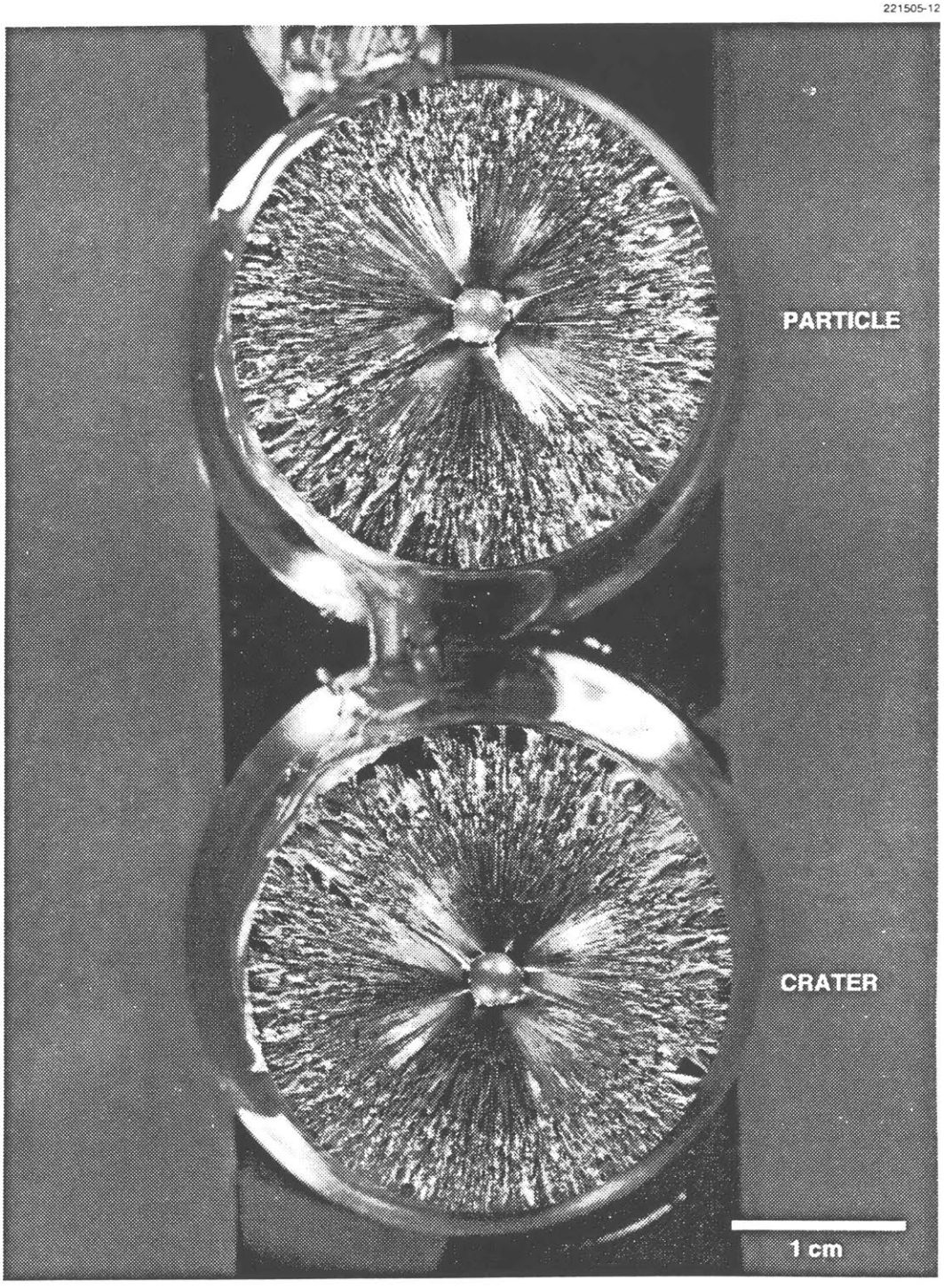

Figure B.30: Typical fracture surfaces initiated by debonding at pole of Nylon sphere. Crack travelled along interface a short distance, and then kinked into the epoxy.

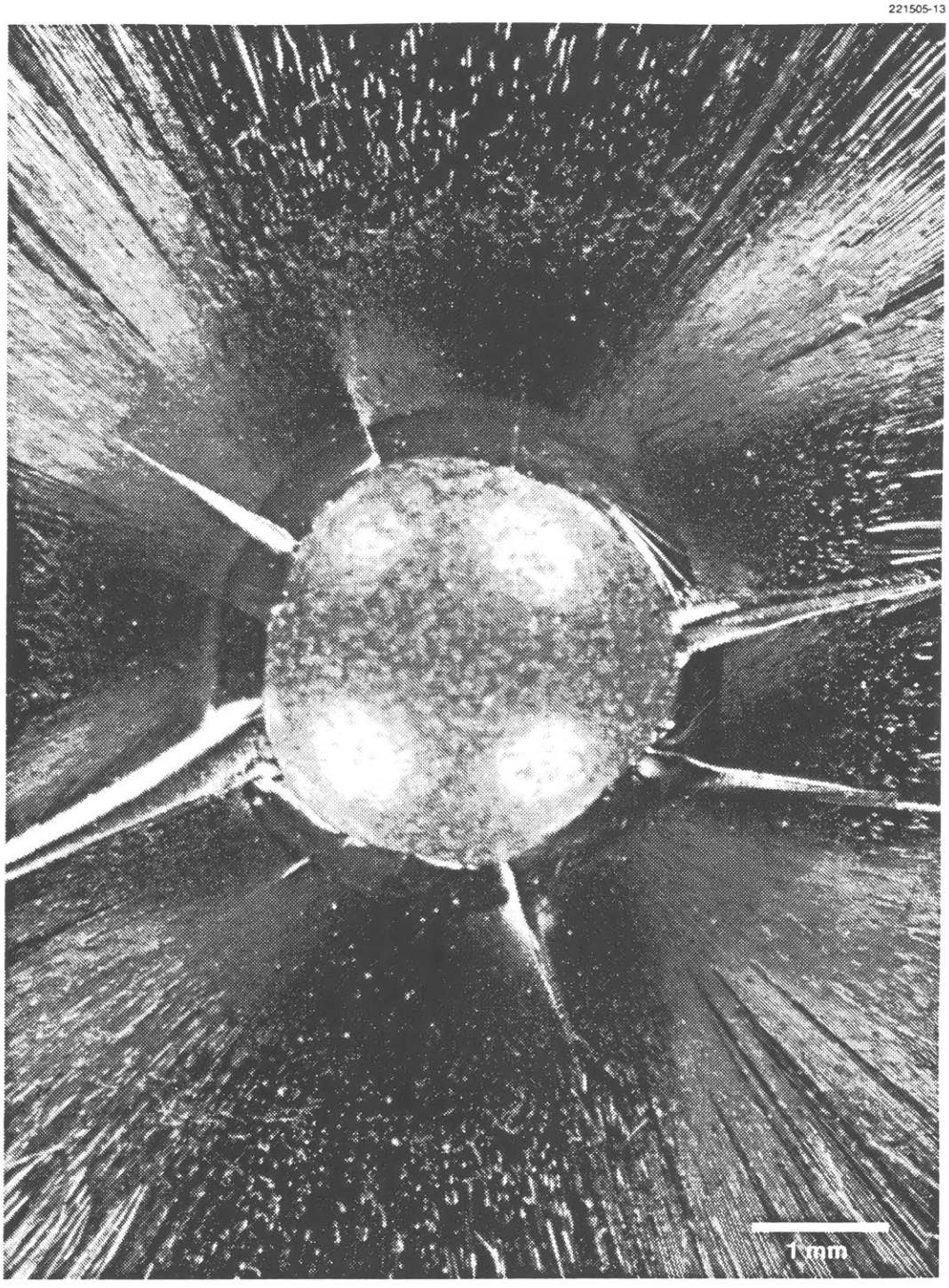

Figure B.31: Photomicrograph of fracture section on previous page, containing Nylon sphere. "Halo" around sphere is epoxy plasticized by water diffusion during curing.

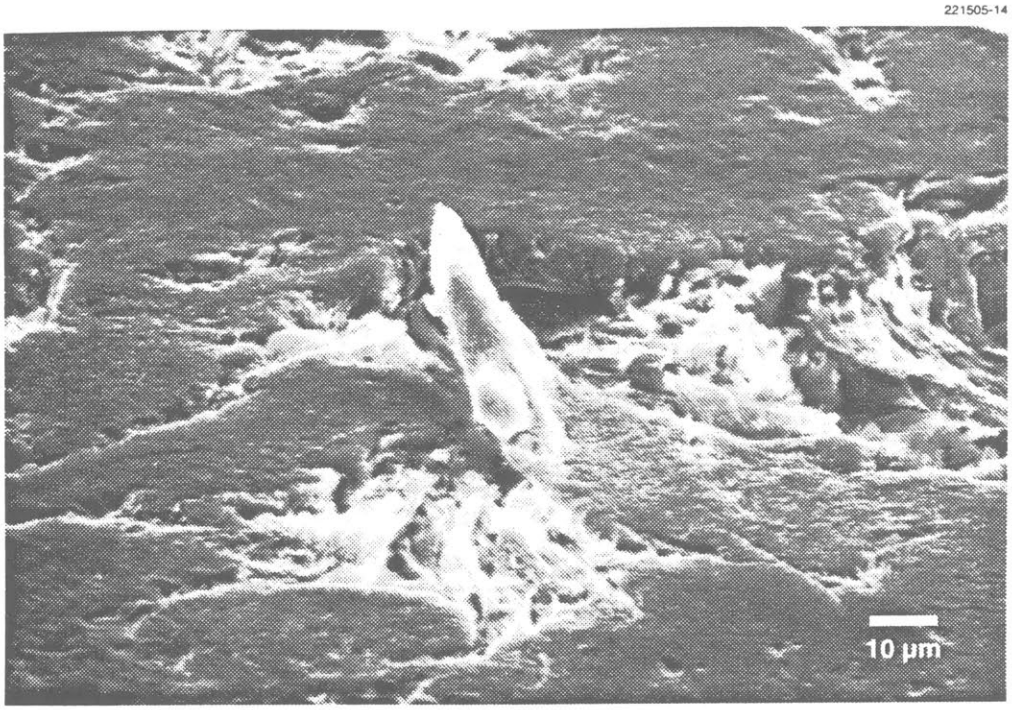

Figure B.32: SEM photomicrograph of typical debonded Nylon sphere in adhesive strength neck specimen. Remnants of epoxy are still attached to surface.

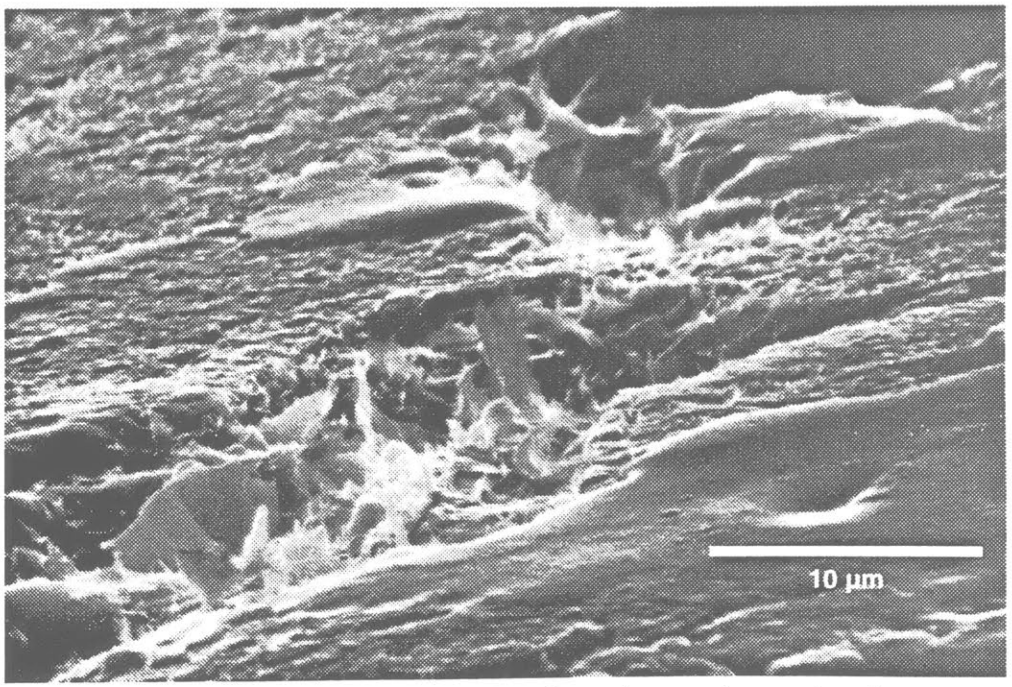

Figure B.33: Higher magnification of surface shown above, showing apparent plastic deformation of epoxy debris remaining on sphere.

Polycarbonate spheres in the as-received condition (cleaned) exhibited such high adhesive strengths that no specimens debonded from the epoxy necks during testing. In all cases, the PC sphere/epoxy interface remained intact until fracture was initiated in the epoxy, near the equator of the sphere. Two examples of this mode of failure are shown in the photographs reproduced in Figure B.34. The striations seen on the fractured epoxy surfaces point back to the origin of the fracture; in both of the cases shown, the origin appears to be adjacent to the sphere, close to its equator. The voids seen in the center of these PC spheres were also present in as-received Nylon spheres (which are less opaque, permitting the voids to be detected with transmitted light) and were formed during fabrication.

The surface markings ("river lines") seen on the fracture surfaces in the SEM images reproduced in Figure B.35 clearly indicate that the fractures originated within the epoxy adjacent to the spheres. In both cases, once a crack had been initiated it propagated across the spheres, leaving striations radiating from the edge. Since debonding of the as-received PC spheres did not occur, the radial stress generated at the particle poles as a result of the maximum applied loads is a measure only of a lower bound to the adhesive strength between PC and epoxy.

The very high adhesive strength developed between epoxy and PC is a function not only of chemistry, but is also influenced strongly by the surface condition of the solid. Figure B.36 contains SEM images showing the surface of PC spheres at two magnifications. These images reveal a uniformly rough surface, very locally three-dimensional, which clearly provides extensive opportunities for liquids to cling to ledges and crevices.

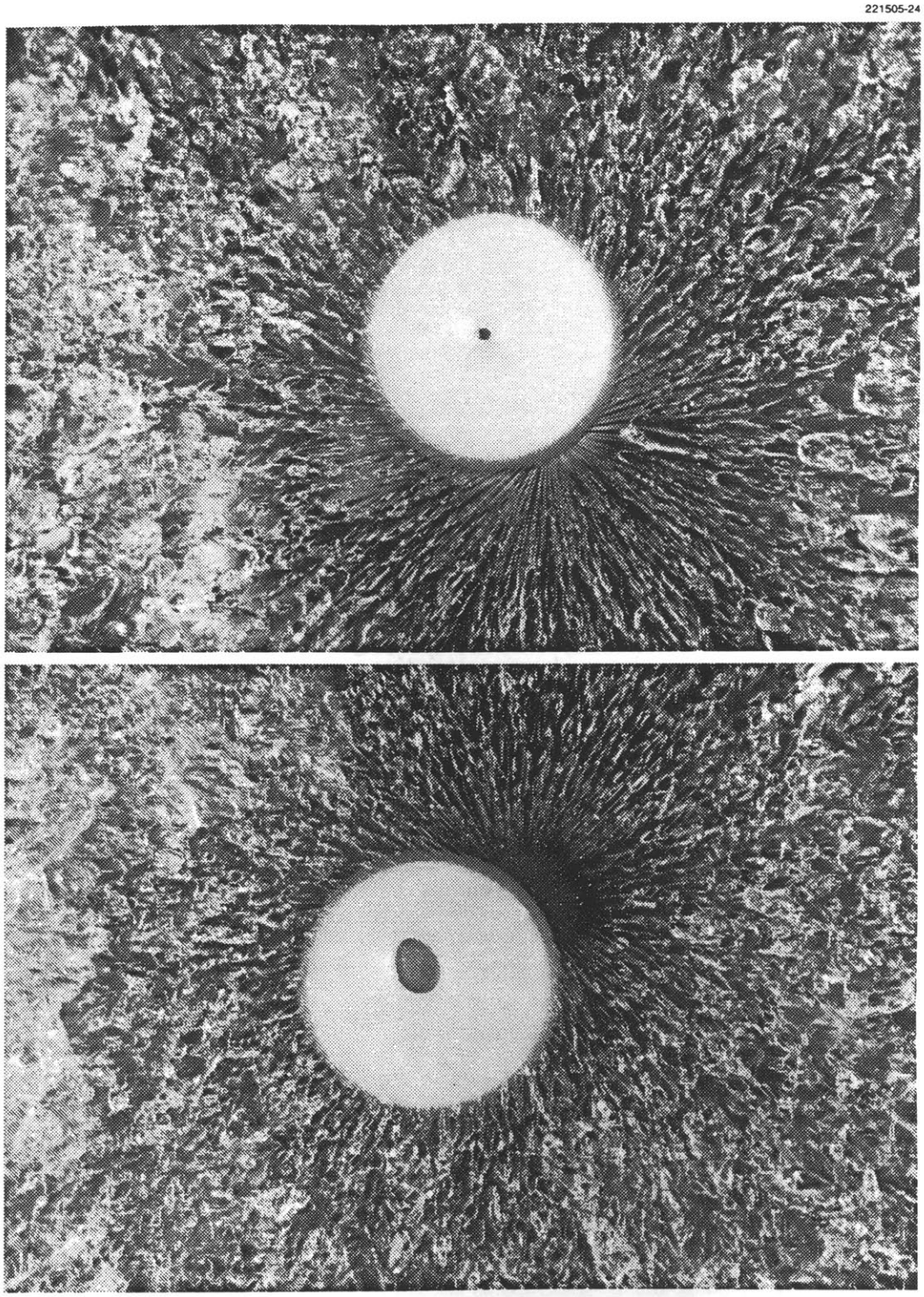

Figure B.34: Typical failure surfaces of neck specimens containing PC spheres. Debonding did not occur: failure resulted from fracture originating within epoxy. Dot in center of spheres is a void formed during fabrication of the spheres.

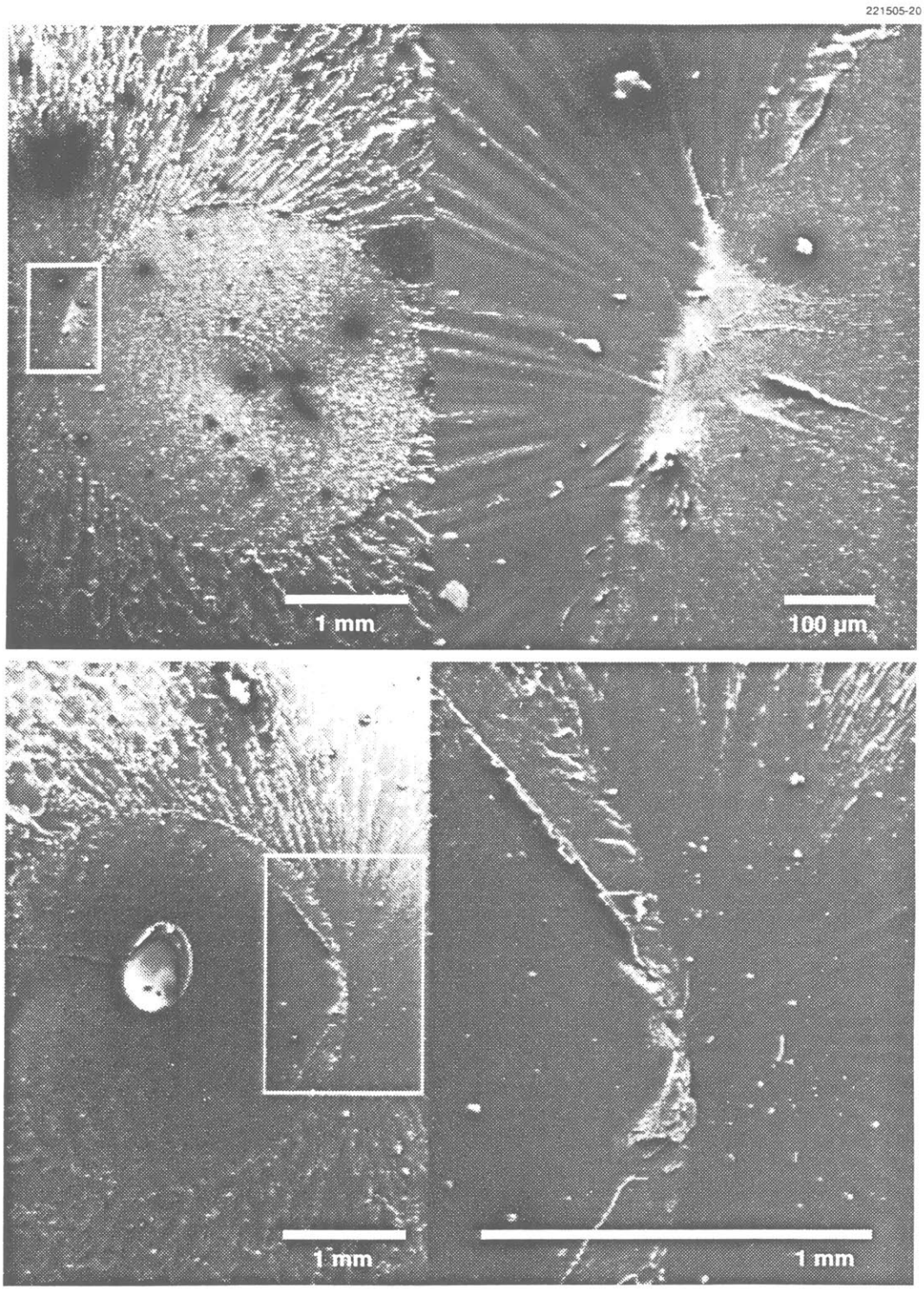

Figure B.35: SEM photomicrographs of fractured PC spheres, showing striations leading back to origins of fracture in epoxy, near the interfaces.

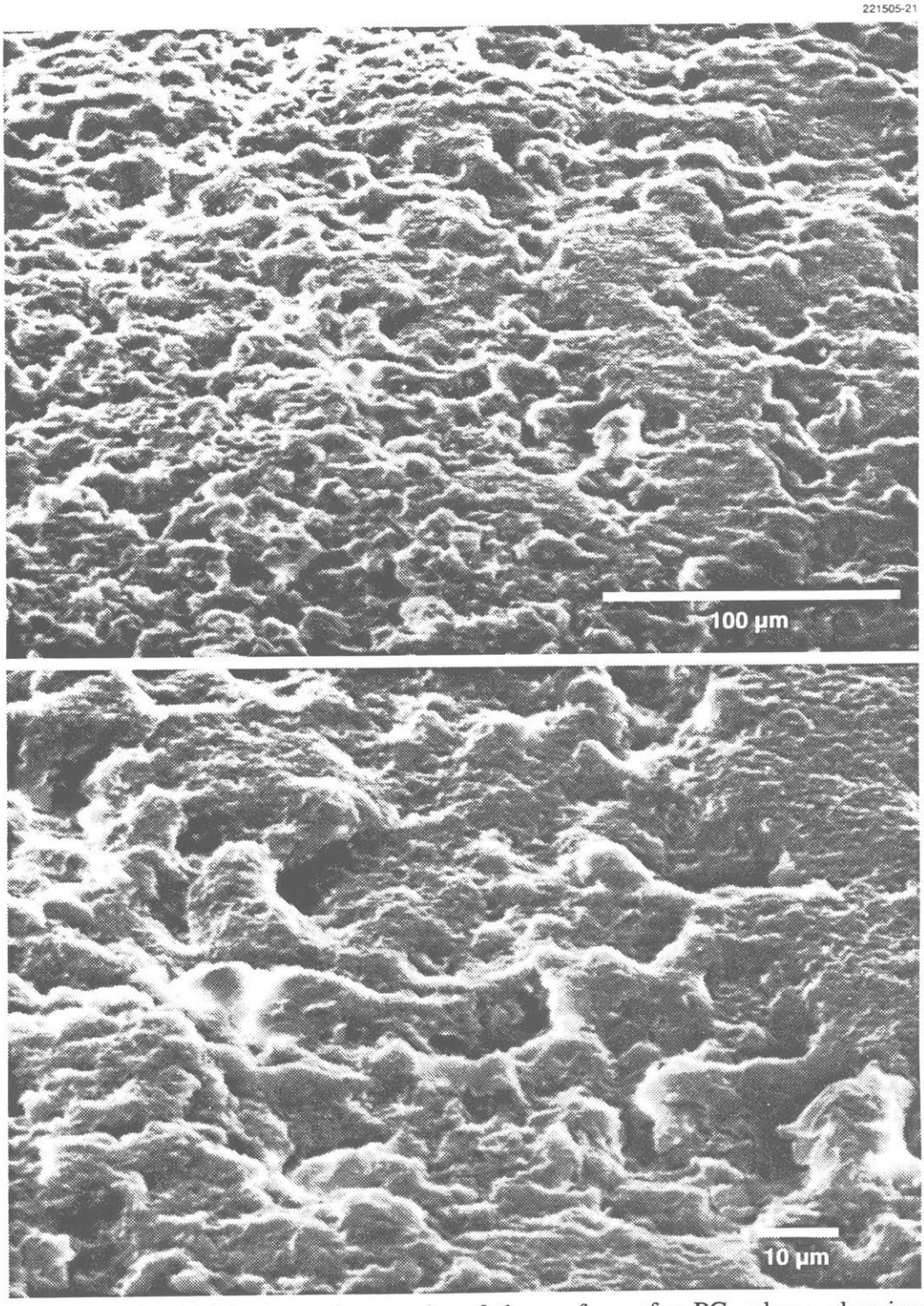

Figure B.36: SEM photomicrographs of the surface of a PC sphere, showing extensive, uniformly distributed three-dimensional features which enhance adhesive strength through mechanical interlocking.

B.6.2 Particle surface modifications

The surface of some PC and glass spheres cast into neck specimens were coated with one or two thin layers of the release agent *Free Kote*©. This is a liquid, proprietary substance that, unlike teflon-based release agents, does not flake off and contaminate the resins it comes in contact with. It requires many coats to be effective, though, so it proved to be an ideal surface modification with which adhesion could be reduced, but not eliminated between the inclusions and epoxy used here in model specimens. Interfacial separation between spheres with reduced adhesion and the epoxy necks took place in a manner similar to the separation of Nylon spheres.

A commercial silane coupling agent (A-1100) was obtained from Union Carbide to attempt to enhance the adhesive strength of epoxy to silica-glass spheres. Several specimens were prepared, after thorough solvent cleaning, by immersion in a 1% A-1100, aqueous solution followed by drying at 100°C for thirty minutes. Similar procedures have been shown to promote chemical bonding of epoxy groups to silica surfaces [180, 181, 182].

Nylon has a surface energy which is almost three times greater than that of Teflon, a polymer which is notoriously difficult to bond to [183]. Consequently, resins more readily wet Nylon surfaces and develop better bonds to Nylon than to Teflon. The bond strength of Nylon to resins has reportedly been enhanced by surface etching and treatment with primers [184]. The SEM photomicrograph of a typical, as-received Nylon sphere used in the model specimens here, shown in Figure B.37, indicates that the surface is quite smooth. Indeed, it appears to have been "smeared" over during the fabrication process. The more highly magnified image in Figure B.38 supports the impression that a low percentage of sub-surface areas escaped the forming process and appear geometrically complex, yet smooth.

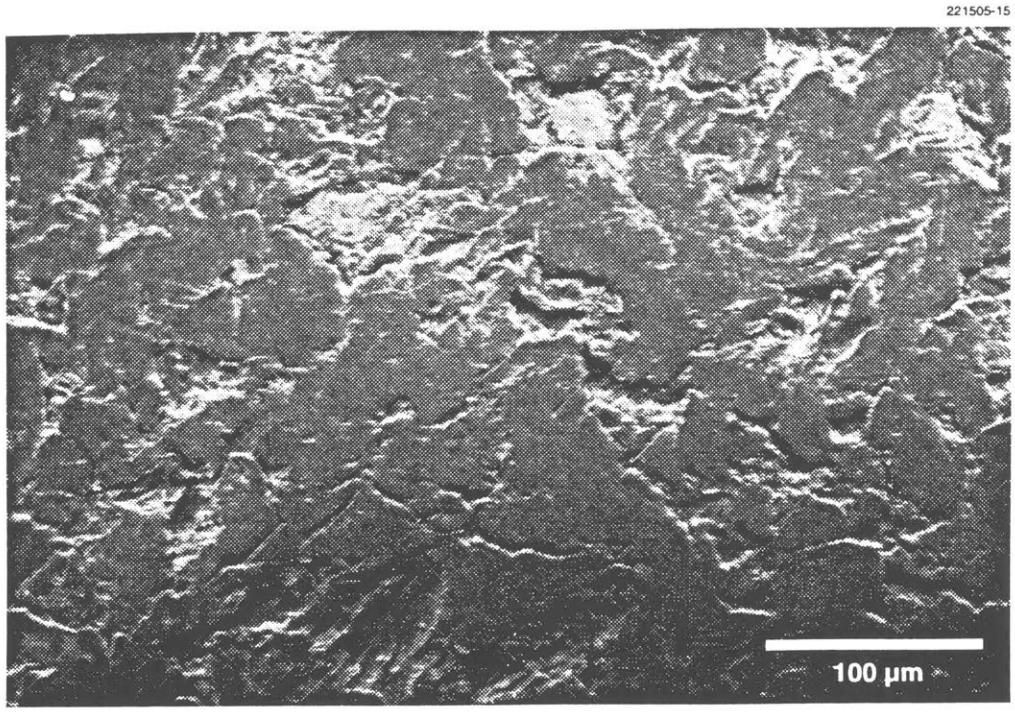

Figure B.37: SEM photomicrograph of surface of Nylon sphere, as received.

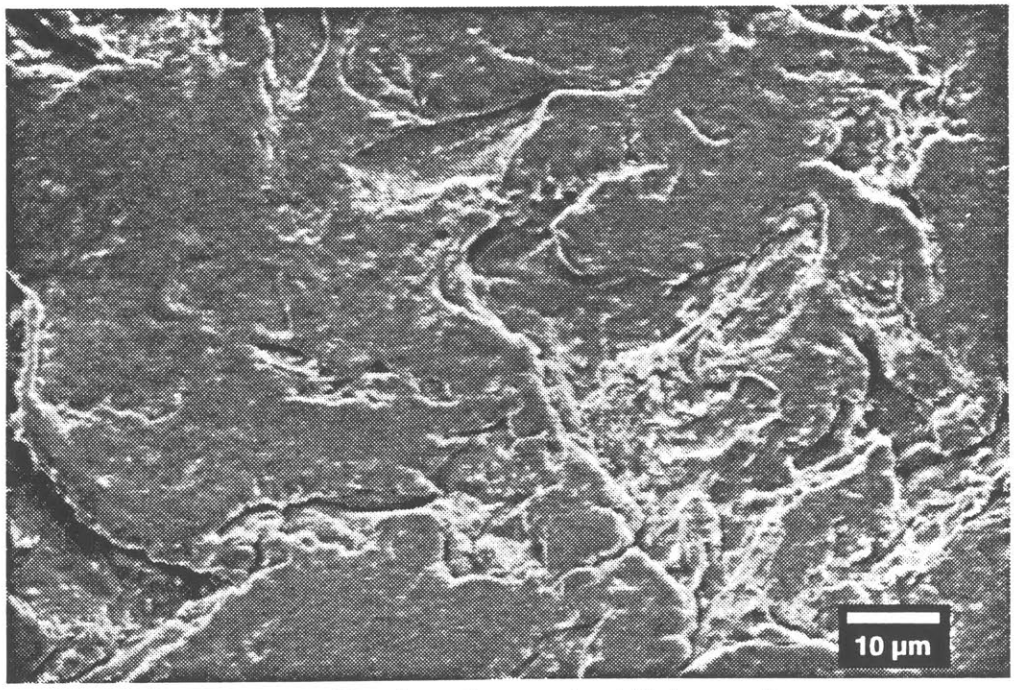

Figure B.38: Higher magnification of as-received Nylon surface.

Improvement of the adhesive bond strength between epoxy and Nylon was attempted through a method established by Shields [184], which reportedly enhanced the adhesive shear strength from 3 to 6 MPa. These data must be viewed qualitatively, however, because the adhesive measurements used were lap shear tests with Nylon plates bonded to steel plates using an epoxy adhesive. The surface preparation appeared to have merit, however, and was followed here.

First, an acid-potassium permanganate solution was used to etch the Nylon. A saturated solution of $KMNO_4$ was prepared at 90°C, to which 2% by weight of H_2SO_4 was added. Nylon specimens were then immersed for five minutes while the temperature was maintained. The specimens were then removed, cleansed with distilled water, and ultrasonically cleaned in isopropanol to remove flakes of $KMNO_4$. A typical surface which resulted from this etching is shown in the SEM image reproduced in Figure B.39. The etching clearly has created many tiny holes, which may improve adhesive strengths through mechanical interlocking [183] (if they are entirely wetted), but surface cracks have been introduced, whose effect upon adhesive strength or toughness may not be beneficial. A closer view of the etched holes and many smaller surface cracks is shown in Figure B.40.

The second step of Shields method was to treat the etched surfaces with a resorcinol-formaldehyde primer. The primer solution was prepared from 5% resorcinol, 5% formaldehyde, 5% NaOH and 85% H_2O. Various procedures of applying this primer were pursued, ranging from air-drying after application with a medicine dropper, to soaking at elevated temperatures followed by different drying and cleaning methods. The optimum method appeared to be soaking of the etched Nylon specimen in the primer solution at 65°C for 30 min, followed by drying with a hand-held dryer ("heat-gun"). Primed specimens were then ultrasonically cleaned in isopropanol for 15 minutes to remove loose scale which would obviously result in poor adhesion.

A photomicrograph of a Nylon surface which had been etched and primed with the

above procedures is shown in Figure B.41. This image shows that the surface holes created by etching are filled in by the primer, creating a patch-work of mechanically attached primer material. The magnified image in Figure B.42 shows one of these patches straddling a crevice created by the etching process.

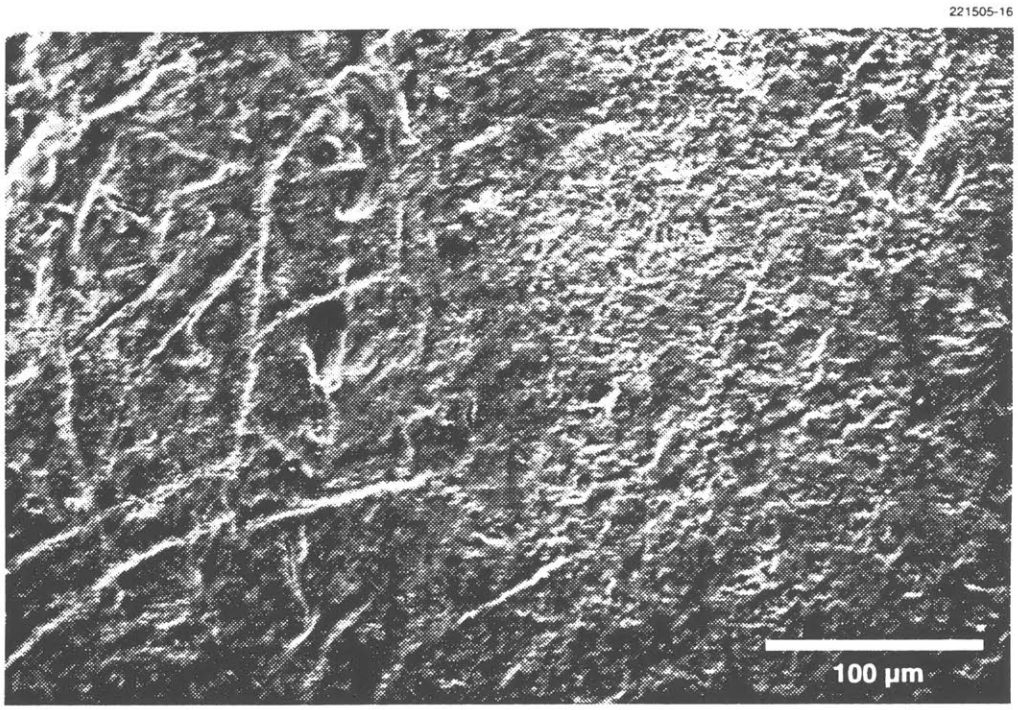

Figure B.39: SEM photomicrograph of surface of Nylon sphere, etched with $KMNO_4$-H_2SO_4 @ 90°C for five minutes and ultrasonicly cleaned in isopropanol.

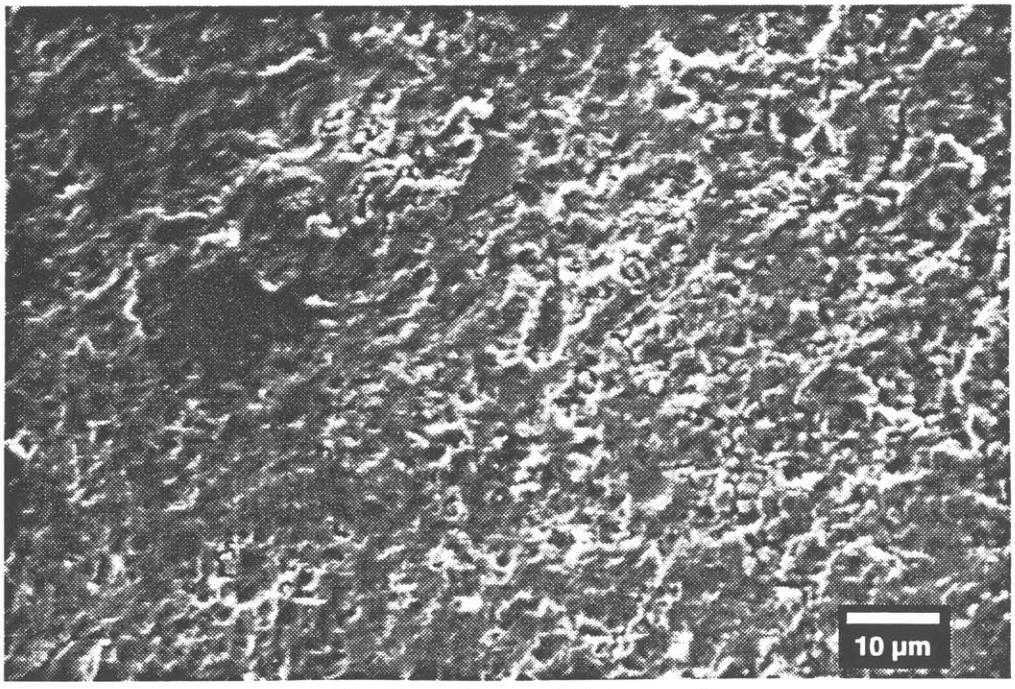

Figure B.40: Higher magnification of etched Nylon surface.

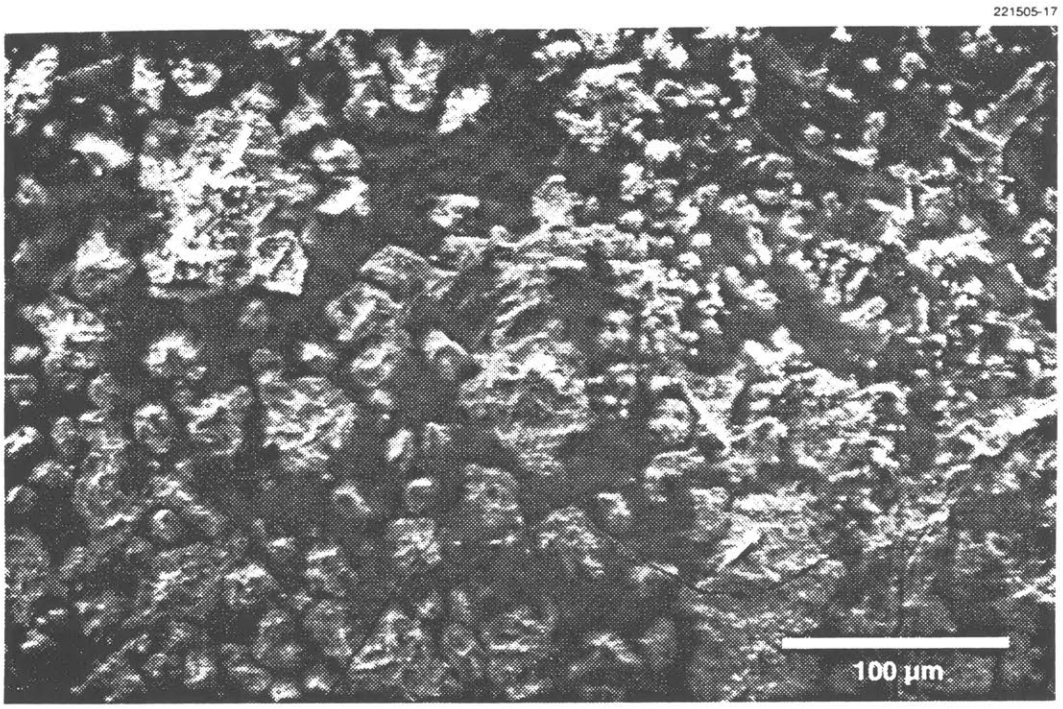

Figure B.41: SEM photomicrograph of surface of Nylon sphere, etched with $KMNO_4$-H_2SO_4 and treated with resorcinol-formaldehyde primer.

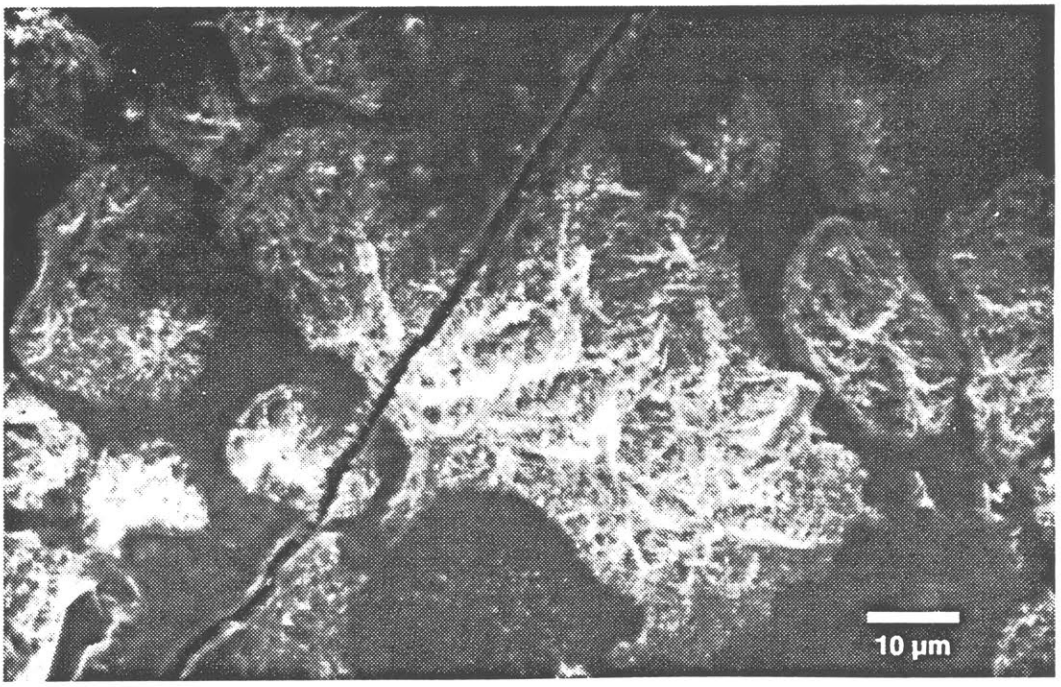

Figure B.42: Higher magnification of etched and primed Nylon surface.

Adhesive strengths between material combinations with little or no chemical bonding are influenced greatly by surface topography. Surface roughening by abrasion [185] or by chemical treatment [186, 188] can give rise to improved adhesive strengths through increased surface area of contact and mechanical "keying" between the two materials.

The effect of surface topology upon adhesion was demonstrated by Evans and Packham, who characterized the adhesive strength of polyethylene to copper as a function of the copper surface features. [187]. They showed that a roughening of the copper surface by oxidation in a proprietary solution greatly enhanced the adhesion strength of polyethylene to it, even if chemical bonding was inhibited by a nitrogen film-coating. The oxidized surfaces were covered with fibrous copper(II) oxide growths, looking very much like anemone.

Remarkably similar growths were observed on a few specimens of etched and primed Nylon spheres in the work reported here. Figures B.43 and B.44 show SEM images of one type of fibrous growth produced on Nylon which looks almost identical to the copper(II) oxide structures shown in [187]. If such structures could be uniformly produced over an entire surface, higher adhesive strengths might result. This goal was attempted through variations in etching and priming solution concentrations, temperatures and application times. The plate-like, floral growths could not be reproduced, but the procedures outlined earlier often gave rise to pointed, branching star-like structures which are shown in the micrographs of Figures B.45 and B.46. These structures appear similar to copper(II) oxide growths on anodized surfaces which demonstrated enhanced adhesion [188].

Despite the obvious surface roughening of Nylon created by the etching and priming procedures discussed above, no consistent effect upon failure modes or enhancement of adhesive strengths was determined, as demonstrated by the data presented in the next section.

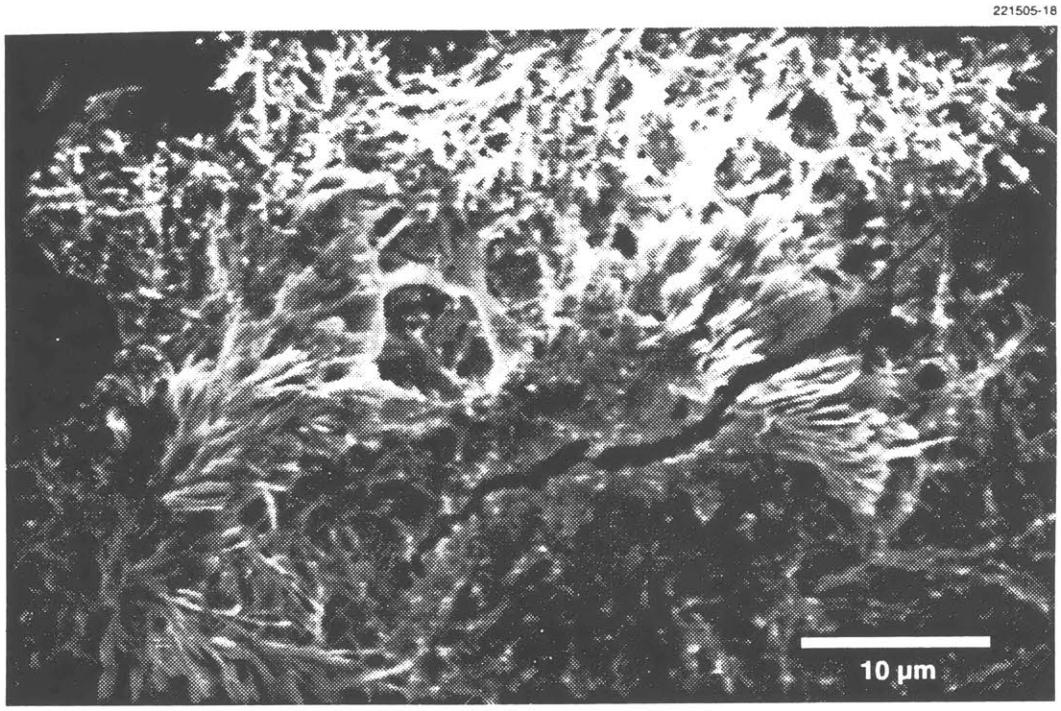

Figure B.43: SEM photomicrograph showing growth of fibrous structures on etched and resorcinol-formaldehyde primed surface of Nylon sphere.

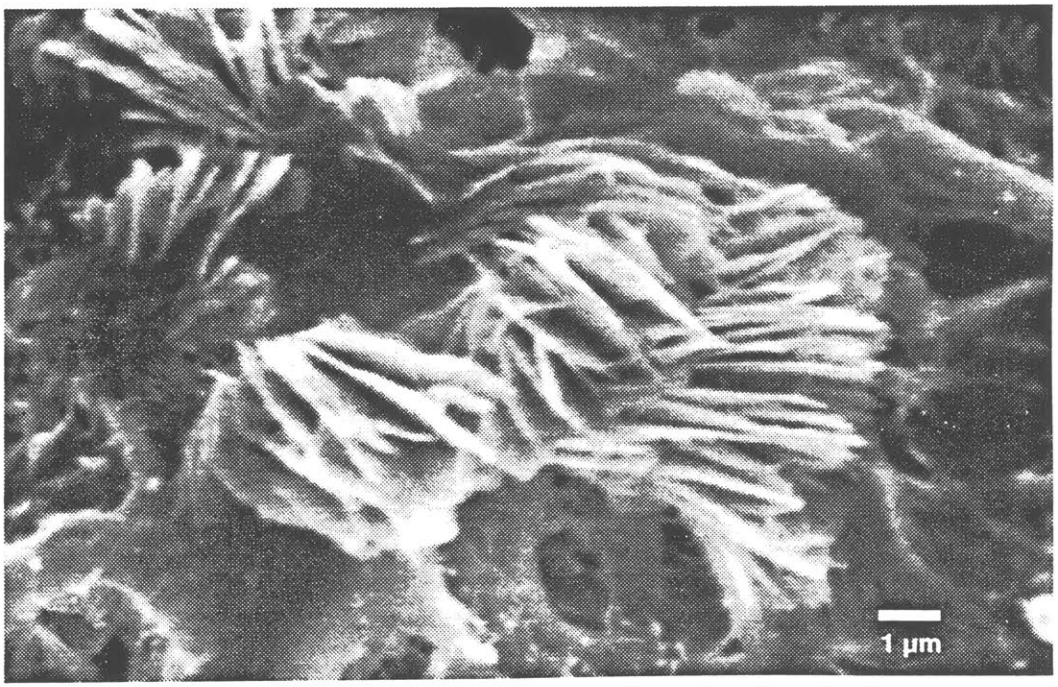

Figure B.44: Higher magnification of above surface, showing platelet structure of the fibrous growths.

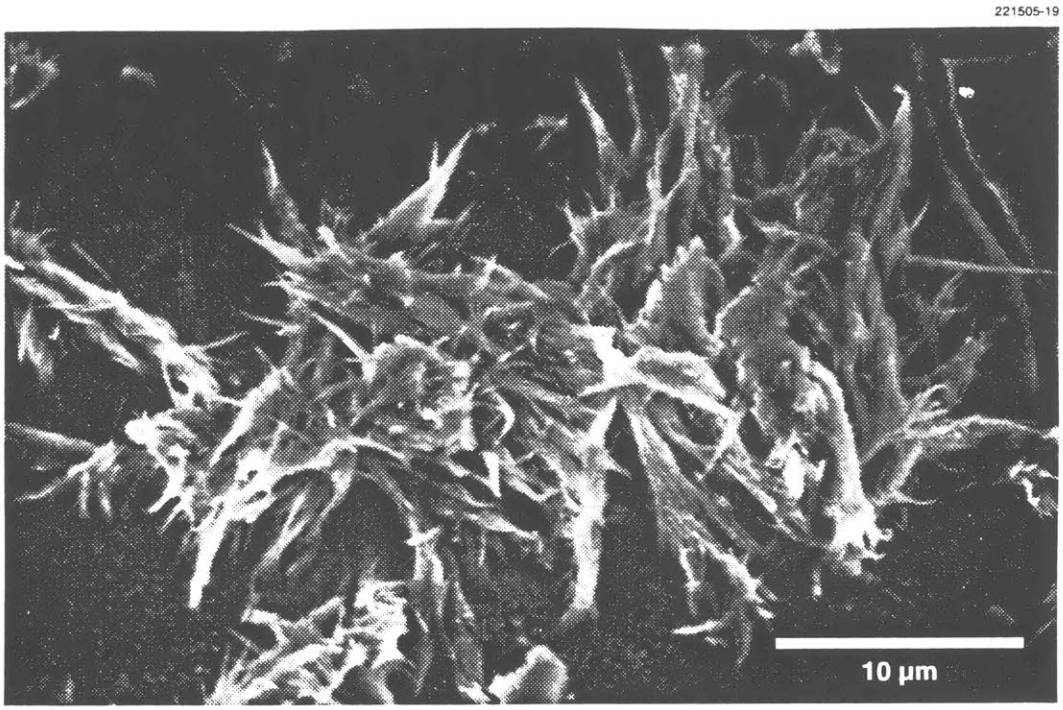

Figure B.45: SEM photomicrograph showing growth of fibrous structures on etched and resorcinol-formaldehyde primed surface of Nylon sphere.

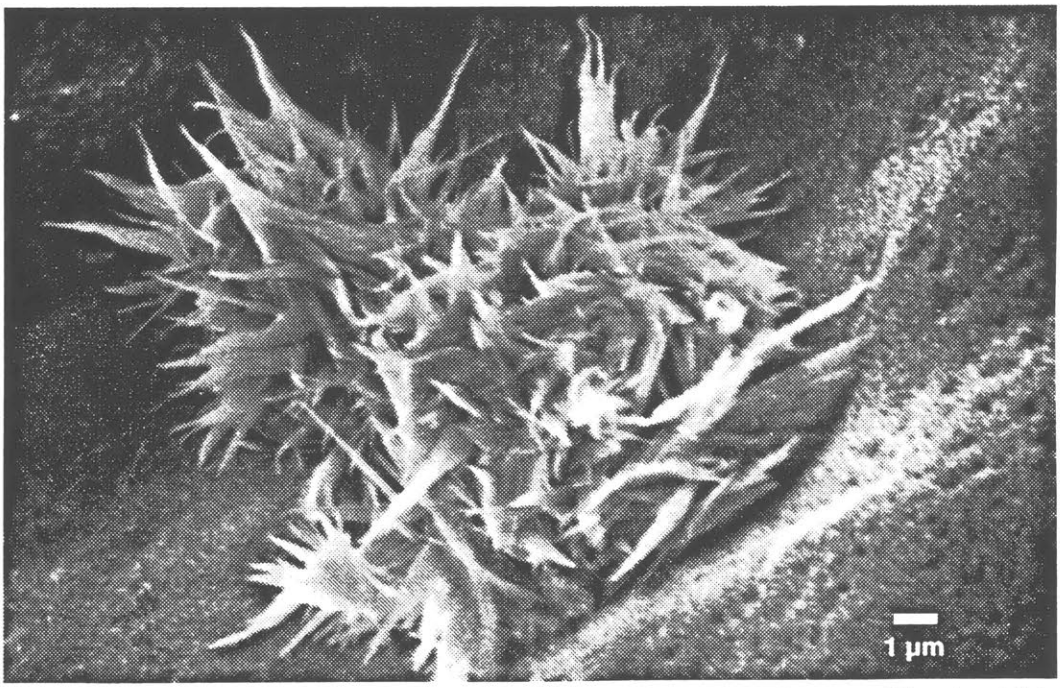

Figure B.46: Higher magnification of above surface, showing star-like dendritic structure of the fibrous growths.

B.6.3 Determination of adhesive strengths

During testing of the adhesive strength neck specimens, initial debonding at poles of spheres occurred when the radial stress across the interface exceeded the strength of the bond, and resulted in the formation of a three-dimensional interfacial crack. Subsequent propagation of this crack proceeded typically in one of two manners. With spheres having low adhesive strengths to epoxy, initial debonding was followed by relatively slow expansion of the interfacial crack towards the equator, until the crack kinked into the epoxy and rapid fracture of the neck section resulted. Debonding of sphere surfaces with greater adhesive strengths occurred at sufficiently high loads that the resulting interfacial cracks rapidly reached the critical flaw size, so that the debonding process could not be temporally distinguished from the fracture process with either the photographic or the load records.

The maximum loads recorded during testing of the neck specimens provides adhesive strength data for all separations of spheres which proceeded from debond sites initiated at poles. A summary of such loads is given in Table B.1, which also includes indications of the nature of the failure process for each neck specimen. Separations which occurred via slow interfacial fractures are indicated in the table by "deb". Specimens which failed by rapid fractures of the epoxy immediately following the initial debonding are indicated by "frac". In the case of as-received (solvent cleaned) PC spheres, no debonding was observed; fractures in these specimens initiated in the epoxy near the equator of spheres and rapidly spread across the neck sections, fracturing the PC spheres in the process.

Table B.1: Summary of adhesion strength neck specimen data.

Material	*Surface Treatment*	*Failure Load* (kN) *and Mode*			
Delrin	Solvent Cleaned	5.16 deb	5.51 deb	6.00 deb	
Nylon	Solvent Cleaned	9.34 deb	11.1 frac	13.8 frac	16.4 frac
	$KMNO_4$-Etched	6.22 deb	7.11 deb	8.45 frac	9.34 frac
	Etched; Resourcinol-	10.2 frac	11.1 frac	11.8 frac	12.0 frac
	Formaldehyde Primer	12.7 frac	13.5 frac	14.0 frac	15.5 frac
Glass	Solvent Cleaned	17.6 frac	18.7 frac	19.8 frac	20.5 frac
	Free-Kote (Release)	14.7 frac	16.4 frac	11.1 deb (2 coats)	
	Silane-coated	15.1 frac	16.2 frac	17.1 frac	
PC	Solvent Cleaned	24.9 frac	24.9 frac	26.0 frac	26.3 frac
	Free-Kote (Release)	12.2 frac	14.9 frac	16.4 frac	16.6 frac
	Free-Kote (2 coats)	10.9 deb	11.6 frac	12.4 deb	13.3 frac

These load data can be combined with the results of the FE analysis, summarized in Figure B.25, to determine the radial stress, σ_r^{app}, applied to each sphere/epoxy interface at the moment when debonding occurred. The spheres were also subjected to a residual radial stress, σ_r^{res}, resulting from the differential thermal contractions between the sphere materials and the epoxy neck, generated during cooling after the post-curing of the epoxy. The net radial stress applied to the interface is simply

$$\sigma_r = \sigma_r^{\text{app}} + \sigma_r^{\text{res}} . \tag{B.6}$$

The residual (thermal) stress can be computed for each sphere material through the use of Equation C.3, where the differential thermal strains, ε_T, are established over the temperature interval from the glass transition temperature of the epoxy, $T_g = 72°C$, to room temperature. The individual thermal strains of the epoxy and the spheres were measured with procedures discussed in Appendix A. Over the interval 72°C→20°C, the measured strains were: ε_{EP}=5380, ε_{NY}=7130, ε_{PC}=3551, and ε_{Gl}=460 $\times -10^{-6}$. Using the elastic constants which were given earlier in the description of the FE procedures, the residual stresses computed for each sphere/epoxy combination are: $\sigma_r^{\text{res}}(\text{NY}) \approx 3$, $\sigma_r^{\text{res}}(\text{PC}) \approx -3$, and $\sigma_r^{\text{res}}(\text{Gl}) \approx -10$ MPa. Only very

slight relaxation of these stresses will have occurred during the room-temperature storage of specimens prior to testing (see Appendix C), so these values are directly substituted into Equation B.6 to arrive at the adhesive strength data which are tabulated below. The elastic and thermal properties of Delrin are assumed similar to those of Nylon, for the purposes of determining the adhesive strengths of Delrin to epoxy given in this table.

Table B.2: Adhesion strengths of listed materials to epoxy; based upon maximum load data, finite element stress analysis and calculated residual stresses.

Material	*Surface Treatment*	*Adhesive Strength* (MPa)				*Mean, St.D.*
Delrin	Solvent Cleaned	14.7	15.5	16.6		15.6, 0.9
Nylon	Solvent Cleaned	24.2	28.2	34.3	40.1	31.7, 6.9
	$KMNO_4$-Etched	17.1	19.1	22.1	24.2	20.6, 3.1
	Etched; Resourcinol-	26.1	28.2	29.8	30.2	31.6, 3.8
	Formaldehyde Primer	31.8	33.6	34.8	38.2	
Glass	Solvent Cleaned	55.3	59.4	63.5	66.1	61.1, 4.7
	Free-Kote (Release)	44.5	50.8	31.2 (2 coats)		
	Silane-coated	46.0	50.1	53.4		49.8, 3.7
PC	Solvent Cleaned	>49.6	>49.6	>53.5	>54.2	>54
	Free-Kote (Release)	22.2	27.8	30.9	31.3	28.0, 4.2
	Free-Kote (2 coats)	19.5	21.0	22.6	24.5	21.9, 2.1

These data indicate that the intrinsic adhesive strength of epoxy to Nylon is approximately twice that of epoxy to Delrin. Contrary to expectation, etching of the Nylon surface drastically reduced its adhesive strength. Despite the many microscopic pits and holes created during the etching process, the global surface apparently remains "smooth"; some of the many cracks in the Nylon surface formed by the etching process apparently acted as initial flaws, so that the apparent bond strength was actually reduced. Priming the etched Nylon surfaces with resorcinol-formaldehyde restored the adhesive strength to the level exhibited by as-received specimens. Use of a less aggressive etching solution in conjunction with the primer might result in higher adhesive strengths between Nylon and resins.

The silica-glass particles exhibited very high adhesive strengths, approximately equal to the yield stress of the epoxy ($\sigma_y \approx 60\,\text{MPa}$). Application of the Free-Kote© release agent appeared to reduce the adhesive strength by about 10 MPa per coat of release. Silane coating the glass particles did not increase their adhesive strength to epoxy. Application of the silane (A-1100) was executed in a manner similar to reported techniques (discussed earlier in this Appendix), but perhaps some aspect of the procedure used here was incorrect. Nonetheless, observations of fractured glass particles in model specimens (discussed in Chapter 4) suggest that the adhesive strength of the as-received glass particles to epoxy exceeds the normal stress experienced by particles in the triaxial stress field ahead of a sharp crack tip in glass-particle filled epoxy composites. Thus, enhancement of epoxy-to-glass adhesive strength is not only unnecessary, but is also undesirable, since toughening by crack trapping requires that particles remain intact and toughening by shielding requires that dilatation (interfacial separation) occurs.

A lower bound to the adhesive strength of epoxy to polycarbonate can be established by the data shown here as approximately 54 MPa. This very high level of adhesion, for a resin to a low surface-energy polymer, is certainly a function of the rough surface of the PC spheres in the as-received condition. Application of one coat of release agent reduced the PC/epoxy adhesive strength to a level comparable to the Nylon/epoxy adhesive strength. The interfacial fracture toughness, however, was not similarly reduced, as evidenced by differences in the extent to which cracks grew along the sphere surfaces after initial debonding.

Following the initial debonding of Nylon spheres from the epoxy necks, interfacial cracks grew toward the equators and nearly separated an entire hemisphere prior to kinking into the epoxy. Debonding of release-coated PC spheres occurred from similar levels of radial stress, but the ensuing interfacial cracks travelled far less distance prior to kinking into the epoxy. The obvious explanation for this difference in behavior, following similar debonding stress, is that the toughness of the PC/epoxy interface remains tougher than the Nylon/epoxy interface, despite the reduction of the PC adhesive strength via release-coating. This conclusion parallels the observations made with the DCB crack-trapping model specimens, in which separation of Nylon rods from the epoxy matrix occurred, but in no case (even with release-coating) did separation of PC rods occur. In the next section, the toughness of interfaces is quantified based upon the measured arcs of interfacial separation of spheres prior to kinking of the cracks into the epoxy necks.

B.6.4 Determination of Interfacial Fracture Toughnesses

Debonding at the polar cap of spheres in the neck specimens introduces a circular crack which is initially normal to the axis of symmetry. While the radius of the crack remains very small relative to the sphere, the mixed-mode energy release rate applied (in spherical coordinates) to the interface, $\mathcal{G}^{\text{int}}$, is virtually identical to the mode I energy release rate, $\mathcal{G}_I^{\text{mat}}$, applied to the neck section (in cylindrical coordinates). Thus, if the toughness of the interface, $\mathcal{G}_c^{\text{int}}$, is less than the toughness of the matrix (epoxy neck), $\mathcal{G}_{Ic}^{\text{mat}}$, the crack will propagate along the interface in response to increased loading. As the crack advances circumferentially towards the equator, $\mathcal{G}^{\text{int}}$ will decline due to the change in orientation of the crack tip with respect to the applied stress field, while $\mathcal{G}_I^{\text{mat}}$ will increase due to the increasing effective crack radius, a (normal to the longitudinal (y) axis). Eventually, conditions become more favorable for fracture through the neck section than for continued fracture along the interface, and the crack will "kink" into the epoxy neck. The following section shows how the toughness of the spherical interfaces in the adhesive strength neck specimens can be determined from the angular position of the crack-path kinking.

B.6.4.1 Kinking criterion

Following the approach of Hutchinson and He [136, 189], the criterion for kinking of cracks from the spherical interface into the epoxy neck material can be stated as

$$\frac{\mathcal{G}_I^{\text{mat}}}{\mathcal{G}_{Ic}^{\text{mat}}} \geq \frac{\mathcal{G}^{\text{int}}}{\mathcal{G}_c^{\text{int}}} . \tag{B.7}$$

As explained above, this criterion will not be met when the semispherical crack is first formed, because $\mathcal{G}^{\text{int}} = \mathcal{G}_I^{\text{mat}}$ initially and $\mathcal{G}_c^{\text{int}} < \mathcal{G}_{Ic}^{\text{mat}}$ for most materials. With increasing load and extending cracks, the kinking criterion is met when the crack reaches the critical kinking radius, a_k. The parameter sought from Equation B.7

is obviously $\mathcal{G}_c^{\text{int}}$, while the other three terms may be determined as follows. The toughness of the neck material, $\mathcal{G}_{Ic}^{\text{mat}}$, is measured in separate experiments. The mode I energy release applied to sections of the neck normal to the y-axis is calculated from the solution for the stress intensity of a three-dimensional, circular crack normal to remote stress [177],

$$K_\circ = \frac{2}{\pi}\sigma_{yy}^{\infty}\sqrt{\pi a}\,, \tag{B.8}$$

using the elastic relation $K^2 = \mathcal{G}E/(1-\nu^2)$. Analytical solutions for the mixed-mode stress intensities of semispherical cracks are not currently available; recent finite element solutions are available, however, and are utilized here.

B.6.4.2 Stress intensities of semispherical cracks

Finite element computations of stress intensities for spherical cap cracks have recently been developed by Xu and Ortiz for decohering particles in both remote uniaxial and hydrostatic tensile stress fields [190]. The analysis assumes that the elastic properties of the sphere are identical to the surrounding medium, which is very nearly the case for the PC and Nylon spheres in epoxy necks tested here. Solutions for K_I and K_{II} were normalized by $K_\circ$ and are plotted in Figure B.47 as a function of the angle subtended from the pole by the crack tip. As the angular position increases, K_I decreases and K_{II} increases for both stress fields, but the rates of change with position are more rapid in the uniaxial stress field than in the case of hydrostatic tension. This results, of course, from Poisson contraction in the former case and from the uniform normal traction in the latter.

The triaxial stress field generated in the central region of the neck specimens is neither uniaxial nor exactly hydrostatic, but is intermediate. Finite element solutions of the stress fields near particles having elastic properties similar (but not equal) to the matrix surrounding them show that remote uniaxial stress (σ_{yy}^{∞}) produces

stress gradients along the surface of the spheres: contours of σ_{yy} and equivalent stress, $\overline{\sigma}$, both indicate minima near the pole (co-located with the axis of loading) and maxima near the equator [191]. In contrast, the finite element solutions of the stresses developed in the neck specimens show that both σ_{yy} and $\overline{\sigma}$ remain constant along the entire surface of the included spheres. The computed radial stresses remain fairly constant over the first 20° from the poles, but diminish toward the equators, as shown earlier in Figure B.24. Consequently, the spheres in neck specimens are not subjected to pure hydrostatic tension. The hydrostatic solutions of He and Ortiz are, nonetheless, judged more appropriate than their uniaxial solutions, for the neck geometry used here.

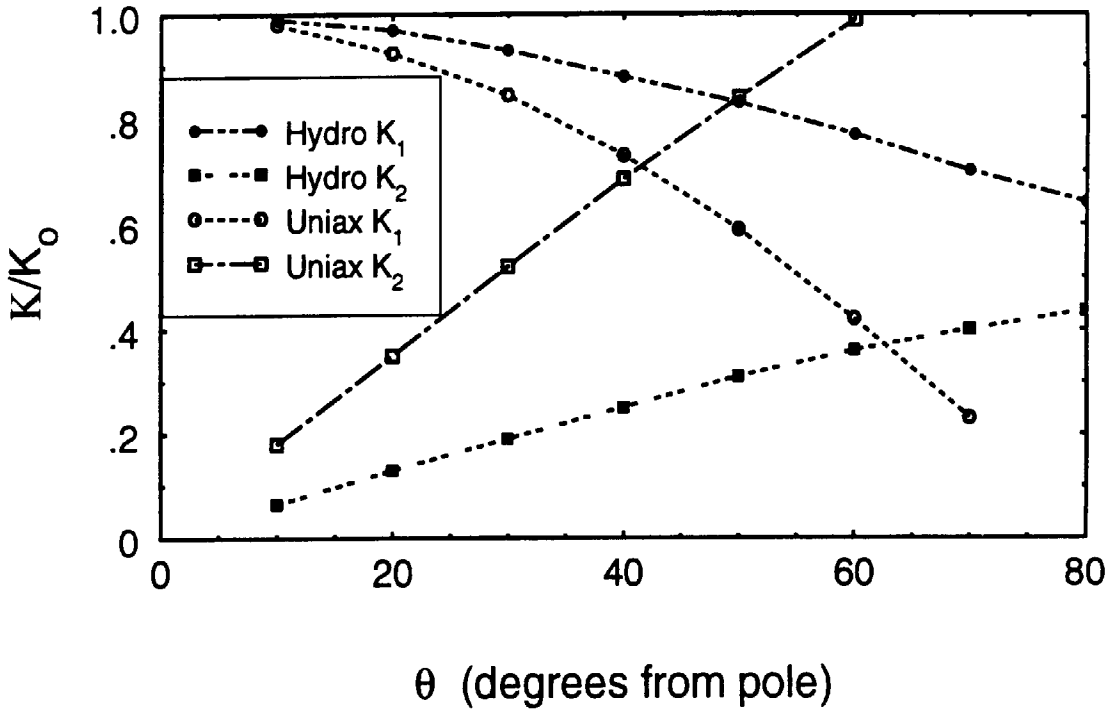

Figure B.47: Stress intensity factors for a spherical crack; from [190].

B.6.4.3 Determination of kinking angles

The toughness of interfaces in the adhesive neck specimens is characterized by the angular positions of the semispherical cracks when they kink into the epoxy neck. The kinking angle is easily determined from examination of the fractured sections as $\theta = \sin^{-1}(a_k/R)$, where a_k is the radius of the circle projected normal to the axis of revolution, exposed by the separation of the interface, and R is the particle radius.

Testing of neck specimens containing as-received PC spheres resulted in no debonding events, so that only a lower bound to the adhesive strength of that material combination could be established, and no toughness information can be deduced. Coating of the PC spheres with a release agent enabled debonding to occur; subsequent fractures along the sphere/epoxy interface extended to angles ranging from 30 to 40°, determined from photographs similar to the one reproduced in Figure B.48.

Following initial debonding in the neck specimens, separation of Nylon/epoxy surfaces extended to kinking angles ranging from 45 to 75°. A typical example shown in Figure B.48 demonstrates a semispherical surface with $a_k/R \sim 0.76$, giving $\theta \approx 50°$. This photomicrograph was taken with transmitted light, because the fracture surface had previously been gold-coated for electron microscopy.

The toughness of silica-glass sphere/epoxy interfaces in the neck specimens was apparently very high, so that little growth of interface cracks followed debonding prior to kinking into the epoxy neck. Shown in Figure B.49 are two examples of interfacial separations of glass spheres. These transmitted light photographs indicate a_k/R ratios of approximately 0.1 and 0.2, which determine kinking angles of about 5 and 10°. These values bracket the range of kinking angles resulting from the testing of all neck specimens containing silica-glass spheres which were not treated with release agents.

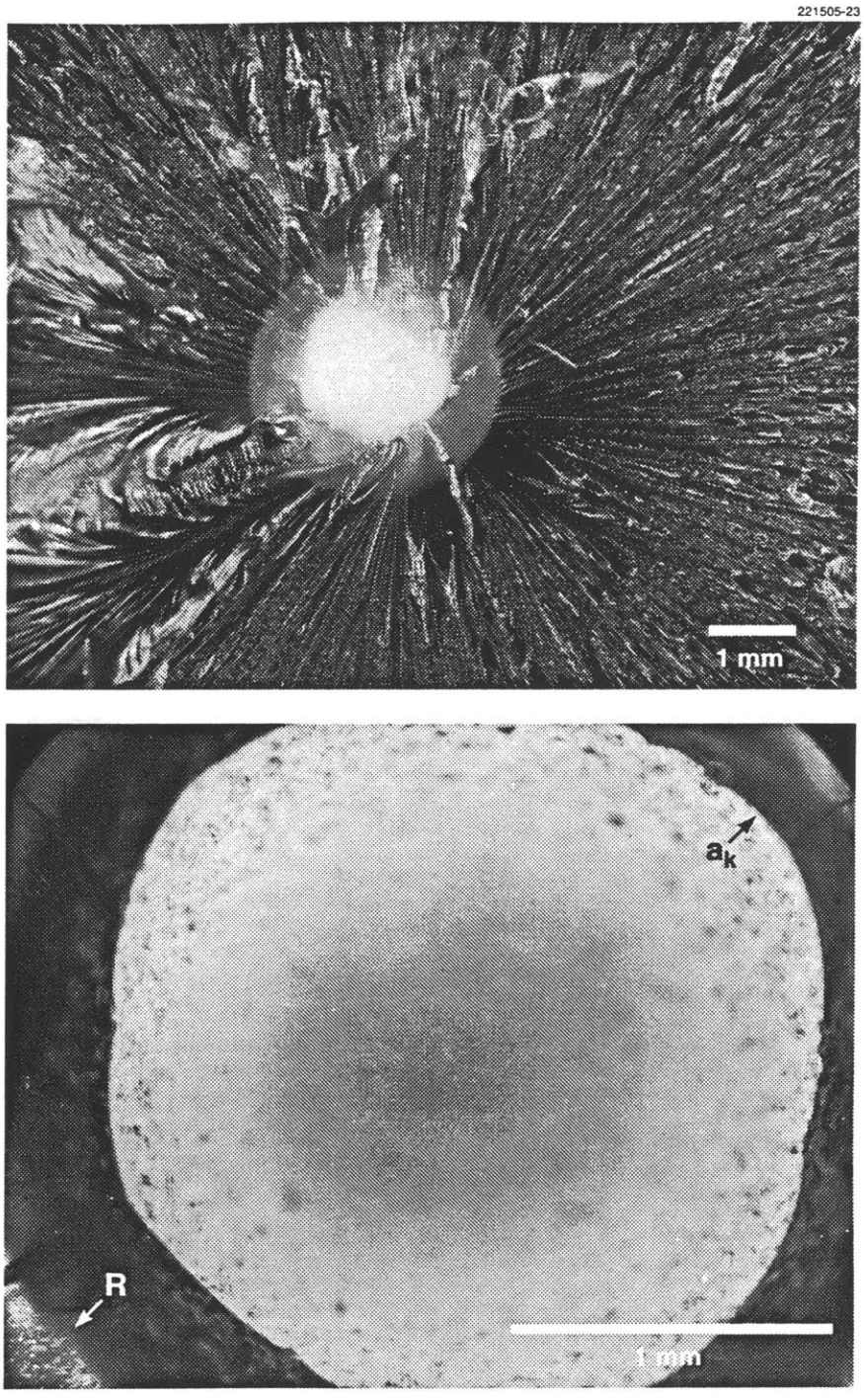

Figure B.48: Surfaces exposed by fracture processes in neck specimens.
Upper photo: release-coated PC sphere with $a_k/R \sim 0.55$.
Lower photo: transmitted light photograph of Nylon sphere with $a_k/R \sim 0.76$.

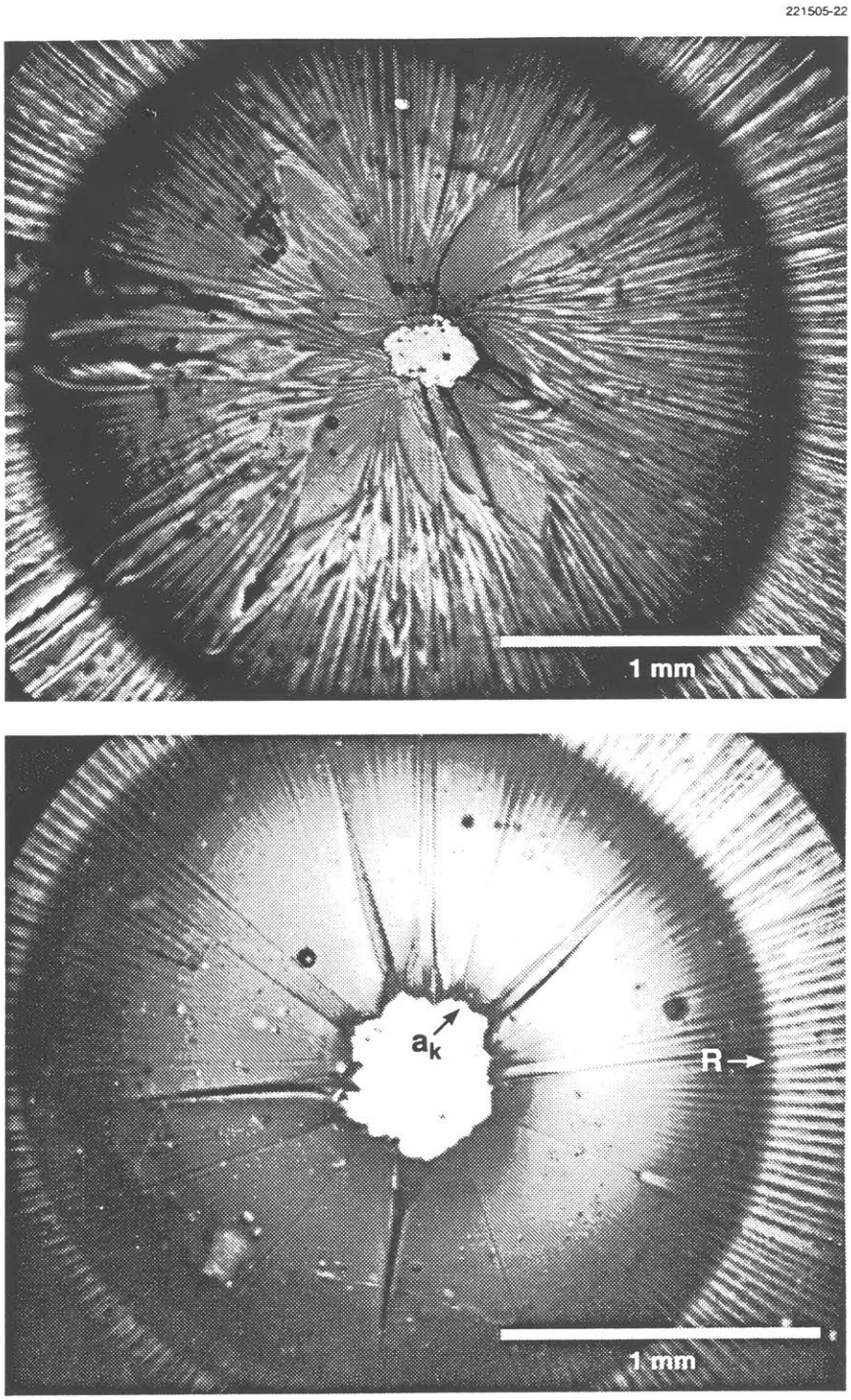

Figure B.49: Transmitted light photomicrographs of fracture surfaces resulting from debonding of glass spheres. Interface cracks advanced to angular positions of approximately 5° and 10° prior to kinking into the epoxy neck sections. The visible bubbles are voids in the glass particles.

B.6.4.4 Fracture toughness calculation

All of the necessary components for the evaluation of interfacial toughness from the neck specimens have been obtained. The close similarity between the elastic constants of PC and Nylon spheres and the neck material (epoxy) results in $\mathcal{E} \approx 0$, so that Equation B.1 becomes

$$\mathcal{G}^{\text{int}} = \frac{(1-\nu^2)}{E}(K_I^2 + K_{II}^2) \,. \tag{B.9}$$

A useful rearrangement of the kinking criterion is

$$\frac{\mathcal{G}_c^{\text{int}}}{\mathcal{G}_{Ic}^{\text{mat}}} = \frac{\mathcal{G}^{\text{int}}}{\mathcal{G}_I^{\text{mat}}} \,, \tag{B.10}$$

since K_I and K_{II} are normalized by K_∞ in Figure B.47, and a sensible measure of $\mathcal{G}_c^{\text{int}}$ is comparison to $\mathcal{G}_{Ic}^{\text{mat}}$.

When the interface cracks kink into the neck sections, $\mathcal{G}_I^{\text{mat}} = K_\infty^2(1-\nu^2)/E$ with $a = a_k$, so that, utilizing Equation B.9, the normalized interface toughness is simply the sum of the squared, normalized stress intensities:

$$\frac{\mathcal{G}_c^{\text{int}}}{\mathcal{G}_{Ic}^{\text{mat}}} = \hat{K}_I^2 + \hat{K}_{II}^2 \tag{B.11}$$

Kinking from the interface between release-coated PC spheres and the epoxy matrix occurred at angles from the pole ranging between 30 and 40°. From the solutions for hydrostatic tension given in Figure B.47, we calculate $0.8 < \mathcal{G}_c^{\text{int}}/\mathcal{G}_{Ic}^{\text{mat}} > 0.9$. For the case of Nylon spheres, kinking angles of between 45 and 75° give $0.6 < \mathcal{G}_c^{\text{int}}/\mathcal{G}_{Ic}^{\text{mat}} > 0.8$.

From data presented in Appendix A, the (arrest and running) toughness of the epoxy at room temperature is approximately $\mathcal{G}_{Ic}^{\text{mat}} = 140\,\text{J/m}^2$. Thus, the toughness of the release-coated PC/epoxy interface is determined to be about $120\pm7\,\text{J/m}^2$, and the toughness of the epoxy/Nylon interface $100\pm15\,\text{J/m}^2$. The toughness of the silica glass/epoxy interfaces is very near that of the epoxy, since kinking from those interfaces into the epoxy consistently occurred at very small angles (5–10°).

Appendix C

Determination of Residual Stresses in Birefringent Composites

This appendix explores some of the issues encountered when using the phenomenon of stress birefringence (photoelasticity) to obtain indications of the residual stresses generated by misfitting inclusions contained within birefringent matrices (in this case, epoxy). Analytical expressions for matrix stresses resulting from differential contractions are summarized from the literature, and then the basic equations of photoelasticity are related. Stresses within the model specimens are calculated and compared to values determined with photoelasticity. Evidence is then shown to indicate that interference fringes persist, with little perturbation, even after a traction-free surface is created (by fracture) within the material. This feature clearly results from *strain*-induced birefringence, so that viscoelastic and plastic behavior of the polymer matrix become relevant. The balance of this appendix discusses a few simple experiments which were performed to address the following fundamental questions: Do stress magnitudes indicated by photomechanics represent the maximum stresses generated during fabrication of composite specimens? How do the photomechanical fringes which accompany the strains vary with time?

C.1 Thermal Stress Analysis of an Inclusion in an Infinite Matrix

C.1.1 Spherical Inclusions

Thermal stresses established in the vicinity of isolated spherical inclusions can be calculated through the use of Selsing's model of a spherical inclusion in a thick-walled sphere. That analysis provides an expression for the hydrostatic pressure, Φ, developed within the inclusion as a result of differential thermal contractions, $\Delta\alpha\,\Delta T$, as a function of the elastic moduli, E_1, E_2, and Poisson's ratios ν_1, ν_2 of the matrix and inclusion, respectively [192]:

$$\Phi = \frac{\Delta\alpha\,\Delta T}{\frac{1+\nu_1}{2E_1} + \frac{1-2\nu_2}{E_2}} . \tag{C.1}$$

Adopting the usual convention of tensile stress being positive, the radial and tangential components of stress in the matrix are given as

$$\sigma_r = -\Phi\left(\frac{R}{r}\right)^3 \qquad \textit{and} \qquad \sigma_\theta = -\frac{\sigma_r}{2} . \tag{C.2}$$

Equation C.1 does not account for variations in α or E as a function of temperature. Though such variations typically remain negligible in ceramics and inorganic glasses such as Selsing worked with, both α and E of the polymers used in the model specimens here experience significant changes over the temperature intervals encountered. To account for temperature-dependent material properties, Equation C.1 should be instituted as

$$\Phi = \int_{T_i}^{T_f} \frac{\Delta\alpha(T)\,T}{\frac{1+\nu_1}{2E_1(T)} + \frac{1-2\nu_2}{E_2(T)}}\,dT , \tag{C.3}$$

where T_i and T_f are the endpoints of the spanned temperature interval and Poisson's ratio is assumed to be constant for both materials.

C.1.2 Cylindrical Inclusions

Matrix stresses in the vicinity of a single, misfitting fiber decrease with the inverse square of radial distance from the axis of the fiber. A peak value of

$$-\sigma_r = \frac{\varepsilon_{T(\perp)}}{\frac{1+\nu_1}{E_1} + \frac{1-\nu_2}{E_2}} \tag{C.4}$$

is given by Shetty for the radial stress component [193], where $\varepsilon_{T(\perp)}$ is the differential thermal contraction between matrix and fiber in the *radial* direction. Clarke and Chiao have shown [194], from the Boussinesq field solution of stresses resulting from a point force (equated to the force resultant of a strained rod), that the influence of differential longitudinal strain upon radial stresses can be represented by adding to the numerator of Equation C.4 the term $(1-2\nu)\varepsilon_{T(\parallel)}$.

Using the equivalent inclusion method of Eshelby, Lu *et al.* obtain the result that, for an infinitely long fiber contained in an infinite matrix, the longitudinal stresses within the matrix must be zero at locations far removed from the fiber ends [195]. They further estimated the effect of finite volume fractions of fibers by recognizing that the longitudinal stress created within a fiber must be balanced by stresses within a volume of matrix associated with each fiber. Consequently, their approximation for longitudinal matrix stress is [195]

$$\sigma_z = \frac{E_1 + E_2}{2} \varepsilon_{T(\parallel)} \frac{f}{(1-\nu)}, \tag{C.5}$$

where f is the volume fraction of fibers (rods), and $\varepsilon_{T(\parallel)}$ is the differential thermal contraction between matrix and fiber in the *longitudinal* direction.

The equations given above may be implemented most accurately by including temperature dependencies and integrating over temperature intervals, as was demonstrated for the case of stresses generated by misfitting spheres.

C.2 Photoelastic Analysis of Inclusion Stresses

C.2.1 Background

Photoelasticity is an experimental technique for the determination of magnitudes and distributions of stresses in model specimens. The basis of the method utilizes the phenomenon of strain birefringence, whereby coherently polarized light passing through a material is split into two vectors, each travelling in the same direction but in mutually orthogonal planes with differing wave speeds. Upon exiting the material, the light waves recombine and travel with the same velocity again, but with a phase separation (retardation). If the light is polarized once again, retardations which are integral multiples of the wavelength of the light source will locally extinguish the light intensity and be manifested as interference fringes. In materials which are strain-birefringent, the magnitude of retardation is proportional to the shear strain encountered by the light waves as they pass through the material; for elastic materials with stresses below yield, the retardation will be proportional to the shear stress. Thus, photoelastic interference fringes can be indicators of contours of constant shear.

Much detail regarding the theory and implementation of photoelastic methods is provided in the classic, two-volume work of Frocht [196] and the more recent, practical volume of Durelli and Riley [197]. The essence of what is required for the following discussions is provided here.

When a monochromatic light source is passed through a circular polarizer, through a birefringent material in a state of plane stress, and then through a circular polarizer again, the resultant interference fringe order, N, at a given planar location is related to the difference in principal stresses at that point by the expression [198]

$$N = \frac{(\sigma_1 - \sigma_2)}{f} t \,, \tag{C.6}$$

where t is the thickness of the specimen and f is known as the "material fringe factor." The fringe factor, f, is a measure of the birefringence sensitivity of the material upon stress, and here will carry the significance of *normal* stress/fringe/thickness.

Magnitudes of $(\sigma_1 - \sigma_2)$ can be determined in a specimen, if f is known, by determining the fringe order, N, produced with a monochromatic light source and circular polarizers. At free surfaces the principal stresses vanish, so they provide a known stress location from which to begin counting fringe orders. In a light field arrangement, where unstressed regions fully transmit the incident light, integer values of N are determined by crossing from a light band over a dark fringe to the edge of the next light band. With a white light source, these alternating bands are brilliant colors; hence, the technique described here, using circular polarizers, yields fringe patterns which are termed "isochromatics," regardless of whether the incident light is white or monochromatic.

Fringe factors are known to vary with time, both as a result of load relaxation at constant strain, and as a result of optical creep at constant stress. Generalizations are difficult to state, however, since time-dependent stress/strain-optical behavior varies greatly between different materials, as exemplified by the following. Constant-load tensile creep tests with the thermosetting resin *Columbia Resin CR-39* demonstrated fringe factors which increased with time, asymptotically reaching values of about 120% of the initial values after 40 minutes under load [199]. Similar tests conducted with a "standard HEX-phthalic epoxy resin" demonstrated a fringe factor which *decreased* with time, reaching a value reduced by about 10% after one hour of loading [200]. The data indicate, nonetheless, that the fringe factors change by only one or two percent during the first minute, so that fringe orders determined quickly (photographed) in a specimen under static loading can be related to fringe factors determined under similar circumstances through Equation C.6.

C.2.2 Three Dimensional Effects

C.2.2.1 Stress freezing technique

The photoelastic determination of stresses, as outlined so far, is limited to elastic, two-dimensional fields in which the principal stress normal to the plane of the specimen is zero, *i.e.* situations of plane stress. A common technique, known as "stress-freezing," can be employed to determine three-dimensional distributions of stress in birefringent models.

In this variation of the standard photoelastic technique, a model specimen is heated to a critical temperature (above T_g) and then subjected to the loads of interest. The temperature of the model is then slowly reduced while the loading is held constant. After ambient temperature is attained, the loading is removed, but the model will remain in a deformed state for a great length of time (typically, years) while creep recovery occurs at ambient temperatures.

A model specimen prepared in this manner may be sliced into thin sections, each of which may be examined in polarized light to obtain stress contours corresponding to planar positions within the three-dimensional model. With proper characterization of the stress/strain-birefringence behavior of the material at the elevated temperature, magnitudes of stresses developed within the model can be related to the actual structure which it represents [201]. While this experimental method has largely been superseded by numerical modeling, it does provide dramatic, 3-D visualizations of stress contours and is particularly revealing in the case of stress concentrations. Careful procedures are required, however, to minimize residual stresses generated during fabrication of specimens and to prevent the perturbation of model stresses during machining processes [202].

C.2.2.2 Determination of stresses near spherical inclusions

A geometrical complication arises in the case of determining stresses in a matrix surrounding a spherical inclusion with the use of photoelasticity. The stress field surrounding a spherical inclusion decays isotropically with a dependence of r^{-3}, so that the difference in principal stresses within planes normal to the direction of light passage will vary with position through the thickness of specimen under examination. The photoelastic technique will, in effect, integrate the stresses through the thickness and indicate an average difference in principal stresses at a given planar location, so that photoelastically indicated stresses will be attenuated from the stresses which actually exist near the inclusions. The actual stresses present can be related to the photoelastic stresses through the following geometrical approximation.

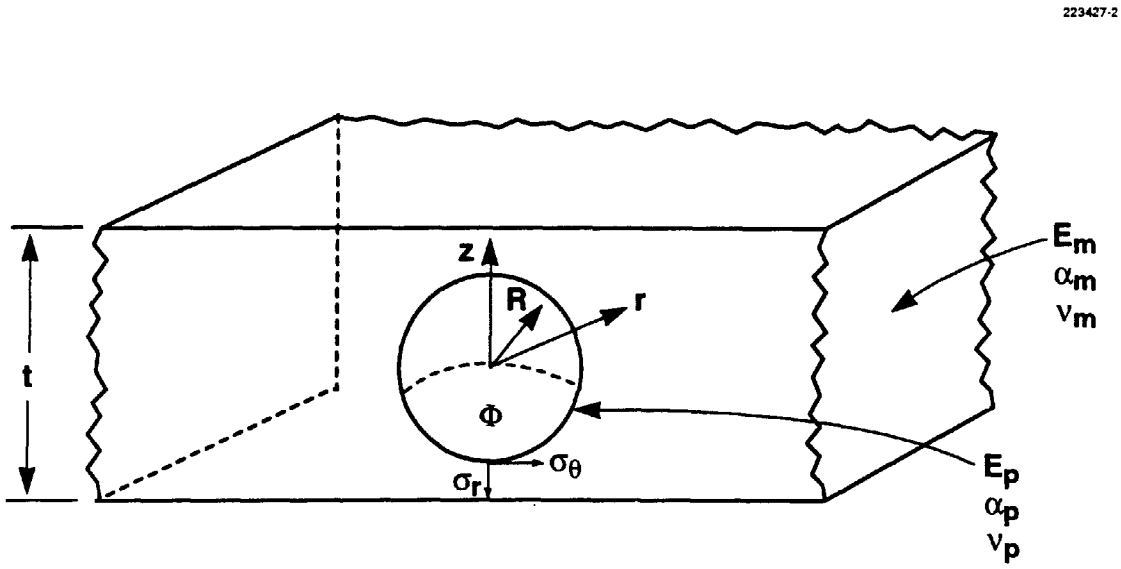

Figure C.1: Geometry of inclusion within slab specimen for photoelastic determination of pressure, Φ, within sphere and misfit stresses in matrix.

The dependence of $(\sigma_1 - \sigma_2)$ upon axial position, z, parallel to the direction of light transmission, can be approximated first writing

$$r(z) = \sqrt{R^2 + z^2} \ , \tag{C.7}$$

where the variables are defined as in Figure C.1. Next, we recognize that the difference in principal stresses as indicated by photoelasticity will be averaged over an infinite number of thin planar slices normal to the direction of light transmission:

$$(\sigma_1 - \sigma_2)_{\text{photo}} \ = \ \frac{1}{t} \int_0^t (\sigma_1 - \sigma_2)(z)\, dz \ . \tag{C.8}$$

Recalling that

$$(\sigma_1 - \sigma_2) \ = \ \frac{3}{2} \Phi \frac{R^3}{r^3} \ , \tag{C.9}$$

where Φ is the magnitude of hydrostatic pressure induced within the inclusion, we substitute Equation C.7 and write that

$$(\sigma_1 - \sigma_2)_{\text{photo}} \ = \ \frac{3}{2} \Phi \frac{R^3}{t} 2 \int_0^{t/2} (R^2 + z^2)^{-3/2}\, dz \ . \tag{C.10}$$

Evaluating the integral, we find that

$$(\sigma_1 - \sigma_2)_{\text{photo}} \ = \ 3\,\Phi \frac{R^3}{t} \left[\frac{\frac{t}{2}}{R^2 \left\{ \left(\frac{t}{2}\right)^2 + R^2 \right\}^{1/2}} \right] \ = \ \Phi \frac{3}{2} \frac{R}{\left\{ \left(\frac{t}{2}\right)^2 + R^2 \right\}^{1/2}} \ . \tag{C.11}$$

Rearranging terms, we obtain the result

$$\Phi \ = \ \frac{2}{3} (\sigma_1 - \sigma_2)_{\text{photo}} \sqrt{\left(\frac{t}{2R}\right)^2 + 1} \ , \tag{C.12}$$

which indicates the geometrical factor necessary to correct for the attenuating effect of material which is radially furthest from the inclusion (and therefore less stressed). Since the pressure within an inclusion is related to the actual matrix stresses at its surface by $\Phi = \frac{2}{3}(\sigma_1 - \sigma_2)$, the stresses actually present near a spherical inclusion are greater than the stresses indicated by photoelasticity, by the factor of $\sqrt{\left(\frac{t}{2R}\right)^2 + 1}$.

C.2.3 Determination of Material Fringe Factors

Photoelastic determination of stresses in a model specimen requires knowledge of the material fringe factor. Calibration tests with uniaxial bars can be performed at increasing load in polarized light to determine the changing fringe order as a function of stress. This procedure, however, does not afford the determination of N with good resolution. Better measurement of N is provided by specimens in which biaxial stresses and stress gradients are present.

The most common specimen geometry for the calibration of the material constant, f, is that of a diametrally compressed disk [203, 204]. A disk which is subjected to two compressive forces, P, acting across a diameter aligned with the y-axis, develops, in addition to the compressive stresses acting in the y-direction, tensile stresses along the x-axis. The exact solution to this elasticity problem was provided by Timoshenko, giving the stresses at the center of the disk as [205]

$$\sigma_y = -\frac{6P}{\pi t D} \qquad and \qquad \sigma_x = \frac{2P}{\pi t D}, \tag{C.13}$$

where D and t are the diameter and thickness of the disk, respectively. At the center of the disk, x and y are principal directions, so that

$$(\sigma_1 - \sigma_2)_{center} = \frac{8P}{\pi t D}. \tag{C.14}$$

Applying Equation C.6 to the center of the disk, we find

$$f = \frac{8P}{\pi D N}. \tag{C.15}$$

Thus, f may be determined easily and accurately by determining the center fringe order in a disk as a function of diametral compressive load.

The method just outlined was employed to determine the fringe factor of the epoxies used as matrix materials in the crack-trapping model specimens. Disks were cast

in PVC tubes cemented to PMMA sheets, resulting in specimens having diameters of 52 mm and thickness of 10 mm. After postcuring, the disks were removed from the molds and the meniscus was removed from each free surface by milling and polishing. The specimens were then annealed at a few degrees below their respective T_g's for a few hours to remove the slight residual stresses developed during casting.

Compression of the disks was performed between polished platens in a displacement-controlled testing machine. A sodium light source with wavelength, $\lambda = 5980\,\mathring{A}$, was directed through a circular polarizing filter into the rear of each disk under compression. A second circular polarizing filter was placed in front, through which photographs were recorded of the fringe patterns developed under load.

A typical sequence of recorded fringe patterns is reproduced in Figure C.2. In (a), the stress-free disk is seen to contain many surface and volume imperfections resulting from inclusion of dust particles and minute voids. The images of fringe patterns in (b)–(d) show increasing center fringe order, N with increasing load. In these images, there appear to be slight perturbations of the fringes at two or three locations. These most likely result from orientation of long molecular chains during the room-temperature initial curing of the specimens; subsequent postcuring and annealing cannot remove birefringent fields induced in this manner [202].

The fringe patterns developed during testing at constant displacement displayed minimal relaxation behavior. This effect was so slight that focused images could be recorded with exposure times on the order of 20 seconds. During this time, the indicated load relaxed by less than one percent. Therefore, not only could accurate calibration data be obtained, but the optical relaxation was seen to result (primarily) from viscoelastic stress relaxation. The data obtained in this manner for the epoxies used in the model specimens ($T_g = 72, 80\,^\circ$C) are plotted in Figure C.3. From the slope of the data it is determined that the epoxy used here has $f = 12.8$ MPa/fringe per mm of model thickness.

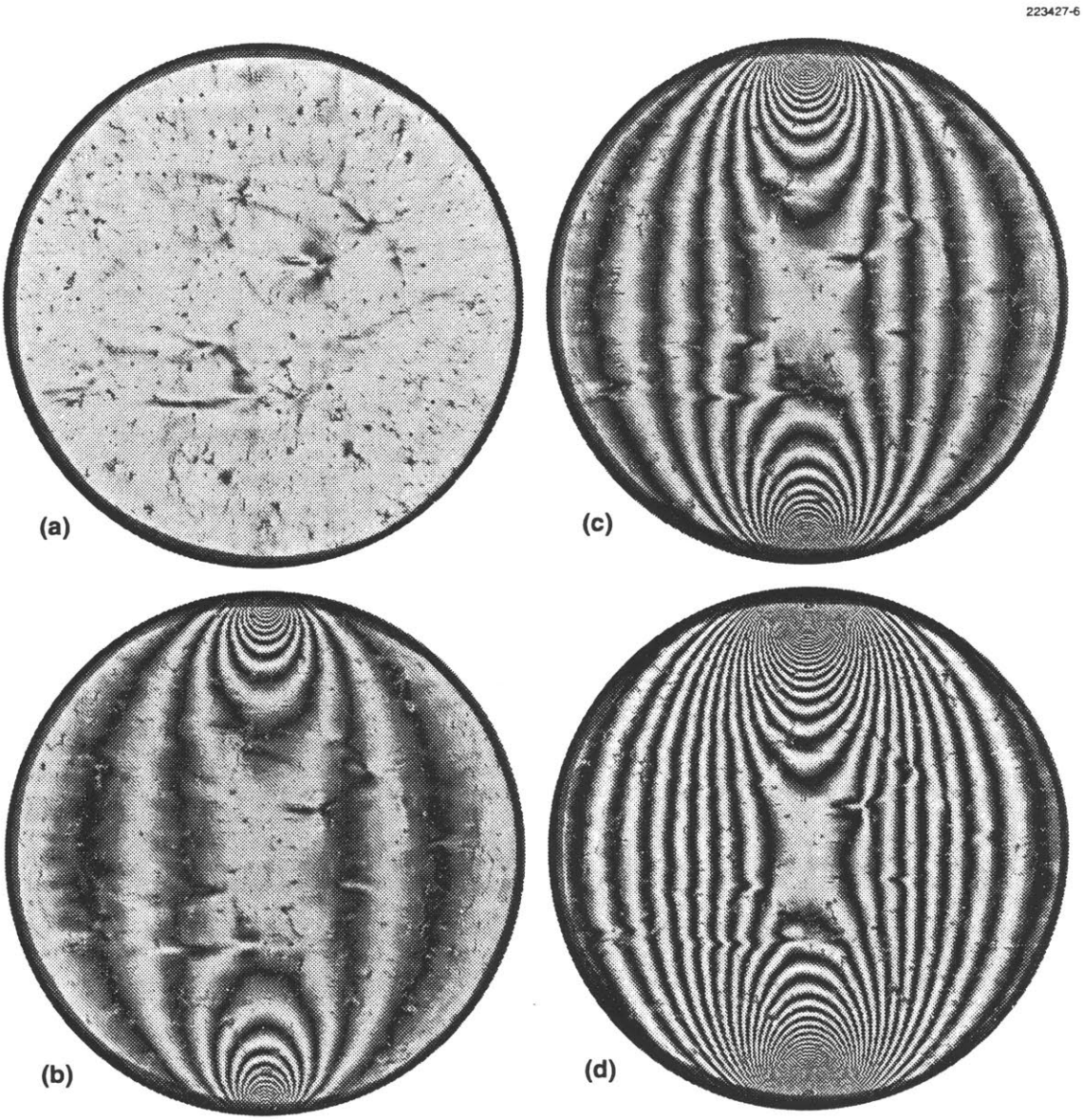

Figure C.2: Diametral compression of epoxy disk for calibration of material f.
(a) P = 0; (b) P = 525 N, $N_c = 2$; (c) P = 1067 N, $N_c = 4$; (d) P = 2090 N, $N_c = 8$.

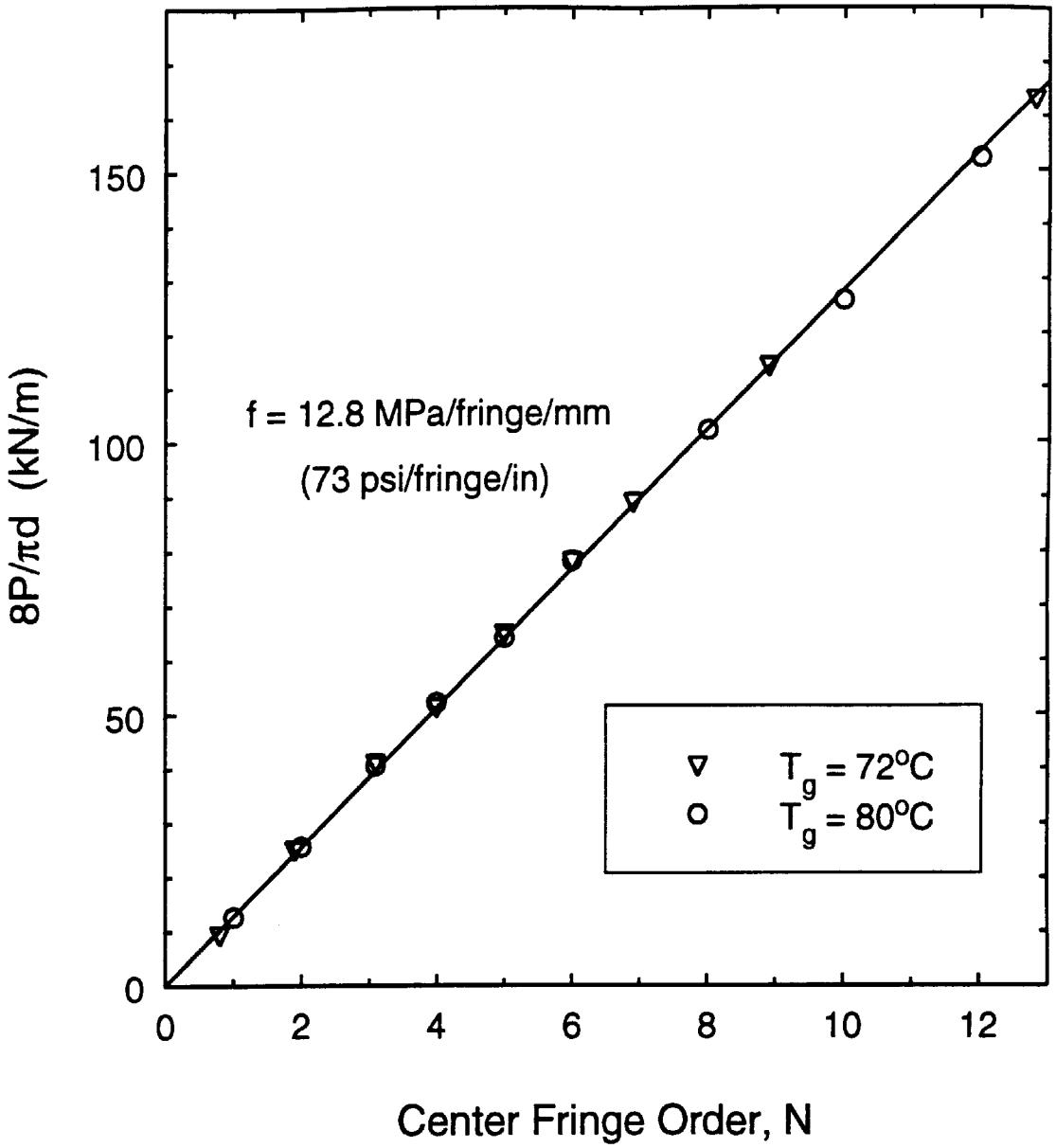

Figure C.3: Determination of fringe factor, f (normal stress), by diametral compression of epoxy disks under quasi-static loading.

C.3 Determination of Thermal Stresses in Model Specimens

C.3.1 Calculated Stresses

Due to different thermal contractions exhibited by the materials used, excursions in temperature generate stresses in and around the inclusions within the crack-trapping model specimens. The first temperature change involved is the initial cooling from the T_g of the epoxy to room temperature. The second interval is from room temperature to -60°C. To enable calculation of the stresses resulting from these temperature excursions, thermal contraction strains were measured for each of the individual materials with a thermomechanical analyzer (TA 2900). A summary of these measurements is tabulated below. This information enables the accurate determination of differential thermal strains ($\int \Delta\alpha(T) T\, dT$) simply as $\varepsilon_T = \varepsilon_m - \varepsilon_p$, where ε_m and ε_p are the individual contraction strains of the matrix and particle, respectively.

Table C.1: Average thermal strains of constituent materials used in the crack-trapping model specimens.

			80°C to 20°C		20°C to -60°C		
Material	*Form*	*Orient.*	$-\varepsilon$ (10^{-6})	*St.Dev.*	$-\varepsilon$ (10^{-6})	*St.Dev.*	*#data*
Epoxy	$T_g = 80$°C	isotr.	7204	532	5625	307	15
Nylon	sphere	random	8086	429	6301	270	10
	rod	radial	6080	126	5606	107	4
	rod	long.	7610	86	6530	109	3
PC	sphere	random	4111	34	4916	113	6
	rod	radial	4357	29	5073	90	5
	rod	long.	4387	72	5117	195	4

Residual thermal stresses in the model specimens at the surface of inclusions (*i.e. maximum matrix stresses*) have been calculated using Equation C.3 for spheres, Equations C.4 and C.5 for rods, and the thermal strains reported in Table C.1. The room-temperature moduli of epoxy, nylon and PC were measured (as described in Appendix A) as 2.5, 2.9 and 2.4 GPa, respectively; moduli at −60°C are 3.5, 3.6 and 3.0 GPa. The integrated effect of temperature-dependent moduli was approximated by taking intermediate values within each temperature interval. For the reduced temperature interval, the measured modulus of the T_g = 80°C epoxy at −20°C is about 3.2 GPa; assuming similar temperature behaviors, moduli of 3.4 and 2.8 are taken for the Nylon and PC at −20°C. For the cooling interval from 80°C to 20°C, moduli of 2.0, 2.2 and 2.1 GPa are taken for the Epoxy, Nylon and PC, respectively. Poisson's ratio was assumed to be 0.37 for the epoxy and 0.35 for the inclusions.

Computed values of maximum matrix stresses are given in Table C.2 for each of the indicated temperature intervals. The actual thermal stresses present in the model specimens were equal to the sum of the stresses generated during the initial cooling, reduced by some unknown amount of relaxation, plus the cooling stresses generated just prior to execution of the crack-trapping experiments. Although the stress relaxation of the epoxy used here is not known, experiments with a similar epoxy (EPON 828, TETA) demonstrated a relaxation time constant, τ_r, in excess of 10^{10} min at room temperature [206]. Assuming similar behavior here, the stresses in model specimens which have been stored for several months will not have time to relax appreciably. (Since $\sigma_{\text{relax}} \propto \sigma_o e^{-t/\tau_r}$) Therefore, the residual stresses during the crack-trapping experiments are taken to be the sum of those generated during the two cooling stages.

Table C.2: Calculated matrix thermal stresses (MPa) at inclusion surfaces.

		80°C to 20°C		20°C to -60°C		Final	
Inclusion	*Material*	σ_r	σ_θ	σ_r	σ_θ	σ_r	σ_θ
Spheres	Nylon	1.8	-0.9	2.2	-1.1	4.0	-2.0
	PC	-6.2	3.1	-2.2	1.1	-8.	4.0
		σ_r	σ_z	σ_r	σ_z	σ_r	σ_z
Rods	Nylon	-1.0	-0.1	-0.4	-0.3	-1.4	-0.4
	PC	-3.7	0.55	-1.0	0.15	-4.7	0.7

C.3.2 Photoelastic Stress Analysis

C.3.2.1 Apparent Stress

To enable the photoelastic determination of stresses present in the model specimens due to differential thermal contractions, plate specimens were prepared of similar epoxy, containing similar inclusions to those used in the crack-trapping specimens. These specimens were placed between circular polarizing filters, and the isochromatic fringes created by the sodium lamp used in the calibration procedure were photographed. Reproductions of typical photographs are provided in Figure C.4.

The specimen shown in the upper photograph of Figure C.4 contains 3.18-mm diameter inclusions (PC sphere, PC and Nylon rods) cast within a 6.5-mm thick plate of epoxy prepared in the same manner as the crack-trapping specimens, giving T_g=80°C. The fringe orders at the surface of the PC sphere, PC rod and Nylon rod are seen to be approximately 2.4, 5.0 and 2.0, respectively. Using Equation C.6, the values of $\Delta\sigma \equiv (\sigma_1 - \sigma_2)$ apparent from the isochromatics are calculated to be 9.8 and 3.9 MPa for the PC and Nylon rods. For the case of the PC sphere, the attenuating 3-D effect analyzed in Section C.2.2.2 needs to be accounted for by multiplying the apparent photoelastic stress by the geometrical factor given in Equation C.12. For the specimen considered here, $\frac{t}{2R} = 2$, giving a correction of $\sqrt{5}$. However, the sphere rests upon lower plane of the plate, so the limits of integration in Equation C.10 need to be from $-t/4$ to $3t/4$ giving (with the multiplier, 2, removed) a slightly higher correction factor of 2.41 for this particular geometry. Thus, for the PC sphere, $\Delta\sigma = 2.4(12.8)2.41/6.5 \approx 11.4$ MPa.

It may quickly be realized that the values of $\Delta\sigma$ just deduced from the isochromatics shown in Figure C.4 are significantly greater than the corresponding values analytically determined earlier and indicated by Table C.2. Experimental imprecision

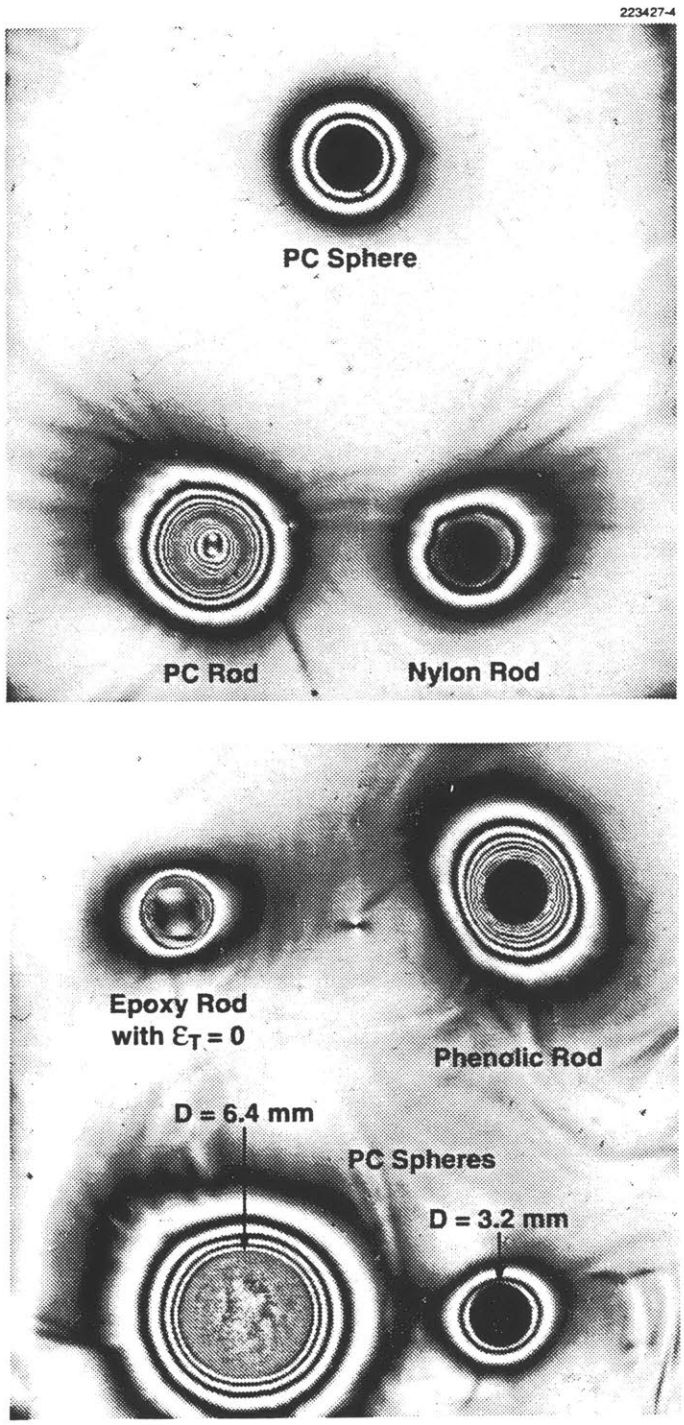

Figure C.4: Isochromatic fringes produced by misfitting thermal strains near inclusions, as labeled, in 6.5-mm thick plate specimens of T_g = 80°C epoxy.

may contribute to the differences between the analytical and photoelastic results, but the major contributor is an effect which appears to be over-looked in all photoelastic studies of composites reported in the literature. It is claimed here that molecular conformation during curing of the matrix, in accommodation of imposed geometries, contributes to the total birefringent field generated within a composite material.

C.3.2.2 Molecular Orientation Effects

Birefringence results from stress-induced orientation of molecules, generating anisotropy in the optical behavior of the material. Additionally, birefringence can result from molecular orientation in the absence of stress. Andrews and Hammack performed a series of experiments with highly oriented polymers (PS and PMMA), showing that the birefringence produced by constant strain, in the absence of stress, was a function of temperature [207]. They further maintain that some "polarizability anisotropy is associated with the hydrocarbon backbone chain of polymers," and that the stress-induced birefringence results from orientation of side groups. This view concurs with statements of Paipetis [202], to the effect that formation of non-random main chains during cold-curing of two stage-curing epoxies (as used here) produces birefringent fields which become locked in place by subsequent cross-linking during postcuring.

To test whether conformational, orientation birefringence contributes to the isochromatic fringes observed in the specimens here, the following simple experiment was performed. A rod of epoxy cured only at room-temperature[1] was cast into a plate of epoxy, along with inclusions similar to those examined before. The plate was allowed to cure at room temperature as usual, and then was given the postcure heating cycle which imparts to the epoxy a T_g of 80°C. In this manner, an inclusion having *exactly* the same thermoelastic properties as the host matrix was fabricated.

[1] To prevent exposure to two elevated postcuring cycles, which would result in a material with a slightly different expansion behavior from the matrix.

The lower photograph of Figure C.4 shows the isochromatic fringes surrounding the thermoelastically matching (epoxy) rod. The fringe order associated with molecular conformation to a rod-inclusion of the same size (3.18 mm) as the PC and Nylon rods, in this particular specimen, appears to be about 1.4. If this value is subtracted from the fringe orders previously determined for the PC and Nylon rods, then the recomputed values of $\Delta\sigma$ are approximately 6 and 1 MPa, respectively. Referring to Table C.2, these values are in reasonable agreement with the analytically determined $\Delta\sigma$ values of 4.3 and 0.9 MPa. In the case of spherical inclusions, the conformational orientation does not develop through the thickness of the specimen, as is the case with rods, but may be expected to develop locally around the surface of the sphere. Therefore, the indicated fringe order of 1.4 resulting from molecular conformation to rods (in these specimens) should be reduced, in the case of spheres, by the geometrical factor determined in Equation C.12. Following through with this logic, we may determine for the 3.18-mm PC sphere (with $N \approx 2.4$ and geometrical factor of 2.4) that $\Delta\sigma \approx [2.4 - (1.4/2.4)]12.8(2.4)/6.5 = 8.6$ MPa. The fringes developed near the larger, 6.4-mm diameter PC sphere are of order $N \approx 4.4$. Since the thickness of the plate is equal to $2R$, the correction factor in Equation C.12 is equal to $\sqrt{2}$. Thus, we compute for the larger PC sphere that $\Delta\sigma \approx [4.4 - (1.4/\sqrt{2})]12.8\sqrt{2}/6.5 = 9.5$ MPa. These values agree quite well with the value of 9.3 MPa determined analytically.

Consequently, it appears that molecular orientation birefringence resulting from conformation to imposed constraints (inclusion surfaces) can strongly influence the photoelastic determination of residual stresses in epoxies cured with bifunctional curing agents that polymerize the epoxy groups first by promoting chain extension and then by crosslinking at elevated temperatures. A simple method was illustrated here by which this effect could be accounted for, resulting in photoelastic stress determination which is in close agreement with stresses calculated from analytical models reported in the literature, in conjunction with careful measurements of the individual thermal strains of constituent materials.

C.4 Rheological Behavior of Fringe Orders

C.4.1 Background

During fracture experiments with epoxy specimens containing steel spherical inclusions, it was observed that the isochromatic fringes induced by misfit strains were influenced little by the creation of a fracture surface within the birefringent fields. The photographs reproduced in Figure C.5 show an example where a fracture path passes tangentially to one sphere and intersects another at its equator. The upper photograph was obtained shortly after the specimen was fractured, while the lower photograph was obtained over two years later. Though the resolution of the fringes in these photographic reproductions is not high, it is apparent that the passage of a traction-free surface through the birefringent fields permitted only very slow decay of the fringe orders near the misfitting spheres.

In the upper photograph of Figure C.5, there appears to be no perturbation of the fringes (within the superimposed white circles) due to the presence of the fracture surface. At first glance, this would imply that the stresses surrounding the sphere had relaxed completely, and the fringes result strictly from residual *strains* which are locked in place. The lower photograph, however, indicates that an anelastic, or viscoelastic, creep of the fringes intersected by the fracture path occurred over a two year period; in contrast, the fringes which were not intersected by the traction-free surface show no apparent creep. Thus, a driving force must exist which causes the creep to be enabled by the traction-free surface. This driving force clearly is a stress which has become frozen into the epoxy surrounding the spheres.

A description of such permanently established stresses is given by Boyce *et al.* in their description of the molecular processes envisaged to be responsible for the plastic flow resistance of amorphous polymers [53] (such as epoxy). It is conceived that the

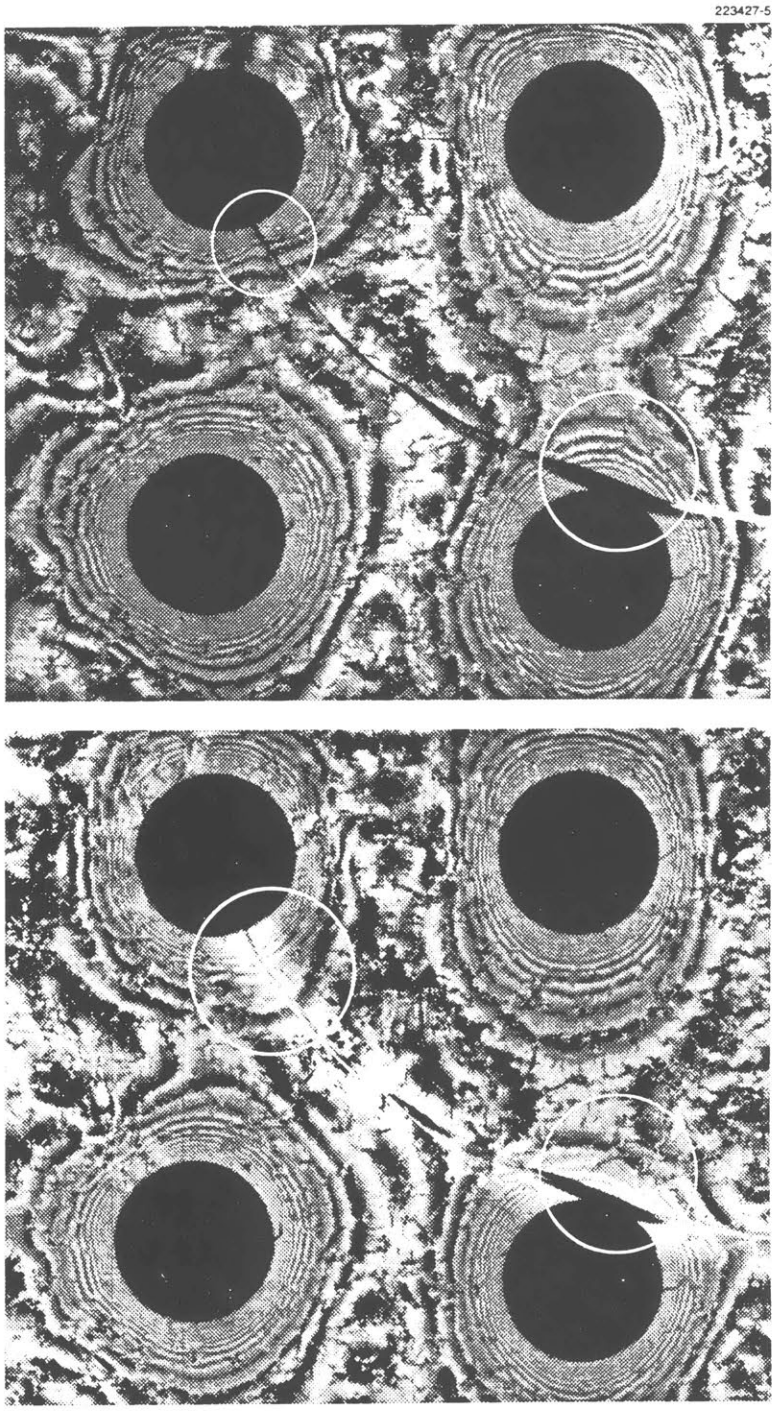

Figure C.5: Post-fracture persistence of isochromatic fringes produced by misfitting thermal strains near steel spheres in epoxy plate. Upper photo, taken immediately after fracture, indicates little change in fringes due to traction-free surface. Lower photo, obtained 29 months later, indicates photomechanical creep of about 20% occurred during the intervening time.

deformation resistance of isotropic glassy polymers results from two components: the initial intermolecular resistance which must be overcome to initiate plastic flow, and an entropic resistance due to physical entanglements between chains. Orientation hardening results from stresses required to rearrange the physical entanglements (which, in the case of cross-linked epoxies, can be quite dense). These stresses are referred to as "back stresses," and become locked in place at temperatures below the glass transition [53].

In the case of the specimens under discussion here, no stresses exceeding yield were created by the differential strains, but the strains were imposed for a great length of time. Consequently, they were "set in place" by viscoelastic deformation of the polymer, allowing the back stresses to be established. Following imposition of the traction-free surface within the back-stress field, viscoelastic relaxation of the back stresses is evidenced by the photographs. The rate of stress decay apparent from these photographs is consistent with exponential time constants on the order of 10^{10} min as measured for similar epoxies at room temperature [206].

The origin of the interference fringes in the specimen shown in Figure C.5, and other, similar specimens, is indeed a stress. As pointed out by Boyce *et al.* , this is evidenced by the complete relaxation of the stress when a specimen possessing back stress is heated to above its glass transition temperature. A clear example of this behavior is shown in Figure C.6, which contains photographs of epoxy disks which had been subjected to diametral compression of an extended period of time. Following removal of the compressive constraint, birefringent fields remained locked in place. Creation of traction-free surfaces by sawing through the disks altered the fringes almost imperceptibly. Heating above the glass transition temperature, however, clearly enabled relaxation of stresses which were incapable of relaxing at room temperature over laboratory time scales. (Relaxation will occur at room temperature, but over a length of time which is a dozen or more orders of magnitude greater than the time

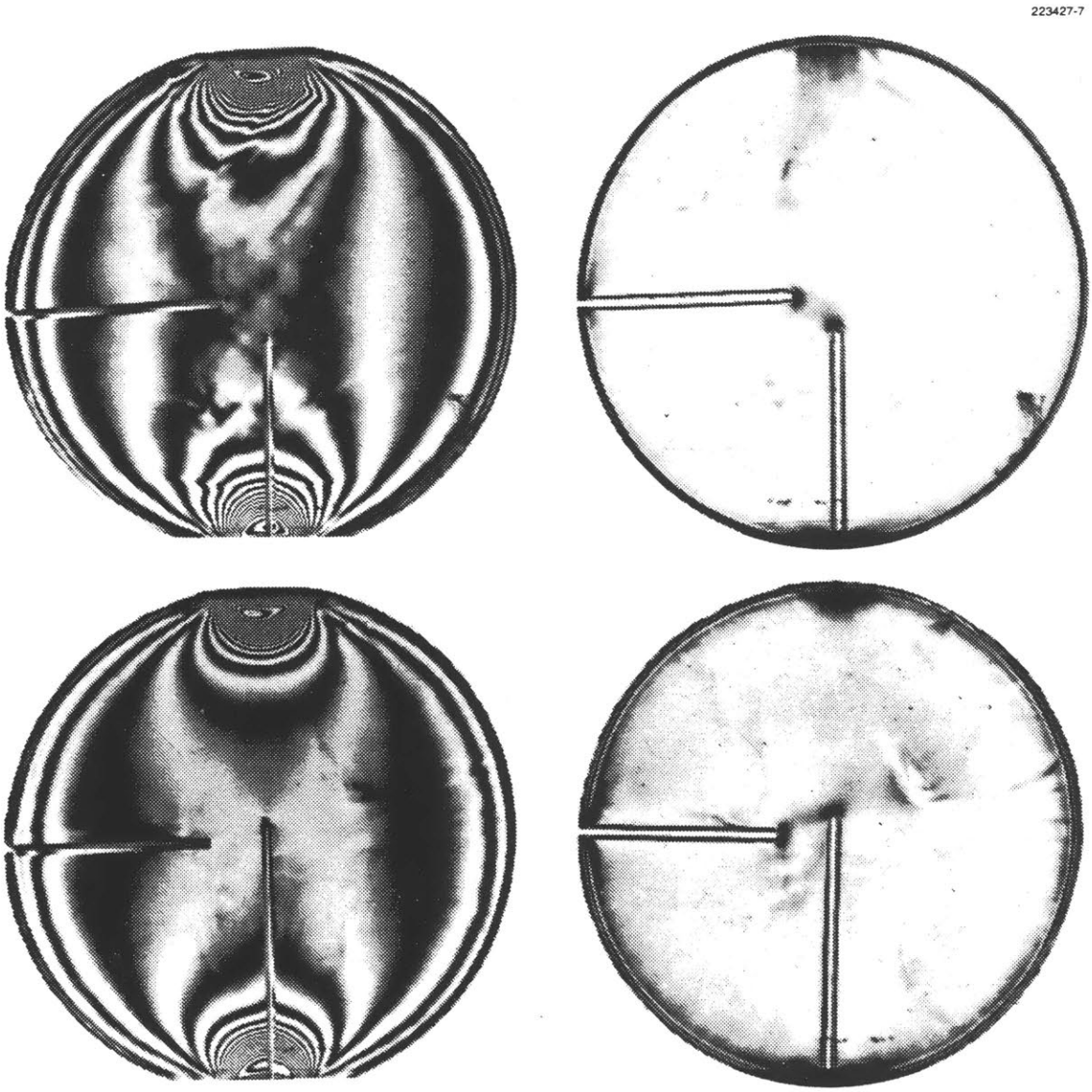

Figure C.6: Demonstration of locked-in isochromatic fringes in epoxy disks which had been subjected to constant compressive strain for 15 days.

required for relaxation enabled by annealing.)

The issue of when, or whether, the birefringent fields surrounding inclusions in glassy polymers indicate the stresses in the matrix surrounding those inclusions may be influenced by the viscoelastic mechanical behavior of the polymer. The effect of mechanical relaxation appears to be slight, for the epoxy used here, as evidenced by little change in the fringe orders near spheres (*not* near the fracture path) in the specimen shown in Figure C.5. Another factor which may have some influence has been reported as optical creep, whereby the fringe order created by a constant level of stress and strain changes with time [199, 200]. To address this issue, for the use of photomechanics in the determination of residual misfit stresses in the epoxy specimens used in this research, the following simple experiments were performed.

C.4.2 Photo-Optical Relaxation Experiments

A series of epoxy disks, 52 mm in diameter and 10-mm thick, were cast in PVC tubes which were cemented to PMMA sheets so that one side of the castings would be smooth. The meniscus was machined flat, the machined surface was polished, and the specimens were annealed to remove and machining-induced stresses. The disks were then placed between two aluminum bars with 10-mm square cross-sections. Bolts between the bars were then tightened, subjecting the disks to a diametral compressive displacement which was kept fixed throughout the period of observation. The disks were observed in polarized light (sodium-wavelength), and photographs of the fringe patterns were recorded at the following times: just after loading ($T = 0^+$), two weeks, and four weeks later. Typical isochromatic fringe patterns obtained from one specimen are reproduced in Figure C.7.

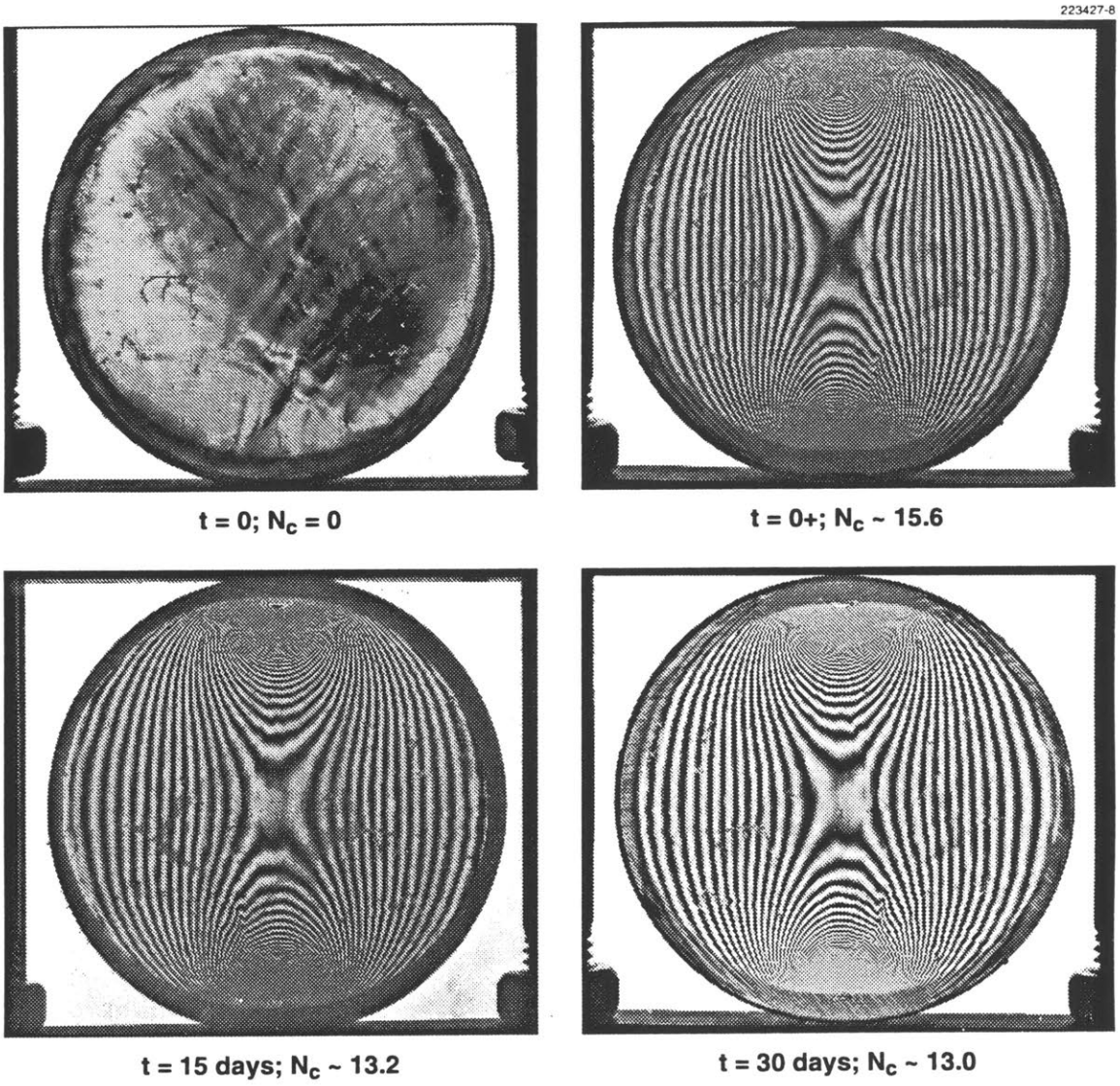

Figure C.7: Typical evolution of isochromatic fringes in epoxy disk subjected to constant diametral compressive strain. Times and center fringe order, N_c, as indicated.

Though more data should have been acquired during the initial stages of relaxation, it is clear that the center fringe order in this disk (and the others tested) asymptotically approached a constant value, following a period of initial relaxation. The magnitude of relaxation reached in the quasi-steady state is on the order of 15%. Levin reports that the optical creep in epoxies subjected to constant stress is on the order of a 10% reduction in the peak fringe value after one hour of loading, and remains nearly constant thereafter [200]. The experiment performed here subjected the disk specimens to imposed displacements, so that mechanical relaxation occurred, in addition to optical relaxation. An extensive study of stress relaxation in similar epoxies indicates that the relaxation time constant is in excess of 10^{10} min, so the stress relaxation which occurred in these disk specimens is judged to be insignificant. This assertion could have been easily verified by measuring the rate of change of stresses in the aluminum bars through the use of strain gages.

The available literature indicates that the mechanical relaxation of similar epoxies [206] proceeds at a rate far slower than the initial optical relaxation [200, 208], which therefore creates the dominating effect upon the significance of observed fringes near inclusions in birefringent matrices. The simple relaxation experiments performed with the disks here show that, with this particular epoxy, the residual stress levels indicated near inclusions decay within a few days to a value which remains relatively constant, at about 85% of the magnitude which was initially established.

Additional data regarding the time-dependence of photomechanical behavior of the epoxy used in this research was obtained during the recovery, or reverse creep, of these disks following their unloading. Those data are presented and discussed in the next section.

C.4.3 Photo-Optical Reverse Creep Experiments

The reverse creep of the center fringe order in the compressed epoxy disks was photographically recorded following release of the diametral compressive constraint. Unlike the relaxation data previously related, data were obtained at intervals spaced closely enough to obtain a good indication of the time dependence of the photo-optical recovery behavior. A typical sequence of images recorded during the recovery of one specimen in reproduced in Figure C.8.

The first frame indicates the magnitude of the steady-state center fringe order that had been established during the compression of the disk. The second frame indicates the fringes which existed after the unloading of the disk, after just enough time had elapsed to allow repositioning of the specimen between polarizing filters and focusing of the camera. The difference in center fringe order between these first two data is a measure of the elastic stress component that was relieved immediately upon unloading of the disk. The remaining birefringence is due to locked-in back stress, which subsequently creeps out of the specimen over an extended period of time.

Plotted in Figure C.9 are data obtained in this manner from three typical epoxy disks, each loaded to initial stresses of significantly different magnitude. Indicated in the figure are the initial, center fringe orders at $t = 0$, the inelastic component remaining 30 seconds after the elastic unloading, and the ensuing creep recovery process spanning over about fifteen months. The data are plotted again in Figure C.10, from which the data in the loaded configuration has been omitted.

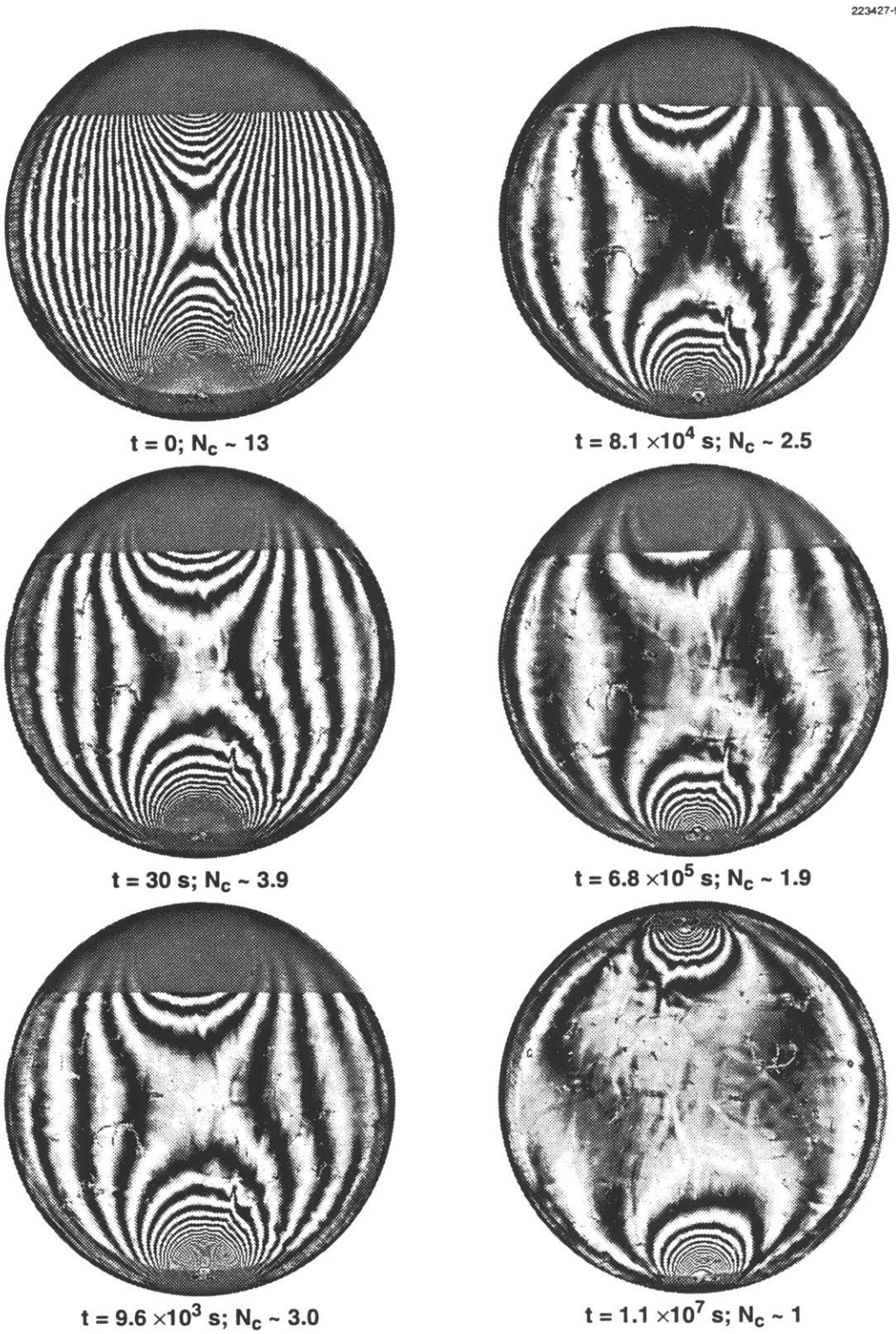

Figure C.8: Typical evolution of isochromatic fringes in epoxy disk relieved of diametral compressive constraint. Times and center fringe order, N_c, as indicated.

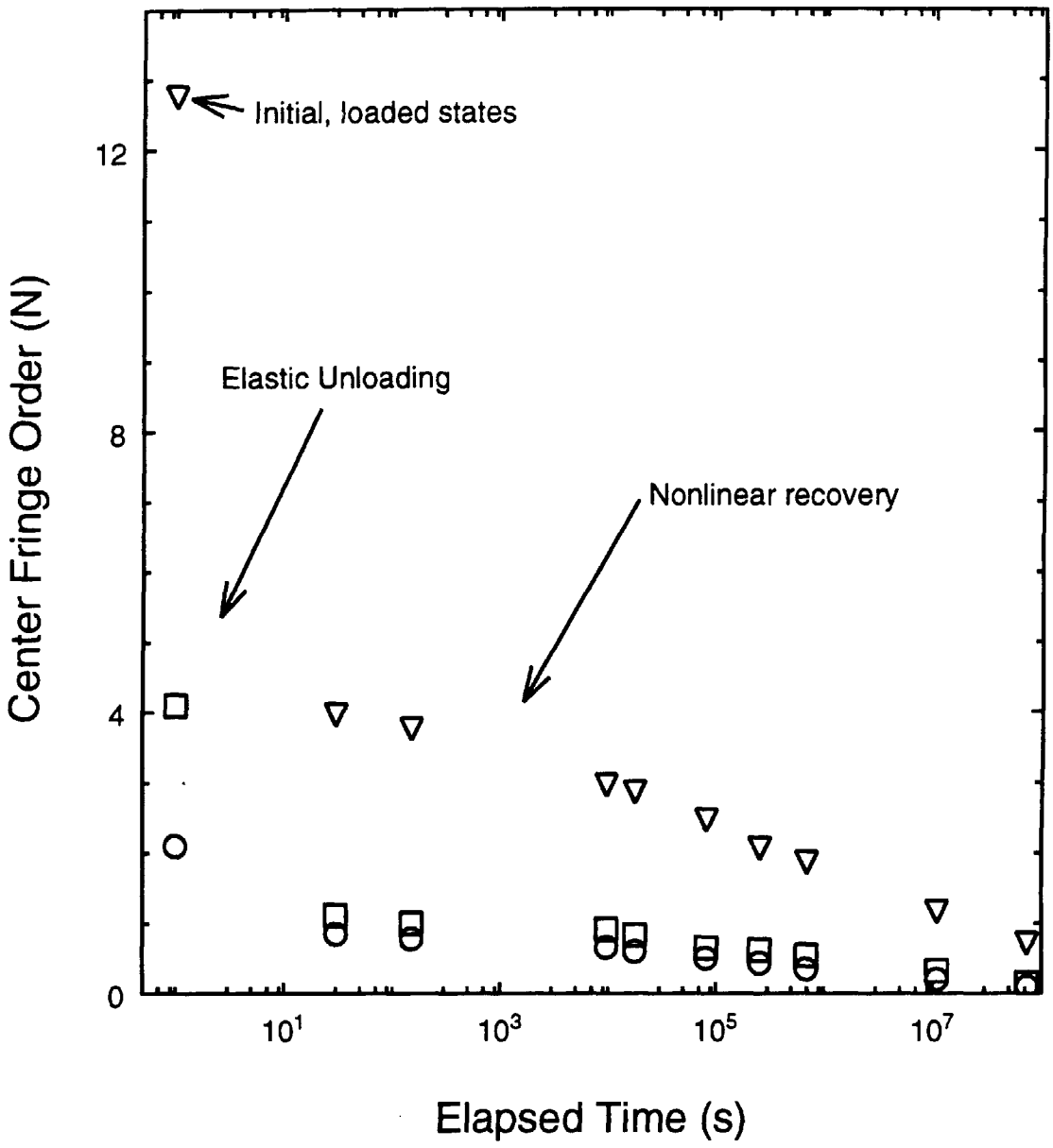

Figure C.9: Photo-Optical creep recovery data, showing initial elastic unloading followed by anelastic/viscoelastic recovery.

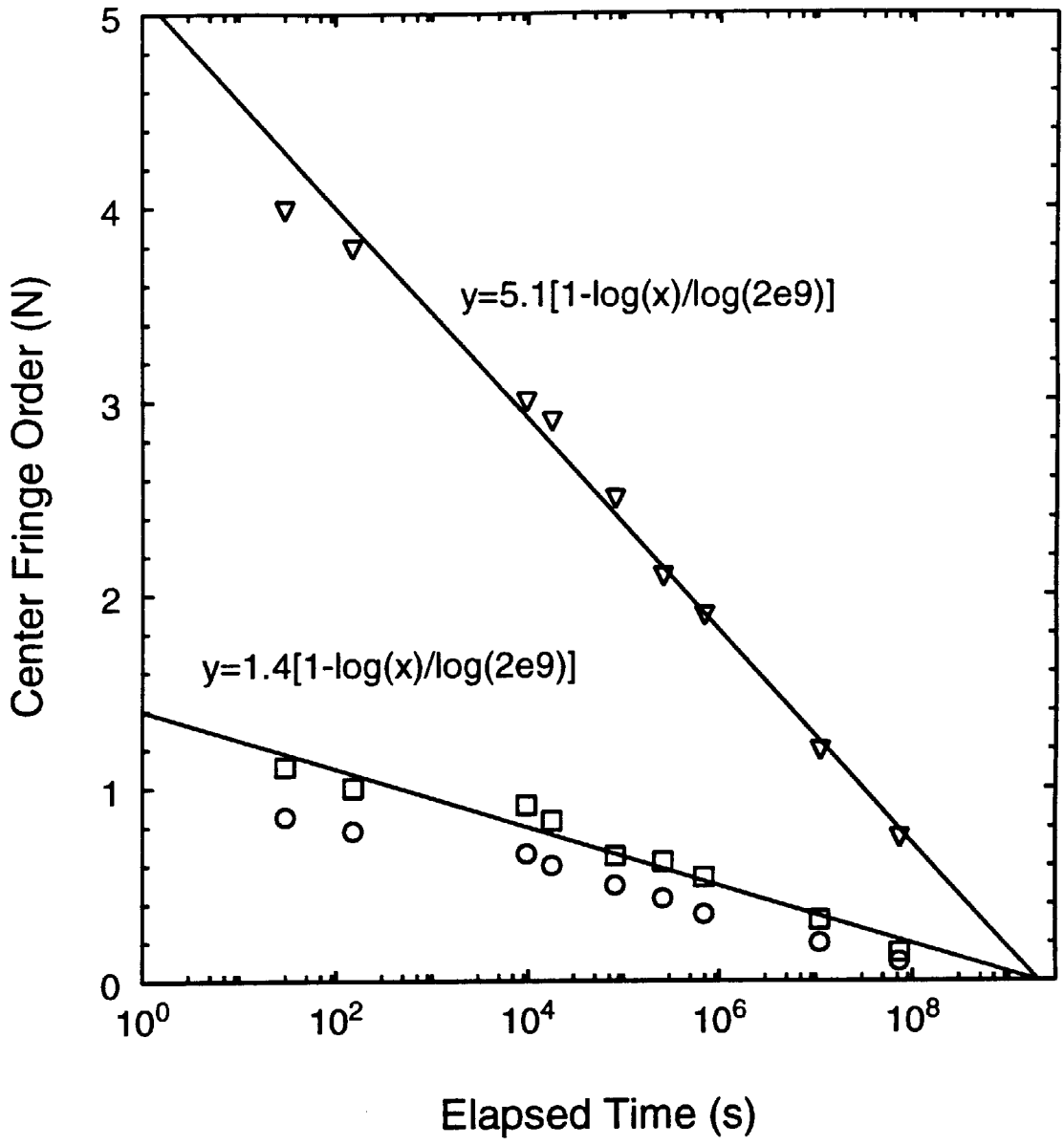

Figure C.10: Photo-Optical creep recovery data, showing fit of data to a log-linear decay, approaching zero at a time of about 2×10^9 s.

Figure C.10 indicates that the center fringe orders during creep recovery of the epoxy specimens did not asymptotically approach some steady-state value, as occurred during the optical relaxation experiment. Rather, the fringes observed during the creep recovery continued to decay steadily with time, so that the data are approximated well by the log-linear functions shown in Figure C.10. Though no physical basis for the log-linear dependency measured can be offered, its implication upon the significance of birefringent fields produced by residual misfit stresses can be inferred.

The optical (reverse) creep in these specimens proceeded at a rate much greater than the mechanical recovery, as evidenced by the finite deformation remaining in specimens which demonstrate little remaining birefringence. Consequently, in specimens which have a traction-free surface passed through them, such as in the fracture specimen shown in Figure C.5, relief of the strain constraint would allow optical creep recovery to proceed at a rate faster than the mechanical recovery. Because fringes are seen to persist despite the intersection of free surfaces, this is additional evidence which supports the view that back stresses in the vicinity of misfitting inclusions (in glassy polymers) are not immediately relaxed by the creation of an intersecting free surface.

As a final note, these experiments clearly would have benefited from the measurement of mechanical relaxation and creep through the use of strain gages or similar techniques. Moreover, while the data presented here is certainly not quantitatively conclusive regarding the time-dependency of photomechanical behavior, they do serve to point out the nature of time-dependent phenomena in birefringent polymers which complicate the use of photomechanics for the determination of residual misfit stresses.

Bibliography

[1] Lilley, J. and Holloway, D.G., "Crazing in epoxy resins," *Philosophical Magazine,* **28** (1973), 215–220.

[2] Meeks, A.C., "Fracture and mechanical properties of epoxy resins and rubber-modified epoxy resins," *Polymer,* **15** (1974), 675–681.

[3] Morgan, R.J. and O'Neal, J.E., "The microscopic failure processes and their relation to the structure of amine-cured bisphenol-A-diglycidyl ether epoxies," *Journal of Materials Science,* **12** (1977), 1966–1980.

[4] LeMay, J.D. and Kelly, F.N., "Structure and ultimate properties of epoxy resins," in *Advances in Polymer Science,* **78** (Springer-Verlag 1986), 115–148.

[5] Yamini, S. and Young, R.J., "The mechanical properties of epoxy resins, Part 2: Effect of plastic deformation upon crack propagation," *Journal of Materials Science,* **15** (1980), 1823–1831.

[6] Kinloch, A.J. and Williams, J.G., "Crack blunting mechanisms in polymers," *Journal of Materials Science,* **15** (1980), 987–996.

[7] Smith, J.W., Kaiser, T. and Roulin-Moloney, A.C., "Deformation-induced volume damage in particulate-filled epoxy resins," *Journal of Materials Science,* **23** (1988), 3833–3842.

[8] Yee, A.F. and Pearson, R.A., "Toughening mechanisms in elastomer-modified epoxies, Part 1: Mechanical studies," *Journal of Materials Science,* **21** (1986), 2462–2474.

[9] Yee, A.F. and Pearson, R.A., "Toughening mechanisms in elastomer-modified epoxies, Part 2: Microscopy studies," *Journal of Materials Science,* **21** (1986), 2475–2488.

[10] Moloney, A.C., Kausch, H.H., Kaiser, T. and Beer, H.R., "Review: Parameters determining the strength and toughness of particulate filled epoxy resins," *Journal of Materials Science,* **22** (1987), 381–393.

[11] Kinloch, A.J., "Mechanics and mechanisms of fracture of thermosetting epoxy polymers," in *Advances in Polymer Science,* **72** (Springer-Verlag 1985), 45–67.

[12] McClintock, F.A. and Argon, A.S., *Mechanical Behavior of Materials* (Addison-Wesley 1966), 110.

[13] *EPON© Resin Structural Reference Manual* (Shell Chemical Co. 1982).

[14] Dayle, A. *Shell Chemist*, private communication (1991).

[15] Prime, R.B. and Sacher, E., "Kinetics of epoxy cure: 2. The system bisphenol-A diglycidyl ether/polyamide," *Polymer,* **13** (1972), 455–458.

[16] Lee, H. and Neville, K., *Handbook of Epoxy Resins* (McGraw-Hill N.Y. 1967).

[17] *Curing chemicals for epoxy resins,* (Harshaw/Filtrol Technical Bulletin Cleveland, Ohio 1991).

[18] Rehage, G. and Borchard, W., "The thermodynamics of the glassy state," in *The Physics of Glassy Polymers,* ed. R. N. Haward (Applied Science, London 1973), 54–107.

[19] Ferry, J.D., *Viscoelastic Properties of Polymers,* (Wiley, N.Y. 1980), 283.

[20] Gee, G., "The glassy state in polymers," *Contemp. Phys.* **11**, (4) (1970), 313–334.

[21] Kovacs, A.J., "Glass transitions in amorphous polymers. Phenomenological study," in *Advances in Polymer Science,* **3** (Springer-Verlag 1964), 394–507.

[22] Gillham, J.K., "Torsional braid analysis: a semimicro thermomechanical approach to polymer characterization," *CRC Critical Reviews in Macromolecular Science* (Jan. 1972), 83–172.

[23] Moy, P. and Karasz, F.E., "The interactions of water with epoxy resins," in *Water in Polymers,* ed. Rowland, S.P. **ACS 127** (American Chemical Society Wash., D.C. 1980), 505–513.

[24] Fava, R.A., "Differential scanning calorimetry of epoxy resins," *Polymer,* **9** (1967), 137–151.

[25] Plazek, D.J. and Frund, "Epoxy resins (DGEBA): The curing and physical aging process," *Journal of Polymer Science, B* **28** (1990), 431–448.

[26] Choy, I.-C. and Plazek, D.J., "The physical properties of bisphenol-based epoxy resins during and after curing," *Journal of Polymer Science, B* **24** (1986), 1303–1320.

[27] Tool, A.Q., *Journal of Research of the National Bureau of Standards,* **5** (1930), 627.

[28] Gray, A.P., "Establishing a correlation between the degree of cure and the glass transition temperature of epoxy resins," *Perkin Elmer Report,* (1972).

[29] Prime, R.B., "Differential scanning calorimetry of the epoxy cure reaction," *Polymer Engineering and Science,* **13**, (5) (1973), 365–371.

[30] Rai, J.S.P. and Mathur, G.N., "Differential scanning calorimetry study of epoxy novalacs," *Polymer Comm.,* **32**, 14 (1991), 439–442.

[31] Petrie, S.E.B., "Thermal behavior of an annealed organic glass," *Journal of Polymer Science: A-2,* **10** (1972), 1255–1272.

[32] Petrie, S.E.B., "The effect of excess thermodynamic properties versus structure formation on the physical properties of glassy polymers," *Journal of Macromolecular Science-Physics,* **B12** (1976), 225–247.

[33] Ophir, Z.H., Emerson, J.A. and Wilkes, G.L., "Sub-T_g annealing studies of rubber-modified and unmodified epoxy systems," *Journal of Applied Physics,* **49**, 10 (1978), 5032–5038.

[34] Alamo, R. and Mandelkern, L., "Origins of endothermic peaks in differential scanning calorimetry," *Journal of Polymer Science: Part B: Polymer Physics,* **24** (1986), 2087–2105.

[35] Chang, T.D., Carr, S.H. and Brittain, J.O., "Studies of epoxy resin systems: Part C: Effect of sub-T_g aging on the physical properties of a fully cured epoxy resin," *Polymer Engineering and Science,* **22**, (18) (1982), 1221–1227.

[36] Kovacs, A.J., "A multiparameter approach for structural recovery of glasses and its implication for their physical properties," *Annals of the New York Academy of Sciences,* **371**, (1981), 38–66.

[37] Nairn, J.A., "Thermoelastic analysis of residual stresses in unidirectional, high-performance composites," *Polymer Composites,* **6**, (2) (1985), 123–130.

[38] Nairn, J.A. and Zoller, P., "Matrix solidification and the resulting residual stresses in composites," *Journal of Materials Science,* **20** (1985), 355–367.

[39] Plepys, A.R. and Farris, R.J., "Evolution of residual stresses in three-dimensionally constrained epoxy resins," *Polymer,* **31**, (10) (1990), 1932–1936.

[40] Vratsanos, M.S. and Farris, R.J., "A novel method for measuring the uniaxial mechanical properties of an epoxy resin during polymerization," *Journal of Applied Polymer Science,* **33** (1987), 915–923.

[41] V. B. Gupta, L. T. Drzal, C. Y-C. Lee and M. J. Rich, "The temperature-dependence of some mechanical properties of a cured epoxy resin system," *Polymer Engineering and Science,* **25**, (13) (1985), 812–823.

[42] ASTM "ANSI/ASTM D638: Standard test method for tensile properties of plastics," in *Annual Book of ASTM Standards* (ASTM Phil. PA 1980), 225–240. (American Chemical Society Wash., D.C. 1980), 505–513.

[43] Williams, J.G. and Ford, H., "Stress–strain relationships for some unreinforced plastics," *Journal of Mechanical Engineering Science,* **6**, (4) (1964), 405–417.

[44] Yamini, S. and Young, R. J., "The mechanical properties of epoxy resins, Part 1: Mechanisms of plastic deformation," *Journal of Materials Science,* **15** (1980), 1814–1822.

[45] X. Caux, G. Coulon and B. Escaig, "Influence of the degree of crosslinking on the plastic deformation behavior of epoxy resins," *Polymer,* **29** (1988), 808–813.

[46] V. T. Truong and B. C. Ennis, "Effect of physical aging on the fracture behavior of crosslinked epoxies," *Polymer Engineering and Science,* **31**, (8) (1991), 548–557.

[47] Struik, L.C.E., *Physical Aging in Amorphous Polymers and Other Materials,* (Elsevier, N.Y. 1978).

[48] Kong, E.S-W., "Physical aging in epoxy matrices and composites," in *Advances in Polymer Science,* **80** (Springer-Verlag 1986), 125–171.

[49] Argon, A.S., "Plastic deformation in glassy polymers," in *Polymeric Materials: Relationships Between Structure and Mechanical Behavior*, eds. Baer and Radcliffe (ASM, Ohio 1975), 411–486.

[50] Argon, A.S., "Inelastic deformation and fracture of glassy solids," in *Materials Science and Technology,* **6**, ed. H. Mughrabi, (VCH Pubs. 1993), 463–508.

[51] Ferry, J.D., *op. cit.*, 30.

[52] Argon, A.S., "Stability of plastic deformation," in *The Inhomogeneity of Plastic Deformation*, ed. Read-Hill (ASM, Ohio 1971), 161–189.

[53] Boyce, M.C., Parks, D.M. and Argon, A.S., "Large inelastic deformation of glassy polymers. Part I: Rate dependent constitutive model," *Mechanics of Materials,* **7** (1988), 15–33.

[54] Petrie, S.E.B., "The Problem of Thermodynamic Equilibrium," in *Polymeric Materials: Relationships Between Structure and Mechanical Behavior*, eds. Baer and Radcliffe (ASM, Ohio 1975), 55–118.

[55] Bowden, P.B., "The yield behavior of glassy polymers," in *The Physics of Glassy Polymers,* ed. R. N. Haward (Applied Science, London 1973), 279–339.

[56] Kambour, R.P. and Robertson, R.E., "The mechanical properties of plastics," in *Polymer Science,* **7**, ed. A.D. Jenkins (North-Holland, London 1972), 687–822.

[57] G'Sell, C. and McKenna, G.B., "Influence of physical ageing on the yield response of model DGEBA/poly(propylene oxide) epoxy glasses," *Polymer,* **33**, (10) (1990), 2103–2113.

[58] M.M. Santore, R.S. Duran and G.B. McKenna, "Volume recovery in epoxy glasses subjected to torsional deformation: the question of rejuvenation," *Polymer,* **32**, (13) (1991), 2377–2381.

[59] Argon, A.S., "A theory for the low-temperature plastic deformation of glassy polymers," *Philosophical Magazine,* **28**, (1973), 839–865.

[60] Argon, A.S. and Bessonov, M.I., "Plastic deformation in polyimides, with new implications on the theory of plastic deformation of glassy polymers," *Philosophical Magazine,* **35**, (4) (1977), 917–933.

[61] Argon, A.S. and Bessonov, M.I., "Plastic flow in glassy polymers," *Polymer Engineering and Science,* **17**, (3) (1977), 174–182.

[62] Oleink, E.F., "Epoxy-aromatic amine networks in the glassy state: structure and properties," in *Advances in Polymer Science,* **80** (Springer-Verlag 1986), 49–99.

[63] Pink, E. and Campbell, J.D., "Deformation characteristics of reinforced epoxy resins, Part 2: An analysis of thermally activated deformation," *Journal of Materials Science,* **9** (1974), 665–672.

[64] Pink, E. and Campbell, J.D., "Deformation characteristics of reinforced epoxy resins, Part 1: The mechanical properties," *Journal of Materials Science,* **9** (1974), 658–6642.

[65] Turner, S., "Creep in glassy polymers," in *The Physics of Glassy Polymers,* ed. R. N. Haward (Applied Science, London 1973), 223–278.

[66] Pink, E., "Structural variations affecting the Eyring analysis of macro deformation in polymers," *Materials Science and Engineering,* **22** (1976), 85–89.

[67] McClintock, F.A. and Argon, A.S., *op. cit.*, 457.

[68] A. S. Argon, "Sources of toughness in polymers," in *Advances in Fracture Research (ICF7),* **4**, eds. K. Salama *et al.*, (Pergamon 1989), 2661–2681.

[69] Broek, D., *Elementary engineering fracture mechanics,* (Martinus Nijhoff 1984).

[70] Kanninen, M.F., and Popelar, C.H., *Advanced fracture mechanics,* (Oxford 1985).

[71] Hutchinson, J.W., *A course on nonlinear fracture mechanics,* (The Technical University of Denmark 1979).

[72] Mower, T.M. and Li, V.C., "Fracture characterization of random short fiber reinforced thermoset resin composites," *Engineering Fracture Mechanics,* **26**, (4) (1987), 593–603.

[73] Kanninen, M.F., "An augmented double cantilever beam model for studying crack propagation and arrest," *International Journal of Fracture,* **9**, (1) (1973), 83–92.

[74] Mostovoy, S. Crosley, P.B. and Ripling, E.J., "Use of crack-line-loaded specimens for measuring plane-strain fracture toughness," *Journal of Materials,* **2** (1967), 661–681.

[75] Gledhill, R.A., Kinloch, A.J., Yamini, S. Young, R.J., "Relationships between mechanical properties of and crack propagation in epoxy resin adhesives," *Polymer* **19** (1978), 574–582.

[76] Cherry, B.W. and Thomson, K.W., "The fracture of highly crosslinked polymers, Part 1: Characterization and fracture toughness," *Journal of Materials Science,* **16** (1981), 1913–1924.

[77] Selby, K. and Miller, L.E., "Fracture toughness and mechanical behavior of an epoxy resin," *Journal of Materials Science,* **10** (1975), 12–24.

[78] Moloney, A.C. and Kausch, H.H., "Direct observations of fracture mechanisms in epoxide resins," *Journal of Materials Science Letters,* **4** (1985), 289–292.

[79] Cantwell, W.J., and Roulin-Moloney, A.C., "Fractography and failure mechanisms of unfilled and particulate filled epoxy resins," in *Fractography and Failure Mechanisms of Polymers and Composites,* ed. Roulin-Moloney (Elsevier 1989), 233–290.

[80] Kinloch, A.J. and Williams, J.G., "Crack blunting mechanisms in polymers," *Journal of Materials Science,* **15** (1980), 987–996.

[81] Low, I.-T. and Mai, Y.-W., "Rate and temperature effects on crack blunting mechanisms in pure and modified epoxies," *Journal of Materials Science,* **24** (1989), 1634–1644.

[82] Williams, J.G., "Thermal crack tip blunting in high speed cracks," in *Advances in Fracture Research (ICF4),* **1**, eds. S.R. Valluri *et al.*, (Pergamon 1985), 731–749.

[83] Scott, J.M., Wells, G.M. and Phillips, D.C., "Low temperature crack propagation in an epoxide resin," *Journal of Materials Science,* **15** (1980), 1436–1448.

[84] Kobayashi, T. and Dally, J.W., "Relation between crack velocity and the stress intensity factor in birefringent polymers," in *Fast Fracture and Crack Arrest, ASTM STP 627,* eds. G.T. Hahn and M.F. Kanninen, (ASTM 1977), 257–273.

[85] Phillips, D.C. and Scott, J.M., "Determination of the K, v diagram of epoxide resins," *Journal of Materials Science Letters,* **9** (1974), 1202–1205.

[86] Stalder, B., Béguelin, Ph., Roulin-Moloney, A.C. and Kausch, H.H., "The graphite gauge and its application to the measurement of crack velocity," *Journal of Materials Science,* **24** (1989), 2262–2274.

[87] R. J. Young and P. W. R. Beaumont, "Failure of brittle polymers by slow crack growth," *Journal of Materials Science,* **10** (1975), 1343–1350.

[88] Cantwell, W.J., Roulin-Moloney, A.C. and Kausch, H.H., "Dynamic crack propagation in the double torsion test geometry," *Journal of Materials Science Letters,* **7** (1988), 976–980.

[89] Cantwell, W.J. and Roulin-Moloney, A.C., "Fast fracture in epoxy resins," *International Journal of Fracture,* **35** (1987), R31–R39.

[90] Döll, W., "Fractography and failure mechanisms of amorphous thermoplastics," in *Fractography and Failure Mechanisms of Polymers and Composites,* ed. Roulin-Moloney (Elsevier 1989), 387–436.

[91] Smekal, A., "Über den Anfangsverlauf der Bruchgeschwindigkeit im Zerreissversuch," *Glast. Ber.,* **23** (1950), 186–189.

[92] Kerkhof, F., "Investigation of the influence of water vapor on crack velocities in glass by ultrasonic fractography," in *Fracture 1969,* ed. Pratt *et al.* (Chapman Hall 1969), 463–473.

[93] Ritchie, R.O. and Bathe, K.J., "On the calibration of the electric potential technique for monitoring crack growth using finite element methods," *International Journal of Fracture,* **15**, (1) (1979), 47–55.

[94] Stalder, B., Béguelin, Ph. and Kausch, H.H., "A simple velocity gauge for measuring crack growth," *International Journal of Fracture,* **22** (1983), R47–R50.

[95] Béguelin, Ph., Stalder, B. and Kausch, H.H., "Application of a new velocity gauge to fracture at high crack velocities," *International Journal of Fracture,* **23** (1983), R7–R10.

[96] Cudré-Mauroux, N., Kausch, H.H., Cantwell, W.J., and Roulin-Moloney, A. C., "High-speed crack propagation in bi-phase materials: an experimental study," *International Journal of Fracture,* **50** (1991), 67–77.

[97] Hall, C., *Polymeric Materials,* (John Wiley 1981), 46.

[98] Timoshenko, S.P. and Goodier, J.N., *Theory of Elasticity,* (McGraw-Hill 1970), 409.

[99] McClintock, F.A. and Argon, A.S., *op. cit.*, 410.

[100] Brinson, H.F., "The viscoelastic-plastic behavior of a ductile polymer," in *Deformation and Fracture of High Polymers,* eds. H.H. Kausch *et al.* (Plenum Press 1972), 397–416.

[101] Galeski, A., Argon, A.S. and Cohen, R.E., "Changes in the morphology of bulk spherulitic Nylon 6 due to plastic deformation," *Macromolecules,* **21** (1988), 2731–2770.

[102] Timoshenko, S.P. and Goodier, J.N., *op. cit.*, 413.

[103] Ashby, M.F., Blunt, F.J. and Bannister, M., "Flow characteristics of highly constrained metal wires," *Acta Metallurgica,* **37**, (7) (1989), 1847–1857.

[104] Akisanya, A.R. and Fleck, N.A., "Fatigue and creep of a constrained metal wire," *Acta Metallurgica,* **41**, (1) (1993), 121–131.

[105] Broek, D., *op. cit.*, 105.

[106] Brown, H.R., "A model for brittle-ductile transitions in polymers," *Journal of Materials Science,* **17** (1982), 469–476.

[107] Williams, J.G., *Fracture Mechanics of Polymers,* (Ellis Horwood 1984), 173.

[108] Kinloch, A.J. and Young, R.J., *Fracture Behavior of Polymers,* (Elsevier 1988), 344.

[109] Murthy, N.S., "Metastable crystalline phases in Nylon 6," *Polymer Communications,* **32**, (10) (1991), 301–305.

[110] Takeda, Y., Keskkula, H. and Paul, D.R., "Toughening of phase-homogenized mixtures of Nylon-6 and poly(*m*-xylene adipamide) with a functionalized block copolymer," *Polymer,* **33**, (16) (1992), 3394–3407.

[111] Broutman, L.J. and Sahu, S., "The effect of interfacial bonding on the toughness of glass filled polymers," *Materials Science and Engineering,* **8** (1971), 98–107.

[112] Faber, K.T., Evans, A.G. and Drory, M.D., "A statistical analysis of crack deflection as a toughening mechanism," in *Fracture Mechanics of Ceramics, Vol. 6,* eds. R. C. Bradt *et al.* (Plenum Press 1983), 77–91.

[113] Kinloch, A.J., Maxwell, D.L. and Young, R.J., "The fracture of hybrid-particulate composites," *Journal of Materials Science,* **20** (1985), 4169–4184.

[114] Cantwell, W.J., Smith, J.W., Kausch, H.H. and Kaiser, T., "Examination of the process of deformation and fracture in a silica-filled epoxy resin," *Journal of Materials Science,* **25** (1990), 633–648.

[115] Spanoudakis, J. and Young, R.J., "Crack propagation in a glass particle-filled epoxy resin *(Part 2: Effect of particle-matrix adhesion)*," *Journal of Materials Science*, **19** (1984), 487–496.

[116] Amdoudi, N. *et al*, "Coated glass beads epoxy composites: influence of the interlayer thickness on pre-yielding and fracture properties," *Journal of Materials Science*, **25** (1990), 1435–1443.

[117] Moloney, A.C., Kausch, H.H. and Stieger, H.R., "The fracture of particulate-filled epoxide resins (Part 1)," *Journal of Materials Science*, **18** (1984), 208–216.

[118] Green, D.J., Nicholson, P.S. and Embury, J.D., "Fracture of a brittle particulate composite *(Part 1: Experimental aspects)*," *Journal of Materials Science*, **14** (1979), 1413–1420.

[119] Green, D.J., Nicholson, P.S. and Embury, J.D., "Crack shape studies in brittle porus materials," *Journal of Materials Science*, **12** (1977), 989–989.

[120] Hutchinson, J.W., "Crack tip shielding by microcracking in brittle solids," *Acta metallurgica*, **35**, (7) (1987), 1605–1619.

[121] Gent, A.N. and Lin, C.W., "Comparison of peel and lap sheer bond strengths for elastic joints with and without residual stresses," *Journal of Adhesion*, **30** (1989), 1-11.

[122] Bogy, D.B., "Two edge-bonded elastic wedges of different materials and wedge angles under surface tractions," *Journal of Applied Mechanics*, **June** (1971), 377–386.

[123] Kinloch, A.J., *Adhesion and Adhesives,* (Chapman and Hall 1987), 188.

[124] Anderson, G.P., DeVries, K.L. and Sharon, G., "Evaluation of Tensile Tests for Adhesive Bonds," in *Delamination and Debonding of Materials, ASTM STP 627*, ed. W.S. Johnson, (ASTM 1985), 115–134.

[125] Kinloch, A.J., *op.cit.,* 211.

[126] Anderson, G.P. and DeVries, K.L., "Predicting bond strengths," *Journal of Adhesion*, **23**, (4) (1987), 289–302.

[127] Kinloch, A.J., *op.cit.,* 214–235.

[128] *Idem, ibid,* 221.

[129] Renton, W.J. and Vinson, J.R., "The efficient design of adhesive bonded joints," *Journal of Adhesion*, **7**, (1975), 175–193.

[130] Kinloch, A.J., *op.cit.*, 231.

[131] *Idem, ibid,* 234.

[132] Anderson, G.P., DeVries, K.L. and Sharon, G., "Evaluation of Adhesive Test Methods," in *Organic Coatings and Applied Polymer Proceedings* **47** (American Chemical Society 1982), 462–466.

[133] Malyshev, B.M. and Salganik, R.L., "The strength of adhesive joints using the theory of cracks," *International Journal of Fracture Mechanics,* 1 (1965), 114–128.

[134] Williams, M.L., "The continuum interpretation for fracture and adhesion," *Journal of Applied Polymer Science,* **13** (1969), 29–40.

[135] Williams, M.L., "The relation of continuum mechanics to adhesive fracture," in *Recent Advances in Adhesion,* ed. L.-H. Lee, (Gordon and Breach 1971), 381–420.

[136] Hutchinson, J.W., "Mixed mode fracture mechanics of interfaces," in *Metal-Ceramic Interfaces,* eds. M. Rühle *et al.*, (Pergamon Press 1989), 295–306.

[137] Rice, J.R., "Elastic fracture mechanics concepts for interface cracks," *Journal of Applied Mechanics*, **55** (1988), 98–103.

[138] Suo, Z. and Hutchinson, J.W., "Sandwich test specimens for measuring interface crack toughness," *Materials Science and Engineering*, **A107** (1989), 135–143.

[139] Jensen, H.M., "Mixed mode interface fracture criteria," *Acta metallurgica et materialia*, **38**, (12) (1990), 2637–2644.

[140] Evans, A.G. and Hutchinson, J.W., "Effects of non-planarity of the mixed mode fracture resistance of bimaterial interfaces," *Acta metallurgica*, **37**, (3) (1989), 909–916.

[141] Cao, H.C. and Evans, A.G., "An experimental study of the fracture resistance of bimaterial interfaces," *Mechanics of Materials*, **7** (1989), 295–304.

[142] Charalambides, P.G., Lund, J. and Evans, A.G., and R. M. McMeeking, "A test specimen for determining the fracture resistance of bimaterial interfaces," *Journal of Applied Mechanics*, **56** (1989), 77–82.

[143] Wang, J.-S., and Suo, Z., "Experimental determination of interfacial toughness curves using Brazil-nut-specimens," *Acta metallurgica et materialia*, **38**, (7) (1990), 1279–1290.

[144] He, M.Y., Cao, H.C. and Evans, A.G., "Mixed-mode fracture: the four-point shear specimen," *Acta metallurgica et materialia*, **38**, (5) (1990), 839–846.

[145] Argon, A.S., Gupta, V., Landis, H.S. and Cornie, J.A., "Intrinsic toughness of interfaces between SiC coatings and substrates of SiC or C fibre," *Journal of Materials Science*, **24** (1989), 1207–1218.

[146] Hull, D., *An Introduction to Composite Materials*, (Cambridge 1988), 48.

[147] Chamis, C.C., "Mechanics of load transfer at the interface," in *Composite Materials, Vol. 2: Interfaces in Polymer Matrix Composites* eds. L.J. Broutman and R.H. Krock, (Academic Press 1974), 31–77.

[148] Koenig, J.L. and Emadipour, H., "Mechanical characterization of the interfacial strength of glass-reinforced composites," *Polymer Composites*, **6**, (3) (1985), 142–150.

[149] Piggot, M.R., "Fiber-matrix interactions," *Polymer Composites*, **3**, (4) (1982), 179–188.

[150] Drzal, L.T. and Madhukar, M., "Fiber-matrix adhesion and its relationship to composite mechanical properties," *Journal of Materials Science*, **28** (1993), 569–610.

[151] Wu, H.F. and Claypool, C.M., "An analytical approach to the microbond test method used in characterizing the fiber-matrix interface," *Journal of Materials Science Letters*, **10**, (1991), 269–262.

[152] Atkinson, C., Avila, J., Betz, E. and Smelser, R.E., "The rod pull out problem: theory and experiment," *Journal of the Mechanics and Physics of Solids*, **30**, (3) (1982), 97–120.

[153] Leung, C.K.Y. and Li, V.C., "New strength-based model for the debonding of discontinuous fibers in an elastic matrix," *Journal of Materials Science*, **26** (1991), 5996–6010.

[154] Broutman, L.J., "Measurement of the fibre-polymer interfacial strength," in *Interfaces in Composites, ASTM STP 452*, (ASTM 1969), 27.

[155] Ikuta, N. *et al.*, "Evaluation of interfacial properties in glass fiber-epoxy resin composites - reconsideration of an embedded single filament shear-strength test," *Journal of Materials Science*, **26** (1991), 4663–4666.

[156] Kenyon, A.S., "Role of the interface in glass-epoxy composites," *Journal of Colloid and Interface Science*, **27**, (4) (1968), 761–771.

[157] Leidner, J. and Woodhams, R.T., "The strength of polymeric composites containing spherical fillers," *Journal of Applied Polymer Science,* **18** (1974), 1639–1654.

[158] J. D. Miller, H. Ishida and F. H. Maurer, "Interfacial role and properties in model composites: fracture surfaces by scanning electron microscopy," *Journal of Materials Science,* **24** (1989), 2555–2570.

[159] M. E. J. Dekkers and D. Heikens, "The effect of interfacial adhesion on the mechanism for craze formation in polystyrene-glass bead composites," *Journal of Materials Science,* **18** (1983), 3281–3287.

[160] G. F. Abate and D. Heikens, "Polymer-filler interaction in polystyrene filled with coated glass spheres: 1. Interfacial adhesion control," *Polymer Communications,* **24** (1983), 137–140.

[161] Farris, R.J., "Dilatation of granular filled elastomers under high rates of strain," *Journal of Applied Polymer Science,* **8** (1964), 25–35.

[162] Smith, J.C., Kermish, G.A. and Fenstermaker, C.A., "Separation of filler particles from the matrix in a particulate-loaded composite subjected to tensile stress," *Journal of Adhesion,* **4** (1972), 109–123.

[163] Sinien, L., Lin, Y., Xiaoguang, Z. and Zongneng, Q., "Microdamage and interfacial adhesion in glass bead-filled high-density polyethylene," *Journal of Materials Science,* **27** (1992), 4633–4638.

[164] van Hartingsveldt, E.A.A. and van Aartsen, J.J., "Interfacial debonding in polyamide-6/glass bead composites," *Polymer,* **30** (1989), 1984–1991.

[165] van Hartingsveldt, E.A.A. and van Aartsen, J.J., "Strain-rate dependence of interfacial adhesion in particle-reinforced polymers," *Polymer,* **32**, (8) (1991), 1482–1487.

[166] Gupta, V., Argon, A.S. and Cornie, J.A., "Interfaces with controlled toughness as mechanical fuses to isolate fibres from damage," *Journal of Materials Science,* **24** (1989), 2031–2040.

[167] Allen, M.G. and Senturia, S.D., "Analysis of critical debonding pressures of stressed thin films in the blister test," *Journal of Adhesion,* **25** (1988), 303–315.

[168] Nutt, G.L., Lai, W., Froeschner, K.E. and King, W.E., "Direct measurement of interface bond strengths," in *Metal-Ceramic Interfaces,* eds. M. Rühle *et al.*, (Pergamon Press 1989), 307–312.

[169] Gupta, V., Argon, A.S., Parks, D.M. and Cornie, J.A., "Measurement of interface strength by a laser spallation technique," *Journal of the Mechanics and Physics of Solids,* **40** (1992), 141–180.

[170] Argon, A.S. and Im, J., "Separation of second phase particles in spheroidized 1045 steel, Cu-0.6Pct Cr alloy, and maraging steel in plastic straining," *Metallurgical Transactions A,* **6** (1975), 839–851.

[171] Argon, A.S., Im, J. and Safoglu, R., "Cavity formation from inclusions in ductile fracture," *Metallurgical Transactions A,* **6** (1975), 825–837.

[172] Argon, A.S., Im, J. and Needleman, A., "Distribution of plastic strain and negative pressure in necked steel and copper bars," *Metallurgical Transactions A,* **6** (1975), 815–824.

[173] Bridgman, P.W., *Studies in Large Plastic Flow and Fracture,* (McGraw-Hill 1952).

[174] Needleman, A., "A numerical study of necking in circular cylindrical bars," *Journal of the Mechanics and Physics of Solids,* **20**, (1972), 11–127.

[175] Im, J., "Inclusion separation in plastic deformation," *S.M. Thesis* (M.I.T. Dept. of Mech. Eng. 1971).

[176] Neuber, H. *Theory of Notch Stresses,* (Edwards 1946), 84–89.

[177] Williams, J.G., *Stress Analysis of Polymers,* (Ellis Horwood 1980), 323.

[178] ANSYS©, *Rev. 4.4A,* (Swanson Analysis Systems, Houston PA 1990).

[179] Wronski, A.S. and Pick, M., "Pyramidal yield criterion for epoxies," *Journal of Materials Science,* **12** (1977), 28–34.

[180] Yu, X.D., Malinconico, M. and Martuscelli, E., "Highly filled particulate composites enhancement of performances by using compound coupling agents," *Journal of Materials Science,* **25** (1990), 3255–3261.

[181] Han, C.D., Sandford, C. and Yoo, H.J., "Effects of titanate coupling agents on the rheological and mechanical properties of filled polyolefins," *Polymer Engineering and Science,* **18**, (11) (1978), 849–854.

[182] Kaas, R.L. and Kardos, J.L., "The interaction of alkoxy silane coupling agents with silica surfaces," *Polymer Engineering and Science,* **11**, (1) (1971), 11–18.

[183] Kinloch, A.J., "Review: The science of adhesion," *Journal of Materials Science,* **15** (1980), 2141–2166.

[184] Shields, J., "Surface pretreatment of plastics for adhesive bonding," *Sira Institute Report,* **R500** (Kent, England 1972).

[185] Kinloch, A.J., *Adhesion and Adhesives,* (Chapman and Hall 1987), 101.

[186] Abu-Isa, I.A., "Iodine treatment of Nylon: Effect on metal plating of the polymer," *Journal of Applied Polymer Science,* **15** (1971), 2865–2876.

[187] Evans, J.R.G and Packham, D.E., "Adhesion of polyethylene to copper: importance of substrate topology," *Journal of Adhesion,* **10** (1979), 39–47.

[188] Evans, J.R.G and Packham, D.E., "Adhesion of polyethylene to metals: the role of substrate topology," *Journal of Adhesion,* **10** (1979), 177-191.

[189] He, M.-Y. and Hutchinson, J.W., "Kinking of a crack out of an interface," *Journal of Applied Mechanics,* **56** (1989), 270–278.

[190] Xu, G. and Ortiz, M., "A variational boundary integral method for the analysis of 3D cracks of arbitrary geometry modeled as continuous distributions of dislocation loops," *International Journal of Numerical Methods in Engineering, in press.*

[191] Huang, Y. and Kinloch, A.J., "Modelling of the toughening mechanisms in rubber-modified epoxy polymers: I," *Journal of Materials Science,* **27** (1992), 2753–2762.

[192] Selsing, J., "Internal stresses in ceramics," *Journal of The American Ceramic Society,* **44** (1961), 419.

[193] Shetty, D.K., "Shear-lag analysis of fiber push-out (indentation) tests for estimating interfacial friction stress in ceramic-matrix composites," *Communications of the American Ceramic Society,* **71**, (2) (1988), C107–C109.

[194] Clarke, D.R. and Chiao, Y-H., "Residual stress induced fracture in glass-sapphire composites: cylindrical geometry," *Acta Metallurgica & Materialla,* **38**, (2) (1990), 259–267.

[195] Lu, T.C. *et al.*, "Matrix cracking in intermetallic composites caused by thermal expansion mismatch," *Acta Metallurgica & Materialla,* **39**, (8) (1991), 1883–1890.

[196] Frocht, M.M., *Photoelasticity,* **1 & 2**, (Wiley 1941 & 1948).

[197] Durelli, A.J. and Riley, W.F., *Introduction to Photomechanics,* (Prentice-Hall 1965).

[198] *Idem, ibid,* 73.

[199] *Idem, ibid,* 114.

[200] Levin, M.M., "Epoxy resins for photoelastic use," in *Photoelasticity*, ed. M. M. Frocht (MacMillan 1963), 145–184.

[201] Frocht, M.M. and Cheng, Y.F., "An experimental study of the laws of double refraction in the plastic state in cellulose-nitrate–foundations for three-dimensional plasticity," in *Photoelasticity*, ed. M. M. Frocht (MacMillan 1963), 195–216.

[202] Paipetis, S.A., "Conventional three-dimensional photoelasticity: A review of principles and materials," in *Photoelasticity in Engineering Practice,* eds. S. A. Paipetis and G. S. Holister (Elsevier 1985), 205–224.

[203] Hendry, A.W., "Chapter 3; Stressed transparent materials in the polariscope," in *Photoelastic Analysis* (Pergamon 1966), 39–50.

[204] Frocht, M.M., "§5.10: The Experimental Basis of the Stress-Optic Law," in *Photoelasticity* **1** (Wiley 1941), 144–149.

[205] Timoshenko, S.P. and Goodier, J.N., *op. cit.,* 123.

[206] Theocaris, P.S., "Time dependence of creep recovery in cross-linked polymers," *Rheologica Acta,* **6**,, (2) (1967), 246–251.

[207] Andrews, R.D. and Hammack, T.J., "Temperature dependence of orientation birefringence of polymers in the glassy and rubber states," *Journal of Polymer Science, C* **5** (1964), 101–112.

[208] Tougui, A., Gamby, D., Lagarde, A. and Brinson, H.F., "Nonlinear photoviscoelasticity: theory and measurement," *Experimental Mechanics* **23**, (3) (1983), 314–321.